APPLICATION OF OPTICAL DIFFRACTION RADIATION TO A NON-INVASIVE LOW-EMITTANCE HIGH-BRIGHTNESS BEAM DIAGNOSTICS

P. KARATAEV*, R. HAMATSU AND T. MUTO
Tokyo Metropolitan University, 1-1 Minamiohsawa, Hachioji, Tokyo 192-0937, Japan

S. ARAKI, H. HAYANO AND J. URAKAWA
KEK: High Energy Accelerator Research Organization, Oho 1-1, Tsukuba 305-0801, Ibaraki-ken, Japan

G. NAUMENKO AND A. POTYLITSYN
Tomsk Polytechnic University, 634050, pr. Lenina 2a, Tomsk, Russia

T. HIROSE
Advanced Research Institute for Science and Engineering, Waseda University, 1-104 Totsukamachi, Shinjuku-ku, Tokyo, 169-8050, Japan

A simple approach for the beam size mesurements with optical diffraction radiation from a slit target is presented. The estimations show that it is possible to measure the beam size with a resolution of about ~1μm. We developed a new approach for calculating diffraction radiation characteristics from a rectangular finite size target with a rectangular opening in it to be able to estimate the influence of the coherent diffraction radiation recoil.

1. Introduction

A high brightness low emittance high-energy beam opens doors in many new fields of the beam physics. For that purpose linear colliders with the energy from a few hundreds of GeV to the TeV energy range and short wavelength free electron lasers have been intensively studied all over the world. To realize such beams a detailed monitoring of different beam parameters is undoubtedly necessary.

Modern accelerators preclude the use of any invasive techniques like transition radiation monitors [1-3] because the electron scattering may lead to significant worsening of the beam parameters.

Optical Diffraction Radiation (ODR) appearing when a charged particle moves in the vicinity of a medium and interacts with the target through its electric field only

* The author to whom the correspondence should be addressed: P. Karataev
Postal address: KEK, Oho 1-1, Tsukuba, Ibaraki-ken, Japan; e-mail: kar_pav@yahoo.com

could be a very precise and useful technique for non-invasive beam diagnostics; however, the effect is not studied experimentally very well.

The first theoretical considerations of DR have appeared about 40 years ago [4-5]. Recent papers considered DR properties and their implementation to beam diagnostics [6-8] in details. The first observation of coherent DR (CDR) (the wavelength is comparable or longer than the longitudinal beam size) in millimeter and sub-millimeter wavelength region has been performed in 1995 [9]. In [10-11] the authors presented the backward CDR investigation and evaluation of the longitudinal beam size using autocorrelation technique.

The first observation of incoherent DR in optical wavelength range from the target edge has been performed by us at the extracted beam of the KEK-Accelerator Test Facility (ATF) [12]. The obtained results are in good agreement with the theoretical predictions based on the model of ideally conducting infinitely thin target. Here we represent a new technique for beam size measurements with ODR. Our estimations show that the resolution of about ~1μm is achievable.

However, for ultrarelativistic particles DR wavelength range is very broad. Due to the coherent effects the beam characteristics could also worsen. Therefore, it is extremely necessary to estimate the distortion of the beam parameters caused by the emission of the DR at the target. In [13] the author considered the transverse kick caused by a tapered collimator, which is usually used in circular and linear colliders to eliminate halo particles from the beam. A similar kick might be caused by a tilted slit target, which we plan to use for beam size measurements at KEK-ATF [14].

2. Beam size effect in optical diffraction radiation.

An approach of the pseudophoton scattering (describing an electric field of the moving charge) by target surface is frequently used to describe the DR and TR phenomena [5-6,11]. The horizontal (x) and vertical (y) polarization components of the DR electric field from an ultarelativistic particle moving close to an ideally reflecting infinitely thin flat target or through a hole of an arbitrary shape in it could be represented in the following general form [5-6]:

$$E_{x,y}(k_x,k_y)=\frac{-ie}{8\pi^4}\int dxdy\int dk'_x dk'_y\left\{\frac{k'_{x,y}e^{i\left(k'_x-\bar{k}_x\right)x+i\left(k'_y-k_y\right)y}}{k'^2_x+k'^2_y+\left(k/\gamma\right)^2}\right\} \qquad (1)$$

Here $\bar{k}_x \equiv k_x - [k/2\gamma^2]\cot(\theta_0)$ [10]. It means that the radiation pattern from a tilted target is shifted by the angle $\gamma^{-2}/2$. For an ultrarelativistic case ($\gamma \sim 10^3$) and large target tilt angles ($\theta_0 = 45$deg.) this shift is negligible and we shall omit it in the future. In Eq. (1) e is the particle charge; $k = 2\pi / \lambda$ is the wave number; γ is the charged particle

Lorentz-factor; $k^{|}_x$ and $k^{|}_y$ are the components of the pseudophoton wave vector; $k_x = k \sin\theta \cos\varphi \approx k\theta_x$ and $k_y = k \sin\theta \sin\varphi \approx k\theta_y$ are the components of the real DR photon wave vector. The spectral angular distribution could be obtained as follows:

$$\frac{d^2W}{d\omega d\Omega} = 4\pi^2 k^2 \left[\left| E_x(k_x, k_y) \right|^2 + \left| E_y(k_x, k_y) \right|^2 \right] \quad (2)$$

Here θ and φ are the polar and azimuthal observation angles, θ_x and θ_y are observation angles measured from the specular reflection direction from the target. Throughout the paper the system of units $\hbar = m_e = c = 1$ is used.

In Eq. (1) the x and y integrals are over the target surface. It is possible to calculate DR from an arbitrarily shaped target numerically. However, usually, theoreticians try to obtain simple solutions for particular cases.

The solution of Eq. (1) for a case when an electron moves through a slit between two tilted semi-infinite planes has been represented in [5-6]. Afterwards, the author of [7] has shown that vertical polarization component is sensitive to the beam size. The expression for the ODR vertical polarization component convoluted with gaussian distribution could be written as:

$$\frac{d^2W_y}{d\omega d\Omega} = \frac{\alpha}{4\pi^2} \frac{\exp\left(-\frac{2\pi a \sin\theta_0}{\lambda} \sqrt{\gamma^{-2} + \theta_x^2} \right)}{\left(\gamma^{-2} + \theta_x^2 + \theta_y^2 \right)} \left[\exp\left(\frac{8\pi^2\sigma^2}{\lambda^2} \left(\gamma^{-2} + \theta_x^2 \right) \right) - \cos\left(\frac{2\pi a \sin\theta_0}{\lambda} \theta_y + 2\psi \right) \right] \quad (3)$$

Here $\psi = \mathrm{arctg}[\theta_y/(\gamma^{-2} + \theta^2_x)^{0.5}]$, a is the slit size, σ is the rms beam size, α is the fine structure constant.

Two-dimensional angular pattern of the vertical polarization component is represented in Figure 1a. In [7] the author proposed to use the minimum-to-maximum ratio of the differential intensity as a parameter for beam size determination (see Figure 1c). However, this method requires a very small angular acceptance. Otherwise, the resolution of the method could be very poor. But the detector sensitivity may not be enough to precisely measure the ODR pattern. In this paper we propose a new method to measure the beam size. From Eq. (3) it is apparent that if the beam size is zero, the photon yield between two peaks (Figure 1a) is zero. However, for a non-zero beam size, the intensity between two peaks is not zero already. It means that all those photons are useful. It is possible to collect them all (integrate over θ_x) and increase the detector sensitivity. We call it as the method of the *projected vertical polarization component* (PVPC). Figure 1b illustrates the PVPC calculated for two beam sizes. Obviously the angular pattern depends on the beam size. As a sensitivity criterion we have chosen the minimum-to-maximum ratio. Figure 1c shows the comparison

between the differential ODR minimum-to-maximum ratio and the PVPC one calculated for the same parameters. One can see that the PVPC is better sensitive to the beam size.

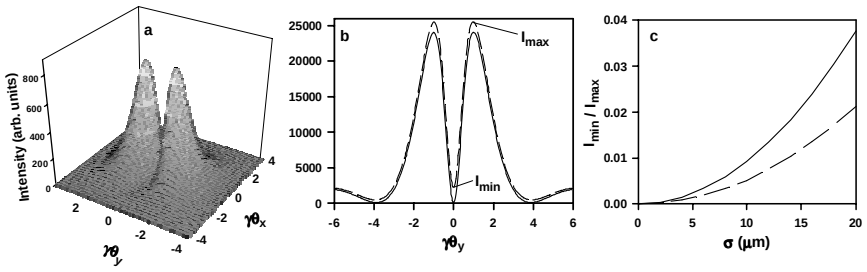

Figure 1. a) Two-dimensional vertical polarization pattern calculated for $\gamma = 2500$, $\lambda = 500$nm, a $\sin\theta_0 = 0.2$mm, $\theta_0 = 45$deg.; b) PVPC calculated for: $\sigma = 0$ – solid line, $\sigma = 30\mu$m – dashed line; c) minimum-to-maximum ratio for PVPC – solid line and differential ODR– dashed line.

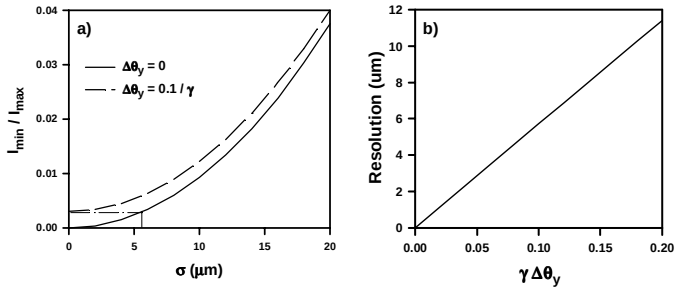

Figure 2. a) Dependences of the minimum-to-maximum ratio for different angular acceptances; b) Dependence of the estimated resolution for beam size measurements with PVPC as a function of the detector angular acceptance

A large detector angular acceptance may significantly distort the angular pattern. Figure 2a represents the minimum-to-maximum ratio of the PVPC versus the beam size calculated for zero and non-zero angular acceptances. One may see that when $\Delta\theta_y \neq 0$, the ratio is not saturated to zero at zero beam size. As a result in the range shown in the picture with dashed-dotted line the beam size effect is very small and the angular pattern almost remains unchanged. This range could be considered as the resolution for the beam size measurement (the smallest beam size, which is possible to measure). The resolution could be improved by reducing the angular acceptance, however the number of photons in that case will be reduced too. Figure 2b shows the dependence of the estimated resolution versus the detector angular acceptance. In the range of

acceptances we have chosen this dependence is linear. From the picture one can see that the resolution of ~1μ is achievable at $\Delta\theta_y = 0.02 / \gamma$.

We should notice here that the real experimental situation is a lot more complicated. The resolution could worsen by the target deformation, contamination of any background sources like synchrotron radiation from the accelerator magnets (since it is polarized two, the contamination could be reduced cutting off one of the polarization components with a polarized) or X-ray background (could be reduced with lead shielding), accuracy of the measurements system, etc. That is why the experimental verification is required.

3. Applicability of DR to non-invasive electron beam diagnostics

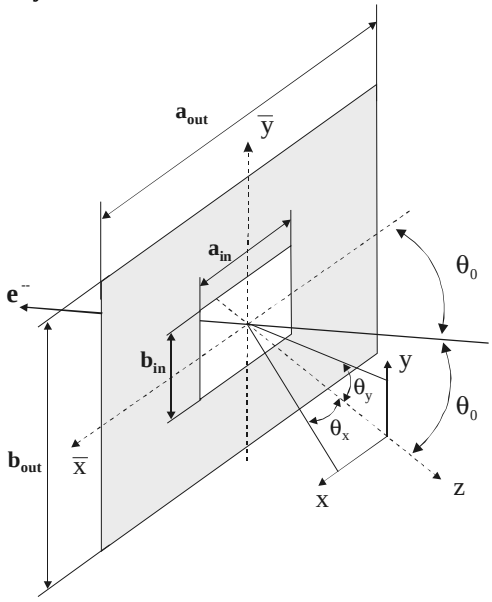

Figure 3. DR geometry from a particle moving through a rectangular opening in a rectangular screen. z axis is directed along the specular reflection.

There are a lot of theoretical papers representing both different approaches for beam size measurements and estimations for real accelerator installations. However, there are no any considerations on the beam characteristics perturbation caused by coherent DR (CDR) from the target. The DR as well as TR spectral range is very broad. For example, during last several years coherent DR in millimeter and sub-millimeter wavelength range has intensively been studied as a possible tool for longitudinal bunch shape measurements [10-11]. Due to the similar coherent effects the electron beam characteristics could worsen.

In our calculations presented above we assumed that the target was infinite. This approximation is usually valid for short wavelengths when the outer target dimensions are much larger than the DR formation zone ($\gamma\lambda / 2\pi$). In reality the target is finite. Therefore, the first step to estimate the transverse kick is to obtain the expression for TR from a target of finite dimensions. Integrating the Eq. (1) over x from $-a_{out}\sin(\theta_0)/2$ to $a_{out}\sin(\theta_0)/2$ and over y from $-b_{out}/2$ to $b_{out}/2$, where a_{out} and b_{out} are horizontal and vertical target dimensions (see Fig. 3), the vertical polarization component of the DR field for a single electron can be represented as:

$$E_y(\theta_x,\theta_y,a_{out},b_{out}) = \frac{ie}{2\pi^3 k}\int_{-\infty}^{\infty} dt \frac{\sin\left[\frac{ka_{out}\sin(\theta_0)}{2}(t-\theta_x)\right]}{(t-\theta_x)(t^2+\theta_x^2+\gamma^{-2})} \times\left\{\theta_y - \exp\left[-\frac{kb_{out}}{2}\sqrt{t^2+\gamma^{-2}}\right]\left[\sqrt{t^2+\gamma^{-2}}\sin\left(\frac{kb_{out}\theta_y}{2}\right)+\theta_y\cos\left(\frac{kb_{out}\theta_y}{2}\right)\right]\right\} \quad (4)$$

In spite of an infinite integration limits the dominant part of the integral is confined within the range of $\Delta t<<1$. The horizontal polarization component (E_x) could be obtained either directly from Eq. (1) or simply exchanging $\theta_x \longleftrightarrow \theta_y$ and $a_{out}\sin(\theta_0)\longleftrightarrow b$ in Eq. (4). By proper integration one may derive an expression for DR field from a particle moving through a rectangular opening in a rectangular screen. The expression could be introduced using the Eq. (4):

$$E_{op(x,y)}(\theta_x,\theta_y,a_{in},a_{out},b_{in},b_{out}) = E_{(x,y)}(\theta_x,\theta_y,a_{out},b_{out}) - E_{(x,y)}(\theta_x,\theta_y,a_{in},b_{in}) \quad (5)$$

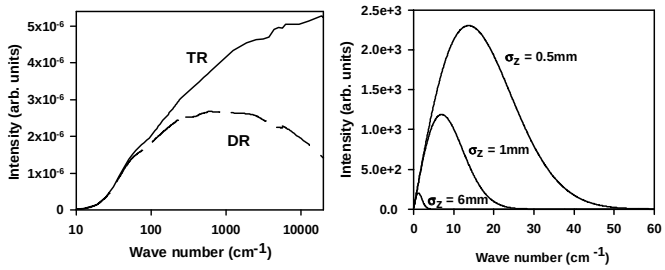

Figure 4. a) TR and DR spectra for a single electron crossing a rectangular target calculated for γ = 2500, 0.2rad angular acceptance, opening dimensions are 5×0.26mm and outer target dimensions are 7×9mm; b) Coherent DR spectra for 10^{10} electrons

Here a_{in} and b_{in} are the horizontal and vertical sizes of the rectangular opening respectively (see Fig. 3). One may notice that Eq. (5) introduces the well-known

Babinet's principle from classical optics.

Figure 4a represents the TR and DR spectra. One may see that in contrast to TR, which is saturated while the wave number increases, DR spectrum decreases exponentially as expected. However, in the soft part both TR and DR intensity is suppressed due to the finite target size.

Table I. Estimated transverse kick.

σ_z	6mm	1mm	0.5mm
Tr. kick	0.028μrad	0.973μrad	3.742μrad

The coherent radiation spectrum per electron could be obtained by multiplying the single electron spectrum by the number electrons N_e and the bunch form factor F, which is usually introduced as the Fourier transform of the longitudinal electron distribution in the bunch [10-11]. The coherent DR spectra for different bunch lengths σ_z are shown in Figure 4b. Integrating over the spectra one may obtain the mean energy E_R emitted by each electron in the bunch in the perpendicular direction as the target is assumed to be inclined with 45 deg. to the beam trajectory. As a result each electron obtains a mean transverse momentum $\Delta P_\perp = E_R/c$. Knowing the transverse and longitudinal momenta one may estimate the transverse kick (see Table I). One may see that for shorter bunches the transverse kick may become significant and exceed the electron angular divergence. Therefore, the beam emittance could be worsen. On the other hand, increasing the outer target dimensions the energy losses due to CDR effect increase, and, as a result, the transverse kick becomes bigger too.

4. Conclusion

In this paper we have presented a new method for the beam size measurements with ODR. We have shown that if all technical and experimental difficulties are solved, it is possible to achieve resolution of about 1μm.

To estimate the coherent radiation recoil we developed a new model for calculating DR characteristics from a particle moving through a rectangular opening in a tilted finite size rectangular screen. The estimations show that for KEK-ATF beam parameters (design bunch length ~6mm and population $\sim 10^{10}$) and the target configuration, which was chosen for the experiment [14], the influence onto the beam parameters is negligible. However, this effect must be taken into account when DR is used for short electron bunch diagnostics. Moreover, for higher energy accelerators ($\gamma > 10^4$), when the DR formation zone is very big, optimization of the target size is required.

It may be noted that the effect of the finite size target leads to essential distortion of the coherent DR spectra and must be taken into account when measurement of the

bunch length is carried out using this technique [9-11].

References

1. J.-I. Choi, H.S. Kang, S.H. Nam, S.S. Chang, in *Proceedings of the 1999 Part. Accel. Conf.*, 1999, edited by A. Luccio and M. Mackay, (IEEE Operations Center, HJ, 1999), p. 2205.
2. D.W.Rule, R.B. Fiorito, W.D.Kimura, in *7th Beam Instrumentation Workshop*, 1996, edited by A. Lumpkin and C. Eyberger, AIP Conf. Proceedings No. **390** (AIP, NY, 1997), p. 510.
3. J.B.Rosenzweig, A.Murokh, and A.Tremaine, in *8th Advanced Accelerator Concepts Workshop*, 1998, edited by W. Lawson, et al., AIP Conf. Proceedings No. **472** (AIP, NY, 1999), p. 38.
4. A. Kazantsev and G. Surdutovich, Soviet Physics - Doklady **7**, p. 990 (1963).
5. M.L. Ter-Mikayelyan, *High Energy Electromagnetic Processes in Condenced Media* (Willey-Interscience, New-York, 1972).
6. R.B. Fiorito and D.W. Rule, Nuclear Instruments and Methods **B173**, p. 67 (2001).
7. M. Castellano, Nuclear Instruments & Methods **A394,** p. 275 (1997).
8. A. Potylitsyn, Nuclear Instruments and Methods **B201**, p. 161 (2003).
9. Y. Shibata, S. Hasebe, K. Ishi, et al., Phys. Rev. **E52,** p. 6787 (1995).
10. A.H.Lumpkin, N.S.Sereno, G.A.Decker, D.W.Rule, in *8th Beam Instrumentation Workshop*, 2000, edited by K. Jacobs and R. Sibley, AIP Conf. Proceedings No. **546** (AIP, NY, 2000), p. 484.
11. M. Castellano, V.A. Verzilov, L. Catani, et al., Phys. Rev. **E63,** p. 056501 (2001).
12. T. Muto, S. Araki, R. Hamatsu, et al., "Observation of incoherent diffraction radiation from a single edge target in the visible light region", Phys. Rev. Letters, **90** (10), pp. 104801, (2003).
13. G.V. Stupakov, Particle Accelerators, 1996, Vol. **56**, p. 83.
14. J. Urakawa, H. Hayano, et al., Nuclear Instruments & Methods **A472**, p. 309 (2001).

GENERATION OF HIGH QUALITY ELECTRON BEAM BY LASER-PLASMA INTERACTION

H. KOTAKI, S. MASUDA, M. KANDO, S. KONDO,
S. KANAZAWA, AND T. HOMMA

Japan Atomic Energy Research Institute, Kizu, Kyoto, Japan
E-mail: kotaki@apr.jaeri.go.jp

K. NAKAJIMA

Japan Atomic Energy Research Institute, Kizu, Kyoto, Japan
and High Energy Accelerator Research Organization, Tsukuba, Ibaraki, Japan
and The Graduate University for Advanced Studies, Hayama, Kanagawa, Japan

We investigate generation of electron beams injected by interaction of two laser pulses. Colliding laser pulses produce a standing wave that injects electrons in plasma into a wakefield excited by a high peak power laser. We make a numerical simulation of the optical injection assuming a plasma density distribution. We find that a high quality intense relativistic electron beam is generated.

1. Introduction

Recently laser-driven plasma accelerators using laser wakefields have been conceived to be the next-generation particle accelerators, promising ultrahigh field particle acceleration and compact size compared with conventional accelerators [1]. The laser wakefield acceleration has been experimentally demonstrated and has great potential to produce ultrahigh field gradients of the order of $\sim$ 100 GeV/m [2−12]. The maximum energy gain has exceeded 100 MeV with an energy spread of $\sim$ 100% due to dephasing and wave-breaking effects in the self-modulated laser wakefield acceleration regime, where thermal plasma electrons are accelerated [8]. The highest energy gain acceleration which exceeded 200 MeV was observed with the injection of an electron beam at an energy matched to the wakefield phase velocity in a fairly underdense plasma [9−12].

Hence, from the point of view of applications for particle accelerators, it is crucial that an ultrashort particle bunch with an energy higher than the trapping threshold should be injected with respect to the correct accel-

eration phase of the wakefield to produce a high quality beam with small momentum spread and good pulse-to-pulse energy stability. The trapped phase space of the wakefield accelerations are typically less than 100 fs temporally and 10 μm spatially, respectively.

Therefore it is essential to inject a very short pulse and a low emittance electron beam into the wakefield. Electron beam injection triggered by an intense ultrashort laser is proposed to an injector of ultrashort electron beams as "optical injection". Presently there are three major schemes: nonlinear wave-breaking injection [13], transverse optical injection [14], and colliding pulse optical injection [15,16]. No proof-of-principle experiment for these schemes has been yet performed because of experimental difficulties. Nonlinear wave-breaking injection uses one pump laser pulse. Transverse optical injection uses two laser pulses; one pump pulse and one injection pulse. The two pulses cross at a focal point. Three laser pulses consisting of a pump pulse for wakefield excitation and two injection pulses for trapping the electrons in plasma make up a colliding optical injector.

In this paper, we present a new optical injection scheme that utilizes two counter-propagating laser pulses.

2. Optical injection of two laser pulses

A plasma electron density oscillation $\delta n_e/n_e$ and an longitudinal electric field eE_z on the center axis of laser pulse propagation are written [1,2]

$$\frac{\delta n_e}{n_e} = \frac{\sqrt{\pi} k_p \sigma_z a^2}{2} \left[1 + \frac{4}{k_p^2 \sigma_r^2}\right] \times \exp\left(-\frac{k_p^2 \sigma_z^2}{4}\right) \sin(k_p \zeta), \tag{1}$$

$$eE_z = \frac{\sqrt{\pi} m_e c^2 k_p^2 \sigma_z a^2}{2} \times \exp\left(-\frac{k_p^2 \sigma_z^2}{4}\right) \cos(k_p \zeta), \tag{2}$$

where c is the speed of light, m_e is the rest mass of the electron, a is the laser strength parameter, $k_p = \omega_p/c$ is the wave number of the plasma, $\omega_p = (4\pi n_e e^2/m_e)^{1/2}$ is the electron plasma frequency, σ_z is the rms-width of the laser pulse in the longitudinal direction, σ_r is the rms-width of the laser pulse in the radial direction, and $\zeta = z - v_p t$ is the longitudinal coordinate in the speed-of-light-frame.

Consider interaction of two laser pulses, a schematic of the interaction is shown in Fig. 1. In this figure, a_0 and a_1 are laser strength parameters of pulse 0 and pulse 1, respectively. When $a_0 > a_1$, wave 0 is dominant

rather than wave 1 in the electron oscillation and the electric field for acceleration. Colliding laser pulses generate a standing wave. The wave injects electrons in plasma into a wakefield excited by the pulse 0. The electrons are accelerated by the wakefield and become a relativistic electron beam.

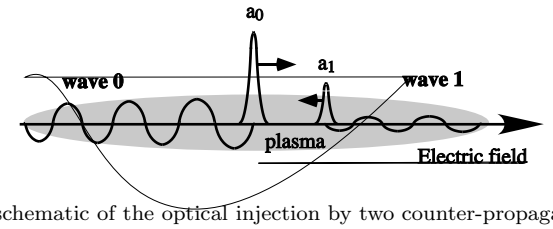

Figure 1. A schematic of the optical injection by two counter-propagate laser pulses.

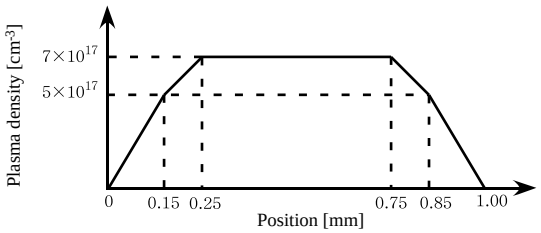

Figure 2. Plasma density distribution used for simulation of the optical injection.

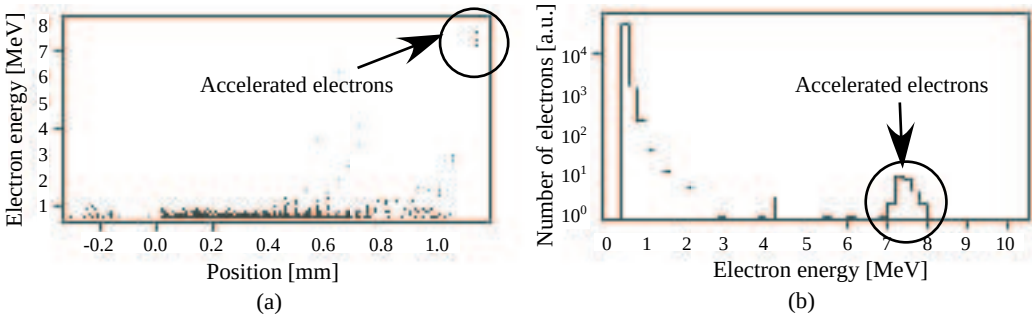

Figure 3. (a) Longitudinal phase space and (b) the energy spectrum of the colliding plasma wave optical injection simulation for $a_0 = 1.0$ and $a_1 = 0.3$ at $n_e = 7{\times}10^{17}$ cm^{-3}.

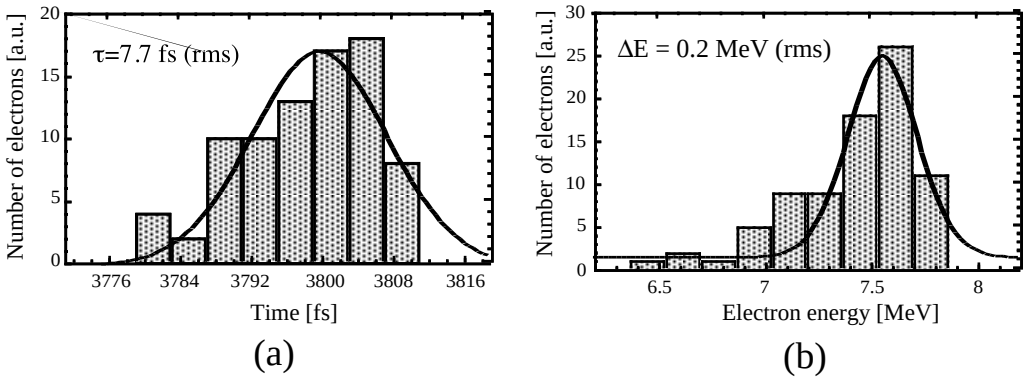

Figure 4. (a) The pulse shape and (b) the energy spectrum of the accelerated electrons for $a_0 = 1.0$ and $a_1 = 0.3$ at $n_e = 7 \times 10^{17}$ cm^{-3}.

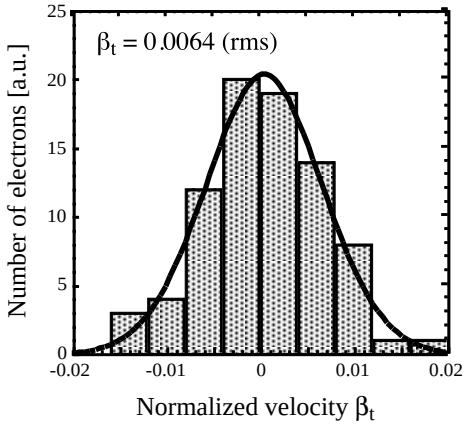

Figure 5. The distribution of the transverse normalized velocity β_t of the accelerated electrons for $a_0 = 1.0$ and $a_1 = 0.3$ at $n_e = 7 \times 10^{17}$ cm^{-3}.

We make a numerical simulation of the optical injection scheme for the plasma density distribution shown in Fig. 2 using a Particle-in-Cell (PIC) code [17]. The plasma density distribution was measured by a Mach-Zehnder interferometer [18]. The electron distribution in a phase space and the energy spectrum for $a_0 = 1.0$ and $a_1 = 0.3$ at $n_e = 7 \times 10^{17}$ cm^{-3} are shown in Figs. 3(a) and (b), respectively. A part of electrons in plasma is trapped

and accelerated in the wakefield excited by the pump pulse. The pulse shape and the energy spectrum of the accelerated electron beam are shown in Figs. 4(a) and (b), respectively. The electron beam has the pulse width of 7.7 fs (rms), the peak energy of 7.5 MeV with the energy spread of 3% (rms) from these figures. The accelerated energy is consistent with Eq. 2 in linear theory. Assuming the electron beam radius of 15 μm, the accelerated electron charge is 26 pC corresponding to the peak current of 1.3 kA. It could be difficult to generate such an ultrashort intense electron beam by means of the conventional RF accelerators.

Figure 5 shows the distribution of the transverse normalized velocities β_t of the accelerated electrons. We can obtain an emittance of the electron beam from $\beta_t = 0.0064$. The unnormalized emittance ε_x of the electron beam is approximately,

$$\varepsilon_x = r_b \beta_t, \tag{3}$$

where r_b is the electron beam radius. The normalized emittance ε_{nx} is

$$\varepsilon_{nx} = \gamma \beta \varepsilon_x, \tag{4}$$

where β is the longitudinal normalized velocity of the electron. For the electron energy of 7.5 MeV γ and β are approximately equal to 14.7 and 1, respectively. Assuming the electron beam radius, $r_b = 15$ μm, the normalized emittance of the accelerated electrons is 0.4 π mm mrad (rms). This emittance is smaller than the best quality beam produced by the conventional RF accelerator technology such as a photocathode RF-gun [12,19].

3. Conclusions

We have explored the generation of high quality electron bunched by using optical injection. Colliding of two two laser pulses injects electrons in plasma into the wakefield and the wakefield accelerates the electrons. We have made a numerical simulation of the optical injection scheme. The colliding plasma wave injection scheme investigated in this paper has the ability to produce relativistic electron bunches with low energy spread and low normalized transverse emittance. We verify the possibility of high quality electron beam generation and acceleration by laser wakefield in a gas-jet plasma.

References

1. T. Tajima and J. M. Dawson, Phy. Rev. Lett. **43**, 267 (1979).

2. K. Nakajima, D. Fisher, T. Kawakubo, H. Nakanishi, A. Ogata, Y. Kato, Y. Kitagawa, R. Kodama, K. Mima, H. Shiraga, K. Suzuki, K. Yamakawa, T. Zhang, Y. Sakawa, T. Shoji, Y. Nishida, N. Yugami, M. Downer, and T. Tajima, Phy. Rev. Lett. **74**, 4428 (1995).
3. D. Umstadter, S. -Y. Chen, A. Maksimchuk, G. Mourou, and R. Wanger, Science **273**, 472 (1996).
4. D. Gordon, K. C. Tzeng, C. E. Clayton, A. E. Dangor, V. Malka, K. A. Marsh, A. Modena, W. B. Mori, P. Muggli, Z. Najmudin, D. Neely, C. Danson, and C. Joshi, Phy. Rev. Lett. **80**, 2133 (1998).
5. A. Modena, Z. Najmudin, A. E. Dangor, C. E. Clayton, K. A. Marsh C. Joshi, V. Malka, C. B. Darrow, and C. Danson, IEEE Trans. Plasma Sci., **24**, 289 (1996).
6. C. I. Moore, A. Ting, K. Krushelnick, E. Esarey, R. F. Hubbard, B. Hafizi, H. R. Burris, C. Manka, and P. Sprangle, Phy. Rev. Lett. **79**, 3909 (1997).
7. K. Nakajima, Nucl. Instr. and Meth. in Phys. Res. **A410**, 514 (1998).
8. T. E. Cowan, A. W. Hunt, T. W. Phillips, S. C. Wilks, M. D. Perry, C. Brown, W. Fountain, S. Hatchett, J. Johnson, M. H. Key, T. Parnell, D. M. Pennington, R. A. Snavely, and Y. Takahashi, Phy. Rev. Lett **84**, 903 (2000).
9. V. Malka, S. Fritzler, E. Lefebvre, M.-M. Aleonard, F. Burgy, J.-P. Chambaret, J.-F. Chemin, K. Krushelnick, G. Malka, S. P. D. Mangles, Z. Najmudin, M. Pittman, J.-P. Rousseau, J.-N. Scheurer, B. Walton, and A. E. Dangor, Science **298**, 1596 (2002).
10. M. Kando, H. Ahn, H. Dewa, H. Kotaki, T. Ueda, M. Uesaka, T. Watanabe, H. Nakanishi, A. Ogata and K. Nakajima, Jpn. J. Appl. Phys. **38**, 967 (1999).
11. H. Dewa, H. Ahn, H. Harano, M. Kando, K. Kinoshita, S. Kondoh, H. Kotaki, K. Nakajima, H. Nakanishi, A. Ogata, H. Sakai, M. Uesaka, T. Ueda, T. Watanabe, K. Yoshii, Nucl. Instr. and Meth. in Phys. Res. A **410**, 357 (1998).
12. K. Nakajima, Nucl. Instr. and Meth. in Phys. Res. **A455**, 140 (2000).
13. S. Bulanov, N. Naumova, F. Pegoraro, and J. Sakai, Phys. Rev. E **58**, R5257 (1998).
14. D. Umstadter, J. K. Kim, and E. Dodd, Phy. Rev. Lett. **76**, 2073 (1996).
15. E. Esarey, R. F. Hubbard, W. P. Leemans, A. Ting, and P. Sprangle, Phy. Rev. Lett. **79**, 2682 (1997).
16. C. B. Schroeder, P. B. Lee, J. S. Wurtela, E. Esarey, and W. P. Leemans, Phy. Rev. E **59**, 6037 (1999).
17. S. Masuda, T. Katsouleas, and A. Ogata, Nucl. Inst. and Meth. A **455**, 172 (2000)
18. H. Kotaki, M. Kando, T. Oketa, S. Masuda, J. K. Koga, S. Kondo, S. Kanazawa, T. Yokoyama, T. Matoba, and K. Nakajima, Phys. Plasmas **9**, 1392 (2002).
19. X. J. Wang, M. Babzien, K. Batchelor, I. Ben-Zvi, R. Malone, I. Pogorelsky, X. Qui, J. Sheehan, J. Sharitka, and T. Srinivasan-Rao, Nucl. Instr. and Meth. A **375** (1996) 82; X. J. Wang, X. Qiu, and I. Ben-Zvi, Phys. Rev. E **54**, 3121 (1996).

POLARIZATION OF FINAL PHOTONS IN NONLINEAR COMPTON SCATTERING FOR LINEARLY POLARIZED LASER

LI DONGGUO*, R.HAMATSU, T. SUMIYOSHI

Dept. of Physics, Tokyo Metropolitan University, Minamiohsawa 1-1, Hachioji, Tokyo 192-0397, Japan
∗ E-mail: leedongguo2000@yahoo.com

KAORU.YOKOYA

High Energy Accelerator Research Organization(KEK), Oho 1-1, Tsukuba-shi, Ibaraki-ken, 305 Japan
E-mail: kaoru.yokoya@kek.jp

T. HIROSE

Advanced Research Institute for Science and Engineering, Waseda University 389-5 Shimooyamada-machi,Machida,Tokyo 194-0202, Japan

Nonlinear Compton scattering of linearly polarized laser beam is discussed in this paper. Using Volkov solution and polarization density matrix, a complete transition probability formula for linearly polarized laser and unpolarized electron is obtained. The polarization properties of final photons are discussed for different condition.

1. Introduction

In the interaction process between electron and laser beams, if laser intensity parameter $\xi \approx \lambda_L[\mathrm{m}]\sqrt{P[\mathrm{GW/m^2}]/27.3}$ increases to a high value, nonlinear Compton scattering(NLCS) happens, i.e. an electron absorbs multi-photons from the laser field and radiates a single photon. Here λ_L and P are the wavelength and power density of laser.

Through the backward Compton scattering of a polarized laser and relativistic electron beam, high energy and polarized X(or γ)-ray can be obtained. At the Accelerator Test Facility of Brookhaven National Laboratory(BNL-ATF), a high intensity picosecond X-ray laser synchrotron source(LSS) through Compton backscattering between a relativis-

tic electron beam with 60MeV and a linearly polarized CO_2 laser beam has been developed [1].

Both high laser intensity and polarization of γ-ray are very important in high energy physics applications, such as the application of polarized laser-Compton scattering in polarized positron generation and in the γ-γ collider. The possibility of the collision of linearly polarized laser for the possible experiments on CP violation.

In Sec.3, an analytical formulas of transition probability, and Monte-Carlo simulation of scattered photons of NLCS for linearly polarized laser are given, and the characters of final polarization are discussed in Sec.4. Finally, the conclusions are given in Sec.5.

2. Kinematics of Nonlinear Compton Scattering

In present paper, we adopt a head-on frame $(e_1, e_2, -k)$ of laser-electron beam system, where 4-vector $e_i = (0, \boldsymbol{e}_i)(i = 1, 2)$, $\boldsymbol{e}_1$ parallels to laser polarization, and $\boldsymbol{e}_2 = -\boldsymbol{k}/|\boldsymbol{k}| \times \boldsymbol{e}_1$. Azimuthal angle ϕ is defined by anti-clockwise direction from $\boldsymbol{e}_1$.

Quantum effect of Compton process is characterized by an invariant parameter $\lambda = 2k{\cdot}p/m^2 \approx 4\omega E/m^2$, where ω is the energy of laser photon, E energy of initial electron, and '$\approx$' means approximation for relativistic incident electron beam.

Final photon energy ω' is expressed by a dimensionless Lorentz invariant parameter x:

$$x = \frac{k{\cdot}k'}{k{\cdot}p} = \frac{n\lambda}{1 + \xi^2 + n\lambda + u^2} \approx \frac{\omega'}{E}, \tag{1}$$

where $u = \sqrt{\frac{n\lambda(1-x)}{x} - (1 + \xi^2)} \approx \gamma\theta$ and θ is scattering polar angle. For a relativistic electron beam, the scattered photons are limited in a narrow cone with solid angle $2/\gamma$. The maximum energy of scattered photons emitted from backward direction(i.e. $\theta = 0$) for given harmonic n is given by $x_{n,max} = n\lambda/(1 + \xi^2 + n\lambda)$.

3. Transition Probability

After using Volkov's solution and polarization density matrix of scattered photons, finally we obtain the differential transition probability formula of nth harmonic NLCS for linearly polarized laser as [3]

$$W_n(x, \phi) = \frac{\alpha m^2 \xi^2}{2q_0} \left[f_{0n} + f_{1n}\xi_1' + f_{3n}\xi_3' \right], \tag{2}$$

where α is the fine structure constant, Stokes parameter $\boldsymbol{\xi}'$ represents the polarization component to be measured by the detector, and functions $f(x,\phi)$ are given by [3]

$$f_{0n} = -\frac{|A_n^{(0)}|^2}{\xi^2} + \left(1 - x + \frac{1}{1-x}\right)\left[|A_n^{(1)}|^2 - A_n^{(0)}A_n^{(2)})\right], \tag{3}$$

$$f_{1n} = \frac{|A_n^{(0)}|^2}{\xi^2} u^2 \sin 2\phi + 2\sqrt{2}\frac{u}{\xi}\sin\phi A_n^{(0)}A_n^{(1)}, \tag{4}$$

$$f_{3n} = -(1 + 2u^2\sin^2\phi)\frac{|A_n^{(0)}|^2}{\xi^2} + 2\left[|A_n^{(1)}|^2 - A_n^{(0)}A_n^{(2)})\right]. \tag{5}$$

Here polarization term f_{1n} is new result, f_{3n} was given by [4], and function $A_n^{(s)}$ is defined by $A_n^{(s)} = \oint \frac{d\phi}{2\pi}\cos^s\phi e^{i[n\phi - \alpha_1\sin\phi + (\alpha_2/2)\sin(2\phi)]}$, $s = 0, 1, 2.$ with arguments $\alpha_1 = -2\sqrt{2}\,\frac{\xi}{\lambda}\frac{xu}{1-x}\cos\phi$, and $\alpha_2 = \frac{\xi^2}{\lambda}\frac{x}{1-x}$.

The energy spectrum of scattered photon is plotted in Figure.1 for $\lambda = 1.0 \times 10^{-4}$ and $\xi = 0.8$. Sharp peaks are seen at the high energy edge only for odd harmonics. Figure.1.(b) shows the energy spectrum of scattered photons whose polarization is parallel or perpendicular to the laser polarization, where the upper(lower) lines for parallel(perpendicular) for each harmonic.

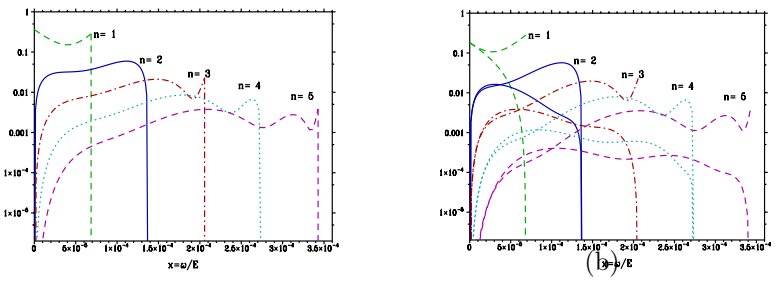

(a) (b)

Figure 1. Energy spectrum, where the transition probability are in units of $\alpha m^2/E$. (b) shows spectrum of scattered photons with polarization.

The code of Monte-Carlo simulation of NLCS for linearly polarized laser has been developed by us. Figure.2 shows the correlation between energy and polar angle of the scattered photons. Scattered photons can be found in the backscattering region $\theta \sim 0$ for odd harmonics. Figure.3.(a)-(c) show the transverse profile of the scattered photons of the first three harmonics. The pattern for the first harmonic has one peak and a dumbbell form,

which is the same as the patterns of dipole radiation in the classical theory. The patterns for the second and third harmonics have two and three peaks. We used the parameters of 2nd CO_2 laser power stage of the Compton scattering experiment in BNL-ATF.

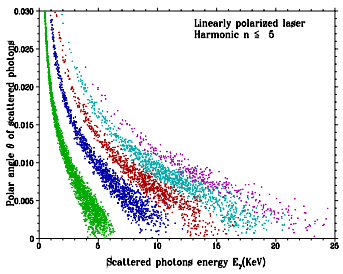

Figure 2. Energy via polar-angle distribution.

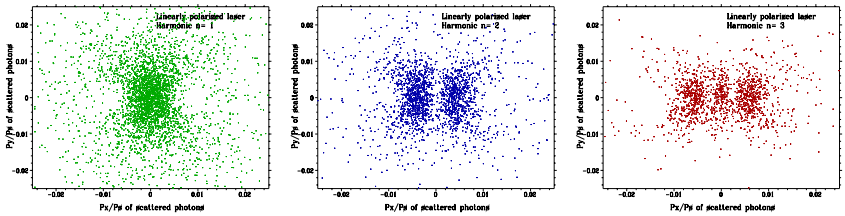

(a) (b) (c)

Figure 3. Transverse profile of scattered photons for linearly polarized laser case, where P_x, P_y and P_s are the momentums of scattered photons.

4. Final photon polarization

Final photon linear polarization(measured value) for n harmonic at (x, ϕ) is given by $\xi_3 = f_{3n}/f_{0n}$, $\xi_1 = f_{1n}/f_{0n}$ [3]. The degree of linear polarization ξ_L and the angle ϕ_L of polarization plane (measured from the polarization plane of the laser) are given by $\xi_L = \sqrt{\xi_1^2 + \xi_3^2}$, $\xi_3 = \xi_L \cos 2\phi_L$ and $\xi_1 = \xi_L \sin 2\phi_L$.

Final polarization in the $(\gamma\theta_x, \gamma\theta_y)$ plane is plotted in Figure.4 for the first third harmonics, where $\lambda = 1$, $\xi = 0.01$, 1.0. The length and direction of the short lines express the degree and direction of polarization. The

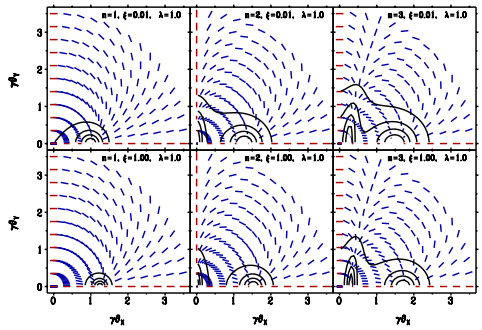

Figure 4. Final polarization in $(\gamma\theta_x, \gamma\theta_y)$ plane.

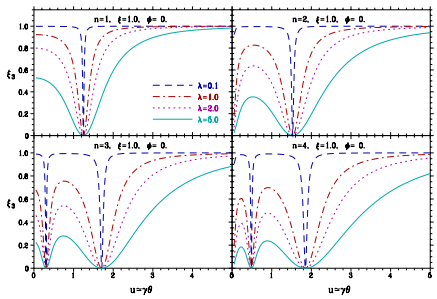

Figure 5. ξ_L vs polar angle $u \approx \gamma\theta$.

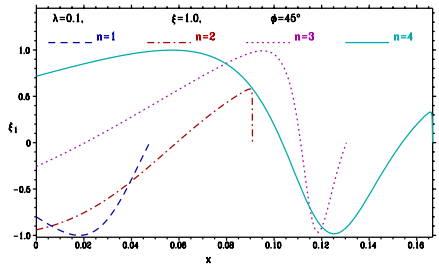

Figure 6. ξ_1 vs energy x on $\phi = 45°$ plane.

polarization degree is also shown by contours (the uppermost contour is 80% and the lowermost 20%).

Final polarization ξ_3 vs polar angle $u \approx \gamma\theta$ is plotted in Figure.5, for the first fourth harmonics under conditions $\phi = 0°$(x-axis, $\xi_1 \equiv 0$ on this

plane), where $\xi = 1$ and $\lambda = 0.1$, 1, 3, 5. One finds $\xi_3 \geq 0$ anywhere on the x-axis and there are $[(n+1)/2]$ zero points where $\xi_3 = 0$. The location of the zeroes is independent of λ as a function of u(Note that it depends on λ as a function of x.). The term of f_{1n} in Eq.(2) is necessary for calculating final photon polarization, as ξ_1 equals zero only correct on the $\phi = 0°$ and $90°$ planes. Figure.6 shows ξ_1 on $\phi = 45°$ plane. One finds the following facts:

1). No final circular polarization appears.

2). When λ is small, the degree of polarization is nearly 100% for any harmonic n and laser strength ξ, except in the vicinity of a few points on the x-axis.

3). Final polarization is parallel to the laser polarization on x-axis ($\phi = 0$). On y-axis ($\phi = 90°$), it is parallel for odd harmonics and perpendicular for even harmonics.

4). For large polar angle θ, the polarization degree is almost 100%.

5). For small polar angle, the polarization decreases as λ, but increases as ξ.

5. Conclusions

NLCS for linearly polarized laser is discussed, and a complete transition probability formula Eq.(2) for linearly polarized laser and unpolarized electron is obtained, where term f_{1n} in Eq.(2) is a new result. Using both f_{1n} and f_{3n}, we can exactly describe the degree and plane direction of final polarization for scattered photons in different azimuthal scattering angle. The polarization properties of final photons are discussed. The code of Monte-Carlo simulation for linearly polarized laser has been developed by us.

References

1. I.V.Pogorelsky, I.Ben-Zvi, T.Hirose etc.,*Phys. Rev. ST Accel. Beams* **3**, 090702 (2000).
2. D.M.Volkov, *Z.Phys.* **94**, 250 (1935).
3. Li.Dongguo, K.Yokoya, T.Hirose, R. Hamastus, 'Transition probability and polarization of final photons in nonlinear Compton scattering for linearly polarized laser', Sep. 2002. To be published by 'Japanese Journal of Applied Physics'.
4. C.Bamber, S.J.Boege, etc., *Phys.Rev.* **D60**, 092004 (1999).
5. V.B.Berestetskii, E.M.Lifshitz and L.P. Pitaevskii, 'Quantum Electrodynamics', 2nd ed.(New York,1982),sec. 40 and sec.87.

IS IT POSSIBLE TO OBTAIN POLARIZED POSITRONS DURING MULTIPLE COMPTON BACKSCATTERING PROCESS?

A.P. POTYLITSYN

Tomsk Polytechnic University, Lenin ave.2A, Tomsk, 634050, Russia
E-mail: pap@phtd.tpu.edu.ru

If a beam of unpolarized positrons (which is considered as a sum of two fractions with opposite helicities) passes through an intense circular polarized laser radiation these fractions may be separated. For high laser flash intensity each positron will interact with $k_0 \gg 1$ laser photons subsequently (linear multiple Compton scattering process). Due to difference in the compton cross-sections for positrons polarized in opposite directions the mean final energy of each fraction will be different. It allows to get a polarized positron beam using the momentum selection (with some intensity loss). Estimations show the possibility to obtain a positron beam with 35% longitudinal polarization and 25% intensity from the initial one for focussed laser flash with total energy 5J and positron beam with energy 5 GeV.

1. In existing projects of electron-positron colliders, the option of polarized electron and positron beams is considered [1,2]. While one can consider the problem of producing the polarized electron beams with required characteristics as having been solved [3], the existing approaches to polarized positrons generation [4-7] do not provide required parameters. In quoted papers the schemes were offered, in which by means of various methods a beam of circularly-polarized (CP) photons with energy of $\sim 10^1$ MeV is generated to be subsequently used for producing the longitudinally polarized positrons during the process of pair creaction in the amorphous converter.

In this paper an alternate approach is discussed - at the first stage the unpolarized positrons are generated by the conventional scheme (interaction of an electron beam with energy of $\sim 10^1$ GeV with an amorphous or crystalline converter), which are accelerated up to energy $\sim 5 \div 10$ GeV and then interact with intense CP laser radiation.

In the scheme of "laser cooling" of an electron beam suggested in the paper [8] , electrons with energy of 5 GeV in head-on collisions with laser photons lose their energy practically without scattering. Thus, as a result of

a multiple Compton scattering (MCS), the electron beam "is decelerated" resulting in some energy distribution, which variance is determined by the electron energy and laser flash parameters. It is clear that the laser cooling process will accompany also the interaction of positrons with laser photons.

If we consider an unpolarized positron beam as a sum of two fractions of the identical intensity with opposite signes of 100% longitudinal polarization, its interaction with CP laser radiation results in different Compton cross-sections for positrons with opposite helicity. After a few collisions positrons with opposite polarization lose a various part of the initial energy, therefore, by means of momentum selection of the resulting beam, it is possible to get a polarized positron beam with some intensity loss.

2. Let us write the Compton cross-section for CP photons after summing over scattered photon polarization [9] (the system of units being used hereinafter is $\hbar = m = c = 1$):

$$\frac{d\sigma}{dy} = \frac{\pi r_0^2}{x}\Big\{\frac{1}{1-y} + 1 - y - s^2 - \xi_{0z}\ P_c\ cy\ \frac{2-y}{1-y} -$$

$$- \xi_z P_c\Big[s_z scy + c_z\Big(\frac{y}{1-y} + yc^2\Big)\Big] + \qquad (1)$$

$$+\xi_{0z}\xi_z\Big[s_z s(1 + c^2 - yc^2) + c_z c\Big(\frac{1}{1-y} + (1-y)c^2\Big)\Big]\Big\} =$$

$$\frac{d\sigma_0}{dy} + P_c\ \xi_{0z}\ \frac{d\sigma_2}{dy} + P_c\ \xi_z \frac{d\sigma_2}{dy} + \xi_{0z}\ \xi_z \frac{d\sigma_3}{dy}\ .$$

Here P_c is the degree of circular polarization of laser photons, $\xi_{0z}(\xi_z)$ is the spin projection of an initial (final) positron on the axis z coincident with the direction of the initial positron momentum, r_0 is the classical electron radius. In (1) standard symbols are used [9]:

$$x = 2pk \approx 4\gamma_0\omega_0\ ,\ y = 1 - \frac{pk'}{pk} \approx \frac{\omega}{\gamma_0}\ ,$$

γ_0 is Lorentz factor of an initial positron; $\omega_0(\omega)$ is energy of an initial (scattered) photon. The factors s, c are determined in the known way [9]:

$$s = 2\sqrt{r(1-r)}\ ,\quad c = 1 - 2r,\ r = \frac{y}{x(1-y)}\ ,$$

where as factors s_z, c_z are obtained in the same coordinate frame for positron scattered at the angle θ_e

$$s_z = s - c\ \theta_e\ ,\quad c_z = c + s\ \theta_e\ .$$

For an ultrarelativistic case $\theta_e = \frac{1}{\gamma_0}\ \frac{\sqrt{y(x-y-xy)}}{1-y}$, so with an accuracy of $\sim \gamma_0^{-1},\ s_z = s,\ c_z = c$.

With the same accuracy, the cross-sections of spin-flip transitions $d\sigma_{+-},\ d\sigma_{-+}$ from states with opposite polarization signs ($\xi_{0z} = +1 \to \xi_z = -1$ and $\xi_{0z} = -1 \to \xi_z = +1$) are equal. It means that the Compton scattering process does not result in considerable polarization of an unpolarized beam. It should be remarked that the formula (1) is not the exact invariant expression (as well as formula (12) in paper [9]). Both expressions may be written in the invariant form with an accuracy of $\sim \gamma_0^{-1}$. The author's conclusion [10] concerning the possibility of polarization of a positron beam as a whole through MCS process was incorrect (it was based on the assumption that the magnitude $\int dy\Big[\frac{d\sigma_{+-}}{dy} - \frac{d\sigma_{-+}}{dy}\Big]$ presents an exact invariant which it was calculated in the rest frame of an initial positron, see also [11]).

3. As follows from (1), the total cross-section of positron interaction with CP photons depends on spin projection (ξ_{0z}):

$$\sigma = \frac{8}{3}\pi r_0^2\ [(1-x) - P_c\ \xi_{0z}\ \frac{x}{4}]\ . \tag{2}$$

In many cases of interest (laser cooling, for example) the relation $x \ll 1$ is satisfied, therefore in (2) the terms $\sim x^2$ and higher are discarded. Let's write the cross-section (2) for 100 % right circular polarization of laser radiation (P_c= +1) and for positrons polarized along the photon momentum and in the opposite direction:

$$\sigma_\pm = \int\limits_0^{x/1+x} \frac{d\sigma_\pm}{dy}\,dy \approx \frac{2\pi r_0^2}{x} \int\limits_0^{x/1+x} \Big[2{-}4\frac{y}{x}(1{+}y){+}4\frac{y^2}{x^2}\big(1{+}2y\big){\pm}\big(2y{-}4\frac{y^2}{x}\big)\Big]dy\ ,$$

Then

$$\sigma_+ = \sigma(P_c = +1,\ \xi_{0z} = +1) = \frac{8}{3}\pi r_0^2(1 - \frac{5}{4}x) = \sigma_T\big(1 - \frac{5}{4}x\big), \tag{3}$$

$$\sigma_- = \sigma(P_c = +1,\ \xi_{0z} = -1) = \sigma_T\big(1 - \frac{3}{4}x\big)\ .$$

Here $\sigma_T = \frac{8}{3}\pi r_0^2$ is the classical Thomson cross-section. It is clear that due to inequality of cross-sections (3), the positrons with various helicities undergo the various number of collisions, that eventually results in difference of average energies $\bar{\gamma}_\pm$ of both fractions of the initial unpolarized beam.

With this distinction being sufficiently great, and the variance of energy distribution for each fraction being enough small, the polarized positron beam can be generated by means of momentum selection.

4. In paper [12], in considering the MCS process by analogy with passage of charged particles through a condensed medium, the partial equations are derived that describe evolution of average energy $\bar{\gamma}$ and energy straggling (distributions variance) Δ for unpolarized electron beam passing through an intense laser flash. The approximate analytical solution was derived there as well:

$$\bar{\gamma} = \frac{\gamma_0}{1 + \frac{\sum^{(1)} l}{\gamma_0}} , \quad \Delta = \frac{\sum^{(2)} l}{\left(1 + \frac{\sum^{(1)} l}{\gamma_0}\right)^4} . \tag{4}$$

In (4) l is the laser flash length ("the thickness" of light target), $\sum^{(n)}$ is the n-order moment of "macroscopic" interaction cross-section:

$$\sum^{(n)} = 2n_L \int\limits_0^{\omega_{max}} \omega^n \frac{d\sigma}{d\omega}\, d\omega = 2n_L \gamma_0^n \int\limits_0^{x/1+x} y^n \frac{d\sigma}{dy}\, dy . \tag{5}$$

Here n_L is the concentration of laser photons, that for "short" laser flash [8] is estimated as follows:

$$n_L = \frac{A}{\omega_0} \frac{1}{\pi r_{ph}^2 l} , \tag{6}$$

A is the laser flash energy; r_{ph} is the minimum radius of the laser beam.

Developing (1) as a series in powers of x and retaining two first summands, we get:

$$\sum^{(1)} = n_L \sigma_T \gamma_0 x\Big(1 - \frac{21}{10}x\Big) , \quad \sum^{(2)} = \frac{7}{10} n_L \sigma_T \gamma_0^2 x^2 \Big(1 - \frac{22}{7}x\Big) . \tag{7}$$

After substitution of the found values for $\sum^{(n)}$ in (4) we have:

$$\bar{\gamma} = \frac{\gamma_0}{1 + n_L \sigma_T l x\Big(1 - \frac{21}{10}x\Big)} , \tag{8}$$

$$\Delta = \gamma_0^2 \frac{\frac{7}{10} n_L\ \sigma_T\ l\ x^2 \Big(1 - \frac{22}{7}x\Big)}{\Big[1 + n_L \sigma_T l x\Big(1 - \frac{21}{10}x\Big)\Big]^4} . \tag{9}$$

Let's write the equation (9) in more evident form:

$$\frac{\gamma_0}{\bar{\gamma}} = 1 + n_L \sigma_T l x\big(1 - \frac{21}{10}x\big) = 1 + \frac{1}{2} k_0\ x\big(1 - \frac{21}{10}x\big) . \tag{10}$$

In approximation $x \ll 1$ the quantity $k_0 = 2n_L\sigma_T\ l$ corresponds to the mean number of scattered photons per an electron of the initial beam (in other words, the average number of collisions of an electron in passing through the "light" target). When expressing the photon concentration n_L in Gaussian laser beam in terms of Rayleigh length z_R and the photon wavelength λ_0, defining minimum radius of the "light" target

$$r_{ph}^2 = \frac{\lambda_0\ Z_R}{2\pi}\ ,$$

one can readily see that the number of collisions is independent of the laser wavelength directly:

$$k_0 = \frac{16}{3}\ \alpha\ \frac{A}{mc^2}\quad \frac{r_0}{Z_R}\ ,$$

here α is the fine structure constant.

The condition of the approximation applicability (4) (and, therefore, (8) and (9) as well) is written as follows:

$$k_0 x^2 \gg 1\ . \tag{11}$$

For electrons with initial energy $E_0 = 5$ GeV having passed through a laser flash of following parameters (see [8]): ω_0=2,5 eV; A=5J; r_{ph}^2=4 μm^2, from (10) one can get $\gamma_0/\bar{\gamma} \approx 8.7$.

Noteworthy is the reasonable agreement with estimates obtained by V. Telnov [8], though the criterion (11) is not satisfied in this case.

5. As it was mentioned above, neglecting by spin flip transitions the evolution of each fraction of polarized positrons can be considered independently.

In this case, the average energy of a fraction and variance may be written in the full analogy with (4):

$$\bar{\gamma}_\pm = \frac{\gamma_0}{1 + \frac{\sum_\pm^{(1)} l}{\gamma_0}}\ ,\quad \Delta_\pm = \frac{\sum_\pm^{(2)}\ l}{\left(1 + \frac{\sum_\pm^{(1)}\ l}{\gamma_0}\right)^4}\ . \tag{12}$$

Here by $\sum_\pm^{(n)}$ the appropriate cross-section moments are denoted:

$$\sum\nolimits_\pm^{(n)} = 2n_L\ \gamma_0^n \int\limits_0^{x/1+x} y^n\ \frac{d\sigma_\pm}{dy}\ dy\ .$$

The calculation of moments involved in (12) and (13) in the same approximation as before, gives the following result:

$$\sum\nolimits_+^{(1)} = n_L\ \sigma_T\ \gamma_0 x\Big(1 - \frac{8}{5}x\Big),\ \ \sum\nolimits_-^{(1)} = n_L\ \sigma_T\ \gamma_0 x\Big(1 - \frac{13}{5}x\Big)\ ;$$

$$\sum\nolimits_{+}^{(2)} = \frac{7}{10}\, n_L\, \sigma_T\, \gamma_0^2\, x^2\Big(1-\frac{35}{14}x\Big),\;\; \sum\nolimits_{-}^{(2)} = \frac{7}{10}\, n_L\, \sigma_T\, \gamma_0^2\, x_0^2\Big(1-\frac{53}{14}x\Big)\,.$$

Thus, the relative width of energy distribution in each fraction is deduced from the relations:

$$\frac{\sqrt{\Delta_+}}{\bar{\gamma_+}} = \frac{\sqrt{\frac{7}{10} n_L \sigma_T l x^2\Big(1-\frac{35}{14}x\Big)}}{1+n_L\sigma_T l x\Big(1-\frac{8}{5}\,x\Big)} = \frac{\sqrt{\frac{7}{20}\;k_0\;x^2\Big(1-\frac{35}{14}x\Big)}}{1+\frac{1}{2}k_0\;x\Big(1-\frac{8}{5}x\Big)}\,, \qquad (13)$$

$$\frac{\sqrt{\Delta_-}}{\bar{\gamma_-}} = \frac{\sqrt{\frac{7}{10} n_L \sigma_T l x^2\Big(1-\frac{53}{14}x\Big)}}{1+n_L\sigma_T l x\Big(1-\frac{13}{5}\,x\Big)} = \frac{\sqrt{\frac{7}{20}\;k_0\;x^2\Big(1-\frac{53}{14}x\Big)}}{1+\frac{1}{2}k_0\;x\Big(1-\frac{13}{5}x\Big)}\,. \qquad (14)$$

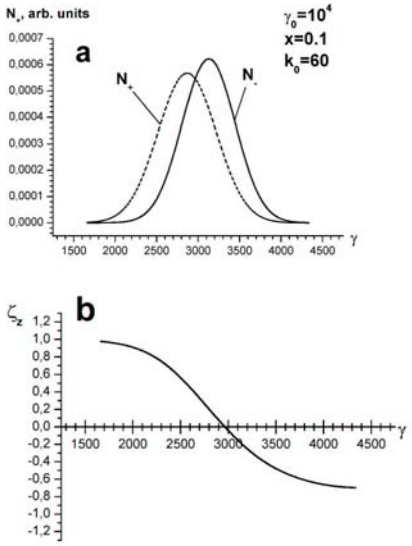

Figure 1. a) Energy distribution of positrons polarized in opposite directions $N_{\pm}(\gamma)$ after passing a laser flash; b) the degree of longitudinal polarization $\xi_z(\gamma)$ versus positrons energy.

Figure 1a presents the distribution for each positron fraction with $\gamma_0 = 10^4$ after passing the laser radiation with flash parameters: A=5J;

λ_0=1 μm, r_{ph}= 4.2 μm(k_0= 60). The distributions were approximated by Gaussians with parameters (12), (13), (14):

$$\bar{\gamma}_+ = 2868,\ \sqrt{\Delta_+}/\bar{\gamma}_+ = 0.12\ ;$$

$$\bar{\gamma}_- = 3129,\ \sqrt{\Delta_-}/\bar{\gamma}_- = 0.10\ .$$

The degree of positron polarization being determined in the ordinary way

$$\xi_z(\gamma) = \frac{N_+ - N_-}{N_+ + N_-} \tag{15}$$

is shown in Figure 1b.

By means of momentum analysis with the fixed acceptance $\Delta p/p = \Delta\gamma/\gamma$= const in proximity to a preset value γ_p one can get a partially polarized positron beam.

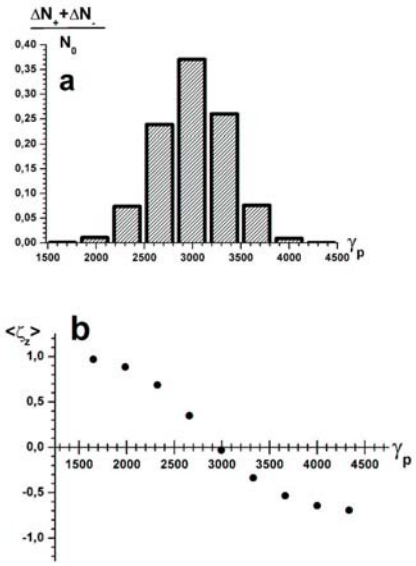

Figure 2. a) Histogram of positron distribution after momentum selection with acceptance $\sigma = \sqrt{\Delta}$ (see Figure 2); b) the degree of positron longitudinal polarization after momentum selection.

Figure 2 presents the polarization degree and intensity of the positron beam resulting from the similar procedure, when after passing a laser flash

the beam had characteristics depicted in Figure 1. For simplicity, the calculations were carried out for uniform acceptance:

$$P = \begin{cases} \text{const}, \ \gamma_p - \frac{1}{2}\sqrt{\Delta} \leq \gamma \leq \gamma_p + \frac{1}{2}\sqrt{\Delta} \\ \\ 0 \qquad \text{off.} \end{cases}$$

As follows from Figure 2, positrons with energy in the interval $\gamma = 2660 \pm 170$ have average polarization $< \xi_z > \approx$ - 0.35, then in the interval $\gamma = 3330 \pm 170$, $< \xi_z > \approx 0.34$, with the positron intensity in each "pocket" reaching $\sim 24\%$ of the initial one.

References

1. J.E. Clendenin, SLAC-PUB-8465, 2000.
2. R.W. Assmann, F. Zimmermann, CERN SL-2001-064.
3. J.E. Clendenin, R. Alley, J. Frish, T. Kotseroglou, G. Mulhollan, D. Schultz, H. Tang, J. Turner and A.D. Yerremian, AIP **421**, 250 (1997).
4. V.E. Balakin, A.A. Mikhailichenko, Preprint INP 79-85, Novosibirsk, 1979.
5. T. Omori, SLAC-R-502, 285 (1997).
6. E.G. Bessonov, A.A. Mikhailichenko, *in: Proc. of V European Particle Accelerator Conference*, 1516 (1998).
7. A.P. Potylitsyn, *Nucl. Instrum. and Meth.* **A398**, 395 (1998).
8. V. Telnov, *Phys. Rev. Lett.* **78**, 4757 (1997).
9. G.L. Kotkin, S.I. Polityko, V.G. Serbo, *Nucl. Inst. Meth.* **A405**, 30 (1998).
10. A.P. Potylitsin, LANL arXiv: physics/0203059.
11. G.L. Kotkin, V.G. Serbo, V.I. Telnov, LANL arXiV: hep-ph/0205139.
12. A. Kolchuzhkin, A. Potylitsyn, S. Strokov, V. Ababiy, Nucl. Inst. and Meth. **B201**, 307 (2003).

1D PIC SIMULATION OF PLASMA CATHODE

S. MASUDA, M. KANDO, H. KOTAKI, S. KONDO,
S. KANAZAWA, T. HONMA AND I. V. SMETANIN
Advanced Photon Research Center, Japan Atomic Energy Research Institute,
8-1 Umemidai, Kizu, Souraku, Kyoto, 619-0215, Japan

K. NAKAJIMA
Advanced Photon Research Center, Japan Atomic Energy Research Institute,
8-1 Umemidai, Kizu, Souraku, Kyoto, 619-0215, Japan
High Energy Accelerator Research Organization,
1-1 Oho, Tsukuba, Ibaraki, 305-0801, Japan

A laser driven plasma cathode experiment is planned using 100TW, 20fs laser system at JAERI-APR. Before the experiment, we made a parameter survey with 1D PIC simulation. We have developed relativistic 1D PIC code to study the propagation of the high intense laser pulse in the plasma and the high energy electron generation. Time evolution of the laser-interaction is simulated. Low emittance electrons with high energy up to several handred MeV are generated. We will report the simulation results of the plasma cathode.

1. Introduction

High energy electrons are generated by focusing an intense ultra short laser pulse into a plasma. The recent experiments demonstrate the high energy electron generation [1,2,3, 4,5] due to the progress on the short laser pulse technology. A laser driven plasma cathode is expected as a high quality electron source. We are preparing the plasma cathode experiment using the 100TW, 20fs Ti:sapphire laser system [6] at JAERI-APR. The peak power up to 100TW is focused into a 7μm spot by an off-axis parabolic mirror with a focal length of 177 mm. Intensity of 10^{20}W/cm^2 can be achieved.

Before conducting the experiment, we made a parameter survey using one dimensional particle-in-cell (1D PIC) simulation code. One dimensional simulation cannot treat the transverse nature of the laser- plasma interaction such as the self-focusing effect. However the 1D code requires

less computer time and computer memory than the 2D and 3D code. It is convenient to use the 1D code for the parameter survey. We will report the results of the simulation of the plasma cathode.

2. 1D PIC Simulation Model

We have developed a 1D PIC (Particle-In-Cell) simulation code to study the interaction of the laser pulse and the plasma. The particle motion and the electromagnetic field are calculated self consistently. The laser-plasma interaction in this code is implemented as follows.

The quantities in the code are normalized based on a quantity characterizing the time evolution of the plasmas, an electron plasma frequency $\omega_{pe} = \sqrt{4\pi e^2 n_{e0}/m_e}$. Where e and m_e are the magnitude of electron charge and the electron mass, respectively. n_{e0} is electron number density. n_{e0} is used as normalization factor. Time t is normalized by ω_{pe} as $t \equiv \omega_{pe}t$, where t of left hand side is normalized time. According to the time, the spacial length x is normalized as $x \equiv xk_{pe}$, here $k_{pe} = \omega_{pe}/c$. The particle velocity is normalized by the speed of light c, $\beta \equiv \mathbf{v}/c$. The electric field $\mathbf{E}$, the magnetic field $\mathbf{B}$, the current density $\mathbf{j}$ and the charge density ρ ;

$$\mathbf{E} \equiv \frac{e\mathbf{E}}{m_e c\omega_{pe}}, \qquad \mathbf{B} \equiv \frac{e\mathbf{B}}{m_e c\omega_{pe}}, \qquad \mathbf{j} \equiv \frac{\mathbf{j}}{en_{e0}c} \qquad \text{and} \qquad \rho \equiv \frac{\rho}{en_{e0}}. \quad (1)$$

Finally, the particle charge q and mass m are also normalized as $q \equiv \frac{q}{e}$ and $m \equiv \frac{m}{m_e}$, respectively.

One dimensional spatial grid is located at $x_i = i\Delta x$. Δx is grid size and i is the index of the grid. The electromagnetic field vectors, E_y, E_z are assigned on x_i and E_x, B_y, B_z are on $x_{i+\frac{1}{2}}$. The current density vector components J_x, J_y, J_z ,which are assigned on the grid same as the electric field vector, are calculated from the particle distribution.

Time evolution of the electromagnetic field is calculated by time integration of the Maxwell equations;

$$\begin{aligned} B^{n+\frac{1}{2}}_{y,i+\frac{1}{2}} &= B^{n-\frac{1}{2}}_{y,i+\frac{1}{2}} + \tfrac{\Delta t}{\Delta x}(E^n_{z,i+1} - E^n_{z,i}) \\ B^{n+\frac{1}{2}}_{z,i+\frac{1}{2}} &= B^{n-\frac{1}{2}}_{z,i+\frac{1}{2}} - \tfrac{\Delta t}{\Delta x}(E^n_{y,i+1} - E^n_{y,i}) \end{aligned} \quad (2)$$

$$\begin{aligned} E^{n+1}_{x,i+\frac{1}{2}} &= E^n_{x,i+\frac{1}{2}} - \Delta t j^{n+\frac{1}{2}}_{x,i+\frac{1}{2}} \\ E^{n+1}_{y,i} &= E^n_{y,i} - \tfrac{\Delta t}{\Delta x}(B^{n+\frac{1}{2}}_{z,i+\frac{1}{2}} - B^{n+\frac{1}{2}}_{z,i-\frac{1}{2}}) - \Delta t j^{n+\frac{1}{2}}_{y,i} \\ E^{n+1}_{z,i} &= E^n_{z,i} + \tfrac{\Delta t}{\Delta x}(B^{n+\frac{1}{2}}_{y,i+\frac{1}{2}} - B^{n+\frac{1}{2}}_{y,i-\frac{1}{2}}) - \Delta t j^{n+\frac{1}{2}}_{z,i}, \end{aligned} \quad (3)$$

where n is the index of time step. B_x is constant in time for one dimentional case.

An open boundary condition for the electromagnetic wave is taken into calculation following Ref [7]. For an electromagnetic wave incident in the $-x$ direction at left side of the system with phase velocity c the relation $k_x E_y - \omega B_z = 0$ is rewritten using time average of E_y and spatial average of B_z as

$$E^n_{y,0} + E^{n+1}_{y,0} + B^{n+\frac{1}{2}}_{z,-\frac{1}{2}} + B^{n+\frac{1}{2}}_{z,\frac{1}{2}} = 0 \tag{4}$$

with the help of $k_x = -\omega$. $B^{n+\frac{1}{2}}_{z,-\frac{1}{2}}$ can be eliminated with

$$\frac{\Delta t}{\Delta x}\frac{B^{n+\frac{1}{2}}_{z,+\frac{1}{2}} - B^{n+\frac{1}{2}}_{z,-\frac{1}{2}}}{\Delta x} + \frac{E^{n+1}_{y,0} - E^n_{y,0}}{\Delta t} = 0. \tag{5}$$

Thus, $E^{n+1}_{y,0}$ at left boundary is obtained;

$$E^{n+1}_{y,0} = -\frac{1 - \Delta x/\Delta t}{1 + \Delta x/\Delta t}E^n_{y,0} - \frac{2}{1 + \Delta x/\Delta t}B^{n+\frac{1}{2}}_{z,\frac{1}{2}}. \tag{6}$$

$E^{n+1}_{z,0}$ is also calculated by similar way. The open boundary condition for E_y and E_z at right side is implemented with same algorithm.

Laser pulse injection is implemented by adding oscillation to the current density at the boundary region;

$$j_{z,i=1} = \frac{2E_L}{\Delta x}g(t)\sin(\omega_L t), \tag{7}$$

where E_L is amplitude of laser electric field, $g(t)$ is the time envelope and ω_L is laser frequency. Time envelope function is given by

$$g(x) = \exp[-\frac{(t - 3\tau_L)^2}{4\tau_L^2}], \tag{8}$$

where τ_L is the pulse length. In this case, the laser electric field is linearly polarized in the z-direction. The laser pulse propagates in the x-direction.

The motion of the particles in the electromagnetic field is calculated by numerically solving the Lorentz force equation for the electrons and ions.

$$\frac{\mathbf{u}^{n+\frac{1}{2}} - \mathbf{u}^{n-\frac{1}{2}}}{\Delta t} = \frac{q}{m}(\mathbf{E}^n + \frac{\mathbf{u}^{n+\frac{1}{2}} + \mathbf{u}^{n-\frac{1}{2}}}{2\gamma^n} \times \mathbf{B}^n) \tag{9}$$

where $\mathbf{u} = \gamma\beta$, $\gamma = 1/\sqrt{1-\beta^2}$, the relativistic factor. The Boris push algorithm is implemented to solve this equation.

The current distribution is calculated from the particle distribution. When the particle is located between x_i and x_{i+1}, the z-component of the current density j_z is

$$\begin{aligned} j_{z,i} &= q_M \frac{u_z}{\gamma} \frac{x_{i+1} - r_x}{\Delta x^2} \\ j_{z,i} &= q_M \frac{u_z}{\gamma} \frac{r_x - x_i}{\Delta x^2}. \end{aligned} \tag{10}$$

The x and y components of the current are calculated by the same manner. All of particles are accumulated to the current density on each grid. Macro particle charge q_M is determined by $q_M = q \int n_s \, dx / N_M$. Where n_s is the initial density distribution of the particles and N_M is number of macro particles.

The electric and magnetic field, the particle position and velocity are advanced in time step by step. At first $\mathbf{B}^{n-\frac{1}{2}}$, $\mathbf{E}^n$, $\mathbf{u}^{n-\frac{1}{2}}$ and $\mathbf{r}^n$ are given initially. The procedure is as following;

1) The magnetic field is advanced half step.

$$\mathbf{B}^n = \mathbf{B}^{n-\frac{1}{2}} - \frac{\Delta t}{2} \nabla \times \mathbf{E}^n \tag{11}$$

2) The particle velocity is advanced full step.

$$\mathbf{u}^{n+\frac{1}{2}} = \mathbf{u}^{n-\frac{1}{2}} - \frac{\mathbf{F}^n}{m} \Delta t \tag{12}$$

3) The magnetic field is advanced half step.

$$\mathbf{B}^{n+\frac{1}{2}} = \mathbf{B}^n - \frac{\Delta t}{2} \nabla \times \mathbf{E}^n \tag{13}$$

4) The particle position is advanced half step.

$$\mathbf{r}^{n+\frac{1}{2}} = \mathbf{r}^n - \frac{\mathbf{u}^{n+\frac{1}{2}}}{\gamma^{n+\frac{1}{2}}} \frac{\Delta t}{2} \tag{14}$$

5) $\mathbf{j}^{n+\frac{1}{2}}$ is calculated from $\mathbf{u}^{n+\frac{1}{2}}$ and $\mathbf{r}^{n+\frac{1}{2}}$.

6) The particle position is advanced half step.

$$\mathbf{r}^{n+1} = \mathbf{r}^{n+\frac{1}{2}} - \frac{\mathbf{u}^{n+\frac{1}{2}}}{\gamma^{n+\frac{1}{2}}} \frac{\Delta t}{2} \tag{15}$$

7) The electric field is advanced full step.

$$\mathbf{E}^{n+1} = \mathbf{E}^n + \Delta t \nabla \times \mathbf{B}^{n+\frac{1}{2}} - \Delta t \mathbf{j}^{n+\frac{1}{2}} \tag{16}$$

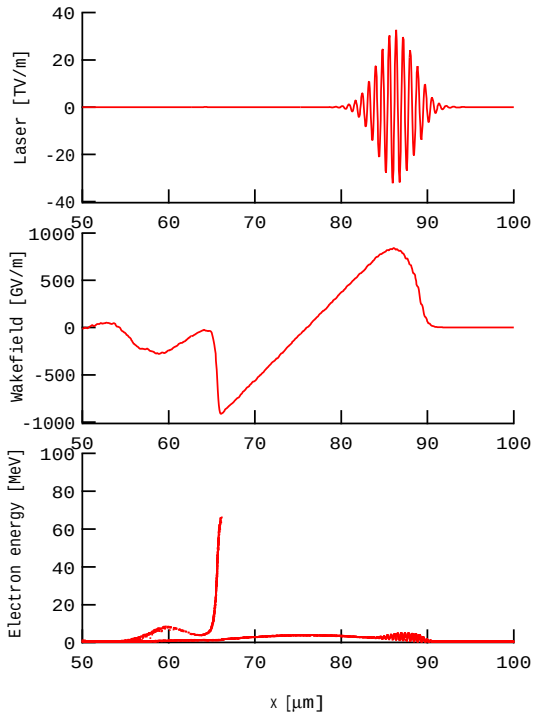

Figure 1. Waveform of the wakefield field excited by the laser pulse and energy distribution of the electrons for $a_0 = 8$. Laser wave length is 800 nm and pulse length is 20 fs (FWHM).

3. Simulation Results

In the 1D simulation presented here, the initial plasma is uniformly distributed between $x = 0$ and $x = 500\mu$m. The 20fs laser pulse is injected from left side ($x = 0$) at $t = 0$. The laser electric field is linearly polarized in z-direction. Figure 1 shows the wake field excited by the laser pulse and the electron energy distribution. The normalized vector potential of the laser a_0 is 8 and the initial plasma density is 10^{19}cm^{-3}. Nonlinear wakefield is excited and the electrons are trapped in the acceleration phase of the wake. The generated electron bunch is very short. The length is the order of 1 μm. The scattering angle of the accelerated electrons is shown in Figure 2. There are three peaks in the scattering angle. Two peaks around 1 and -1 rad. are due to the scattering by the laser ponderomotive acceleration [8]. The electrons trapped in the wakefield have small scattering angle. It is es-

timated from the Figure 2 that the divergence $\sqrt{<(\beta_z/\beta_x)^2>}$ is 1.2×10^{-3} for high energy electrons.

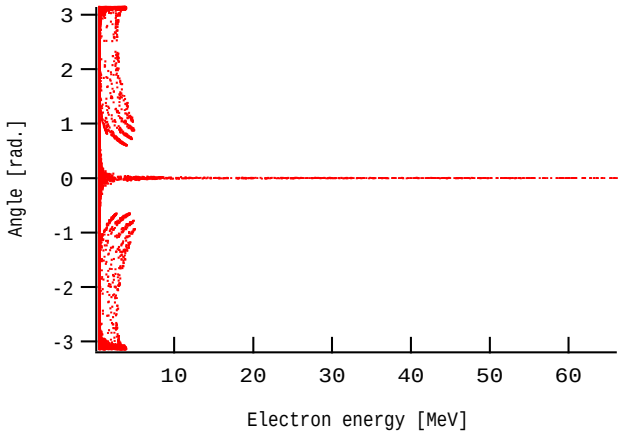

Figure 2. Scattering angle as a function of electron energy. The simulation parameter is the same as in Figure 1.

The energy of electron increases in time as the wakefield propagates in the plasma. The time evolution of the maximum electron energy is plotted in Figure 3. It is seen that the electron is alternately accelerated and decelerated for the plasma density over $1\times10^{19}\mathrm{cm}^{-3}$. This is due to the phase slipping because the dephasing length decreases with increasing in the plasma density. Maximum energy gain is obtained at the plasma density around $7\times10^{18}\mathrm{cm}^{-3}$. The electron energy reaches 300 MeV.

4. Summary

1D PIC simulation is conducted for the plasma cathode experiment at JAERI-APR. When the 100TW, 20fs laser pulse is focused into the plasma, high energy electrons over 300 MeV are generated. Although 1D simulation cannot treat transverse characteristics, estimation of the emittance is possible by supposing that transverse interaction region is the same as the laser spot size (7μm). In our case, the normalized emittance is the order of $1\ \pi$ mm-mrad and 10^9-10^{10} electrons are accelerated by the wakefield.

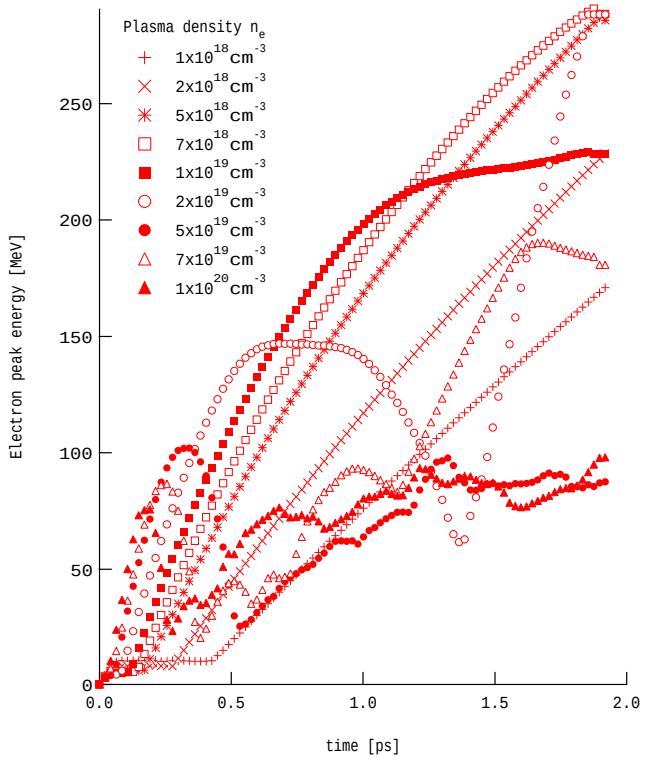

Figure 3. Time evolution of peak energy of the electrons.

References

1. D. Gordon, K. C. Tzeng, C. E. Clayton, A. E. Dangor, V. Malka, K. A. Marsh, A. Modena, W. B. Mori, P. Muggli, Z. Najmudin, D. Needy, C. Danson and C. Joshi, *Phys. Rev. Lett.* **80**, 2133 (1988)
2. C. Gahn, G. D. Tsakiris, A. Pukhov, J. Meyer-ter-Vehn, G. Pretzler, P. Thirof, D. Habs and K. J. Witte, *Phys. Rev. Lett.* **83**, 4772 (1999)
3. X. Wang, M. Kirshnan, N. Saleh, H. Wang and D. Umstadter, *Phys. Rev. Lett.* **84**, 5324 (2001)
4. V. Malka, J. Faure, J. R. Marques, F. Amiranoff, J. P. Rousseau, S. Ranc, J. P. Chambaret, Z. Najmudin, B. Walton, P. Mora and S. Solodov *Phys. Plasmas,* **8**, 2605 (2001)
5. M. I. K. Santala, Z. Najmudin, E. L. Clarke, M. Tatarakis, K. Krushelnick, A. E. Dangor, A. Malka, J. Faure, R. Allott and R. J. Clarke, *Phys. Rev. Lett.* **86**, 5324 (2001)
6. K. Yamakawa, M. Aoyama, S. Matsuoka, T. Kase, Y. Akahane and H.

Takuma, *Opt. Lett.* **23**, 1468 (1998)
7. C. K. Birdsall and A. B. Langdon, *"Plasma Physics via Computer Simulation"* IOP Pub., (1991)
8. F.V. Hartemann, S. N. Fochs, G. P. Le Sage, N. C. Luhmann Jr., J. G. Woodworth, M. D. Perry, Y. J. Chen and A. K. Kerman *Phys. Rev. E* **51**, 4833 (1995)

BOILING THE VACUUM WITH AN X-RAY FREE ELECTRON LASER

A. RINGWALD

Deutsches Elektronen-Synchrotron DESY,
Notkestraße 85,
D-22607 Hamburg, Germany
E-mail: andreas.ringwald@desy.de

X-ray free electron lasers will be constructed in this decade, both at SLAC in the form of the so-called Linac Coherent Light Source as well as at DESY, where the so-called TESLA XFEL laboratory uses techniques developed for the design of the TeV energy superconducting electron-positron linear accelerator TESLA. Such X-ray lasers may allow also for high-field science applications by exploiting the possibility to focus their beams to a spot with a small radius, hopefully in the range of the laser wavelength. Along this route one obtains very large electric fields, much larger than those obtainable with any optical laser of the same power. We consider here the possibility of obtaining an electric field so high that electron-positron pairs are spontaneously produced in vacuum (Schwinger pair production) and review the prospects to verify this non-perturbative production mechanism for the first time in the laboratory.

1. Introduction

Spontaneous particle creation from vacuum induced by an external field was first proposed in the context of e^+e^- pair production in a static, spatially uniform electric field[1] and is often referred to as the Schwinger[2] mechanism. It is one of the most intriguing non-linear phenomena in quantum field theory. Its consideration is theoretically important, since it requires one to go beyond perturbation theory, and its eventual experimental observation probes the theory in the domain of strong fields. Moreover, this mechanism has been applied to many problems in contemporary physics, ranging from black hole quantum evaporation[3] and e^+e^- creation in the vicinity of charged black holes[4], giving rise possibly to gamma ray bursts[5], to particle production in hadronic collisions[6] and in the early universe[7], to mention only a few. One may consult the monographs[8] for a review of further applications, concrete calculations and a detailed bibliography.

It is known since the early 1930's that in the background of a static, spatially uniform electric field the vacuum in quantum electrodynamics (QED) is unstable and, in principle, sparks with spontaneous emission of e^+e^- pairs[1]. However, a sizeable rate for spontaneous pair production requires extraordinary strong electric field strengths $\mathcal{E}$ of order or above the critical value

$$\mathcal{E}_c \equiv \frac{m_e\, c^2}{e\, \lambda\!\!\!^{-}_e} = \frac{m_e^2\, c^3}{e\, \hbar} \simeq 1.3 \cdot 10^{18}\ \mathrm{V/m}\,. \tag{1}$$

Otherwise, for $\mathcal{E} \ll \mathcal{E}_c$, the work of the field on a unit charge e over the Compton wavelength of the electron $\lambda\!\!\!^{-}_e = \hbar/(m_e c)$ is much smaller than the rest energy $2\, m_e c^2$ of the produced e^+e^- pair, the process can occur only via quantum tunneling, and its rate is exponentially suppressed, $\propto \exp[-\pi\, \frac{\mathcal{E}_c}{\mathcal{E}}]$.

Unfortunately, it seems inconceivable to produce macroscopic static fields with electric field strengths of the order of the critical field (1) in the laboratory. In view of this difficulty, in the early 1970's the question was raised whether intense optical lasers could be employed to study the Schwinger mechanism[9,10]. Yet, it was found that all available and conceivable optical lasers did not have enough power density to allow for a sizeable pair creation rate[9,10,11,12,13,14,15,16,17,18,19]. At about the same time, the thorough investigation of the question started whether the necessary superstrong fields around $\mathcal{E}_c$ can be generated microscopically and transiently in the Coulomb field of colliding heavy ions with $Z_1 + Z_2 > Z_c \approx 170$[20]. At the present time, clear experimental signals for spontaneous positron creation in heavy ion collisions are still missing and could only be expected from collisions with a prolonged lifetime[21].

Meanwhile, there are definite plans for the construction of X-ray free electron lasers (FEL), both at SLAC, where the so-called Linac Coherent Light Source[22,23] (LCLS) is under construction, as well as at DESY, where the so-called TESLA XFEL uses techniques developed for the design of the TeV energy superconducting e^+e^- linear accelerator TESLA[24,25,26]. Such X-ray lasers may possibly allow also for high-field science applications[27,28,29,30,31]: One could make use of not only the high energy and transverse coherence of the X-ray beams, but also of the possibility to focus them to a spot with a small radius σ, hopefully in the range of the laser wavelength, $\sigma \gtrsim \lambda \simeq \mathcal{O}(0.1)$ nm. In this way one might obtain very large electric fields,

$$\mathcal{E} = \sqrt{\mu_0\, c\, \frac{P}{\pi\sigma^2}} \;=\; 1.1 \cdot 10^{17}\ \frac{\mathrm{V}}{\mathrm{m}}\ \left(\frac{P}{1\ \mathrm{TW}}\right)^{1/2}\ \left(\frac{0.1\ \mathrm{nm}}{\sigma}\right)\,, \tag{2}$$

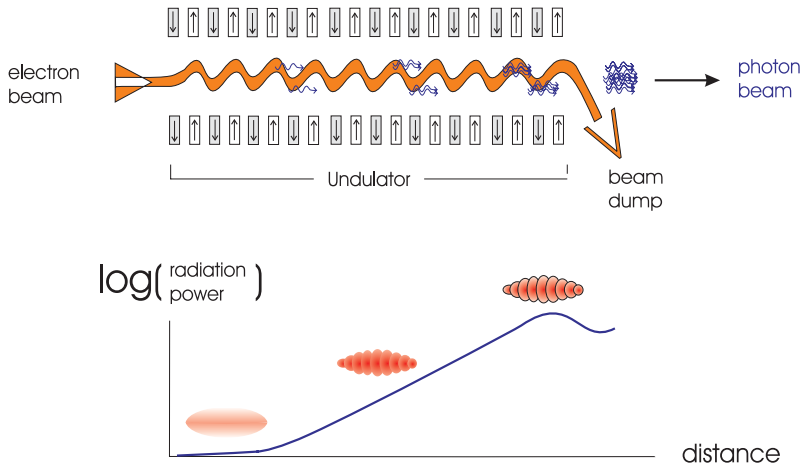

Figure 1. Principle of a single-pass X-ray free electron laser in the self amplified spontaneous emission mode[26].

much larger than those obtainable with any optical laser of the same peak power P. Thus, X-ray FELs may be employed possibly as vacuum boilers[28].

In this contribution, I will review recent work on spontaneous e^+e^- pair production at the focus of future X-ray FELs[32,33,34,35] and discuss the prospects to verify this non-perturbative production mechanism for the first time in the laboratory.

2. X-Ray Free Electron Lasers

Let us start by briefly reviewing the principle of X-ray free electron lasers.

Conventional lasers yield radiation typically in the optical band. The reason is that in these devices the gain comes from stimulated emission from electrons bound to atoms, either in a crystal, liquid dye, or a gas. The amplification medium of free electron lasers[36], on the other hand, is *free*, i.e. unbounded, electrons in bunches accelerated to relativistic velocities with a characteristic longitudinal charge density modulation (cf. Fig. 1).

The basic principle of a single-pass free electron laser operating in the self amplified spontaneous emission (SASE) mode[37] is as follows. It functions by passing an electron beam pulse of energy E_e of small cross section and high peak current through an undulator – a long periodic magnetic structure (cf. Fig. 1). The interaction of the emitted synchrotron radiation, with opening angle

$$1/\gamma = m_e c^2/E_e = 2 \cdot 10^{-5} \ \ (25 \text{ GeV}/E_e) \ , \tag{3}$$

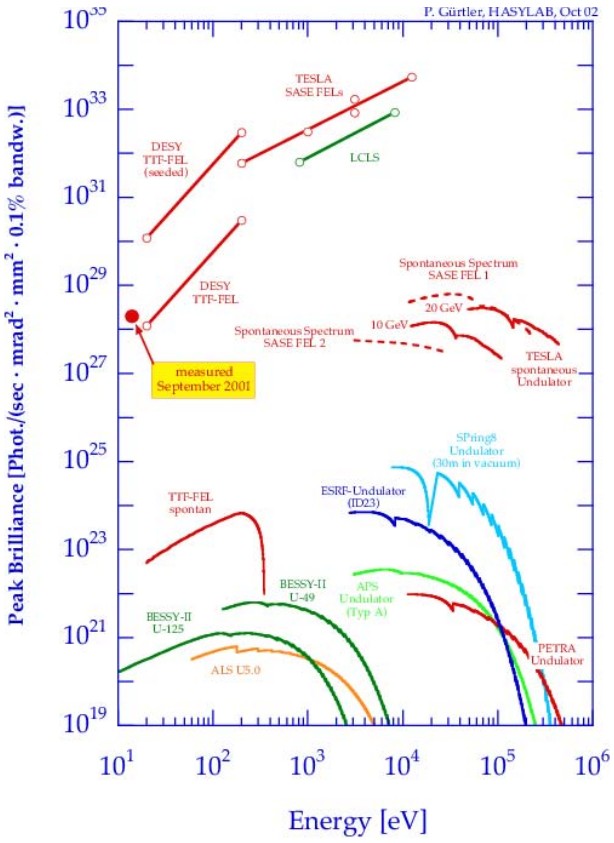

Figure 2. Spectral peak brilliance of X-ray FELs and undulators for spontaneous radiation at TESLA, together with that of third generation synchrotron radiation sources[26]. For comparison, the spontaneous spectrum of an X-ray FEL undulator is shown.

where m_e is the electron mass, with the electron beam pulse within the undulator leads to the buildup of a longitudinal charge density modulation (micro bunching), if a resonance condition,

$$\lambda = \frac{\lambda_U}{2\gamma^2}\left(1+\frac{K_U^2}{2}\right) = 0.3\ \text{nm}\ \left(\frac{\lambda_U}{1\,\text{m}}\right)\left(\frac{1/\gamma}{2\cdot 10^{-5}}\right)^2\left(\frac{1+K_U^2/2}{3/2}\right), \quad (4)$$

is met. Here, λ is the wavelength of the emitted radiation, λ_U is the length of the magnetic period of the undulator, and K_U is the undulator parame-

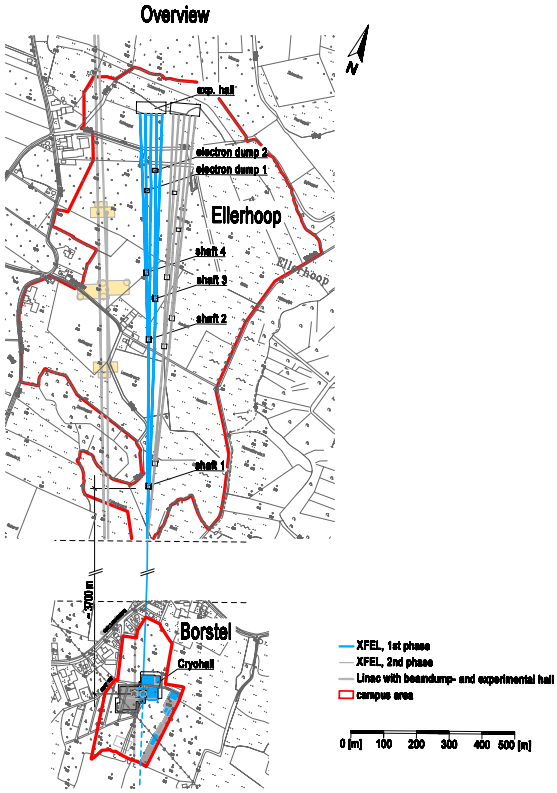

Figure 3. The TESLA XFEL campus North-West of the DESY laboratory[26], whose commissioning is expected in 2010. The XFEL electron beam is accelerated by a dedicated 20 GeV linear accelerator (linac) starting at a supply hall ≈ 4 km south of the XFEL laboratory. The XFEL linac tunnel runs under a small angle of 2° with respect to the tunnel of the future TESLA linac, which is shown in grey color.

ter,

$$K_{\mathrm{U}} = \frac{e\lambda_{\mathrm{U}} B_{\mathrm{U}}}{2\pi m_e c}\,, \tag{5}$$

which gives the ratio between the average deflection angle of the electrons in the undulator magnetic field B_{U} from the forward direction and the typical opening cone of the synchrotron radiation. The undulator parameter should be of order one on resonance. The electrons in the developing micro bunches eventually radiate coherently – the gain in radiation power P,

$$P \propto e^2\, N_e^2\, B_{\mathrm{U}}^2\, \gamma^2\,, \tag{6}$$

over the one from incoherent spontaneous synchrotron radiation ($P \propto N_e$) being proportional to the number $N_e \geq 10^9$ of electrons in a bunch (cf. Fig. 2) – and the number of emitted photons grows exponentially until saturation is reached. The radiation has a high power, short pulse length, narrow bandwidth, is fully polarized, transversely coherent, and has a tunable wavelength.

The concept of using a high energy electron linear accelerator for building an X-ray FEL was first proposed for the Stanford Linear Accelerator[22]. The LCLS at SLAC is expected to provide the first X-ray laser beams in 2008. The feasibility of a single-pass FEL operating in the SASE mode has been demonstrated recently down to a wavelength of 80 nm using electron bunches of high charge density and low emittance from the linear accelerator at the TESLA test facility (TTF) at DESY[38] (cf. Fig. 2). Some characteristics of the radiation from the planned X-ray FELs at the TESLA XFEL laboratory[26] (cf. Fig. 3), whose commissioning is expected in 2010, are listed in Table 1.

Table 1. Properties of X-ray FELs at the TESLA XFEL laboratory.

	unit	SASE 1	SASE 3	SASE 5
wavelength	nm	$0.1 \div 0.5$	$0.1 \div 0.24$	$0.4 \div 5.8$
bandwidth (FWHM)	%	0.08	0.08	$0.29 \div 0.7$
peak power	GW	37	22	$110 \div 200$
average power	W	210	125	$610 \div 1100$
photon beam size (rms)	μm	43	53	$25 \div 38$
peak power density	W/m^2	$6 \cdot 10^{18}$	$3 \cdot 10^{18}$	$6 \cdot 10^{19}$

3. Semi-classical Rate Estimates

We now turn to the main subject of our contribution, namely the spontaneous pair production at the focus of future X-ray FELs. We will elaborate in this section on a simplified approximation concerning the electromagnetic field of the laser radiation which retains the main features of the general case but nevertheless allows to obtain final expressions for the pair production rate in closed form. This should be sufficient for an order-of-magnitude estimate of critical parameters to be aimed at to get an observable effect.

It is well known that no pairs are produced in the background of a light-like static, spatially uniform electromagnetic field[2], characterized invariantly by

$$\mathcal{F} \equiv \frac{1}{4} F_{\mu\nu} F^{\mu\nu} \equiv -\frac{1}{2} (\mathbf{E}^2 - c^2 \mathbf{B}^2) = 0 \,, \tag{7}$$

Table 2. Laser parameters and derived quantities relevant for estimates of the rate of spontaneous e^+e^- pair production. The column labeled "Optical" lists parameters which are typical for a petawatt-class (1 PW = 10^{15} W) optical laser, focused to the diffraction limit, $\sigma = \lambda$. The column labeled "Design" displays design parameters of the planned X-ray FELs at DESY (Table 1). Similar values apply for LCLS. The column labeled "Focus: Available" shows typical values which can be achieved with present day methods of X-ray focusing: It assumes that the X-ray FEL X-ray beam can be focused to a rms spot radius of $\sigma \simeq 21$ nm with an energy extraction efficiency of 1 %. The column labeled "Focus: Goal" shows parameters which are theoretically possible by increasing the energy extraction of LCLS (by the tapered undulator technique) and by a yet unspecified method of diffraction-limited focusing of X-rays.

Laser Parameters				
	Optical	**X-ray FEL**		
	Focus: Diffraction limit	Design	Focus: Available	Focus: Goal
λ	1 μm	0.4 nm	0.4 nm	0.15 nm
$\hbar\omega = \frac{hc}{\lambda}$	1.2 eV	3.1 keV	3.1 keV	8.3 keV
P	1 PW	110 GW	1.1 GW	5 TW
σ	1 μm	26 μm	21 nm	0.15 nm
$\triangle t$	500 fs ÷ 20 ps	0.04 fs	0.04 fs	0.08 ps
Derived Quantities				
$S = \frac{P}{\pi\sigma^2}$	3×10^{26} $\frac{\mathrm{W}}{\mathrm{m}^2}$	5×10^{19} $\frac{\mathrm{W}}{\mathrm{m}^2}$	8×10^{23} $\frac{\mathrm{W}}{\mathrm{m}^2}$	7×10^{31} $\frac{\mathrm{W}}{\mathrm{m}^2}$
$\mathcal{E} = \sqrt{\mu_0\, c\, S}$	4×10^{14} $\frac{\mathrm{V}}{\mathrm{m}}$	1×10^{11} $\frac{\mathrm{V}}{\mathrm{m}}$	2×10^{13} $\frac{\mathrm{V}}{\mathrm{m}}$	2×10^{17} $\frac{\mathrm{V}}{\mathrm{m}}$
$\mathcal{E}/\mathcal{E}_c$	3×10^{-4}	1×10^{-7}	1×10^{-5}	0.1
$\frac{\hbar\omega}{m_e c^2}$	2×10^{-6}	0.006	0.006	0.02
$\eta = \frac{\hbar\omega}{e\,\mathcal{E}\lambda_c}$	9×10^{-3}	6×10^{4}	5×10^{2}	0.1

$$\mathcal{G} \equiv \frac{1}{4}\, F_{\mu\nu}\tilde{F}^{\mu\nu} \equiv c\,\mathbf{E}\cdot\mathbf{B} = 0\,, \tag{8}$$

where $F^{\mu\nu}$ is the electromagnetic field strength tensor and $\tilde{F}^{\mu\nu} = (1/2)\,\epsilon^{\mu\nu\alpha\beta}F_{\alpha\beta}$ its dual. It has been argued that fields produced by focusing laser beams are very close to such a light-like electromagnetic field, leading to an essential suppression of pair creation[12]. Yet, in a focused wave there are regions near the focus where $\mathcal{F} < 0$ and pair production is possible[9,27]. For other fields, $\mathcal{F}$ and $\mathcal{G}$ do not vanish, and pair production becomes possible, unless $\mathcal{G} = 0$, $\mathcal{F} > 0$, corresponding to a pure magnetic field in an appropriate coordinate system[2]. In particular, one expects pair creation in the background of a spatially uniform electric field oscillating with a frequency ω, say

$$\mathbf{E}(t) = (0, 0, \mathcal{E}\cos(\omega t))\,, \qquad \mathbf{B}(t) = (0, 0, 0)\,, \tag{9}$$

which has $\mathcal{G} = 0$, $\mathcal{F} < 0$. As emphasized in Refs.[13,15,16,28], such a field may

be created in an antinode of the standing wave produced by a superposition of two coherent laser beams with wavelength

$$\lambda = \frac{2\pi c}{\omega}\,, \tag{10}$$

and, indeed, it may be considered as spatially uniform at distances much less than the wavelength.

Thus, for definiteness, we assume that every X-ray laser pulse is split into two equal parts and recombined to form a standing wave with locations where the electromagnetic field has the form (9) and where the peak electric field is given by Eq. (2). Alternatively, one may consider pair creation in the overlap region of two lasers, whose beams make a fixed angle to each other[19]. Furthermore, we assume that the field amplitude $\mathcal{E}$ is much smaller than the critical field, and the photon energy is much smaller than the rest energy of the electron,

$$\mathcal{E} \ll \mathcal{E}_c\,, \qquad \hbar\omega \ll m_e c^2\,; \tag{11}$$

conditions which are well satisfied at realistic X-ray lasers (cf. Table 2). Under these conditions, it is possible to compute the rate of e^+e^- pair production in a semi-classical manner, using generalized WKB or imaginary-time (instanton) methods[10,11,18,19,39]. Here, the ratio η of the energy of the laser photons over the work of the field on a unit charge e over the Compton wavelength of the electron,

$$\eta = \frac{\hbar\omega}{e\mathcal{E}\lambda\!\!\!^{-}_e} = \frac{\hbar\,\omega}{m_e c^2}\,\frac{\mathcal{E}_c}{\mathcal{E}} = \frac{m_e c\,\omega}{e\,\mathcal{E}}\,, \tag{12}$$

plays the role of an adiabaticity parameter. Indeed, the probability that an e^+e^- pair is produced per unit time and unit volume,

$$w = \frac{\mathrm{d}\, n_{e^+e^-}}{\mathrm{d}^3x\,\mathrm{d}t}\,, \tag{13}$$

depends on the laser frequency only through the adiabaticity parameter η and reads, in the limiting cases of small and large η, as follows[32,35]

$$w \simeq \frac{c}{4\,\pi^3 \lambda\!\!\!^{-}_e{}^4} \times \tag{14}$$

$$\times \begin{cases} \frac{\sqrt{2}}{\pi}\left(\frac{\mathcal{E}}{\mathcal{E}_c}\right)^{\frac{5}{2}} \exp\left[-\pi\,\frac{\mathcal{E}_c}{\mathcal{E}}\left(1-\frac{1}{8}\eta^2+\mathcal{O}(\eta^4)\right)\right]\,, & :\eta \ll 1\,, \\ \sqrt{\frac{\pi}{2}}\left(\frac{\hbar\,\omega}{m_e c^2}\right)^{\frac{5}{2}} \sum_{n>2\frac{m_e c^2}{\hbar\omega}} \left(\frac{\mathrm{e}}{4\eta}\right)^{2n} \mathrm{e}^{-2\left(n-2\frac{m_e c^2}{\hbar\omega}\right)} \times & \\ \times\, \mathrm{Erfi}\left(\sqrt{2\left(n-2\frac{m_e c^2}{\hbar\omega}\right)}\right) & :\eta \gg 1\,, \end{cases}$$

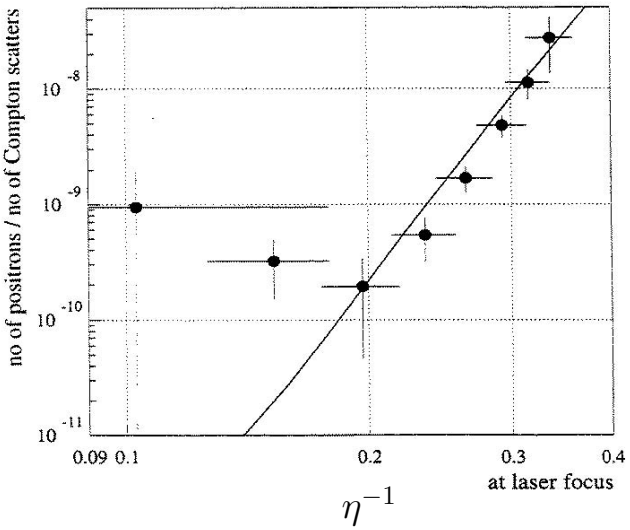

Figure 4. The positron rate per laser shot as a function of the inverse of the adiabaticity parameter, η^{-1}, as measured by the SLAC experiment E-144[40]. The line is a power law fit to the data which gives $R_{e+} \propto \eta^{-2n}$, with $n = 5.1 \pm 0.2\,(\text{stat})^{+0.5}_{-0.8}\,(\text{syst})$.

where Erfi is the imaginary error function. This result agrees in the adiabatic high-field, low-frequency limit, $\eta \ll 1$, with the non-perturbative Schwinger result[2] for a static, spatially uniform field, if a proper average over an oscillation period is made. In the non-adiabatic low-field, high-frequency limit, $\eta \gg 1$, on the other hand, it resembles a perturbative result: it corresponds to the $\geq n$-th order perturbation theory, n being the minimum number of quanta required to create an e^+e^- pair: $n \gtrsim 2\, m_e c^2/(\hbar\omega) \gg 1$.

At this point it seems appropriate to discuss the question whether – as argued in Ref.[27] – the non-perturbative Schwinger pair creation mechanism has already been demonstrated by the SLAC experiment E-144[40]. This experiment studied positron production in the collision of 46.6 GeV/c electrons with terawatt optical ($\lambda = 527$ μm) laser pulses. In the rest frame of the incident electrons, an electrical field strength of about 38 % of the critical field (1), $\mathcal{E} \simeq 5 \cdot 10^{17}$ V/m, was reached. The values of the adiabaticity parameter η probed were therefore in the range $\eta \simeq 3 \div 10$ (cf. Fig. 4), i.e. in the non-adiabatic, perturbative multi-photon regime. Correspondingly, in Refs.[40,41] the data were convincingly interpreted in terms of

multi-photon light-by-light scattering. Indeed, the observed positron production rate scales as $R_{e^+} \propto \eta^{-10}$ (cf. Fig. 4). This is in good agreement with the fact that the rate of perturbative multi-photon reactions involving n laser photons is proportional to η^{-2n} for $\eta \gg 1$, Eq. (14), and with the kinematic requirement that five photons are needed to produce a pair near threshold.

For an X-ray laser ($\hbar\omega \simeq 1 \div 10$ keV), the adiabatic, non-perturbative, strong field regime, $\eta \lesssim 1$, starts to apply for $\mathcal{E} \gtrsim \hbar\omega\, \mathcal{E}_c/(m_e c^2) \sim 10^{15\div 16}$ V/m (cf. Eq. (12)). An inspection of the rate (14) leads then to the conclusion that one needs an electric field of about $0.1\,\mathcal{E}_c \sim 10^{17}$ V/m in order to get an appreciable amount of spontaneously produced e^+e^- pairs[32]. To this end one needs either a terawatt X-ray or a tens of exawatt optical laser.

In Table 2 we have summarized the relevant parameters for the planned X-ray FELs[32]. We conclude that the power densities and electric fields which can be reached with presently available technique (column labeled "Focus: Available" in Table 2) are far too small for a sizeable effect. On the other hand, if the energy extraction can be improved considerably, such that the peak power of the planned X-ray FELs can be increased to the terawatt region, and if X-ray optics can be improved[42] to approach the diffraction limit of focusing, leading to a spot size in the 0.1 nanometer range, then there is ample room (c. f. column labeled "Focus: Goal" in Table 2) for an investigation of the Schwinger pair production mechanism at X-ray FELs. At the moment it is hard to predict whether this goal will be reached before the commissioning of exawatt-zettawatt optical lasers[43].

4. Quantum Kinetic Studies

More information about the details of the Schwinger mechanism accessible at the focus of an X-ray laser can be obtained via approaches based on quantum kinetics. In Refs.[33,34], quantum Vlasov equations, derived within a mean-field treatment of QED[44], were employed to obtain a description of the time evolution of the momentum distribution function for the particles produced via vacuum decay in the background of a spatially uniform external electric field of the form (9). It was found that – for realistic laser parameters (cf. Table 2) – pair production will occur in cycles that proceed in tune with the laser frequency (cf. Fig. 5). The peak density of produced pairs, however, is frequency independent, with the consequence that several hundred pairs could be produced per laser period, in accord with the

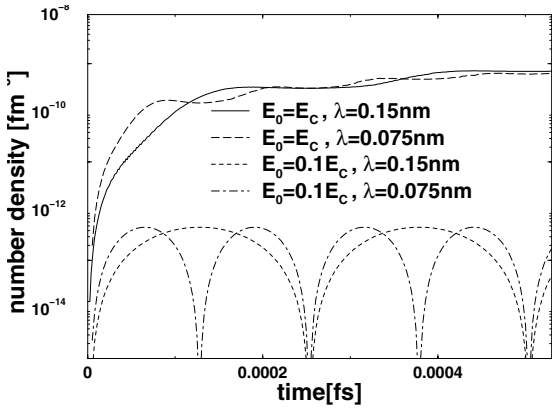

Figure 5. Time evolution of the number density of produced e^+e^- pairs at the focus of an X-ray laser[33]. In strong fields, particles accumulate, leading to the almost complete occupation of available momentum states. In weak fields, repeated cycles of particle creation and annihilation occur in tune with the laser frequency.

Schwinger rate. For even higher peak electric fields, $\mathcal{E} \gtrsim 0.25\,\mathcal{E}_c$ – possibly achievable at a 9 TW X-ray FEL (cf. Table 2) – particle accumulation and the consequent formation of a plasma of spontaneously produced pairs is predicted[34] (cf. Fig. 6). The evolution of the particle number in the plasma will exhibit then non-Markovian aspects, and the plasma's internal currents will generate an electric field whose interference with that of the laser leads to plasma oscillations[34]. This feature persists even if – in distinction to Refs.[33,34] – one takes into account collision terms in the quantum Vlasov equations[45].

5. Conclusions

We have considered the possibility to study non-perturbative spontaneous e^+e^- pair creation from vacuum for the first time in the laboratory. We have seen that for this application still some improvement in X-ray FEL technology over the presently considered design parameters is necessary. Intensive development in technical areas, particularly in that of X-ray optics, will be needed in order to achieve the required ultra-high power densities. It should be pointed out, however, that even though progress to achieve such a demanding goal is rather slow and laborious, the rewards that may be gained in this unique regime are so extraordinary that looking into TESLA XFEL's or LCLS's extension to this regime merits serious considerations.

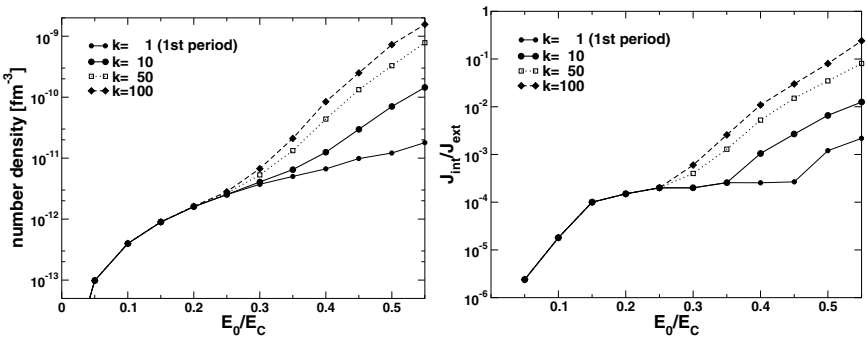

Figure 6. *Left:* Peak particle number density versus laser field strength[34]. The qualitative change at $E_0 \approx 0.25\, E_c$ marks the onset of particle accumulation. *Right:* Internal to external peak current ratio[34]: field-current feedback becomes important for $E_0 \gtrsim 0.25\, E_c$.

No doubt, there will be unprecedented opportunities to use these intense X-rays in order to explore some issues of fundamental physics that have eluded man's probing so far.

References

1. F. Sauter, Z. Phys. **69**, 742 (1931); W. Heisenberg and H. Euler, Z. Phys. **98**, 714 (1936).
2. J. Schwinger, Phys. Rev. **82**, 664 (1951).
3. S. W. Hawking, Nature **248**, 30 (1974); Commun. Math. Phys. **43**, 199 (1975); T. Damour and R. Ruffini, Phys. Rev. D **14**, 332 (1976); G. W. Gibbons and M. J. Perry, Proc. Roy. Soc. Lond. **358**, 467 (1978); S. P. Gavrilov and D. M. Gitman, Phys. Rev. D **53**, 7162 (1996); M. K. Parikh and F. Wilczek, Phys. Rev. Lett. **85**, 5042 (2000).
4. T. Damour and R. Ruffini, Phys. Rev. Lett. **35**, 463 (1975).
5. G. Preparata, R. Ruffini and S. S. Xue, Astron. Astrophys. **338**, L87 (1998); J. Korean Phys. Soc. **42**, S99 (2003); R. Ruffini, C. L. Bianco, P. Chardonnet, F. Fraschetti, L. Vitagliano and S. S. Xue, astro-ph/0302557; L. Vitagliano, these proceedings; S. S. Xue, these proceedings.
6. A. Casher, H. Neuberger, and S. Nussinov, Phys. Rev. D **20**, 179 (1979); B. Andersson, G. Gustafson, G. Ingelman, and T. Sjöstrand, Phys. Rept. **97**, 31 (1983); T. S. Biro, H. B. Nielsen, and J. Knoll, Nucl. Phys. B **245**, 449 (1984).
7. L. Parker, Phys. Rev. **183**, 1057 (1969); N. D. Birrell and P. C. Davies, *Quantum Fields in Curved Space* (Cambridge University Press, 1982).
8. W. Greiner, B. Müller, and J. Rafelski, *Quantum Electrodynamics of Strong Fields* (Springer-Verlag, Berlin, 1985); A. A. Grib, S. G. Mamaev, and V. M. Mostepanenko, *Vacuum Quantum Effects in Strong Fields* (Atomiz-

dat, Moscow, 1988; Friedmann Laboratory Publishing, St. Petersburg, 1994); E. S. Fradkin, D. M. Gitman, and Sh. M. Shvartsman, *Quantum Electrodynamics with Unstable Vacuum* (Springer-Verlag, Berlin, 1991).
9. F. V. Bunkin and I. I. Tugov, Dokl. Akad. Nauk Ser. Fiz. **187**, 541 (1969) [Sov. Phys. Dokl. **14**, 678 (1970)].
10. E. Brezin and C. Itzykson, Phys. Rev. D **2**, 1191 (1970).
11. V. S. Popov, Pisma Zh. Eksp. Teor. Fiz. **13**, 261 (1971) [JETP Lett. **13**, 185 (1971)]; V. S. Popov, Zh. Eksp. Teor. Fiz. **61**, 1334 (1971) [Sov. Phys. JETP **34**, 709 (1972)]. V. S. Popov, Pisma Zh. Eksp. Teor. Fiz. **18**, 435 (1973) [JETP Lett. **18**, 255 (1974)]; V. S. Popov, Yad. Fiz. **19**, 1140 (1974) [Sov. J. Nucl. Phys. **19**, 584 (1974)].
12. G. J. Troup and H. S. Perlman, Phys. Rev. D **6**, 2299 (1972).
13. V. S. Popov, Zh. Eksp. Teor. Fiz. **62**, 1248 (1972) [Sov. Phys. JETP **35**, 659 (1972)]; V. S. Popov and M. S. Marinov, Yad. Fiz. **16**, 809 (1972) [Sov. J. Nucl. Phys. **16**, 449 (1973)].
14. N. B. Narozhnyi and A. I. Nikishov, Zh. Eksp. Teor. Fiz. **65**, 862 (1973) [Sov. Phys. JETP **38**, 427 (1974)].
15. V. M. Mostepanenko and V. M. Frolov, Yad. Fiz. **19**, 885 (1974) [Sov. J. Nucl. Phys. **19**, 451 (1974)].
16. M. S. Marinov and V. S. Popov, Fortsch. Phys. **25**, 373 (1977).
17. J. I. Katz, Astrophys. J. Supp. **127**, 371 (2000).
18. G. Dunne and T. Hall, Phys. Rev. D **58**, 105022 (1998).
19. H. M. Fried, Y. Gabellini, B. H. McKellar, and J. Avan, Phys. Rev. D **63**, 125001 (2001).
20. Ya. B. Zel'dovich and V. S. Popov, Usp. Fiz. Nauk **105**, 403 (1971) [Sov. Phys. Usp. **14**, 673 (1972)]; B. Müller, J. Rafelski, and W. Greiner, Z. Phys. **257**, 62 (1972); *ibid.* **257**, 183 (1972).
21. W. Greiner and J. Reinhardt, in *Quantum Aspects of Beam Physics*, Proc. 15th Advanced ICFA Beam Dynamics Workshop, Monterey, Calif., 4-9 Jan 1998, ed. P. Chen (World Scientific, Singapore, 1998), p. 438.
22. J. Arthur *et al.* [LCLS Design Study Group Collaboration], SLAC-R-0521 (1998).
23. I. Lindau, M. Cornacchia and J. Arthur, in *Workshop On The Development Of Future Linear Electron-Positron Colliders For Particle Physics Studies And For Research Using Free Electron Lasers*, eds. G. Jarlskog, U. Mjörnmark and T. Sjöstrand (Lund University, 1999), pp. 153-161.
24. R. Brinkmann, G. Materlik, J. Rossbach and A. Wagner, Hamburg, Germany: DESY (1997) 1183 p. Hamburg DESY - DESY-97-048 (97/05,rec.Sep.) 1183 p. (ECFA 97-182).
25. G. Materlik and T. Wroblewski, in *Workshop On The Development Of Future Linear Electron-Positron Colliders For Particle Physics Studies And For Research Using Free Electron Lasers* , eds. G. Jarlskog, U. Mjörnmark and T. Sjöstrand (Lund University, 1999), pp. 39-58.
26. G. Materlik and T. Tschentscher, *TESLA: The superconducting electron positron linear collider with an integrated X-ray laser laboratory. Technical design report. Pt. 5: The X-ray free electron laser*, DESY-01-011; R. Brinkmann

et al., *TESLA XFEL: First stage of the X-ray laser laboratory. Technical design report, supplement*, DESY-02-167
27. A. C. Melissinos, in *Quantum Aspects of Beam Physics*, Proc. 15th Advanced ICFA Beam Dynamics Workshop, Monterey, Calif., 4-9 Jan 1998, ed. P. Chen (World Scientific, Singapore, 1998), p. 564.
28. P. Chen and C. Pellegrini, in *Quantum Aspects of Beam Physics*, Proc. 15th Advanced ICFA Beam Dynamics Workshop, Monterey, Calif., 4-9 Jan 1998, ed. P. Chen (World Scientific, Singapore, 1998), p. 571.
29. P. Chen and T. Tajima, Phys. Rev. Lett. **83**, 256 (1999).
30. T. Tajima, "Fundamental Physics with an X-Ray Free Electron Laser," to be published.
31. A. Ringwald, in Workshop on *Electromagnetic Probes of Fundamental Physics*, Erice, Sicily, Italy, 16-21 Oct 2001, hep-ph/0112254.
32. A. Ringwald, Phys. Lett. B **510**, 107 (2001).
33. R. Alkofer, M. B. Hecht, C. D. Roberts, S. M. Schmidt and D. V. Vinnik, Phys. Rev. Lett. **87**, 193902 (2001).
34. C. D. Roberts, S. M. Schmidt and D. V. Vinnik, Phys. Rev. Lett. **89**, 153901 (2002).
35. V. S. Popov, JETP Lett. **74**, 133 (2001) [Pisma Zh. Eksp. Teor. Fiz. **74**, 151 (2001)]; JETP **94**, 1057 (2002) [Zh. Eksp. Teor. Fiz. **121**, 1235 (2002)].
36. J. M. Madey, J. Appl. Phys. **42**, 1971 (1906).
37. A. M. Kondratenko and E. L. Saldin, Part. Accel. **10**, 207 (1980); R. Bonifacio, C. Pellegrini, and L. M. Narducci, Opt. Commun. **50**, 373 (1984).
38. J. Andruszkow *et al.* [TESLA Collaboration], Phys. Rev. Lett. **85**, 3825 (2000).
39. S. P. Kim and D. N. Page, Phys. Rev. D **65**, 105002 (2002).
40. D. L. Burke *et al.*, Phys. Rev. Lett. **79**, 1626 (1997).
41. C. Bamber *et al.*, Phys. Rev. D **60**, 092004 (1999).
42. J. B. Hastings *et al.*, "X-ray Laser Physics", in *LCLS – The First Experiments* (September 2000).
43. T. Tajima and G. Mourou, Phys. Rev. ST Accel. Beams **5**, 031301 (2002); T. Esirkepov, S. Bulanov and T. Tajima, these proceedings.
44. S. A. Smolyansky, G. Röpke, S. M. Schmidt, D. Blaschke, V. D. Toneev and A. V. Prozorkevich, hep-ph/9712377; S. M. Schmidt, D. Blaschke, G. Röpke, S. A. Smolyansky, A. V. Prozorkevich and V. D. Toneev, Int. J. Mod. Phys. E **7**, 709 (1998); Y. Kluger, E. Mottola and J. M. Eisenberg, Phys. Rev. D **58**, 125015 (1998); J. C. Bloch, C. D. Roberts and S. M. Schmidt, Phys. Rev. D **61**, 117502 (2000).
45. R. Ruffini, L. Vitagliano and S. S. Xue, Phys. Lett. B **559**, 12 (2003); S. S. Xue, these proceedings.

UNRUH EFFECT AS PARTICULAR FRENET SERRET VACUUM RADIATION AND DETECTION PROPOSALS

HARET C. ROSU

Applied Mathematics and Computational Systems
Potosinian Institute of Scientific and Technological Research
Apdo Postal 3-74 Tangamanga, San Luis Potosí, SLP, Mexico

The paradigmatic Unruh radiation is an ideal and simple case of stationary scalar vacuum radiation patterns related to worldlines defined as Frenet-Serret curves. We briefly review the corresponding body of theoretical literature as well as the proposals that have been suggested to detect these types of quantum field radiation patterns.

1. Frenet-Serret Worldlines and Vacuum Radiation Patterns

A thermal radiation effect due to vacuum oscillations in quantum field theory has been discussed by Unruh in 1976,[1] using the so-called *detector method*. This was based on the first order perturbation calculation of the excitation rate of a quantum particle considered as a two-level field detector around its classical trajectory. Slightly earlier, Davies obtained a similar result using a *mirror model*,[2] that implies the calculation of the Bogoliubov coefficient β, like in particle production in astrophysics and cosmology. A 'thermodynamic' temperature, $T_V = \frac{\hbar}{2\pi c k_B} \cdot a$, directly proportional to the proper linear acceleration a is the main feature of this vacuum radiation pointing to a new universal quantum field thermal effect. Moreover, a direct link to the Hawking radiation in black hole physics could be thought of through the equivalence principle. On the other hand, in a little noticed paper of 1981, Letaw [3] studied by means of Frenet-Serret tetrads and the same detector method the stationary world lines on which relativistic quantum particles with a linear coupling to the scalar vacuum have time-independent excitation spectra. These worldlines are characterized by the requirement that the geodetic interval between two points depends only on the proper time interval. Letaw employed a generalization of the Frenet-Serret equations to the four-dimensional Minkowski space in which the worldlines are characterized by the curvature κ and two torsions τ_1 and τ_2 instead of a single one as in the common three-dimensional space. Mathematically, this means a change of dimension of the antisymmetric matrix of curvature

invariants

$$\begin{pmatrix} 0 & \kappa & 0 \\ -\kappa & 0 & \tau \\ 0 & -\tau & 0 \end{pmatrix} \Longrightarrow \begin{pmatrix} 0 & -\kappa(s) & 0 & 0 \\ \kappa(s) & 0 & -\tau_1(s) & 0 \\ 0 & \tau_1(s) & 0 & -\tau_2(s) \\ 0 & 0 & \tau_2(s) & 0 \end{pmatrix} , \tag{1}$$

where s is the proper time parameter along the classical Frenet-Serret trajectory. Not surprisingly, the curvature invariants are the proper acceleration and angular velocity of the world line. Solving the generalized Frenet-Serret equations for the simple case of constant invariants leads to six classes of stationary world lines. He also demonstrated the equivalence of the timelike Killing vector field orbits and the stationary world lines. Last but not least, Letaw did some calculations of the vacuum excitation spectra of detectors on the sample of six families of stationary world lines, i.e., of the following cosine Fourier transform

$$S(E,\tau) = 2\pi\rho(E)\int_{-\infty}^{0} ds\langle 0|\phi(x(\tau))\phi(x(\tau+s))|0\rangle\cos(Es) , \tag{2}$$

E is the energy difference between the two levels of the particle considered as detector of the vacuum spectra, $\rho(E)$ is the density of states of the detected vacuum 'quasiparticles', and $\langle 0|\phi(x(\tau))\phi(x(\tau+s))|0\rangle$ is the expectation value of the Wightman autocorrelation function in the ground state of the particle. Letaw's work is a generalization of Unruh's result concerning the excitation of a scalar particle detector moving with constant linear acceleration in the vacuum of flat spacetime. Unruh's result became famous because of Unruh's interpretation that the detector behaves as if in contact with a bath of scalar 'particles' with energies in a Planck spectrum of temperature proportional to $a/2\pi$ ($\hbar\,, c\,, k_B = 1$). The connection with the Hawking radiation and its paradigmatic nature led many theoretical physicists to focus on Unruh's effect and there is a strong need for an experimental confirmation of the effect as a consequence of long debate.[4] It is the main goal of this short survey to present the ideas that have been generated over the years in this respect.

1.1. *The Six Stationary Scalar Frenet-Serret Radiation Spectra*

We quote here those vacuum excitation spectra $S(E,\tau)$ that are independent of proper time τ, i.e., stationary.

1. Inertial (uncurved) worldlines $\quad \kappa = \tau_1 = \tau_2 = 0$

$S_0(E) = \frac{E^3}{4\pi^2}$.

The interpretation is a normal vacuum spectrum, i.e., as given by a vacuum of zero point energy per mode $E/2$ and density of states $E^2/2\pi^2$.

2. Hyperbolic worldlines $\quad \kappa \neq 0$, $\tau_1 = \tau_2 = 0$

$S_\kappa(\epsilon_\kappa) = \frac{\epsilon_\kappa^3}{2\pi^2(e^{2\pi\epsilon_\kappa}-1)}$.

This is the unique noninertial case that is torsionless. The employed variable is $\epsilon_\kappa = E/\kappa$.The excitation spectrum is Planckian allowing the interpretation of $\kappa/2\pi$ as 'thermodynamic' temperature.

3. Ultratorsional (helical) worldlines $\quad |\kappa| < |\tau_1| \neq 0,\ \tau_2 = 0,\ \rho^2 = \tau_1^2 - \kappa^2$

$$S^{\rm u}_{\tau_1}(\epsilon_\rho) \overset{\kappa/\rho\to\infty}{\longrightarrow} S^{\rm p}_{\tau_1}(\epsilon_\kappa)\ .$$

The excitation spectrum is an analytic function corresponding to the case 4 below only in the limit $\kappa \gg \rho$. Letaw plotted the numerical integral for $S^{\rm u}_{\tau_1}(\epsilon_\rho)$, where $\epsilon_\rho = E/\rho$ for various values of κ/ρ.

4. Paratorsional (semicubical parabolic) worldlines $\quad \kappa = \tau_1 \neq 0,\ \tau_2 = 0$

$$S^{\rm p}_{\tau_1}(\epsilon_\kappa) = \tfrac{\epsilon_\kappa^2}{8\pi^2\sqrt{3}} e^{-2\sqrt{3}\epsilon_\kappa}\ .$$

The excitation spectrum is analytic, and since there are two equal curvature invariants one can use the dimensionless energy variable ϵ_κ. It is worth noting that $S^{\rm p}_{\tau_1}$, being a monomial times an exponential, is quite close to the Wien-type spectrum $S_W \propto \epsilon^3 e^{-{\rm const.}\epsilon}$.

5. Infratorsional (catenary) worldlines $\quad |\kappa| > |\tau_1| \neq 0,\ \tau_2 = 0,\ \sigma^2 = \kappa^2 - \tau_1^2$

$$S_\kappa(\epsilon_\kappa) \overset{0\leftarrow\tau/\sigma}{\longleftarrow} S^{\rm i}_{\tau_1}(\epsilon_\sigma) \overset{\tau/\sigma\to\infty}{\longrightarrow} S^{\rm p}_{\tau_1}(\epsilon_\kappa).$$

In general, the catenary spectrum cannot be found analytically. It is an intermediate case, which for $\tau/\sigma \to 0$ tends to S_κ, whereas for $\tau/\sigma \to \infty$ tends toward $S^{\rm p}_{\tau_1}$.

6. Hypertorsional (variable pitch helicoid) worldlines $\quad \tau_2 \neq 0$

S_{τ_2} is not analytic.

The hypertorsional worldlines are rotating with constant $a_\perp$ to the rotation plane. The excitation spectrum is given in this case by a two-parameter set of curves. These trajectories are a superposition of the constant linearly accelerated motion and uniform circular motion. According to Letaw, the spatial path of a two-level detector on this world line is helicoid of variable pitch that decreases to zero at proper time interval $\tau = 0$ and increases thereafter. The corresponding vacuum spectra have not been calculated by Letaw, not even numerically.

1.2. *Conclusions from the stationary scalar cases*

Examining the six scalar stationary cases we see that only the hyperbolic worldlines, having just one nonzero curvature invariant, allow for a Planckian excitation spectrum and lead to a strictly one-to-one mapping between the curvature invariant κ and the 'thermodynamic' temperature ($T_\kappa = T_V = \kappa/2\pi$). The excitation spectrum due to semicubical parabolas can be fitted by Wien type spectra, the

radiometric parameter corresponding to both curvature and torsion. The other stationary cases, being nonanalytical, lead to approximate determination of the curvature invariants, defining locally the classical worldline on which a relativistic quantum particle moves. This explains why the Unruh effect became so prominent with regard to the other five types of stationary Frenet-Serret scalar spectra.

For the important case of electromagnetic vacuum fluctuations the FS formalism has not been used in a direct way. However, Hacyan and Sarmiento [6] developed a procedure by which they provided nonanalytic formulas (cosine Fourier transform integrals) for the spectral energy density, flux density, and stress density of the vacuum radiation in terms of the electromagnetic Wightman functions calculated by means of the two Killing vectors associated to circular trajectories.

2. Detection Proposals

Because the curvature thermodynamic temperature is given by $T_\kappa = \frac{\hbar}{2\pi ck}\, a$ this leads to $T_\kappa = 4 \cdot 10^{-23}\, a$ and one needs accelerations greater than $10^{20} g_\oplus$ to have 'thermal' effects of only a few Kelvin degrees. On the other hand, one should focus below the Schwinger acceleration for copious spontaneous pair creation out of QED vacuum, $a_{\rm Schw} \approx m_e c^3/\hbar \approx 10^{29}\ m/s^2 \approx 10^{28}\ g_\oplus$. Thus the optimal range for detecting a possible Unruh effect entails eight orders of magnitude in proper acceleration

$$10^{20} g_\oplus \leq a \leq 10^{28}\ g_\oplus\ , \tag{3}$$

There are indeed several physical settings (for reviews, see [5]) in which accelerations can be achieved only a few orders below the Schwinger acceleration and forthcoming technological advances could test routinely those acceleration scales. The Unruh effect, if it exists, can be revealed as a tiny thermal-like signal in the background of by far more powerful effects.

The following is the list of proposals.

2.1. *Unruh Effect in Storage Rings* ($a \sim 10^{22} g_\oplus$, $T_\kappa = 1200\, K$)

J.S. Bell and J.M. Leinaas imagined the first laboratory phenomenon connected to the Unruh effect. During 1983-1987 they published a number of papers on the idea that the depolarising effects in electron storage rings could be interpreted in terms of Unruh effect.[7]However, the incomplete radiative polarization of the electrons in storage rings has been first predicted in early sixties by Sokolov and Ternov,[8] as an effect due to the spin-flip synchrotron radiation in the framework of QED. Their approach successfully provides the observed maximum polarization of electrons at storage rings, $P_{max} = \frac{8\sqrt{3}}{15} = 0.924$.[11] Besides, the circular vacuum noise is not sufficiently "universal" since it always depends on both acceleration and velocity. This appears as a 'drawback' of the *storage ring electron radiometry*,[12] not to mention the very intricate spin physics.

The polarization calculated by Bell and Leinaas is very similar in shape to a formula for the polarization as a function of the electron gyromagnetic factor g obtained by Derbenev and Kondratenko,[9] in 1973 that is considered the standard QED accelerator result for the polarization of beams. Their function $P_{DK}(g)$ is a combination of exponential and polynomial terms in the anomalous part of the gyromagnetic factor of the electron. Barber and Mane [10] have shown that the DK and BL formalisms for the equilibrium degree of radiative electron polarization are not so different as they might look. They also obtained an even more general formula for the equilibrium polarization than the DK and BL ones and from their formula they estimated as negligible the differences between them.

Recently, the spin-flip synchrotron radiation has been experimentally shown to be important in the hard part of the spectrum in the axial channeling of electrons in the energy range 35-243 GeV incident on a W single crystal.[13] This may revive the interest in the BL interpretation, especially in the cleaner planar channeling case.[14]

One can also recall that K.T. McDonald applied the Unruh temperature formula for a rapid calculation of the damping in a linear focusing channel.[15] This is a transport system at accelerators that confines the motion of charged particles along straight central rays by means of a potential quadratic in the transverse spatial coordinates. He used the same idea about two decades ago to reproduce Sands' results on the limits of damping of the phase volume of beams in electron storage rings.

2.2. *Unruh Effect and the Physics of Traps* ($a \sim 10^{21} g_{\oplus}$, $T_{\kappa} = 2.4\,K$)

The very successful and precise physics of traps could help detecting the circular thermal-like vacuum noise. The proposal belongs to J. Rogers [16] being one of the most attractive. The idea of Rogers is to place a small superconducting Penning trap in a microwave cavity. A single electron is constrained to move in a cyclotron orbit around the trap axis by a uniform magnetic field (Rogers' figure is B = 150 kGs). The circular proper acceleration is $a = 6 \times 10^{21} g_{\oplus}$ corresponding to T = 2.4 K. The velocity of the electron is maintained fixed ($\beta = 0.6$) by means of a circularly polarized wave at the electron cyclotron frequency, compensating also for the irradiated power. The static quadrupole electric field of the trap creates a quadratic potential well along the trap axis in which the electron oscillates. The axial frequency is 10.5 GHz (more than 150 times the typical experimental situation [17]) for the device scale chosen by Rogers. This is the measured frequency since it is known that the best way of observing the electron motion from the outside world is through the measurement of the current due to the induced charge on the cap electrodes of the trap, as a consequence of the axial motion of the electron along the symmetry axis.[17] At 10.5 GHz the difference in energy densities between the circular electromagnetic vacuum noise and the universal linear scalar noise are negligible (see Fig. 2 in Rogers' work). Even better experimental setups in this context could be

electrons in cylindrical Penning traps with the trap itself representing the microwave cavity.[18]

2.3. *Unruh Effect and Nonadiabatic Casimir Effect* ($a \sim 10^{20} g_{\oplus}$, $T \sim 1\,K$)

Yablonovitch,[19] proposed a *plasma front* as an experimental equivalent of a *fast moving mirror*. Plasma fronts can be created when a gas is suddenly photoionized. The argument is that the phase shift of the zero-point electromagnetic field transmitted through a plasma window whose index of refraction is falling with time (from 1 to 0) is the same as when reflected from an accelerating mirror. Consider the case of hyperbolic motion. Since the velocity is

$$v = c \tanh(a\tau/c) \tag{4}$$

where τ is the observer's proper time, the Doppler shift frequency will be

$$\omega_D = \omega_0 \sqrt{\frac{1 - v/c}{1 + v/c}} = \omega_0 \exp(-a\tau/c) \tag{5}$$

and consequently a plane wave of frequency ω_0 turns into a wave with a time-dependent frequency. Such waves are called chirped waves in nonlinear optics and acoustics. Eq. (5) represents an *exponential chirping* valid also for Schwartzschild black holes with the substitution $a = c^4/4GM$ (G is Newton's constant and M is the mass parameter of the Schwarzschild black hole).

The technique of producing plasma fronts/windows in a gas by laser breakdown, and the associated frequency upshifting phenomena (there are also downshifts) of the electromagnetic waves interacting with such windows, are well settled since about twenty years. Blue shifts of about 10% have been usually observed in the transmitted laser photon energy.

In his paper, Yablonovitch works out a very simple model of a *linear* chirping due to a refractive index linearly decreasing with time, $n(t) = n_0 - \dot{n}t$, implying a Doppler shift of the form $\omega \rightarrow \omega[1 + \frac{\dot{n}}{n}t] \sim \omega[1 + \frac{a}{c}t]$. To have accelerations $a = 10^{20} g_{\oplus}$ the laser pulses should be less than 1 picosecond. Even more promising may be the nonadiabatic photoionization of a semiconductor crystal in which case the refractive index can be reduced from 3.5 to 0 on the timescale of the optical pulse. As discussed by Yablonovitch, the pump laser has to be tuned just below the Urbach tail of a direct-gap semiconductor in order to create weakly bound virtual electron-hole pairs. These pairs contribute a large reactive component to the photocurrent since they are readily polarized. The background is due to the bremsstrahlung emission produced by real electron-hole pairs, and to diminish it one needs a crystal with a big Urbach slope (the Urbach tail is an exponential behavior of the absorption coefficient).

In addition, Eberlein,[20] elaborated on Schwinger's interpretation of sonoluminescence in terms of zero point fluctuations and asserted that whenever *an interface*

between two dielectrics or a dielectric and the vacuum moves noninertially photons are created, i.e., the Unruh effect occurs. An interesting discussion in favor of "dielectric windows" rather than the "plasma window" is provided by Dodonov *et al.*[21] Moreover, Grishchuk, Haus, and Bergman,[22] discussed a nonlinear Mach-Zhender configuration to generate radiation through the optical squeezing of zero-point fluctuations interacting with a *moving index grating* that is also reminiscent of Unruh effect.

2.4. *Unruh Effect and Channeling* ($a \sim 10^{30} g_\oplus$, $T_\kappa \sim 10^{11}\, K$?)

Relativistic particles can acquire extremely high transverse accelerations when they are channeled through crystals. Darbinian and collaborators [23] related this physical setting to Unruh radiation.

The idea is to measure the *Unruh radiation emitted in the Compton scattering of the channeled particles with the Planck spectrum of the inertial crystal vacuum*. The main argument is that the crystallographic fields act with large transverse accelerations on the channeled particles. The estimated transverse proper acceleration for positrons channeled in the (110) plane of a diamond crystal is $a = 10^{25}\gamma$ cm/s^2, and at a $\gamma = 10^8$ one could reach 10^{33} cm/s^2 $= 10^{30} g_\oplus$. Working first in the particle instantaneous rest frame, Darbinian *et al* derived the spectral angular distribution of the Unruh photons in that frame. By Lorentz transformation to the lab system they got the number of Unruh photons per unit length of crystal and averaged over the channeling diameter. At about $\gamma = 10^8$ the Unruh intensity, i.e., the intensity per unit pathlength of the Compton scattering on the Planck vacuum spectrum becomes comparable with the Bethe-Heitler bremsstrahlung ($dN_\gamma/dE \propto 1/E$, and mean polar emission angle $\theta = 1/\gamma$).

Similar calculations have been applied by the same group,[24] to get an estimate of the Unruh radiation generated by TeV electrons in a uniform magnetic field as well as in a circularly polarized laser field but the conclusions are not optimistic because of the huge synchrotron background.

2.5. *Unruh Radiation and Ultraintense Lasers* ($a \sim 10^{25} g_\oplus$, $T_\kappa = 1.2\, 10^6\, K$)

A Unruh signal could be obtained in electron Petawatt-class laser interaction according to a proposal put forth by Chen and Tajima in 1999.[25] Uniform acceleration through the usual quantum vacuum (Minkowski vacuum) of the electromagnetic field distorts the two-point function of the zero-point fluctuations in such a way that

$$\langle E_i(-\tau/2) E_j(+\tau/2)\rangle = \frac{4\hbar}{\pi c^3}\, \delta_{ij}\, \frac{(a/c)^4}{\sinh^4(a\tau/2c)}\ . \tag{6}$$

The main point of Tajima and Chen is to introduce the so-called laser strength (ponderomotive) parameter $a_0 = \frac{eE_0}{mc\omega_0}$ in this formula and in all their estimations. They calculate the Unruh radiation based on the autocorrelation function in Eq. (6).

The accelerated electron is assumed "classical", i.e., with well-defined acceleration, velocity, and position. This allows to introduce a Lorentz transformation so that the electron is described in its instantaneous proper frame. In the words of Chen and Tajima "the electron reacts to the vacuum fluctuations with a nonrelativistic quivering motion in its proper frame" that triggers additional (Unruh) radiation besides the classical Larmor radiation.

The important claim of Chen and Tajima is that there is a blind spot in the Larmor angular distribution for azimuthal angle $\Delta\phi = 10^{-3}$ and polar angle $\Delta\theta \ll 1/a_0$ where the Unruh thermal-like signal could be revealed. Since at each half cycle the electron almost suddenly becomes relativistic, with constant $\gamma \sim a_0$, the Unruh radiation is boosted along the direction of polarization in the lab frame. Moreover, they showed that the autocorrelation function, and therefore the Unruh signal, tend to diminish more rapidly than that from Larmor within the laser half cycle. This should induce a sharper time structure for the former that could help its detection.

2.6. *Unruh Radiation in Quantum Optics* *(moderate a could work)*

This is a very recent proposal in several versions due to a Scully collaboration.[26] The idea is to enhance the thermal Unruh radiation signal from an accelerating He^+ ion used as a two-level type detector of transition frequency ω passing through a high Q "single mode" cavity of frequency ν in the vicinity of the atomic frequency ω. The enhancement is very significant, in the sense that for reasonable values of the parameters, the effective Boltzmann factor turns from the usual exponential behaviour to a linear dependence in $\alpha/2\pi\omega$, where $\alpha = a/c$. Employing quantum optics calculations, they showed that this type of Unruh effect is due to nonadiabatic transitions stemming from the counter-rotating term $\hat{a}_k^+\hat{\sigma}^+$ in the time-dependent atom-field interaction Hamiltonian. The Larmor radiation lobes ($\sim \sin^2\theta$) will certainly be present but the blind spot in the forward direction of motion could be hopefully used for the detection of this nonadiabatic thermal effect.

3. Conclusion

Although the Unruh radiative effect is interpreted as a thermal effect of the noninertially and nonadiabatically-produced vacuum state, its thermal features are quite distinct of the usual thermal thermodynamics effects. For example, it is a highly correlated state with EPR-type correlations,[27] and not a thermal uncorrelated state as the equilibrium states in statistical thermodynamics. Some of the most feasible proposals are related to nonadiabatic conditions (i.e., capable of producing very rapid oscillations) for those cases in which the nonadiabaticity parameter depends on the proper acceleration. It is only for this reason that an association with Unruh's effect is mentioned. A direct detection of the scalar vacuum spectra has not been proposed so far. It requires noninertial propagation of a source such as a dislocation or a vortex through the corresponding phonon medium. For more details the interested reader can look at the extended version in electronic preprint form.[28]

Acknowledgements

The author very much appreciates the invitation of Dr. Pisin Chen to QABP3 and the kindness of the hosts at Higashi-Hiroshima. He also is very grateful to Prof. Marlan O. Scully and people in his group for discussions on the 'Unruh mazer' proposal.

References

1. W.G. Unruh, Phys. Rev. D **14**, 870 (1976)
2. P. Davies, J. Phys. A **8**, 609 (1975)
3. J.R. Letaw, Phys. Rev. D **23**, 1709 (1981); J.D. Pfautsch, "Quantum Field Theory in Stationary Coordinate Systems", Ph.D. Thesis, Univ. of Texas at Austin (1981)
4. A.O. Barut, J.P. Dowling, Phys. Rev. A **41**, 2277 (1990)
5. H.C. Rosu, Gravitation & Cosmology **7**, 1 (2001), gr-qc/9406012; H.C. Rosu, in *Artificial Black Holes*, pp 307-334 (World Scientific, 2002), gr-qc/0012083
6. S. Hacyan, A. Sarmiento, Phys. Rev. D **40**, 2641 (1989)
7. J.S. Bell, J.M. Leinaas, Nucl. Phys. B **212**, 131 (1983); *ibidem* B **284**, 488 (1987); J.S. Bell, R.J. Hughes, J.M. Leinaas, Z. Phys. C **28**, 75 (1985)
8. A.A. Sokolov, I.M. Ternov, Dokl. Akad. Nauk. SSSR **153**, 1052-1054 (1963) [Sov. Phys. Dokl. **8**, 1203 ((1964)]
9. Ya.S. Derbenev, A.M. Kondratenko, Sov. Phys. JETP **37**, 968 (1973)
10. D.P. Barber, S.R. Mane, Phys. Rev. A **37**, 456 (1988)
11. J.R. Johnson, R. Prepost, D.E. Wiser, J.J. Murray, R.F. Schwitters, C.K. Sinclair, Nucl. Instr. and Methods **204**, 261 (1983)
12. M. Kühne, in *New Developments and Applications in Optical Radiometry*, Inst. Phys. Conf. Ser. No. 92, IOP Publishing Ltd, (1989)
13. K. Kirsebom et al., Phys. Rev. Lett. **87**, 054801 (2001). For theory, see A.V. Korol, A.V. Solov'yov and W. Greiner, J. Phys. G: Nucl. Part. Phys. **28**, 627 (2002)
14. U. Uggerhoj, private communication at QABP-3.
15. K.T. McDonald, in QABP-1 (World Scientific, 1999) pp. 643-648, physics/0003061
16. J. Rogers, Phys. Rev. Lett. **61**, 2113 (1988)
17. L.S. Brown, G. Gabrielse, Rev. Mod. Phys. **58**, 233 (1986)
18. J. Tan, G. Gabrielse, Appl. Phys. Lett. **55**, 2144 (1989); Phys. Rev. A **48**, 3105 (1993)
19. E.Yablonovitch, Phys. Rev. Lett. **62**, 1742 (1989)
20. C. Eberlein, Phys. Rev. Lett. **76**, 3842 (1996); Phys. Rev. A **53**, 2772 (1996)
21. V.V. Dodonov, A.B. Klimov, D.E. Nikonov, Phys. Rev. A **47**, 4422 (1993)
22. L. Grishchuk, H.A. Haus, K. Bergman, Phys. Rev. D **46**, 1440 (1992)
23. S.M. Darbinian, K.A. Ispirian, A.T. Margarian, preprint Yerevan Phys.Inst. YERPHY-1188(65)-89 (August 1989)
24. S.M. Darbinian, K.A. Ispiryan, M.K. Ispiryan, A.T. Margaryan, JETP Lett. **51**, 110 (1990)
25. P. Chen, T. Tajima, Phys. Rev. Lett. **83**, 256 (1999)
26. M.O. Scully, V.V. Kocharovsky, A. Belyanin, F. Capasso, E. Fry, "Enhancing Unruh Acceleration Radiation via Cavity Quantum Electrodynamics", to be published (2003)
27. L.N. Pringle, Phys. Rev. D **39**, 2178 (1989); D.N. Klyshko, Phys. Lett. A **154**, 433 (1991)
28. H.C. Rosu, "Frenet-Serret Vacuum Radiation, Detection Proposals and Related Topics", hep-th/0301128 (2003)

QUANTUM EXCITATION-FREE RADIATION EMISSION INCLUDING MULTIPLE SCATTERING

ULRIK I. UGGERHØJ

Department of Physics and Astronomy, University of Aarhus
DK-8000 Aarhus C, Denmark

In order to increase the luminosity of electron-positron colliders it is desirable to find a means to reduce the phase-space of the beams. The transverse cooling of positrons imposed by the quantum excitation-free radiation emission in a single crystal is considered as a potential route to achieving ultra-cold beams. An analysis of the problem is presented, including an evaluation of the contribution from multiple scattering during the passage. The analysis shows that an emittance reduction may be achieved in special cases, but in general the emittance will increase as a result of the multiple scattering.

1. Introduction

In a series of theoretical papers, the quantum excitation-free radiation emission in a single crystal has been discussed [1,2]. It is shown that the transverse action - and thereby the emittance - decreases exponentially towards the minimum value $\hbar/2$, corresponding to an emittance of half of the Compton wavelength. This applies as long as the radiation is in the undulator regime where the angle of emission is larger than the pitch angle. On the other hand, experiments [3] have been performed which in agreement with theoretical expectations based on a completely different analysis show that positrons in contrast to electrons generally suffer heating instead of cooling. The present work is motivated by two things: The desire to estimate the potential of single crystals as 'devices' for the production of ultra-cold beams and a wish to find a consensus between two apparently different theoretical approaches and experimental results. In the following the outline of [2] is followed, with the inclusion of multiple scattering, and it is shown that for the experiment one should indeed expect heating as concluded from both theories. Finally, it is shown that in special cases it is expected that transverse cooling can be achieved.

2. Channeling, multiple scattering and dechanneling

The large fields present near the nuclei in solid materials may in the case of single crystals add coherently such that a penetrating particle experiences a continuous field along its direction of motion - the so-called continuum approximation [4]. If further the particle is incident with a sufficiently small angle to a particular crystallographic direction, inside the so-called Lindhard angle, the negatively/positively charged particle is constrained to move near/far from the nuclei and the electron clouds surrounding these. This is the channeling phenomenon [4] which has found widespread applications in physics. For a general introduction to channeling and applications, see eg. [5]. The critical angle for planar channeling is given by

$$\psi_p = \sqrt{4Z_1 Z_2 e^2 N d_p C a_{\mathrm{TF}}/pv} \tag{1}$$

where $Z_1 e$ is the charge of the penetrating particle, $Z_2 e$ that of the lattice nuclei, p the momentum, v the velocity, $N d_p$ is the planar density of atoms, N being the atomic density and d_p the planar spacing, $C \simeq \sqrt{3}$ is Lindhard's constant and a_{TF} is the Thomas-Fermi screening distance.

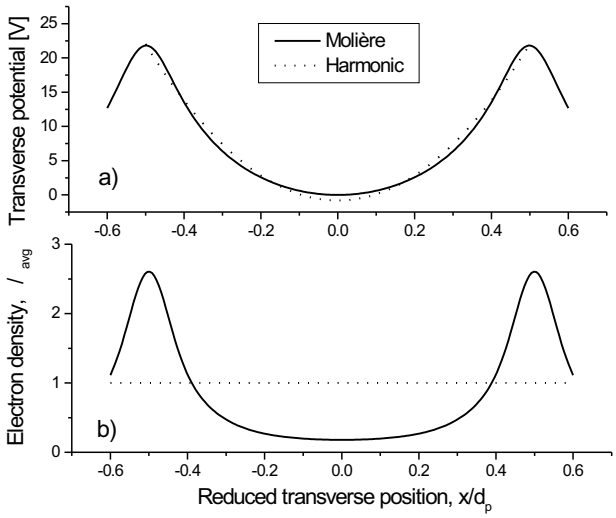

Figure 1. *The figure shows as a function of reduced transverse position, x/d_p, a) the transverse potential in the Molière and harmonic approximations and b) the electron density calculated from Poisson's equation.*

In the continuum approximation, the resulting transverse potential leads to a continuously focusing environment in which photon emission may take place without recoil to the emitting particle, the recoil being absorbed by the lattice. This is the so-called 'semi-classical channeling radiation reaction' [1,2]. In the previous papers on this phenomenon two main assumptions are made: The particle is moving in a harmonic potential and the energy of the photons emitted is small compared to the energy of the particle. Disregarding for the moment the potentially important case of axially channeled positrons along a crystal axis, this leaves only planar channeled positrons since channeled electrons are in a strongly anharmonic potential. Axially channeled positrons may be confined to a region between certain strings if their transverse energy is very low, so-called proper channeled positrons. In this case the transverse potential can be well approximated by a harmonic potential, see e.g. [6]. As seen from figure 1a, the harmonic approximation is clearly well suited for positive particles.

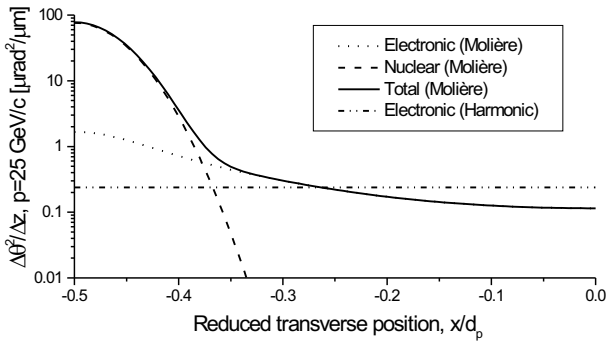

Figure 2. *The squared scattering angle per unit distance, $\Delta\theta^2/\Delta z$, as a function of reduced transverse position, x/d_p, for a $p = 25$ GeV/c beam in silicon.*

The transfer of channeled particles to states above the barrier, so-called random, is referred to as dechanneling. The length, L_{D}, over which a planar channeled beam of protons has been reduced to the fraction 1/e of the initial intensity by transfer to the random beam is given for $\gamma \gg 1$ by [7], [8]:

$$L_{\mathrm{D}} = \frac{256}{9\pi^2} \frac{pv}{\ln(2\gamma mc^2/I) - 1} \frac{a_{\mathrm{TF}} d_p}{Z_1 e^2} \tag{2}$$

where I is the ionisation potential. Eq. (2) has been shown to be in good

agreement with measured values of L_{D} at room temperature [8]. Due to the dependence of electron density on transverse position, see figure 1a, the dechanneling process which is a result of the multiple scattering depends itself on the transverse position and therefore on the transverse energy. In figure 2 is shown the squared scattering angle per unit distance, $\Delta\theta^2/\Delta z$, for a $p = 25$ GeV/c beam in silicon. For low transverse energies, the multiple scattering is dominated by the interaction with electrons and it is observed that $\Delta\theta^2/\Delta z$ is almost a factor of two lower for the more accurate Molière approximation than for the harmonic potential (for the Molière approximation, see e.g. [9]).

3. Quantum excitation-free radiation emission including multiple scattering

Following [2] the time evolution of the longitudinal Lorentz factor, $\gamma_z \equiv \sqrt{m^2c^4 + p_z^2c^2}/mc^2 = E_z/mc^2$, in a continuous focusing environment is given by the differential equation

$$\frac{\mathrm{d}\gamma_z(t)}{\mathrm{d}t} = -\Gamma_c G\gamma_z^{3/2} J_x(t) \tag{3}$$

i.e. it couples to the transverse action, $J_x = E_x/\omega_z$, which evolves as

$$\frac{\mathrm{d}J_x(t)}{\mathrm{d}t} = -\Gamma_c J_x - \frac{3}{4}\Gamma_c G\gamma_z^{1/2}(t) J_x^2(t) \tag{4}$$

leading to two coupled differential equations, both in the absence of multiple scattering. Here $\Gamma_c = 2r_eK/3mc$ is given by the focusing parameter, K, related to the transverse potential height, U_0, and planar spacing, d_p, as $U_0 = K(d_p/2)^2/2$ and $G = \sqrt{K/m^3c^4}$ is a convenient constant expressing the focusing strength.

The solution is given as

$$J_x(t) = J_{x0}(1 + \frac{5}{8}\gamma_{z0}^2\theta_{p0}^2(1 - \exp(-\Gamma_c t)))^{-3/5}\exp(-\Gamma_c t) \tag{5}$$

and

$$\gamma_z(t) = \gamma_{z0}(1 + \frac{5}{8}\gamma_{z0}^2\theta_{p0}^2(1 - \exp(-\Gamma_c t)))^{-4/5} \tag{6}$$

where $\theta_{p0} = \sqrt{2GJ_{x0}/\gamma_{z0}^{3/2}}$ is the initial pitch angle, J_{x0} the transverse action and γ_{z0} the longitudinal Lorentz factor upon entry.

To include multiple scattering we use the analysis for the dechanneling length, L_{D}, of positive particles with $\gamma \gg 1$. The dechanneling process

arises due to a steady increase of the transverse energy imposed by multiple scattering, i.e. the transverse energy increases as $\mathrm{d}E_x/\mathrm{d}z = U_0/L_\mathrm{D}$. Therefore the transverse action increases as $\mathrm{d}J_x/\mathrm{d}t = U_0 c/L_\mathrm{D}\omega_z$, but since the effective dechanneling length depends on the transverse energy approximately as $L_\mathrm{D} = L_{\mathrm{D}0}U_0/J_x\omega_z$, the transverse action changes according to

$$\mathrm{d}J_x/\mathrm{d}t = c/L_{\mathrm{D}0}J_x \tag{7}$$

Here $L_{\mathrm{D}0}$ denotes the dechanneling length for states where $E_x \simeq U_0$. This is found by dividing the squared scattering angle for $x = 0$ by the average over x of the squared scattering angles shown in figure and multiplying the dechanneling length from eq. (2) by this ratio, i.e.

$$L_{\mathrm{D}0} = L_\mathrm{D} d_p \Delta\theta^2(d_p/2)/2 \int_0^{d_p/2} \Delta\theta^2(x)\mathrm{d}x \tag{8}$$

Thus, by combining eqs. (4) and (7), the result is

$$\frac{\mathrm{d}J_x(t)}{\mathrm{d}t} = (\frac{c}{L_{\mathrm{D}0}} - \Gamma_c)J_x - \frac{3}{4}\Gamma_c G\gamma_z^{1/2}(t)J_x^2(t) \tag{9}$$

whereas $\gamma_z(t)$ remains unaffected. By a change of variables $\Gamma_c' = \Gamma_c(1 - c/\Gamma_c L_{\mathrm{D}0}$ and $G' = G(1 - c/\Gamma_c L_{\mathrm{D}0})^{-1}$ the same type of coupled differential equations as eqs. (3) and (4) are obtained with solutions given by eqs. (5) and (6) with Γ_c' and G' instead of Γ_c and G and with a new pitch angle, $\theta_{p0}' = (1 - c/\Gamma_c L_{\mathrm{D}0})^{-1/2}\theta_{p0}$. To get the true pitch angle as a function of time the inverse transformation is applied, i.e. $\theta_p = (1 - c/\Gamma_c L_{\mathrm{D}0})^{1/2}\theta_p'$ where $\theta_p' = \sqrt{2G'J_x'/\gamma_z'^{3/2}}$ is the modified pitch angle. As expected and seen from the results below, a good measure of the depth at which the cooling effect starts to appear is given by $c\tau_c = c/\Gamma_c$.

4. Results

In figure 3 is shown the pitch angle calculated as a function of normalized penetration time, t/τ_c, for 25 GeV positrons in a (110) diamond, with and without inclusion of the multiple scattering. It is seen that while the cooling starts around $t/\tau_c = 0.1$ without multiple scattering, it is postponed to values above $t/\tau_c \simeq 5$ when this additional effect is taken into account. Since there is always an incoherent contribution to the radiation emission which typically takes place as in an amorphous medium, it is important to note the scale of $c\tau_c$ compared to the amorphous radiation length, X_0, which for diamond is 122 mm. It is thus not possible to utilize planar channeling in diamond for cooling of a 25 GeV beam of positrons for an

angle of incidence near ψ_p. However, for smaller angles the cooling starts already at $\simeq 0.1t/\tau_c$, i.e. a 10 mm thick diamond would suffice to initiate the cooling.

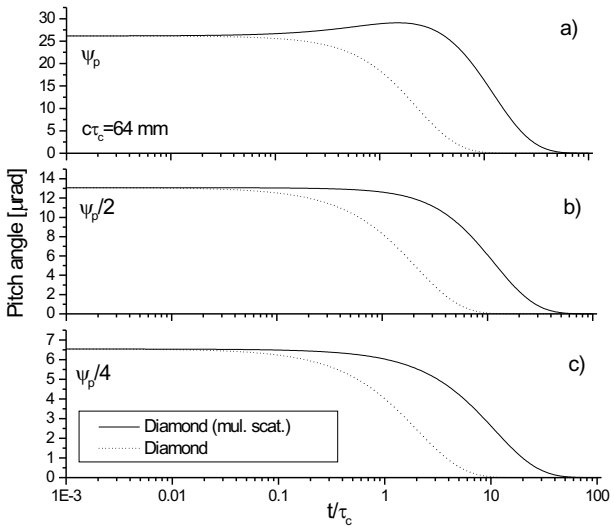

Figure 3. *The pitch angle in diamond (110) as a function of normalized penetration time, t/τ_c. The full drawn curve is calculated including multiple scattering while the dotted line excludes this contribution. The graphs a), b) and c) are for incidence angles ψ_p, $\psi_p/2$ and $\psi_p/4$, respectively.*

In figure 4 is shown the different behaviours for several angles of incidence, calculated for tungsten (110). Strong cooling is found to appear early for small values of the angle of incidence, but for tungsten $c\tau_c \simeq 8X_0$ which means that even for small angles there will be a strong influence from incoherent scattering.

In figure 5 is shown results for silicon and germanium showing that for light materials, where the lattice is not very compact as in diamond, the influence of multiple scattering is much stronger than for heavier ones.

To get an impression of the variation of the cooling effect as a function of energy in figure 6 is shown the results for 4 different energies. Clearly, as the energy increases, the influence of multiple scattering diminishes and cooling starts earlier.

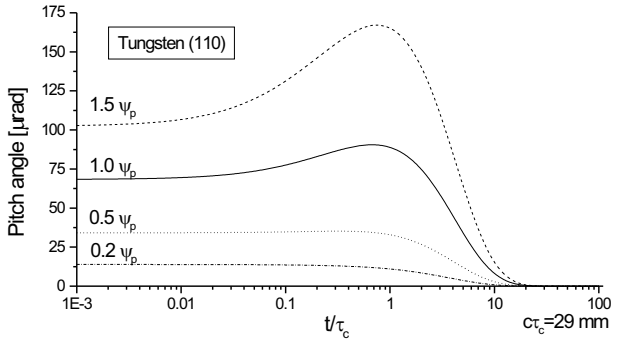

Figure 4. *The pitch angles in tungsten (110) as a function of normalized penetration time, t/τ_c, for 4 different angles of incidence as indicated. The positron energy is set to 25 GeV and all curves are calculated including multiple scattering.*

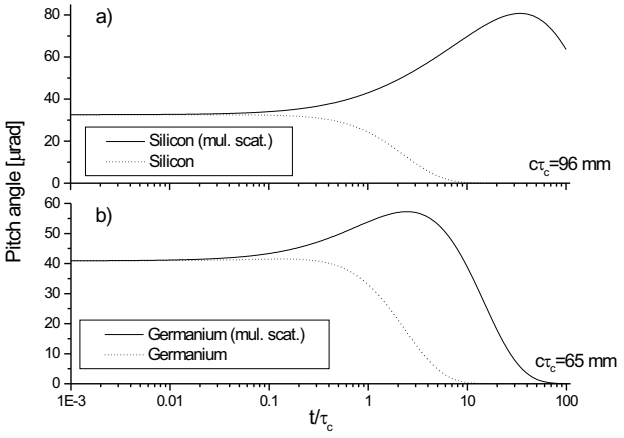

Figure 5. *The pitch angle in a) silicon and b) germanium (110) as a function of normalized penetration time, t/τ_c. In each case, the initial pitch angle equals the planar critical angle, ψ_p, and the full curves are calculated including multiple scattering while the dotted curves do not include this effect.*

As a crude estimate, the axial potential can be approximated by a harmonic potential with barrier height equal to that found by the Molière potential. The two kinds of motions in the planar and axial channeling

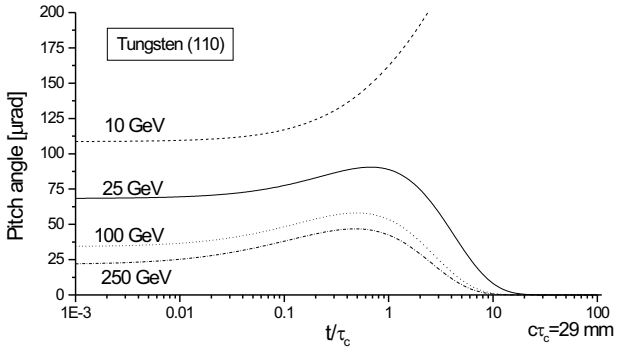

Figure 6. *The pitch angle in tungsten (110) as a function of normalized penetration time, t/τ_c, for 4 different energies as indicated. In each case, the initial pitch angle equals the planar critical angle, ψ_p, and all curves are calculated including multiple scattering.*

cases are very different and it is not expected to get anything but an indication of the magnitude of the effect from this analysis. However, in figure 7 is shown the results obtained by this procedure for two energies and we note that in this case the characteristic cooling length is *much* shorter than X_0. This indicates that the much stronger axial fields may indeed provide substantial cooling.

Such an experiment has been performed by NA43 at CERN, see [3], and compared to a theoretical analysis by Kononets, see [10]. It was found, in agreement with this theory, that positrons suffered heating in contrast to electrons. In figure 8 is shown results under the same crude estimation method for the axial case as mentioned above. The actual value of the crystal thickness in the experiment is given by the vertical dashed line and it is seen - as observed in the experiment - that for all angles of incidence positrons suffer heating.

In [11] calculations of the transverse cooling including multiple scattering have also been performed. However, in order to present a fully self-consistent model, the authors have chosen to model the electron density by solving the Poisson equation for the harmonic potential. This yields an electron density which is constant as a function of transverse position and may underestimate the net cooling effect as a cause of this. On the other hand, in [11] scattering 'on fluctuations of the planar potential', i.e. the nuclear

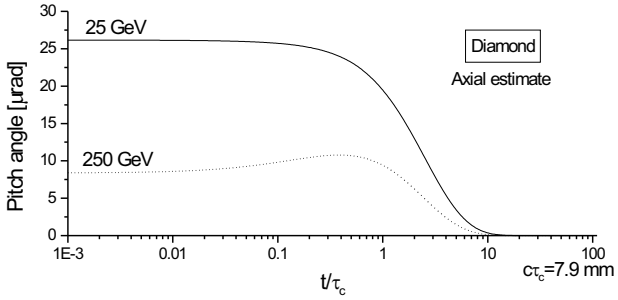

Figure 7. *The estimated axial pitch angle in diamond as a function of normalized penetration time, t/τ_c, for 2 different energies as indicated. In each case, the initial pitch angle equals the planar critical angle, ψ_p, and both curves are calculated including multiple scattering.*

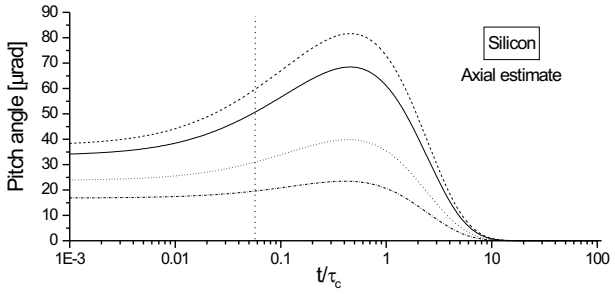

Figure 8. *The estimated axial pitch angle in silicon as a function of normalized penetration time, t/τ_c, for 4 different angles of incidence. All curves are calculated including multiple scattering.*

contribution is not taken into account either. The analysis presented here supplements that of Baier and Katkov [11] in producing essentially the same conclusion by use of a different approach: Only under special circumstances may a penetrating particle experience a net cooling effect.

5. Conclusions

Qualitative agreement among two different theoretical approaches and an experiment on radiative angular cooling is shown. This gives considerable confidence in the predictions, especially of the semi-classical channeling radiation reaction approach. Furthermore, for this approach multiple scattering is included to obtain a more realistic estimate of the cooling properties. Rough estimates show that for existing positron beams a strong cooling effect may be achievable by means of axial channeling in a $\simeq 20$ mm thick diamond crystal. There are however still open questions which deserve attention, among others that of dilution of the longitudinal phase-space due to the severe straggling in energy loss and the possibility of cooling simultaneously in both transverse directions by proper axial channeling or channeling in carbon nanotubes [12].

6. Acknowledgments

I am grateful for having benefitted substantially from encouraging discussions with P. Chen, T. Tajima, H. Rosu and J. Ellison. Furthermore, I wish to thank V. Baier for drawing my attention to the paper [11]. A 'Steno' grant from the Danish Natural Science Research Council is gratefully acknowledged.

Finally, I wish to thank Pisin Chen for his kind invitation to attend a workshop with a (for me) hitherto unseen fraction of visionary physicists.

References

1. Z. Huang, P. Chen and R.D. Ruth, Phys. Rev. Lett. **74**, 1759 (1995)
2. Z. Huang, P. Chen and R.D. Ruth, Nucl. Instr. Meth. B **119**, 192 (1996)
3. A. Baurichter *et al.*, Phys. Rev. Lett. **79**, 3415 (1997)
4. J. Lindhard, Mat. Fys. Medd. Dan. Vid. Selsk. **34**, 1 (1965)
5. A.H. Sørensen and E. Uggerhøj, Nucl. Sci. Appl. **3**, 147 (1989)
6. Ph. Lervig, J. Lindhard and V. Nielsen, Nucl. Phys. **A96**, 481 (1967)
7. V.M. Biryukov *et al.*, Physics-Uspekhi **37**, 937 (1994)
8. V.M. Biryukov *et al.*, Nucl. Instr. Meth. B **86**, 245 (1994)
9. V.M. Biryukov, Y.A. Chesnokov and V.I. Kotov, Crystal Channeling and Its Application at High-Energy Accelerators, Springer-Verlag (1997)
10. Yu.V. Kononets, Nucl. Instr. Meth. B **135**, 40 (1998)
11. V.N. Baier and V.M. Katkov, Phys. Lett. A **232**, 456 (1997)
12. T. Tajima, private communication, 2003

FLYING MIRRORS – RELATIVISTIC PLASMA WAKE CAUSTIC LIGHT INTENSIFICATION

T. ESIRKEPOV, S. V. BULANOV AND T. TAJIMA
Advanced Photon Research Center, JAERI, Kyoto-fu 619-0215, Japan
E-mail: timur@apr.jaeri.go.jp

A method to generate ultrahigh intense electromagnetic fields is presented. This method, in principle, allows us to achieve the Schwinger limit of the electric field. The method is demonstrated with the help of two- and three-dimensional particle-in-cell simulations.

1. Introduction

The invention of chirped pulse amplification (CPA) method and recent development of laser technology led to a stunning increase of the light intensity in a laser focal spot[1]. Electrons in laser-induced plasma become relativistic at intensities $I \sim 10^{18}\mathrm{W/cm^2}$. The ion motion strongly affect the relativistic plasma dynamics starting from $I \gtrsim (m_i/m_e) \times 10^{18}\mathrm{W/cm^2}$, as demonstrated in the review[2]. Nowaday lasers produce pulses, whose intensity is approaching to $10^{22}\mathrm{W/cm^2}$. At intensities of the order of $10^{23} - 10^{24}\mathrm{W/cm^2}$ the effect of radiation reaction force come into play[3]. Further, starting from the intensity $10^{25}\mathrm{W/cm^2}$ we have to treat electrons in the framework of the quantum electrodynamics (QED)[4].

At intensity of the order of $10^{29}\mathrm{W/cm^2}$, which corresponds to the QED critical electric field, light can generate particle-antiparticle pairs from vacuum. There are several ways to achieve such an intensity. One way was demonstrated in the experiments [5], where high-energy bunch of electrons interacts with counterpropagating intense laser pulse. In the reference frame of electrons the electric field magnitude of the incident radiation was approximately 25% of the QED critical field.

Technically feasible way, in principle, is to increase the power of the contemporary laser system by 7 orders of magnitude. Another way is to increase the frequency of the laser radiation and then focus it into a tiny region. In this method X-ray lasers with present-day power can be used,

if one can focus such a radiation[6]. To achive more "moderate" intensities, $10^{24} - 10^{25}\mathrm{W/cm}^2$, another scheme was suggested in the paper[7], where a quasi-soliton wave between two foils is pumped by the external laser field up to ultrahigh magnitude.

In this paper we consider a scheme based on the laser frequency upshifting and the pulse compression. These two phenomena were discussed and demonstrated experimentally in a broad variety of configurations, where they were caused, in general, by different mechanisms. In particular, the wave amplification reflected at the moving relativistic electron slab has been discussed in references[8,9], the backward Thompson scattering at relativistic electron bunch was considered in references[10,11], the reflection at the moving ionization fronts has been studied in references[12,13,14,15,16,17], various schemes of the counter-propagating laser pulses in underdense plasma and a use of parametric instabilities were discussed in references[18,19,20,21].

2. Mirrors in the plasma wake wave

Here we consider a plasma wakefield in the wavebreaking regime as a tool for generating a coherent radiation of ultra-high intensity.

Consider the following scenario. A short intense laser pulse (the "*driver*") induces wakefield in an underdense plasma. Its group velocity equals to zero, and its phase velocity $v_{ph} = \beta_{ph} c$ is equal to the group velocity of the laser pulse in the plasma. The corresponding Lorentz factor is $\gamma_{ph} = \left(1 - \beta_{ph}^2\right)^{-1/2} \approx \omega_d/\omega_{pe}$, where ω_d is the *driver* pulse frequency, ω_{pe} is the Langmuir frequency. The nonlinearity of strong wakefield causes a nonlinear wave profile, including the steepening of the wave and formation of the cusps in the electron density[22]. This amounts to the wavebreaking regime[2]. Theoretically the electron density in the cusp depends on the coordinate as $\propto (x - v_{ph}t)^{-2/3}$ and tends to infinity, but remains integrable[2]. Sufficiently weak counter-propagating laser pulse (the "*source*") will be partially reflected from the cusp. The amount of the reflected energy scales with γ_{ph} as γ_{ph}^{-4}, as it is shown below. Thus the cusp acts as a mirror flying with the relativistic velocity v_{ph}. The frequency of the reflected radiation is up-shifted by the factor $(1 + \beta_{ph})/(1 - \beta_{ph}) \approx 4\gamma_{ph}^2$, in accordance with the Einstein formula. The reflection is small, but the frequency up-shift is very high, and the intensity of the reflected radiation is much greater than that of the *source* pulse.

It is important that the relativistic dependence of the Langmuir frequency on the driver pulse amplitude results in the horseshoe-shaped pat-

tern of the wakefield in two-dimensional (2D) and three-dimensional (3D) configurations, since the driver pulse has a finite transverse size. Each cusp in the electron density has a shape close to a parabaloid. Because now we have a curved mirror, the frequency $\tilde{\omega}_s$ of the reflected radiation depends on angle:

$$\tilde{\omega}_s = \frac{1+\beta_{ph}}{1-\beta_{ph}\cos\theta}\omega_s\,, \tag{1}$$

where ω_s is the *source* pulse frequency, and θ is the angle of the reflected wave vector in the laboratory frame. The reflected light is focused. The focal spot size is of the order of the diffraction limited size. In the reference frame of the cusp it is $\lambda_s\left(\left(1-\beta_{ph}\right)/\left(1+\beta_{ph}\right)\right)^{1/2} \approx \lambda_s/(2\gamma_{ph})$, where λ_s is the wavelength of the *source* pulse. In the laboratory frame the focal spot size will be approximately $\lambda_s/(4\gamma_{ph}^2)$ along the paraboloid axis, and $\approx \lambda_s/(2\gamma_{ph})$ in the transverse direction.

With the ideal realization of the above dynamics, the resulting intensity in the focal spot of the *source* pulse, reflected and focused by the electron density cusp, is increased by the factor of the order of $\gamma_{ph}^{-4} \times (4\gamma_{ph})^2 \times (2\gamma_{ph}D/\lambda_s)^2 = 64(D/\lambda_s)^2\gamma_{ph}^2$, where D is the diameter of the efficiently reflected portion of the *source* pulse.

In order to calculate the reflection coefficient, we consider the interaction of an electromagnetic wave with a spike of the electron density formed in a breaking Langmuir wave. In the laboratory frame, this interaction can be described by the wave equation

$$\partial_{tt}A_z - c^2\left(\partial_{xx}+\partial_{yy}\right)A_z + \frac{4\pi e^2 n\left(x-v_{ph}t\right)}{m_e\gamma_e}A_z = 0\,, \tag{2}$$

where A_z is the z-component of the vector potential, γ_e is the electron Lorentz factor, near the maximum of the density it is $\gamma_e \approx \gamma_{ph}$.

In the reference frame comoving with the plasma wake wave, equation (2) has the same form, whereas the electron density now reads $n(x-v_{ph}t) \approx n_0(2/9)^{1/3}\gamma_{ph}\left(v_{ph}\gamma_{ph}/\omega_{pe}x'\right)^{2/3}$ in the vicinity of the cusp[2]. The transformation of coordinates to the moving frame is given by $t' = (t-v_{ph}x/c^2)\gamma_{ph}$, $x' = (x-v_{ph}t)\gamma_{ph}$, $y' = y$, $z' = z$.

Consider the vector potential in the form $A_z = \left(A_0\exp\left(ik_x'x'\right) + A_R(x')\right)\exp\left(i\left(\omega't' - k_y'y'\right)\right)$, where A_0 and A_R correspond to the incident and reflected waves, and $\omega' = (\omega+v_{ph}k_x)\gamma_{ph}$, $k_x' = (k_x+v_{ph}\omega/c^2)\gamma_{ph}$, $k_y' = k_y$ are the frequency and wave vector in the moving frame, and $k_x' > 0$. Using this ansatz, from equation (2) we obtain

for the reflected wave in the moving frame

$$\frac{d^2 A_R}{dx'^2} + \left(q^2 - \frac{g}{x'^{2/3}}\right) A_R = A_0 \frac{g}{x'^{2/3}} \exp\left(ik'_x x'\right) , \tag{3}$$

where $q^2 = \omega'^2/c^2 - k'^2_y \geq k'^2_x > 0$ and $g = (2/9)^{1/3} k_{pe}^{4/3} \gamma_{ph}^{2/3}$.Assuming $\omega_d \gg \omega_{pe}$, and considering the amplitude A_R to be much smaller than A_0 at $x' \to \infty$, we find the reflected wave:

$$A_R(x') = i^{4/3} g \Gamma(2/3) A_0 \exp\left(-iqx'\right) / q(q + k'_x)^{1/3} , \tag{4}$$

where Γ is the Euler gamma function, $q > 0$. Performing the inverse Lorentz transformation to the laboratory frame, we obtain that the frequency of the reflected wave is defined by Eq.(1). In the case of normal incidence ($k_y = 0$), the electric field magnitude in the reflected wave is increased by the factor $(8/9)^{1/3}\Gamma(2/3)(\omega_s/\omega_d)^{4/3}$. The length of the reflected pulse is $\approx 4\gamma_{ph}^2$ times shorter than the length of the incident pulse. Therefore, the reflection coefficient scales as $\propto \gamma_{ph}^{-4}$.

If we take the electron plasma density $n_e = 10^{17}\mathrm{cm}^{-3}$, the *driver* pulse wavelength 1μm and intensity $I_d = 10^{19}\mathrm{W/cm}^2$, *source* pulse wavelength 1μm and intensity $I_s = 10^{18}\mathrm{W/cm}^2$, and the diameter of the efficiently reflected portion of the *source* $D = 500\mu$m, we obtain that the intensity of the reflected and focused light is of the order of $10^{29}\mathrm{W/cm}^2$. We see, that the scheme described above can be used to achieve the QED critical electric field with present-day technology.

3. Three-dimensional Particle-in-Cell simulation

To demonstrate the feasibility of the effect of the light reflection and focusing by the breaking plasma wake wave, we performed three-dimensional (3D) particle-in-cell (PIC) simulations using the code REMP (Relativistic Electro-Magnetic Particle-mesh code). The code is massively parallel and fully vectorized, it uses the 'current density decomposition' method[23]. In the simulations the *driver* laser pulse propagates in the direction of the x-axis. Its dimensionless amplitude is $a_d = 1.7$ which corresponds to peak intensity $4 \times 10^{18}\mathrm{W/cm}^2 \times (1\mu\mathrm{m}/\lambda_d)^2$, where λ_d is the laser wavelength. The *driver* is linearly polarized along the z-axis, it has gaussian shape, its FWHM size is $3\lambda_d \times 6\lambda_d \times 6\lambda_d$. The *source* pulse propagates in the opposite direction. Its wavelength is two times greater than the wavelength of the *driver* pulse, $\lambda_s = 2\lambda_d$. The *source* pulse amplitude is chosen to be small, $a_s = 0.05$, to reduce a distortion of the plasma wake wave. The pulse shape is rectangular in the x-direction and Gaussian in the transverse direction,

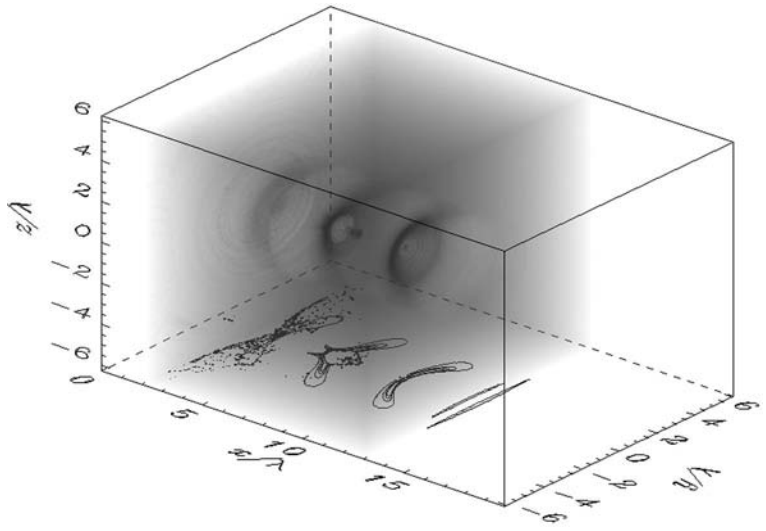

Figure 1. The electron density in the wake of the *driver* laser pulse at $t = 16 \times 2\pi/\omega_d$.

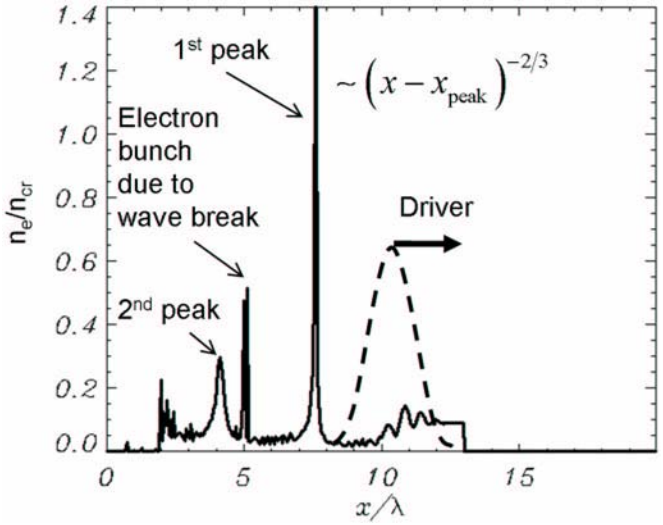

Figure 2. The profile of the electron density along the *driver* laser pulse propagation axis at $t = 14 \times 2\pi/\omega_d$.

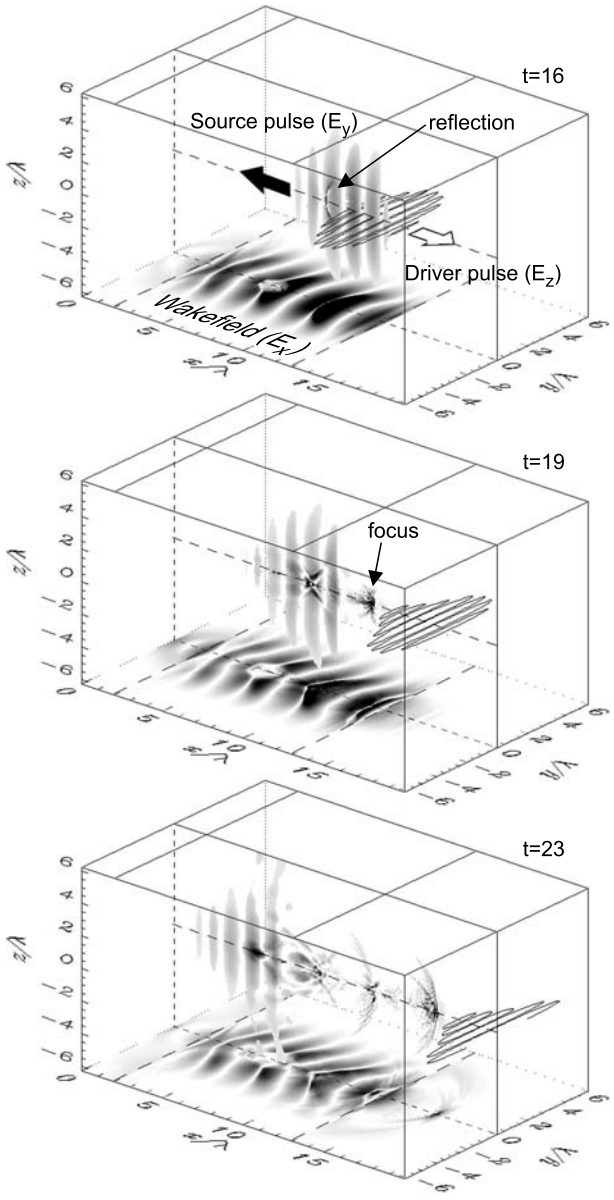

Figure 3. The cross-sections of the electric field components. The $(x, y, z = -6\lambda_d)$-plane: $E_x(x, y, z = 0)$ (colorscale), the plane $(x, y, z = 0)$: $E_z(x, y, z = 0)$ (curves), the plane $(x, y = 0, z)$: $E_y(x, y = 0, z)$ (colorscale) at $t = 16, 19, 23 \times 2\pi/\omega_d$.

its size is $6\lambda_d \times 6\lambda_d \times 6\lambda_d$. To distinguish the electromagnetic radiation of the *driver* and *source* pulses, we set the *source* pulse to be linearly polarized in the direction perpendicular to the *driver* pulse polarization, i. e. along the y-axis. The laser pulses propagate in the underdense plasma slab with the electron density $n_e = 0.09 n_c r$, which corresponds to the Langmuir frequency $\omega_{pe} = 0.3\omega_d$. The plasma slab is localized at $2\lambda_d < x < 13\lambda_d$.

The simulations were performed on 720 processors of the supercomputer HP Alpha Server SC ES40 at APRC-JAERI. The grid size is $2200 \times 1950 \times 1920$, the mesh size is $dx = \lambda_d/100$, total number of quasiparticles is 10^{10} (ten billion). The boundary conditions are absorbing on the x-axis and periodic in the transverse directon, both for the electromagnetic fields and quasi-particles. We emphasize that the simulation grid is set to be fine enough to resolve the huge frequency up-shift, given by Eq.(1).

The simulation results are presented in Figs. 1-3. Fig. 1 shows the plasma wake wave induced by the *driver* laser pulse, as modulations in the electron density. We see the electron density cusps in the form of paraboloids. They move with velocity $v_{ph} \approx 0.87c$, the corresponding gamma-factor is $\gamma_{ph} \approx 2$. Their transverse size is much larger than the wavelength of the counterpropagating *source* laser pulse. Fig. 2 shows the electron density profile along the axis of the *driver* pulse propagation. The wake wave dynamics is close to wave-beaking regime. Each cusp is a semi-transparent parabolic mirror which reflects a part of the *source* laser pulse radiation.

In Fig. 3 we present the cross-sections of the electric field components. The cross-section of the x-component of the electric field projected onto the $(x, y, z = -6\lambda_d)$-plane represents the longitudinal wakefield. The *driver* laser pulse is seen in the cross-section of the z-component of the electric field in the $(x, y, z = 0)$-plane The *source* laser pulse and its reflection is seen in the cross-section of the y-component of the electric field in the $(x, y = 0, z)$-plane. The part of the *source* pulse is reflected from the paraboloidal cusp, and focused into a small region. The reflected part has the same number of cycles as the *source* pulse. The wavelength and duration of the reflected pulse are appriximately 14 times less than the wavelength and duration of the *source* pulse, in agreement with Eq.(1) since $(1 + \beta_{ph})/(1 - \beta_{ph}) \approx 14.4$. The focal spot size of the reflected radiation is much smaller than the wavelength of the *source* pulse. The electric field in the focal spot is approximately 16 times higher than in the *source* pulse, therefore the intensity increases 256 times, in accordance with theoretical estimations above.

In Fig. 3 we see that the part of the *source* pulse radiation is reflected from the flying paraboloidal mirrors, then it focused giving the peak intensity in the focal spot, and finally it is defocused and propagates as a spherical short wave train, whose frequency depend on the angle from the paraboloid mirror axis, in agreement with Eq.(1). The main part of the reflected light power is concentrated whithin the angle $\sim 1/\gamma_{ph}$. This coherent high-frequency beam resembles a searchlight.

We emphasize that the efficient reflection is achievable only when the wakefield is close to the wave-breaking regime, and the cusps in the electron density are formed. As we see in the simulations, the reflection and focusing is quite robust, and even distorted (to some extent) wake wave can efficiently reflect and focus the *source* pulse radiation. We also see that despite the small reflection coefficient, the colossal frequency up-shift and focusing by a sufficiently wide (transversely) wake wave give us a huge increase of the light intensity.

4. Conclusion

We have demostrated the scheme of the relativistic plasma wake caustic light intensification, which can be achieved due to the reflection and focusing of light from the cusps of the electron density in the plasma wake wave in the wave-breaking regime. The presented results of 3D PIC simulations provide us a proof of principle of the electromagnetic field intensification during reflection of the laser radiation at the flying paraboloidal relativistic mirrors in the plasma wake wave.

Acknowledgments

We appreciate the help of APRC computer group. We thank J. Koga, K. Mima, G. Mourou, K. Nishihara, F. Pegoraro, V. Telnov, M. Yamagiwa for the discussion.

References

1. D. Strickland, and G. Mourou, Opt. Commun. **56**, 219 (1985); G. A. Mourou, C. P. J. Barty, and M. D. Perry, Phys. Today **51**, No. 1, 22 (1998); T. Tajima, and G. Mourou, Phys. Rev. ST-AB **5**, 031301 (2002).
2. S. V. Bulanov, et. al. in: Reviews of Plasma Physics. Vol. 22, ed. by V.D. Shafranov (Kluwer Academic / Plenum Publishers, NY, 2001), p. 227.
3. A. Zhidkov, et al., Phys. Rev. Lett. **88**, 185002 (2002).
4. S. V. Bulanov, et al., Interaction of charged particles with ultra strong electromagnetic waves..., in this issue.

5. C. Bamber, et. al., Phys. Rev. D **60**, 092004 (1999).
6. A. Ringwald, Phys. Lett. B **510**, 107 (2001).
7. B. Shen, and M. Y. Yu, Phys. Rev. Lett. **89**, 275004 (2002).
8. K. Landecker, Phys. Rev. **86**, 852 (1952)
9. L. A. Ostrovskii, Soviet Physics Uspekhi **116**, 315 (1976).
10. F. R. Arutyunian, and V. A. Tumanian, Phys. Lett. **4**, 176 (1963).
11. Y. Li, et. al., Phys. Rev. ST Accel. Beams **5**, 044701 (2002).
12. V. I. Semenova, Sov. Radiophys. Quantum Electron. **10**, 599 (1967).
13. W. B. Mori, Phys. Rev. A **44**, 5118 (1991).
14. R. L. Savage, Jr., C. Joshi, and W. B. Mori, Phys. Rev. Lett. **68**, 946 (1992).
15. W. B. Mori, et. al., Phys. Rev. Lett. **74**, 542 (1995).
16. M. I. Bakunov, et. al., Phys. Plasmas **8**, 2987 (2001).
17. J. M. Dias, et. al., Phys. Rev. E **65**, 036404 (2002)
18. G. Shvets, et. al., Phys. Rev. Lett. **81**, 4879 (1998).
19. G. Shvets, and A. Pukhov, Phys. Rev. E **59**, 1033 (1999).
20. Z.-M. Sheng, et al., Phys. Rev. E **62**, 7258 (2000).
21. Y. Ping, et. al., Phys. Rev. E **62**, R4532 (2000).
22. A. I. Akhiezer, and R. V. Polovin, Sov Phys. JETP **30**, 915 (1956).
23. T. Zh. Esirkepov, Comput. Phys. Comm. **135**, 144 (2001).

QUANTUM THEORY OF LASER - BEAM COMPTON INTERACTION AND STIMULATED ELECTRON - POSITRON ANNIHILATION IN A STRONG FIELD

I. V. SMETANIN* AND K. NAKAJIMA**

*Advanced Photon Research Center, JAERI, Kizu, Kyoto, 619-0215 Japan

**High- Energy Accelerator research Organization (KEK), Tsukuba, Ibaraki, 305-0801 Japan

Quantum effects in spontaneous and stimulated Compton laser-beam interactions are considered in the frame of the Klein-Gordon theory. We derive a quantum kinetic equation for the process of laser cooling of electron beams. Nonlinear theory of coherent π-pulse generation in the quantum x-ray Compton FEL is presented. A scheme of coherent stimulated annihilation of electron-positron pairs and stimulated emission of γ-ray photons is proposed.

1. Introduction

Interaction of relativistic electron beams with ultrashort laser pulses at high intensities has been intensively studied for decades which leads to the progress in accelerator technology and development of new radiation sources. One of the most important is the Compton interaction regime which dominates in the radiative cooling of relativistic electron beams,[1,2] x-ray free-electron lasers[3,4] (FEL) and γ-ray photon sources.[5] Nonlinear Compton scattering has been proposed for coherent pair creation in linear colliders.[6]

Quantum effects in the laser-beam Compton scattering are caused by the recoil effect. In the laser cooling of electron beams,[1,2] the limit of beam emittance and energy spread is determined by the quantum fluctuations caused by a discrete change in momentum and energy in a photon scattering event. In the Compton FEL, with an advancement of lasing toward the x-ray and γ-ray spectral domains, increasing quantum recoil will pull electrons out of the energy interval of resonant photon emission, and a new essentially quantum interaction regime emrges.[3,4]

In this paper, we have developed the quantum theory of coherent laser-beam Compton interaction at high intensities using the Klein-Gordon field theory. The quantum kinetic equation which describes the evolution of the energy and momentum distribution function of electron beam in the laser cooling scheme is derived. Theory of the x-ray Compton FEL in the quantum regime, in which FEL becomes a two-level quantum oscilator with a completely inverted active medium, is presented. Using analogy between Compton and electron-positron annihilation processes, a new regime of stimulated coherent annihilation and pair creation in the strong laser field is proposed. Generation of coherent π-pulses of high-intensity x-ray and γ-radiation is discussed.

2. Quantum Kinetics of the Laser Cooling of Relativistic Electron Beam

To describe the Compton interaction of laser and electron beam, we start with the Hamiltonian[7] which includes the interaction of Klein-Gordon scalar field with the quantized electromagnetic field in the momentum representation, the Lorentz gauge $A^0 = 0$ is chosen ($\hbar = c = 1$)

$$\begin{aligned}\mathcal{H}_{int} = \sum_{\mathbf{p}} \sum_{\mathbf{k},\lambda} & - \mu_{\mathbf{k}}(\mathbf{p}-\mathbf{k}) \left[(\mathbf{e}_{\mathbf{k},\lambda}, \mathbf{p}) c_{\mathbf{k},\lambda} a^+_{\mathbf{p}} a_{\mathbf{p}-\mathbf{k}} + (\mathbf{e}^*_{\mathbf{k},\lambda}, \mathbf{p}) c^+_{\mathbf{k},\lambda} a^+_{\mathbf{p}-\mathbf{k}} a_{\mathbf{p}} \right] \\ & - \mu_i(\mathbf{p}-\mathbf{k}_i) \left[(\mathbf{e}_i, \mathbf{p}) c_i a^+_{\mathbf{p}} a_{\mathbf{p}-\mathbf{k}_i} + (\mathbf{e}^*_i, \mathbf{p}) c^+_i a^+_{\mathbf{p}-\mathbf{k}_i} a_{\mathbf{p}} \right] \\ & + g_{\mathbf{k}}(\mathbf{p}-\mathbf{q}) \left[(\mathbf{e}_{\mathbf{k},\lambda}, \mathbf{e}^*_i) c_{\mathbf{k},\lambda} c^+_i a^+_{\mathbf{p}} a_{\mathbf{p}-\mathbf{q}} + (\mathbf{e}^*_{\mathbf{k},\lambda}, \mathbf{e}_i) c_i c^+_{\mathbf{k},\lambda} a^+_{\mathbf{p}-\mathbf{q}} a_{\mathbf{p}} \right] \quad (1)\end{aligned}$$

Here $a^+_{\mathbf{p}}, a_{\mathbf{p}}$ are the field operators for the electron of momentum $\mathbf{p}$ and of energy $\varepsilon_{\mathbf{p}}$, c^+, c are the photon operators, $\{\mathbf{k}, \lambda\}$ represents the scattered mode of electromagnetic field of a wave vector $\mathbf{k}$ and polarization number λ, and $\mathbf{e}_{\mathbf{k},\lambda}$ is the polarization vector, the incident laser pulse is modelled by the single mode $\{\mathbf{k}_i, \lambda_i\}$, with the polarization vector $\mathbf{e}_i$. The coefficients in Eq.(1) are $\mu_{\mathbf{k}}(\mathbf{p}) = e(2V\omega_k \varepsilon_{\mathbf{p}+\mathbf{k}} \varepsilon_{\mathbf{p}})^{-1/2}$, $g_{\mathbf{k}}(\mathbf{p}) = e^2(4V^2 \omega_k \omega_i \varepsilon_{\mathbf{p}+\mathbf{q}} \varepsilon_{\mathbf{p}})^{-1/2}$, $\mathbf{q} = \mathbf{k} - \mathbf{k}_i$ is the total change in momentum of an electron, V is the quantization volume, and sum is over scattered modes $\{\mathbf{k}, \lambda\} \neq \{\mathbf{k}_i, \lambda_i\}$.

In the laser cooling of electron beam, spontaneous Compton scattering dominates. We will consider here the linear Compton regime, when an electron interacts with only one photon of the laser field. Solving the Heizenberg equations for both the electron and photon operators in the lowest unvanishing order of perturbation theory we have for the electron

distribution function $f(\mathbf{p}) =< a_{\mathbf{p}}^{+} a_{\mathbf{p}} >$ the following evolution equation

$$\frac{d}{dt} f(\mathbf{p}) \; = \; 2 \sum_{\mathbf{k},\lambda} \{ G_{\mathbf{k},\lambda}(\mathbf{p}+\mathbf{q}) f(\mathbf{p}+\mathbf{q}) \; - \; G_{\mathbf{k},\lambda}(\mathbf{p}) f(\mathbf{p}) \}, \tag{2}$$

with the coefficients are

$$\begin{aligned} G_{\mathbf{k},\lambda}(\mathbf{p}) = | & \frac{\mu_i(\mathbf{p}-\mathbf{k}) \mu_{\mathbf{k}}(\mathbf{p}-\mathbf{k}) (\mathbf{e}_i, \mathbf{p}-\mathbf{k}) (\mathbf{e}^{*}_{\mathbf{k},\lambda}, \mathbf{p})}{\varepsilon_{\mathbf{p}-\mathbf{k}} - \varepsilon_{\mathbf{p}-\mathbf{q}} + \omega_i} \\ & + \; \frac{\mu_{\mathbf{k}}(\mathbf{p}-\mathbf{q}) \mu_i(\mathbf{p}) (\mathbf{e}_i, \mathbf{p}) (\mathbf{e}^{*}_{\mathbf{k},\lambda}, \mathbf{p}+\mathbf{k}_i)}{\varepsilon_{\mathbf{p}+\mathbf{k}_i} - \varepsilon_{\mathbf{p}-\mathbf{q}} - \omega_k} \\ & - \; g_{\mathbf{k}}(\mathbf{p}-\mathbf{q}) (\mathbf{e}^{*}_{\mathbf{k},\lambda}, \mathbf{e}_i) \, |^2 \, n_i \, \frac{\sin(\varepsilon_{\mathbf{p}} - \varepsilon_{\mathbf{p}-\mathbf{q}} - \omega_k + \omega_i) t}{\varepsilon_{\mathbf{p}} - \varepsilon_{\mathbf{p}-\mathbf{q}} - \omega_k + \omega_i}. \end{aligned} \tag{3}$$

Here, $n_i =< c_i^{+} c_i >= I_i / c\hbar\omega_i$ is the density number of photons in the pumping wave of intensity I_i. Equation (2) is a typical "decay" kinetic equation, the right hand side of which (i.e., the collision integral) represents the balance of electrons in the state $\mid \mathbf{p} >$. The term $\sin(\Delta t)/\Delta$ corresponds to the energy conservation law.

Expanding right hand side of Eq. (2) to the second-order of small parameter $|k|/|p|$, we have a diffusion-like kinetic equation

$$\frac{d}{dt} f(\mathbf{p}) \; = A(p) f(p) + \sum_{\nu} B_{\nu} \frac{\partial f}{\partial p_{\nu}} + \frac{1}{2} \sum_{\nu,\xi} C_{\nu,\xi} \frac{\partial^2 f}{\partial p_{\nu} \partial p_{\xi}} + ... \tag{4}$$

Here the coefficients are $A \; = \; \sum_{k,\lambda} [G_{k,\lambda}(p+q) - G_{k,\lambda}(p)]$, $B_{\nu} \; = \; \sum_{k,\lambda} G_{k,\lambda}(p+q) q_{\nu}$ and $C_{\nu,\xi} = \sum_{k,\lambda} G_{k,\lambda}(p+q) q_{\nu} q_{\xi}$. The first two terms in the right hand side are classical and describe the cooling and decrease in energy of electron beam . The term with the second derivative contains the Plank constant and describes the diffusive growth of the beam energy spread. To illustrate competition between these two processes, let us consider the 1D approximation. Keeping only the longitudinal momentum p_z, after integration over all the scattered photon modes, we have

$$\frac{d}{dt} f(p_z) = \frac{8}{3} \pi r_0^2 I_i \gamma^2 \left[\frac{c}{\varepsilon_p} f + \frac{\partial f}{\partial p_z} + \frac{88}{15} \hbar k_i \gamma^2 \frac{\partial^2 f}{\partial p_z^2} \right] \tag{5}$$

Here γ is the Lorentz factor of electrons. In the classical cooling regime, when the quantum recoil (i.e., the second derivative term) is negligible, solution to Eq. (5) describes a decreasing with time energy spread $\sigma(t) \sim \sigma_0(1 - st)$, the cooling rate is $s \approx 8/3\pi r_0^2 I_i$, r_0 is the classical radius of an electron. It is easy to estimate that quantum diffusion heating will stop the cooling process at the energy spread $\sigma_q \sim (88/15)\hbar\omega_i$ which is of the order of the energy of scattered photon.

3. Quantum Limit in the x-ray FEL Theory

In the x-ray Compton FEL, the stimulated Compton scattering dominates, in which electrons interact resonantly with the pump and the only scattered electromagnetic mode. The resonant energy $\varepsilon_o = mc^2(1-\omega/kc)^{-2}$ corresponds to the synchronism of an electron with the slow ponderomotive wave of frequency $\omega = \omega_s - \omega_i$ and wavenumber $k = k_s + k_i$, $\omega_{i,s}$ and $k_{i,s}$ are the frequencies and wave numbers of pumping (i) and signal (s) waves respectively. The energy interval of resonant photon emission in an FEL $\Delta\varepsilon/\varepsilon_o \approx max\{(4N)^{-1}, \Delta\gamma/\gamma, \Delta\Theta^2/2\}$ is determined by the finite length of interaction region $L = N\lambda_i$, beam energy spread $\Delta\gamma/\gamma$ and divergence $\Delta\Theta$ caused by beam emittance.[3]

Quantum operation regime in an FEL emerges when the quantum emitted $\hbar\omega_s \simeq 4\gamma^2\hbar\omega_i$ exceeds $\Delta\varepsilon$: as a result of recoil in Compton scattering, an electron is expelled from the energy interval of resonant photon emission.[3,4] Assuming pump laser wavelength $\lambda_i \simeq 1\mu m$ and energy of electron beam $\varepsilon = 5$MeV, the quantum emitted is $\hbar\omega_s \approx 0.5$keV (soft x-ray region), and the quantum regime becomes attainable at $\Delta\varepsilon/\varepsilon \sim 10^{-4}$.

To describe lasing in the quantum regime, we will use the Klein - Gordon equation.[4] Assuming vector potentials be $A_i \exp(i[k_i z + \omega_i t])$ for the pump and $A_s \exp(i[k_s z - \omega_s t])$ for the signal waves, we have in the 1D approximation that the dynamics of electrons is reduced to the resonant excitation of an anharmonic oscillator, the system of discrete levels of which $\Psi = \sum a_n \exp(\frac{i}{\hbar}[p_n z - \varepsilon_n t])$ is characterized by the eigen momenta $p_n = p_o + n\hbar(\omega_i + \omega_s)/c$, $n = 0, \pm 1, \pm 2..$ and energies $\varepsilon(p_n) = \sqrt{p_n^2c^2 + m^2c^4}\ldots$. The anharmonicity $\Delta_n = \frac{\varepsilon_n - \varepsilon_{n-1}}{\hbar} - \omega \approx \Delta_0 + n\delta$, $\delta = 8\hbar\omega_s^{1/2}\omega_i^{3/2}/mc^2$ is negligible in conventional FEL schemes, but in the quantum x-ray Compton FEL becomes significant $\delta\tau_{in} \gg 1$, $\tau_{in} = N\lambda_i/c$ is the electron time-of-flight in the optical undulator. As a result[4], FEL dynamics is reduced to the transition between only two quantum levels which are in resonance with the signal mode ($n = 0, -1$, for definiteness).

Evolution of the amplitudes of resonant levels in the interaction region is guided by the following equations which can be found from the Klein-Gordon equation[4]

$$\frac{\partial a_0}{\partial z} = -\frac{i}{4\hbar c}\frac{e^2 A_i A_s^*}{\sqrt{\varepsilon_o \varepsilon_{-1}}} \exp(-i\Delta_0 t)\, a_{-1} \ ,$$
$$\frac{\partial a_{-1}}{\partial z} = -\frac{i}{4\hbar c}\frac{e^2 A_i^* A_s}{\sqrt{\varepsilon_0 \varepsilon_{-1}}} \exp(i\Delta_0 t)\, a_0 \qquad (6)$$

The wave equation for the signal wave amplitude is

$$\frac{\partial A_s}{\partial z} + \frac{1}{c}\frac{\partial A_s}{\partial t} = i\frac{2\pi e^2 A_i}{\omega_s\sqrt{\varepsilon_0\varepsilon_{-1}}}\int_0^\infty d\varepsilon_0 f(\varepsilon_0)a_0 a_{-1}\exp(-i\Delta_0 t), \qquad (7)$$

with $f(\varepsilon_0)$ is the initial energy distribution of electrons in the bunch, no depletion of pumping wave $A_i \approx const$ is assumed.

Thus the lasing in the two-level x-ray FEL is described by the closed self-consistent nonlinear system of equations (6)-(7), which is analogous to the Maxwell-Bloch system of equations in nonlinear optics.

Assuming exact resonance $\Delta_0 = 0$, Eqs. (6) are easily integrated by introduction of the pulse area for the signal mode $\chi(z) = \frac{\mu}{c\hbar}\int_0^z E_s(z)dz$, $\mu = e^2 E_i/m\omega_i^{1/2}\omega_s^{3/2}$ is the characteristic dipole moment of the resonant transition, and the field strength amplitudes $E_{i,s}$ are used instead of corresponding vector potentials. Optimum for the FEL lasing injection of the electron beam corresponds to the the inverted state $a_0|_{z=0} = 1$, $a_{-1}|_{z=0} = 0$, and the solution to Eq. (6) is

$$a_0(z) = \cos(\chi/2), \qquad a_{-1}(z) = -i\sin(\chi/2) \qquad (8)$$

The signal pulse area is then guided by the pendulum equation

$$\frac{\partial^2\chi}{\partial z^2} = \alpha^2\,\sin\chi, \qquad \alpha = \sqrt{\frac{2\pi n_e e^4 E_i^2}{\hbar\omega_s^2\omega_i m^2 c^2}}, \qquad (9)$$

α is the linear ($\chi \ll 1$) gain coefficient. As a result, we have for the output signal intensity[4]

$$I_s(L) = dn^{-2}(\frac{\alpha L}{\kappa}, \kappa)I_s(0). \qquad (10)$$

Here $dn(x, y)$ is the Jacobi elliptic tangent, $\kappa = \sqrt{1 + I_s(0)/I_b}$, $I_b = \hbar\omega_s n_e c$, and $I_s(0)$ is the initial ($z = 0$) signal intensity.

According to Eq.(10), the output intensity $I_s(L)$ of the high-frequency signal is a periodic function of the interaction length L. Maximum output intensity

$$I_s(L_m) = I_s(0) + I_b \qquad (11)$$

is achieved for a sequence of optimal lengths $L_m = \alpha^{-1}\kappa K(\kappa)(2m + 1)$, $m = 0, 1, \ldots$, $K(\kappa)$ is a complete elliptic integral. In this optimum regime, each electron will emit one x-ray photon coherently and inversion will be completely removed in one pass. FEL output radiation then forms the high-intensity π-pulse ($\chi(L_m) = \pi$) of coherent x-ray radiation.

Coherent generation of x-ray photons can be realized at conditions close to that of the recent experiment,[8] in which ∼6keV spontaneous photons were produced in the scattering of 600MW 200psec CO_2 ($\lambda_i = 10.6\mu$m) laser pulses by 60MeV electrons. At the laser intensity $I_i = 3 \cdot 10^{15}\mathrm{W/cm}^2$ (normalized amplitude $a \sim 0.5$) and the electron beam density $n_e = 10^{17}\mathrm{cm}^{-3}$, the linear gain coefficient is $\alpha \approx 7.6\mathrm{cm}^{-1}$. In the x-ray π-pulse regime each electron ($6{\cdot}10^9$ for 1nC bunch) will emit x-ray photon coherently, and the output intensity is $I_s \simeq I_b = \hbar\omega_s n_e c \approx 3 \cdot 10^{12}\mathrm{W/cm}^2$.

4. Stimulated Coherent Annihilation in the Strong Field

It is well known[7] that the processes of Compton scattering and electron-positron pair annihilation have a deep analogy with each other, which is reflected in the structure of corresponding matrix elements. This fact allows us to propose, in analogy with the discussed in the previous section model of x-ray quantum FEL, a new mechanism of stimulated pair creation and annihilation in the strong electromagnetic field.

Let us consider the relativistic electron-positron beam interacting with a strong counter-propagating laser pulse. If the energy of laser photon in the beam reference frame exceeds mc^2, m is the rest mass of electron, coherent stimulated generation of γ-ray photons becomes possible. Let the vector potential of the γ-ray photons is $A_1 \exp(i[k_1 z - \omega_1 t])$, and that of the laser pulse is $A_2 \exp(i[k_2 z + \omega_2 t])$. In the Klein-Gordon theory, the annihilation Hamiltonian can be written in the form[7] ($\hbar = c = 1$)

$$H = \sum_p \{g_p^* a_p^+ b_{p'}^+ + g_p b_p a_{p'}\} \delta(p + p' - (k_1 - k_2)) \tag{12}$$

Here a_p^+, b_p^+ are the creation operators for electrons and positrons of the momentum p and energy ε_p, respectively, and a_p, b_p are the corresponding annihilation operators, $g_p = \frac{e^2}{4\sqrt{\varepsilon_p \varepsilon_{p'}}}(A_2 A_1^*)$ is the coupling constant. Delta function express the energy and momentum conservation laws for the pair creation and annihilation, $p + p' = k_1 - k_2 \equiv q$ and $\varepsilon_p + \varepsilon_{p'} = \omega_1 + \omega_2$,respectively.

Electron-positron pair in the electromagnetic field can be considered as a two-level system, in which the upper state consists in one electron, one positron and N pair of photons, and the lower state is (N+1) photon pairs. Really, one can easy find the Bogolubov transformation which diagonalizes the Hamiltonian (12) with the eigen energy

$$\Omega_p = \sqrt{(\varepsilon_p + \varepsilon_{q-p})^2 + 4|g_p|^2} \tag{13}$$

which can be considered as the Rabi frequency of the effective two-level system. Rabi frequency characterizes the rate of pair creation and annihilation at given external field.

To describe the nonlinear evolution of the electron-positron pair in the interaction region and coherent generation of coherent γ-rays, we will use the Klein - Gordon equation and seek its solution for electrons and positrons in the form

$$\begin{aligned}\Psi_e(z,t) &= \sum_p \sqrt{\frac{mc^2}{2V\varepsilon_p}} u_p^{(-)}(z) \exp\left(\frac{i}{\hbar}[pz-\varepsilon_p t]\right) \\ &+ \sqrt{\frac{mc^2}{2V\varepsilon_{q-p}}} v_{q-p}^{(-)}(t) \exp\left(-\frac{i}{\hbar}[(q-p)z-\varepsilon_{q-p}t]\right) \\ \Psi_p(z,t) &= \sum_p \sqrt{\frac{mc^2}{2V\varepsilon_{q-p}}} u_p^{(+)}(z) \exp\left(\frac{i}{\hbar}[(q-p)z-\varepsilon_{q-p}t]\right) \\ &+ \sqrt{\frac{mc^2}{2V\varepsilon_p}} v_p^{(+)}(z) \exp\left(-\frac{i}{\hbar}[pz-\varepsilon_p t]\right) \end{aligned} \tag{14}$$

where the momentum and the energy of particles satisfy the above conservation law. The amplitudes of the upper $u(z)$ and lower $v(t)$ states of the two-level electron-positron system are assumed to be slow varying functions, and after substitution in the Klein - Gordon equation we have

$$\frac{\partial u_p^{(\pm)}}{\partial z} = -i\frac{e^2(A_1A_2^*)}{4\hbar\sqrt{\varepsilon_p\varepsilon_{-p-q}}} v_p^{(\pm)} \qquad \frac{\partial v_p^{(\pm)}}{\partial z} = -i\frac{e^2(A_1^*A_2)}{4\hbar\sqrt{\varepsilon_p\varepsilon_{-p-q}}} u_p^{(\pm)} \tag{15}$$

We will assume that electromagnetic modes have equal polarizations, and one of the waves (counter-propagating) is sufficiently strong to neglect its depletion. Evolution of the second (high-frequency) electromagnetic wave is described by the Maxwell equations with the current density of the Klein - Gordon field

$$\left(\frac{\partial}{\partial z}+\frac{1}{c}\frac{\partial}{\partial t}\right) A_1 = i\frac{2\pi e^2 A_2 n}{\omega_1\sqrt{\varepsilon_p\varepsilon_{q-p}}} \int d\varepsilon_p \left(u_p^{(-)}v_p^{(-)} + u_p^{(+)}v_p^{(+)}\right) \tag{16}$$

where n is the density of electron- positron pairs. Equations (15), (16) are analogous to Eqs. (6), (7) for the x-ray Compton FEL in the quantum regime, and forms closed self-consistent system of Maxwell-Bloch equations which allows solutions of the self-induced transparency type with the generation of π-pulses of coherent γ-rays.

By analogy with the case of two-level quantum FEL, we introduce the pulse area $\chi_1(z) = \frac{\mu_1}{c\hbar}\int_0^z E_1(z)dz$ with the characteristic dipole momentum

of the two-level system under consideration $\mu_1 = \frac{e^2c^2}{2\omega_1\omega_2\sqrt{\varepsilon_p\varepsilon_{-p-q}}}$. Boundary conditions $u_p^{(\pm)}|_{z=0} = 1$, $v_p^{(\pm)}|_{z=0} = 0$ corresponds to the case of stimulated annihilation of electron-positron pairs and coherent γ-ray emission, for which Eqs. (15) results in solutions $u_p^{(\pm)} = \cos(\chi_1/2)$, $v_p^{(\pm)} = -i\sin(\chi_1/2)$. For the opposite process of the stimulated generation of electron-positron pairs in the strong external laser and γ-ray photon fields, boundary conditions are $v_p^{(\pm)}|_{z=0} = 1$, $u_p^{(\pm)}|_{z=0} = 0$, and solution to Eqs. (15) becomes $u_p^{(\pm)} = -i\sin(\chi_1/2)$, $v_p^{(\pm)} = \cos(\chi_1/2)$.

Evolution of the pulse area for the amplified γ-ray signal is guided by the pendulum equation (8) with the linear gain coefficient

$$\alpha' = \sqrt{\frac{\pi e^4 E_2^2 nc^2}{\hbar\omega_1\omega_2^2\varepsilon_p\varepsilon_{q-p}}} \tag{17}$$

Intensity of the coherently generated γ-ray field in the process of stimulated annihilation depends on the interaction distance z in analogous to Eq. (10) way, $I_1(z) = dn^{-2}\left(\frac{\alpha' z}{\kappa'}, \kappa'\right) I_1(0)$, where parameter is $\kappa' = \sqrt{1 + I_1(0)/I_m}$, $I_1(0)$ is the initial intensity of the γ-ray photon flux, determined by the spontaneous pair annihilation. For the process of stimulated pair creation, the argument in this solution has to be shifted by the half of the period of the Jacobi dn function, $K(\kappa')$. The parmeter $I_m = \hbar\omega_1 nc$ is the maximum intensity of the amplified γ-ray wave which can be attained as a result of annihilation of positrons and electrons having the equal beam densities n. By analogy with Eq. (11), the maximum intensity can be achieved for the interaction distance $L_{\max} = \kappa' K(\kappa')/\alpha'$, $I_1(L_{\max}) = I_1(0) + I_m$, which corresponds to the formation of the π-pulse of the γ-ray photons, $\chi_1(L_{\max}) = \pi$, with the complete removal of inversion (i.e., annihilation) in the electron-positron pair two-level system.

Let us make some estimates. The optimum interaction conditions correspond to the case when in the center-of-mass reference frame both photons have equal energies $\hbar\omega_1' \approx \hbar\omega_2' \approx mc^2$ and electron and positron are nonrelativistic and have a small kinetic energies. Let the second electromagnetic field is formed by the super-strong laser pulse. The gamma factor for this moving reference frame is $\gamma_0 \approx mc^2/2\hbar\omega_2 \sim 2.5 \times 10^5$ for the frequency $\hbar\omega_2 \sim 1eV$ in the laboratory frame, which corresponds to the energy of co-propagating electron and positron beams of ˜125 GeV. The linear gain coefficient is $\alpha \approx \left(\pi r_0 n a^2/2\gamma_0^3\right)^{1/2} \approx 0.53 \times 10^{-2} a \left(n/10^{24} cm^{-3}\right)^{1/2} cm^{-1}$ where $a = eA_2/mc^2$ is the normalized vector potential amplitude of the laser field The coherent γ -ray field generated

has the frequency $\hbar\omega_1 \approx 4\gamma_0^2\hbar\omega_2 \approx 2mc^2\gamma_0 \approx 250$GeV and π-pulse intensity $I_m \sim 1.2 \times 10^{27} \left(n/10^{24}cm^{-3}\right) W/cm^2$. The length of formation of coherent π-pulse of γ radiation $L_{\max} \sim \alpha^{-1}$and can be less than 1mm at $a \sim 2 \times 10^3$ which corresponds to laser pulse intensity $\sim 5.5 \times 10^{24} W/cm^2$ at 1μm wavelength.

References

1. P. Sprangle and E. Esarey, *Phys. Fluids* **B4**, 2241 (1992).
2. V. Telnov, *Phys. Rev. Lett.* **80**, 4757 (1997).
3. P. Dobiash, P. Meystre, M. O. Scully, *IEEE J. Quantum Electron.* **19,** 1812 (1983); J. Gea-Banacloche et al., ibid., **23,** 1558 (1987).
4. I. V. Smetanin, *Laser Physics* **7**, 318 (1997); E. M. Belenov et al., *JETP* **105,** 808 (1994).
5. P. Sprangle et al., *J. Appl. Phys.* **72,** 5032 (1992).
6. P. Chen and V. Telnov, *Phys. Rev. Lett.* **63**, 1796 (1989).
7. V. B. Berestetskii, E. M. Lifshitz, L. P. Pitaevskii, *Quantum Electrodynamics.* Oxford: Pergamon 1978.
8. I. V. Pogorelsky, I. Ben-Zvi, X. J. Wang, T. Hirose, *Nucl. Instr. Meth. Phys. Res.* **A455**, 176 (2000).

INTERACTION OF CHARGED PARTICLES WITH ULTRA STRONG ELECTROMAGNETIC WAVES IN THE RADIATION DOMINANT REGIME

S. V. BULANOV, T. ZH. ESIRKEPOV, J. KOGA, AND T. TAJIMA
Advanced Photon Research Center, Kansai Research Establishment
Japan Atomic Energy Research Institute 8-1 Umemidai, Kizu, Souraku,
Kyoto 619-0215, Japan
E-mail: bulanov@apr.jaeri.go.jp

The plasma particle interaction with a relativistically intense electromagnetic wave under the conditions when the radiation reaction effects are dominant is considered. We analyze the radiation damping effects on the electron motion inside the circularly polarized planar wave and inside a subcycle crossed-field electromagnetic pulse. We consider the ion acceleration due to the radiation pressure action on a thin plasma slab. The results of 2D and 3D PIC simulations are presented.

1. Introduction

Acceleration of charged particles by an electromagnetic wave provides an example of one of the most fundamental processes in physics. When the electromagnetic wave becomes relativistically intense, i.e. when the charged particle's quiver energy it's above the rest mass energy, particle dynamics both within the classical and quantum description acquires remarkable properties which differ from the properties of the nonrelativistic particle interaction with the electromagnetic wave (see Refs. [1,2]). As the electromagnetic wave intensity increase to the ultrahigh intense level, the charged particle velocity will approach the speed of light and in the Lorentz force the magnetic term can not be neglected compared to the electric term. Because of the combined action of the E and B fields in the limit of relativistic intensity of the electromagnetic wave, the longitudinal component of the particle momentum becomes much larger than the transverse one. However, for a finite (long enough) length electromagnetic pulse the net energy gain is almost zero according to the so-called Woodward - Lawson theorem (see for example Ref. [3], and literature cited in). However, the condition for the theorem may be broken in a variety of ways, e.g. such as radiation damping due to the intense acceleration [4-6].

In the present paper we shall address mainly the regimes of the charged particle interaction with an electromagnetic wave when the radiation reaction force plays a dominant role. The nonlinear interaction of charged particles with relativistically strong electromagnetic fields is of great interest for astrophysics (see Refs. [6,7]). In addition, it is of great interest for the laser-matter interaction, when the laser pulse power range is in the multi-petawatt regime. With the advent of very powerful laser sources in recent years these regimes have become available for experimental studies [8]. When the petawatt radiation of the laser pulse with a wavelength equal to $0.8\mu m$ is focused to a one-wavelength focus spot, its intensity reaches the value $5 \cdot 10^{22} W / cm^2$. In this case its dimensionless amplitude $a_0 = eE_0 / m_e \omega_0 c$ is about 160. Here E_0 and ω_0 are the electric field and the frequency of the electromagnetic wave, respectively. The threshold of the relativistic regime discussed above corresponds to $a_0 = 1$ and an intensity $1.38 \cdot 10^{18} W / cm^2$. In the case of a circularly polarized electromagnetic wave in a collisionless plasma the quivering electron energy is related to the wave amplitude as $\mathcal{E} = m_e c^2 \sqrt{1 + a_0^2}$ (see Ref. [9]). The quivering electron radiates a wave with a frequency spectrum ranging up to the frequency $\omega_m = \omega_0 \gamma^3$, where the relativistic gamma factor is equal to $\gamma = \mathcal{E} / m_e c^2$. As a result, there is a radiation reaction force acting on the particle. Here $r_e = e^2 / m_e c^2 = 2.8 \cdot 10^{-13} cm$ and $\lambda = 2\pi / \omega$ are the classical electron radius and the laser light wavelength, respectively. By comparing the radiation reaction force with the Lorentz force $f_R \approx 8\pi^2 m_e r_e c^2 \gamma^2 a_0^2 / 3\lambda^2$, we find that the radiation damping effects become dominant for the wave with the amplitude $a_0 > \left(3\lambda / 4\pi r_e\right)^{1/3}$.

We see that for a $0.8\,\mu m$ wavelength laser the role of the radiation effects becomes important for $a_0 > 408$. This corresponds to the radiation intensity $3.5 \cdot 10^{23} W / cm^2$ and to a $2.6\,PW$ laser pulse focused to a one-wavelength focus spot. As it has been noticed recently [10], during interaction of the laser light with plasmas in the high amplitude range, a substantial portion of the incident light energy is transformed into electromagnetic radiation in the X-ray domain.

2. Electron interaction with a circularly polarized electromagnetic wave in a plasma in the radiation dominant regime

The investigations of free electron radiation during its interaction with an electromagnetic wave have always, starting from the work of J. J. Thomson, been of great significance. The literature devoted to studies of the electromagnetic wave – particle interaction is vast (see for example, Refs. [1-3, 11-13]).

Below in this Section we shall consider a relativistic electron interacting with a circularly polarized electromagnetic wave. In the case of a circularly polarized electromagnetic wave the fact that the charged particle moves along a circular trajectory simplifies its motion description, and one may borrow the expressions for the properties of the radiation emitted by the particle from the theory of synchrotron radiation [14,15]. Taking into account the effects of the radiation damping force, equations of the electron motion can be written as

$$\frac{d\mathbf{p}}{dt} = e\mathbf{E} + \frac{e}{c}\mathbf{v}\times\mathbf{B} + \mathbf{f}_R, \quad \frac{d\mathbf{x}}{dt} = \frac{\mathbf{p}}{m\gamma}. \tag{1}$$

Here, the particle momentum $\mathbf{p}$, velocity $\mathbf{v}$, and the Lorentz factor γ are $\mathbf{v} = d\mathbf{x}/dt$, $\gamma = \sqrt{1+|\mathbf{p}|^2/m_e^2c^2}$, and the radiation force $\mathbf{f}_R$ is approximately equal to,

$$\mathbf{f}_R = -\frac{2e^4}{3m_e^5c^7}\frac{\mathbf{p}}{\gamma}\left[\left(m_ec\gamma\mathbf{E} + \mathbf{p}\times\mathbf{B}\right)^2 - (\mathbf{p}\cdot\mathbf{E})^2\right]. \tag{2}$$

Here, we retained the leading term in the ultrarelativistic limit in the radiation force given by the expression presented in the text-book [1].

The electromagnetic wave is assumed to propagate in plasma with the velocity v_{ph} along the *x*-direction. It is given by the vector potential $\mathbf{A} = a_0(m_ec^2/e)\left(\mathbf{e}_y\cos\psi + \mathbf{e}_z\sin\psi\right)$, where $\psi = \omega(t - x/v_{ph})$. The electric and magnetic fields are $\mathbf{E} = -c^{-1}\partial\mathbf{A}/\partial t$ and $\mathbf{B} = \nabla\times\mathbf{A}$.

When the radiation damping force is taken into account the longitudinal component of the force (the radiation pressure) does not vanish. We assume that in this case the particle does not move along the *x*-axis because the radiation pressure force is balanced by the force due to the charge separation electric field in the plasma (see Refs. [13,16]). The *x*-component of a total force on the particle vanishes: $eE_x + e(v_yB_z - v_zB_y)/c = 0$, and the particle coordinate along the *x*-axis is equal to *x=0*. Here, the *x*-component of the electric field E_x that occurs due to the electric charge separation in the plasma. In the transverse

direction the particle rotates along a circle. From equations (1, 2) we obtain for the transverse components of the particle momentum with

$$\dot{p}_y = -a_0 m_e c\omega \sin\omega t - \dot{y}\Phi(a_0,\gamma), \tag{3}$$

$$\dot{p}_z = a_0 m_e c\omega \cos\omega t - \dot{z}\Phi(a_0,\gamma) \tag{4}$$

$$\Phi(a_0,\gamma) = \frac{2}{3}\left(\frac{e\omega a_0}{c}\right)^2 (\gamma^2 - p^2\sin^2\varphi), \tag{5}$$

where we introduced a phase φ between the particle rotation and the wave field, i.e. $p_y + ip_z = p\exp(i\omega t + i\varphi)$ and $\dot{y} + i\dot{z} = (p_y + ip_z)/m_e\gamma$. From equations (3, 4) we find for the particle momentum

$$a_0^2 = \left(\frac{p}{m_e c}\right)^2 + \varepsilon_{rad}^2 \frac{p^2}{m_e^2 c^2 + p^2}\left[a_0^2 + \left(\frac{p}{m_e c}\right)^4\right]^2. \tag{6}$$

Here the dimensionless parameter ε_{rad} is

$$\varepsilon_{rad} = (4\pi r_e / 3\lambda). \tag{7}$$

We see that in the limit of a relatively low amplitude laser pulse, when $1 \ll a_0 \ll a_{rad} = \varepsilon_{rad}^{-1/3}$, the particle momentum depends on the laser pulse amplitude as $p = m_e c a_0$, and in the limit $a_{rad} \ll a_0 \ll \varepsilon_{rad}^{-1/3} \equiv a_{rad}$ the momentum dependence on a_0 is given by $p = m_e c(a_0/\varepsilon_{rad})^{1/4}$ as it is illustrated in Figure 1.

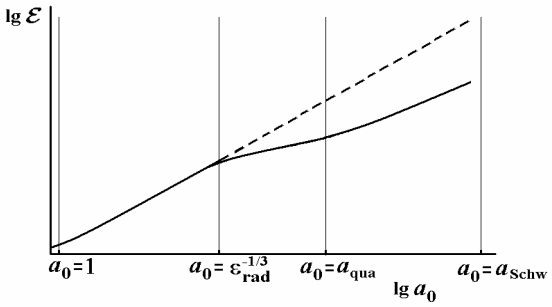

Figure 1. Double logarithm dependence of the particle energy on the dimensionless amplitude of the laser pulse. The dashed line corresponds to the dependence $\mathcal{E} = m_e c^2\sqrt{1 + a_0^2}$.

The Pointing vector of the electromagnetic wave is $\mathbf{P} = c\,\mathbf{E}\times\mathbf{B}/4\pi = \mathbf{v}_g E^2/4\pi$. The total scattering cross section is defined as

the ratio of the electromagnetic energy reemitted by the particle $eE(p/m_e\gamma)\sin\varphi$ with respect to the value of the Pointing vector. It reads

$$\sigma = \sigma_T \frac{p\left[a_0^{\,2}\left(m_e c\right)^4 + p^4\right]}{\left(a_0 m_e c\right)^2\left(m_e^{\,2}c^2 + p^2\right)^{1/2}}, \tag{8}$$

where the particle momentum p dependence on the wave amplitude a_0 is given by equation (6) and $\sigma_T = 8\pi r_e^{\,2}/3 = 6.65\cdot 10^{-25} cm^2$ is the Thomson cross section. In the limit of low laser pulse amplitude, when $1 \ll a_0 \ll a_{rad}$, the scattering cross section depends on the laser pulse amplitude as $\sigma \approx \sigma_T a_0^{\,2}(1 + a_0^{\,2})$, and in the limit $a_{rad} \ll a_0 \ll a_{rad}^{\,3}$ it is given by $\sigma \approx \sigma_T a_{rad}^{\,3}/a_0$ with a maximum of $\sigma \approx \sigma_T a_{rad}^{\,2}$ at $a_0 \approx a_{rad}$ [16].

Quantum physics effects become important when the photon, generated due to the Compton scattering, has the energy of the order of the electron energy, i.e. $\hbar\omega_m \approx \mathcal{E}_e$. (In the quantum regime in addition to the damping effects due to radiation, recoil effects due to the stochastic emission of photons have to be taken into account, thus making the motion explicitly stochastic similar to a Brownian particle subject to a noisy environment. However, we do not discuss here the quantum fluctuations of the electron orbit similar to the quantum fluctuations of the trajectory of an electron moving in a magnetic field [15]. The electron with the energy $\mathcal{E}_e = m_e c^2\gamma$ rotates with the frequency ω in the circularly polarized wave propagating in plasma and it emits photons with frequency $\omega_m = \omega\gamma^3$ [1]. We obtain that quantum effects come into play when $\gamma \geq \gamma_{qua} = \left(m_e c^2/\hbar\omega\right)^{1/2}$. For the electron interacting with one micron laser light we find $\gamma_q \approx 600$. From the previous analysis of the radiation effects we have for the electron gamma factor $\gamma = (a_0/\varepsilon_{rad})^{1/4}$. This is why the quantum limit is

$$a_{qua} = \frac{2e^2 m_e c}{3\hbar^2\omega} = \frac{1}{3\pi}\frac{r_e\lambda}{\lambda\!\!\!^{-}_c{}^2}, \tag{9}$$

where the Compton length is $\lambda\!\!\!^{-}_c = \hbar/m_e c$. For the equivalent electric field of the electromagnetic wave it yields

$$E_{qua} = \frac{2em_e^{\,2}c^2}{3\hbar^2} = \frac{2}{3}\frac{\lambda\!\!\!^{-}_c}{r_e}E_{Schw}. \tag{10}$$

Here $E_{Schw} = m_e{}^2 c^3 / e\hbar$ is the Schwinger electric field [17]. The quantum limit electric field E_q is in a factor $3/2\alpha = 3e^2/2\hbar c$, i.e. approximately 200 times, smaller than the Schwinger electric field.

In the radiation dominant regime in the quantum limit we have instead the equation (6)

$$a_0{}^2 - \left(p/m_e c\right)^2 = \varepsilon_{rad}{}^2 \left(p/m_e c\right)^8 \mathrm{U}^2(\Upsilon). \qquad (11)$$

Here the dimensionless variable Υ is $\Upsilon = \left(\hbar\omega / m_e c^2\right)\left(p/m_e c\right)^2$ and the function $U(\Upsilon)$ can be expressed via the Airy function and its derivative (see Refs. [2,18]). In classical limit, for $\Upsilon \ll 1$, the function $U(\Upsilon) \approx 1$, and in the quantum limit, when $\Upsilon \gg 1$, we have $U(\Upsilon) \approx (128\pi/81\sqrt{3})\Upsilon^{-4/3}$. Substituting this expression into equation (11) we find the electron momentum as a function of the electromagnetic wave amplitude in the limit $a_0 > a_q : p \approx 1.693 m_e c \left(\hbar\omega / m_e c^2\right)\left(a_0/\varepsilon_{rad}\right)^{3/4}$, as it is shown in Fig. 1.

For a one micron laser pulse interaction with plasmas, as it is well known, the relativistic effects become important for $a_0 \geq 1$, which corresponds to the radiation intensity above $I_{rel} = 1.38 \cdot 10^{18} W/cm^2$. The radiation dominant regime begins at $a_0 \approx a_{rad}$ with $a_{rad} \approx 400$, i.e. for the laser light intensity of the order of $I_{rad} = 3 \cdot 10^{23} W/cm^2$. Quantum physics effects come into play at $a_0 \approx a_q = 2500$, which gives $I_q = 1.38 \cdot 10^{26} W/cm^2$. We reach a limit when the nonlinear quantum electrodynamics effects with the electron-positron pair creation in the vacuum come into play, when the laser pulse electric field becomes equal to the Schwinger electric field $E_{Schw} = m_e{}^2 c^3 / e\hbar$, which corresponds to $a_{Schw} = m_e c^2 / \hbar\omega = 5 \cdot 10^5$ and $I_{Schw} = 3 \cdot 10^{29} W/cm^2$.

Above we have considered the charged particle interaction with the electromagnetic wave in a plasma when the radiation pressure force is balanced by the electric field due to the electric charge separation. As is well known, when the electromagnetic wave packet interacts with a charged particle at rest before the interaction in vacuum, the particle momentum and the Lorentz factor are given by $p_{||} = m_e c\, a_0{}^2/2$, $p_{\perp} = m_e c\, a_0$, $\gamma = 1 + a_0{}^2/2$ [1,3]. In the ultrarelativistic limit, when $a_0 \gg 1$ the longitudinal component of the particle momentum is much larger than the transversal component. The particle drift velocity along the direction of the wave propagation is equal to $v_{||} = p_{||}/2m_e\gamma = c a_0{}^2/(2 + a_0{}^2)$. We perform the Lorentz transformation into the reference frame moving with the particle drift velocity $v_{||}$. We find that

in the moving reference frame the dimensionless amplitude value of the laser pulse is the same as its value in the laboratory reference frame: $\overline{a}_0 = a_0$. This is a consequence of the fact that the transverse component of a four vector does dot change during the Lorentz transformation. In contrast, the parameter ε_{rad}, given by (7), is not a Lorentz invariant. We can find that it is $\overline{\varepsilon}_{rad} = (4\pi r_e / 3\overline{\lambda}) = \varepsilon_{rad} / \left(1 + a_0{}^2\right)^{1/2}$, where we have used the fact that the wavelength of the laser pulse in the moving reference frame is equal to $\overline{\lambda} = \left[(c + v_{||})/(c - v_{||})\right]^{1/2} \lambda = \left(1 + a_0{}^2\right)^{1/2} \lambda$. The limit of the radiation dominant regime now reads as $a_0{}^3 \gg \overline{\varepsilon}_{rad}{}^{-1}$ or $a_0 \gg \varepsilon_{rad}{}^{-1/2}$. It is easy to show that quantum effects, in the case of the charged particle interaction with the electromagnetic wave in vacuum, become important when the wave electric field reaches the Schwinger limit.

3. Scattering of the laser light on small clusters and the interaction of a super-intense laser pulse with a thin foil

We have considered above the light scattering on a charged particle within the framework of the single particle-light interaction. Another approach to study the radiation dominant regimes for the laser – plasma interaction is connected with the usage of targets with their size significantly smaller than the wavelength of the laser radiation. The examples of such the interaction can be provided by small cluster targets and a thin foil target.

3.1. *The laser-cluster interaction*

The laser – cluster interaction is accompanied by the efficient transformation of the laser light energy into the energy of the scattered electromagnetic wave [19]. In typical situations the cluster size is smaller than the wavelength of the laser light. In this case the scattering occurs in the collective regime and the scattering cross section increases as N^2. Here, N is the number of electrons involved into the scattering process. Typical value of the electron number in the cluster can be estimated to be equal to $N = 10^8$. We see that the parameter $a_{rad} = (4\pi N r_e / \lambda)^{-1/3}$ becomes ≈ 500 times larger. It corresponds to the laser intensity of the order of $I_q = 10^{18} W / cm^2$. Thus in this regime we can model the radiation dominant laser plasma interaction using the moderate power lasers and provide a source of powerful ultra-short electromagnetic bursts.

When the cluster is exposed to a strong enough electromagnetic wave the electrons are pushed away within a few laser cycles. The electron bunch moves with acceleration and hence, it generates coherent EM radiation. This radiation was identified in the 3D PIC simulation corresponding to Figure 2. The electron bunch makes a few oscillations almost without decaying. It generates a short pulse of high-intense antenna-like EM radiation shown in Fig. 2, see Ref. [20]. Due to coherent motion of electrons the magnitude of radiation reaction is significant. Therefore this case provides an example of the radiation-dominant regime of laser-plasma interaction, where a bunch of electrons behaves as a single ultra-relativistic particle.

Even in the relatively low intensity limit the radiation damping may play an important role leading to the saturation of resonances [20]. For example, in the case of electrically non-neutral spherical cluster the electrostatic component of the electric field is radial: $\mathbf{E} = 4\pi e n \mathbf{r}$ with the electric charge density inside the cluster *en*. Incorporating this electric field into the equations of the particle motion, we obtain instead (6) equation

$$a_0^{\,2} - \left(\frac{p}{m_e c}\right)^2 \left[1 - \frac{\delta m_e c}{(m_e^{\,2}c^2 - p^2)^{1/2}}\right]^2 = \varepsilon_{rad}^{\,2} \frac{p^2}{m_e^{\,2}c^2 + p^2}$$

$$\left\{a_0^{\,2} + \delta\left(\frac{p}{m_e c}\right)^2 \left[1 - \left(\frac{p}{m_e c}\right)^2\right]^{1/2} + \left(\frac{p}{m_e c}\right)^4 \left[1 - \frac{\delta m_e c}{(m_e^{\,2}c^2 - p^2)^{1/2}}\right]^2\right\}^2 . \quad (12)$$

Here $\delta = (\omega_{pe}/\omega)^2$. This equation has a form of the equation for the amplitude of driven oscillations for a nonlinear oscillator in the presence of damping. Here the nonlinearity comes from the relativistic dependence of the particle mass on its energy. From the left hand side of this equation we see that in the limit of a small amplitude wave a resonance appears at $\delta = 1$. If the ratio $\varepsilon_{rad}/a_0 \ll 1$, the resonance saturates at the amplitude $a_m \approx a_0/\varepsilon_{rad}$. As it is well known the nonlinear dependence of the oscillator frequency on the oscillation amplitude results in appearance of the region with three stationary solutions and the hysteresis (see Ref. [21]). Typical resonance curves are presented in Figure 3, where the transverse momentum versus the parameter δ for different values of the e. m. wave amplitude a_0 are shown. In Figure 4 we present the dependence of the particle momentum on the wave amplitude.

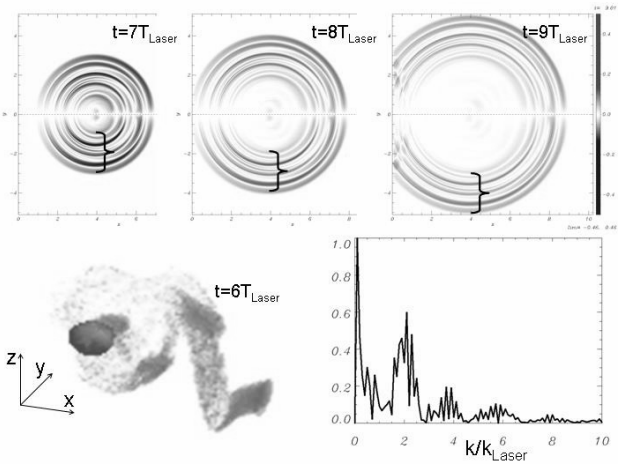

Figure 2. Coherent radiation from the cluster. Electromagnetic field pattern at t=7T, t=8T and t=9T (upper row), where T is the period of laser radiation. Electron and ion density distribution (lower left hand side frame). The frequency spectrum of emitted radiation (lower right hand side frame).

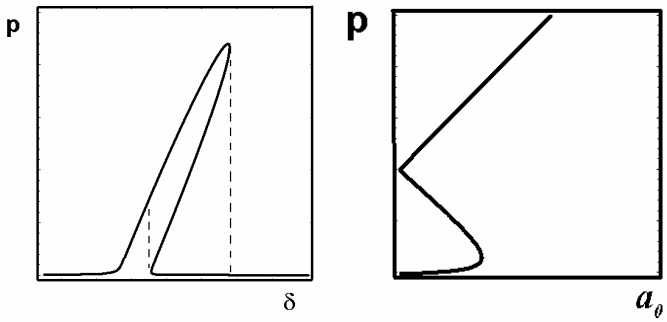

Figure 3. Transverse momentum versus the parameter δ (l.h.s. frame).
Figure 4. Particle momentum versus e.m. wave amplitude (r.h.s. frame).

We see that for a relatively small amplitude wave ($a_0 < \delta$) we have a region where we have three branches of the solution. The momentum depends on a_0 , as a_0 / δ for the first branch, it changes from 1 at $a_0 \approx \delta$ to $\approx \delta$ at small a_0 , and then is increases monotonously for the third branch. On the third branch the momentum increases as a_0 for $a_0 < \varepsilon_{rad}^{-1/3}$, which corresponds to the negligibly

small effects of the radiation damping, and then it grows as $(a_0 / \varepsilon_{rad})^{1/4}$ for $a_0 > \varepsilon_{rad}^{-1/3}$ in the radiation dominated regime.

3.2. *High efficiency ion acceleration during the laser-foil interaction*

It is well known that the interaction of a laser with a thin target can produce a copious high energy proton beam with superior transverse emittance. The proton generation is a direct consequence of the electron acceleration. The electrons that are violently accelerated in the laser field can attract protons behind them. In the radiation dominant regime the proton acceleration process acquires novel features. In this case the proton slab moves with almost the same velocity as the electron slab and the acceleration is realized through direct action of the radiation pressure force. This regime is illustrated in Figures 5-7.

Here the linearly polarized (with s-polarization) laser pulse interacts with a thin foil target. The laser pulse has the size $10\lambda \times 10\lambda$ and the amplitude $a_0 = 316$. The foil density is equal to $n = 16 n_{cr}$ and its thickness is $\lambda / 4$. During the laser foil interaction the laser pulse deforms the foil into the "cocoon", which confines the laser radiation (see Figures 6 and 7). The leading part of the foil moves with relativistic velocity. This results in the reflection of the laser light at the relativistic mirror. Since the reflected radiation has a substantially lower amplitude and frequency compared with the initial amplitude and frequency, the energy of the laser pulse is almost completely transformed into proton energy. The energy spectrum of the electrons and protons is shown in Figure 8. We see that the fast proton energy is 3.5 times larger than the electron energy.

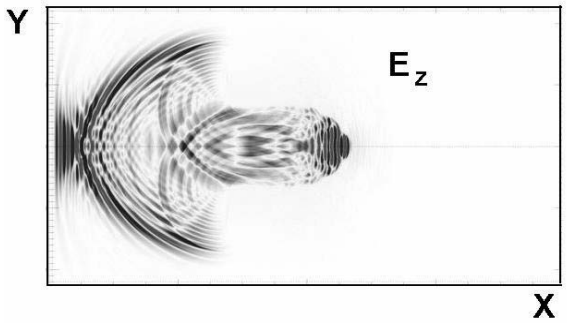

Figure 5. Distribution of the z-component of the electric field in the x,y plane at t=87.5T, where T is the laser radiation period.

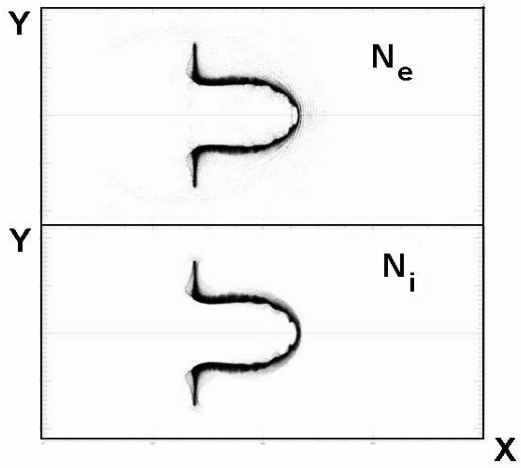

Figure 6. Distribution of the electron (upper frame) and the ion (lower frame) denstity in the x,y plane at t=87.5T.

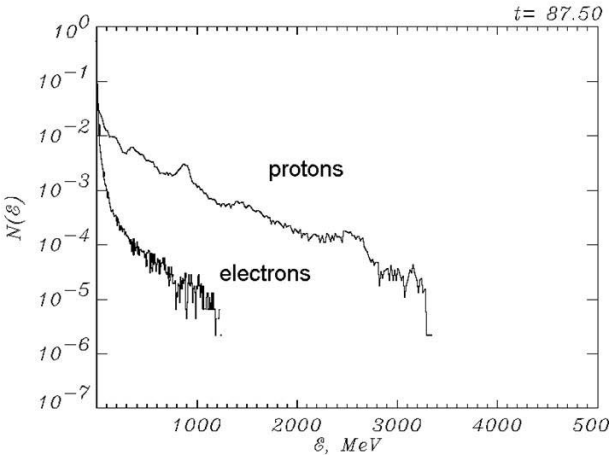

Figure 7. The electron and the ion energy spectra at t=87.5T.

4. Intensification of the Electromagnetic Radiation during its Interaction with the "Flying Mirror" formed in the Wake behind the Laser Pulse

Today's technology tells us that the power of the most powerful laser that could be built is limited by the available pump source. As it has been discussed by Tajima and Mourou in Ref. [5] the largest laser that could be used as a pump, at present is the National Ignition Facility (NIF) in the US and the

Laser Megajoule in France. Assuming that we could compress the beam over 10fs, with a 70% efficiency compressor we would obtain a power close to 0.1×10^{21} W or 0.1 zettawatt.

Using another approach [22], ultra high intensity electromagnetic radiation limit can be reached as a result of subsequent laser radiation frequency up-shifting and focusing into a one-wavelength focus spot. Within the framework of this scheme we use the properties of the wake field generated in underdense plasmas by the ultra-short relativistically strong laser pulse – driver. The electron density modulation within nonlinear wake plasma waves can be regarded as high density plasma shells moving with velocity v_{ph} close to the speed of light in vacuum. The second laser pulse, which counter propagates with respect to the driver pulse, may now be reflected back at these relativistic electron shells with frequency upshifting and compression of the reflected pulse. We may say that in a wake behind the laser pulse – driver we see "flying relativistic mirrors". As a result the wavelength of the reflected wave becomes a factor $4\gamma_{ph}{}^2 \gg 1$ shorter.

Within the framework of this scheme it is important that the relativistic dependence of the Langmuir frequency on the wave amplitude results in the formation of wake waves with curved fronts that have a form close to a paraboloid. The electromagnetic wave reflection at the paraboloid flying mirror leads to the electromagnetic wave focusing. The resulting intensity in the laboratory frame increases by a factor $16\gamma_{ph}{}^6 (R_0 / \lambda)^2$. This value must be multiplied on the reflection coefficient which is smaller than one. Calculation of the reflection coefficient shows that it is about $\gamma_{ph}{}^{-4}$. As a result we can have the electromagnetic wave intensification of a factor $\approx 16(R_0 / \lambda)^2 \gamma_{ph}{}^2$.

Take the example of the wakefield excitation in a gas of density $10^{19} cm^{-3}$. This means the Lorentz factor associated with the phase velocity of the wakefield is related to ω / ω_{pe}, which is on the order of 10. Thus a laser pulse intensification of the order of 10^4 may be realized for $R_0 / \lambda \approx 10$. For the plasma density equal to $10^{17} cm^{-3}$ the Lorentz factor associated with the wake field phase velocity is equal to 100, and the laser pulse intensification may reach 10^6. In this case one finds if one has a laser of 1PW and focuses it down to the intensity of $10^{22} W / cm^2$, the relativistic engineering of this intensification may lead to the intensity of $10^{28} W / cm^2$. We see that the reflected radiation intensity can approach the Schwinger limit. In this range of electromagnetic field intensity it becomes possible to investigate the fundamental problems of the current physics using presently available laser devices.

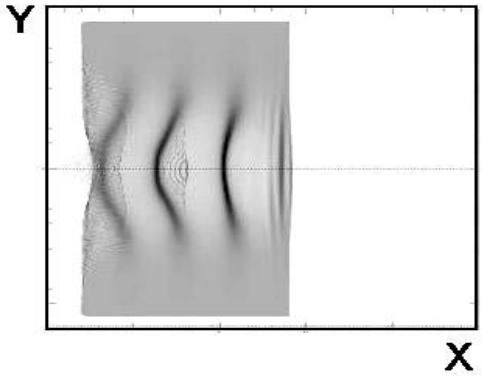

Figure 8. Paraboloidal modulations of the electron density in the wakewave.

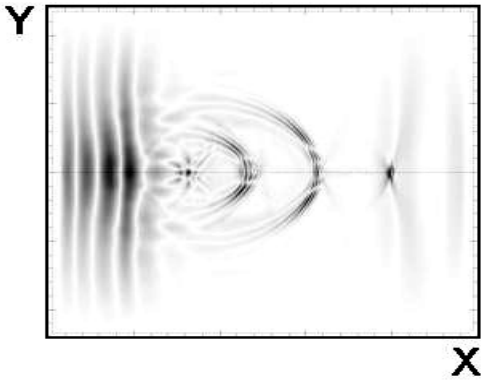

Figure 9. The projections of the electric field components.

Now we present the results of 2D PIC simulations of the laser pulse reflection at the "flying mirrors". The results of the simulations are presented in Figures 8 and 9. Figure 8 shows the paraboloidal modulations of the electron density in the wake behind the driver laser pulse. Their transverse size is larger than the reflecting laser pulse wavelength. In Figure 9 we present the z-component of the electric field. We see that the reflected laser light has its wavelength substantially shorter than in the incident wave as well as its focusing in a region with size also much smaller than the wavelength of the incident pulse. For the parameters of the simulations the phase velocity of the wake wave corresponds to $\beta_{ph} = 0.87$, i. e. $\gamma_{ph} = 2$. The reflected light has a frequency a factor 14 higher than the incident radiation in perfect agreement with the expression $(1 + \beta_{ph})/(1 - \beta_{ph}) \approx 14.4$. The electric field of the reflected

radiation is at about 16 times higher than in the incident pulse, i. e. the intensity increases 256 times. These results provide us a proof of principle of the electromagnetic field intensification during reflection of the laser radiation at the flying paraboloidal relativistic mirrors in the wake plasma waves.

References

1. L. D. Landau and E. M. Lifshits, *The Classical Theory of Fields* (Pergamon Press, Oxford, 1980).
2. V. B. Beresteskii, E. M. Lifshitz and L. P. Pitaevskii, *Quantum Electrodynamics* (Pergamon, Oxford, 1982).
3. F. V. Hartemann, *High-Field Electrodynamics* (CRC Press, NY, 2002).
4. D. M. Fradkin, *Phys. Rev. Lett***. 42**, 1209 (1979).
5. T. Tajima and G. Mourou, G., *Phys. Rev,* **STAB 5**, 031301 (2002).
6. J. E. Gunn and J. P. Ostriker, *Phys. Rev. Lett*. **22**, 728 (1969).
7. V. S. Berezinskii, S. V. Bulanov, V. L. Ginzburg, V. A. Dogiel. and V. S. Ptuskin, *Astrophysics of Cosmic Rays* (Elsevier, Amsterdam,1990).
8. G. Mourou, C. P. J. Barty and M. D. Perry, *Phys. Today* **51**, 22 (1998).
9. A.I. Akhiezer and R. V. Polovin, *Sov Phys. JETP* **30**, 915 (1956).
10. A. Zhidkov, et al., *Phys, Rev. Lett.* **88**, 185002 (2002).
11. A. I. Nikishov and V. I. Ritus, *Sov. Phys. JETP* **19**, 529 (1964).
12. E. S. Sharachik and G. T. Schappert, *Phys. Rev.* **D 1**, 2378 (1970).
13. Ya. B. Zel'dovich, *Sov. Phys. Usp*. **18,** 79 (1975).
14. V. L. Ginzburg and S. I. Syrovatskii, *Ann. Rev. Astron. Astrophys*. **3**, 297 (1965).
15. A. A. Sokolov and I. M. Ternov, *Synchrotron Radiation* (Pergamon Press, NY, 1968).
16. Ya. B. Zel'dovich and A. F. Illarionov, *JETP* **34**, 467 (1972).
17. J. Schwinger, *Phys. Rev.* **82**, 664 (1951).
18. V. I. Ritus, in: *Proceedings of the P. N. Lebedev Physics Institute of Acad. Sci. USSR,* **vol. 111** (Moscow, Nauka, 1979), p.5.
19. Y. Kishimoto, and T. Tajima, in: *High Field Science*, eds. Tajima, T., Mima, K. and Baldis, H. (Plenum, NY, 1999) p.85.
20. G. A. Askar'yan and S. V. Bulanov, *Sov. Tech. Phys. Lett.* **9**, 533 (1983).
21. L. D. Landau and E. M. Lifshits, *Mechanics* (Pergamon Press, Oxford, 1980).
22. T. Zh. Esirkepov, S. V. Bulanov and T. Tajima, in: *Present Proceedings*.
23. S. V. Bulanov, et al., in: *Reviews of Plasma Physics*. **Vol. 22**, ed. by V.D. Shafranov, (Kluwer Academic / Plenum Publishers, NY, 2001), p. 227.

ELECTRON-POSITRON PAIR-BEAM PRODUCTION AND ACCELERATION IN ULTRA-STRONG LASER-PLASMA INTERACTIONS

KAZUHISA NAKAJIMA

High Energy Accelerator Research Organization
1-1 Oho, Tsukuba, Ibaraki, 305-0801, Japan
E-mail: nakajima@post.kek.jp

Recent tremendous advances of ultraintense lasers have enabled the production of positrons via pair creation in ultrastrong fields in plasma. This process produces an electron-positron pair beam with relativistic energy in an overdense plasma, where an ultraintense ultrashort laser pulse propagates. We propose an intense pair-beam production and its acceleration up to high energies via consecutive interactions with ultrastrong laser fields. Applications of pair-beams provide a new concept of laser-plasma accelerators and an electron-positron collider in a micro-scale size.

1. Introduction

The recent progress of ultraintense lasers makes it possible to conceive a novel concept on production and acceleration of an intense electron-positron pair beam, and its application to an electron-positron collider. The strong laser field can produce plasmas through quantum mechanical tunneling ionization mechanism, and accelerate produced electrons and ions to generate a relativistic electron beam and energetic ions in plasmas. This process will be followed by creation of electron-positron pairs through interaction of relativistic electrons with a Coulomb field of a nucleus in plasma ions or a strong laser field. In the ultraintense laser intensities more than 10^{21} W/cm^2, the pair-production rate rises quickly to enormous values. Since the pair-production occurs in the presence of the laser field and the electrostatic field generated by an ultraintense laser pulse, the produced pairs will be accelerated by the coherent action of those fields to form a relativistic beam. This pair-beam will be useful for applications to high energy collider physics as an electron-positron beam source if it can be accelerated to a very high energy and focused to a very small spot size.

In this paper, the possible pair-production processes in strong laser-

plasma interactions are investigated to estimate the number of electron-positron pairs in terms of the laser intensity and the plasma density. We propose acceleration and focusing of the pair beam by the ponderomotive acceleration scheme to compose a high energy electron-positron collider with very high luminosity.

2. Pair production processes in laser fields

2.1. *Multiphoton pair creation in a Coulomb field*

The creation of an electron-positron pair in the vicinity of a nucleus with charge Z is a process of extremely large multiphoton order, given by

$$n\omega_L + Z \to e^+e^- \tag{1}$$

where a very large number of photons of the order of $n \sim 2m_ec^2/\hbar\omega_L$ must be absorbed for any laser frequency ω_L to create a pair. The pair creation rate per nucleus is expected to be of order[1]

$$W \sim \exp\left[-\frac{m_ec^2}{\hbar\omega_L}\right] \sim \exp[-10^6]\ \mathrm{sec}^{-1}. \tag{2}$$

The cross section for this process is so small at optical frequencies as to make it completely negligible in laser-plasma interactions.

2.2. *Pair creation by relativistic electrons*

Focused laser pulses produce plasmas in matter. Electrons can be accelerated to relativistic energy by electrostatic wakefields collectively generated by intense short laser pulses in plasmas or by direct laser fields as the quiver motion of electrons becomes relativistic. When the incident electron kinetic energy exceeds the pair-production threshold $2m_ec^2$, the high energy electron can produce an electron-positron pair by scattering in the Coulomb potential of a nucleus in the process, often called "trident process".

$$e + Z \to e'e^+e^-. \tag{3}$$

The cross section for the trident pair-production process is first calculated by Bhabha as[2]

$$\sigma_T = \frac{(\alpha r_eZ)^2}{128}\left(\ln\gamma^2 - \frac{161}{60} + c_1 + c_2 + c_3\right)(\gamma-3)^4, \tag{4}$$

where α is the fine structure constant, $r_e = e^2/m_ec^2$ is the classical electron radius, Z is the nuclear charge, and γ is the Lorentz factor of the electron

with the kinetic energy E_v, defined by $\gamma = 1 + E_v/(m_e c^2)$. The symbols c_1, c_2, and c_3 are lengthy algebraic functions of γ, given by Bhabha's paper[2]. The more exact calculation can be approximated over most of the energy range near the trident production threshold as[3]

$$\sigma_T \approx 9.6 \times 10^{-4} \frac{(\alpha r_e Z)^2}{(\gamma - 3)^{3.6}}. \tag{5}$$

2.3. *Pair creation by an incident non-laser photon*

An incident non-laser photon can produce an electron-positron pair in presence of a laser field in the process

$$\omega + n\omega_L \to e^+ e^-. \tag{6}$$

For $n = 1$, this pair production in two-photon collision is known as Breit-Wheeler process[4] of which the cross section for unpolarized photons is given by

$$\sigma_{pair} = \frac{1}{2}\pi r_e^2 (1 - \beta^2) \left((3 - \beta^4) \ln \frac{1 + \beta}{1 - \beta} - 2\beta(2 - \beta^2) \right), \tag{7}$$

where $\beta = (1 - m_e^2 c^4/(\hbar^2 \omega \omega_L))^{1/2}$. The multiphoton Breit-Wheeler process is considered as the trident process

$$e + n\omega_L \to e' e^+ e^-. \tag{8}$$

In this process an incoming high energy electron emits a virtual photon that decays into an electron-positron pair in the presence of the absorption of n laser photons. From the energy-momentum conservation for the trident process, the threshold electron Lorentz factor for a head-on collision between laser and electron is given by

$$\gamma > \frac{2 m_e c^2}{n \hbar \omega_L} \left(1 + \frac{\langle e^2 \mathbf{A}^2 \rangle}{m_e^2 c^4} \right), \tag{9}$$

where $\mathbf{A}$ is the vector potential of a laser field[5].

Schwinger[6] predicted that the spontaneous breakdown of vacuum occurs in a strong static electric field at the critical value,

$$E_c = \frac{m_e^2 c^3}{e\hbar} = 1.32 \times 10^{16} \text{ V/cm}. \tag{10}$$

The physical meaning of this critical field can be interpreted as follows. A charge e moving through the uniform electric field E_c over the distance permitted by the uncertainty relations, i.e., the Compton wavelength $\lambda_C =$

$\hbar/m_e c$ gains the energy, which should be at least equal to the rest mass, $eE_c\lambda_C = m_e c^2$. The pair production in vacuum in the presence of a strong laser field has been discussed by Brezin and Itzykson[7] using the normalized vector potential of the laser field,

$$a_0 = \left[\frac{e|\langle A_\mu A^\mu\rangle|}{m_e^2}\right]^{1/2} = \frac{eE_{\rm rms}}{\omega_0 m_e c}, \tag{11}$$

where $\langle\rangle$ denotes the average over one period of the field, $E_{\rm rms}$ is the root mean-square electric field and ω_0 is the laser angular frequency. The pair production probabilities per unit time-unit volume are derived for two cases: in the perturbative regime, $a_0 \ll 1$,

$$w \simeq \frac{\alpha E^2}{4\hbar}\left(\frac{eE}{2m_e\omega_0 c}\right)^{4m_e c^2/\hbar\omega_0}, \tag{12}$$

and in the static (zero frequency) regime, $a_0 \gg 1$,

$$w \simeq \frac{\alpha E^2}{\pi\hbar}\exp\left(-\frac{\pi m_e^2 c^3}{e\hbar E}\right). \tag{13}$$

In the perturbative regime $n = 2m_e c^2/\hbar\omega_0$ is the number of photons required to produce the pair. In the static regime the behavior of the rate can be understood as a quantum-mechanical tunneling. This is analogous to ionization, where a pair is bound in vacuum with binding energy $V_0 \sim 2m_e c^2$.

3. Electron acceleration in plasmas

In order to produce electron-positron pairs in plasma via the trident process in the presence of either nuclear charge fields or laser fields, initially plasma electrons must be accelerated up to relativistic energy for both cases. For a nonrelativistic plasma wave, the acceleration gradients are limited to the order of the wave-breaking field given by

$$eE_0[\text{eV/cm}] = m_e c\omega_p \simeq 0.96 n_e^{1/2}[\text{cm}^{-3}], \tag{14}$$

where $\omega_p = (4\pi n_e e^2/m_e)^{1/2}$ is the electron plasma frequency and n_e is the ambient electron plasma density. It means that the plasma density of $n_e = 10^{18}$ cm^{-3} can sustain the acceleration gradient of 100 GeV/m. The recent laser-plasma interaction experiments have demonstrated relativistic electron acceleration exceeding > 200 MeV for the laser strength parameter $a_0 \sim 1$[8,9]. Here we estimate the energy of electrons accelerated by ultraintense laser pulses in plasmas.

3.1. *Basic equations for particle acceleration in plasma*

The laser electromagnetic field and electron space charge field can be expressed by the vector potential $\mathbf{A}$ and the scaler potential Φ as

$$\mathbf{E} = -\frac{1}{c}\frac{\partial \mathbf{A}}{\partial t} - \nabla\Phi, \qquad \mathbf{B} = \nabla \times \mathbf{A} \tag{15}$$

The equation of a particle motion is written as

$$\frac{d\mathbf{p}}{dt} = -\left(e\mathbf{E} + \frac{\mathbf{v}}{c} \times \mathbf{B}\right) = \left(e\Phi + \frac{1}{c}\frac{\partial A}{\partial t}\right) - \frac{\mathbf{v}}{c} \times (\nabla \times \mathbf{A}), \tag{16}$$

where $d/dt \equiv \partial/\partial t + \mathbf{v} \cdot \nabla$. The equation of a particle energy is given by

$$\frac{d\gamma mc^2}{dt} = -e\mathbf{v} \cdot \left(\nabla\Phi + \frac{1}{c}\frac{\partial A}{\partial t}\right). \tag{17}$$

The vector potential and the scaler potential can be obtained from the Maxwell's equations and the continuity equation of plasma density n

$$\left(\frac{1}{c^2}\frac{\partial^2}{\partial t^2} - \nabla^2\right)\mathbf{A} = \frac{4\pi}{c}\mathbf{j} - \nabla\left(\frac{1}{c}\frac{\partial\Phi}{\partial t} + \nabla \cdot \mathbf{A}\right), \tag{18}$$

$$\nabla \cdot \left(\nabla\Phi + \frac{1}{c}\frac{\partial \mathbf{A}}{\partial t}\right) = -4\pi\rho, \tag{19}$$

$$\frac{\partial n}{\partial t} + \nabla \cdot n\mathbf{v} = 0 \tag{20}$$

where $\mathbf{j} = \langle -en\mathbf{v}\rangle$ is the current density and $\rho = \langle -en\rangle$ is the charge density, respectively.

In a 1-dimensional laser field according to the Coulomb gauge $\nabla \cdot \mathbf{A} = 0$, letting the axial field $A_z = 0$, the vector potential is expressed as

$$\mathbf{A} = A_x\mathbf{e}_x + A_y\mathbf{e}_y \quad \text{(the circular polarization)}, \tag{21}$$

$$\mathbf{A} = A_x\mathbf{e}_x \qquad \text{(the linear polarization)}. \tag{22}$$

Considering the laser pulse frame propagating at a group velocity in plasma $v_g = c(1-\omega_p^2/\omega_0^2)^{1/2}$, the momentum equation can be transformed to a new variable $\zeta - v_g t$. From the transverse component of the equation,

$$\frac{d}{d\zeta}\left(\mathbf{p}_\perp - \frac{e}{c}\mathbf{A}_\perp\right) = 0. \tag{23}$$

This gives conservation of canonical transverse momentum

$$\mathbf{p}_\perp = \frac{e}{c}\mathbf{A}_\perp. \tag{24}$$

Then the electron quiver velocity is given by $\mathbf{v}_\perp = \mathbf{p}/(\gamma m) = (e/\gamma mc)\mathbf{A}_\perp$ where the Lorentz factor $\gamma = (1-\beta^2)^{-1/2}$ and $\beta = v/c$. Defining the normalized vector potential, $\mathbf{a} \equiv e\mathbf{A}/(mc^2)$, the normalized particle velocity is written as $\beta_\perp = \mathbf{a}_\perp/\gamma$.

The longitudinal component of the energy equation derives

$$\frac{d}{d\zeta}\left(p_z - \frac{\gamma mc^2}{v_g} + \frac{e}{v_g}\Phi\right) = 0. \tag{25}$$

This gives

$$\gamma(1-\beta_g\beta_z) - \phi = \gamma_0(1-\beta_g\beta_0) \tag{26}$$

where $\beta_g = v_g/c$ is the normalized group velocity and $\phi \equiv e\Phi/mc^2$ is the normalized scaler potential of the electron space charge field, assuming that prior to the laser-particle interaction, $\gamma = \gamma_0$, $\beta_z = \beta_0$ and $\mathbf{a}_\perp = \phi = 0$. Using the relation $\gamma = \gamma_\perp\gamma_z$ where $\gamma_\perp = \sqrt{1+\mathbf{a}_\perp^2}$, and $\gamma_z = 1/\sqrt{1-\beta_z^2}$, these two equations can be solved on the normalized velocity β and the energy γ as

$$\beta_\perp = \frac{\mathbf{a}}{\gamma},\ \beta_z = \frac{\beta_g\gamma_\perp^2 \pm H_0[H_0^2 - (1-\beta_g^2)\gamma_\perp^2]^{1/2}}{H_0^2 + \beta_g^2\gamma_\perp^2}, \tag{27}$$

and

$$\gamma = \frac{H_0^2 + \beta_g^2\gamma_\perp^2}{H_0 \mp \beta_g[H_0^2 - (1-\beta_g^2)\gamma_\perp^2]^{1/2}}, \tag{28}$$

where $H_0 = \gamma_0(1-\beta_g\beta_0) + \phi$.

The space-charge potential ϕ is obtained from the continuity equation and the Poisson's equation:

$$\frac{\partial n}{\partial t} + \nabla\cdot(n\beta) = 0, \tag{29}$$

$$\nabla^2\phi = k_p^2\left(\frac{n}{n_e} - 1\right), \tag{30}$$

where $k_p = \omega_p/c$ is the plasma wave number. In an initial equilibrium prior to the laser pulse, the space-charge potential is negligible, i.e. $\phi = 0$. Assuming $n = n(\zeta)$, the continuity equation becomes

$$\frac{d}{d\zeta}\left[n(\beta_g - \beta_z)\right] = 0. \tag{31}$$

This derives the electron density in plasma as

$$n = n_e\frac{\beta_g - \beta_0}{\beta_g - \beta_z}. \tag{32}$$

Assuming that the group velocity is close to the vacuum speed of the light , i.e. $\beta_g \approx 1$, the Poisson's equation is

$$\frac{d^2\psi}{d\zeta^2} = \frac{\hat{k}_p^2}{2}\left[\frac{1+a^2}{(1+\psi)^2} - 1\right], \tag{33}$$

where $\psi = \phi/\gamma_0(1-\beta_0)$ and $\hat{k_p} = k_p/\gamma_0^{3/2}(1-\beta_0)$. This is the nonlinear wake equation on the electrostatic potential ψ driven by the ponderomotive potential $\mathbf{a}(\zeta)$ of a laser pulse. In the short pulse limit of $c\tau_L \ll \lambda_p/2\pi$, where τ_L is the laser pulse duration and λ_p is the plasma wavelength, the wake excitation is negligible: $|\psi| \ll 1$. In the long pulse limit of $c\tau_L \gg \lambda_p/2\pi$, the electrostatic potential is given by

$$\psi \approx \langle(1+\mathbf{a}^2)^{1/2}\rangle - 1 \cong (1+a_0^2/2)^{1/2} - 1, \tag{34}$$

for the linearly polarized laser pulse. The amplitude of the normalized vector potential is given by

$$a_0 = (2e^2\lambda_0^2 I/\pi m_e^2 c^5)^{1/2} \cong 0.855\times 10^{-9}\lambda_0[\mu\mathrm{m}]I^{1/2}[\mathrm{W/cm^2}], \tag{35}$$

where λ_0 is the laser wavelength and I is the laser intensity.

3.2. *Production of a high energy ultrashort intense electron beam in plasmas*

In the short pulse limit, $\phi = 0$, the maximum and minimum energies of electrons by the laser field is given by

$$\gamma_{\mathrm{max,min}} = \gamma_g^2\gamma_0(1-\beta_g\beta_0) \pm \gamma_b\beta_g[\gamma_g^2\gamma_0^2(\beta_g-\beta_0)^2 - \mathbf{a}^2]^{1/2}, \tag{36}$$

where $\gamma_g = (1-\beta_g^2)^{-1/2}$. For initially stationary plasma electrons, $\phi = \gamma_L - 1$, where $\gamma_L = (1+a_0^2/2)^{1/2}$ in the long pulse limit, the final accelerated energy is

$$\gamma = (2\gamma_g^2 - 1)\gamma_L \tag{37}$$

The dispersion relation of relativistically strong electromagnetic waves is

$$\omega^2 = k^2c^2 + \omega_p^2/\gamma_L. \tag{38}$$

This gives a group velocity of the intense laser pulses:

$$\beta_g = \left(1 - \frac{\omega_p^2}{\gamma_L\omega_0^2}\right)^{1/2} = \left(1 - \frac{n_e}{\gamma_L n_c}\right)^{1/2}, \tag{39}$$

where $n_c = \pi/(r_e\lambda_L^2)$ is the critical plasma density. It implies that the laser pulses can propagate overdense plasmas for $n_e < \gamma_L n_c$. This corresponds to the relativistic transparency of overdense plasmas. As $\gamma_g = \omega_0\sqrt{\gamma_L}/\omega_p = (\gamma_L n_c/n_e)^{1/2}$, the final energy is given by

$$\gamma = 2\gamma_L^2 n_c/n_e - \gamma_L \approx a_0^2 n_c/n_e. \tag{40}$$

The density n_1 of accelerated electrons can be calculated from Eq. (32) as

$$n_1 = n_e\beta_g/|\beta_g - \beta_z| = (2\gamma_g^2 - 1)n_e = 2\gamma_L n_c - n_e \approx \sqrt{2}a_0 n_c \tag{41}$$

Finally the intense laser pulse propagating the plasma with thickness Δ an electron beam with bunch length,

$$l_b = \Delta|\beta_z - \beta_g|/\beta_g = \Delta/(2\gamma_g^2 - 1) \cong n_e\Delta/(2\gamma_L n_c) \approx n_e\Delta/(\sqrt{2}a_0 n_c). \tag{42}$$

As an example, the intense laser pulse of the wavelength $\lambda_0 = 0.8\mu$m with the intensity $I = 2.1 \times 10^{20}$ W/cm^2 ($a_0 = 10$) can accelerate electrons up to the energy of 1.6 GeV in a plasma of the electron density $n_e = 5.3 \times 10^{19}$ cm^{-3}. An electron beam produced from a plasma with thickness $\Delta = 100$ μm is compressed to the bunch length $l_b = 0.2$ μm (700 attoseconds) with density of $n_1 = 2.4 \times 10^{22}$. The results of the particle-in-cell simulation can show such high energy high intensity electron beam production in plasmas[10].

4. Pair-beam production yield in plasmas

4.1. *A trident process in the nuclear field*

The pair creation rate by means of the trident process in a volume of which the characteristic length $l\lambda$ is

$$\frac{dN_p}{dt} = (l\lambda_0)^3 n_i n_e \sigma_T v_e, \tag{43}$$

where n_i is the ion (nucleus) density, n_e is the electron density and $v_e = \beta c = (c/\gamma)(\gamma^2 - 1)^{1/2}$ is the velocity of the electron. In a plasma containing of charge $Z_i = n_e/n_i$,

$$\frac{dN_p}{dt} = \frac{9.6\pi^2}{10^4}\left(\frac{c}{\lambda_0}\right) l^3\alpha^2\frac{Z^2}{Z_i}\left(\frac{n_e}{n_c}\right)^2(\gamma - 3)^3.6(\gamma^2 - 1)^{1/2}/\gamma. \tag{44}$$

Substituting Eq. (40) into the electron energy $\gamma \gg 3$, the pair production yield is given by

$$N_{pair} \approx \frac{0.48\pi^3}{10^3}\alpha^2 a_0^8 Z^3\left(\frac{n_c}{n_e}\right)^2\left(\frac{r_0}{\lambda_0}\right)^2\left(\frac{\Delta}{\lambda_0}\right)^2 \tag{45}$$

$$\approx 2.8 \times 10^{-45} Z^3 I^4[\mathrm{W/cm^2}] n_e^{-2}[\mathrm{cm^{-3}}] r_0^2[\mu\mathrm{m}]\Delta^2[\mu\mathrm{m}], \tag{46}$$

where r_0 is the laser spot radius and Δ is the plasma thickness. As an example, when a laser pulse with $I = 1 \times 10^{22}$ W/cm^2 focused on the spot size of $r_0 = 10$ μm is propagating a thickness of $\Delta = 100$ μm in the Xe ($Z = 54$) plasma with density $n_e = 1 \times 10^{20}$ W/cm^{-3}, the number of pairs produced is $N_{pair} \approx 4.4 \times 10^{14}$.

4.2. *A trident process in the counter-propagating laser field in plasma*

If an electron moves through the electric field with 4-momentum p_μ ($\gamma = p_0/m_e c$), a nonzero Lorentz and gauge invariant parameter can be formed as[5]

$$\chi^2 = -\frac{\langle (e(p_\mu - eA_\mu)F^{\mu\nu})^2 \rangle}{(m_e c^2)^6}, \tag{47}$$

where $\langle\ \rangle$ denotes the average over one period of the field. Using a four-potential of the laser field,

$$\mathbf{A}^\mu = [0, A_1(kx), A_2(kx), 0]. \tag{48}$$

and a four-dimensional wave vector,

$$k_\mu = (\omega_0, \mathbf{k}),\ kx = \omega_0 t - \mathbf{kx}, \tag{49}$$

this invariant parameter is

$$\chi^2 = \frac{(pk)^2}{(m_e c^2)^4} \frac{(e\mathbf{A})^2}{(m_e c^2)^2}. \tag{50}$$

For a head-on collision between an electron and a laser field,

$$\chi = \frac{2cp_0\hbar\omega_0}{(m_e c^2)^2} a = 2\gamma \frac{e\hbar E_L}{m_e^2 c^3} = \frac{2\gamma E_L}{E_c} = 2\gamma a \frac{\hbar\omega_0}{m_e c^2} = 2\gamma a_0 \frac{\lambda_C}{\lambda_0}, \tag{51}$$

where $\lambda_C/2\pi = \hbar/m_e c \approx 3.86 \times 10^{-11}$ cm is the Compton wavelength of the electron.

Let us consider the N_e electrons with energy $\gamma m_e c^2$ crossing the laser field with E_L. Integrating the probability over volume ΔV and time Δt for each electron crossing, i.e. $\Delta V = (\lambda_C/2\pi)^3$ and $\Delta t = \tau_L/2\gamma$ for the time of interaction with laser pulse of duration τ_L in the electron rest frame, assuming that a pulse length is smaller than the Rayleigh length. The number of pairs produced per laser shot is given by

$$N_{pair} \cong N_e \left(\frac{\lambda_c}{2\pi}\right)^3 \frac{\tau_L \alpha E_c^2}{2\gamma\pi\hbar} \chi^2 \exp\left[-\frac{\pi}{\chi}\right] \tag{52}$$

$$= 4N_e \gamma a_0^2 \left(\frac{\lambda_C}{\lambda_0}\right) \left(\frac{c\tau_L}{\lambda_0}\right) \exp\left[-\frac{\pi}{\chi}\right]. \tag{53}$$

Substituting Eq. (40) into the electron energy γ, the pair production yield is

$$N_{pair} \cong \frac{8\pi^3 a_0^4}{\alpha}\left(\frac{r_0^2\Delta}{\lambda_0^3}\right)\left(\frac{c\tau_L}{\lambda_0}\right)\exp\left[-\frac{\pi}{\chi}\right], \\ \approx 5\times 10^{-33} I^2[\mathrm{W/cm^2}] r_0^2[\mu\mathrm{m}]\Delta[\mu\mathrm{m}]\tau_L[\mathrm{fs}]\exp[-\pi/\chi]. \quad (54)$$

where the invariant parameter is

$$\chi \cong \frac{4\pi^2}{\alpha}\frac{a_0^3}{n_e\lambda_0^3} \approx 3.38\times 10^{-12}\frac{I^{3/2}[\mathrm{W/cm^2}]}{n_e[\mathrm{cm^{-3}}]}. \quad (55)$$

As an example, when a laser pulse with $I = 1\times 10^{22}$ W/cm^2 and $\tau_L = 20$ fs focused on the spot size of $r_0 = 10$ μm is propagating a thickness of $\Delta 100$ μm in plasma of density $n_e = 1\times 10^{20}$ cm^{-3}, the number of pairs produced is $N_{pair} \approx 9\times 10^{16}$ with $\chi \cong 34$. In Figure 1, the number of pair production yields for two processes calculated from Eqs. (46), and (54) are shown as a function of the laser intensity.

5. Relativistic ponderomotive acceleration and focusing of a pair beam

High energy booster acceleration of a pair-beam can be accomplished by the relativistic ponderomotive acceleration with focusing in vacuum or tenuous plasma. In the ponderomotive acceleration[11], the final energy is obtained approximately by $\gamma_f \approx a_0^2$ for a particle initially at rest. The accelerated final energy is written as

$$E_f[\mathrm{GeV}] \approx 0.37\times 10^{-21} I[\mathrm{W/cm^2}]\lambda_0^2[\mu\mathrm{m}]. \quad (56)$$

As an example, the laser intensity $I = 1\times 10^{24}$ W/cm^2 of λ_0 μm can accelerate the electron beam up to 240 GeV.

The focusing of an electron beam will be accomplished by the higher order Hermite-Gaussian modes. The focusing force is obtained from the ponderomotive potential U as $F_r/m_e c^2 = \partial U/\partial r$. In the fundamental Hermite-Gaussian mode referred to as a Gaussian mode, the ponderomotive potential propagating in vacuum is given by

$$U_0(r,z,t) = a_0^2\frac{\sigma_{\perp 0}^2}{\sigma_\perp^2}\exp\left[-\frac{r^2}{2\sigma_\perp^2} - \frac{(z-ct)^2}{2\sigma_z^2}\right], \quad (57)$$

where $\sigma_{\perp 0}$ is the rms spot size at $z = 0$, $\sigma_\perp = \sigma_{\perp 0}\sqrt{1+z^2/Z_R^2}$ the rms spot size at z, Z_R the Rayleigh length, and σ_z the rms laser pulse length. Since $\partial U_0/\partial r < 0$, the ponderomotive potential of a Gaussian mode exerts

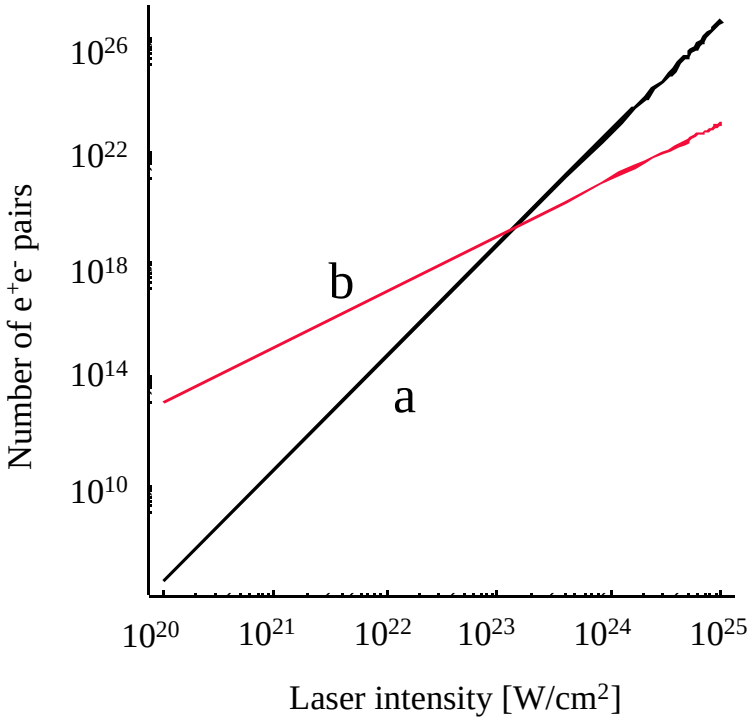

Figure 1. The number of pair production yields for two trident processes as a function of the laser intensity: **a** for the trident process in the nuclear field and **b** for the trident process in the counter-propagating laser field. The pair production yields are calculated for the parameters, $\tau_L = 20$ fs, $r_0 = 10\mu$m, $n_e = 1 \times 10^{20}$ cm^{-3}, $\Delta = 100\mu$m and $Z = 54$.

defocusing forces on off-axis particles that are quickly expelled from the laser beam in the radial direction. The focusing force can be produced by superposition of a Gaussian mode and higher order modes of which the ponderomotive potential creates a potential well in the radial direction[12]:

$$U_1(r,z,t) = a_1^2 \frac{r^2\sigma_{\perp 0}^2}{\sigma_\perp^4} \exp\left[-\frac{r^2}{2\sigma_\perp^2} - \frac{(z-ct)^2}{2\sigma_z^2}\right], \tag{58}$$

where a_1 is the dimension less vector potential of the first order mode. The focusing strength at $r = 0$, and $z - ct = 0$ is

$$K_F = \frac{F_r}{\gamma m_e c^2 r} = \frac{\partial U}{\gamma r \partial r} = \frac{2a_1^2 - a_0^2}{\gamma \sigma_{\perp 0}^2}, \tag{59}$$

where $U = U_0 + U_1$ is the total ponderomotive potential. Then the beam

envelope equation on the rms beam radius σ_{rb} is written as

$$\frac{d^2\sigma_{rb}}{dz^2} + K_F\sigma_{rb} - \frac{r_e N_b}{\sqrt{2\pi}\beta^2\gamma^3\sigma_{rb}\sigma_{zb}} - \frac{\varepsilon_b^2}{\sigma_{rb}^3} = 0, \tag{60}$$

where N_b is the number of electrons in the bunch, σ_{zb} the rms bunch length, $\varepsilon_b = \varepsilon/(\gamma\beta)$ the geometrical beam emittance, and ε_n is the normalized beam emittance. In this equation the third term and the fourth term are attributed to a space charge force and the thermal emittance, respectively. The equilibrium beam radius is obtained from $d^2\sigma_{rb}/dz^2 = 0$.

5.1. *A focused beam size limited by the space charge force*

First let us consider an equilibrium beam size of the electrons or the positrons focused by the laser ponderomotive potential well in the case of the radial expansion of the beam due to the space charge force. The equilibrium beam size is given by the focusing strength at $r = 0$, and $z - ct = 0$ is

$$\sigma_{rb} \approx \frac{\sqrt{r_e N}}{(2\pi)^{1/4}K_F^{1/2}\beta\gamma^{3/2}\sigma_{zb}^{1/2}} = \frac{\sqrt{r_e N}}{(2\pi)^{1/4}(2a_1^2 - a_0^2)^{1/4}\sigma_{zb}^{1/2}}\frac{\sigma_{\perp 0}}{\gamma}. \tag{61}$$

Assuming $a_1 = a_0$, $\sigma_{\perp 0} = r_0/2$, and $\sigma_{zb} \approx \lambda_0/2\pi$, an estimate of the beam size is

$$\sigma_{rb} \approx \frac{(2\pi r_0)^{1/4}}{2a_0^{5/2}}\sqrt{\frac{r_e N}{\lambda_0}}. \tag{62}$$

This is rewritten in terms of the laser intensity as

$$\sigma_{rb}[\mathrm{pm}] \approx 2 \times 10^{24}\frac{\sqrt{N}}{I^{5/4}[\mathrm{W/cm^2}]}\frac{r_0[\mu\mathrm{m}]}{\lambda_0^3[\mu\mathrm{m}]}. \tag{63}$$

As an example, for $N = 1 \times 10^{10}$, $\lambda_0 = 0.8$ μm, the laser pulse of the peak intensity of $I = 1.0 \times 10^{22}$ can focus the spot radius to $\sigma_{rb} \approx 1.2$ nm.

5.2. *A focused beam size limited by the thermal emittance*

If an electron-positron pair beam is focused, the space chrage force will be neglected. The focused beam size can be limited by equilibrium between the ponderomotive focusing and the thermal emittance expansion:

$$\sigma_{rb} \approx \frac{\sqrt{\varepsilon_b}}{K_F^{1/4}} = \frac{\gamma^{1/4}\sqrt{\varepsilon_b\sigma_\perp 0}}{(2a_1^2 - a_0^2)^{1/4}}, \tag{64}$$

Assuming $a_1 = a_0$, $\sigma_{\perp 0} = r_0/2$, $\varepsilon_b \approx \varepsilon_n/\gamma \approx \lambda_0/(2\pi a_0^4)$, an estimate of the beam size is

$$\sigma_{rb} \approx \frac{\sqrt{\varepsilon_n \sigma_{\perp 0}}}{a_0} = \frac{1}{2a_0^2}\sqrt{\frac{\lambda_0 r_0}{\pi}}. \tag{65}$$

This is rewritten in terms of the laser intensity as

$$\sigma_{rb}[\mathrm{pm}] \approx \frac{4\times 10^{23}}{I[\mathrm{W/cm^2}]}\sqrt{\frac{r_0}{\lambda_0}}. \tag{66}$$

As an example, for $\lambda_0 = 0.8\mu$m and $r_0 = 10\mu$m, the laser pulse of the peak intensity of $I = 1.0\times 10^{22}$ can focus the spot radius to $\sigma_{rb} \approx 0.14$ nm.

5.3. *Application to a high energy electron-positron collider*

It is conceivable that two counter propagating laser-accelerated beams make it possible to produce the e^+e^-, e^-e^-, and e^+e^+ high energy collisions. The colliding beam energy is given by Eq. (56). We can estimate the collision luminosity for the new concept collider from above discussions on the accelerated energy and the focused beam size due to the ponderomotive acceleration mechanism.

In the space charge limited case, the collider luminosity will be given by

$$L = \frac{N^2 f_{rep}}{4\pi\sigma_{rb}^2} \approx \frac{a_0^5 \lambda_0 N f_{rep}}{\sqrt{2}\pi^{3/2} r_e r_0^2}, \tag{67}$$

where f_{rep} is the repetition frequency of the colliding laser pulses. In terms of the laser intensity, the collision luminosity is

$$L[\mathrm{cm^{-2}s^{-1}}] = 2\times 10^{-30} I^{5/2}[\mathrm{W/cm^2}]\lambda_0^6[\mu\mathrm{m}] r_0^{-2}[\mu\mathrm{m}] N f_{rep}[\mathrm{Hz}]. \tag{68}$$

In the emittance-limited case, where the electron-positron pair beam is collided with no separation, the luminosity results in

$$L = \frac{N^2 f_{rep}}{4\pi\sigma_{rb}^2} \approx \frac{a_0^4 \lambda_0 N^2 f_{rep}}{r_0 \lambda_0}. \tag{69}$$

In terms of the laser intensity, the collision luminosity is

$$L[\mathrm{cm^{-2}s^{-1}}] = 5.3\times 10^{-27} I^2[\mathrm{W/cm^2}]\lambda_0^3[\mu\mathrm{m}] r_0^{-1}[\mu\mathrm{m}] N^2 f_{rep}[\mathrm{Hz}]. \tag{70}$$

As an example, in order to accelerate the pair beams to the center-of-mass collision energy of 10 GeV, the laser intensity of $I = 2.1\times 10^{22}$ W/cm^2 is required. For $N = 1\times 10^{10}$, $\lambda_0 = 0.8\mu$m, $r_0 = 10\mu$m, and $f_{rep} = 10$ Hz, the space-charge limited luminosity is 3.35×10^{34} cm^{-2}s^{-1} and the emittance limited luminosity becomes 1.2×10^{38} cm^{-2}s^{-1}. This is four orders of magnitude higher than the conventional B factories.

6. Conclusions

The pair-production processes in ultra-strong laser-plasma interactions have been investigated to estimate the number of electron-positron pairs in terms of the laser intensity and the plasma density. Since the pair-production occurs in the presence of the laser field and the electrostatic field generated by an ultraintense laser pulse, the produced pairs will be accelerated by the coherent action of those fields to form a relativistic beam. This pair-beam will be useful for applications to high energy collider physics as an electron-positron beam source if it can be accelerated to a very high energy and focused to a very small spot size by the ponderomotive acceleration mechanism. We propose a new concept of a high energy, high luminosity electron-positron collider driven by the ultra-strong lasers in a micro-scale size.

References

1. M. H. Mittelman, *Phys. Rev.* **A35**, 4624 (1987).
2. H. J. Bhabha, *Proc. R. Soc.* **152**, 559 (1935).
3. J. W. Shearer,J. Garrison, J. Wong, and J. E. Swain, *Phys. Rev.* **A8**, 1582 (1973).
4. G. Breit and J. A. Wheeler, *Phys. Rev.* **46**, 1087(1934).
5. W. Becker, *Laser and Particle Beams* **9**, 603 (1991).
6. J. Schwinger, *Phys. Rev.* **82**, 664 (1951).
7. E. Brezin and C. Itzykson, *Phys. Rev.* **D2**, 1191 (1970).
8. H. Dewa et al., *Nucl. Inst. and Meth.* **A410** 357 (1998) ; M. Kando et al., *Jpn. J. Appl. Phys.* **38** L967 (1999).
9. V. Malka et al., *Sciece* **298**, 1596 (2002).
10. J. Koga, K. Nakajima, and K. Nakagawa, *AIP Conf. Proc.* **611**, 126(2002).
11. F. V. Hartemann et al., *Phys. Rev.***E51**, 4833(1995).
12. G. V. Stupakov and M. S. Zolotorev, *Phys. Rev. Lett.* **86**, 5274(2001).

QUANTUM ASPECTS OF SUPER-STRONG FIELD INTERACTIONS

HIROSHI TAKAHASHI[†]

Brookhaven National Laboratory.
Upton ,
New York, 11973 ,, USA
E-mail: takahash@bnl.gov

Quantum aspect of interaction between high intensity laser and electron plasma has been studied in point of view of coherent state formalism In the previous paper, I present a theoretical foundation based on quantum-mechanical- and coherent-state-formalism for analyzing the interactions between the high-intensity laser and electron plasma in a many electron system. In this paper the group theoretical methods are studied for dealing with many modes created in the target under the super strong laser irradiation. The methodology based on the exponential Hilbert space approach are studied for analyzing the modes interacting system where non linear mode interaction becomes prominent over the linear space analysis**.**

1. Introduction

1.1.

In my previous paper[1], I discussed a theoretical foundation based on quantum-mechanical- and coherent-state-formalism for analyzing the interactions between the high-intensity laser and electron plasma in a many photon-electron system. The Two times Green Function method developed by Matsubara [2] is used for giving quantum theoretical foundation on the free electron laser for both low and high intensity lasers [3,4]. The analysis base on the multiple excitation of fock type number state becomes complex to be solved, the high intensity laser are treated as the classical field and the equation of motion under classical field can be derived. By using this classical field, the formalism can be greatly simplified, and the many correlation associated the plasma under high intensity laser can be obtained in the analytical form. However the quantum aspect of the laser electrons interacting system is not expressed clearly in this formalism,

In order to clarify, the quantum effect for the laser, the coherent state description for the laser field is more appropriate than classical field presentation.
or getting the dispersion formula, for free electron laser, the total Hamiltonian of the system are expanded with the creation (a^+, A^+) and annihilation (a, A) operators of

[†] Work partially supported by grant 2-4570.5 of the Swiss National Science Foundation.

the relativistic electron which moved in the wiggler magnetic field and the laser photon and the coulomb interaction between relativistic electrons are described using their density operators of (a^+ a) , and the two times Green function of photon are obtained by solving the equation of the motion for the Green function for photon << [A^+, A]>>
For high intensity laser, the equation of motion for multiple photons states are created, the very large number of the states are involved, but the many photons are behaves same way so that these states are treated as the group and the large numbers of the states are grouped together and the number of states dealing with the equation motion for the analysis are reduced. Classical formalism for electro magnetic fields equivalent with the coherent states.
When a high intensity laser irradiation on the target, not only many photons but also the higher atomic excitation will be occurs, and these can be analyzed by many kind coherent states of atomic, squeezed , super-radiant [4-6] as discussed in the previous paper [2].

Note of A^2 term in the Hamitonian

To derive the dispersion relation for the photon in the strong laser irradiation to electron plasma, the energy difference between the two dressed relativistic electron was assumed to be small in the previous paper. However, it is not negligible in the case when the large momentum change of electrons occurs as the strong laser irradiation. In the relativistic electron which wave function is approximated as the schrodinger type equation, the electron motion by strong laser irradiation is affected by the square of photon amplitude A^2 term in the formalism. As you find the formalism using the schrodinger type equation in the semi-classical formalism A**2 term will play important role for high intensity laser irradiation, due to creating the pondermotive potential . For dealing with relativistic electron, we have to use the Dirac equation under high laser field which used for the Compton scattering study[9]. The relativistic electron wave function under strong laser field is derived as

Using this formalism, we can derive the dispersion formula in the similar way as the above non-relativistic electron plasma,
In my previous paper for high intensity laser, we derived the dispersion relation for the laser photon, this classical EM field formalism are treated as the similar to the static magnetic Wiggler field. so that it might not properly treated the higher order process such as scattering of laser. Although first order transition of Compton scattering can be described as discussed in our referenced paper Where the relativistic electron wave function are obtained by solving the Dirac equation under strong laser described as A cos (Θ).
When the wave function of relativistic electron ha the form of

Where u(p) is bi-spinor, p is a constant four vector determining the state , $p^2=m^2$, q =p – a e/ 4(pk)]

$$\psi_p = [1+\frac{e}{2(k_1 P)}(\gamma k_1)(\gamma a_1)\cos(k_1 x)]\frac{u(p)}{\sqrt{(2p_0)}}e^{-iqx+iS} \quad (4)$$

where

$$S = -e\frac{pa_1}{k_1 p}\sin(k_1 x)+\frac{e^2 a_1^2}{8(k_1 p)}\sin(2k_1 x)$$

The cross section for compton scattering of high intensity laser is derived by us using the Dirac wave function (eq.(4) for getting the scattering matrix amplitude of equation (5) 5i

$$\sum_{polar}\left|M_{f\ i}^{(s)}\right|^2 = 16\pi e^2 m^2\left[-A_0^2+(2+\frac{(k_1 k_2)^2}{(pk_1)(pk_2)})\xi_1^{\ 2}(A_1^2-A_1 A_1)\right]$$

whe

where $A_n(s,\kappa,\eta)$ *and*

$$A_n(s,\kappa,\eta)=\frac{1}{2\pi}\int_{-\pi}^{\pi}d\phi\cos^n(\phi)e^{i[-k\sin\phi-\eta\sin(2\phi)+s\phi]}$$

$$W_s = N\int\ \sum_{polar}\left|M_{f\ i}^{(s)}\right|^2\left[\frac{d_1^3 q'}{(2\pi)_1^3)(2q_0 2q'_0)}\frac{\left[a_2\right]^2}{(16\pi)}(2\pi)^4\right]$$

$$.\left[(q+sk_1\pm k_2-q')\right]$$

$p^2=m^2$, $q_\mu = p_\mu - [a_1^2\ e^2/\ 4(p\ k_1)]k_{1\mu}$;

$n=1,2.$

where κ *and* η *are*

$$\kappa=(\frac{(a_1 p)}{(pk_1)}-\frac{(a_1 p')}{(p'k_1)})$$

$$\eta=\frac{e^2 a_1^2}{8}[\frac{1}{(pk_1)}-\frac{1}{(p'k_1)}]$$

(11)

2. Many modes interacting system (analysis by Exponential Hilbert space)

When Strong laser is irradiating target, many modes of the photon, electron, even nucleon fields through the photo-nuclear reaction will be involved, and the many mode of the coherent states are involved and the interaction between these modes are came in the analysis. To deal with these high numbers of modes, straight forward extension of the above formalism is too much complicated in the same way as the multi-photons excitation .
To deal with this many body problem, group theoretical approach can be applied in the similar way for the analysis for nuclear, atomic physics.
The system in which many modes are interacting has some symmetry structure, and to analyze this system, group theory associated with this symmetry is imposed. When this group can be factorized into subgroups so that there is no interaction between subgroups, it can be solved more simple way. However due to quantum fluctuation came in the physical system, the interaction between subgroups can be occurs through quantum fluctuations and it can not be neglected. In this way the quantum aspect are came in the analysis of the many body problems structured as the some hierarchy character.
To analyze the interacting many mode system, the second quantization method applied in the field theory simplify greatly the formalism for the interacting mode systems. When the total Hamiltonian is composed of the many independent mode, it will be expressed with the creation operator and annihilation operators of the each modes. And the coherent wave function are used for expressing the wave function describing the mode, the equation of motion for each mode are solved independently from the other modes, the formalism becomes factorized and can be solved without difficulty, but when it is treated quantum mechanically, between modes, there is interaction through quantum fluctuation. We need take into account quantum effect, although if the mode is composed of many particles, and the momentum of mode is large, the effect of the quantum fluctuation becomes small so that the classical description for the mode can be justified.
When the many modes are interacting through interaction with the intermediate mode, the Hamiltonian can be expressed with the non-linear interaction. This non-linear interaction play very important role for whole structure behavior of the system term similar way as the turbulence of the hydraulic dynamics. The soliton behavior observed from the computer analysis will be created through this non linear interaction. Thus the quantum effect for each mode are small but the effect through this non linear interaction become large effect for analysis of global behavior.
To derive the analytical method for this mode interacting, the exponential Hilbert space which was proposed by Klauder will be very useful tool. In this formalism, the Coherent state which defined as the annihilation operator A to

the state Pai > can be expressed with the complex value z >. More extended state expressed as Sum zip

Exponential For Mode A is defined and the Hilbert space which is built as the polynomial of the operator A is expanded.

The foundation of the quantum behavior will be constructed in solid foundation as the similar way as the quantum physics foundation built upon the Hilbert space.
By using this exponential Hilbert Space, the symmetry associated with the whole system will be imposed with the sound mathematical foundation.
With group structure are imposed, The use of the exponential Hilbert space greatly simplify the formalism.
Klauder developed the formalism for the interacting mode system by extending the Hilbert space to the Exponential Hilbert space [ ], This was carried out in the similar way developed the coherent state is an abstraction of the Fock space for boson field using the wide class of the field operator representation. He provided the methodology deal with many interacting mode fields can be useful for analysis of the system which has own interacting subgroup structure.
The Hamiltonian of the His dynamically system
His general formula for the fields of Dynamics based on the Hamiltonian of the form of the form

$$H = \sum A_k^{\dagger} \omega_{kl} A_l + \sum g_{klm} A_k^{\dagger} A_l^{\dagger} A_m + h.c. + \sum v_{klm\nu} A_k^{\dagger} A_l^{\dagger} A_m A_\nu , \quad (2.13)$$

(2.1)

which is including the terms representing production and decay , scattering , etc. For the analysis of the strong laser relativistic electron system since we are dealing with the relativistic system which is imposed by Lorentz group, The imposing the Lorentz group to the every mode from the beginning greatly simplified the formulation. By using the an equal time field algebra which characterized by family of formally self-adjoint field operator Wl(x) , l=1,2,…L with comutation relation of as

(2.2)
Here clmn are the structure constants of Lie group. When we choose the real function of f(x), g(x) then

$$\left\lceil W_l(f), W_m(g) \right\rceil = ic_{lmn} W_n(fg)$$

(2.3)

The unitary group element in canonical coordinates are given as

(4.3) where f (x) it is representation of these field operators. We are seeking, the using these function and unitary operators the overcomplete family of states

$$\phi'\left[f_l\right] = e^{-i\,\mathrm{Im}(\xi,\phi'[f_l])} U\left[f_l\right]\phi_0$$

(4.4)

for some choice of ξ and of φ'[f_l]∈h. We insist on an

$$(\phi'\left[f_l\right], \phi'\left[f_l\right]) = N' \;\; N\, e^{-(\phi'[f_l],\phi'[f_l])}$$

(4.5)

The group law reads

$$U\left[f_l\right] U\left[f_l\right] \equiv U\left[(f.f)_l)\right]$$

where f.f symbolize the parameter combination law characterizing the group. To straight forward extension of the above formalism becomes complicated.

Acknowlegements

The author thanks to Profs. M. Namiki, Nakjima , A. Yu for their valuable discussion .

References

[1] Hiroshi Takahashi " Theory of the free electron laser". Physica 123 C (1984) 225-237 North-Holland Amsterdam

[2] T. Kwan., J.M.Dawson, and A.T. Lin. Phys. Rev. 16A (1977)

[3]Hiroshi Takahashi "Interaction between a Plasma and a Strong Electromagnetic Wave " Physica 98C (1980) 313-324

[4] Tadashi Toyoda and Karl Widermuth " Charged Schroedinger particle in a c-number radiation field" Phy. Rev. 10D, p2391 (1980)

[5] Yosio Ohnuki and Taro Kashiwa "Coherent State of Fermi Operators and the Path Integral" Prog. Theo. Physics, 60. 548, (1978)

[6] F.T.Arecchi, E.Courtens, R. Gilmore and H. Thomas " Atomic coherent states in Quantum Optics" Phys. Rev A, 6, 2211, 1972.

[7} John Klauder " Exponential Hibert Space: Fock Space Revited" Journal of Mathematical Phyisics . 11 , 233. (1970)

[8] D. Horn ,R.Siver “ Coherent Prouction of Pion “ Annals of Physics 66. 509. (1971)
(9) Roy Gluber “ Coherent and Incoherent States of the radiation Field. Physical Review 131, 2766, (1963)

TOWARDS AIGO, AN ATOM-BASED INTERFEROMETRIC GRAVITATIONAL-WAVE OBSERVATORY

RAYMOND Y. CHIAO and ACHILLES D. SPELIOTOPOULOS
Department of Physics, University of California, Berkeley, CA 94720-7300

It is shown that the use of atom interferometry allows for the construction of AIGO, the Atom-based Interferometric Gravitational-wave Observatory, that, for the same sensitivity, is expected to be orders of magnitude smaller than traditional laser-based observatories as LIGO or LISA. A design for AIGO is introduced, and the technologies required for its construction is presented. For meter-sized AIGOs with fringe sensitivity limited by shot noise, the sensitivity of AIGO to gravitational waves is compared with the 4 km-size LIGO. A road map for experimentally verifying the feasibility of AIGO is outlined.

1. Introduction

We propose a research program that will lay the foundations for the construction of AIGO, an Atom-based Interferometric Gravitational-wave Observatory. For the same sensitivity, AIGO is expected to be orders of magnitude smaller than the laser-based observatories such as LIGO and LISA.

Roughly speaking, since an atom weighs much more than a photon, an atom's response to gravitational waves (GWs) should be much greater than that of a photon (see **III-F** below). Hence atoms will be much more sensitive to GWs than light. This increase in sensitivity can be exploited by making use of the quantum phase of an atomic DeBroglie matter wave. The DeBroglie wavelength of a particle depends inversely on its velocity. When a GW passes through an atom interferometer, the velocities of the atoms—and hence their DeBroglie wavelengths—will be slightly perturbed. By suitably designing the interferometer, this perturbation in the DeBroglie wavelength causes a phase shift, which will result in a shift in the interference pattern that—like LIGO and LISA—can then be measured interferometrically, and used to determine the properties of the GW.

While classical-based systems such as LIGO and LISA place classical test masses (mirrors) a certain distance way from the central beam splitter

of the interferometer, and measures slight shifts in their *positions* through light-based interferometry, quantum-based systems such as AIGO throw out quantum test masses (atoms) with certain velocities, and measures the quantum phase shift due to slight shifts in their *velocities* through atom-based interferometry. A GW can readily change the velocities of nonrelativistic atoms, but it cannot change the velocity c—or even the frequency—of photons (although it can slightly change their directions) Stated in terms of general relativity, since *nonrelativistic* atoms, which follow *timelike* geodesics, are used in AIGO, they are very sensitive to changes in the local Riemann curvature of spacetime due to the passage of a GW. This is in contrast to the case of *ultrarelativistic* particles, such as photons, which rigidly follow *null* geodesics, and are therefore relatively insensitive to such changes.

Consequently, we find that for AIGO the perpendicular length of the "arms" of the interferometer $L_\perp$, should be much shorter than that of LIGO's for the same sensitivity to GWs. Defining $L_{AIGO} \equiv L_\perp$, in AIGO's operating range this length scale is given by

$$L_{AIGO} = \left\{ \frac{\hbar\omega}{mc^2} \frac{L_{LIGO}\lambda_{GW}}{4\pi} \right\}^{1/2}, \tag{1}$$

if the interferometers have the same phase sensitivity (see **III-F**). Here L_{LIGO} is the effective optical path length of LIGO's arms, λ_{GW} is the wavelength of the GW to be detected, ω is the frequency of the laser used in LIGO, and m is the mass of the atom used in AIGO. Due to the factor $\hbar\omega/mc^2 \simeq 3.1 \times 10^{-10}$ (i.e., the "weight" of a 1.06 μm photon relative to the "weight" of a helium atom), L_{AIGO} is smaller than L_{LIGO} by many orders of magnitude. For the helium–atom-based AIGO that has a sensitivity comparable to LIGO in LIGO's operating frequency band, $L_{AIGO}/L_{LIGO} < 3 \times 10^{-5}$. Similarly, comparing AIGO to LISA within its frequency band, $L_{AIGO}/L_{LISA} < 1 \times 10^{-4}$. As a consequence, meter-sized AIGOs could in principle be constructed with sensitivities comparable to LIGO: We hereby propose a radically different route for the construction of gravitational-wave observatories than the traditional light-based systems.

In the preliminary phase of this research program, we propose to explore the range of potential physical systems and available technologies that can be implemented in the construction of a space-based AIGO. As we shall outline below, the great majority of the various technologies needed to construct AIGO have already been demonstrated *separately* in various atom diffraction and interferometry experiments since Stern's early demonstra-

tion of the diffraction of helium atoms by alkali-halide crystals. However, they have *not* been integrated into the construction of a whole atom interferometer with a design and a sensitivity that can be used to detect, measure, and observe GWs. Moreover, atom interferometers that can be constructed from crystal diffraction gratings have not been demonstrated as of yet, although Bonse-Hart-type neutron interferometers based on single-crystal silicon ingots have been used to measure gravitational effects [1]. These crystal-based atom interferometers would be needed to construct a meter-scale AIGO. Nanofabricated transmission gratings with a periodicity of 20 nm could also be used, but would result in an AIGO many times longer.

The overarching objective of this preliminary research program is to determine the feasibility of constructing AIGOs, and to establish the technologies needed for their implementation. To this end, we have in this paper outlined the design of a specific AIGO configuration, and calculated the phase shifts expected to be seen by this AIGO resulting from the passage of GWs. Using this analysis as a guide, we have estimated the specifications of an interferometer needed to measure GWs, and we have outlined the technologies that could be used in reaching these specifications. The experimental plan in this preliminary phase will focus on gathering the needed experimental results required to finalize the design of AIGO.

2. Background and Review of Research

In this section we review some of the relevant research in atom interferometers, and in GW detectors.

2.1. *Atom Interferometry*

The diffraction of helium atoms off crystalline surfaces was first seen by Stern in 1929 [2] (see [3] for a complete overview). Using a room-temperature helium-atom beam, and a pressure manometer as a detector, clear diffraction peaks could be seen for helium diffracting off of both NaCl and LiF cleaved single-crystal surfaces. Due to its unique properties, research in the diffraction of helium atoms continues [16], and the construction of a scanning helium-atom microscope is actively being pursued [5].

While the diffraction of atoms has been used to construct atom interferometers (see for example [6]), these interferometers have been based on fabricated transmission gratings with a periodicity of typically 100 nm, and are typically three orders of magnitude larger than the lattice constant for

most crystals. The crystalline lattice of silicon has been used to construct an Bonse-Hart-type interferometer [1], but using neutrons and not atoms.

2.2. *LIGO, LISA, and the Detection of GWs*

The great majority of the current experimental searches for GWs are based on laser interferometry. These detectors are scalable by design to a size where the detection of GWs become feasible. A number of research groups located throughout the world [7] are expecting to begin to collect data soon: GEO600, German-British collaboration; VIRGO, a French-Italian collaboration; TAMA300, a Japanese effort; and ACIGA, an Australian effort. The current US-based, international collaboration, is LIGO (Laser Interferometer Gravitational-wave Observatory). In addition, a space-based laser interferometer system LISA (Laser Interferometer Space Antenna) is currently in the initial planning stage. We will focus specifically on LIGO in this section.

LIGO is a set of three interferometers based at two locations separated by 3020 km: Hanford, Washington and Livingston, Louisiana. All three instruments are based on Michelson interferometers with Fabry-Perot arms. The physical length of the each arm of the main LIGO interferometer is 4 km, and with a Fabry-Perot interferometer in each arm, the optical path of the arm is increased 150-fold. At the end of each arm is a massive mirror suspended vertically within a vacuum chamber, and the location of this mirror must be held in position within 10^{-10} to 10^{-13} m with respect to the center of the interferometer. An analysis of the response of LIGO within the approximation of freely-falling mirrors will be given in **III-F**. We shall, for now, give a qualitative discription of the physics underlying LIGO.

Consider a freely-fally test mass m placed a certain distance L away from an observer. When a GW passes the system, the wave is expected to slightly shift the position of the test mass. It will, however, also shift the position of the observer. Consequently, only the *difference*—the geodesic *deviation*—in the distance x^i between the observer and the test mass can be measured. From [9], x^i obeys the geodesic deviation equation.

$$\frac{d^2x_i}{dt^2} = -R^{GW}_{0i0j}x^j, \tag{2}$$

where R^{GW}_{0i0j} is the Riemann curvature tensor for the GW. In deriving Eq. (2), the long-wavelength limit—expected to be valid for GWs from astrophysical sources—was taken. The GW slightly shifts the position of the test mass, and this shift is proportional to L; the longer L, the larger

the shift. By measuring the changes in x^i it is in principle possible to detect the presence of a GW.

The laser interferometry used by LIGO provides a means of accurately doing so over large distances, and in LIGO, the test mass are mirrors suspended by piano wire off of a fixed frame. The shift in the mirror's position causes a phase shift that produces an interference pattern that can, in principle, be seen. However, while laser interferometry provides the most accurate means to measure this shift, it is important to note that it is the response of the test masses to the passage of the GW that is measured, *not* that of the photons in the interferometer.

Because the mirrors of LIGO are suspended off of piano wire, they are not in free-fall. They form pendula, and undergo simple harmonic motion when a GW passes through. There are resonance effects which cause an increase in sensitivity between $10 - 100$ Hz, but a decrease in sensitivities at higher frequencies. For low frequencies, seismic noise in the mirror's suspension system will also cause a decrease in the sensitivity. Because the mirrors have to be as freely-falling as possible, an active noise cancellation scheme has to be used to fix the position of the mirror relative to the center beam splitter.

Construction of LIGO began in 1996, and the main interferometers were commissioned in 2001 [8]. The first science runs were started in June of 2002, and these data are currently being analyzed. The installation of Advanced LIGO—designed to be used for GW astronomy—is expected to begin in 2006.

3. An Atom-based Interferometric Gravitational-wave Observatory (AIGO)

In this section we outline the basic design of a proposed version of AIGO, and the technologies that could be used to construct it. We also derive the phase-shifts expected for this AIGO, and use this calculation as a guide to determine the specifications of AIGO based on current technology.

3.1. *Theoretical Basis*

In this subsection we outline the conceptual foundations for AIGO, a matter-wave interferometer for measuring GWs. To focus on the underlying physics, we consider an interferometer in free fall in Low Earth Orbit (LEO) (see [10]). In this idealized interferometer, the very large ground-based acceleration-dependent effects seen in [1] are not present. In addition, orbital

Figure 1. 1a is a sketch of the the spacetime diagram of the atom interferometry measurement and 1b is its corresponding spatial projection (not to scale). An atomic beam is coherently split at A, and recombined coherently at B.

dynamics can be used to eliminate the need for mirrors in the construction of this interferometer (and their complications), and the essential physics become readily apparent. In **III-E** we shall provide the detail analysis of the phase shifts expected for the proposed space-based AIGO.

With its conceptual roots in the work of [11,12,13], we consider an atom interferometer in LEO at a distance $r^i(t)$ from the center of the Earth. We choose a local coordinate system X^μ fixed on the center-of-mass (CM) of the apparatus. We then release an atom traveling along the orbit of the CM (see Fig. 1a). At t_A, a transmission diffraction grating is used to coherently split the atomic beam. One possible geodesic for the atom is γ_1 where the atom is given a velocity $\vec{v}_\perp$ at the beam splitter that is perpendicular to the CM's orbit. The other path corresponds to a geodesic γ_2 with velocity $-\vec{v}_\perp$. If the beam is split coherently, it will *not* possible to determine which geodesic any individual atom will take because the atom behaves quantum mechanically. Because the spatial projection of both γ_1 and γ_2 correspond to LEOs, the two paths will intersect with one another again after a time T as shown in Fig. 1b. A second transmission diffraction-grating beam splitter is then used to recombine the two paths coherently at t_B, and detectors are then be used to determine the interference pattern, and through it the phase shift $\Delta\phi$ that the atom picks up between the two possible geodesics. Importantly, the combined spacetime path $\gamma = \gamma_1 \cup \gamma_2$ is closed (see Fig. 1a), and forms the boundary of a spacetime surface $\mathcal{D}$.

As usual, we take the linearized gravity limit $g_{\mu\nu} = \eta_{\mu\nu} + h^E_{\mu\nu} + h^{GW}_{\mu\nu}$ where $\eta_{\mu\nu}$ is the flat spacetime metric, and $h^E_{\mu\nu}$ is the deviations from the flat metric due to the Earth. The components h^E_{0i} form the Lense-Thirring field of the rotating Earth that causes frame dragging, and, as usual, $h^E_{00} = -2GM/r$ is proportional to the Newtonian potential. Next, $h^{GW}_{\mu\nu}$—whose components are often called are the strain—are fluctuations in the flat spacetime metric due to the passage of a GW. We shall work in the transverse-traceless (TT) gauge [9] where $\partial^\mu h^{GW}_{\mu\nu} = 0$ and $\eta^{\mu\nu} h^{GW}_{\mu\nu} = 0$. As usual, we consider the GW to be in the long-wavelenth limit.

The Schrödinger equation for the atom the the CM frame is

$$i\hbar\frac{\partial\psi}{\partial t} = -\frac{\hbar^2}{2m}\nabla^2\psi + i(\hbar N^E_i + \hbar N^{GW}_i)\nabla^i\psi - mN^E_0\psi, \tag{3}$$

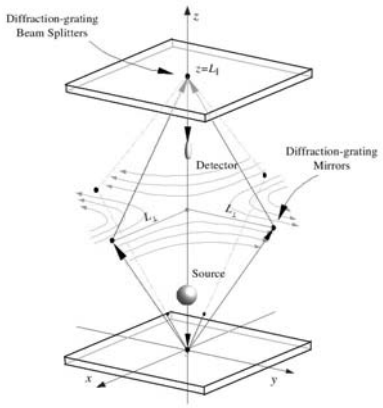

Figure 2. Sketch of "octahedral" interferometer with diffraction-grating beam splitters and diffraction-grating mirrors left out for clarity. The quadrupolar pattern for the + polarization of a GW perpendicularly incident on the detector is shown on the center plane (not to scale).

where ψ is the wavefunction, m is the mass of the atom, and using the usual techniques,

$$N_0^E = \frac{1}{4}X^iX^j\partial_i\partial_j h_{00}(r(t)) + \frac{1}{2}X^jX^k\frac{dr^i}{dt}\partial_j\partial_k h_{0i}(r(t)),$$
$$N_i^E = X^j\partial_j h_{0i}(r(t)) - \frac{1}{2}X^jX^k\partial_j\partial_k h_{0i}(r(t)), \quad (4)$$

where $\partial_i f = \partial f/\partial x^i$. From [13], $N_\mu^E = (N_0^E, N_i^E)$ is the four-velocity field acting on the test particle induced by the tidal field of the Earth as seen by an observer at the CM (see also [14]). Similarly,

$$N_i^{GW} = \dot{h}_{ij}^{GW}x^i/2, \quad (5)$$

is the tidal velocity field induced by the GW in the long-wavelenth approximation. Note that in the TT gauge, $N_0^{GW} = 0$.

Unlike R_{0i0j}^E, R_{0i0j}^{GW} varies rapidly with time, and the above approximation no longer holds. Contributions to $\Delta\phi$ due to the GW depend on the details of the interferometer, and we differ this analysis to **III-E**.

The wave-packet of the atom propagates along either γ_1 or γ_2. Taking the eikonal approximation $\psi = e^{imS/\hbar}\psi_0$, where ψ_0 is the solution of Eq. (3)

in the absence of (N_0, N_i),

$$\frac{\partial S}{\partial t} = -\frac{1}{2}|\nabla S|^2 + (N_i^E + N_i^{GW})\nabla^i S + N_0, \qquad 0 = \frac{\psi_0}{2}\nabla^2 S + (\nabla_i S - N_i^E - N_i^{GW})\nabla^i \psi_0. \tag{6}$$

From Eq. (4), $\nabla^i N_i^E = 0$, and in the TT-gauge, $\nabla^i N_i^{GW} = 0$ as well. Thus, Eq. (6) becomes

$$\frac{\partial S}{\partial t} = N_0^E, \qquad \nabla_i S = N_i^E + N_i^{GW}, \tag{7}$$

neglecting terms of $\mathcal{O}(N^2)$. Solving Eq. (7)

$$S(X) = \int_0^{X^\mu} (N_\mu^E + N_\mu^{GW}) d\tilde{X}^\mu, \tag{8}$$

integrated along γ_1 or γ_2. Thus,

$$\Delta\phi = \frac{m}{\hbar}\int_{\gamma_2} (N_\mu^E + N_\mu^{GW}) d\tilde{X}^\mu - \frac{m}{\hbar}\int_{\gamma_1} (N_\mu^E + N_\mu^{GW}) d\tilde{X}^\mu = \frac{m}{\hbar}\int_{\mathcal{D}} (R_{0i0j}^E(r(t)) + R_{0i0j}^{GW}) \tilde{X}^i d\tilde{t} d\tilde{X}^j \tag{9}$$

by Stokes' theorem.

Consider the contribution $\Delta\phi^E$ to $\Delta\phi$ from the curvature of the Earth. Since the normal to $\mathcal{D}$ is a spacelike vector,

$$\Delta\phi^E \approx \frac{m}{\hbar}|\bar{R}_{0i0j}^E|\mathcal{A}T \tag{10}$$

where $\bar{R}_{0i0j}^E$ is the average of R_{0i0j}^E over $\mathcal{D}$, and we have assumed that R_{0i0j}^E varies slowly within $\mathcal{D}$. For the Space Station with an orbit of 90 minutes, this is a good approximation. The area $\mathcal{A}$ is that contained within the two intersecting orbits in Fig. 1b, and T is the transit time.

3.2. *A Proposed AIGO Configuration: The "Octahedral" Interferometer*

Based on our analysis of an idealized atom interferometer in the previous section, we expect that quantum phase shifts of the atoms in an interferometer will be sensitive to the local curvature of the spacetime. Moreover, due to the overall factor of $m/\hbar$, small changes in the total Riemann curvature tensor from the passage of GWs could in principle be seen. Motivated by this qualitative result, we shall present in this section a specific design for a space-based AIGO along with an outline of the technologies can could be used in its construction.

Detailed analysis of the response of this interferometer to the passage of GWs will be done in the next section. However, some knowledge of the

Grating Size	$\delta\varphi_{shot} = 10^{-9}$, $L_\perp = 5.0$ m			$\delta\varphi_{shot} = 10^{-10}$, $L_\perp = 1.6$ m		
	T_0 (K)	P_0 (atm)	$L_\parallel$ (m)	T_0 (K)	P_0 (atm)	$L_\parallel$ (m)
10 nm	5.2	19	230	5.2	1900	75
20 nm	5.2	19	476	5.2	1900	151
Si (5.43 Å)	5.2	19	7.8	40	5400	11
BeCo (2.61 Å)	15	31	2.6	40	5400	4.32

operating parameters and sizes of the interferometer must of known before any technologies that could be used in its construction can be proposed. Based on an analysis given in **III-G**, Table I lists some of the possible operating parameters for AIGO.

The overall design of this proposed configuration for AIGO is shown in Fig. 2. It is a balanced interferometer with an octahedral shape. An atomic source emits a high-intensity beam of atoms that strikes a beam splitter which splits the beam along the $\pm x$ and $\pm y$ direction. One of the beams in the x-direction and one of the beams in the y-direction are capped-off, and the other two beams are reflected by mirrors, and recombined at the final beam splitter. The flexibility in choosing which beams to cap enables parity discrimination to be done on the signal. In addition, unlike LIGO, this "octahedral" configuration for AIGO is able to measure the local curvature from *any* source. The Sagnac effect, or the local curvature of the Earth can thus be used to calibrate the interferometer.

We propose to make the beam splitters and the mirrors from diffraction gratings. These gratings will either be nanofrabricated, such as the one shown in Fig. 3, used in transmission, or using the cleaved-surface periodic structures of crystalline materials, used in reflection. The sketch of AIGO in Fig. 2 shows crystal gratings being used in reflection. As we shall see in **III-G**, the width $L_\perp$ and length $L_\parallel$ will be determined by three parameters: the sensitivity of the interferometer $\delta\varphi_{shot}$, the type of GW the interferometer is designed to detect, and the grating period a. Generally, the higher the sensitivity, the smaller $L_\perp$, and the smaller the a, the shorter $L_\parallel$.

As we can see from Table 1, an "octahedral" AIGO made using a BeCo crystal with a lattice constant of 2.606Åwould have an aspect ratio of $L_\parallel/L_\perp = 2.7$ for a shot-noise-limited sensitivity of $\delta\varphi_{shot} = 10^{-10}$. However, an atom interferometer using crystal-lattice reflection gratings has never been demonstrated before, and, as we shall see below, there may be some question of whether the atomic beams in such an interferometer will

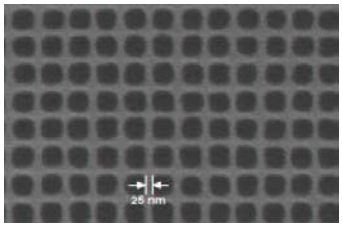

Figure 3. Photographs of a 100 nm periodicity transmission grating with 25 nm features fabricated for atom interferometry. From Space Nanotechnology Laboratory (www.snl.mit.edu/projects.html).

maintain its phase coherence. A 20 nm nanofabricated transmission grating at the same sensitivity would have an aspect ratio of 95, and would be much longer. Nevertheless, atom interferometers using transmission gratings have been demonstrated [6], nanofrabricated transmission gratings with a periodicity of 32 nm have been made [4], and 10 nm periodicity gratings are within the goals of current nanotechnology research. Thus, there is a trade-off in size of the interferometer versus risk of its development through the choice of grating types. Because of its inherent advantage in the size of the interferometer, we will focus on development of crystal-based diffraction grating systems.

The "octahedral" configuration for AIGO can be divided into four subsystems. We analyze and describe the possible technologies that can be used in each subsystem to construct AIGO.

3.2.1. *Atom Source Subsystem*

Helium is the atom of choice for AIGO-type interferometers (see **III-G**).There are several reasons for this. First, we shall see that the low temperatures needed for a high-intensity atom source suggests the use of gaseous or liquid helium for reasonable parameter ranges of AIGO sensitivities. Second, helium atoms would not stick to the proposed optical elements, i.e., the mirrors and beam-splitters made from crystals or nanofabricated gratings that are necessary for the construction of the interferometer. Third, the use of helium atoms would allow a reasonably high probability of elastic, and hence coherent, atomic diffraction and reflection processes; diffraction of helium atoms is well established [16]. Fourth, the construction of helium-atom mirrors based on thin silicon wafer technology, which has also already been demonstrated [17], lends itself naturally to the design of

a pressure-based "quantum accumulator" detector for the interferometer, which is described below.

Standard supersonic sources are already well developed for noble gases, including helium [18]. A jet of gas from a high-pressure reservoir escapes supersonically in free expansion through a nozzle, which consists of a small orifice, typically 10 to 100 microns in diameter, into a differentially pumped low-pressure chamber with a larger orifice at its output end called the "skimmer". This skimmer has the appropriate geometry so as to skim away the outer components of the rapidly expanding gas jet, thus leaving only the intense, low-temperature central component of the atomic beam to enter into another differentially pumped chamber, where the beam is further collimated by a slit at its output end. The beam could be further collimated by means of a second slit at the output end of yet another differentially pumped chamber, before it enters the main vacuum chamber containing the atom interferometer [6]. Thus, with successive stages of differential pumping by means of diffusion pumps, one can maintain an ultra-high vacuum of the main chamber inside which the optical elements are placed.

Based on the calculations given in **III-B**, for an AIGO sensitivity of $\delta\varphi_{shot} \simeq 10^{-9}$, we would need a helium atom source intensity of $\simeq 10^{18}$ atoms per sec, which should be achievable with a standard gas-based supersonic source such as that described above. However, for the higher AIGO sensitivities of $\delta\varphi_{shot} \simeq 10^{-10}$, we would need to go to a liquid-based supersonic source, since a liquid can have much larger number density of atoms than a gas. At intensities higher than 10^{-9}, it becomes difficult construct a gas-based source, even from a supersonic source, to emit these many atoms per second. In addition, the density of atoms in the beam can be so high that collisions between atoms in the beam can occur while they traverse the interferometer [15]. These collisions can potentially induce decoherence in the beam, and wash-out the interference fringes. Thus, for sensitivities above 10^{-9}, we would consider instead liquid based sources where reservoir consisting of liquid helium which emerges supersonically through a nozzle into a low pressure chamber. Such sources have recently be constructed by Toennies' group (www.gwdg.de/~mpisfto/www.e/superfluid_e.html), where *in vacuo* filamental beams of superfluid helium have been made.

3.2.2. *Atomic Beam Optical Elements: Mirrors and Beam Splitters*

We propose to explore two different routes for the fabrication of mirrors and beam splitters needed for the construction of AIGO. First, we shall

consider cleaved surfaces of single crystals for such optical elements, which we know yield such near-perfect crystalline surfaces. These crystals would be used to construct mirrors and beam splitters. Various diffraction orders from such surfaces have already been observed for helium atoms [16]. Furthermore, Holst and Allison have demonstrated that the flexible, thin, hydrogen-passivated single-crystal silicon wafer surface Si(111)-(1 × 1)H can be used as a mirror for focusing helium atom beams [17]. Using this helium-based mirror, scanning helium-atom microscopes are presently being developed [5].

Second, we shall consider the nanofabricated gratings which have previously been used for demonstrating matter-wave interferometry with various atoms and molecules (see [6]). Gratings with square array of holes having a 100 nm period with 25 nm features have been fabricated (see Fig 3).

Both routes have their advantages and disadvantages. On the one hand, crystals have smaller grating periods, and hence typically yield smaller interferometer sizes. However, the use of crystalline surfaces requires an ultra-high vacuum environment. On the other hand, nanofabricated gratings can be flexible in their design, and can also be easier to align than crystals due to their larger grating periods. However, their use entails the construction of much longer AIGO interferometers.

3.2.3. *Laser Interferometer Alignment Subsystem*

It is important for space-based AIGOs to develop laser interferometry for positioning and aligning the various optical elements of the atom interferometer. This is a difficult engineering task. As we shall argue below, there are no fundamental physical obstacles to achieving this goal.

Unlike LIGO, where the mirrors of the interferometer are in free fall, i.e., placed as pendula on the end of kilometer-long interferometer arms, here in AIGO, the mirrors and beam splitters must be bolted to some underlying mechanically rigid structure. (The fringe shift in AIGO is due to deflections in the motion of the *atoms*, and not of the *mirrors* as in LIGO, by the GW; see **III-E**). Furthermore, the size of AIGO is on the order of meters, and not of kilometers as in the case of LIGO, or of millions of kilometers as in the case of LISA. This should make this engineering task orders of magnitude easier for AIGO than for LIGO. In addition, the active-feedback-mechanism technology developed for LIGO to stabilize the mirror–central-beam-splitter distance could be transfered to AIGO if needed.

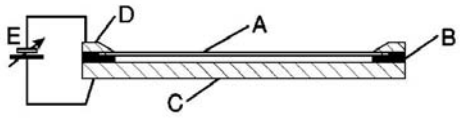

Figure 4. Schematic of a mirror for helium atoms from [20].

Nevertheless, for the crystal-based AIGO interferometers the positioning and aligning of the various optical elements must be accomplished on the scale of Ångströms. Furthermore, in order to observe the "white-light fringe," it would be necessary to balance the two arms of the interferometer also on the scale of Ångströms. Such careful measurements of distances are difficult, but not impossible, and are certainly much easier than the even more stringent requirements for LIGO and LISA. The fundamental sensitivity of the laser interferometer in distance measurements necessary to make such measurements arises from the photon-shot noise limit

$$\delta\varphi_{laser} \simeq \frac{1}{\sqrt{N_{photon}}} \simeq \frac{1\text{Å}}{1\mu\text{m}} \simeq 10^{-4}, \tag{11}$$

where N_{photon} is the number of photons in a given measurement time interval. Hence we would need $N_{photon} \simeq 10^8$ in order to perform these measurements. This is not difficult achieve with standard lasers.

For nanofabricated-grating-based AIGOs, similar considerations apply. Although grating periods for these AIGOs are typically three orders of magnitude larger than for the crystal-based AIGOs, the longitudinal length scales are correspondingly larger, so that the required fractional precision for position measurements using the laser interferometry subsystem is about the same in both cases.

3.2.4. *Detector Subsystem*

For detecting the high-intensity helium atom beams at the output port of AIGOs, we propose to use a "quantum accumulator detector," i.e., a pressure detector of the beam emerging from the atom interferometer. This detector works on the principle of momentum conservation during elastic, specular reflections of the helium atoms from a thin silicon wafer supported

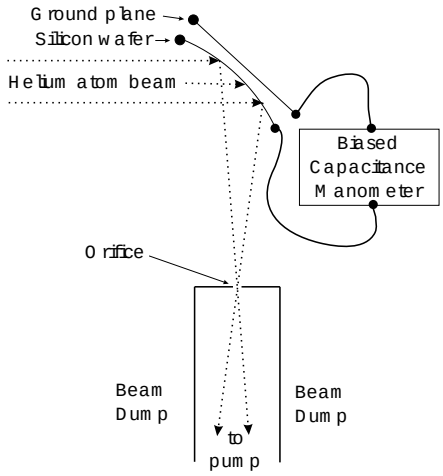

Figure 5. The "quantum accumulator detector," i.e., a pressure detector for the helium atom beam emerging from the output port of the atom interferometer.

at its boundary by a spacer separating it from the ground plane (see Fig. 4). The impacts of 10^{20} helium atoms per second (in order to have $\delta\varphi_{shot} \simeq 10^{-10}$ in a typical bandwidth of 1 Hz) in a beam moving with a typical velocity of 200 m/s, elastically reflected at 45° from the center of the silicon wafer, yields a typical force of 20 dynes. A capacitor consisting of the silicon wafer which is metalized on its back side and the ground plane, is used here to measure the pressure due to this beam impinging on the wafer, by means of a biased capacitance manometer. The beam is also focused through a small orifice into a "beam dump" (i. e., a diffusion pump) by the mirror formed by the bias voltage on the silicon wafer. The quantum shot-noise limit should be achievable with this detector.

3.3. *Preliminary Experiments: The Test Interferometer*

The ultimate goal of this research program is to construct an AIGO with the sensitivity to detect, measure, and observe GWs, and the experiments planned in this preliminary phase of the research program are designed to support this goal. Based on these experiments, a better assessment of the feasibility of can be made.

Table II is a preliminary sketch of the AIGO development effort and how these experiments fit within the whole development plan. The right two columns list the performance goals, and the expected subsystem con-

figurations of the space-based AIGO based on the preliminary considerations outlined in **III-B**. The interferometer is divided into subsystems, and aside from the laser-interferometer-alignment subsystem, specific preliminary experiments are listed on the left column to develop understanding of the fundamental physics of the subsystem in support of the eventual space-based-AIGO performance goals. Based on the analysis in **III-B**, it is expected that the development of laser-interferometer-alignment system will be more an issue of careful engineering than of any underlying physics, and we do not plan much research in this subsystem in these preliminary experiments.

The first part of the experimental plan focuses on evaluating and selecting candidate crystals could be used in the space-based AIGO. We will either need to set up a test rig for measuring the properties of such mirrors and beam splitters in an ultra-high vacuum scattering chamber, or to use existing facilities, such as those in Berkeley's chemistry department, in order to make such measurements. In particular, we propose to measure the probabilities of the scattering of helium atoms into the various diffraction orders for the passivated cleaved silicon surfaces Si(111), Si (100), and Si(110), using standard passivation techniques, to find out their suitability for a helium atom interferometer, as well as other candidates, such as surfaces of LiF, BeCo, etc. We would also need to obtain nanofabricated gratings, such as the MIT Space Nanotechnology Laboratory, etc., but we will also explore the possibility of using the Berkeley EECS microfabrication facility to make these gratings.

In dividing each subsystem into separate parts, and designing experiments to understand the fundamental physics underlying each subsystem, we can at most ensure that each subsystem, separately, can be designed. To ensure that these subsystems can be integrated into an interferometer, we propose to construct a test interferometer, which, like the Bonse-Hart neutron interferometer used by Collela, Overhauser, and Werner [1], would be formed out of one large piece of monolithic, single-crystal silicon ingot. Silicon ingots with diameters of 12 inches are commercially available, and ingots with diameters of up to 22 inches can be obtained from Silicon Crystals, Inc., 2620 Mercantile Dr., Rancho Cordova, CA 95742 (www.siliconcrystals.com/services.html). This would serve as a ground-based test of a simplified version of the proposed "octahedral" interferometer described above, which would combine into an integrated whole all the crucial elements of an atom interferometer, including beam splitters and mirrors. Thus the question of how the decoherence occurring at these

Sub-System	*Preliminary Experiments*	*Space-based Interferometer* Low-intensity sources	*Space-based Interferometer* High-intensity sources
Source	- Effusive noble-gas source - Supersonic noble-gas source	Supersonic noble-gas source with $\Delta\varphi_{shot} \sim 10^{-7}$	Liquid-based atom source with $\Delta\varphi_{shot} \sim 10^{-10}$
"Optics" (Mirrors and Beam Splitters)	- Prepare crystal samples - Explore candidate crystals - Measure diffraction intensities - Demonstrate optical elements	Crystal-based	Crystal-based
Laser Interferometer Alignment	- Construct high-accuracy laser interferometer	Laser-interferometer based	Laser-interferometer based
Detector	- Accumulators - Metastable noble-gas detectors	Quantum-accumulator detectors	Quantum-accumulator detectors

elements would degrade the visibility of the resulting interference fringes could be answered experimentally.

In the test interferometer, an incoming helium atom beam from a supersonic source "S" enters a rhomboidal interferometer (see Fig. 6). This beam from the atom source would be introduced by means of a mirror cleaved out of a pedestal located at the position marked "S", oriented in such a way so as to reflect an incident beam into the plane of the interferometer and directed towards the initial beam splitter. This incoming beam is coherently split by this beam splitter (a crystalline reflective diffraction grating) into an upper path and a lower path. These two beams are reflected by the top and bottom mirrors towards the final beam splitter (also a crystalline reflective diffraction grating), where they are coherently recombined into a single outgoing beam directed towards the detector "D," in a time-reversed version of the initial beam-splitting process. Thus the interferometer consists of four optical elements at the four corners of a rhombus, the top and bottom elements being two mirrors, and the left and right elements being the initial and final beam splitters. These elements, indicated by the heavy lines, are first etched out of a single, underlying silicon crystal base. The surfaces for the beam splitters and mirrors are then cleaved from the etched crystal, and then passivated to preserve its surface crystalline structure, and thus to ensure well-defined diffraction peaks of the beam. A metastable gas detector will primarily be used for these experiments. In the metastable gas detector, an electron beam is used to excite the helium atoms to a metastable excited state. When a metastable helium atom strikes a metal surface, an electron is released and is detected by an electron multiplier.

This test interferometer possesses automatically balanced arms, so that a "white-light" fringe should be readily observable, provided that no substantial decoherence of the quantum mechanical phase of the helium atoms occurs at the beam splitters, mirrors, or along the paths of the beam.

When the plane of the interferometer is horizontal, there should be a large detectable Sagnac phase shift due to the Earth's rotation. If the plane of the interferometer is tilted towards the vertical, a large detectable phase shift due to the Earth's gravitational acceleration g should be observable, similar to that observed in the neutron interferometer [1].

Decoherence and the Debye-Waller factor Quantum interference requires that there exists no possibility of "which-path" information for the helium atom inside the interferometer. This places stringent limits on the decoherence of the atom beam as it is diffracted from the beam splitters, and reflected off the mirrors. (Scattering of atoms in the beam off of background gas is assumed to be negligible). In particular, the diffraction and reflection processes have to be elastic. A measure of the inelastic versus elastic components of these process is based on the Debye-Waller factor W in the intensity ratio $I/I_0 = \exp(-2W)$, where I is the diffracted (or reflected) intensity and I_0 is the incident intensity. This factor W is a measure of the fluctuations of the locations of the atoms in the crystal that diffracts the incident helium beam. For diffracted helium beams,

$$W = B/a^2, \tag{12}$$

where a is the lattice constant of the silicon crystal, and B is measured to be 0.45 Å^2 at room temperature [19]. The rule of thumb in the atomic beam community is that [3]

$$\frac{W}{12} < 0.1 \ , \tag{13}$$

for sharp, elastic diffraction patterns to be seen. However, our requirement for observing interference is more stringent: We require that the probability of emitting even a single phonon during the diffraction process be negligible. The criterion for predominantly single-phonon processes is that [21]

$$\frac{W}{12} < 0.01. \tag{14}$$

For the proposed test interferometer, $W/12 = 1.3 \times 10^{-3}$ at room temperature and decreases at lower temperatures. Thus it is highly probable that the *zero-phonon* process is the dominant one, and therefore quantum phase coherence is expected. However, this conclusion must be checked experimentally in the proposed test interferometer.

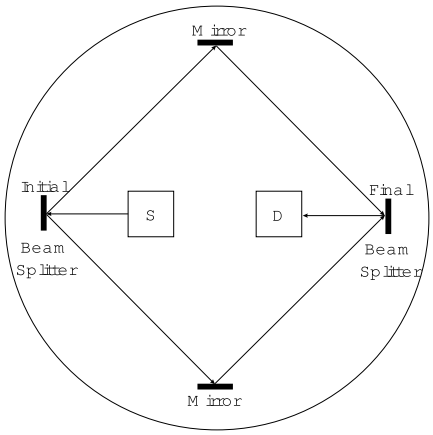

Figure 6. Schematic of the proposed test interferometer, which is a Bonse-Hart-type interferometer for helium atoms formed out of a single crystal of silicon.

3.4. *Expected Phase Shifts*

In this section we estimate the phase shifts expected for AIGO in the space-based, octahedral configuration described above. In the free-fall environment of LEO, only the local curvature of spacetime will determine the paths of the atoms in the interferometer. In **III-B** we have already estimated the contribution of the Riemann curvature of the Earth $\Delta\phi^E$ to the total phase shift. We shall focus here only on the GW component of the phase shift, and neglect the effect of the Earth's curvature on the motion of the atoms. Since $R^E_{0i0j} \sim 10^{-6}$ s^{-2}, while for a GW with a frequency of 10^4 Hz and strain of 10^{-21} has a $R^{GW}_{0i0j} \sim 10^{-12}$ s^{-2}, this is a good approximation.

We consider a GW incident along the longitudinal axis of the interferometer. Along this axis, the x- and y-axes of the interferometer look like the Michelson interferometer used by LIGO. Like LIGO, the $\times$ polarization does not produce a measureable signal; this polarization tends to move the atoms perpendicular to their path. The + polarization, on the other hand, *does* contribute and will tend to speed-up and slow-down the particle along each axis separately.

As usual, we choose as our origin the initial beam splitter at the base of the interferometer (see Fig. 2). The net phase shift for a single atom in

the continuous atom beam traveling along the x-axis versus the y-axis is,

$$\Delta\phi^{GW} = \frac{1}{\hbar}(S_x - S_y), \tag{15}$$

where

$$S_x = \int_{\gamma_x} \left(\frac{1}{2}mv_i v^i - mN_i^{GW} v^i\right), \qquad S_y = \int_{\gamma_y} \left(\frac{1}{2}mv_i v^i - mN_i^{GW} v^i\right), \tag{16}$$

are the classical action for a particle traveling along the x-axis (γ_x) and y-axis (γ_y) respectively. N_i^{GW} is given in Eq. (5), and it is straightforward to see that either S_x or S_y leads to the Hamiltonian for the Schrödinger equation (3).

While a continuous atom source will most likely be used in AIGO, for clarity in this derivation of the phase shift of AIGO due to the passage of a GW let us consider a pulse source for that throws out $N_{\Delta t}$ atoms at intervals of Δt; the continuous source to be recovered by letting $\Delta t \to 0$ appropriately. For the atoms traveling along the x-axis released at time $t_n = n\Delta t$,

$$\begin{aligned} v_{0x} &= v_\perp, \qquad & x_0(t) &= v_\perp(t - t_n), \\ v_{0z} &= v_\parallel, \qquad & z_0(t) &= v_\parallel(t - t_n), \end{aligned} \tag{17}$$

for $t_n < t < t_n + T/2$, where $T/2$ is the time for the atom to travel from the beam splitter to the mirror, while

$$\begin{aligned} v_{0x} &= -v_\perp, \qquad & x_0(t) &= L_\perp - v_\perp(t - t_n), \\ v_{0z} &= v_\parallel, \qquad & z_0(t) &= v_\parallel(t - t_n), \end{aligned} \tag{18}$$

for $t_n + T/2 < t < t_n + T$. Due to the mirrors, there is a jump discontinuity in v_{0x}. Similar equations hold for the path along the y axis. It is clear that $L_\parallel = v_\parallel T$, and $L_\perp = v_\perp T/2$.

At $t > 0$ a GW in the long-wavelenth limit with strain h_{ij}^{GW} with a + polarization passes through the interferometer traveling parallel to the z-axis. The paths of the atoms will be slightly perturbed so that $x = x_0 + x_1$ and $y = y_0 + y_1$, where x_1 and y_1 are deviations from the free-space paths x_0 and y_0. These perturbations satisfy the geodesic deviation equations of motion in Eq. (2). The GW does not affect motion along the z-axis. Then, writing $v_x = v_{0x} + v_{1x}$, for the bunch of atoms released at $t = t_n$,

$$S_x = \frac{m}{2}(v_\parallel^2 + v_\perp^2)T + m\int_{t_n}^{t_n+T} v_{0x}\left\{v_{1x} - \frac{1}{2}h_{xx}^{GW} x_0 v_{0x}\right\} dt. \tag{19}$$

After successive integration by parts and use of Eq. (2),

$$S_x = \frac{m}{2}(v_\parallel^2+v_\perp^2)T+m\left\{L_\perp\left(v_{1x}(t_n+T^-/2)-v_{1x}(t_n+T^+/2)+h_{xx}^{GW}(t_n+T/2)v_\perp\right)-\frac{v_\perp^2}{2}\int_{t_n}^{t_n+T}h_{xx}(t)dt\right\}, \tag{20}$$

where $v_{1x}(t_n+T^-/2)\equiv\lim_{\epsilon\to 0}v_1(t_n+T/2-\epsilon)$ is the value of v_{1x} right before the mirror, and $v_{1x}(t+n+T^+/2)\equiv\lim_{\epsilon\to 0}v_1(t_n+T/2+\epsilon)$ is the value of v_{1x} right after the mirror. The jump condition of the x-velocity at the mirror requires that $v_{1x}(t_n+T^-/2)=-v_{1x}(t_n+T^+/2)$; everything is reflected. Integrating Eq. (2), we get

$$v_{1x}(t_n+T^-/2)=\frac{L_\perp}{2}\dot{h}_{xx}^{GW}(t_n+T/2)-\frac{v_\perp}{2}\left\{h_{xx}^{GW}(t_n+T/2)-h_{xx}^{GW}(t_n)\right\}, \tag{21}$$

so that for the + polarization where $h_{xx}=-h_{yy}$,

$$\Delta\phi^{GW}=\frac{2m}{\hbar}L_\perp^2\left\{\dot{h}_{xx}^{GW}(t_n+T/2)+2\frac{h_{xx}(t_n)}{2}-\frac{1}{2T^2}\int_{t_n}^{t_n+T}h_{xx}^{GW}(t)dt\right\}. \tag{22}$$

Taking now the Fourier transform of $h_{xx}^{GW}(t)$,

$$h_{xx}^{GW}=\int_{-\infty}^{\infty}\frac{d\omega}{2\pi}h_+(\omega)e^{i\omega t}, \tag{23}$$

we find the following frequency response,

$$\Delta\phi_{AIGO}(\omega)=\frac{2m}{\hbar}L_\perp^2 ih_+(\omega)\omega e^{i\omega t/2}\left\{1-\frac{2i}{\omega T}\left[\cos\frac{\omega T}{2}-\frac{\sin\omega T/2}{\omega T/2}\right]-\frac{\sin\omega t/2}{\omega T/2}\right\}. \tag{24}$$

for the phase shift.

The resonance apparent at T us due to the finite size of the interferometer, and the relatively slow velocity of the atom compared to the GW. When $\omega T >> 2\pi$,

$$|\Delta\phi_{AIGO}|\approx\frac{2m}{\hbar}L_\perp^2|h_+(\omega)|\omega. \tag{25}$$

In this limit T is much *longer* than the period of the GW, and the time behavior of the GW can be discerned. As we shall see, it is in this limit that AIGO is most sensitive to gravitational waves, and we shall focus on this limit when discussing the size and design of the interferometer.

In the other limit where $\omega T << 2\pi$

$$|\Delta\phi_{AIGO}|\approx\frac{m}{3\hbar}L_\perp^2|h_+^{GW}(\omega)|\omega=\frac{2m}{3\hbar}|R_{0x0x}(\omega)|L_\perp^2 T. \tag{26}$$

In this limit T is *shorter* than the period of the GW, and in this limit, the time behavior of $R^{GW}_{0x0x}(t)$ cannot be discerned, and is effectively a constant for each bunch of atoms passing through the interferometer. As expected, Eq. (26) reduces Eq. (10) in the static limit. Note, however, that $|\Delta\phi_{AIGO}|$ is proportional to ωT, which is very small is this limit. Consequently, AIGO will not be as sensitive to GWs in this limit.

As we see from Eq. (22), the phase shift $\Delta\phi^{GW}$ depends explicitly on the transit time T of the atom through the interferometer, which can be very slow. Thus, it seems that due to this relatively long transit time, AIGO would appear to be a slowly-responding interferometer. This would be incorrect. Each bunch of atoms travels through the interferometer as a group, and a sequence of $\Delta\phi(T)$, $\Delta\phi(T+\Delta t)$, $\Delta\phi(T+2\Delta t)$, $\ldots$, can then be measured. Each measurement of the phase shift corresponds to a value of h^{GW}_{xx} at a different time, and using Eq. (22), the time dependence of h^{GW}_{xx} can in principle be reconstructed. Thus, what determines overall response-time of AIGO not the transit time of the atom, but rather the integration time of the interferometer.

As we can see from Eq. (25), unlike $\Delta\phi_{LIGO}$, $\Delta\phi_{AIGO}$ depends on the *square* of $L_\perp$, and not simply on $L_\perp$. As we shall see in the next section, this difference in the power-law dependence of the phase shift on the size of the interferometer is due to the fact that while LIGO measures fluctuations in the *positions* of classical test masses (the mirrors of LIGO's interferometer) due to the passage of a GW, AIGO measures fluctuations in the *velocity* of quantum test masses (the atoms used in AIGO).

3.5. *AIGO and LIGO: The Underlying Physics*

In this section, we delineate the physics underlying both AIGO and LIGO, and compare their relative sensitivities to GWs from astrophysical sources. We shall emphasize only the physics here, and our arguments will be more physical than formal. Consequently, we shall consider the effects of a GW passing over freely-falling particles only, and neglect all other external forces on the system. We begin with the classical dynamics arising from the geodesic deviation equations of motion from Eq. (2); on a classical level, both AIGO and LIGO are governed by it. For LIGO, one considers a test mass (a mirror) at a distance L^i from the center of mass (the central beam splitter) of the apparatus, which is the origin of the coordinate system. When a GW passes over the apparatus, it causes small shifts ξ^i in this distance as observed by an observer at the origin. Thus, we can write

$x^i = L^i + \xi^i$, where $\left|\xi^i\right| << \left|L^i\right|$, and

$$\frac{d^2\xi_i}{dt^2} \approx -R^{GW}_{0i0j} L^j. \tag{27}$$

To lowest order,

$$\xi_i \approx -L^j \int_0^t dt' \int_0^{t'} dt'' R^{GW}_{0i0j}(t'') = \frac{1}{2} L^j h^{GW}_{ij}, \tag{28}$$

where for $t \leq 0$, $h^{GW}_{ij} \equiv 0$. Thus, in LIGO one puts a mass (a mirror) at $t = 0$ a certain distance L^i away from the center, and observes fluctuations in its *position* due to the passage of a GW. In AIGO, on the other hand, one throws out a test mass (an atom) at $t = 0$ with a velocity V_i from the center, and observes deviations in its *velocity*, and thus its path in spacetime, due to the passage of a GW. To see this, we write $v_i = V_i + \beta_i$, where $|\beta_i| << |V_i|$. Then

$$\frac{d\beta_i}{dt} \approx -R^{GW}_{0i0j} V^j t. \tag{29}$$

Once again to lowest order,

$$\beta_i \approx -V^j \int_0^t dt' R^{GW}_{0i0j}(t') = \frac{1}{2} V^j \dot{h}^{GW}_{ij} \tag{30}$$

where $\dot{h}^{GW}_{ij}$ is the rate of change of the strain field h^{GW}_{ij} of the GW. The parallelism between the displacement ξ^i in LIGO, and the velocity shift β_i in AIGO, are readily apparent. Classically, the velocity shift β_i is extremely small, and virtually impossible to measure. Quantum mechanically, however, this velocity shift can be measured by means of quantum interference.

A quantum particle has a DeBroglie wavelength $\lambda_{DB} = 2\pi\hbar/mv$, where m is the mass of the particle and v is its speed. Changes in the particle's speed Δv result in changes to its local DeBroglie wavelength, and hence its quantum phase. This phase shift could be measured by means of an atom interferometer, as we have described above. Indeed, Eq.(25) can rewritten as

$$\Delta\phi_{AIGO} = \frac{2\pi}{\lambda_{\perp dB}} \Delta L_{eff} \ , \tag{31}$$

where $\lambda_{\perp DB} = 2\pi\hbar/mv_\perp$ and

$$\Delta L_{eff} = 4\pi \Delta v T = 4\pi L_\perp \left|\dot{h}^{GW}_{ij}\right| T. \tag{32}$$

Thus, the quantum phase in AIGO is a cumulative effect depending on the total history of the atom in the presence of the GW. Note that in AIGO

it is the phase of the atom which is *directly* acted upon by the GW, and used in the measurement. This is *not* the case in LIGO, where any means to measure the deviations in the position of the test mass, can be used. In LIGO, light-based interferometry is used to measure these deviations, and the test mass is a freely-falling mirror in the interferometer, and the phase shift is given by LIGO is given by

$$\Delta\phi_{LIGO} = \frac{2\pi}{\lambda}\Delta L_{LIGO}, \tag{33}$$

where $\lambda = 2\pi/k$ is the wavelength of the laser, ΔL_{LIGO} is the optical path length difference of LIGO induced by the GW, and where for the two arms of the interferometer,

$$\Delta L_{LIGO} \ = 150\left|h_{ij}^{GW}L^i\right|, \tag{34}$$

where the factor of 150 accounts for multiple reflections within each arm of LIGO. Thus, the phase in LIGO depends on the instantaneous position of the test particle (i.e., the mirror) in the presence of the GW. Note that in LIGO the photons used in making the measurement are *not* the particles being acted on by the GW: It is only the test mass (i.e., the mirror) which is being acted on. Thus, even though the velocity of the test mass is small in AIGO, the effect of a GW on the particle may still may be large.

3.5.1. *Comparison of AIGO and LIGO*

To compare the ability of AIGO to detect GWs to LIGO's, we consider a + polarized, monochromatic GW with frequency ν_{BW} and amplitude h_+ incident on both AIGO and LIGO. Then

$$\frac{\Delta\phi_{AIGO}}{\Delta\phi_{LIGO}} = \frac{\lambda}{\lambda_{\perp DB}}\frac{\Delta L_{eff}}{L_{LIGO}h_+}. \tag{35}$$

Then if the sensitivity of AIGO is equal to LIGO, $\Delta\phi_{AIGO}/\Delta\phi_{LIGO} = 1$, and from Eq. (32),

$$L_{AIGO} = \left\{\frac{\hbar\omega}{mc^2}\frac{L_{LIGO}\lambda_{GW}}{4\pi}\right\}^{1/2}, \tag{36}$$

where ω is the frequency of the laser. LIGO's designed operating frequency range is from 10 Hz to 10^4 Hz, and we find that $L_{AIGO}/L_{LIGO} < 3\times10^{-5}$ for helium atoms. For the same size, AIGO is orders of magnitude more sensitive than LIGO.

From Eq. (33) we see that $\Delta\phi_{LIGO}$ increases with decreasing λ. We are proposing to construct AIGO using atoms whose DeBroglie wavelength

is in the x-ray region, much shorter than LIGO's current lasers. However, even if x-ray lasers can be constructed for LIGO, we see that

$$L_{AIGO} = \left\{ \frac{v_\perp}{c} \frac{L_{LIGO}\lambda_{GW}}{4\pi} \right\}^{1/2}, \tag{37}$$

where we have set $\lambda = \lambda_{\perp DB}$ in Eq. (35). For a helium-atom-based AIGO using silicon crystal gratings, $v_\perp = 389$ m/s (see below), and $L_{AIGO}/L_{LIGO} < 0.23$, and is still over 4 times shorter than LIGO.

3.5.2. *Matter-wave Interferometry and the Detection of Gravitational Effects*

The relative sizes of AIGO compared with LIGO given in Eqs. (36) and (37) would seem to be counterintuitive. AIGO makes use of slowly-moving, nonrelativistic atoms to make its measurements, while LIGO would seem to make use of fast-moving photons. Thus, at first glance it would seem that AIGO should be *less* sensitive to GWs than LIGO by some power of $v_\perp/c$. This, however, would be an erroneous argument. As outlined in **II-B** and in the above, it is *not* effect of GW on the *photons* used in the laser interferometer that is being measured in LIGO; it is the effect of the GW on the test masses (the *mirrors*) *which are at rest* that is being measured. Indeed, it is precisely because the atoms are *nonrelativistic* that the effect of GWs on their motions are much more readily measurable than their effect on photons.

Again, a GW can readily change the velocities of nonrelativistic atoms, but it cannot change the velocity c—or even the frequency—of photons (although it can slightly change their directions). Photons are constrained to have a zero 4-momentum, and must travel along *null* geodesics between to events in spacetime. Massive particles such as atoms, however, can only travel along *timelike* geodesics, and for nonrelativistic particles, there are an *many* available paths between two events depending on the velocity of the atom. Thus, roughly speaking, an atom's path is much more readily shifted than a photon's. Consequently, we would expect that the sensitivity to detecting GWs to *decrease* if ultrarelativistic particles—which behave like photons—are used instead of slow-moving, nonrelativistic atoms.

Equations (25), (35), and the conclusion that the sensitivity of atom-based interferometers to GWs is *larger* in comparison to light-based interferometers, are also surprising when compared to the results of Bordé [22]. Using the standard formalism for quantum field theory in the presence of linearized gravity, he considered the phase shift that a GW would induce

on a generic atom interferometer constructed using nonrelativistic, spin 1/2 atoms. His starting point was the Dirac equation in curved spacetime, and he derived an incorrect expression (Eq.(92) of [22]) for the quantum phase shift. In his expression, the power-law dependencies on $\lambda_{\perp DB}$ and λ is very much different than ours, and lead him to the erroneous conclusion that atom-based interferometers are no more sensitive to GWs than light-based interferometers.

However, it is well known [9] that when dealing with GWs, the effect of the GW on *all parts* of the system, including the observer, must be included; this leads naturally to the geodesic *deviation* equation of motion, which scales linearly with the distance between the center of mass of the apparatus, and the rest of the instrument. Unlike electromagnetic waves, no part of an atom interferometer can be shielded from the GW. Bordé's governing Hamiltonian (Eq. (89) of [22]) that does not scale correctly with the size of the interferometer, and this is the reason why he calculated the incorrect expression for the quantum phase shift.

3.6. *Potential Sensitivity*

3.6.1. *Sizing AIGO*

As mentioned in **III-E**, phase shifts measured by AIGO scales quadratically with it width $L_\perp$. Thus, the larger the interferometer, the larger the expected phase shift. How large of a $L_\perp$ is needed to measure a specific GW depends on the sensitivity of the interferometer, however. This sensitivity, in turn, depends on the design details of the device, and, most critically, on its signal-to-noise ratio. A reliable analysis of the signal-to-noise ratio of AIGO is not possible without an instrument on hand. However, the sensitivity of the final space-based interferometer cannot exceed the fundamental shot-noise limit, and for the supersonic sources described in **III-B** an estimate for the shot-noise sensitivity $\delta\varphi_{shot}$ can be estimated, and given a range of GWs to be detected, $L_\perp$ can then be determined.

What is not obvious from Eq. (25) is that the length $L_\parallel$ of AIGO is also set by $\delta\varphi_{shot}$ as well once a periodicity a of the grating used in the interferometer. Note, that

$$\sin\theta = \frac{v_a}{v_\parallel} \tag{38}$$

where $v_a = 2\pi\hbar/ma$ and θ is the angle that the atom is diffracted off the surface of the beam splitter in Fig. (2). Then, $v_\parallel = v_a/\sin\theta$ and $v_\perp = v_a/\cos\theta$. $L_\perp$ is set by the GW, and $\delta\varphi_{shot}$ while $v_\perp$, to a great

extent, is determined by a. This sets the time-of-flight T for the atom through the interferometer, and thus the aspect ratio of the interferometer $L_\parallel/L_\perp = 2/\tan\theta$. The interferometer is "sized" once $\Delta\phi_{shot}$, a, $v_\parallel$, and a representative $h_+\nu_{GW}$ is given.

However, $\Delta\phi_{shot}$ is determined by the rate of atoms emitted from the source $\dot{N}$, the integration time τ, and the contrast $C \equiv (I_{\max} - I_{\min})/(I_{\max} + I_{\min})$,

$$\delta\varphi_{shot} = \frac{1}{\sqrt{\dot{N}\tau}}\,\frac{1}{C}, \tag{39}$$

and for a given initial density of atoms in the source, $\dot{N}$ increases with increased $v_\parallel$. Thus, for the high-intensity beams needed for AIGO, AIGO can be run "hot" with a large $v_\parallel$ for the atoms in the beam and a lower pressure at the atom source, or it can be run "cold" with a correspondingly higher pressure at the atom source. The first choice will give a longer $L_\parallel$ and the second choice will give a shorter $L_\parallel$. In either case, supersonic sources described in **III-B** will have to be used to decrease $\delta\varphi_{shot}$ to the level needed to observe GW.

For the supersonic sources outlined in **III-B**, the temperature of the gas inside the source is

$$T_0 = \frac{\gamma - 1}{2\gamma}\frac{m v_\parallel^2}{k_B}, \tag{40}$$

where γ is the ratio C_P/C_V of the heat capacity of the gas at constant pressure to the heat capacity at constant volume, and comes from the isentropic expansion of the gas out of a the high-pressure source [18]. For an ideal gas $\gamma = 5/3$. The internal pressure P_0 of the source is

$$P_0 = \frac{m v_\parallel \dot{N}}{A^*}\,\frac{\sqrt{\gamma^2 - 1}}{2\gamma}\left(\frac{\gamma + 1}{2}\right)^{\frac{1}{\gamma - 1}}, \tag{41}$$

where A^* is an effective cross-sectional area of the nozzle of the supersonic source. While we would wish to make $L_\parallel$ as small as possible, to have sufficient $\delta\varphi_{shot}$, P_0 will soon become so high that at some given T_0 that the gas inside the source will condense into a liquid. Moreover, the density of the atoms in the beam will be so high that the collision time between atoms will be shorter than the transit time of the atoms through the interferometer risking decoherence of the atoms through collisions. For these practical reasons, we propose to use helium in AIGO, even though Eq. (25) would argue for using heavier atoms; helium remains a gas at very low temperatures and high pressures. It is also the reason we suggested the

development of liquid-based sources in **III-B**, which would not be bound by this constraint on $\dot{N}$.

From Eqs (40) and (41), T_0 scales as $1/a^2$ while P_0 scales as $1/a$. The difficulties of running gas-based sources at high-P_0 and low-T_0 are even greater for larger a. As a consequence, AIGOs constructed from nanofabricated transmission gratings will have much longer aspect ratios than AIGOs constructed from crystal gratings.

Based on these considerations, a representative set of the size and operating of parameters for AIGO listed in Table (1) can be determined for $\delta\varphi_{shot} = 10^{-9}$ and $\delta\varphi_{shot} = 10^{-10}$. Notice that for $\delta\varphi_{shot} = 10^{-9}$ it is possible to construct an AIGO using a supersonic source and any one of the four gratings. This is no longer possible for $\delta\varphi_{shot} = 10^{-10}$. The nanofabricated grating would have to be run at such high P_0 that it would not be feasible. Even for the crystal grating the needed running P_0 may be too high. Thus, for $\delta\varphi < 10^{-10}$ a liquid-based source would have to be used.

3.6.2. *AIGO Sensitivities*

Given the crystal-grating-based AIGO in Table (1), we now determine the *spectrum* GWs that can potentially be detected with it for various $\delta\varphi_{shot}$.

From the overview given in **III-B**, it is not possible to know C without building the actual interferometer, although for silicon-based beam splitters and mirrors it is expected to be very high. We will set $C \approx 1$ in this estimate of AIGO's sensitivity. The integration time is primarily set by the atomic source and $\dot{N}$; the higher the $\dot{N}$, the shorter τ can be. Thus,

$$\tau \approx \begin{cases} \alpha/\nu_{GW}, \text{ if } \tau < 1/\nu_0 \\ 1/\nu_0 \qquad \text{if } \tau > 1/\nu_0 \end{cases} \tag{42}$$

for some α and ν_0 set by $\dot{N}$, and $1/\nu_0$ is the integration time of the interferometer. Eq. (42) states that for GWs below ν_0, the source is emitting enough atoms that the signal can be sampled α-times in one period of the GW; above ν_0, it can only be sampled once. For the supersonic sources described in **III-B**, a reasonable estimate of α and ν_0 would be 10 and 1 Hz, respectively.

For $L_\perp = 1.6$ m, fig. (7) gives the expected sensitivity for AIGO constructed using a silicon-crystal grating for various $\delta\varphi_s$. This size of the interferometer was chosen as an extreme example the size advantage that AIGO has over LIGO; other sizes of interferometers can be chosen. The change in the slope of the graphs of AIGO sensitivity at 60 Hz is due to

the finite transit time T of the atoms through the interferometer; for frequencies higher than 60 Hz the phase shift is governed by Eq. (25) and for frequencies lower than 60 Hz, it is governed by Eq. (26). (Note that near 60 Hz the phase shift oscillates with ω, but this is cannot be seen on this graph due its scale. The second change in slope occurs at ν_0 Hz, and is due to Eq. (42). The graph of the expected sources and strengths of GWs from various astronomical sources on which Fig. (7) is based is from [23] and was compiled by Thorne; it is most likely dated. Note that the amplitude h of the GW is plotted against the frequency f and not $h/\sqrt{f}$ as is the current practice. The sensitivity of LIGO, for example, is expected to be better than that shown in the figure. However, this figure does outline in a single graph the target sensitivity for both LIGO and LISA, and the potential sensitivity of AIGO can be compared to both. We see that at the very minimum, it is expected that AIGO can fill the gap in the sensitivies of LIGO and LISA for GWs with frequences between 0.1 and 10 Hz

It should be emphasized that the choice $L_\perp = 1.6$ m was arbitrary. By making the interferometer bigger, the same sensitivity can be obtained with a larger $\delta\varphi_{shot}$. The relevant parameter is $\delta\varphi_{shot}/L_\perp^2$, which, unlike LIGO, depends on the *square* of $L_\perp$. Thus, by making $L_\perp$ ten times larger, the same middle graph on fig. (7) with only a 10^{-8} instead of 10^{-10}. Moreover, decreasing $L_\perp$ also increases T by a factor of 10 (for the same source-temperature), which will shift the first break point of the slope of the graphs to 6 Hz, close to ν_0, and increasing the region where AIGO is most sensitive.

4. Conclusion

The ultimate goal of this research program is to construct an AIGO with the sensitivity to detect, measure, and observe GWs. As AIGO is a new concept, we have given a detailed description of the physics underlying the concept, and have estimated the potential of its gain in sensitivity to GWs over LIGO. In all, the tremendous increase in the capability to measure astrophysical GWs with AIGO that may be had over LIGO and LISA, argues strongly for this research program. At the very minimum, it is expected that AIGO can fill the gap in the sensitivities of LIGO and LISA for GWs with frequencies between 0.1 and 10 Hz (see Fig. 7).

References

1. R. Collela, A. W. Overhauser, and S. A. Werner, Phys. Rev. Lett. **23**, 1472 (1975).

2. O. Stern, Naturwissensch, **17** 291 (1929).
3. U. Valbusa, in *Atomic and Molecular Beam Methods*, Vol. 2, edited by G. Scoles (Oxford University Press, New York, 1992), p. 327.
4. www.elec.gla.ac.uk/groups/nano/litho/32nmgrating.html
5. www-sp.phy.cam.ac.uk/research/mirror.php3
6. J. Schmiedmayer, M. S. Chapman, C. R. Ekstrom, T. D. Hammond, D. A. Kokorowski, A. Lenef, R. A. Rubenstein, E. T. Smith, and D. E. Pritchard, in *Atom Interferometry*, edited by P. R. Berman (Academic Press, San Diego, 1997), p. 2.
7. G. Gonzáles , *Gravitational Wave Detectors: A Report From LIGO-Land* , gr-qc/0303117 .
8. B. Barish , *LIGO Overview, NSF Annual Review 23-Oct-02* , www.ligo.caltech.edu/LIGO-web/conferences/nsf-reviews.html.
9. C. W. Misner , K. S. Thorne , and J. A. Wheeler , *Gravitation* (W. H. Freeman and Company , San Francisco , 1973), Chapters 1, 35.
10. R. Y. Chiao and A. D. Speliotopoulos , *Quantum Interference to Measure Spacetime Curvature: A Proposed Experiment at the Intersection of Quantum Mechanics and General Relativity* , `gr-qc/0303027`.
11. L. Stodolsky , Gen. Rel. Grav. **11** , 391 (1979).
12. J. Anandan , Phys. Rev. **15** , 1448 (1977).
13. A. D. Speliotopoulos and R. Y. Chiao , *The Coupling of Linearized Gravity to Non-Relativistic Test Particles: Dynamics in the General Laboratory Frame* , gr-qc/0302045 .
14. A. D. Speliotopoulos , Phys. Rev. **D51** , 1701 (1995).
15. The Pauli exclusion principle would suppress decoherence arising from the collisions between cold, fermionic ^{3}He atoms in a dense beam of spin-polarized ^{3}He atoms, making the visibility of interference fringes for this kind of atomic beam very high. We thank T. Hänsch for pointing this out to us.
16. K. H. Rieder and T. Engel, Phys. Rev. Lett **45**, 824 (1980).
17. B. Holst and W. Allison in *Atomic and Molecular Beams: the State of the Art 2000*, edited by R. Campargue (Springer Verlag, New York, 2001), p. 183.
18. D. R. Miller, in *Atomic and Molecular Beam Methods*, Vol. 1, edited by G. Scoles (Oxford University Press, New York, 1988), p. 14.
19. N. M. Butt, J. Bashir, B. T. M. Willis, and G. Heger, Acta Cryst. A**44**, 396 (1988).
20. R. J. Wilson, B. Holst, and W. Allison, Rev. Sci. Instr. **70**, 2960 (1999).
21. J. H. Weare, J. Chem. Phys. **61**, 2900 (1974).
22. C. J. Bordé, in *Atom Interferometry*, edited by P. R. Berman (Academic Press, San Diego, 1997), p. 275.
23. D. G. Blair in *The Detection of Gravitational Waves* , ed. by D. G. Blair , (Cambridge University Press , New York , 1991).

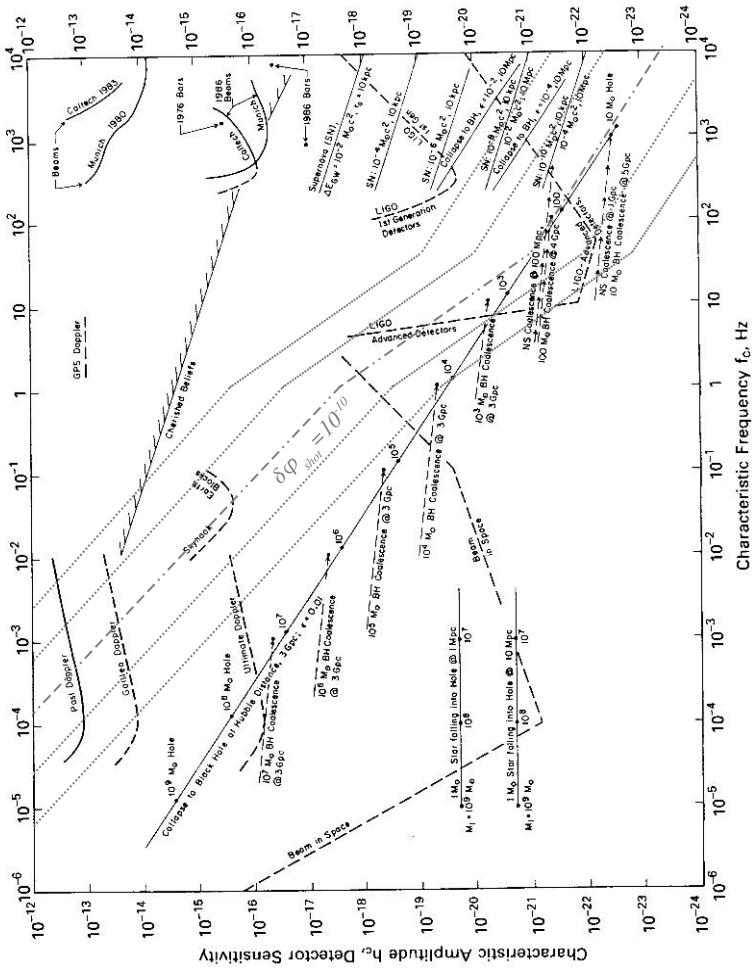

Figure 7. Plot of expected AIGO sensitivities for various shot-noise-limited fringe sensitivities. The center dot-dash line is the $\Delta\phi_{shot} = 10^{-10}$ line. The two dotted lines below, and the two dotted lines below this center line corresponds to the increase or decrease, respectively, of this sensitivity by an order of magnitude each. (Original figure from
[23].

GRAVITATIONAL-WAVE INDUCED EFFECTS IN STORAGE RINGS BEAM DYNAMICS

DONG DONG* AND CHAO–GUANG HUANG†

Institute of High Energy Physics, Chinese Academy of Sciences, P. O. Box 918, Beijing 100039, China

Since Einstein predicted the existence of gravitational waves in nature, more than eighty years passed. Several methods such as Weber antenna, laser interference to directly detect the gravitational waves have been proposed and developed. Unfortunately, untill now, no confirmative gravitational wave signal has been observed directly. Here, we propose a new method to directly detect the gravitational waves by monitoring the motion of charged particles in the storage ring.

Suppose that a plane gravitational wave is incident on a simple quadruple oscillator consisting of charged particles moving in a storage ring. The metric of spacetime with a plane gravitational wave propagating along z-axis is given in $c = 1$ unit by

$$ds^2 = -dt^2 + (1 + h_+)dx^2 + (1 - h_+)dy^2 + 2h_\times dxdy + dz^2, \qquad (1)$$

where $h_+(\ll 1)$ and $h_\times(\ll 1)$ are two independent polarizations. Its effect on a storage ring and beam position monitors (BPM) is negligible because they are fixed on the ground and because the gravitational wave is extremely weak. However, the gravitational wave will lead to the moving particles in the storage ring deviating from their original orbits. The deviation n^μ will be recorded by BPM. The equation of the deviation for the moving particles with the rest mass m_0 and the 4-velocity U^μ is

$$\frac{D^2 n^\mu}{d\tau^2} + R^\mu{}_{\alpha\beta\gamma} U^\alpha (x^\beta - x_o^\beta) U^\gamma = \frac{1}{m_0} \frac{DF^\mu}{dx^\alpha} n^\alpha, \qquad (2)$$

where $R^\mu{}_{\alpha\beta\gamma}$ is the curvature tensor of the spacetime, x_0^β the coordinates of the center of the storage ring, and F^μ the four-vector of the Lorentz force.

*dongd@mail.ihep.ac.cn

†huangcg@mail.ihep.ac.cn

When the storage ring is placed on the x–y plane with the center at the origin of the coordinates, equation (2) may reduce to

$$\frac{d^2n^1}{dt^2} + \omega_a^2 n^1 = \frac{1}{2}\left(\frac{\partial^2 h_+}{\partial t^2}\cdot x + \frac{\partial^2 h_\times}{\partial t^2}\cdot y\right) \tag{3}$$

$$\frac{d^2n^2}{dt^2} + \omega_a^2 n^2 = \frac{1}{2}\left(\frac{\partial^2 h_\times}{\partial t^2}\cdot x - \frac{\partial^2 h_+}{\partial t^2}\cdot y\right) \tag{4}$$

under the simplified assumptions that (i) the magnetic field B is in the z-axis, (ii) n^0 and n^3 are negligible, and (iii) the variations of U^0 and U^3 are negligible. In equations (3) and (4), $\omega_a^2 = \omega_o^2 + \omega_o\omega_B$, where $\omega_0 = qB/m$ is the angular velocity of the charged particles in the storage ring, $\omega_B = qRB'(r)/m$ the angular velocity induced by the gradient of B in radial direction on the x–y plane, q and $m = m_0/\sqrt{1-\omega_0^2R^2}$ the charge and the moving mass of each charged particle, respectively, and R the radius of the orbit of the charged particles.

For simplicity, we consider the sinusoidal plane gravitational wave with the angular frequency ω_g and the wavelength λ_g, *i.e.*, $h_+ = A_+\cos(\omega_g t - 2\pi z/\lambda_g)$ and $h_\times = A_\times\cos(\omega_g t - 2\pi z/\lambda_g)$. The solution of the equations (3) and (4) is

$$n^1 = A_1\cos(\omega_a t + \varphi_1) + \frac{\omega_g^2(A_+x + A_\times y)}{2(\omega_g^2 - \omega_a^2)}\cos(\omega_g t) \tag{5}$$

$$n^2 = A_2\cos(\omega_a t + \varphi_2) + \frac{\omega_g^2(A_\times x - A_+ y)}{2(\omega_g^2 - \omega_a^2)}\cos(\omega_g t). \tag{6}$$

Obviously, both the deviations n^1 and n^2 caused by the gravitational wave have sharp maximums at the angular frequency $\omega_g = \omega_a$. Namely, the gravitational wave with such an angular frequency is in resonance with the rotations of the charged particle in the storage ring.

It is well known that the charged particles in circular motion will have synchrotron radiation, which results in the damping of the motion. If the damping with a rate η is considered, the factor $\omega_g^2/(\omega_g^2 - \omega_a^2)$ in the second term in equations (5) and (6) should be replaced by the quality factor $Q = \omega_g/2\eta$ at the resonance frequency. In order to estimate the quality factor due to the minimum synchrotron radiation and the sensitivity to gravitational waves, let's consider two running storage rings. The first one is SPring-8. It has the radius of about 227 m. The position of electrons can be determined within the precision of 1 μm. The energy of the electron is 8 Gev. The angular velocity is then about $6\times10^6\mathrm{s}^{-1}$. The quality factor for the synchrotron radiation is about 10^4. Therefore, one might detect the

1 MHz gravitational wave on SPring-8 with the dimensionless amplitude $h = \sqrt{A_+^2 + A_\times^2}$ of 10^{-13}. Obviously, such a sensitivity is still too low to detect the gravitational wave. The second example is the storage ring of RHIC has the radius of radius 605 m. The Au nuclei are accelerated to an energy 300 GeV. The angular velocity is then about $5 \times 10^5 \mathrm{s}^{-1}$. The quality factor due to the synchrotron radiation is as high as 10^{12}. Then, one might have a chance to detect the 100 KHz gravitational wave on RHIC with the dimensionless amplitude $h = 10^{-21}$ if the position of nuclei can be determined with the precision of 1 μm. Of course, one should not be so optimistic because of the existence of other potential damping effects. Clearly, to make the storage ring as a realistic detector, one has to, at least, rebuilt the storage ring and analyze other potential effects which might decrease the quality factor.

Usually, the frequency of the gravitational waves generated in astrophysical process is lower than 10^4 Hz. One might argue that it is impossible to use the storage ring to search the gravitational waves because the resonance frequency is too high. However, the high frequency gravitational radiation may be generated, on one hand, by the coalescence of two small black holes with radii less than 1 km or by the oscillation of cosmic strings. On the other hand, the angular velocity of particles moving in a storage ring may be lowered to $2\pi \mathrm{s}^{-1}$, so that we might have an opportunity to detect the gravitational waves with a frequency of 1 Hz by monitoring the motion of charged particles in the storage ring.

In conclusion, the charged particles moving in a storage ring could be used as a detector of gravitational waves. Its working frequency band can spread from 1Hz to 10^7Hz. The favorite working frequency is between 10^4Hz and 10^7Hz. It would open a new window for detecting the gravitational waves, because the electromagnetic detectors are sensitive to the gravitational waves with 10^8Hz or higher, while the traditional detectors, including mechanical and optical devices, are sensitive to the waves with the frequency below 10^4 Hz and the pulsar timing and the cosmic microwave anisotropy work in the even low frequency band.

Acknowledgements

We would like to thank Profs./Drs. S. Kurokawa, S. Date, T. P. Li, Z. Y. Guo, S. Boughn, Y. L. Yan, L. M. Song, and Y. Z. Zhang for helpful discussions and critical comments. One of authors (Dong) thanks Prof. K. Nakahara for his hospitality at the Institute of High Energy Physics in

Japan. The project is in part supported by National Science Foundation of China under Grant No.10175070.

References

1. For example, see: Misner, C. W., Thorn, K. S., and Wheeler, J. A., Gravitation, (W. H. Freeman and Company, San Francisco, 1973).
2. J. Weber, Detection and Generation of Gravitational Waves, *Phys. Rev.* **D**, **117** 307-313 (1960).
3. J. Hough and S. Rowan, Gravitational Wave Detector by Interferometry (Ground and Space), http://www.livingreviews.org/Articles/Volume3/2000-3hough/index.html and references therein.
4. http://www.ligo.caltech.edu/
5. http://www.virgo.infn.it/
6. http://lisa.jpl.nasa.gov/

COSMOLOGICAL FINAL FOCUS SYSTEMS

JOHN IRWIN AND MARINA SHMAKOVA

SLAC, Stanford University, Stanford, CA 94309

We develop the many striking parallels between the dynamics of light streams from distant galaxies and particle beams in accelerator final focus systems. Notably the deflections of light by mass clumps are identical to the kicks arising from the long-range beam-beam interactions of two counter-rotating particle beams (known as parasitic crossings). These deflections have sextupolar as well as quadrupolar components. We estimate the strength of such distortions for a variety of circumstances and argue that the sextupolar distortions from clumping within clusters may be observable. This possibility is enhanced by the facts that i) the sextupolar distortions of background galaxies is a factor of 5 smaller than the quadrupolar distortion, ii) the angular orientation of the sextupolar and quadrupolar distortions from a mass distribution would be correlated, appearing as a slightly curved image, iii) these effects should be spatially clumped on the sky.

1. Introduction

The dynamics for a light stream from a distant galaxy which is collected by an earth-based telescope is shown to be analogous to the dynamics of a particle beam in a final focus system in an accelerator [1]. The beam emittance is well-defined and is similar to that found in present generation accelerators. The dynamics is well approximated by drifts and thin-lens kicks from clusters of matter. The thin-lens kicks are mathematically identical to the kicks arising from parasitic crossings of beams in accelerators. The usual weak gravitational lensing analysis (for recent review see [2], [3] and references therein) restricts itself to the creation of quadrupole moments in the observed light bundle, but here we propose that the sextupole moments, and even octupole moments, may also be observable if the light stream passes close to a dark matter clump. The clump need only have a mass of 10^9 solar masses. We present the mathematics which determines the map from observed image to the source image, and the relationship

of that map to the observed moments of the galaxy images. Finally, we report the beginning of our studies of galaxy images in the Hubble deep fields. The magnitude of background sextupole-moments is a factor of 5 smaller than the background quadrupole moments.

2. Final focus analogy

The dynamics governing the light stream from a distant galaxy collected by an earth-based telescope is analogous to the dynamics of a particle beam for two reasons: the dynamics is governed by a Hamiltonian, and the emittance is small. Paths of photons are determined within general relativity by an action principle $I = \int_1^2 g_{\mu\nu}(x) \frac{dx^\mu}{d\lambda} \frac{dx^\nu}{d\lambda} d\lambda$, hence there is a Langrangian $L = \frac{1}{2} g_{\mu\nu}(x) \frac{dx^\mu}{d\lambda} \frac{dx^\nu}{d\lambda}$, a canonical momentum $p_\mu = g_{\mu\nu}(x) \frac{dx^\nu}{d\lambda}$, and a Hamiltonian $H = \frac{1}{2} g^{\mu\nu}(x) p_\mu p_\nu$, defining the trajectory given by Hamilton's equations $\frac{dx^\mu}{d\lambda} = \frac{\partial H}{\partial p_\mu}$; $\frac{dp^\mu}{d\lambda} = -\frac{\partial H}{\partial x_\mu}$. Since the metric is changing very slowly with time and the gravitational fields are weak, the Newtonian approximation is adequate $g_{00} = -1 - \phi$. For non-relativistic particles $\frac{d^2 x^i}{dt^2} = -\frac{\partial \phi}{\partial x^i}$. Light ray deflections can be calculated from non-relativistic trajectories by multiplying deflection angles by 2.

The emittance can be calculated at the entrance to the telescope. For a 2 m diameter telescope aperture and a galaxy image that has an rms angular radius of 0.1", the emittance is 0.5 mm-mr (millimeter-milliradians). 1" corresponds to $5 \cdot 10^{-6}$ radians. 0.1" is about 2 "drizzled" pixels in the Hubble deep fields.

Furthermore, the light beam dynamics are similar to those of a final focus system, because the telescope translates arrival angles into position on the focal plane rendering the position on the surface of the collecting aperture irrelevant, i.e. only 2 dimensions of the full 4 dimensional phase space is important for the dynamics. The system can be approximated by a series of drifts and thin-lens kicks because the distance between kicks is the order of 500 Mpc (about 1.5 billion light years) whereas the longitudinal size of the mass distributions giving rise to the light bending is usually smaller than 500 kpc (1.5 million light years)(for review see [4]).

The deflection angles are rarely larger than 10^{-4} radian, so one can integrate along the undeflected trajectory to find the magnitude of the

thin-lens kick. At a distance x from a point mass the result is

$$\Delta\left[\frac{dx}{ds}\right] = \frac{2}{c}\int \frac{F_x}{m} = -2\int_{-\infty}^{\infty} \frac{GM}{(x^2+s^2)}\frac{x}{(x^2+s^2)^{1/2}}ds = -\frac{4GM}{x}. \quad (1)$$

This $1/r$ kick is similar to the electric field of a line-charge in electrostatics. The potential function is $2\Phi(r) = 4GM\ \ Ln\,[r]$, which is the Green's function for the 2D Laplace equation, $\nabla^2\Phi(\vec{r}) = 4\pi\, G\,\Sigma(\vec{r}) = 4\pi\, G\int_{-\infty}^{\infty}\rho\,(\vec{r},s)\,ds$. In other words, the situation is identical to the parasitic crossings in beamlines. The factor 2 is inserted to obtain potential for light ray deflections from the potential for non-relativistic particle deflections.

3. Multipole analysis

The $Ln[r]$ potential can be written in Cartesian coordinates as $Ln[r] = Re(Ln[x+iy])$. This is an example of the fact that solutions to $\nabla^2\Phi = 0$ can be written as the real part of an analytic function. We will use a standard complex variable notation, $w = x + iy$. We will assume that the light beam is passing the mass distribution at position (x_0, y_0) and expand about this position to get a multipole expansion for the deflections. For a point mass (or outside a spherically symmetric distribution)

$$Ln\,[w_0+w] = Ln\,[w_0] + Ln\left[1+\frac{w}{w_0}\right] = Const - \sum_{n\geq 1}\frac{1}{n}\left[-\frac{w}{w_0}\right]^n.$$

By also introducing the variable $\bar{w} = x - iy$, and noting that derivative operators can be defined by

$$\frac{\partial}{\partial w} = \frac{1}{2}\left(\frac{\partial}{\partial x} - i\frac{\partial}{\partial y}\right) \equiv \partial \text{ and } \ \frac{\partial}{\partial \bar{w}} = \frac{1}{2}\left(\frac{\partial}{\partial x} + i\frac{\partial}{\partial y}\right) \equiv \bar{\partial}$$

to correctly give $\frac{\partial}{\partial w}w = \frac{\partial}{\partial \bar{w}}\bar{w} = 1$ and $\frac{\partial}{\partial w}\bar{w} = \frac{\partial}{\partial \bar{w}}w = 0$, we are able to express the horizontal and vertical kicks, given by $\delta x' = -\frac{\partial(2\Phi)}{\partial x}$ and $\delta y' = -\frac{\partial(2\Phi)}{\partial y}$, by the single equation $\delta w' = -2\frac{\partial(2\Phi)}{\partial \bar{w}}$.

Returning to the logarithmic potential we get

$$2\Phi = 4MG\,\mathrm{Re}(Ln\,[w_0+w]) = -2MG\sum_{n\geq 1}\frac{1}{n}\left\{\left[-\frac{w}{w_0}\right]^n + \left[-\frac{\bar{w}}{\bar{w}_0}\right]^n\right\} + const$$

from which it follows that

$$\delta w' = -2\frac{\partial(2\Phi)}{\partial \bar{w}} = -\frac{4MG}{w_0}\sum_{n\geq 1}\left[-\frac{\bar{w}}{\bar{w}_0}\right]^{n-1}$$

These are the usual multipole kicks (dipole, quadrupole, sextupole, octupole).

A general potential distribution can be written

$$\Phi(w,\bar{w}) = \Phi_0 + \partial\Phi\, w + \bar{\partial}\Phi\, \bar{w} + \tfrac{1}{2}\left[\partial^2\Phi\, w^2 + 2\,\partial\bar{\partial}\Phi\, w\bar{w} + \bar{\partial}^2\Phi\bar{w}^2\right] + \tfrac{1}{3!}\left[\partial^3\Phi\, w^3 + 3\,\partial^2\bar{\partial}\Phi\, w^2\bar{w} + 3\,\partial\bar{\partial}^2\Phi\, w\bar{w}^2 + \bar{\partial}^3\Phi\,\bar{w}^3\right] + \ldots$$

from which we see there are additional kick terms all of which contain

$$\frac{\partial}{\partial w}\frac{\partial}{\partial \bar{w}}\ \Phi = \ \frac{1}{4}\left(\frac{\partial^2}{\partial x^2} + \frac{\partial^2}{\partial y^2}\right)\ \Phi = \ \frac{1}{4}\nabla^2\Phi \ \ = \ \ \pi\, G\, \Sigma(\vec{r}).$$

In other words the additional terms will be zero unless Σ(r) or its derivatives are unequal to zero at the light-path centroid.

4. Multipole kick-strength estimates

In our sample of deep field galaxies, the average angular size of the core of distant galaxies in the Hubble deep field is $\theta_G \approx 0.1$". At a distance of 1000 Mpc, where the light path passes a rich cluster, the footprint size would be about 0.5 kpc. A rich cluster of mass $M_C = 5\cdot 10^{14} M_\odot$ would give a light-beam passing at its edge, at a distance from the center of $r_C = 500$kpc , a dipole kick of strength θ_C^D :

$$\theta_C^D = \frac{4GM_C}{r_C} \approx 30 \text{ arc sec}, \qquad \text{implying} \quad \frac{\theta_C^D}{\theta_G} \approx 300.$$

The strength of the quadrupole kick θ_C^Q would be:

$$\theta_C^Q = \frac{4GM_C}{r_C}\left(\frac{r_G}{r_C}\right) \approx 0.03 \text{ arc sec}, \qquad \text{implying} \quad \frac{\theta_C^Q}{\theta_G} \approx 0.3,$$

and the sextupole kick-strength θ_C^S would be

$$\theta_C^S = \frac{4GM_C}{r_C}\left(\frac{r_G}{r_C}\right)^2 \approx 3\cdot 10^{-5} \text{ arc sec}, \qquad \text{implying} \quad \frac{\theta_C^S}{\theta_G} \approx 3\cdot 10^{-4}.$$

This is a hopelessly small number. On the other hand, if the dark-matter clump had a mass equal to $M_C = 5\cdot 10^{10} M_\odot$ and a light-beam is passing at a much smaller distance from the center of the cluster at $r_C = 5$kpc then the quadrupole kick-strength would be the same but the sextupole kick-strength would be 100 times larger:

$$\theta_C^S = \frac{4GM_C}{r_C}\left(\frac{r_G}{r_C}\right)^2 \approx 3\cdot 10^{-3} \text{ arc sec}, \qquad \text{implying} \quad \frac{\theta_C^S}{\theta_G} \approx 0.03.$$

As we will see later, this is approximately the value of the rms sextupole moments of the background galaxies in the Hubble deep field. One could hope to detect such a kick.

5. Finding kick-strengths from image moments

If the source had no quadrupole or sextupole moment one could easily deduce the strength of the kick that would have produced the measured moment. Let the superscripts S and T designate the source and telescope image, respectively. The condition that the source have no quadrupole moments can be written

$$0 = M_{20}^S \equiv \int w_S^2 \; i_S(w_S, \bar{w}_S) \; dx_S dy_S.$$

We will now change from source variables to telescope variables (the map we can deduce goes from the telescope image to the source, in reverse because both the position and the slope are known at the telescope), $w_S = w_T + a\bar{w}_T$. Under this transformation

$$i_S(w_S, \bar{w}_S) = i_T(w_T\left(w_S\right), \bar{w}_T\left(w_S\right)) \cdot \left| \begin{array}{cc} \frac{\partial w_T}{\partial w_S} & \frac{\partial \bar{w}_T}{\partial w_S} \\ \frac{\partial w_T}{\partial \bar{w}_S} & \frac{\partial \bar{w}_T}{\partial \bar{w}_S} \end{array} \right|.$$

We end up with

$$\begin{array}{c} M_{20}^S = \int w_S(w_T, \bar{w}_T)^2 \; i_T(w_T, \bar{w}_T) \; dx_T dy_T \\ = \int \left(w_T + a\bar{w}_T\right)^2 \; i_T(w_T, \bar{w}_T) \; dx_T dy_T \\ = \int \left(w_T^2 + 2a w_T \bar{w}_T + a^2 \bar{w}_T^2\right) \; i_T(w_T, \bar{w}_T) \; dx_T dy_T \\ = M_{20}^T + 2a \; M_{11}^T + a^2 \; M_{02}^T \end{array}.$$

Under the assumption that the original galaxy had no quadrupole moment this can be solved for the map coefficient a

$$a = -\frac{M_{20}}{M_{11}} \frac{1}{1 + \sqrt{1 - \frac{|M_{20}|^2}{M_{11}^2}}} \quad \text{and} \quad a \approx -\frac{M_{20}}{2M_{11}} \quad \text{for} \quad \frac{|M_{20}|}{M_{11}} \ll 1.$$

The coefficient a is related to the kick strength through a geometrical factor $a = \frac{D_{LS}}{D_S} \frac{\theta_C^Q}{\theta_G}$. Here D_{LS} is the distance from the source to the lensing matter and D_S is the distance from the telescope to the source galaxy. The ratio of these distances reflects the fact that the apparent displacement of a point in the image due to a kick at the lens plane will be given by the kick strength time this distance ratio.

Similarly the sextupole strength can be found from

$$0 = M_{30}^S \equiv \int w_S^3 \; i_S(w_S, \bar{w}_S) \; dx_S dy_S,$$

yielding

$$\begin{aligned} M_{30}^S &= \int w_S(w_T,\bar{w}_T)^3\ i_T(w_T,\bar{w}_T)\ dx_T dy_T \\ &= \int \left(w_T + a\,\bar{w}_T + b\,\bar{w}_T^2\right)^3\ i_T(w_T,\bar{w}_T)\ dx_T dy_T \\ &= \int \left(w_T^3 + 3b\,w_T^2\bar{w}_T^2 + 3a\,w_T^2\bar{w}_T + \ldots\right)\ i_T(w_T,\bar{w}_T)\ dx_T dy_T \\ &= M_{30}^T + 3b\ M_{22}^T + 3a\,M_{21}^T + \ldots \end{aligned}$$

For small b and negligible $a \cdot M_{21}$, $b = -\frac{M_{30}}{3M_{22}}$. Note that if M_{21} is non-zero, the quadrupole kick can also create a sextupole moment. Non-zero M_{21} requires symmetry breaking and in general will be much smaller than M_{22}, which is equal to $< r^4 >$. Still with a expected to be much larger than b one must pay attention to the possibility that contributions may arise from a non-zero M_{21}.

6. The Hubble deep fields

We have used the software SExtractor [5] to identify and extract galaxy images from the Hubble deep field. This software requires a number of input decisions that affect which galaxies are selected and how their boundaries are defined. One will end up with noisy boundaries (and noisy sextupole moments) for the images unless thresholds are set to be considerably larger than the noise floor. We have used the factor 10 for this input parameter. There is also a subtlety with the convolution matrix for the filter that determines the footprint. In general, less convolution is better.

The extracted images were transferred to the *Mathematica*(www.wolfram.com) computing environment where we could use the full power of the image processing available there. Figure 1 shows contour plots and 3-D images of two of these galaxies. Such images gave us a sense of what we were looking at, and allowed us, for example, to eliminate all galaxies that had two or more maxima. After filtering we had more than 600 high-z galaxies in our selected sample for each Hubble deep field. We measured the sextupole moments for these galaxies, and found them to be about a factor of 5 smaller than the quadrupole moments: they have a dimensionless rms strength of about bσ=0.03. The rms size of the galaxy is introduced to create the dimensionless measure sought. A cautionary note! Our result for this sextupole strength depends on the threshold setting for galaxy intensity. Nevertheless, the sextupole moments are small, as we had hoped (see Figure 2).

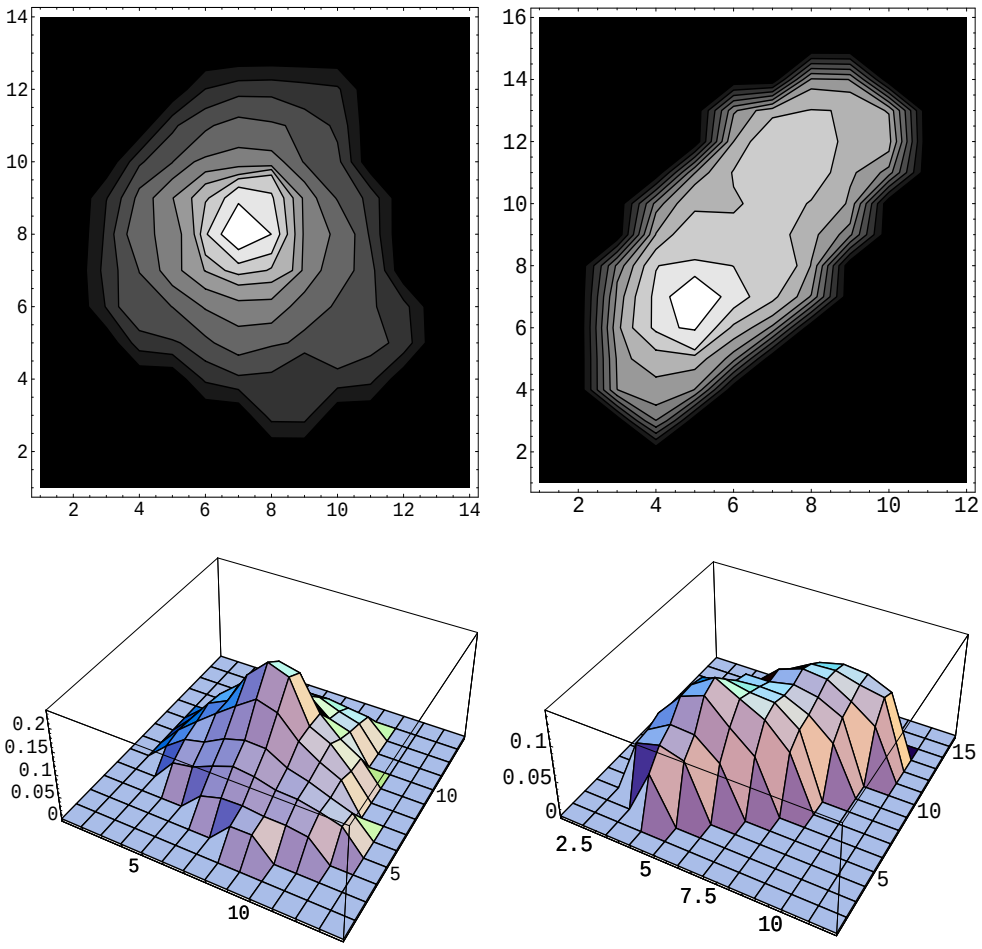

Figure 1. Two galaxy images (contour plots and 3-D plots of surface brightnessfrom the Hubble north field).

7. Correlations and clumping

A careful look at the induced quadrupole and sextupole moments from a kick reveals that together they give a small curvature to the image. This is equivalent to saying that the orientation of the induced sextupolar distortion has its minimum aligned with the minimum of the quadrupolar distortion. We have looked for such a correlation in our galaxy images, and refer to these as "curved" galaxies. We have taken the sample of "curved"

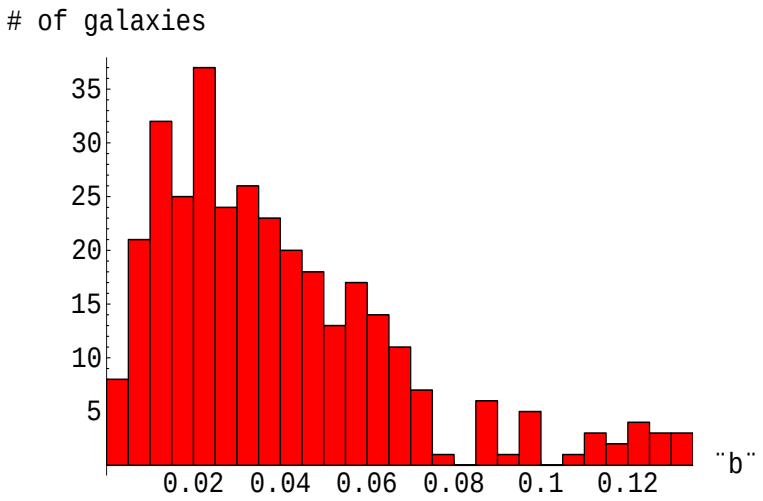

Figure 2. The sextupole strength of faint, z > 0.8 galaxies from Hubble Deep Field (North) data.

galaxies and investigated how these galaxies are arranged on the sky, looking for evidence of clumping. Our conjecture was that if there were clusters of dark matter with sub-clumps of order $10^{10} M_{\odot}$ then the galaxy light paths passing through the cluster might pass near a small clump and become curved. Indeed we have observed statistically significant clumping of curved galaxies in both of the Hubble deep fields. (A random choice of galaxies would give the observed clumping in each field with a probability less than 0.03. Taking the fields together, the probability is less than 1 part per thousand that our result occurs by chance.) However it remains to rule out other possible sources for this clumping. We have determined that if one takes a set of galaxies of a certain slice in z having the same number of members as our curved sample, then clumping is evident as one might expect, since galaxies are known to be clumped. It is also known that high-z galaxies have more complex shapes than low-z galaxies. We are currently investigating whether this correlation can explain our observations.

8. Conclusion (Future plans)

If indeed one can establish that some of the images of distant galaxies are curved because of the presence of small dark matter clumps within larger

dark matter clusters, then one might hope to develop a method that would determine the power spectrum of mass structure in the universe on a much smaller angular scale than has been previously possible. To carry out such a program would require the study of larger fields than it is possible with the Hubble, though there are plans for enlarging the Hubble deep field studies. The two fields we have been studying are each about two minutes across, each corresponding to only one part in 2 10^7 of its hemisphere.

Our observations indicate it would be difficult to make these measurements in the presence of atmospheric turbulence. Even a good earth-based point-spread function (PSF) of 0.4" is 6 times larger than the Hubble PSF of 0.07". And the radius of the typical galaxy image we are using is only slightly larger than the Hubble PSF. Fortunately a mission is planned that would do high-resolution lensing from space, known as SNAP (Supernovae Acceleration Probe)[6]. The weak-lensing program for SNAP plans to scan an area of either 300 or 1000 sq. degrees. This would be from 3 10^5 to 10^6 larger than the Hubble deep fields.

We would like to thank Tony Tyson, David Wittman and the Bell-Lab group for encouraging our work and providing us with the orientation and tools needed to get started. We thank Ron Ruth and Pisin Chen for providing support and encouragement for our work at SLAC.

References

1. T. O. Raubenheimer and F. Zimmermann, Rev. Mod. Phys. **72**, 95 (2000).
2. M. Bartelmann and P. Schneider, arXiv:astro-ph/9912508.
3. Y. Mellier, arXiv:astro-ph/9812172.
4. P. J. Peebles, "Principles Of Physical Cosmology," Princeton, USA: Univ. Pr. (1994).
5. E. Bertin and S. Arnouts, Astron. Astrophys. Suppl. Ser.**117**, 393 (1996)
6. J. Rhodes, A. Refregier and R. Massey [the SNAP Collaboration], arXiv:astro-ph/0304417; R. Massey *et al.*, arXiv:astro-ph/0304418; A. Refregier *et al.*, arXiv:astro-ph/0304419.

SPONTANEOUS GRAVITATIONAL INSTABILITY OF STAR DISTRIBUTION IN A NONROTATING GALAXY

ALEX CHAO

Stanford Linear Accelerator Center, 2575 Sand Hill Road, Menlo Park, CA 94025, USA

E-mail: achao@slac.stanford.edu

Gravitational instability of the distribution of stars in a galaxy is a well-known phenomenon in astrophysics. This work is a preliminary attempt to analyze this effect using the standard tools developed in accelerator physics. The result is first applied to nonrotating gallaxies with spherical and planar symmetries. Extensions to rotating galaxies are not studied here.

1. Introduction

Consider a distribution of stars in a galaxy described by a distribution density $\rho(\vec{x}, \vec{v}, t)$ in the phase space $(\vec{x}, \vec{v})$. We wish to analyze the stability of this distribution of stars under the influence of their collective gravitational force. To simplify the problem, we will use a flat Euclidean space-time and will consider Newtonian, nonrelativistic dynamics only. The instability does not assume a specific cosmological model other than Newtonian gravity. If this approach turns out successful, a large arsenal of analysis tools can be transported from accelerator physics to this problem.

The instability we are interested in is self-generated, i.e. it occurs spontaneously. In particular, it does not require an initial "seed" fluctuation at the birth of the galaxy. The instability growth pattern as well as its rate of growth are intrinsic properties of the system. This gravitational instability is a wel-known problem; its first analysis was almost a century ago [1]. What we do in the following is to treat the same problem using the standard techniques developed in the study of collective instabilities in circular accelerators [2].

2. Dispersion Relation

Consider a particular star in the galaxy. The equations of motion of this star are

$$\begin{aligned}\dot{\vec{x}} &= \vec{v} \\ \dot{\vec{v}} &= G\int d\vec{v}'\int d\vec{x}'\,\frac{\rho(\vec{x}',\vec{v}',t)(\vec{x}'-\vec{x})}{|\vec{x}'-\vec{x}|^3}\end{aligned} \tag{1}$$

Note that these equations do not depend on the mass of the star under consideration.

Evolution of ρ is described by the Vlasov equation

$$\begin{aligned}&\frac{\partial\rho}{\partial t}+\frac{\partial\rho}{\partial\vec{x}}\cdot\dot{\vec{x}}+\frac{\partial\rho}{\partial\vec{v}}\cdot\dot{\vec{v}} \\ &=\frac{\partial\rho}{\partial t}+\frac{\partial\rho}{\partial\vec{x}}\cdot\vec{v}+\frac{\partial\rho}{\partial\vec{v}}\cdot G\int d\vec{v}'\int d\vec{x}'\,\frac{\rho(\vec{x}',\vec{v}',t)(\vec{x}'-\vec{x})}{|\vec{x}'-\vec{x}|^3} \\ &=0\end{aligned} \tag{2}$$

Let the galaxy distribution be given by an unperturbed distribution ρ_0 plus some small perturbation. Let the unperturbed distribution ρ_0 depend only on $\vec{v}$,

$$\rho_0=\rho_0(\vec{v}) \tag{3}$$

This unperturbed distribution is uniform in $\vec{x}$, i.e. it is uniform in the infinite 3-D space. The function $\rho_0(\vec{v})$ is so far unrestricted, and is to be prescribed externally.

The perturbation around ρ_0 will have some structure in t and in $\vec{x}$. We Fourier decompose this structure and write

$$\rho(\vec{x},\vec{v},t)=\rho_0(\vec{v})+\Delta\rho(\vec{v})\,e^{-i\omega t+i\vec{k}\cdot\vec{x}} \tag{4}$$

The quantity $\Delta\rho$ is considered to be infinetisimal compared with ρ_0.

Substituting Eq.(4) into Eq.(2) and keeping only first order in $\Delta\rho$ yield

$$-i(\omega-\vec{v}\cdot\vec{k})\Delta\rho(\vec{v})+G\left(\int d\vec{v}'\,\Delta\rho(\vec{v}')\right)\frac{\partial\rho_0(\vec{v})}{\partial\vec{v}}\cdot\vec{q}(\vec{k})=0 \tag{5}$$

where

$$\vec{q}(\vec{k})\equiv\int d\vec{x}'\frac{e^{i\vec{k}\cdot(\vec{x}'-\vec{x})}(\vec{x}'-\vec{x})}{|\vec{x}'-\vec{x}|^3}=\int d\vec{y}\,\frac{e^{i\vec{k}\cdot\vec{y}}\,\vec{y}}{|\vec{y}|^3} \tag{6}$$

is a well-defined quantity depending only on $\vec{k}$; it is the Fourier transform of the Newton kernel, and might be called the graviton propagator. In fact,

avoiding the singularity at the origin $\vec{k} = \vec{0}$, it can be shown that

$$\vec{q}(\vec{k}) = \frac{4\pi i}{|\vec{k}|^2}\,\vec{k} \tag{7}$$

Eq.(5) can be rewritten as

$$\Delta\rho(\vec{v}) = -iG\left(\int d\vec{v}'\,\Delta\rho(\vec{v}')\right)\,\frac{\frac{\partial\rho_0(\vec{v})}{\partial\vec{v}}\cdot\vec{q}(\vec{k})}{\omega - \vec{v}\cdot\vec{k}} \tag{8}$$

Integrating both sides over $\vec{v}$ and canceling out the mutual factor of $\int d\vec{v}'\,\Delta\rho(\vec{v}')$ then gives a dispersion relation that must be satisfied by ω and $\vec{k}$,

$$1 = -iG\int d\vec{v}\frac{\frac{\partial\rho_0(\vec{v})}{\partial\vec{v}}\cdot\vec{q}(\vec{k})}{\omega - \vec{v}\cdot\vec{k}} \tag{9}$$

We need to solve this dispersion relation for a given $\rho_0(\vec{v})$ to find the most unstable pattern of perturbation and its corresponding growth rate, as will be described next. This result, we hope, could say something about the characteristic dimension of galaxies.

3. Uniform Isotropic Galaxy

We next consider an unperturbed distribution that depends only on the magnitude of $\vec{v}$, i.e., let

$$\rho_0 = \rho_0(|\vec{v}|^2) \tag{10}$$

which gives

$$\frac{\partial\rho_0}{\partial\vec{v}} = 2\vec{v}\,\rho_0'(|\vec{v}|^2) \tag{11}$$

This is the case of a uniform isotropic (spherically symmetric) galaxy. Normalization condition is

$$\begin{aligned}\int_0^\infty 4\pi v^2 dv\,\rho_0(v^2) &= \rho_m \\ &= \text{volume mass density of stars}\end{aligned} \tag{12}$$

Substituting Eqs.(7) and (11) into Eq.(9) then gives

$$1 = \frac{8\pi G}{|\vec{k}|^2}\int d\vec{v}\,\rho_0'(|\vec{v}|^2)\frac{\vec{v}\cdot\vec{k}}{\omega - \vec{v}\cdot\vec{k}} \tag{13}$$

Let $\vec{k} = (0, 0, k)$, and choose coordinates so that $\vec{v} = v(\sin\theta\cos\phi, \sin\theta\sin\phi, \cos\theta)$, Eq.(13) becomes, with a change of variable $u = \cos\theta$,

$$1 = \frac{16\pi^2 G}{k} \int_0^\infty v^3 dv\, \rho_0'(v^2) \int_{-1}^1 du\, \frac{u}{\omega - kvu} \tag{14}$$

One must refrain from performing the integration over u at this time. Proper treatment of the singularity is first necessary. We then follow the standard technique used in accelerator physics on Landau damping [3]. The treatment amounts to adding an infinitesimal positive imaginary part to ω, i.e. $\omega \to \omega + i\epsilon$,

$$\begin{aligned}
\mathcal{I}(\omega, kv) &\equiv \int_{-1}^1 du\, \frac{u}{\omega - kvu} \\
&\to \int_{-1}^1 du\, \frac{u}{\omega + i\epsilon - kvu} \\
&= \text{P.V.} \int_{-1}^1 du\, \frac{u}{\omega - kvu} - i\frac{\pi\omega}{k^2v^2}\, H\left(1 - \left|\frac{\omega}{kv}\right|\right) \\
&= -\frac{2}{kv} - \frac{\omega}{k^2v^2} \ln\left|\frac{\omega - kv}{\omega + kv}\right| - i\frac{\pi\omega}{k^2v^2}\, H\left(1 - \left|\frac{\omega}{kv}\right|\right)
\end{aligned} \tag{15}$$

where P.V. means taking the principal value of the integral, and $H(x) = 1$ for $x > 0$ and 0 for $x < 0$ is the step function.

To be specific, we next take a uniform distribution of ρ_0,

$$\rho_0(v^2) = \begin{cases} \frac{3\rho_m}{4\pi v_0^3} & \text{if } v^2 < v_0^2 \\ 0 & \text{otherwise} \end{cases} \tag{16}$$

with

$$\rho_0'(v^2) = -\frac{3\rho_m}{8\pi v_0^4} \delta(v - v_0) \tag{17}$$

The quantity v_0^2 is related to the "temperature" of the stars. Substituting Eq.(17) into Eq.(14) gives the dispersion relation

$$1 = -\frac{6\pi G\rho_m}{kv_0} \mathcal{I}(\omega, kv_0) \tag{18}$$

Substituting Eq.(15) into Eq.(18) then gives

$$\lambda = \frac{1}{2 + x \ln\left|\frac{x-1}{x+1}\right| + i\pi x\, H(1 - |x|)} \tag{19}$$

where

$$\lambda = \frac{6\pi G\rho_m}{k^2 v_0^2} \quad \text{and} \quad x = \frac{\omega}{kv_0} \tag{20}$$

4. Stability Condition

We next need to compute the instability growth rate, which is given by the imaginary part of ω, as a function of k. The star distribution $\rho_0(\vec{v})$ is unstable when ω is complex with a positive imaginary part. We need to compute x as a function of λ using Eq.(19) in order to obtain ω as a function of k.

In general x is complex, but at the edge of instability, x is real. The edge of stability can be seen by plotting the RHS of Eq.(19) as x is scanned along the real axis from $-\infty$ to ∞. Fig.1 shows the real and imaginary parts of the RHS of Eq.(19) in such a scan. The horizontal and vertical axes of Fig.1 are the real and imaginary parts of the RHS of Eq.(19) respectively. As x is scanned from $-\infty$ to ∞, the RHS of Eq.(19) traces out a cherry-shaped diagram, including the "stem" of the cherry running from $-\infty$ to 0 along the real axis. If λ lies inside this cherry diagram (including the stem), the galaxy distribution is stable. Since λ is necessarily real and positive, the stability condition therefore reads

$$\lambda < \frac{1}{2} \tag{21}$$

Eq.(21) indicates that a hot universe (high temperature, i.e. large v_0) is more stable than a cold universe. This is expected due to the Landau damping mechanism. It also indicates that the star distribution is unstable for long-wavelength perturbations (small k). The threshold wavelength is given by $2\pi/k_{\rm th}$, where

$$k_{\rm th} = \frac{\sqrt{12\pi G\rho_m}}{v_0} \tag{22}$$

Perturbations with wavelength longer than that corresponding to Eq.(22) are unstable. One might expect that the galaxy will have a dimension of the order of this wavelength because if the galaxy had a larger dimension, it would have broken up due to the instability. There will be more discussions on this point later.

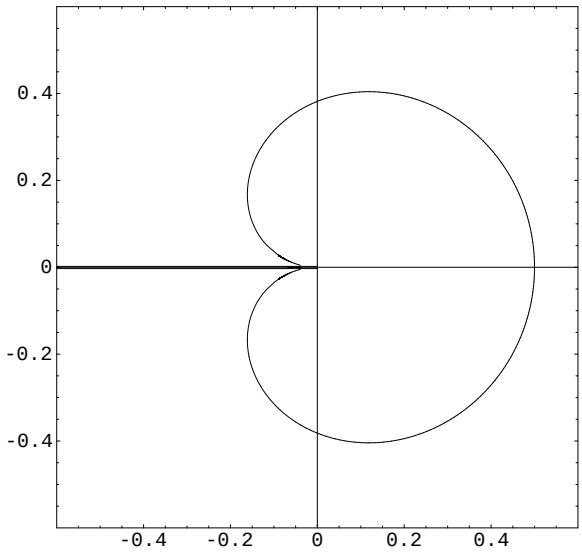

Figure 1. Stability diagram for the galaxy distribution.

5. Spontaneous Gravitational Instability

When $\lambda > 1/2$, ω will be complex. The instability growth rate will be determined by the imaginary part of ω,

$$\tau^{-1} = \mathrm{Im}(\omega) \tag{23}$$

We need to go back to Eq.(19), but modify it slightly for complex ω. Let

$$\frac{\omega}{kv_0} = x + iy, \quad (y > 0) \tag{24}$$

Eq.(19) then becomes

$$\lambda = \frac{1}{2 + \left(\frac{x+iy}{2}\right) \ln\left[\frac{(x-1)^2+y^2}{(x+1)^2+y^2}\right] + (ix - y)\left[\tan^{-1}\left(\frac{x+1}{y}\right) - \tan^{-1}\left(\frac{x-1}{y}\right)\right]} \tag{25}$$

When $y \to 0^+$, we obtain Eq.(19) as it should.

We will need to solve Eq.(25) for x and y for given $\lambda > \frac{1}{2}$. It turns out that in this range there is always one solution with purely imaginary ω, i.e. $x = 0$, and

$$\lambda = \frac{1}{2 - 2y \tan^{-1}\left(\frac{1}{y}\right)} \tag{26}$$

or, written out explicitly,

$$\frac{6\pi G\rho_m}{k^2 v_0^2} = \frac{1}{2 - \frac{2\tau^{-1}}{kv_0}\tan^{-1}\left(\frac{kv_0}{\tau^{-1}}\right)} \tag{27}$$

We need to find τ^{-1} as a function of k. To do so, we first scale the variables by

$$u = \frac{kv_0}{\sqrt{6\pi G\rho_m}}, \quad v = \frac{\tau^{-1}}{\sqrt{6\pi G\rho_m}} \tag{28}$$

and then

$$\frac{1}{u^2} = \frac{1}{2 - 2\left(\frac{v}{u}\right)\tan^{-1}\left(\frac{u}{v}\right)} \tag{29}$$

Fig.2 shows the result.

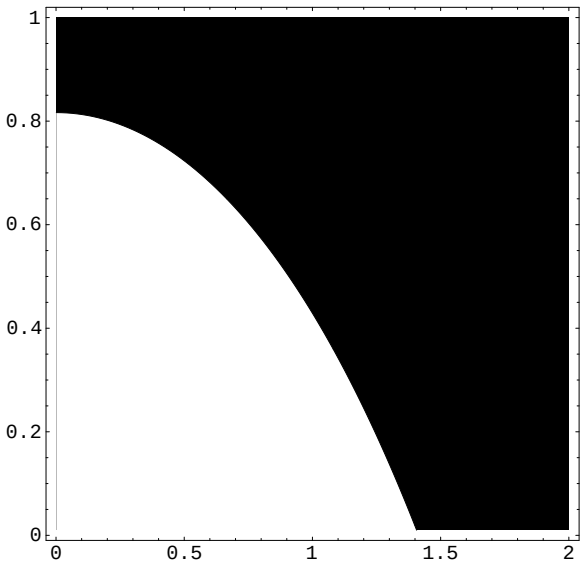

Figure 2. v vs u according to Eq.(29).

As seen from Fig.2, the growth rate vanishes ($v = 0$) when $u = \sqrt{2}$, corresponding to $\lambda = 1/2$, i.e. at the stability boundary. This is of course expected. Fig.2 also shows that instability occurs fastest for small u, i.e. small k and large wavelegnth. The growth rate is maximum at $u = 0$ with

$v = \sqrt{2/3}$. This means the maximum growth rate occurs for perturbation of infinite wavelength, and is given by

$$(\tau^{-1})_{\max} = \sqrt{4\pi G\rho_m} \tag{30}$$

Note that the growth rate is independent of v_0, even though there is still the condition that the distribution is unstable, i.e. $\lambda > 1/2$, which does depend on v_0 and can be cast into the form (see Eq.(22))

$$k < \frac{\sqrt{3}}{v_0}(\tau^{-1})_{\max} \tag{31}$$

The fastest instability corresponds to $k = 0$, or an instability wavelength of infinity.[a]

According to Eq.(31), all stable galaxies must have a dimension smaller than a critical value, i.e.

$$\text{galaxy dimension} < \frac{2\pi v_0}{\sqrt{12\pi G\rho_m}} \tag{32}$$

The stability is provided through Landau damping. When the temperature $v_0 \to 0$, no galaxies can be stable. Eqs.(30) and (32) are our main results.

6. Numerical Estimates

For a numerical application, we take estimates from the Milky Way,

$$\rho_m = 2 \times 10^{-23} \text{ g/cm}^3$$
$$v_0 = 200 \text{ km/s}$$

We obtain a maximum growth time of $\tau_{\max} = 7\times10^6$ years for perturbations with very large wavelengths. For stability, the galaxy dimension must be smaller than 14000 light-years, which seems to be consistent with the size of the Milky Way.

7. Discussions

- The case studied so far is that of a galaxy with uniform distribution of stars. One direction of generalization is to consider galaxies with a finite spherically symmetric distribution. One attempt was made

[a]This result depends on our assumption of Newtonian dynamics of action-at-a-distance. Perturbation at one location instantly affects locations infinitely far away. If this action-at-a-distance effect is appropriately removed, it is expected that the instability for perturbations with very large wavelengths will be weakened.

and included in Appendix A. Our finding here is that a spherically symmetric distribution of the Haissinski type (to be explained in Appendix A) does not exist.

- Appendix B gives an extension to a planar galaxy, still nonrotating. The unperturbed distribution does exist and is given in Appendix B. However, this planar distribution is found, as shown in Appendix C, to be always stable against perturbations that do not involve transverse structures. Any instability of the planar galaxy will therefore have to have a sufficiently complex pattern.
- It is conceivable that the same analysis can be applied to the dynamics of galaxies in a galaxy cluster, instead of stars in a galaxy. In that case, $\rho(\vec{x}, \vec{v}, t)$ describes the distribution of galaxies in the galaxy cluster. We might then take the corresponding numerical values

$$\rho_m = 10^{-31} \text{ g/cm}^3$$
$$v_0 = 1000 \text{ km/s}$$

  We obtain a growth time of $\tau_{\max} = 1 \times 10^{11}$ years. The galaxy cluster dimension should be smaller than 1×10^9 light-years. These values do not seem to be too unreasonable.
- For more detailed applications, we will have to include the rotation of the galaxy into the analysis. The unperturbed distribution will then involve also the angular momentum. The analysis is much more involved but should be straightforward.
- Still further extensions might include the special relativity and general relativity to replace Newtonian gravity and to avoid the "action at a distance" problem.

References

1. See for example, P.L. Palmer, "Stability of Collisionless Stellar Systems", Kluwer Academic Publishers, The Netherlands, 1994, and references quoted therein.
2. See for example, Alexander W. Chao, "Physics of Collective Beam Instabilities in High Energy Accelerators", John Wiley & Sons, New York, 1993, and references quoted therein.
3. L.D. Landau, J. Phys. USSR 10, 25 (1946).
4. J. Haissinski, Nuovo Cimento 18B, 72 (1973).

Appendix A

So far we have considered the stability of a galaxy whose unperturbed distribution is uniform in the infinite space and is nonrotating. As a first (unsuccessful) attempt of genralization, we will look for an unperturbed distribution that is isotropic, nonrotating, and finite in size. To do so, we first note that Eq.(1) is derivable from a Hamiltonian

$$H = \frac{\vec{v}^2}{2} - G \int d\vec{v}' \int d\vec{x}' \, \frac{\rho(\vec{x}', \vec{v}', t)}{|\vec{x}' - \vec{x}|} \tag{33}$$

We then make the observation that one possible unperturbed distribution is that it is a function of this Hamiltonian, i.e.

$$\rho_0(\vec{x}, \vec{v}) = \rho_0(H) \tag{34}$$

For example, one may choose

$$\rho_0(\vec{x}, \vec{v}) = \mathcal{N} e^{-H/\sigma_v^2} = \mathcal{N} \exp\left[-\frac{1}{\sigma_v^2} \left(\frac{\vec{v}^2}{2} - G \int d\vec{v}' \int d\vec{x}' \, \frac{\rho_0(\vec{x}', \vec{v}')}{|\vec{x}' - \vec{x}|} \right) \right] \tag{35}$$

where σ_v is the rms of the magnitude of $\vec{v}$, and is a prescribed input parameter in this model. The quantity $\mathcal{N}$ is a normalization so that integrating ρ_0 over $\vec{x}$ and $\vec{v}$ gives the total mass of the galaxy M. Note that Eqs.(34) and (35) are not a useful ansatz for a rotating galaxy because it assumes a distribution that is isotropic in $\vec{v}$.

Equation (35) is a self-consistent equation for ρ_0. It is equivalent to the Haissinski equation in accelerator physics [4]. Our job is to solve for ρ_0 from Eq.(35). It turns out that the distribution factorizes,

$$\rho_0(\vec{x}, \vec{v}) = \frac{e^{-\vec{v}^2/2\sigma_v^2}}{(\sqrt{2\pi}\,\sigma_v)^3} \; \rho_m(\vec{x}) \tag{36}$$

The quantity ρ_m is then the mass volume density of the stars in the galaxy, now a function of $\vec{x}$. Substituting Eq.(36) into Eq.(35) yields self-consistent equation for $\rho_m(\vec{x})$,

$$\rho_m(\vec{x}) = (\sqrt{2\pi}\,\sigma_v)^3 \, \mathcal{N} \exp\left[\frac{G}{\sigma_v^2} \int d\vec{x}' \, \frac{\rho_m(\vec{x}')}{|\vec{x}' - \vec{x}|} \right] \tag{37}$$

If we now assume ρ_m is also isotropic, i.e. $\rho_m(\vec{x}) = \rho_m(r)$ in spherical coordinates, then Eq.(37) becomes

$$\rho_m(r) = (\sqrt{2\pi}\,\sigma_v)^3 \, \mathcal{N} \exp\left[\frac{4\pi G}{\sigma_v^2} \int_0^\infty r'^2 dr' \, \frac{\rho_m(r')}{\max(r, r')} \right] \tag{38}$$

It turns out that no solution exisits that satisfies Eq.(38) while is also normalizable to a finite total mass of the galaxy. This means that an isotropic unperturbed distribution of the Haissinski type does not exist.

Appendix B

A planar distribution avoids the singularity problem that leads to the failure of a Haissinski type distribution in the spherical case. Use cylindrical coordinates $(\vec{x}_\perp, z)$, and let the unperturbed distribution be independent of $\vec{x}_\perp$ and factorizable in such a way that

$$\rho_0(\vec{x}_\perp, \vec{v}_\perp, z, v_z) = \rho_\perp(\vec{v}_\perp)\, \rho_z(z, v_z) \tag{39}$$

where we demand

$$\int d\vec{v}_\perp\, \rho_\perp(\vec{v}_\perp) = 1 \tag{40}$$

$$\int dz \int dv_z\, \rho_z(z, v_z) = \Sigma$$

$$= \text{surface mass density of stars} \tag{41}$$

This unperturbed distribution is that of an infinite disk of finite thickness.

We will first need the equations of motion,

$$\begin{aligned} \dot{\vec{x}}_\perp &= \vec{v}_\perp \\ \dot{\vec{v}}_\perp &= \vec{0} \\ \dot{z} &= v_z \\ \dot{v}_z &= 2\pi G \int dv'_z \int dz'\, \rho_z(z', v'_z)\, \mathrm{sgn}(z' - z) \end{aligned} \tag{42}$$

Equation (42) is derivable from first principles, as well as from Eq.(1). The corresponding Hamiltonian is

$$\begin{aligned} H_\perp &= \frac{\vec{v}_\perp^{\,2}}{2} \\ H_z &= \frac{v_z^2}{2} + 2\pi G \int dv'_z \int dz'\, \rho_z(z', v'_z)\, |z' - z| \end{aligned} \tag{43}$$

We then form the Haissinski ansatz

$$\begin{aligned} \rho_\perp &= \frac{1}{2\pi\sigma_{v\perp}^2} e^{-\vec{v}_\perp^{\,2}/2\sigma_{v\perp}^2} \\ \rho_z &= \mathcal{N} \exp\left[-\frac{1}{\sigma_{vz}^2} \left(\frac{v_z^2}{2} + 2\pi G \int dv'_z \int dz'\, \rho_z(z', v'_z)\, |z' - z| \right) \right] \end{aligned} \tag{44}$$

where $\sigma_{v\perp}$ relates to the transverse temperature, and σ_{vz} relates to the longitudinal temperature. The fact that the transverse and longitudinal motions decouple allows the two different temperatures.

Note that although a gaussian form of $\rho_\perp$ is most natural, this assumption is not compulsary. Any normalized form is acceptable, without affecting our following analysis.

Writing ρ_z as

$$\rho_z(z,v_z) = \frac{1}{\sqrt{2\pi}\,\sigma_{vz}} e^{-v_z^2/2\sigma_{vz}^2}\,\rho_m(z), \quad \text{with} \quad \int_{-\infty}^{\infty} dz\,\rho_m(z) = \Sigma \tag{45}$$

then gives the Haissinski equation

$$\rho_m(z) = \sqrt{2\pi}\,\sigma_{vz}\,\mathcal{N}\,\exp\left[-\frac{2\pi G}{\sigma_{vz}^2}\int dz'\,\rho_m(z')\,|z'-z|\right] \tag{46}$$

Equation (46) can be manipulated to yield

$$\left(\frac{\rho_m'}{\rho_m}\right)' + \frac{4\pi G}{\sigma_{vz}^2}\,\rho_m = 0 \tag{47}$$

where a prime means taking derivative with respect to z. We then make a transformation to the scaled variables u and w,

$$z = u\,\frac{\sigma_{vz}^2}{G\Sigma}, \quad \rho_m = w\,\frac{G\Sigma^2}{\sigma_{vz}^2} \tag{48}$$

to obtain

$$\left(\frac{w'}{w}\right)' + 4\pi w = 0 \tag{49}$$

where a prime now means taking derivative with respect to u. The Haissinki equation (46) is rewritten as

$$w(u) = \sqrt{2\pi}\,\frac{\sigma_{vz}^3\mathcal{N}}{G\Sigma^2}\exp\left[-2\pi\int_{-\infty}^{\infty} du'\,w(u')|u'-u|\right] \tag{50}$$

There is also the normalization condition

$$\int_{-\infty}^{\infty} du\,w(u) = 1 \tag{51}$$

as well as the condition that $w'(0) = 0$. The planar unperturbed distribution has an exponential tail in $|z|$. The distribution found numerically by MATHEMATICA is shown in Fig.3.

Given the function $w(u)$, the planar unperturbed distribution is summarized as

$$\rho_z(z,v_z) = \frac{G\Sigma^2}{(2\pi)^{1/2}\sigma_{vz}^3}\,\exp\left(-\frac{v_z^2}{2\sigma_{vz}^2}\right) w\left(\frac{G\Sigma}{\sigma_{vz}^2}\,z\right) \tag{52}$$

$$\rho_0(\vec{v}_\perp,z,v_z) = \frac{G\Sigma^2}{(2\pi)^{3/2}\sigma_{v\perp}^2\sigma_{vz}^3}\,\exp\left(-\frac{\vec{v}_\perp^{\,2}}{2\sigma_{v\perp}^2} - \frac{v_z^2}{2\sigma_{vz}^2}\right) w\left(\frac{G\Sigma}{\sigma_{vz}^2}\,z\right) \tag{53}$$

The thickness of the planar distribution is $\approx \sigma_{vz}^2/G\Sigma$. This thickness corresponds, not surprisingly, to an equipartition of the longitudinal potential and kinetic energies.

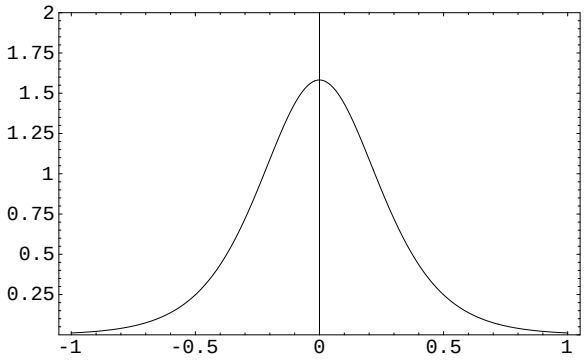

Figure 3. Planar unperturbed star distribution $w(u)$ vs u. $w(0) \approx 1.5822$.

Appendix C

To study the gravitational stability of the planar unperturbed distribution Eqs.(52, 53), we need to analyze the behavior of its infinitesimal perturbations. We have examined perturbations of the type

$$\rho(\vec{x}_\perp, \vec{v}_\perp, z, v_z) = \rho_\perp(\vec{v}_\perp)\,[\rho_z(z, v_z) + \Delta\rho(z, v_z, t)] \tag{54}$$

i.e. the perturbation occurs only in the *longitudinal* (z, v_z) dimension. We found that such perturbations are always stable. Analysis leading to this conclusion is given in the Appendix. Instabilities of a planar galaxy will therefore have to involve the transverse coordinates in forms different from Eq.(54).

The Vlasov equation, to first order in $\Delta\rho$, reads

$$\frac{\partial\Delta\rho}{\partial\tau} + \frac{\partial\Delta\rho}{\partial u}v + \frac{\partial\Delta\rho}{\partial v}\frac{w'(u)}{w(u)} - \sqrt{2\pi}\,v e^{-v^2/2} w(u) \int dv' \int du'\,\Delta\rho(u', v')\,\mathrm{sgn}(u' - u) \;=\; 0 \tag{55}$$

where we have introduced the scaled dimensionless variables

$$u = \frac{G\Sigma}{\sigma_{vz}^2}\,z, \quad v = \frac{v_z}{\sigma_{vz}}, \quad \tau = \frac{G\Sigma}{\sigma_{vz}}\,t \tag{56}$$

The function w'/w in the third term is the gravitational focusing coming from the unperturbed distribution of the stars.

To proceed, we first try to linearize the problem (thus losing Landau damping) for small u. In doing so, however, to be self-consistent, we must

at the same time linearize the unperturbed distribution ρ_z, i.e.

$$w \approx w(0)e^{-2\pi w(0)u^2}$$
$$\rho_z \approx \frac{G\Sigma^2 w(0)}{\sqrt{2\pi}\,\sigma_{vz}^3}\, e^{-v^2/2-2\pi w(0)u^2} \tag{57}$$

Substituting Eq.(57) into Eq.(55) gives

$$\frac{\partial\Delta\rho}{\partial\tau} - \omega_0\frac{\partial\Delta\rho}{\partial\phi} - \sqrt{2\pi}\,\omega_0^2 r\sin\phi\;\frac{\omega_0^2}{4\pi}\,e^{-\omega_0^2 r^2/2}$$
$$\times\int_0^\infty r'dr'\int_0^{2\pi} d\phi'\,\Delta\rho(r',\phi',\tau)\,\mathrm{sgn}(r'\cos\phi' - r\cos\phi) \;=\; 0 \tag{58}$$

where

$$u = r\cos\phi, \quad \frac{v}{\omega_0} = r\sin\phi, \quad \omega_0 = \sqrt{4\pi w(0)} \tag{59}$$

Consider a collective mode

$$\Delta\rho = e^{-i\Omega\tau}\sum_{m=-\infty}^{\infty} R_m(r)e^{-im\phi} \tag{60}$$

Charge conservation requires that

$$\int_0^\infty 4\pi r dr\, R_0(r) = 0 \tag{61}$$

Eq.(58) becomes

$$-i\Omega R_m(r) + im\omega_0 R_m(r) - \frac{\omega_0^4}{4\pi\sqrt{2\pi}}\,r\,e^{-\omega_0^2 r^2/2}\int_0^{2\pi}\sin\phi\,d\phi\,e^{im\phi}$$
$$\times\int_0^\infty r'dr'\int_0^{2\pi} d\phi'\sum_{m'=-\infty}^{\infty} R_{m'}(r')e^{-im'\phi'}\,\mathrm{sgn}(r'\cos\phi' - r\cos\phi) \;=\; 0 \tag{62}$$

Integration over ϕ' and after some algebraic manipulations, we obtain

$$-i\Omega R_m(r) + im\omega_0 R_m(r) - \frac{\omega_0^4}{\sqrt{2\pi}}\,e^{-\omega_0^2 r^2/2}\int_0^\infty r'dr'\sum_{m'=-\infty}^{\infty} R_{m'}(r')$$
$$\times\, i^{m-m'-1}m\int_{-\infty}^{\infty}\frac{dk}{k^2}J_m(kr)J_{m'}(kr') \;=\; 0 \tag{63}$$

The case of $m = 0$ is a special mode. It is the static eigenmode with

$$\Omega = 0, \quad m = 0 \tag{64}$$

while the corresponding eigenfunction $R_0(r)$ is arbitrary as long as it satisfies Eq.(61).

We now decompose $R_m(r)$ as

$$R_m(r) = \left(\frac{\omega_0 r}{\sqrt{2}}\right)^{|m|} e^{-\omega_0^2 r^2/2} \sum_{n=0}^{\infty} a_{mn}\, L_n^{(|m|)}\left(\frac{\omega_0^2 r^2}{2}\right) \tag{65}$$

where $L_n^{(m)}$'s are the generalized Laguerre polynomials. Using their orthogonality properties, and applying to both sides of Eq.(63) by (for chosen m and n)

$$\int_0^{\infty} r dr \left(\frac{\omega_0 r}{\sqrt{2}}\right)^{|m|} L_n^{(|m|)}\left(\frac{\omega_0^2 r^2}{2}\right) \tag{66}$$

we obtain

$$\begin{aligned} & -i(\Omega - m\omega_0)\, a_{mn} \qquad (67) \\ & -\sqrt{2}\,\omega_0 \sum_{\substack{m'=-\infty \\ m+m'=\text{even}}}^{\infty} \sum_{n'=0}^{\infty} a_{m'n'} \frac{m\, i^{|m|-|m'|-1}(|m|+|m'|+2n+2n'-3)!!}{(|m|+n)!n'!\, 2^{2n+2n'+|m|+|m'|}} \;=\; 0 \end{aligned}$$

The infinite matrix equation (67) is then solved for the eigenmode frequency Ω. Instability of the perturbations of type Eq.(54) is to be identified with complex solution of Ω, but it is found that all eigenvalues of Ω are real. We conclude that the planar galaxy is stable against longitudinal perturbations of the form (54). The largest "frequency shift" occurs for the $m = 1$ mode with $\Omega/\omega_0 \approx 1.37$. Instabilities, if any, will have to involve transverse dynamics.

THE SEARCH FOR QUANTUM GRAVITY USING MATTER INTERFEROMETERS

R BINGHAM

Rutherford Appleton Laboratory
Chilton, Didcot, Oxfordshire OX11 0QX, UK

One of the biggest unsolved problems in fundamental physics is the unification of quantum mechanics and gravity. One of the consequences of unification could be the existence of "incoherent conformal waves" in gravitational fields due to quantum mechanical zero-point fluctuations. Recent theories have demonstrated that these fluctuations change the first order correlation function of matter-waves. A spacecraft mission called Hyper is being designed to conduct matter-wave experiments in space. An order of magnitude improvement may be gained by going into orbit reducing the effects of environmental interactions. The results of such experiments are to put constraints on the upper bands of measurements of de-coherence of a matter-wave interferometer due to quantum fluctuations.

1. Introduction

The physics of the very small is based on quantum theory, and physics on the largest scales is based on Einstein's theory of general relativity, which interprets gravity as the curvature of space-time. There can be no unification of physics, which does not include them both. Superstring theory (Green et al 1987) and its recent extension to the more general theory of branes is probably the best candidate, but the links with experiment are very tenuous.

One hundred years ago, when Planck introduced the constant named after him, he also introduced the Planck scales, which combined this constant with the velocity of light c and Newton's gravitational constant G to give the fundamental

Planck time $T_{planck} = (\hbar G / c^5)^{1/2} \approx 5\times10^{-44} s$; Planck length $cT_{planck} = (G\hbar / c^3)^{\frac{1}{2}} \approx 10^{-35} m$; Planck mass $M_{planck} = (\hbar c / G)^{\frac{1}{2}} \approx 10^{-8} kg.$

Experiments on quantum gravity require access to these scales. When compared with atomic scales, the time and length are very small and the mass is extremely large. To access these scales directly using accelerators would require 10^{19}GeV accelerators, well beyond any conceivable experiments.

The atomic scales were first accessed through Brownian motion, using Einstein's theory for the thermal fluctuations of small particles (1905). By interpreting the motion of these particles as due to random collisions with atoms, Einstein was able to deduce many atomic properties, even though each individual atom was too small to be observed directly in his time. The advantage of this method is that it depends for its success on the square root of the ratio of the atomic scale to macroscopic scales, and not any integer power of the ratio. This was crucial for this method, and led to the most accurate estimates of Avogadro's number at the time, and thus to the universal recognition of the reality of atoms.

Quantum decoherence is also a fluctuation phenomenon, and satisfies the same scaling laws as for Brownian motion. Modern experimental methods are so much in advance of those of Einstein's time, that we are now in a position to consider accessing the Planck scales by a method analogous to Brownian motion (Percival 1997). This is why quantum decoherence due to space-time fluctuations have been suggested as a method to study quantum gravity effects at the Planck scale. (Ellis et al 1984, Percival et al 1997). The basic idea is that space-time does not vary smoothly as in Euclidean or Minkovski geometries but has topological discontinuities. Both semi-classical analysis and String theory supports the concept of space-time quantum decoherence at the Planck scale. Combining the sensitivity of atom interferometers at the quantum level to the greatly reduced "noise" environment of space the possibility of using a "macroscopic" instrument to investigate a microsystem is now a real possibility.

The curvature of space-time produces changes in "proper time", the time measured by moving clocks, for sufficiently short time intervals, of the order of the Planck time, the proper time fluctuates strongly due to quantum fluctuations. For longer time intervals, proper time is dominated by a steady drift due to smooth space-time. Proper time is therefore made up of the quantum fluctuations plus the steady drift. The boundary separating the shorter time scale fluctuations from the longer time scale drifts, marked by a time τ_0, which is approximately around the Planck time, $T_{planck} \approx 5\times10^{-44} s$.

Atom interferometers are ideal in measuring decoherence effects and will be able to put upper limits on quantum fluctuations which will help guide the theoretical work. Decoherence can be caused by other less interesting processes

such as black body radiation, collisions with atoms and molecules, and even interactions with its own components. By performing the experiments in space some of the environmental problems such as natural vibrations can be reduced allowing a more accurate measurement.

Search for evidence of space-time granularity deteriorating the coherence of matter waves. One of the biggest unsolved problems in fundamental physics is the unification of quantum mechanics and gravity. One consequence of the unification will be the existence of so called incoherent conformal waves in gravitational fields due to quantum mechanical zero-point fluctuations. These fluctuations granulate the space-time and lead presumably to an observable decoherence of matter waves. New theories have been developed to describe the changes of first order correlation function of matter-waves under the presence of space-time granularity as a function of parameters like the atomic mass or like the geometry of the atomic trajectories. Investigations with atom interferometers will open up a new field in quantum gravity, which a large impact on the grand unification theories or on the superposition principle in quantum mechanics. Atom interferometers in space will improve on laboratory experiments putting upper bounds to quantum fluctuations that can be used to test theories.

2. Ground based tests and limits.

The detection of the decoherence due to these fluctuations on the Planck scale would provide experimental access to quantum gravity effects on this scale analogous to the access to atomic scales provided by Brownian motion. The properties of the Planck-scale quantum fluctuations in space-time are open to investigation by studying their cumulative effects in matter interferometers, by analogy with the cumulative effects of atomic collisions on the motion of small macroscopic particles.

Quantum coherence is powerful tool for investigating properties of the micro system of quantum fluctuations with a macroscopic instrument such as an atom interferometer. More specifically it has been advocated as a way of studying phenomena leading to quantum decoherence induced by quantum gravity effects (Percival & Strunz 1997). In particular the papers by Pervical and co-workers show how incoherent conformal waves in the gravitational field, which are produced by quantum mechanical zero point fluctuations, interact with wave packets of massive particles. The non-linear interaction between the quantum fluctuations cause a decoherence of the quantum wave packets of massive particles.

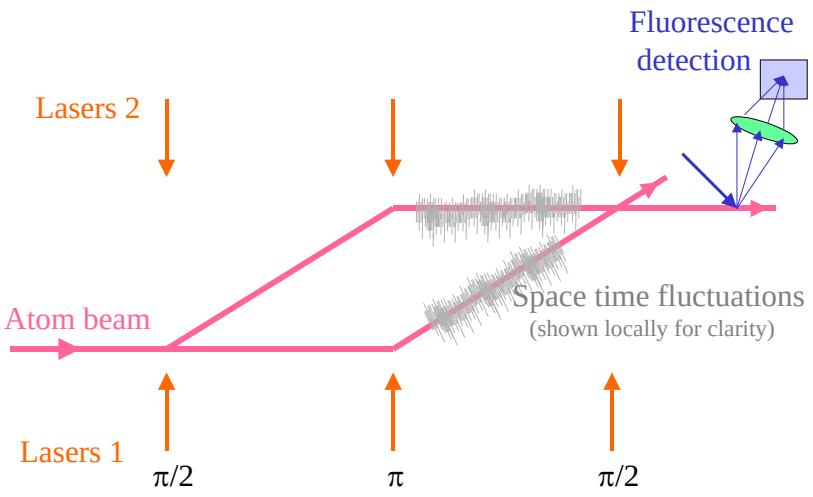

Figure 1.

An atom is a quantum clock with a very high frequency proportional to its mass. In an atom interferometer, Fig.1, an atomic wavepacket is split into two coherent wave packets that follow different paths before recombining. The phase change of each wavepacket is proportional to the proper time along its path, resulting in constructive or destructive interference when the wavepackets recombine. Where the phases differ by an even multiple of π, there is constructive interference, and where they differ by an odd multiple, there is destructive interference. The interference pattern contains information about the time difference between the two paths, the phases of the atoms depend on the paths followed. The phase change $\phi(t)$ over a proper time interval, T, is $\phi(T) = \Omega T$, where $\Omega = mc^2/\hbar$ is the quantum angular frequency associated with the rest mass, m of the atom. Note that the phase change for large scales where space-time is smooth is proportional to time. On the other hand quantum gravity fluctuations in space-time are irregular and produce stochastic phase shifts described as with any stochastic process like Brownian motion is a diffusion process proportional to $T^{\frac{1}{2}}$, the regular phase due to smooth space-time shift is proportional to T. Therefore, in the simplest model, the intrinsic space-time fluctuations lead to an additional fluctuating phase which is proportional to the regular phase charge $\phi(T)$ multiplied by a fluctuation factor $(\tau_o / T)^{\frac{1}{2}}$ resulting in a fluctuating phase $\delta\phi(T) = (\tau_o T)^{\frac{1}{2}}\Omega$ where τ_o is close to the Planck time T_{planck} [Percival 1997]. Due to the different paths in the

interferometer the atoms experience different space-time fluctuations resulting in a decoherence observed in the interference pattern. Because of the locality of the beams smooth space-time produces the same phase shift in both arms of the interferometer and any decoherence is then due to quantum fluctuations. The wave function experiences a quantum random walk in phase due to fluctuations on scales less than τ_o close to the Planck time. Figure 2 represents the total phase shift for times less then τ_0, close to the Planck time T_{planck}, the graph is roughly parabolic due to space-time fluctuations.

For longer times the phase shift is linear in time being dominated by smooth space-time. From the formula for $\delta\phi(T)$ it follows that the best atom interferometers are those with relatively large atomic mass which increases Ω and large drift times.

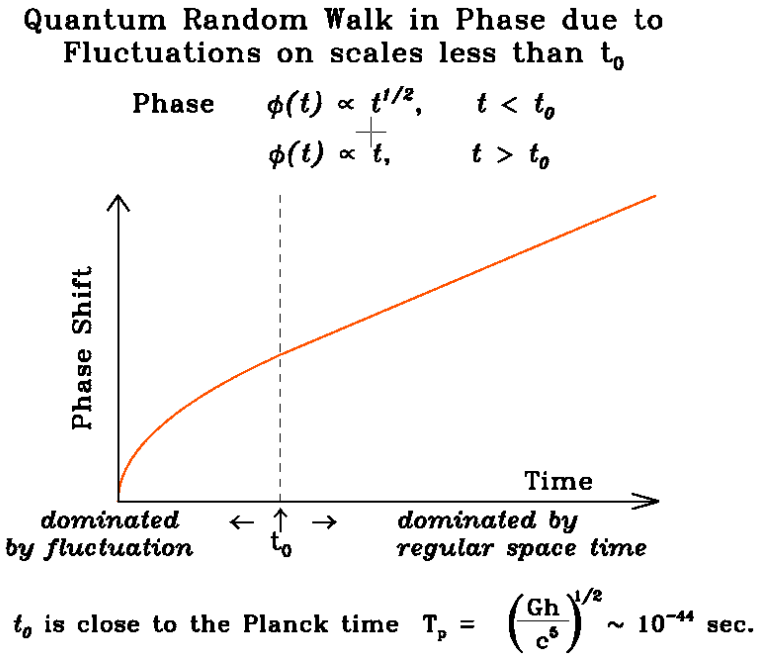

Figure 2.

The most promising source of space-time quantum gravity fluctuations for experimental detection by atom interferometers is zero-point energy fluctuations. A well-known effect of zero-point energy is the Casimir force (1948) which describes a quantum electrodynamical force of the vacuum observed recently by

Lamoreaux (1997) and Mohideen & Roy (1999). Recently Powers and Percival (2000) have shown how non-linear incoherent conformal waves in the gravitational field produced by quantum mechanical zero-point fluctuations, interact with the wave-packets of massive particles causing decoherence. Previous studies of decoherence include non-propagating interactions conformal fluctuations by Sanchez - Gomez (1993), a Newtonian gravitational model by Kay (1998). The most recent work by Power and Percival (2000) considered sources of the conformal field and amplitudes and coherence properties of the resulting fluctuations. A drawback of their model is that a classical model for quantum fluctuations is used which does not guarantee that all the essential physics is included. Conformal metric fluctuations are also considered since the deviation in the Minkowski metric is equal in all dimensions making the problem mathematically easier to deal with. Theories of quantum gravity predict a cut-off wavelength for conformal gravitational waves related to the Planck length cT_{planck} such that $\lambda_{cut-off} = \lambda cT_{planck}$ and a cut-off frequency $\omega_m = 2\pi c / \lambda_{cut-off}$, where λ is in the range $10^2 - 10^6$. For a matter wave interferometer using particles of mass m separated in space by a distance large compared with the correlation length for a time T Powers and Percival (2000) estimate λ to be

$$\lambda = \left(\sqrt{\frac{\pi}{2}} \frac{M^2 c^4 T_{planck} T}{\hbar^2 (\delta\rho / \rho(o))} \right)^{\frac{1}{7}}$$

where $\rho(o)$ is the density matrix of the wavepacket at time $T = 0$ and $\delta\rho$ is the change due to space-time fluctuations, $\delta\rho / \rho(o)$ represent the decoherence. Recent atom interferometer experiments by Peters et al. (1997), using cesium atoms separated for $0.32s$ detected a loss of contrast of about 3% putting a lower bound on λ of $\lambda > 18$. In contrast accelerator based experiments put an upper bound of λ which in current experiments is still above the theoretical prediction of 10^6 and unlikely to improve significantly in the foreseeable future.

3. Improved tests with Hyper.

The results of decoherence in the two-path atom interferometer investigated by Percival and Strunz (1997) hold if the separation of the wavepackets is large compared to the width of the wavepacket. In this case it will be the loss of coherence between the two wave packets that will be noticed. If not then the loss of coherence within the wavepacket is important factor. The approach of

Power(1999) includes both. It also includes the nonlinearity in the gravitational field equations, without which the ordinary commutative structure of space-time gives the same fluctuating contribution to both arms of an interferometer, and thus no net effect on the interference pattern. Both approaches neglect the back-reaction of the matter on the space-time metric, and make a semiclassical approximation to the space-time fluctuations. These approximations could be removed using ordinary Feynman diagram expansions. But there remains the need for a cut-off because the gravitational field is not renormalizable. If the claims of superstring theory and its modern extensions are to be believed, it does not have the renormalization problems of field theory, and could presumably therefore be used to make precise predictions of the size of the fluctuations, without approximation, and thus subject the theory to direct experimental test using matter interferometers. The difficulty here seems largely cultural: there is no tradition of applying superstring theory directly to laboratory or space experiments of this kind.

Improvements in the sensitivity by reducing background noise and vibrational noise in the apparatus and increasing the mass and time of flight in atom interferometer experiments will raise the bound on λ although the $1/7^{th}$ power dependence results in a small rise. The recent experiments that show no evidence of space-time fluctuations require suppression of interference, which can be achieved by increasing the separation of the wave packets, which can be done using HYPER. An order of magnitude improvement may be gained by going into orbit reducing the effects of environmental interactions, taking the experiments into the domain of theory. The final result of such experiments is to put constraints on the upper bounds of measurements of decoherence which quantum fluctuations, which can be used to test some quantum theories of gravity. The proposed HYPER mission would increase our understanding and provide a test bed for many of the quantum gravity theories.

3.1. ***Acknowledgements***

I would like to thank M. Sandford, B. Kent and I.C. Percival for fruitful discussions.

References

1. R P Feynman, Lectures on Gravitation, California Institute of Technology, (1971)
2. S W Hawking, **D53**, 3099, (1996)

3. M Green, J Schwarz and E Witten, *Superstring Theory*, Cambridge University Press, Cambridge, (1987)
4. J Ellis, J S Hagelin, D V Nanopolous and M Srednicki, *Nucl. Phys*. B241, 381, (1984)
5. I C Percival, W T Stunz, *Proc. R. Soc. Lond. A.*, **453**, 431, (1997)
6. A Einstein, *Ann.d.Physik*, **17**, 549, (1905)
7. I C Percival, *Physics Today*, **10**, 43, (1997)
8. H B G Casimir, *Proc. K. Akad. Wet*., **51**, 793, (1948)
9. S K Lamoreaux, *Phys. Rev. Lett*., **78**, 5, (1997)
10. U Mohideen and R Roy, *Phys. Rev. Lett*., **81**, 4549, (1999)
11. J L Sanchez-Gomez in Stochastic evolution of quantum states in open systems and in measurement processes. ed. L Diosi, G B Lukacs, World Scientific, Singapore, (1993)
12. B Kay, *Class. Quant. Grav*., 15, L89, (1998)
13. W L Power and I C Percival, *Proc. Roy. Soc. Lond. A*., **456**, 955, (2000)
14. W L Power, *Proc. Roy. Soc. Lond. A*., **455**, 991, (1996)

ELECTRON-POSITRON-PHOTON PLASMA AROUND A COLLAPSING STAR

R. RUFFINI, L. VITAGLIANO AND S.-S. XUE

We describe electron-positron pairs creation around an electrically charged star core collapsing to an electromagnetic black hole (EMBH), as well as pairs annihilation into photons. We use the kinetic Vlasov equation formalism for the pairs and photons and show that a regime of plasma oscillations is established around the core. As a byproduct of our analysis we can provide an estimate for the thermalization time scale.

1. Dynamics of Dyadosphere

Dyadosphere was first introduced in Ref. 1 as the region surrounding an electromagnetic black hole (EMBH) in which the electromagnetic field strength exceeds the critical value $\mathcal{E}_{\rm c}$ for electron-positron pair creation via the mechanism *à là* Heisenberg-Euler-Schwinger.[2,3] The relevance of the dyadosphere around an EMBH, for the astrophysics of gamma-ray busts has been discussed in Refs. 1, 4–6 (the external radius of dyadosphere will be denoted by $r_{\rm ds}$). In those papers the pair production in dyadosphere has been described as an electrostatic problem: instantaneously a massive body collapses to an EMBH whose charge is large enough that the electric field strength $\mathcal{E}$ exceeds $\mathcal{E}_{\rm c}$ and the Schwinger process is triggered in the entire dyadosphere; moreover the pairs are produced at rest and remain at rest during the whole history of their production; finally they instantaneously thermalize to a plasma configuration (see Fig. 1). These ansatz, formulated for the sake of simplicity, allow one to estimate the number density of pairs produced as well as the energy density deposited on the pairs in a straightforward manner. We relax the hypothesis that the large electric field is instantaneously built up and take the following dynamical point of view:

(1) A spherically symmetric star core endowed with electric, say positive, charge Q, collapses. We assume that the electromagnetic field strength $\mathcal{E}$ on the surface of the core is amplified to $\mathcal{E}_{\rm c}$ during the collapse and the Schwinger process begins.

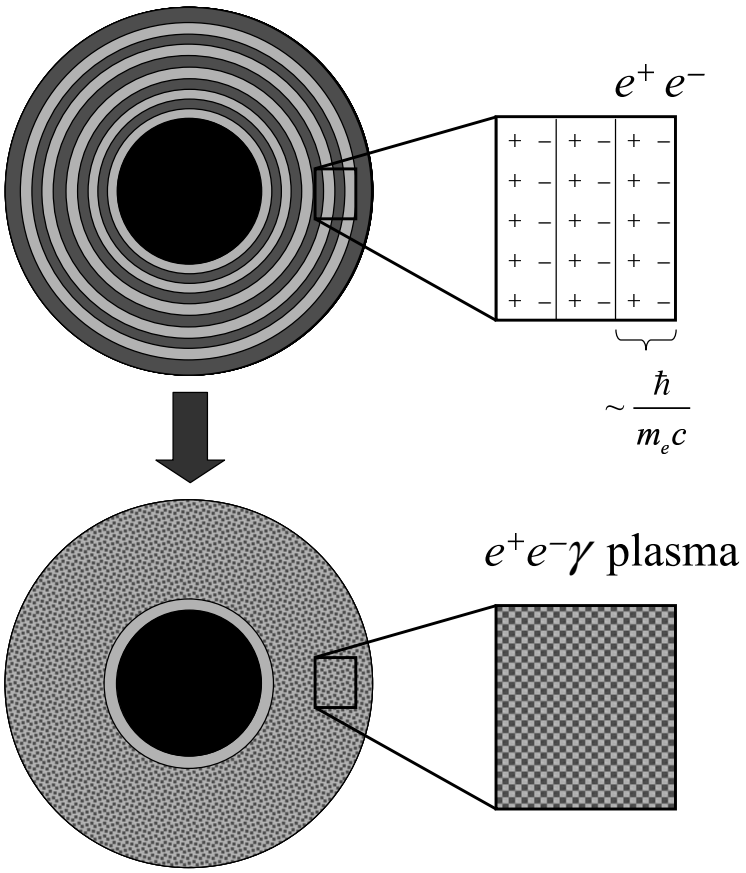

Figure 1. Vacuum polarization process of energy extraction from an EMBH. Pairs are created by vacuum polarization in the dyadosphere and the system thermalizes to a neutral plama configuration (see Ref. [1] for details).

(2) The pairs produced by the vacuum polarization progressively screen the electromagnetic field of the core, thus reducing its strength. Furthermore the charges (electrons and positrons) are accelerated by the Lorentz force in the electromagnetic field. Finally particles and antiparticles annihilate into photons.

An enormous amount of pairs ($N \sim \frac{Q}{e}\frac{r_{\rm ds}}{\lambda_{\rm C}}$, where $\lambda_{\rm C}$ is the Compton length of the electron) is produced, as claimed in Refs. 1, 4–6, if the core charge is not annihilated by the charge of the accelerated electrons during the gravitational collapse (see Ref. 7). Therefore it is useful to study the

dynamics of the electron-positron-photon plasma in the electric field of the core in some details. This will be the main object of the next section. As a byproduct of the analysis we obtain an estimate for the time scale needed for the thermalization of the system.

In Ref. 8 it was suggested that the exact solution of Einstein-Maxwell equations describing the gravitational collapse of a thin charged shell can be used as a simplyfied analytical model for the gravitational collapse of a charged core; it was also discussed in some details the amplification of electromagnetic field strength on the surface of the core. Here we briefly review some of the results of Ref. 8. The region of space-time external to the core is Reissner-Nordström with line element

$$ds^2 = -f dt^2 + f^{-1} dr^2 + r^2 d\Omega^2 \tag{1}$$

in Schwarzschild like coordinate (t, r, θ, ϕ), where $d\Omega^2 = d\theta^2 + \cos^2\theta d\phi^2$, $f = f(r) = 1 - \frac{2M}{r} + \frac{Q^2}{r^2}$; M is the total energy of the core as measured at infinity and Q is its total charge. Let us label with R and T the radial and time-like coordinate of the shell, then the equation of motion of the core is (cfr. Ref. 8)

$$\frac{dR}{dT} = -\frac{f(R)}{H(R)}\sqrt{H^2(R) - f(R)} \tag{2}$$

where $H(R) = \frac{M}{M_0} - \frac{M_0^2+Q^2}{2M_0 R}$; M_0 is the rest mass of the shell. The analytical solution of Eq. (2) was found in Ref. 8 in the form $T = T(R)$. According to a static observer $\mathcal{O}$ placed at the event $x_0 \equiv (R, T(R), \theta_0, \phi_0)$ the core collapses with speed given by

$$V^* \equiv -\frac{dR^*}{dT^*} = \sqrt{1 - \frac{f(R)}{H^2(R)}} \leq 1 \tag{3}$$

where $dR^* \equiv f^{-1/2} dR$ and $dT^* \equiv f^{1/2} dT$ are spatial and temporal proper distances as measured by $\mathcal{O}$. In Fig. 2 we plot V^* as a function of R for a core with $M = M_0 = 20 M_\odot$[a] and $\xi \equiv \frac{Q}{M} = 10^{-3}, 10^{-2}, 10^{-1}$. Recall that dyadosphere radius is given by[1]

$$r_{\rm ds} = \sqrt{\frac{eQ\hbar}{m_e^2 c^3}}, \tag{4}$$

where c is the speed of light; e and m_e are electron charge and mass respectively. Then note that $V^*_{\rm ds} \equiv V^*|_{R=r_{\rm ds}} \simeq 0.2c$ for $\xi = 0.1$.

[a]The condition $M_0 = M$ corresponds to a shell starting its collapse at rest at infinity.

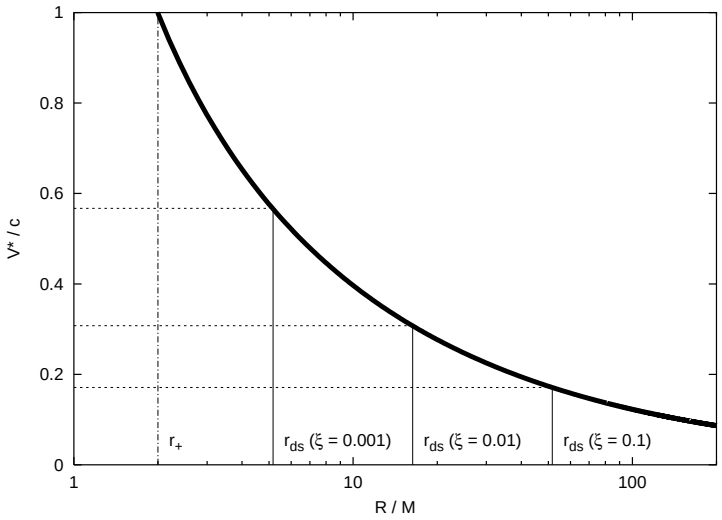

Figure 2. Collapse velocity of a charged star of mass $M_0 = M = 20M_\odot$ as measured by static observers as a function of the radial coordinate of the star surface. As the charge is not too large ($\xi \lesssim 0.1$) there is not much difference between collapse velocities of stars with different charge. Dyadosphere radii for different charge to mass ratios ($\xi = 10^{-3}, 10^{-2}, 10^{-1}$) are indicated in the plot together with the corresponding velocity.

2. Plasma oscillations and screening

We now turn to the pair creation taking place during the gravitational collapse. The gravitational fields of the core is considered classical; the gravitational effects of the electron-positrons-photons plasma are neglected.

The most detailed framework for studying electromagnetic vacuum polarization and particle-antiparticle scattering around an electromagnetic collapsing core is quantum electrodynamics in the classical external electromagnetic field of the core on the Reissner-Nordström space-time around the core itself. Of course a number of approximations is needed in order to make the problem be tractable. Let us discuss such approximations.

(Homogeneity) First of all, the static Reissner-Nordström space-time region external to the collapsing core is naturally splitted in space (hypersurfaces orthogonal to the static Killing field) and time. In the local frames associated with static observers, the electromagnetic field of the core is purely electric. Moreover, we will see that the length scale L over which the electric field as well as the particle number densities vary, is much larger than the length scale l which is

charachteristic of the electron–positron motion. Thus we can divide dyadosphere into small regions D_i

$$\begin{aligned} &D_i : r_i \leq r \leq r_{i+1} = r_i + \varepsilon; \\ &r_+ \leq r_i \leq r_{\mathrm{ds}} \qquad \varepsilon \lesssim l \end{aligned} \tag{5}$$

such that for any i the system formed by the electric field and the pairs can be considered homogeneous in D_i.

(Flat space-time) For, in geometric units, the electron charge e is much larger than the electron mass m_e, the gravitational acceleration is negligible with respect to electric acceleration for sufficiently large electric field strengths (even much less than $\mathcal{E}_c$), therefore we will neglect the curvature of space-time and use the local frame of a static observer as a globally inertial frame of the Minkowski space-time.

(Mean field) The number of pairs is so high that a semiclassical formalism and mean field approach can be used, in which the total electromagnetic field (core electromagnetic field and screen field due to pairs) is considered to be classical, while the electron-positron field is quantized. It has been shown[9−11] that, if we neglect scattering between particles, the semiclassical evolution of the homogeneous system in a flat space-time is well described by a Boltzmann-Vlasov-Maxwell system of partial differential equations, where the electrons and positrons are described by a distribution function $f_e = f_e(t, \mathbf{p})$ in the phase space, where t is the inertial time and $\mathbf{p}$ the 3−momentum of electrons. Finally we use the method presented in Ref. 13 to simplify such a Boltzmann-Vlasov-Maxwell system.

Let us summarize results in Ref. 13: we obtained the following system of ordinary differential equations which simultaneously describes the creation and evolution of electron-positron pairs in a strong electric field as well as the annihilation of pairs into photons:

$$\begin{cases} \frac{d}{dt} n_e = S(\mathcal{E}) - 2n_e^2 \sigma_1 \rho_e^{-1} \left|\pi_{e\|}\right| + 2n_\gamma^2 \sigma_2 \\ \frac{d}{dt} n_\gamma = 4n_e^2 \sigma_1 \rho_e^{-1} \left|\pi_{e\|}\right| - 4n_\gamma^2 \sigma_2 \\ \frac{d}{dt} \rho_e = e n_e \mathcal{E} \rho_e^{-1} \left|\pi_{e\|}\right| + \frac{1}{2} \mathcal{E} j_p(\mathcal{E}) - 2n_e \rho_e \sigma_1 \rho_e^{-1} \left|\pi_{e\|}\right| + 2n_\gamma \rho_\gamma \sigma_2 \\ \frac{d}{dt} \rho_\gamma = 4n_e \rho_e \sigma_1 \rho_e^{-1} \left|\pi_{e\|}\right| - 4n_\gamma \rho_\gamma \sigma_2 \\ \frac{d}{dt} \pi_{e\|} = e n_e \mathcal{E} - 2n_e \pi_{e\|} \sigma_1 \rho_e^{-1} \left|\pi_{e\|}\right| \\ \frac{d}{dt} \mathcal{E} = -2e n_e \rho_e^{-1} \left|\pi_{e\|}\right| - j_p(\mathcal{E}) \end{cases}, \tag{6}$$

where n_e (n_γ) is the electron (photon) number-density, ρ_e (ρ_γ) is the electron (photon) energy-density, $\pi_{e\|}$ is the density of electron radial momentum and $\mathcal{E}$ the electric field strength. Finally $S(\mathcal{E})$ is the Schwinger prob-

ability rate of pair creation, $j_p(\mathcal{E})$ is the polarization current-density, $\sigma_{1,2}$ are total cross sections for the processes $e^+e^- \rightleftarrows \gamma\gamma$ and the corresponding terms describe probability rates of pair annihilation into photons and vice versa. System (6) was numerically integrated in Ref. 13.

Here it has to be integrated once for each of the regions D_i (see (5)) with initial conditions

$$n_e = n_\gamma = \rho_e = \rho_\gamma = \pi_{e\|} = 0; \quad \mathcal{E}_0 = \tfrac{Q}{r_i^2}. \tag{7}$$

Let us recall the main results of the numerical integration. The system undergoes plasma oscillations:

(1) the electric field oscillates with lower and lower amplitude around 0;
(2) electrons and positrons oscillates back and forth in the radial direction with ultrarelativistic velocity;
(3) the oscillating charges are trapped in a thin shell whose radial dimension is given by the elongation $\Delta l = |l - l_0|$ of the oscillations, where l_0 is the radial coordinate of the centre of oscillation and

$$l = \int_0^t \tfrac{\pi_{e\|}}{\rho_e} dt. \tag{8}$$

Note that $\frac{\pi_{e\|}}{\rho_e} \equiv v$ is the radial mean velocity of charges (we plot the elongation Δl as a function of time in Fig. 3);
(4) the lifetime Δt of the oscillation is of the order of $10^2 - 10^4 \tau_{\mathrm{C}}$ (see Fig. 3).
(5) in the time Δt the system thermalizes in the sense that both number and energy equipartition between electron–positron pairs and photon are approached.

In Fig. 4 we plot electrons mean velocity v as a function of the elongation during the first half period of oscillation, which shows precisely the oscillatory behaviour.

3. Conclusions

In a paper under preparation[7] we are examining the conditions under which the charge of the collapsing core is not annihilated due to vacuum polarization as a consequence of the above plasma oscillations.

Note that $e^+e^- \rightleftarrows \gamma\gamma$ scatterings is marginal at early times ($t \ll \Delta t$) since the cross sections $\sigma_{1,2}$ are negligible in the beginning of pair production.[13] However at late times ($t \gtrsim \Delta t$) the system is expected to

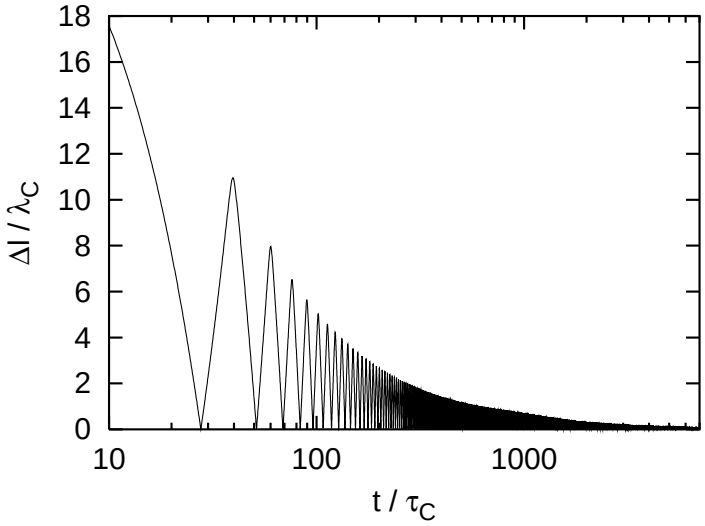

Figure 3. Electrons elongation as function of time in the case $r = \frac{1}{3} r_{\rm ds}$. The oscillations are damped in a time of the order of $10^3 \tau_{\rm C}$.

relax to a plasma configuration of thermal equilibrium.[13] Thus a regime of thermalized electrons-positrons-photons plasma begins in which the system can be described by hydrodynamic equations. It is shown in Refs. 12, 14 that the equations of hydrodynamic imply the expansion of the system. In "brief" the system reaches the ultrarelativistic velocities required in a realistic model for GRBs. It is worthy to remark that the time scale of hydrodynamic evolution ($t \sim 0.1 s$) is, in any case, much larger than the time scale Δt needed for thermalization.

References

1. G. Preparata, R. Ruffini and S.-S. Xue, *A&A* **338**, L87 (1998).
2. W. Heisenberg and H. Euler, *Zeits. Phys.* **98** (1935) 714.
3. J. Schwinger, *Phys. Rev.* **82**, 664 (1951).
4. R. Ruffini, C. L. Bianco, P. Chardonnet, F. Fraschetti and S.-S. Xue, *ApJ* **555**, L107 (2001).
5. R. Ruffini, C. L. Bianco, P. Chardonnet, F. Fraschetti and S.-S. Xue, *ApJ* **555**, L113 (2001).
6. R. Ruffini, C. L. Bianco, P. Chardonnet, F. Fraschetti and S.-S. Xue, *ApJ* **555**, L117 (2001).
7. R. Ruffini, L. Vitagliano and S.-S. Xue, in preparation.

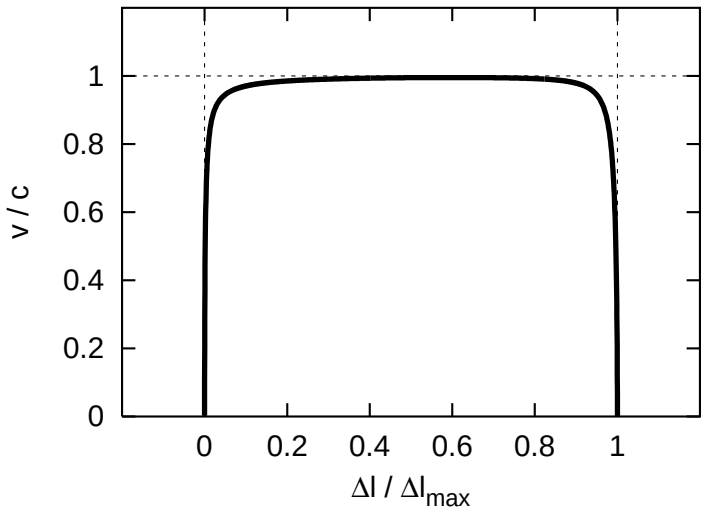

Figure 4. Electrons mean velocity as a function of the elongation during the first half oscillation. The plot summarize the oscillatory behaviour: as the electrons move, the mean velocity grows up from 0 to the speed of light and then falls down at 0 again.

8. C. Cherubini, R. Ruffini and L. Vitagliano, *Phys. Lett.* **B545**, 226 (2002).
9. Y. Kluger, J. M. Eisenberg, B. Svetitsky, F. Cooper and E. Mottola, *Phys. Rev. Lett.* **67**, 2427 (1991).
10. Y. Kluger, J. M. Eisenberg, B. Svetitsky, F. Cooper and E. Mottola, *Phys. Rev.* **D45**, 4659 (1992).
11. F. Cooper, J. M. Eisenberg, Y. Kluger, E. Mottola and B. Svetitsky, *Phys. Rev.* **D48**, 190 (1993).
12. R. Ruffini, J. D. Salmonson, J. R. Wilson and S.-S. Xue, *A&A* **359**, 855 (2000).
13. R. Ruffini, L. Vitagliano and S.-S. Xue, *Phys. Lett.* **B559** (2003) 12.
14. R. Ruffini, L. Vitagliano and S.-S. Xue, (2003) *in these proceedings.*

PLASMA EXPANSION IN THE GEOMETRY OF A COLLAPSING STAR

R. RUFFINI, L. VITAGLIANO AND S.-S. XUE

We describe the evolution of an electron-positron-photon plasma created by Sauter–Heisenberg–Euler–Schwinger mechanism around a collapsing charged star core in the Reissner-Nordström geometry external to the core, in view of the application in the framework of the EMBH theory for gamma ray bursts.

1. Introduction

In 1975, following the work on the energetics of black holes,[1] Damour and Ruffini[2] pointed out the existence of the vacuum polarization process *à là* Sauter–Heisenberg–Euler–Schwinger[3,4] around black holes endowed with electromagnetic structure (EMBHs), whose electric field strength exceeds the Schwinger critical value $\mathcal{E}_{\rm c} = \frac{m_e^2 c^3}{e\hbar}$, where c is the speed of light, e and m_e are electron charge and mass respectively. Damour and Ruffini gave reasons to believe that this process is almost reversible in the sense introduced by Christodoulou and Ruffini[1] and that it extracts the mass energy of an EMBH very efficiently: this have been proved in Ref. 5. The vacuum polarization process around an EMBH offered a natural mechanism for explaining the Gamma Ray Bursts (GRBs), just discovered at the time. Moreover the mechanism had a most peculiar prediction: the characteristic energetics of the burst should be of the order of 10^{54} ergs; while nothing at the time was known about either the distances or the energetics of GRBs.

More recently, after the discovery of the afterglow of GRBs and their cosmological distance, the idea by Damour and Ruffini has been reconsidered in Refs. 6–9 where the EMBH model for GRBs is developed. The evidence is now that through the observations of GRBs we are witnessing the formation of an EMBH and therefore are following the process of gravitational collapse in real time. Even more importantly, the tremendous energies involved in the energetics of these sources have their origin in the extractable energy of black holes.

Various models have been proposed in order to extract the rotational energy of black holes by processes of relativistic magnetohydrodynamics

(see, e.g., Ref. 10). It should be expected, however, that these processes are relevant over the long time scales characteristic of accretion processes. In the present case of GRBs a sudden mechanism appears to be at work on time scales of the order of few seconds or shorter and they are naturally explained by the vacuum polarization process introduced in Ref. 2.

All considerations on the electric charge of stars have been traditionally directed towards the presence of a net charge on the star surface in a steady state condition, from the classic work by Shvartsman[11] all the way to the fundamental book by Punsly.[12] The charge separation can occur in stars endowed with rotation and magnetic field and surrounded by plasma, as in the case of Goldreich and Julian,[13] or in the case of absence of both magnetic field and rotation, the electrostatic processes can be related to the depth of the gravitational well, as in the treatment of Shvartsman.[11] However, in neither case is it possible to reach the condition of the overcritical field needed for pair creation.

The basic new conceptual point is that GRBs are the most violent transient phenomenon in the universe and therefore in order to realize the condition for their occurrence, one must look at a transient phenomenon. We propose as a candidate the most transient phenomenon possibly occurring in the life of a star: the gravitational collapse. The condition for the creation of the supercritical electromagnetic field required in the Damour and Ruffini work has to be achieved during the process of gravitational collapse which lasts less than ~ 30 seconds for a mass of $10M_\odot$ and the relevant part of the process may be as short as 10^{-2} or even 10^{-3} seconds. It is appropriate to consider a numerical example here[14] (see Fig. 1). We compare and contrast the gravitational collapse of a star in the two limiting cases in which its core of $M = 3M_\odot$ and radius $R = R_\odot$ is either endowed with rotation or with electromagnetic structure. The two possible outcomes of the process of gravitational collapse are considered: either a neutron star of radius of 10km or a black hole.

In the case of rotation the core has been assumed to have a rotational period of ~ 15 days. For such an initial configuration we have:

$$E_{rot} \simeq 7\times10^{-12}E_{tot} \ll |E_{grav}| \simeq 6\times10^{-6}E_{tot} \ll E_{bar} \simeq 4.4\times10^{5}\mathrm{cm}\,. \quad (1)$$

In the collapse to a neutron star we have:

$$E_{rot} \simeq 0.01E_{tot} \ll |E_{grav}| \simeq 0.1E_{tot} \ll E_{bar} \simeq 4.4\times10^{5}\mathrm{cm}\,. \quad (2)$$

The very large increase in the rotational energy is clearly due to the process of gravitational collapse: such a storage of rotational energy is the well

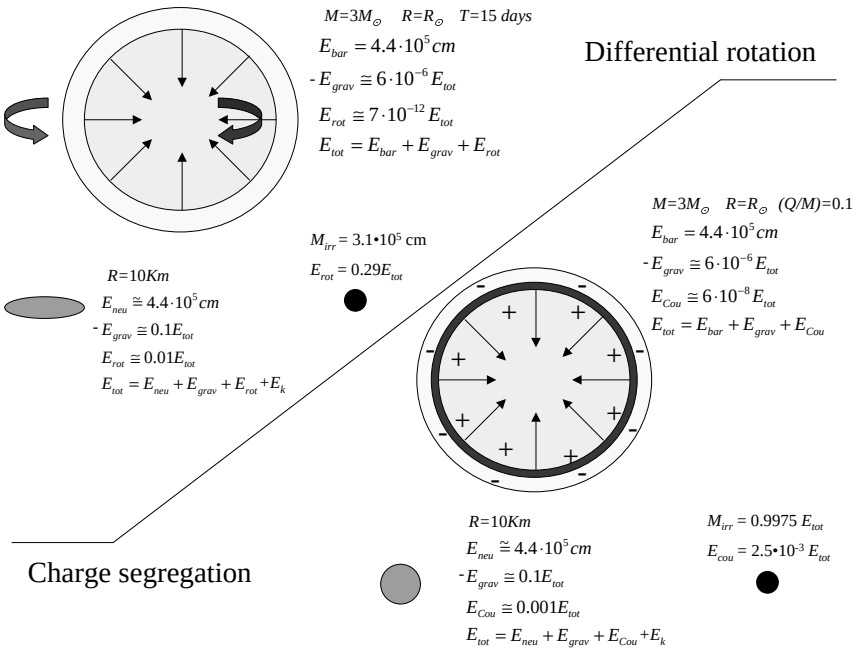

Figure 1. Comparing and contrasting gravitational collapse to a neutron star and to a black hole for a star core endowed with rotation or electromagnetic structure. Reproduced from Ref. [14] with the kind permission of the author.

known process explaining the pulsar phenomena. The collapse to a black hole has been estimated *assuming* the mass–energy formula.[1] The overall energetics, for the chosen set of parameters, leads to a solution corresponding to an extreme black hole, for which in principle 29% of the energy is extractable.

The similar process in the electromagnetic case starts from an initial neutral star with a magnetosphere oppositely charged from a core with

$$\frac{Q}{M\sqrt{G}} = 0.1 \ . \tag{3}$$

Let us first evaluate the amount of polarization needed in order to reach the above relativistic condition. Recalling that the charge to mass ratio of a proton is $q_p/\left(m_p\sqrt{G}\right) = 1.1 \times 10^{18}$, it is enough to have an excess of one quantum of charge every 10^{19} nucleons in the core of the collapsing star to obtain such an EMBH after the occurrence of the gravitational collapse. Physically this means that we are dealing with a process of charge segregation between the core and the outer part of the star which has the opposite sign of net charge in order to enforce the overall charge neutrality

condition.

We then have:

$$E_{cou} \simeq 6\times10^{-8}E_{tot} \ll |E_{grav}| \simeq 6\times10^{-6}E_{tot} \ll E_{bar} \simeq 4.4\times10^{5}\mathrm{cm}\,. \quad (4)$$

In the collapse to the neutron star configuration we have:

$$E_{Cou} \simeq 0.001E_{tot} \ll |E_{grav}| \simeq 0.1E_{tot} \ll E_{bar} \simeq 4.4\times10^{5}\mathrm{cm}\,. \quad (5)$$

Once again, the amplification of the electromagnetic energy is due to the process of gravitational collapse. Again, *assuming* the mass–energy formula, the collapse to a black hole for the chosen set of parameters leads to:

$$M_{\rm ir} = 0.9975E_{tot}\,, \quad E_{Cou} = 2.5\times10^{-3}E_{tot}\,. \quad (6)$$

It is during such a process of gravitational collapse to an EMBH that the overcritical field is reached.

The process of charge segregation between the inner core and the oppositely charged outer shell is likely due to the combined effects of rotation and magnetic fields in the earliest phases of the gravitational collapse of the progenitor star or to a process of ionization. In the following we will forget about the outer shell and will treat the inner core as an electrically charged collapsing star.

2. Energy extraction from a supercritical EMBH

We know from the Christodoulou-Ruffini mass formula[1] that the mass energy of an EMBH is the sum of the irreducible mass and the electromagnetic energy:

$$M = M_{\rm ir} + \frac{Q^2}{2r_+}, \quad (7)$$

where Q is the charge and r_+ is the radius of the horizon. Moreover in Ref. 5 it is shown that the electromagnetic energy $\frac{Q^2}{2r_+}$ is stored throughout the region external to the EMBH and can be extracted. If the condition

$$\frac{Q}{r_+^2} \geq \mathcal{E}_{\rm c} \quad (8)$$

is fulfilled the leading extraction process is a *collective* process based on the electron-positron plasma generated by Schwinger mechanism in the supercritical electric field of the EMBH.[5] The condition (8) implies

$$\frac{GM/c^2}{\lambda_{\rm C}}\left(\frac{e}{\sqrt{G}m_e}\right)^{-1} \simeq 2\cdot10^{-6}\frac{M}{M_\odot} \leq \xi \leq 1 \quad (9)$$

and therefore this vacuum polarization process can occur only for an EMBH with mass smaller than $2\cdot10^6 M_\odot$. The electron-positron pairs are produced in the dyadosphere of the EMBH,[6] the spherical region whose radius $r_{\rm ds}$ satisfies $\mathcal{E}_{\rm c} \equiv \frac{Q}{r_{\rm ds}^2}$. We have

$$r_{\rm ds} = \sqrt{\frac{eQ\hbar}{m_e^2 c^3}}\,. \tag{10}$$

The number of particles created is[6]

$$N_{\rm ds} = \frac{1}{3}\left(\frac{r_{\rm ds}}{\lambda_{\rm C}}\right)\left(1-\frac{r_+}{r_{\rm ds}}\right)\left[4+\frac{r_+}{r_{\rm ds}}+\left(\frac{r_+}{r_{\rm ds}}\right)^2\right]\frac{Q}{e} \simeq \frac{4}{3}\left(\frac{r_{\rm ds}}{\lambda_{\rm C}}\right)\frac{Q}{e}\,. \tag{11}$$

The total energy stored in the dyadosphere is[6]

$$E_{\rm ds}^{\rm tot} = \left(1-\frac{r_+}{r_{\rm ds}}\right)\left[1-\left(\frac{r_+}{r_{\rm ds}}\right)^4\right]\frac{Q^2}{2r_+} \simeq \frac{Q^2}{2r_+}\,. \tag{12}$$

The mean energy per particle produced in the dyadosphere $\langle E\rangle_{\rm ds} = \frac{E_{\rm ds}^{\rm tot}}{N_{\rm ds}}$ is then

$$\langle E\rangle_{\rm ds} = \frac{3}{2}\frac{1-\left(\frac{r_+}{r_{\rm ds}}\right)^4}{4+\frac{r_+}{r_{\rm ds}}+\left(\frac{r_+}{r_{\rm ds}}\right)^2}\left(\frac{\lambda_{\rm C}}{r_{\rm ds}}\right)\frac{Qe}{r_+} \simeq \frac{3}{8}\left(\frac{\lambda_{\rm C}}{r_{\rm ds}}\right)\frac{Qe}{r_+}\,, \tag{13}$$

which can be rewritten as

$$\langle E\rangle_{\rm ds} \simeq \frac{3}{8}\left(\frac{r_{\rm ds}}{r_+}\right)\ m_e c^2 \sim \sqrt{\frac{\xi}{M/M_\odot}}10^5 keV\,. \tag{14}$$

Such a process of vacuum polarization, occurring not at the horizon but in the extended dyadosphere region ($r_+ \le r \le r_{\rm ds}$) around an EMBH, has been observed to reach the maximum efficiency limit of 50% of the total mass-energy for an extreme EMBH (see e.g. Ref. 6). As discussed in Ref. 5 the e^+e^- creation process occurs at the expense of the Coulomb energy and does not affect the irreducible mass, which does not depend of the electromagnetic energy. In this sense, $\delta M_{\rm ir} = 0$ and the transformation is fully reversible.

3. The EMBH Theory

In a series of papers,[6–9] Ruffini and collaborators have developed the EMBH theory for GRBs, which has the advantage, despite its simplicity, that all eras following the process of gravitational collapse to the EMBH are described by precise field equations which can then be numerically integrated.

Starting from the vacuum polarization process *à là* Sauter–Heisenberg–Euler–Schwinger in the overcritical field of an EMBH first computed in Ref. 2, Ruffini et al. developed the dyadosphere concept.[6]

The dynamics of the e^+e^-–pairs and electromagnetic radiation of the plasma generated in the dyadosphere propagating away from the EMBH in a sharp pulse (PEM pulse) has been studied by the Rome group and validated by the numerical codes developed at Livermore Lab.[15,16]

The collision of the still optically thick e^+e^-–pairs and electromagnetic radiation plasma with the baryonic matter of the remnant of the progenitor star has been again studied by the Rome group and validated by the Livermore Lab codes.[15,16] The further evolution of the sharp pulse of pairs, electromagnetic radiation and baryons (PEMB pulse) has been followed for increasing values of the gamma factor until the condition of transparency is reached.[17]

As this PEMB pulse reaches transparency the proper GRB (P-GRB) is emitted[8] and a pulse of accelerated baryonic matter (the ABM pulse) is injected into the interstellar medium (ISM) giving rise to an afterglow. Thus in GRBs we can distinguish an injector phase and a beam-target phase. The injector phase includes the process of gravitational collapse, the formation of the dyadosphere, as well as the PEM pulse, the engulfment of the baryonic matter of the remnant and the PEMB pulse. The injector phase terminates with the P-GRB emission. The beam-target phase addresses the interaction of the ABM pulse, namely the beam generated during the injection phase, with the ISM as the target. It gives rise to the E-APE (Extended Afterglow Peak Emission) and the decaying part of the afterglow. The existence of both the P-GRB and the E-Ape is shown in Fig. 2, where the fit of observational data relative to GRB 991216 within the EMBH theory is reported.

4. Gravitational Collapse of an Electrically Charged Core: Formation of Dyadosphere

We now turn to the details of the formation of dyadosphere. If the electric field of a charged star core is stable against vacuum polarization during the gravitational collapse,[18] then an enormous amount of pairs can be created by Schwinger mechanism. Moreover the pairs thermalize to a positrons-electrons-photons plasma configuration (see Refs. 6, 19, 20). Such a plasma undergoes a relativistic expansion. The evolution of the system and the details of GRB emission, along the lines summarized in the previous section,

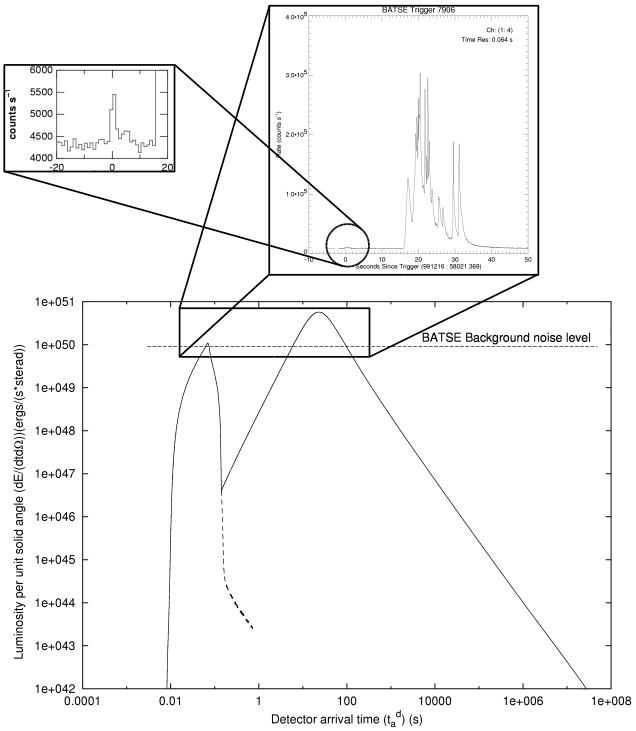

Figure 2. The overall description of the EMBH theory applied to GRB 991216. The BATSE noise threshold is represented and the observations both of the P-GRB and of the E-APE are clearly shown in the subpanels. The continuos line in the picture represents the theoretical prediction of the EMBH model.

were described in Refs. 6–8, 15–17. In the latter papers the time scale of the gravitational collapse is neglected with respect to the hydrodynamic time scale. In this paper we relax this approximation: our main aim is to describe how the plasma expansion occurs *during* the gravitational collapse. In a forthcoming paper[18] we will discuss how the expansion is affected by the strong gravitational field near the horizon of the forming EMBH.

In Refs. 20 and 21 it was suggested that the exact solution of Einstein-Maxwell equations describing the gravitational collapse of a thin charged shell can be used as an analytical model for the gravitational collapse of a charged core. First we briefly review some of the results of Ref. 21. The region of space-time external to the collasping core is Reissner-Nordström

with line element, in Schwarzschild like coordinates (t, r, θ, ϕ),

$$ds^2 = -\alpha^2 dt^2 + \alpha^{-2} dr^2 + r^2 d\Omega^2, \tag{15}$$

where $d\Omega^2 = d\theta^2 + \sin^2\theta d\phi^2$, $\alpha^2 = \alpha^2(r) = 1 - \frac{2M}{r} + \frac{Q^2}{r^2}$, M is the total energy of the core as measured at infinity and Q is its total charge. Let us label with r_0 and t_0 the radial and time-like coordinates of the shell, then the electromagnetic field strength on the surface of the core is $\mathcal{E} = \mathcal{E}(r_0) = \frac{Q}{r_0^2}$ and the equation of core's collapse is[21]

$$\frac{dr_0}{dt_0} = -\frac{\alpha^2(r_0)}{H(r_0)}\sqrt{H^2(r_0) - \alpha^2(r_0)} \tag{16}$$

where $H(r_0) = \frac{M}{M_0} - \frac{M_0^2+Q^2}{2M_0 r_0}$ and M_0 is the rest mass of the shell. The analytical solution of Eq. (16) was found in Ref. 21 in the form

$$t_0 = t_0(r_0). \tag{17}$$

Dyadosphere is formed since the instant $t_{\rm ds} = t_0(r_{\rm ds})$ when $\mathcal{E} = \mathcal{E}_{\rm c}$. In the following we put $t_{\rm ds} = 0$.

5. Formation of e^+e^- Pairs around a Collapsing Charged Core

For $t < t_{\rm ds}$, $\mathcal{E} < \mathcal{E}_{\rm c}$ and the Schwinger process of e^+e^- pairs creation is exponentially suppressed. For $t > t_{\rm ds}$ the Schwinger process becomes relevant and e^+e^- pairs are created. As shown in Refs. 19,20 the pairs created at radius $r_0 < r_{\rm ds}$ oscillate with ultrarelativistic velocity and partially annihilate into photons. At the same time the electric field oscillates around zero and the amplitude of such oscillations decreases in time: in a time of the order of $10^2 - 10^4\ \hbar/m_e c^2$ the electric field is effectively screened to about the critical value; more precisely, the average of the electric field $\mathcal{E}$ over one period of oscillation is 0, but the average of $\mathcal{E}^2$ is of the order of $\mathcal{E}_c^2$. As a result an energy density has been deposited[5] on the pairs and the photons given by

$$\epsilon_0(r_0) = \frac{1}{8\pi}\left[\mathcal{E}^2(r_0) - \mathcal{E}_c^2\right] = \frac{\mathcal{E}_c^2}{8\pi}\left[\left(\frac{r_{\rm ds}}{r_0}\right)^4 - 1\right]. \tag{18}$$

The pairs and the photons are expected to thermalize[6,19,20], to an $e^+e^-\gamma$ plasma equilibrium configuration:

$$n_{e^+} = n_{e^-} \simeq n_\gamma = n_0, \tag{19}$$

(where $n_\bullet$ is the proper number density of particles of type $\bullet$), and reach an average temperature T_0 such that

$$\epsilon\left(T_0\right) \equiv \epsilon_\gamma\left(T_0\right) + \epsilon_{e^+}\left(T_0\right) + \epsilon_{e^-}\left(T_0\right) = \epsilon_0; \tag{20}$$

here $\epsilon_\bullet\left(T\right)$ is the equilibrium proper energy density at temperature T for the species $\bullet$. Then $n_{e^\pm}$ (n_γ) are given by Fermi (Bose) integrals once the temperature T_0 is known.

6. Plasma's Expansion

The highly energetic plasma so formed undergoes a relativistic expansion. As will be shown, the expansion (hydrodynamic) time-scale is much bigger than both the pair creation and the thermalization time-scales, then the process can be described as follows: at any time t_0 it begins to expand a slab of plasma of thickness $\Delta l = \alpha^{-1}\Delta r$ (as measured by static observers) produced at radius $r_0 = r_0\left(t_0\right)$. Δl can be chosen very small in comparison with $r_{\rm ds}$ so that, in particular, the temperature T is approximately constant in the slab. Moreover Δl has to be much bigger than the quantum length scale ($\sim \hbar/m_e c$).

We can follow the expansion of each slab of plasma by using conservation of energy and number of particles. Note that Eqs. (20) and (19) provide initial data for the problem of the expansion. We describe the expansion of a single slab using the following approximations:

(1) the geometry in which the expansion occurs is Reissner-Nordström with line-element given by (15). In particular we will denote by ξ^a the static vector field normalized at unity at spatial infinity, and by $\left\{\Sigma_t\right\}_t$ the family of space-like hypersurfaces orthogonal to ξ^a (t being the Killing time);
(2) the plasma is assumed to be a neutral perfect fluid characterized by proper energy density ϵ, proper pressure p, proper particle (electrons, positrons and photons) number density n and 4−velocity u^a;
(3) at any instant, electrons, positrons and photons in a single slab are assumed to be at thermal equilibrium with temperature T, possibly different from slab to slab. The slabs are uncorrelated in the sense that they do not share energy nor particles. In other words the expansion of each slab is adiabatic; this will be checked *a posteriori* (see also Ref. 16);
(4) the thickness $\Delta l = \alpha^{-1}\Delta r$ of a slab as measured by static observers is constant.

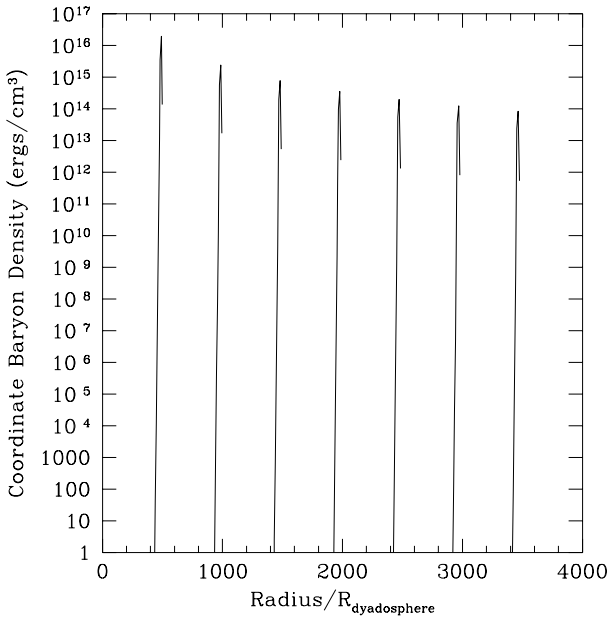

Figure 3. A sequence of snapshots of coordinate baryon energy density is shown from the numerical solution of partial differential continuity equations. This run correspond to an EMBH of mass $M = 10^3 M_\odot$ and charge to mass ratio $\xi \equiv Q/M = 0.1$.

The last approximation is justified by the result in Ref. 16, where it is shown, by numerical integration of the partial differential continuity equations, that the baryon energy density of an expanding slab of plasma enriched with nucleons from the remnant of the progenitor star is localized in a region of constant thickness (see Fig. 3).

Given the above assumptions, both the energy momentum–tensor $T^{ab} = (\epsilon + p)\, u^a u^b + p g^{ab}$ and the electron (positron) –number current $n_e^a = n_e u^a$ are conserved:

$$\nabla_b T^{ab} = 0, \tag{21}$$

$$\nabla_b n_e^b = 0. \tag{22}$$

In particular, using assumption (4) one can reduce the partial differential continuity equations (21) and (22) to ordinary differential equations for the radial coordinate r and the temperature T of the single slab as functions of time (see Ref. 16). The equation of motion of a single slab can be

numerically integrated with initial conditions

$$r\left(t_0\right) = r_0, \tag{23}$$

$$\left.\frac{dr}{dt}\right|_{t=t_0} = 0, \tag{24}$$

$$T\left(t_0\right) = T_0. \tag{25}$$

The overall motion of the plasma is the superposition of motions of single shells. The typical plasma expansion curves are shown in Fig. 4 from the numerical integration of the equations of motion.

The curvature of space–time strongly affects the motion of plasma in the vicinity of the EMBH horizon and in turn the phenomenology of the GRB. We discuss these issues in a forthcoming paper.[18]

References

1. D. Christodoulou and R. Ruffini, *Phys. Rev.* **D4**, 3552 (1971).
2. T. Damour, R. Ruffini, *Phys. Rev. Lett.* **35**, 463 (1975).
3. W. Heisenberg and H. Euler, *Zeits. Phys.* **98**, 714 (1935).
4. J. Schwinger, *Phys. Rev.* **98**, 714 (1951).
5. R. Ruffini, L. Vitagliano, *Phys. Lett. B* **545** (2002) 233.
6. G. Preparata, R. Ruffini and S.-S. Xue, *A&A* **338**, L87 (1998).
7. R. Ruffini, C. L. Bianco, P. Chardonnet, F. Fraschetti and S.-S. Xue, *ApJ* **555**, L107 (2001).
8. R. Ruffini, C. L. Bianco, P. Chardonnet, F. Fraschetti and S.-S. Xue, *ApJ* **555**, L113 (2001).
9. R. Ruffini, C. L. Bianco, P. Chardonnet, F. Fraschetti and S.-S. Xue, *ApJ* **555**, L117 (2001).
10. R. Ruffini and J.R. Wilson, *Phys. Rev.* **D12**, 2959 (1975).
11. V.F. Shvartsman, *Sov. Phys. JETP* **33**, 475 (1970).
12. B. Punsly, *Black Hole Gravitohydromagnetics*, Springer, 2001.
13. P. Goldreich and W.H. Julian, *Ap. J.* **157**, 869 (1969).
14. R. Ruffini, in *Proceedings of the Ninth Marcel Grossmann Meeting on General Relativity*, Gurzadyan V.G., Jantzen R.T. & Ruffini R. editors, World Scientific, Singapore (2002).
15. R. Ruffini, J. D. Salmonson, J. R. Wilson and S.-S. Xue, *A&A* **350**, 334 (1999).
16. R. Ruffini, J. D. Salmonson, J. R. Wilson and S.-S. Xue, *A&A* **359**, 855 (2000).
17. C. L. Bianco, R. Ruffini, S.-S. Xue, *A&A* **368**, 377 (2000).
18. R. Ruffini, L. Vitagliano and S.-S. Xue, (2003) *in preparation.*
19. R. Ruffini, L. Vitagliano and S.-S. Xue, *Phys. Lett.* **B559**, 12 (2003).
20. R. Ruffini, L. Vitagliano and S.-S. Xue, (2003) *in these proceedings.*
21. C. Cherubini, R. Ruffini and L. Vitagliano, *Phys. Lett.* **B545**, 226 (2002).

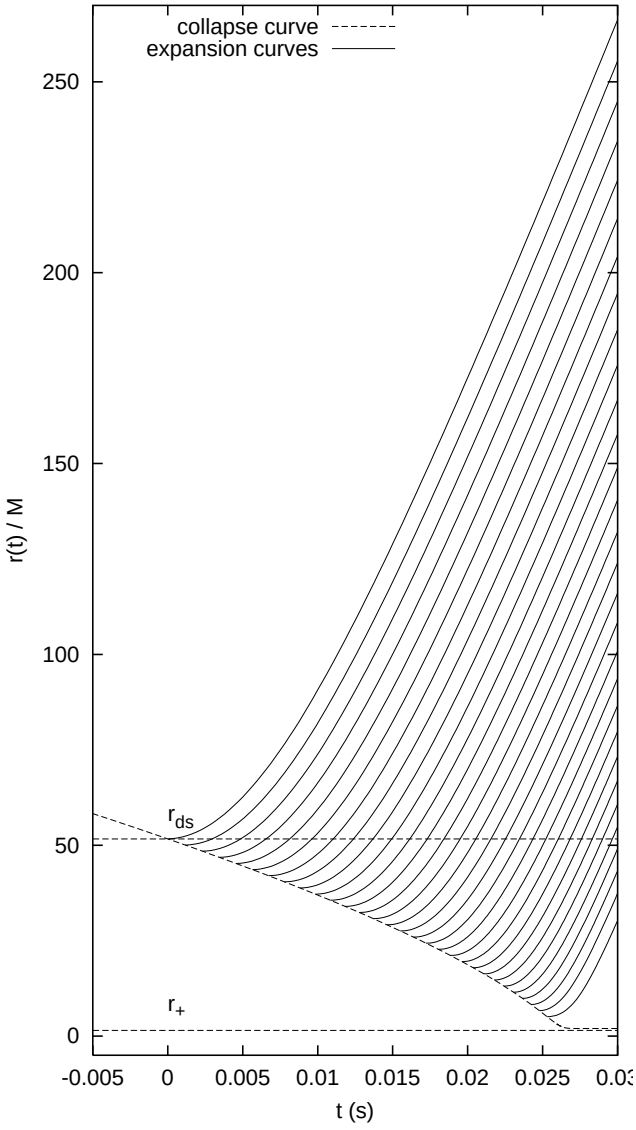

Figure 4. Collapse curve of an elettromagnetic star core (dashed line) as derived by Eq. (16) in the case $M = M_0 = 20M_\odot$, $Q = 0.1M$ and expansion curves of plasma.

GENERALIZED UNCERTAINTY PRINCIPLE AND DARK MATTER

PISIN CHEN

Stanford Linear Accelerator Center
Stanford University, Stanford, CA 94309, USA

There have been proposals that primordial black hole remnants (BHRs) are the dark matter, but the idea is somewhat vague. Recently we argued that the generalized uncertainty principle (GUP) may prevent black holes from evaporating completely, in a similar way that the standard uncertainty principle prevents the hydrogen atom from collapsing. We further noted that the hybrid inflation model provides a plausible mechanism for production of large numbers of small black holes. Combining these we suggested that the dark matter might be composed of Planck-size BHRs. In this paper we briefly review these arguments, and discuss the reheating temperature as a result of black hole evaporation.

1. Introduction

It is by now widely accepted that dark matter (DM) constitutes a substantial fraction of the present critical energy density in the universe. However, the nature of DM remains an open problem. There exist many DM candidates, among which a contending category is weakly interacting massive particles, or WIMPs. It has been suggested that primordial black holes (PBHs)[1,2] are a natural candidate for WIMPs[3]. More recent studies[4] based on the PBH production from the "blue spectrum" of inflation demand that the spectral index $n \sim 1.3$, but this possibility may be ruled out by the recent WMAP experiment[5].

In the standard view of black hole thermodynamics, based on the entropy expression of Bekenstein[6] and the temperature expression of Hawking[7], a small black hole should emit blackbody radiation, thereby becoming lighter and hotter, leading to an explosive end when the mass approaches zero. However Hawking's calculation assumes a classical background metric and ignores the radiation reaction, assumptions which must break down as the black hole becomes very small and light. Thus it does not provide an answer as to whether a small black hole should evaporate

entirely, or leave something else behind, which we refer to as a black hole remnant (BHR).

Numerous calculations of black hole radiation properties have been made from different points of view[8], and some hint at the existence of remnants, but none appears to give a definitive answer. A cogent argument against the existence of BHRs can be made[9]: since there is no evident symmetry or quantum number preventing it, a black hole should radiate entirely away to photons and other ordinary stable particles and vacuum, just like any unstable quantum system.

In a series of recent papers[10,11], a generalized uncertainty principle (GUP)[12,13,14] was invoked to argue the contrary, that the total collapse of a black hole may be prevented by dynamics and not by symmetry, just like the prevention of hydrogen atom from collapse by the uncertainty principle[15]. These arguments then lead to a modified black hole entropy and temperature, and as a consequence the existence of a BHR at around the Planck mass. This notion was then combined with hybrid inflation model[16,17,18,19] and it was shown that primordial BHRs might in principle be the primary source for dark matte[11]. In this paper we briefly reproduce these arguments, and include additional discussion on the reheating temperature as a result of black hole evaporation.

2. Generalized Uncertainty Principle

As a result of string theory[12] or general considerations of quantum mechanics and gravity[13,14], the GUP gives the position uncertainty as

$$\Delta x \geq \frac{\hbar}{\Delta p} + l_p^2 \frac{\Delta p}{\hbar} \ , \tag{1}$$

where $l_p = (G\hbar/c^3)^{1/2} \approx 1.6 \times 10^{-33}$cm is the Planck length. A heuristic derivation may also be made on dimensional grounds. We think of a particle such as an electron being observed by means of a photon with momentum p. The usual Heisenberg argument leads to an electron position uncertainty given by the first term in Eq.(1). But we should add to this a term due to the gravitational interaction of the electron with the photon, and that term must be proportional to G times the photon energy, or Gpc. Since the electron momentum uncertainty Δp will be of order of p, we see that on dimensional grounds the extra term must be of order $G\Delta p/c^3$, as given in Eq.(1). Note that there is no $\hbar$ in the extra term when expressed in this way. The position uncertainty has a minimum value of $\Delta x = 2l_p$, so the Planck distance, l_p, plays the role of a fundamental length.

3. Black Hole Remnant

The characteristic energy E of the emitted photons may be estimated from the uncertainty principle. In the vicinity of the black hole surface there is an intrinsic uncertainty in the position of any particle of about the Schwarzschild radius, $\Delta x \approx r_s$, due to the behavior of its field lines[20] - as well as on dimensional grounds. This leads to a momentum uncertainty

$$\Delta p \approx \frac{\hbar}{\Delta x} = \frac{\hbar}{r_s} = \frac{\hbar c^2}{2GM_{\rm BH}} \ , \tag{2}$$

and hence to an energy uncertainty of $\Delta pc \approx \hbar c^3/2GM_{\rm BH}$. We identify this as the characteristic energy of the emitted photon, and thus as a characteristic temperature; it agrees with the Hawking temperature up to a factor 4π, which we will henceforth include as a "calibration factor" and write (with $k_B = 1$),

$$T_{\rm H} \approx \frac{\hbar c^3}{8\pi GM_{\rm BH}} = \frac{M_p^2 c^2}{8\pi M_{\rm BH}} \ , \tag{3}$$

where $M_p = (\hbar c/G)^{1/2} \approx 1.2 \times 10^{19}$GeV is the Planck mass.

The blackbody energy output rate of BH is given by

$$\dot{x} = \frac{1}{t_{ch}(x_i^3 - 3t/t_{ch})^{2/3}} \ , \tag{4}$$

where $x = M_{\rm BH}/M_p$ and x_i refers to the initial mass of the hole. $t_{ch} = 60(16)^2\pi t_p \approx 4.8 \times 10^4 t_p$ is a characteristic time for BH evaporation, and $t_p = (\hbar G/c^5)^{1/2} \approx 0.54 \times 10^{-43}$sec is the Planck time. The black hole thus evaporates to zero mass in a time given by $t/t_{ch} = x_i^3/3$, and the rate of radiation has an infinite spike at the end of the process.

The momentum uncertainty according to the GUP is

$$\frac{\Delta p}{\hbar} \approx \frac{\Delta x}{2l_p^2}\Big[1 \mp \sqrt{1 - 4l_p^2/(\Delta x)^2}\Big] \ . \tag{5}$$

Therefore the modified black hole temperature becomes

$$T_{\rm GUP} = \frac{M_p c^2}{4\pi} x\Big[1 \mp \sqrt{1 - 1/x^2}\Big] \ . \tag{6}$$

This agrees with the Hawking result for large mass if the negative sign is chosen, whereas the positive sign has no evident physical meaning. Note that the temperature becomes complex and unphysical for mass less than the Planck mass and Schwarzschild radius less than $2l_p$. At the Planck mass the slope is infinite, which corresponds to zero heat capacity of the black hole, and the evaporation comes to a stop.

If there are g species of relativistic particles, then the BH evaporation rate is

$$\dot{x} = -\frac{16g}{t_{ch}} x^6 \Big[1 - \sqrt{1 - 1/x^2}\Big]^4 \ . \tag{7}$$

Thus the hole with an initial mass x_i evaporates to a Planck mass remnant in a time given by

$$\begin{aligned} \tau &= \frac{t_{ch}}{16g}\Big[\frac{8}{3}x_i^3 - 8x_i - \frac{1}{x_i} + \frac{8}{3}(x_i^2-1)^{3/2} - 4\sqrt{x_i^2-1} + 4\cos^{-1}\frac{1}{x_i} + \frac{19}{3}\Big] \\ &\approx \frac{x_i^3}{3g} t_{ch}, \qquad\qquad x_i \gg 1 \ . \end{aligned} \tag{8}$$

The energy output given by Eq.(7) is finite at the end point where $x = 1$, i.e., $dx/dt|_{x=1} = -16g/t_{ch}$, whereas for the Hawking case it is infinite at the endpoint where $x = 0$. The present result thus appears to be more physically reasonable. The evaporation time in the $x_i \gg 1$ limit agrees with the standard Hawking picture.

4. Hybrid Inflation and Black Hole Production

The hybrid inflation, first proposed by A. Linde[16], can naturally induce large number of small PBHs[21]. In the hybrid inflation model two inflaton fields, (ϕ, ψ), are invoked. Governed by the inflation potential, ϕ first executes a "slow-roll" down the potential, and is responsible for the more than 60 e-folds expansion while ψ remains zero. When ϕ eventually reduces to a critical value, it triggers a phase transition that results in a "rapid-fall" of the energy density of the ψ field, which lasts only for a few e-folds, that ends the inflation.

The evolution of the ψ field during the second stage inflation, measured backward from the end, is

$$\psi(N[t]) = \psi_e \exp(-sN[t]) \ , \tag{9}$$

where $N(t) = H_*(t_e - t)$ is the number of e-folds from t to t_e, H_* is the Hubble parameter during inflation, and s is a numerical factor of the order unity.

Quantum fluctuations of ψ induce variations of the starting time of the second stage inflation, i.e., $\delta t = \delta\psi/\dot{\psi}$. This translates into perturbations on the number of e-folds, $\delta N = H_*\delta\psi/\dot{\psi}$, and therefore the curvature contrasts, $\delta\rho/\rho \equiv \delta$. With an initial density contrast $\delta(m) \equiv \delta\rho/\rho|_m$, the probability that a region of mass m becomes a PBH is[23]

$$P(m) \sim \delta(m) e^{-w^2/2\delta^2} \ . \tag{10}$$

Let us assume that the universe had inflated e^{N_c} times during the second stage of inflation. It can be shown[21] that

$$e^{N_c} \sim \left(\frac{2M_p}{sH_*}\right)^{1/s} , \tag{11}$$

and the curvature perturbations reentered the horizon at time

$$t \sim t_h = H_*^{-1} e^{3N_c} . \tag{12}$$

At this time if the density contrast was $\delta \sim 1$, then BHs with size $r_s \sim H_*^{-1} e^{3N_c}$ would form with an initial mass

$$M_{\rm BH}{}_i \simeq \frac{M_p^2}{H_*} e^{3N_c} . \tag{13}$$

Following the numerical example given in Ref.21, we let $H_* \sim 5 \times 10^{13}$ GeV and $s \sim 3$. Then the density contrast can be shown to be $\delta \sim 1/7$, and the fraction of matter in the BH is thus $P(m) \sim 10^{-2}$. From Eq.(11), $e^{N_c} \sim 54$. So the total number of e-folds is $N_c \sim 4$. The black holes were produced at the moment $t_h \sim 2 \times 10^{-33}$ sec, and had a typical mass $M_{\rm BH}{}_i \sim 4 \times 10^{10} M_p$. Let $g \sim 100$. Then the time it took for the BHs to reduce to remnants, according to Eq.(8), is

$$\tau \sim \frac{x_i^3}{3g} t_{ch} \sim 5 \times 10^{-10} \text{sec} . \tag{14}$$

The "black hole epoch" thus ended in time for baryogenesis and other subsequent epochs in the standard cosmology. As suggested in Ref.21, such a post-inflation PBH evaporation provides an interesting mechanism for reheating.

5. Black Hole Remnants as Dark Matter

This process also provides a natural way to create cold dark matter. Although in our example $P(m) \sim 10^{-2}$, PBHs would soon dominate the energy density by the time $t \sim P(m)^{-2} t_h \sim 2 \times 10^{-29}$s, because the original relativistic particles would be diluted much faster than non-relativistic PBHs. By the time $t \sim \tau$, all the initial BH mass (x_i) had turned into radiation except one unit of M_p preserved by each BHR. As BH evaporation rate rises sharply towards the end, the universe at $t \sim \tau$ was dominated by the BH evaporated radiation.

Roughly, $\Omega_{{\rm BHR},\tau} \sim 1/x_i$ and $\Omega_{\gamma,\tau} \sim 1$ at $t \sim \tau$, and since the universe resumed its standard evolution after the black hole epoch ($t > \tau$), we find

the density parameter for the BHR at present to be

$$\Omega_{\rm BHR,0} \sim \Big(\frac{t_{eq}}{\tau}\Big)^{1/2}\Big(\frac{t_0}{t_{eq}}\Big)^{2/3}\frac{1}{x_i}\Omega_{\gamma,0}\ , \tag{15}$$

where $t_0 \sim 4\times 10^{17}$s is the present time, and t_{eq} is the time when the density contributions from radiation and matter were equal. It is clear from our construction that $(t_{eq}/\tau)^{1/2} \sim x_i$. So $t_{eq} \sim 10^{12}$ sec, which is close to what the standard cosmology assumes, and Eq.(15) is reduced to a simple and interesting relationship:

$$\Omega_{\rm BHR,0} \sim \Big(\frac{t_0}{t_{eq}}\Big)^{2/3}\Omega_{\gamma,0} \sim 10^4\Omega_{\gamma,0}\ . \tag{16}$$

In the present epoch, $\Omega_{\gamma,0} \sim 10^{-4}$. So we find $\Omega_{\rm BHR,0} \sim \mathcal{O}(1)$, about the right amount for dark matter!

6. Black Hole Epoch and Reheating Temperature

As discussed above, shortly after PBHs were produced the density of the universe was dominated by the BHs. Eventually the universe was reheated through their continuous evaporation. To simplify the discussion we ignore BH accretions of the radiation as well as BH mergers. Then under Hubble expansion the effective reheating temperature at the end of the black hole epoch, or $t \sim \tau$, can be expressed as

$$T_r(\tau[x_i]) = \frac{1}{x_i - 1}\int_1^{x_i} dx T_{\rm GUP}(x)\frac{a(t[x])}{a(\tau[x_i])}\ , \tag{17}$$

where $a(t)$ is the scale factor. Since $x_i \gg 1$, the evaporation only became effective near the late times during this black hole epoch, when the energy density was dominated by the BH radiation. As a further approximation we assume radiation dominance throughout the BH epoch so that $a(t) \propto t^{1/2}$. Expressing t in terms of x using Eq.(7), we find

$$T_r(\tau[x_i]) \approx \frac{M_p c^2}{16\pi(x_i-1)}\Big[2\log(2x_i) - 1\Big] + \mathcal{O}\Big(\frac{1}{x_i^3}\Big)\ . \tag{18}$$

In our model $x_i \sim 4\times 10^{10}$. So $T_r(\tau[x_i]) \sim 1.3\times 10^8$ GeV, which is sufficiently lower than the Planck and the GUT scales, but higher than the baryogenesis scale.

7. Acknowledgements

I deeply appreciate my early collaborations and fruitful discussions with Ronald J. Adler. I also thank S. Dimopoulos, A. Green, A. Linde, M. Shmakova, and K. Thompson for helpful discussions. This work is supported by the Department of Energy under Contract No. DE-AC03-76SF00515.

References

1. Ya. B. Zeldovich and I. D. Novikov, *Sov. Astron.* **10**, 602 (1966).
2. S. W. Hawking, *Mon. Not. R. Astron. Soc.* **152**, 75 (1971).
3. J. H. MacGibbon, *Nature* **329**, 308 (1987); J. D. Barrow, E. J. Copeland, A. R. Liddle, *Phys. Rev. D* **46**, 645 (1992).
4. B. J. Carr, J. H. Gilbert, and J. E. Lidsey, *Phys. Rev. D* **50**, 4853 (1994); J. E. Lidsey, B. J. Carr, and J. H. Gilbert, arXiv: astro-ph/9406028.
5. D. N. Spergel *et al.*, arXiv: astrop-ph/0302209, submitted to *Astrophys. J.*
6. J. D. Bekenstein, *Phys. Rev. D* **7**, 2333 (1973); *Lett. al Nuovo Cimento* **4**, 737 (1972).
7. S. W. Hawking, *Comm. Math. Phys.* **43**, 199 (1974).
8. See, for example, M. K. Parikh and F. Wilczek, *Phys. Rev. Lett.* **85**, 5042 (2000), and references therein.
9. L. Susskind, private communications (2001); *J. Math. Phys.* **36**, 6377 (1995).
10. R. J. Adler, P. Chen, and D. Santiago, *Gen. Rel. Grav.* **33 (12)**, 2101 (2001).
11. P. Chen, arXiv: astro-ph/0303349; submitted to *Phys. Rev. Lett.*
12. G. Veneziano, *Europhys. Lett.* **2**, 199 (1986); E. Witten, *Phys. Today*, Apr. 24 (1996).
13. R. J. Adler and D. I. Santiago, *Mod. Phys. Lett.* **A14**, 1371 (1999).
14. M. Maggiore, *Phys. Lett.* **B304**, 65 (1993); F. Scardigli, *Phys. Lett.* **B452**, 39 (1999).
15. R. Shankar, *Principles of Quantum Mechanics*, 2nd ed. (Plenum, 1994).
16. A. Linde, *Phys. Lett.* **B259**, 38 (1991); *Phys. Rev. D* **49**, 748 (1994).
17. E. J. Copeland, A. R. Liddle, D. H. Lyth, E. D. Stewart, and D. Wands, *Phys. Rev. D* **49**, 6410 (1994).
18. L. Randall, M. Soljacic, and A. H. Guth, *Nucl. Phys.* **472**, 408 (1996).
19. For a recent review, see D. H. Lyth and A. Riotto, *Phys. Rep.* **314**, 1 (1999); A. Linde, *Phys. Rep.* **333-334**, 575 (2000).
20. R. S. Hanni and R. Ruffini, in *Black Holes*, eds. C. DeWitt and B. S. DeWitt, R57 (Gordon and Breach, 1973); R. J. Adler and T. K. Das, *Phys. Rev. D* **14**, 2474 (1976).
21. J. Garcia-Bellido, A. Linde, and D. Wands, *Phys. Rev. D* **54**, 6040 (1996).
22. A. R. Liddle and D. H. Lyth, *Phys. Rep.* **231**, 1 (1993).
23. B. J. Carr and S. W. Hawking, *Mon. Not. R. Astron. Soc.* **168**, 399 (1974); B. J. Carr, *Astrophys. J.* **201**, 1 (1975).

CP VIOLATION OF THE EARLY UNIVERSE AND THE MASS SCALE OF HEAVY MAJORANA NEUTRINOS

TAKUYA MOROZUMI *

Graduate School of Science, Hiroshima University,
1-3-1, Kagami-yama, Higashi-Hiroshima, Japan 739-8526
E-mail: morozumi@hiroshima-u.ac.jp

Recent study on CP violation of leptogenesis is briefly discussed with emphasis on CP violation of the seesaw model and Majorana mass scale bound from the leptogesis

1. Introduction

Where did anti-matter disappear ? The ratio of baryon number density and photon number density of our universe ; $n_B/n_\gamma \simeq 10^{-9\sim-10}$ The photon number density of our universe can be estimated with $3K$ background black body radiation. Particle physics model for generating baryon number asymmetry must account for this number. There are famous Sakharov's [1] three conditions for baryogenesis.

- $B-L$ violation at high energy
- CP violation
- Thermal non-equilibrium

The first condition is modified from the original one after we know the sum of the baryon and lepton number is not conserved due to anomaly. The washing out effect is significant when the temperture of our universe was higher than $T\rangle$ 100(GeV) $\sim$ 1(TeV). Because of this effect, a simple baryogenesis scenario based on GUT model does not work and primordial $B+L$ generated before the anomolous effect is frozen will be washed out as $(B+L)_{prim.}\exp[-\frac{t}{\tau}]$. By considering the chemical equilibrium condition

*Work partially supported by grant no. 13640290 from the ministry of education, science, and culture of japan

for various processes, the present baryon number becomes proportional to $B-L$.

$$B_{now} = \frac{8N_g + 4N_H}{22N_g + 13N_H}(B-L)_{primordial} \simeq \frac{1}{3}(B-L)_{prim.}. \quad (1)$$

Therefore, in order to generate the present baryon number, $B-L$ must be broken at high energy. This may be a guide for construction of the models for baryogenesis as well as new physics model beyond the standard model. In the seesaw models, the heavy Majorana neutrinos are introduced and the primordial lepton number can be produced. Moreover,baryons are stable in zero temperature and primordial $B-L$ is generated through leptogenesis [2].

$$(B-L)_{prim.} = -L_{prim.} \quad (2)$$

Therefore the present baryon number is determined from $L_{prim.}$

$$B_{now} \simeq -\frac{1}{3}L_{prim.}. \quad (3)$$

Next we come to CP violation. The standard model can not account for the baryogenesis, though it is good at explaining the present measured CP violation phenomena observed in K and B meson system. We need some new source of CP violation other than Kobayashi Maskawa phase. On the otherhand, in the seesaw models =(standard model + heavy Majorana neutrinos), there are CP violation phases and some of them are related to leptogenesis. $B-L$ can be broken and the other two conditions (CP violation and thermal non-equilibrium) may be satisfied. In this talk, I will explain:

- CP violation of the seesaw models
- How well can we predict the baryon number asymmetry based on a specific seesaw model ?
- How can we test the model in the laboratory experiments ?

Let's start how three conditions of the baryogensis are satisfied in the seesaw models. By adding N heavy Majorana neutrinos N_R to the standard three generation left-handed neutrinos $\nu_{Li}(i = 1 \sim 3)$, the lepton sector of the seesaw model is given by the following Lagrangian:

$$\begin{aligned} \mathrm{L} = & -\overline{\psi_{Li}} y_{D\,ij} \tilde{\phi} N_{Rj} - \overline{\psi_{Li}} y_{l\,ij} \phi l_{Rj} \\ & - \frac{1}{2} \overline{(N_{Ri})^c} M_{Rij} N_{Rj} + h.c., \end{aligned} \tag{4}$$

where ${\psi^T}_{Li} = (\nu_{Li}, l_{Li})$. Without loss of generality, we can choose a basis in which both charged lepton and Majorana mass terms are real diagonal, i.e., $M_{Rij} = M_{Ri}\delta_{ij}$ and $y_{lij} = y_{li}\delta_{ij}$. In the broken phase of Higgs potential,

$$L = -[\overline{\nu_L} m_D N_R + \frac{1}{2} \overline{(N_R)^c} M_R N_R + \overline{l_L} m_l l_R] - h.c. \tag{5}$$

where $l = e, \mu, \tau$ are charged leptons.

$$\begin{aligned} m_D &= \frac{v}{\sqrt{2}} y_D \\ m_l &= \frac{v}{\sqrt{2}} y_l \end{aligned} \tag{6}$$

In the basis, the charged lepton mass matrix and Majorana mass matix are given as; $m_l = diag.(m_e, m_\mu, m_\tau)$. and $M_R = diag.(M_1, M_2, ...M_N)$. The lepton number is broken because it is related to the symmetry with respect to the phase rotation for charged leptons (both left and right) and left-handed neutrinos. If there were not the Majorana mass term M_R, we can define lepton number as the vectorial phase rotation for neutrinos with both chiralties, i.e., ν_L and N_R. However, the Majorana mass term prevents us from defining the conserved lepton number. Because Majorana neutrinos N_R do not have lepton number, the lepton number is explicitly broken in the Dirac mass term m_D The primordial lepton number is produced form N_R decays due to the Dirac mass term m_D. In the basis which we adopt, $m_D(y_D)$ is a general complex $(3, N)$ matrix. How many independent CP violating phases in m_D ? $Im(m_D) \neq 0$ implies CP violation;

$$CP[\overline{\nu_L} m_D N_R] CP^{-1} = \overline{N_R} m_D^T \nu_L. \tag{7}$$

$$m_D = \begin{pmatrix} m_{11}\ m_{12}\ ..\ m_{1N} \\ m_{21}\ m_{22}\ ..\ m_{2N} \\ m_{31}\ m_{32}\ ..\ m_{3N} \end{pmatrix} \tag{8}$$

From $3N$ imaginary parts in m_D, there are $3N-3$ independent CP phases. -3 comes out because we can still make the phase rotation as:

$$\begin{aligned} l_i &\to \exp(i\theta_i) l_i \\ \nu_{Li} &\to \exp(i\theta_i) \nu_{Li}, \end{aligned} \tag{9}$$

and accordingly three CP phases are absorbed into the field's redefinition.

$$m_D \to \begin{pmatrix} \exp(i\theta_1) & 0 & 0 \\ 0 & \exp(i\theta_2) & 0 \\ 0 & 0 & \exp(i\theta_3) \end{pmatrix} \begin{pmatrix} m_{11}\ m_{12}\ ..\ m_{1N} \\ m_{21}\ m_{22}\ ..\ m_{2N} \\ m_{31}\ m_{32}\ ..\ m_{3N} \end{pmatrix}, \quad (10)$$

$3N-3$ phases become physical CP violating phases. Depending on the number of Majorana neutrinos, we have
$N=1$ (no CP violation)
$N=2$ three CP violating phases
$N=3$ six CP violating phases
We note the following decomposition is always possible:

$$\begin{pmatrix} m_{11}\ m_{12}\ ..\ m_{1N} \\ m_{21}\ m_{22}\ ..\ m_{2N} \\ m_{31}\ m_{32}\ ..\ m_{3N} \end{pmatrix} = U_L \begin{pmatrix} m_1 & 0 & .. & 0 \\ 0 & m_2 & .. & 0 \\ 0 & 0 & m_3 & 0 \end{pmatrix} V_R, \\ = U_L m V_R \quad (11)$$

where $U_L(3,3)$ Unitary: $V_R(N,N)$ Unitary matrices. Seesaw model is an attractive model since it may explain the smallness of the neutrino masses compared with other charged fermions. From the hypothetical heavy Majorana neutrinos' exchanged Feynman diagram, and small Majorana neutrino mass terms $\overline{\nu_{Li}} {m_{eff}}_{ij} {\nu_{Lj}}^c$ are generated:

$$m_{eff} = -m_D \frac{1}{M_R} m_D^T. \quad (12)$$

In the symmetric universe of the early universe, heavy Majorana neutrinos can decay into Higgs and lepton pairs. The relevant interaction terms are:

$$L = y_{D\,ij} \bar{l_{Li}} N_{Rj} \phi^- \\ -y_{D\,ij} \bar{\nu_{Li}} N_{Rj} \phi^0 \quad (13)$$

$$N \leftrightarrow l^{\mp} \phi^{\pm} \quad (14)$$

When the temprature cooled down compared with $M \rangle T$, the inverse deca is suppressed and the production of lepton and higgs particle occurs:

$$N \to l^{\mp} \phi^{\pm} \quad (15)$$

If CP symmetry is broken, the primordial lepton number $L_{prim.}$ is proportional to CP asymmetry. occur as:

$$\epsilon_1 = \frac{\Gamma[N \to l^- \phi^+] - \Gamma[N \to l^+ \phi^-]}{\Gamma[N \to l^- \phi^+] + \Gamma[N \to l^+ \phi^-]} \quad (16)$$

The lepton number is converted into baryon number in anomolous process. The mechanism generating $L_{primordial}$ is similar to "Direct CP violation" in K and B physics. $\Gamma[B^+ \to K^+\pi^0] - \Gamma[B^- \to K^-\pi^0] \sim Im(a_0 {a_1}^*)\sin(\delta_0 - \delta_1)$

$$\begin{aligned} Amp.(B^+ \to K^+\pi^0) &= a_0 exp(i\delta_0) + a_1 exp(i\delta_1) \\ Amp.(B^- \to K^-\pi^0) &= a_0^* exp(i\delta_0) + a_1^* exp(i\delta_1) \end{aligned} \tag{17}$$

where δ is strong phase. In the standard model, CP violation $Im(a_0 {a_1}^*)$ is determined by a single Kobayashi Maskawa phase.
In the expanding universe,e.g.,in the Friedmann Universe: $ds^2 = dt^2 - a(t)^2(dx^2 + dy^2 + dz^2)$, time evolution of the number density of heavy Majorana neutrino $n(t)$ and lepton number density $L(t)$.

$$\begin{aligned} &\frac{dn(t)}{dt} + 3Hn(t) = -\Gamma_N(n - n_{eq.}). \\ &\frac{dL(t)}{dt} + 3HL(t) = (\Gamma[N \to l^-\phi^+] - \Gamma[N \to l^+\phi^-])(n - n_{eq}), \end{aligned} \tag{18}$$

where we omit the temperture dependence of the decay width Γ_N and the terms which is related to washingout effects of the lepton number. Using the relation between the temperture and time in radiation dominated era, $t = \sqrt{\frac{45}{16\pi^3 g^*}}\frac{M_{pl}}{T^2}$, we can solve the evolution equation. We must set the initial condition such as at $T = 10^{16}$(GeV),

$$n = n_{eq}, L = 0$$

The result depends on Γ_N, " Direct CP violation" (ϵ_1) $\Gamma[N \to l^-\phi^+] - \Gamma[N \to l^+\phi^-]$ and expansion rate of the universe (Hubble) $H = \frac{\dot{a}}{a}$. $L_{primodial}$ is efficiently produced if the non-equilibrium condition is satisfied.

$$H \rangle \Gamma_N \tag{19}$$

If this is the case, we may obtain large deviation of n from the thermal equilibrium density n_{eq}.
Now we briefly discuss how we can test the leptogenesis in the laboratory experiments. CP violation of neutrino oscillations is a place to see the CP violation related to leptogenesis.

$$P(\nu_\mu \to \nu_e) - P(\bar{\nu_\mu} \to \bar{\nu_e}) = 4J[\sin(\frac{\Delta m_{12}^2 L}{2E}) + \sin(\frac{\Delta m_{23}^2 L}{2E}) + \sin(\frac{\Delta m_{31}^2 L}{2E})].$$

$$J = Im\left(U_{e1}U_{\mu 1}^* U_{e2}^* U_{\mu 2}\right).$$

The lepton mixing matrix U can be obtained from the diagonalization of m_{eff}. We may expect the correlation between CP violation for leptogenesis and CP violation in neutrino oscillation because both may come from imaginary part in m_D.

$$L_{prim.} \sim Im(m_D^\dagger m_D)^2_{ij}, (i \neq j): \quad -U^\dagger m_D \frac{1}{M} {m_D}^T U^* = \begin{pmatrix} n_1 & 0 & 0 \\ 0 & n_2 & 0 \\ 0 & 0 & n_3 \end{pmatrix}$$

$L \leftarrow Im(m_D) \rightarrow Im(U) \rightarrow J$.
Both J and L are related to CP phases in m_D. However, the correlaton may not be manifest in the most general case. This is because, there are many CP violating phases in seesaw model and there are no one to one correspondance between CP violation of high energy and low energy. To start with, we first count the number independent parameters.

model	(3,N)	(3,3)	(3,2)
M	N	3	2
$Re(m_D)$	3 N	9	6
$Im(m_D)$	3N-3	6(3)	3 (1)
total	7N-3	18	11

Even in the minimal seesaw model ($N = 2$), there are 11 parameters which are more than low energy observables 7.

mixing angles	$2 + \|U_{e3}\|$
Δm^2	2 (solar, atm.)
neutrinoless double β	$\|(m_{eff})_{ee}\|$
CP violation in oscillation	1 (ΔP)
total	7

We adopt four high energy physical quantities as input. For example, Heavy Majorana masses (M_1, M_2) and their decay widths Γ_1, Γ_2 can be chosen. We can fix 11 parameters of the minimal seesaw (3,2) model.
7 (low energy observables)+ 4 (high energy observables)=11. m_D in (3,2) model can be parametrized as [3]:

$$\begin{aligned} m_D &= \begin{pmatrix} m_{11} & m_{12} \\ m_{21} & m_{22} \\ m_{31} & m_{32} \end{pmatrix} = U_L \begin{pmatrix} 0 & 0 \\ m_2 & 0 \\ 0 & m_3 \end{pmatrix} V_R \\ &= U_L m V_R. \end{aligned} \tag{20}$$

U_L: 3×3 , V_R:2×2 unitary matrix.

$$U_L = O(\theta_{L23})U(\theta_{L13}, \delta_L)O(\theta_{L12})diag.(1, \exp[-i\frac{\gamma_L}{2}], \exp[i\frac{\gamma_L}{2}])$$
$$V_R = \begin{pmatrix} c_R & s_R \\ -s_R & c_R \end{pmatrix} \begin{pmatrix} \exp(-i\frac{\gamma_R}{2}) & 0 \\ 0 & \exp(i\frac{\gamma_R}{2}) \end{pmatrix}.$$

Among 3 CP phases$(\delta_L, \gamma_L, \gamma_R)$ γ_R is related to leptogenesis.

$$\begin{aligned} \epsilon_1 &\sim \Gamma[N_1 \to l^- \phi^+] - \Gamma[N_1 \to l^+ \phi^-] \sim -Im[(m_D^\dagger m_D)_{12}^2] \\ &\sim -({m_3}^2 - {m_2}^2)^2 {s_R}^2 {c_R}^2 \sin 2\gamma_R. \end{aligned}$$

By using the light neutrino mass eigenvalue equation $det.(m_{eff} m_{eff}^\dagger - n^2) = 0$, we can extract the leptogenesis phase as;

$$\cos 2\gamma_R = \frac{n_2^2 + n_3^2 - x_1^2 - x_2^2}{2(x_1 x_2 - n_2 n_3)}, \tag{21}$$

where, $x_i = \frac{({m_D}^\dagger m_D)_{ii}}{M_i}$ and $\left(\frac{V}{M_i}\right)^2$ with $V = \sqrt{4\pi}v$ Combining the above formulae, we get:

$$\epsilon_1 = -\frac{3M_1}{4x_1 V^2} \sqrt{((n_-)^2 - (x_-)^2)\,((x_+)^2 - (n_+)^2)}, \tag{22}$$

where $n_\pm = n_3 \pm n_2$ and $x_\pm = x_1 \pm x_2$. The lower bound of M_1 can obtained because lepton number asymmetry ϵ_1 is proportional to M_1. In an analysis [3], we showed $M_1 \rangle 1 \times 10^{11}$ GeV.

References

1. Sakharov, *Pisma Zh.Eksp.Teor.Fiz.* **5**, 32-35 (1967).
2. M. Fukugita and T. Yanagida *Phys.Lett.* **B174**, 45 (1986).
3. T. Endoh, S. Kaneko, S. K. Kang, T. Morozumi, M. Tanimoto, Phys.Rev.Lett.**89**:231601,2002

ULTRA-HIGH ENERGY COSMIC RAYS AND VIOLATION OF LORENTZ INVARIANCE INDUCED BY EXTERNAL FIELD

HUMITAKA SATO

Department of Physics, Konan University
Okamoto, Kobe658-8501, JAPAN
E-mail: satoh@konan-u.ac.jp

High-energy end of the cosmic-ray spectrum has provided us to check a validity of the Lorentz Invariance and the Relativity principle, through the observation of the so-called GZK cut-off. It is claimed in this report that the comoving reference frame in the expanding universe might define the preferable inertia frame, in contradiction to the relativity principle. If the present universe has been permeated by tensor fields in a manner like it has been done by Higgs scalar field , the limiting particle velocity of each species splits to different values depending on the coupling coefficients to these external fields.

1. Historical Introduction

Energy spectrum of the cosmic rays extends by a power-law over more than ten decimal, decreasing in a power-law like $E^{-\gamma}$ with energy E and $\gamma \sim 2.5$. Then a natural question is whether the high-energy end in the energy spectrum does exist or not. In 1966, a very clear-cut prediction was presented, which introduced a definite upper-limit in the power-low energy spectrum, which is called now as GZK(Greisen-Zatepin-Kuzmin) cut-off.[1]

This cut-off prediction was invoked by the discovery of "3K radiation" in 1965, which is now called as CMB(cosmic microwave background). Although CMB was observed just on the earth, CMB was supposed to fill up in the whole cosmic space uniformly, even in the extra-galactic space, as the relics of "hot" big-bang. Therefore it became crucial to check the presence of CMB in the extra-galactic space, in order to settle the big debates between the steady state cosmology and Gamow's hot big-bang cosmology. As an advocator of the steady-state cosmology, Fred Hoyle tried hard to present two types of counter arguments, one was about exotic interstellar dusts which masks the extragalactic view in this wave-band and another one was

how much degree the high-energy cosmic radiations(γ-rays,X-rays,electron-positron,etc) are masked by the extra-galactic presence of CMB. Hoyle's motivation of the latter argument was to point out a contradiction of the hot big-bang cosmology but this argument had created a rich implication of CMB toward the high-energy cosmic radiations, including the GZK cut-off.

Since then, the GZK cut-off energy of about 10^{20}eV became an experimental target for the cosmic-ray physicist. Observation of the EAS(extensive air shower) started also in Japan and EAS-group led by K. Suga constructed the array of detectors in the suburb of Tokyo, a dense array in the site of the research institute and several remote stations at the sites of elementary school, the city office and so on. It was the autumn of 1971 when they announced that their detector had catched a huge EAS with energy over GZK cut-off in 1970. In following February, the workshop was organized in order to discuss this puzzling EAS event.

At the workshop, I gave a talk by the title "Very high-energy cosmic-rays and the limitation of relativity principle".[2] If the high-energy end does not exist contrary to the GZK cut-off prediction, we could enumerate three possible ways of resolution, 1) "3K"radiation is local, 2)source of such cosmic ray is local(within mean-free-path), 3) cosmic ray is not proton but some exotic primary. At the workshop of 1972, I added the fourth possibility 4) violation of relativity principle. Later the paper was written by the title "Ultra-high Energy cosmic rays, Hot universe and Absolute reference frame".[3]

Although the energy estimation of this 1970-event was not accurate enough to claim the existence of super-GZK cut-off cosmic rays, this event promoted very much the effort toward a construction of bigger array in Akeno. This new big array, AGASA, finally presented more assured experimental evidences of super-GZK cut-off after 1997. Experimental data suggesting super-GZK cosmic rays given by AGASA[4] as well as FlysEyes gave a great impact towards the bigger new observational projects such as Auger, EUSO[5] , and others.

In such trend of research, an implication of the super-GZK cosmic ray has been discussed widely. In different from the situation in 1972, the first possible way(local "3K") has been eliminated and other three possibilities have been discussed; a) exotic local source such as cosmic string, mini black hole,etc.(so-called top-down scenario), b)exotic primaries such as neutrinos, neutrino with Z-burst in Galactic halo, etc, and finally c)violation of Lorentz invariance.

Even for the last possibility, there are variety of arguments.[6,?,8,9] In this

report, a specific toy model of violation of Lorentz invariance is proposed and an extension of Lorentz invariance with non-unique limiting velocities is discussed.

2. Comoving Frame in the Expanding Universe and Relativity Principle

In the expanding universe, we can clearly identify preferential inertia frames: (1)rest frame of baryon matter, (2)rest frame of astronomical objects, (3)frame in which CMB is isotropic, (4) frame in which the Hubble flow is observed isotropic. Furthermore, these four frames are approximately identical within a relative velocity difference of several hundreds km/sec. These inertia frames have a concrete physical effect when we understand the structure formation in the expanding universe.[9]

According to recent theoretical view on the early universe, these cosmological frames are considered to have the same physical origin; spontaneous selection of the inertia frame in which the primordial black body radiation is isotropic via a reheating at Inflation. But even in the vacuum universe without material substance, the creation of the expanding universe itself is the browken state of Lorentz invariance. That is a formation of comoving frame perpendicular to the time direction. We call this cosmological and comoving frame as C-frame.

In spite of a lucid presence of the C-frame, however, the Lorentz invariance is supposed to hold in any local physical phenomena. The relativity principle does not respect this lucid presence. Whatever lucid this presence is, it has no physical effect. That is the spirit of the relativity since Galileo. In the derivation of GZK cut-off, the relativity principle is used as usual but its situation is very special because the Lorentz factor relative to the C-frame is as large as $\gamma \sim 10^{11}$, which is far beyond the Lorentz factor in the particles the accelerators of about $\gamma \sim 10^5$.

Here we should not confuse the two meanings of "high energy". One is an invariant energy(or center of mass energy) defined such as ,

$$p^\mu p_\mu = E^2 - P^2 = Q^2$$

,where p^μ is total four momentum of the system. Another one is energy relative to a specific reference frame and it will be defined in the following manner as

$$N^\mu p_\mu = 1 \cdot E - 0 \cdot P = E$$

, where N^μ is a four vector specifing the frame. For the C-frame, the component is given as $N^\mu(1,0,0,0)$ in the C-frame. The Relativity principle claims that the cross section of collision, σ, does depend solely on Q but does not depend on $N^\mu p_\mu$, such as $\sigma(Q)$ but not as $\sigma(Q, N^\mu p_\mu)$. In our early paper[3], the cut-off function in the momentum space was assumed to depend on $N^\mu p_\mu$ and the cross section involved to the GZK was altered not to give the cut-off of the spectrum.

In the discussion of GZK cut-off, Q is $\sim 10^{8.5}$eV, which is rather low energy in high-energy physics, but, $N^\mu p_\mu \sim 10^{20}$eV is extraordinarily large even in high-energy physics. The uniqueness of the GZK cut-off lies on the largeness of $N^\mu p_\mu$, but not on the so-called energy frontier of the high-energy physics, e.g., Energy frontier for supersymmetry, GUT, Planck scale, etc., those are talking about large Q but not on the largeness of $N^\mu p_\mu$.

3. A Toy Model of Lorentz-Invariance Violation

Consider the following Lagrangian for a Dirac particle A,

$$L_A = \frac{i}{2}\bar{\psi}\gamma_\mu\partial^\mu\psi - \alpha_A\phi\bar{\psi}\psi + \frac{i}{2}g_A F_{\mu\nu}\bar{\psi}\gamma^\mu\partial^\nu\psi,$$

where ψ is the Dirac field of A, ϕ is Higgs scalar field with coupling coefficient α_A and $F_{\mu\nu}$ is a tensor field with coupling coefficient g_A.The first term in the right hand side is kinetic term and the second one is the Yukawa coupling term which creates mass by Higgs mechanism. In this Lagrangian, the dynamical parts of ϕ and $F^{\mu\nu}$ has been omitted and ϕ and $F^{\mu\nu}$ are both taken as an external field. They are un-removable given field in the present state of universe. Non-zero value of $<\phi>$ gives the mass, $m_A = \alpha_A <\phi>$, to this Dirac particle.

Next we assume that some component of the tensor field has got some non-zero value as followings,

$$<F^{00}> = B \neq 0 \ \text{ and } <F^{\mu\nu}> = 0 \ \text{ for other components.}$$

B is supposed to be constant in space and time but can be slowly changing with cosmological spacetime scale. Then the dispersion relation for plain wave is given as[10]

$$p^\mu p_\mu - m_A^2 c^2 = -2g_A B(E/c)^2$$

, where only the first order terms of B has been retained and the higher term of B has been neglected.

This relation is rewritten by denoting the three momentum as p as

$$(1 + g_A B)(E/c)^2 = p^2 + m_A^2 c^2,$$

where c is the universal constant introduced at the definition of the space-time length by space length and time length.

Renormalizing the velocity and mass as followings

$$c_A^2 = \frac{c^2}{1 + g_A B} \quad \text{and} \quad m_{AB}^2 = (1 + g_A B) m_A^2,$$

the conventional energy-momentum relation is resumed

$$E^2 = p^2 c_A^2 + m_{AB}^2 c_A^4.$$

but now c_A is depending on particle species through g_A, that is, the limiting velocity, velocity in the limit of $E \to \infty$, is depending on the particle species.

Here we remark some difference between the Higgs scalar ϕ and the tensor external field $F^{\mu\nu}$. Different from a scalar field , we have adopted the C-frame as the preferential frame and the above energy-momentum relation holds only in the C-frame. If we modified the Lorentz transformation with psudo-Lorentz factor

$$\gamma_A = \frac{1}{\sqrt{1 - \left(\frac{v}{c_A}\right)^2}} \quad \text{instead of} \quad \gamma = \frac{1}{\sqrt{1 - \left(\frac{v}{c}\right)^2}},$$

the above relation keeps its form. However the Lorentz invariance apparently breaks down if we consider a system consisting of pariticles of different species.

The perturbative super string theory has suggested an existence of various hidden fields such as the above tensor field.[11] If we assume a vector field A_μ in stead of $F_{\mu\nu}$ as the external field, the Lagrangian is written,[13]

$$L_A = \frac{i}{2} \bar{\psi} \gamma_\mu \partial^\mu \psi - m_A \bar{\psi} \psi - f_A V_\mu \bar{\psi} \gamma^\mu \psi.$$

, where the Higgs term is now rewritten by the mass term. Here we assume

$$< V_0 >= V \neq 0 \quad \text{and} \quad < V_\mu = 0 > \quad \text{for all other components}$$

and the the dispersion relation becomes like

$$E^2 - p^2 c^2 - m_A^2 c^4 = -2 f_A V E.$$

If we define as

$$c_A(E) = \frac{c}{1+\frac{f_A V}{E}}, \quad m_{AV}^2 = (1+f_A V/E)^2[m_A^2 + (f_A V)^2/c^4],$$

the above dispersion relation resume a pseudo-conventional form like

$$E^2 = p^2 c_A(E)^2 + m_{AV}^2 c_A(E)^4.$$

$c_A(E)$ has anomaly in the limit of $E \to 0$ but this limit would need a quantum mechanical correction. The violation of Lorentz invariance would dominate in the vector case similar to the scalar or Higgs case. Then the tensor case is necessary as the toy model which exhibits the violation of Lorentz invariance in the limit of large γ

4. Boost Particle-Transformation in the External Field

The above argument can be discussed from a different viewpoint. We can consider two types of transformation, boost particle-transformation and the Lorentz transformation.[12] The Lorentz transformation is just a change of reference frame for the description of the same phenomena and is sometime called "passive" transformation. The boost particle-transformation is "active" transformation, where particle's energy-momentum are changed actually. Relativity principle claims that the boosted state and the original state seen from the transformed reference frame are identical. For the system of particles, this is trivial and the classification into "Boost" and "Lorentz" has no particular meaning.

However some complication comes in when we consider the system consisting of particles and external given field. In the Lorentz transformation, both the particle's energy-momentum and the components of the external field are transformed. Therefore the relative relation between particle and external field does not changed. In the boost particle-transformation, however, particle's energy-momentum are transformed but the field configuration is kept unchanged. Therefore two states of the particles relative to the field are different. In this way, the actively boosted state of particle is not identical with the passively Lorentz transformed state having the same particle state but different field configuration. Thus we call this situation as an "apparent" violation of Lorentz invariance but it is in fact a misconduct of the Lorentz transformation.

What we have done in the previous section is something like this. In the actual universe, the external fields like $F^{\mu\nu}$ are totally unknown to us upto now and "misconduct" of application of the Lorentz transformation

could happen. Conversely we also say that the apparent violation implies a finding of the hidden external fields.

5. Eigen State of the Limiting Velocity and GZK cut-off

Without touching on the origin of various limiting velocity, we can rise a question how much degree the universality of limiting velocity has been checked by direct experiment. The assumption of non-equality of the limiting velocity of a charged particle and light velocity is equivalent to the introduction of the Lorentz non-invariant term of the electromagnetic field into the Lagrangian.[16] In general, this is true for any non-universal assumptions of the limiting velocity.[15]

Coleman and Glashow also discussed this assumption, firstly in order to explain the neutrino oscillation.[14] They also pointed out that the high-energy phenomena might disclose an apparent degeneracy of limiting velocity and reveal a splitting into a fine structure. They called various limiting velocity as eigen state of velocity. They have shown also that this modification does not hurt the standard theory of interaction based on the gauge field theory.[15] The discussion in the section 3 is concerned the origin of such an ad hoc assumption of the eigen state of limiting velocity.

If we introduce the particle species dependent c_A, the GZK cut-off discussion could be modified very much. By the head-on collision between the cosmic-ray proton and the CMB photon, Δ particle is produced if the following condition is satisfied.[10]

$$(E_p + E_\gamma)^2 - (p_p + p_\gamma)^2 c_\Delta^2 > m_\Delta^2 c_\Delta^4,$$

while the proton obeys to $E_p^2 = p_p^2 c_p^2 + m_p^2 c_p^4$. In the situation of $E_p \gg m_p c_p^2$ and $|c_\Delta - c_p| \ll c_p$, the condition becomes as followings

$$-\frac{c_\Delta - c_p}{c_p} E_p^2 + 2E_p E_\gamma > \frac{m_\pi^2 c^4}{2}$$

In the conventional case, $c_\Delta - c_p = 0$ and the threshold energy is obtained $E_p > m_\pi^2 c^4 / 4E_\gamma$.

If $(c_\Delta - c_p) \neq 0$, the above equation gives a quite different result; the cut-off disappears for $(c_\Delta - c_p) > 0$ and the cut-off energy decreases compared with the GZK cut-off for $(c_\Delta - c_p) < 0$. For example, the above equation does not have solution if

$$\frac{c_\Delta - c_p}{c_p} > 2\left(\frac{E_\gamma}{m_\pi c^2}\right)^2 \sim 10^{-22},$$

the cut-off does not exist.

On the other hand, for $(c_\Delta - c_p) < 0$, the cut-off energy is modified as

$$E_{GZK}\left[1 - \frac{|c_\Delta - c_p|}{2c_p}\left(\frac{m_\pi c^2}{E_\gamma}\right)^2\right] \quad \text{for} \quad \frac{|c_\Delta - c_p|}{2c_p}\left(\frac{m_\pi c^2}{E_\gamma}\right)^2 < 1$$

and

$$\sqrt{\frac{c_p}{2|c_\Delta - c_p|}}m_\pi c^2 \quad \text{for} \quad \frac{|c_\Delta - c_p|}{c_p}m_\pi^2 c^4 \gg E_\gamma^2$$

6. Paradigm of Spontaneous Symmetry Breakdown

One of the achievement of the 20-century Physics was discovery of various symmetry hidden deep in the diversity of superficial phenomena: we can point out many symmetries such as rotational and boost symmetry of 3-space, past-future symmetry in mechanics, duality symmetry between electro- and magneto-fields, Lorentz symmetry of spacetime, discrete symmetry in atomic structure of solid, particle-antiparticle symmetry, isospin symmetry of nuclear force, chiral symmetry, "eight-fold symmetry", supersymmetry, colour symmetry and so on. Particularly, in the late of 1970's, theory of fundamental interactions among elementary particles was formulated into the unified-gauge-theory, based on internal or local symmetry hidden in electro-weak and strong interactions among quarks and leptons.

This unification of the fundamental interaction was accomplished, however, by one extra idea called "spontaneous symmetry breakdown(SSB)", which is schematically written as

$$[\text{observed law}] = [\text{symmetric law}]\text{x}[\text{SSB}].$$

That is, the symmetric law itself is not realized in this universe because the universe is not empty but the external field called Higgs field has permeated by . The most essential difference of the Higgs field from a conventional field is that it is un-removable from the universe. Then the genuine symmetric law looses its chance to exhibit its original form in this universe.

This SSB has introduced a new ingredient about the concept of physics law, that is, the physics law itself is symmetric but our actual universe is not in a state of exact symmetry. This may be re-phrased also as followings; physics law is universal but our universe is not universal entity, or, physics law itself does not exhibit its original form in our universe where we live in. We call this kind of idea as the SSB paradigm.[8]

In fact, some symmetries are not exact but show a tiny breakdown, like in case of CP-asymmetry. The actual composition of cosmic matter

does not obey the particle-antiparticle symmetry in spite of CPT-symmetry in physics law itself. Following these considerations, we are tempted to think that any symmetry might be not exact in this actual universe, which has come into an existence through various spontaneous selections of non-universal parameters.

Lorentz invariance claims that there is no preferential inertia frame; that is the central dogma of relativity principle. However, in our universe filled with the CMB and cosmic matter, we can clearly identify the preferential frame, which we have called the C-frame. In the inflationay scenario, CMB is supposed to be created in association with some SSB of the vacuum state of quantum field theory. Some features of the particle interaction in this universe is supposed to have inherited the parameters chosen by a dynamical process of this SSB. Furthermore, the SSB paradigm is now extended to the creation of spacetime from higher dimensional space through a dynamical process similar to SSB. Thus we can speculate also the exact Lorentz symmetry might have been violated dynamically in "our universe", that is spontaneous breaking of Lorentz symmetry.[11]

Lorentz symmetry, however, has been built in all fundamental concepts of modern physics, such as Dirac field, spin, renormalization group of quantum field theory, and so on. Therefore, the violation of this symmetry can not be introduced so easily. One of the outcomes of the relativity principle is the equivalence of all inertia frame. However this equivalence has not been directly proved so much.[17] Only the accelerator experiments has proved this equivalence up to some Lorentz factor of $\gamma_{\rm acce} \sim 10^5$. In this respect, the GZK cut-off has an unique status for the experimental verification of the equivalence of all inertia frames and the validity limit may be extended up to $\gamma_{\rm GZK} \sim 10^{11}$. Following to the SSB paradigm, this verification has coupled with the universality of the limiting velocity. And if there were not the GZK cut-off, that may imply a finding of a un-removable hidden external field of tensor type. The SSB paradigm anyway describes our universe as "un-universal" universe.

References

1. K.Greisen:Phys. Rev. Lett. **16**, 748(1966).
   G.Zatsepin and V.A.Kuzmin:JETP Phys. Lett., **4**, 78(1966).
2. H. Sato:"Uchuusen-Kenkyu"(japanese journal of "Cosmic-Ray Research"), **17**, 183(1972).
3. H. Sato and T. Tati: Prog. Theor. Phys. **47**, 1788(1972).
4. M. Takeda, et al(AGASA group): Phys.Rev. Lett.,**81**, 1163(1998).
5. Y. Takahashi: Paper in this issue.

6. H. Sato: *Black Holes and High Energy Astrophysics*, ed.by H. Sato and N. Sugiyama, Universal Academy Presss, 401 (1998).
7. G. Amelino-Camelia,J. Ellis, N. E. Mavromatos, D. V. Nanopoulous and S. Sarkar: Nature **393**, 763 (1998).
8. H. Sato: *SpaceFactory on International Space Station*, ed.by T. Ebisuzaki, T. Takahashi and T. Handa, Universal Academy Presss,131 (2000); astro-ph/0005218.
9. H. Sato: Journal of Physical Society of Japan, Vol 70, SupplementB, 64 (2001).
10. O. Bertolami and C. S. Carvalho: Phys. ReV. **D61**, 103002 (2000).
11. V.A. Kostelecky and S.Samuel: Phys. Rev.,**D39**, 683(1989).
12. D. Colladay and V. A. Kostelecky: Phys. Rev. **D55**,6760 (1997).
13. D. Colladay and V. A. Kostelecky: Phys. Rev.**D58** 116002(1998).
    V.A.Kostelecky and C.D.Lane: Phys. Rev. **D60**,116010 (1999) .
    M. S. Berger and V. A. Kostelecky: Phys. Rev., **D65**, 091701 (2002).
14. S. Coleman and S. L. Glashow: Phys. Lett. **B405**, 249 (1997).
15. S. Coleman and S. L. Glashow: Phys. Rev. **D59**, 116008 (1999).
16. G. L. Green, M. S. Dewey, E. G. Kessler and E. Fischbach: Phys. Rev. **D44**, 2216 (1991).
17. M. P. Haugan and C. W. Will: *Physics Today* **May**, 69 (1987),

BRIDGING PARTICLE ASTROPHYSICS AND COSMOLOGY VIA ULTRA HIGH ENERGY COSMIC RAYS

W-Y. PAUCHY HWANG

Center for Academic Excellence on Cosmology and Particle Astrophysics,
Department of Physics, National Taiwan University,
Taipei 106, Taiwan, R.O.C.
E-mail: wyhwang@phys.ntu.edu.tw

The present Cosmos consists of about 65% "dark energy", 30% dark matter, and 5% baryons, all embedded in a cosmic medium of 2.73° K cosmic microwave background (CMB) and 1.95° K cosmic neutrino background (CνB). Based on the conventional particle astrophysics, we may describe the propagation of ultra high energy cosmic rays (UHECR's) in the cosmic medium, but interactions of UHECR's with the atmosphere or the detector would require a better knowledge of particle physics at PeV's ("PeV particle physics). In this paper, I wish to describe how UHECR's serve as a natural bridge over which we may walk from particle astrophysics to cosmology.

1. Cosmology

1.1. *The Discoveries of 1992 and 1999*

In retrospect as well as in my personal views, the cosmology has transformed itself, at the turn of the new century, into an experimental science primarily due to two major discoveries, the 1992 discovery[1] of anisotropies in the cosmic microwave background (CMB) and the 1999 discovery of the accelerating universe via Type Ia supernova observations.[2] The significance of the turning point that cosmology is becoming a true science, as I see it, is that it will be remembered as a historic moment in the civilization of the mankind, especially in the scientific history of how the human beings develop their understandings towards the environments.

The 1992 discovery[1] of anisotropies, at a level of 10^{-5}, associated with the cosmic microwave background (CMB) has helped to identify the physics of the early universe as a prime research area in astronomy and in particle astrophysics, theoretically and observationally[3]. CMB anisotropies and polarizations, the latter beginning to be observed most recently[4,5], either

primary (as imprinted on the last scattering surface when the universe was about 300,000 years old) or secondary (as might be caused by the interactions of CMB photons with large-scale structures along the line of sight), are linked closely to the inhomogeneities produced in the early universe. Although such inhomogeneities are often attributed to quantum fluctuations produced at the early inflationary epoch, as amplified by many orders of magnitude through the inflation, it is nevertheless of importance to note that phase transitions, an inevitable process in the hot big bang era, might also have played an important role of amplifying, as well as generating, inhomogeneities as seen to be associated with our universe.

The 1999 discovery of the accelerating expansion of our present universe, as based upon Type Ia supernova observations[2], has suggested the existence of yet another form of energy, the so-called "dark energy" as coined by M.S.Turner. The fraction of "dark energy" in the present universe is by no means small, about 65 % of the total energy content in order to account for the supernova type Ia observational data.[2]

1.2. *The Standard Cosmology*

A prevailing view regarding our universe is that it originates from the joint making of Einstein's general relativity and the cosmological principle while the observed anisotropies associated with the cosmic microwave background (CMB), at the level of about one part in 100,000, provide a measure of quantum fluctuations in the inflation era. This is the standard cosmology,which we often use as the benchmark in tackling the various problems at hand.

Based upon the cosmological principle which states that our universe is homogeneous and isotropic, we introduce the Robertson-Walker metric to describe our universe.[6]

$$ds^2 = dt^2 - R^2(t)\{\frac{dr^2}{1-kr^2} + r^2 d\theta^2 + r^2 sin^2\theta d\phi^2\}. \qquad (1)$$

Here the parameter k is the spatial curvature with $k = +1,\ -1$, and 0 describing an open, closed, and flat universe, respectively. The scale factor $R(t)$ provides a measure of the size of the universe at time t.

To the approximation that anisotropies can be neglected, the universe may be described by a perfect fluid, i.e., a fluid with the energy-momentum tensor $T^{\mu}{}_{\nu} = diag\,(\rho,\ ,\ -p,\ -p,\ -p)$ where ρ is the energy density and p the pressure. Thus, the Einstein equation, $G^{\mu}{}_{\nu} = 8\pi G_N T^{\mu}{}_{\nu} + \Lambda g^{\mu}{}_{\nu}$, gives rise to only two independent equations, i.e., from $(\mu,\ \nu) = (0,\ 0)$ and $(i,\ i)$ components,

$$\frac{\dot{R}^2}{R^2} + \frac{k}{R^2} = \frac{8\pi G_N}{3}\rho + \frac{\Lambda}{3}. \tag{2}$$

$$2\frac{\ddot{R}}{R} + \frac{\dot{R}^2}{R^2} + \frac{k}{R^2} = -8\pi G_N\ p + \Lambda. \tag{3}$$

Combining with the equation of state (EOS), i.e. the relation between the pressure p and the energy density ρ, we can then solve the three functions $R(t)$, $\rho(t)$, and $p(t)$ from the three equations. Note that the above two equations yields

$$\frac{\ddot{R}}{R} = -\frac{4\pi G_N}{3}(\rho + 3p) + \frac{\Lambda}{3}, \tag{4}$$

showing either that there is a positive cosmological constant or that $\rho + 3p$ must be somehow negative, if the major conclusion of the Supernovae Cosmology Projects are correct,[2] i.e. the expansion of our universe still accelerating ($\frac{\ddot{R}}{R} > 0$).

It might be useful to remind our readers a few important results based on these equations. First of all, we assume a simple equation of state, $p = w\rho$, and obtain, from Eqs. (2) and (3),

$$2\frac{\ddot{R}}{R} + (1+3w)(\frac{\dot{R}^2}{R^2} + \frac{k}{R^2}) - (1+w)\Lambda = 0, \tag{5}$$

so that, with $p = -\rho$ and $k = 0$, we find

$$\ddot{R} - \frac{\dot{R}^2}{R} = 0, \tag{6}$$

which has an exponentially growing, or decaying, solution $R \propto e^{\pm\alpha t}$, compatible with the so-called "inflation" or "big inflation". In other words, the idea of "inflation" is perfectly consistent with both Einstein's general relativity and the cosmological principle.

To realize the inflation scenario, we may consider the simplest case of a real scalar field $\phi(t)$,

$$\rho = \frac{1}{2}\dot{\phi}^2 + V(\phi), \qquad p = \frac{1}{2}\dot{\phi}^2 - V(\phi), \tag{7}$$

so that, when the "kinetic" term $\frac{1}{2}\dot{\phi}^2$ is negligible, we have an equation of state, $p \sim -\rho$. That is, a universe filled with only matter in the form of such fields can be inflating for a while until the potential term loses its grip.

In addition to its possible role as the "inflaton" responsible for inflation, such field has also been invoked to explain the accelerating expansion of the present universe, as dubbed as "quintessence"[7] or "spintessence".[8]

1.3. *The Hot Big Bang*

Another simple consequence in the standard cosmology is to derive the continuity equation from Eqs. (2) and (3):

$$d(\rho R^3) + pd(R^3) = 0. \tag{8}$$

We see that $\rho \propto R^{-4}$ for a radiation-dominated universe ($p = \rho/3$) while $\rho \propto R^{-3}$ for a matter-dominated universe ($p << \rho$). When the universe was young enough or $R \to 0$, the universe would have to be dominated by radiations, leading to the idea of "big bang" or "hot big bang". The "dark energy", as invoked to explain the accelerating expansion of the present universe, could be in the form of a positive cosmological constant Λ or "quintessence",[7,8] or caused by evolution of extra dimensions.[9] Dark energy in the form of the cosmological constant remains as a constant when R changes. It is clear that dark energy will become negligible when R is small enough, or when the universe was young enough. In the standard cosmology, therefore, our universe began with an exponential "inflation" to saw the seed for the "hot big bang", to be followed by a matter-dominated universe, and eventually entering the present era of being dominated by "dark energy".

Another useful note is that, over the last three decades, the standard model of particle physics has been established to a precision level of 10^{-5} or better in the electroweak sector while to a level of about one percent on strong interactions. In the standard model, the electroweak (EW) phase transition, which endows masses to the various particles, and the QCD phase transition, which gives rise to confinement of quarks and gluons within hadrons in the true QCD vacuum, are two well-established phenomena. Presumably, the EW and QCD phase transitions would have taken place in the early universe, respectively, at around $10^{-11}\,sec$ and at a time between $10^{-5}\,sec$ and $10^{-4}\,sec$, or at the temperature of about $300\,GeV$ and of about $150\,MeV$, respectively. While it is imperative to understand the roles of the EW and QCD phase transitions in the early universe, none of ordinary particles would assume the meaning of "mass" before the EW phase transition had ever occurred while a nucleon had yet to be formed before the QCD phase transition took place.

For the radiation-dominated early epochs of the universe with $k = 0$ and $\Lambda = 0$ (for the sake of simple arguments), we may deduce, also from Eqs. (2) and (3),

$$\rho = \frac{3}{32\pi G_N} t^{-2}, \qquad T = \{\frac{3c^2}{32\pi G_N a}\}^{\frac{1}{4}} t^{-\frac{1}{2}} \cong 10^{10} t^{-1/2} (^\circ K). \tag{9}$$

These equations tell us a few important times in the early universe, such as $10^{-11} sec$ when the temperature T is around 300 GeV during which the electroweak (EW) phase transition is expected to occur, or somewhere between $10^{-5} sec$ ($T \cong 300\ MeV$) and $10^{-4} sec$ ($T \cong 100\ MeV$) during which quarks and gluons underwent the QCD confinement phase transition. We may use "the radiation" as a "thermometer" for measuring the temperature of the universe, or the instant (the age) of the universe.

At $t \sim 10^{-11} sec$ or $T \sim 300\, GeV$, we have

$$\rho_\gamma \sim 6.4 \times 10^{22} gm/cm^3, \quad \rho_m \sim 3.2 \times 10^{12} gm/cm^3. \tag{10}$$

Just above the electroweak phase transition, all particles of the familiar kinds are massless. The fact that ρ_γ was bigger than ρ_m by 10 orders of magnitude is something beyond anyone's imagination. Thermal equilibrium would not distinguish one species of massless particles from another massless species. Something is terribly "wrong", either there was not thermal equilibrium at such early times or the initial condition is completely "biased". In this paper, however, I shall not dwell on such problem and proceed to discuss other issues.

At $t \sim 10^{-5} sec$ or $T \sim 300\, MeV$, we have

$$\rho_\gamma \sim 6.4 \times 10^{10} gm/cm^3, \quad \rho_m \sim 3.2 \times 10^{3} gm/cm^3. \tag{11}$$

Or, slightly later when QCD phase transition has completed, at $t \sim 10^{-4} sec$ or $T \sim 100\, MeV$, we have

$$\rho_\gamma \sim 6.4 \times 10^{8} gm/cm^3, \quad \rho_m \sim 1.0 \times 10^{2} gm/cm^3. \tag{12}$$

At $10^{-5} sec$ or $300\, MeV$, before QCD phase transition took place, chemical equilibrium would still be an issue (which we no longer try to tackle) but the universe is definitely a strangeness-rich system. The phase transition will bring about large numbers of strange baryons which decay quickly into nucleons. Since we are working near the critical temperature, $T \sim 150\, MeV$, the masses $m_i^*(T)$ for the various baryons will be an important input for any decent predictions. In fact, the various axial couplings g_A^{i*} would determine the decay rates of strange baryons and would have to be

understood. It seems that QCD sum rules in a more versatile context[10] would be something which we could use to tackle these problems.

At $t \sim 1\,sec$ or $T \sim 1\,MeV$, we have

$$\rho_\gamma \sim 6.4 gm/cm^3, \quad \rho_m \sim 1.0 \times 10^{-4} gm/cm^3. \tag{13}$$

Nucleosynthesis began to take place in a radiation-dominated environment, until $t \sim 10\tau_n \sim 15\,min$ when all neutrons decay or get imprisoned in ^4He. The fact that $m_n^* - m_p^*$ is comparable with the temperature ($1\,MeV$) to begin with and the mass difference controls the neutron decay rate suggest that we must understand more precisely its temperature dependence, but here the method of QCD sum rules is fairly reliable.

At the "last scattering surface", $t \sim 300,000\,years$ or $T \sim 5.4 \times 10^{2\,\circ} K$ when the universe just turned transparent for photons, we have

$$\rho_\gamma \sim 6.4 \times 10^{-26} gm/cm^3, \quad \rho_m \sim 3.2 \times 10^{-24} gm/cm^3. \tag{14}$$

Now, the matter already began to dominate but the dark energy component remains far less important. Protons and helium nuclei are already stable objects for quite a while, and nucleon properties are what we are seeing today.

1.4. *A Short Summary of the Present Universe*

To sum up, CMB observations indicate that our universe is flat, or that the energy density is of the critical value, $8.0 \times 10^{-30} gm/cm^3$. CMB and Supernovae observations indicate that 65 % of the presence universe is in the form of "dark energy", 30 % in the form of "dark matter", and about 5 % in the baryon content. The radiation content of the present universe is $5 \times 10^{-35} g/cm^3$, as estimated from the 2.73° K black-body radiation. As we extrapolate back in time, $t \to 0$, we anticipate $R \to 0$, a very small universe as compared to the present one. We would first get back to the "matter epoch" when the matter content is the dominant component of the universe. As the time is even earlier, the universe would necessarily be dominated by the radiation. At present, we have already entered the "dark" age as the dark energy dominates over all the rest.

2. Ultra High Energy Cosmic Rays (UHECR's)

2.1. *Observations of Cosmic Rays near* $10^{20}\,eV$

The observation of ultra high energy cosmic rays (UHECR's) beyond the Greisen-Zatsepin-Kuzmin (GZK) cutoff energy presents an outstanding

puzzle in astrophysics and cosmology.[11] It has long been anticipated that the highest energy cosmic rays would be protons from outside the galaxy, but there is an upper limit of the highest energy in the observed proton spectrum, commonly referred to as the GZK cutoff,[12] as the protons travelling from intergalactic distances should experience energy losses owing to pion productions by interacting with photons in the cosmic background radiation.

2.2. *Propagation of UHECR's in the Cosmic Medium*

The 2.73 K cosmic microwave background (CMB) of the photons satisfies the Planck's ideal black-body radiation formula, with the number density $n_\gamma = 16\pi\zeta(3)\left(kT/hc\right)^3 = 413$ photons per cm^3 and the mean energy per photon $\epsilon_\gamma = \pi^4 kT/30\zeta(3) = 6.35 \times 10^{-4}$ eV, where $\zeta(3) = 1.20$ is the Riemann Zeta function. When the nucleon with 4-momentum $p = (E, \mathbf{p})$ interacts with the photon with 4-momentum $k = (\epsilon, \mathbf{k})$, and compose into a system with the center of mass energy squared S, we have

$$E = \left(S - m_N^2\right)/2\epsilon \left(1 - \sqrt{1 - m_N^2/E^2}\cos\theta\right), \tag{15}$$

where θ is the angle between $\mathbf{p}$ and $\mathbf{k}$. θ cannot be zero since a nucleon cannot catch up a photon moving in the same direction, and the energy of the nucleon E must be very large near the pion photoproduction process $N + \gamma_{CMB} \to \pi + N$, therefore we have,

$$E \approx \left(S - m_N^2\right)/2\epsilon\left(1 - \cos\theta\right). \tag{16}$$

The threshold energy for pion production $N + \gamma_{CMB} \to \pi + N$ is

$$E \approx \left(2m_N m_\pi + m_\pi^2\right)/4\epsilon = 1.10 \times 10^{20} \text{ eV}, \tag{17}$$

and the threshold energy for producing the Δ resonance $N + \gamma_{CMB} \to \Delta \to \pi + N$ is

$$E \approx \left(m_\Delta^2 - m_N^2\right)/4\epsilon = 2.52 \times 10^{20} \text{ eV}. \tag{18}$$

The neutron has a mean life time $\tau_n = 887$ s in its rest reference frame. Due to time dilation, the lifetime of a moving particle is dilated by a factor $\gamma_n = E_n/m_n$. Thus, we have, for a neutron at the pion production threshold,

$$l_n \approx c\gamma_n\tau_n = 3.12 \times 10^{24} \text{ cm} = 1.01 \text{ Mpc}, \tag{19}$$

and, for a neutron near the Δ resonance threshold,

$$l_n \approx c\gamma_n\tau_n = 7.11 \times 10^{24} \text{ cm} = 2.30 \text{ Mpc}. \tag{20}$$

Therefore the neutron fraction around the GZK cutoff is expected to be negligibly small for nucleons coming from a source with distance of considerably more than a few Mpc.

To take into account the detailed features of the pion photoproduction reactions, $N + \gamma_{CMB} \to \pi + N$, we may employ the low energy theorem [18] or the chiral quark model [19]. In this approximation, we have[19]

$$A(p\gamma \to \pi^+ n) = \sqrt{2}\left(A^- + A^0\right), \tag{21}$$

$$A(n\gamma \to \pi^- p) = \sqrt{2}\left(A^- - A^0\right), \tag{22}$$

$$A(p\gamma \to \pi^0 p) = A^+ + A^0, \tag{23}$$

$$A(n\gamma \to \pi^0 n) = A^+ - A^0, \tag{24}$$

where the isospin amplitudes $A^{\pm,0}$ can be expanded in terms of the ratio between pion mass and nucleon mass $\eta = m_\pi/m_N$

$$A^- = 1 + O(\eta^2), \quad A^+ = A^0 = -\eta/2 + O(\eta^2). \tag{25}$$

Thus, we obtain

$$\frac{\sigma(n\gamma \to \pi^- p)}{\sigma(p\gamma \to \pi^+ n)} = \frac{(1+\eta/2)^2}{(1-\eta/2)^2} \approx 1.34, \tag{26}$$

which is in excellent agreement with the experimental data [20], and

$$\frac{\sigma(p\gamma \to \pi^0 p)}{\sigma(p\gamma \to \pi^+ n)} = \frac{\eta^2}{2(1-\eta/2)^2} \approx 0.01, \tag{27}$$

$$\frac{\sigma(n\gamma \to \pi^0 n)}{\sigma(p\gamma \to \pi^+ n)} = \frac{O(\eta^4)}{2(1-\eta/2)^2} \approx O(\eta^4), \tag{28}$$

which means that the neutral pion production processes, $p+\gamma_{CMB} \to \pi^0+p$ and $n+\gamma_{CMB} \to \pi^0+n$, can be neglected. Adopting an average cross section $\sigma(p\gamma \to \pi^+ n) = 200$ μb [12,14] above the pion photoproduction threshold, we have the mean free path of interaction for the proton

$$\lambda_p = \frac{1}{n_\gamma \sigma(p\gamma \to \pi^+ n)} = 1.21 \times 10^{25} \text{ cm} = 3.92 \text{ Mpc}, \tag{29}$$

and that for the neutron

$$\lambda_n = \frac{1}{n_\gamma \sigma(n\gamma \to \pi^+ p)} = 9.04 \times 10^{24} \text{ cm} = 2.93 \text{ Mpc}. \tag{30}$$

It is interesting to note that the protons and neutrons change into each other via charged pion production by the relic photons in the travel until the nucleon energies degraded to below the GZK cutoff. There is always a

certain amount of neutron fraction for nucleons above the pion photoproduction threshold, since the protons can always change into neutrons via the charged pion photoproduction. Though the neutrons change more fast into protons via both beta decay or charged pion photoproduction (with effective mean free path $\lambda_n^{\rm eff} = l_n\lambda_n/(l_n + \lambda_n)$), these produced protons continue to change into neutrons if their energy is still above the pion production threshold. As a consequence, there is always a non-trivial neutron fraction in the nucleon cosmic rays above the GZK cutoff. Assuming that the nucleons with energy above the GZK cutoff are from a point source with uniform nucleon spectrum at a distance far away, the neutron/proton ratio would soon reach the equilibrium value of $\lambda_n^{\rm eff}/\lambda_p \approx 0.19$ at the pion production threshold and 0.33 at the Δ production threshold, independent of the neutron/proton ratio of the source.[13]

2.3. *On the Origin of Ultra High Energy Cosmic Rays*

Stecker suggested[14] that the particles with energy above the GZK cutoff may come from within the local "supercluster" of galaxies of which we are a part. Thus, the "GZK cutoff" would not be a true cutoff, but a suppression of the ultrahigh energy cosmic ray flux owing to the limitation of the propagation distance, which we refer to as the GZK zone. According to Stecker's suggestion, the observed cosmic ray events above the GZK cutoff come from sources within the GZK zone, i.e., not far from us in a few tens of Mpc.

The "Z-bursts" [15,16,17] hypothesis was also introduced to account for the highest energy cosmic ray events observed by far, but with the bursts taking place within the GZK zone.[14] The reason is that the "Z-bursts" are from the Z-boson annihilations of the ultrahigh energy neutrino (antineutrino) cosmic rays with the relic neutrinos (antineutrinos) in the cosmic background. The "Z-bursts" could produce nucleon cosmic rays beyond the GZK energy if taking place within the GZK zone, as the energy of the produced Z-bosons would be high enough by the collision of ultrahigh energy neutrino beams with the relic neutrinos of non-zero mass.

The possibility that the UHECR's above the GZK cutoff energy may in fact be neutrinos rather than protons or nuclei is to be explored briefly in the next section on "PeV Particle Physics".

3. PeV Particle Physics

Noting that we now have evidences of observing UHECR's near or even above $10^{20}\,eV$, we wish to address the next basic question of how such UHECR particle initiates a gigantic shower in the atmosphere or how they would interact with a "detector" if it would ever be made. This leads to what I would call "PeV Particle Physics" (PPP), or particle physics in the energy range of $10^{15}\,eV$ (PeV). It is simple to estimate the center-of-mass squared S when a UHECR particle of $10^{20}\,eV$ energy interacts with a nucleon in the atmosphere or in the hypothetical detector:

$$S \equiv (p_1 + p_2)^2 \cong 2p_1 \cdot p_2 \cong 2E_1 m_N \cong 2 \times 10^{29}\,eV^2, \tag{31}$$

giving rise to a CM energy of 450 TeV, or a half PeV, way above the temperature for the EW phase transition. At these energies, photons and neutrinos would not be very different in view of full electroweak unification while supersymmetry (SUSY) might be at its full working. Quarks inside the target nucleon or, if the UHECR particle is also a hadron, in the UHECR would experience interactions slightly different from photons and neutrinos and if SUSY would be the primary story at such energies such distinction between quarks and leptons would be even smaller.

A serious study of PeV Particle Physics is much needed if the observed UHECR's above the GZK cutoff, or some of them, are in fact neutrinos. Such neutrinos could come from anywhere in the Universe, way beyond the so-called "GZK zone", a restriction for UHECR protons but not for neutrinos.

Do we have a natural sources for UHECR neutrinos with energies above $10^{20}\,eV$ or even higher? The situation seems much better off than the neutrinos needed for initiating the so-call "Z-bursts". If a proton is accelerated in the region of the jet or accretion disk near a supermassive black hole, such as quasars or active galactic nuclei (AGN), there is a good reason to believe that it could be accelerated to an energy way above the GZK cutoff energy. Such proton, when propagating in the cosmic medium, converts itself into a bunch of particles, including neutrinos above the GZK cutoff energies, eventually to stablize the nucleon content against the GZK instability. These are what we call "GZK neutrinos", neutrinos coming from a UHECR nucleon propagating in the cosmic medium.

So, the interactions of UHECR's with the atmosphere or with the "detector" offer us the first glimpse of PeV particle physics in action. I suspect that PPP will soon become a very active research area in particle physics,

even before CERN's LHC comes into operation.

4. Taiwan CosPA Project in a Glimpse

I would like to give our distinguished audience a very sketchy description of the project which we are undertaking, for the sake of explaining to you how we are engaging ourselves in the prime research area in cosmology while offering our interested colleagues collaborative opportunities in the near future.

The Project in Search of Academic Excellence on "Cosmology and Particle Astrophysics (CosPA)", a multi-institutional research project[21] funded for a period of four years beginning from January 2000 by the Ministry of Education of R.O.C. (Taiwan) and dubbed as "Taiwan CosPA Project", consists of five subprojects and an overseeing project and aims at building up Taiwan's astronomy through research efforts in the hotly-contested areas of cosmology and particle astrophysics. The total budget of the project is at the level of about 15 million U.S. dollars over 4 Years. At the point of this writing, we have submitted our request for funding over the subsequent four years (2004.4 - 2008.3).

The five subprojects and their missions or science goals are described very briefly as follows:

- **Subproject No. 1:** Array for Microwave Background Radiation (AMiBA): From Construction and Operation to Data Acquisition and Analysis (P.I.: Paul T.-P. Ho).
- **Subproject No. 2:** Experimental Particle Physics Studies on Issues related to "Early Universe, Dark Matter, and Inflation" (P.I.: W. S. Hou).
- **Subproject No. 3:** Theoretical Studies of Cosmology and Particle Astrophysics (P.I.: W-Y. Pauchy Hwang).
- **Subproject No. 4:** Frontier Observation in Optical and Infrared Astronomy (P.I.: Typhoon Lee).
- **Subproject No. 5:** National Infrastructure (P.I.: Wing Ip).

On Subproject No. 1 for radio astronomy, we wish to complete, by the end of 2003, the construction of 7-element AMiBA geared toward the measurement of the CMB polarizations. While making use of the 7-element array for scientific studies, we will be moving on to complete, by the end of 2005, the full 19-element AMiBA so that systematic SZ surveys of high-z clusters could be conducted and accomplished well before ESO's Planck

Surveyor comes into operation. The 6-meter easy-to-rotate platform and mount, with excellent pointing cabability, will be on site (Mauna Loa, Hawaii) during the summer of 2003 and it will accommodate 19 1.2m dishes in its full capacity.

On Subproject No. 2 for particle astrophysics, the experimental high energy physics team based at National Taiwan University is the basic manpower infrastructure to carry out the experiments related to dark matter, the early universe, and/or inflation. The group has been an active player in the KEK/Belle Collaboration on the B & CP studies - they were in the news of major discovery, both in July 2001 and in February 2002. During the first year of this project, the team has completed the feasibility study of a dark matter search. Lately, their interests have switched to neutrino astrophysics and now is attempting to build a prototype neutrino telescope for the detection of very high energy cosmic neutrinos. In addition, the group attempts to phase-in a meaningful participation of the GLAST project (NASA / DOE), but outside the present CosPA framework.

On Subproject No. 3 for theoretical studies of cosmology and particle astrophysics, the science goal is to make significant progresses, hopefully some breakthroughs, in the prime area of cosmology, i.e. the physics of the early universe. Subjects under intensive studies include CMB polarization and anisotropy, dark energy and the accelerating universe, noncommutative spacetime and cosmology, roles of phase transitions in the early universe, and physics of ultra high energy cosmic rays (UHECR's). Starting from 2002, we also phase in an experimental component "laboratory astrophysics", as a new way to supplement the inadequacy of astrophysics studies through observations or numerical simulations.

On Subproject No. 4 for optical and infrared astronomy, an agreement between National Taiwan University and Canada-French-Hawaii Telescope (CFHT) Corporation was ironed out in July 2001 in order that the CosPA team will participate the construction efforts of the Wide-Field Infrared Camera (WIRCam) and that the CosPA team will have 68 nights,over the next six-year period, to use CFHT/WIRCam to conduct the large-scale-structure (LSS) survey to complement the SZ survey of the AMiBA.

On Subproject No. 5 for national infrastructure, we are trying to make the links between education and research so that there will be adequate young manpower to sustain the growth of the astronomy as a field. Through this sub-project, we establish, on top of the Lu-lin Mountain, an observatory which house small research telescopes such as the TAOS survey network telescopes.

It is of some interest to note that CosPA's overall scientific objectives sit amazingly well on top of the CPU/BPA/NRC report, released April 2002 by the U.S. National Research Council. There are currently many other projects around the world, with a scale similar to our CosPA project, such as Center for Cosmology at University of Chicago, several distinguished projects going on at California Institute of Technology, Kavli Institute for Particle Astrophysics and Cosmology at Stanford University, and Research Center for the Early Universe (RESCEU) at University of Tokyo. Cosmology has indeed become a hotly-contested area of forefront research in physics and astronomy.

5. Prospects

The present Cosmos consists of about 65% "dark energy", 30% dark matter, and 5% baryons, all embedded in a cosmic medium of $2.73^\circ\, K$ cosmic microwave background (CMB) and $1.95^\circ\, K$ cosmic neutrino background (CνB). While we may employ conventional particle astrophysics to describe the propagation of ultra high energy cosmic rays (UHECR's) in the cosmic medium, interactions of UHECR's with the atmosphere or the detector would require a better knowledge of particle physics at PeV's ("PeV particle physics). In this paper, I have described how UHECR's may serve as a natural bridge over which we may walk from particle astrophysics to cosmology.

I also wish to stress that, at the turn of the century, cosmology is transforming itself into an experimental science. It has become the main-stream research in astronomy, as well as in particle astrophysics. In Taiwan, we are joining this red-hot race through the Taiwan CosPA Project. The project, if successfully carried out, should help us to build a world-class, research-based, respectable astronomy in Taiwan.

Acknowledgments

This work is supported primarily through the Taiwan CosPA Project, as funded by the Ministry of Education (89-N-FA01-1-0 up to 89-N-FA01-1-5). It is also supported in part by National Science Council of R.O.C. (NSC 90-2112-M002-028 & NSC 91-2112-M002-041).

References

1. G. Smoot *et al.*, Astrophys. J. **396**, L1 (1992); C. Bennett *et al.*, Astrophys. J. **396**, L7 (1992); E. Wright *et aql.*, Astrophys. J. **396**, L11 (1992).
2. S. Perlmutter *et al.* [Supernova Cosmology Project], Astrophys. J. **517**, 565 (1999); A. G. Riess *et al.* [Supernova Search Team], Astron. J. **116**, 1009 (1998).
3. C. L. Bennett, M. S. Turner, and M. White, Physics Today, November 1997, p. 32, for an early general review.
4. E.M. Leitch *et al.*, arXiv:astro-ph/0209476, September 2002; J. Kovac *et al.*, arXiv:astro-ph/0209478, September 2002.
5. A. Kogut *et al.*, arXiv:astro-ph/0302213, February 2003; submitted to The Astrophysical Journal.
6. E.W. Kolb and M.S. Turner, *The Early universe*, *Addison-Wesley Publishing Co.* (1994).
7. R.R. Caldwell, R. Dave, and P.J. Steinhardt, Phys. Rev. Lett. **80**, 1582 (1998).
8. Je-An Gu and W-Y. P. Hwang, Phys. Lett. **B517**, 1 (2001).
9. Je-An Gu and W-Y. P. Hwang, Phys. Rev. **D66**, 024003-1 (2002).
10. W-Y. P. Hwang, Z. Phys. **C75**, 701 (1997); W-Y. P. Hwang, Nucl. Phys. **A663 & 664**, 1039c (2000).
11. For some reviews, see, e.g., P. Sokolsky, AAPPS Bulletin **13**, 11 (2003); F. Halzen, astro-ph/0111059; S. Sarkar, hep-ph/0202013; M. Nagano and A.A. Watson, Rev. Mod. Phys. **72**, 689 (2000).
12. K. Greisen, Phys. Rev. Lett. **16**, 748 (1966); G.T. Zatsepin and V.A. Kuzmin, Pis'ma Zh. Eksp. Tero. Fiz. **4**, 114 (1966) [JETP Lett. **4**, 78 (1966)].
13. W-Y. P. Hwang and Bo-Qiang Ma, "Neutrons and Antiprotons in Ultrahigh Energy Cosmic Rays", preprint 2003, submitted to Phys. Lett. B.
14. F.W. Stecker, Phys. Rev. Lett. **21**, 1016 (1968). For an extensive review with recent progress, see, F.W. Stecker, astro-ph/0101072.
15. T. Weiler, Phys. Rev. Lett. **49**, 234 (1982); Astrophys. J. **285**, 495 (1984); Astropart. Phys. **11**, 303 (1999).
16. D. Fargion, B. Mele, and A. Salis, Astrophys. J. **517**, 725 (1999).
17. G. Gelmini and G. Varieschi, Phys. Rev. Lett. **82**, 5202 (1999); **84**, 1378 (2000); hep-ph/0201273.
18. G.F. Chew, M.L. Goldberger, F.E. Low, and Y. Nambu, Phys. Rev. **106**, 1345 (1957); S. Fubini, G. Furlan, and C. Rossetti, Nuovo Cimento **40**, 1171 (1965); M.S. Bhatia and P. Narayanaswamy, Phys. Rev. **172**, 1742 (1968).
19. Z. Li, Phys. Rev. **D 50**, 5639 (1994).
20. T. Fujii *et al.*, Phys. Rev. Lett. **28**, 1672 (1972); J. Pine and M. Bazin, Phys. Rev. **132**, 2735 (1963).
21. W-Y. P. Hwang, AAPPS Bulletin **12**, 5 (2002).

THE LAMB SHIFT AND ULTRA HIGH ENERGY COSMIC RAYS

SHE-SHENG XUE

I.C.R.A. and Physics Department, University of Rome "La Sapienza", I-00185 Rome, Italy

E-mail: xue@icra.it

On the analogy with the Lamb shift, we study the vacuum effect that proton's electric field interacts with virtual particles in the vacuum. We find a possible quantum instability that triggered by an external force, proton's electric field interacting with virtual particles spontaneously induces a quantum force that back reacts on the proton in the direction of the external trigger force. Such a quantum-induced force accelerates the proton runaway, by gaining the zero-point energy from the vacuum ($\sim 10^{-5}$ eV/cm). This effect possibly accounts for the mysterious origin and spectrum of ultra high-energy cosmic ray (UHECR) events above 10^{20}eV, and explains the puzzle why the GZK cutoff is absent. The candidates of these events could be primary protons from the early Universe.

The effective Lagrangian for a proton. The Lamb shift[1] shows that the energy level $2S_{\frac{1}{2}}$ of the hydrogen atom spectrum is shifted *upward* +1008MHz, compared with $2P_{\frac{1}{2}}$. This implies that QED vacuum effects drain the zero-point energy to a hydrogen atom. We relate these vacuum effects to the origin of UHECR events.

Considering a proton interacting with virtual particles in the vacuum, we introduce (i) Ψ and A_μ describing a proton field and its gauge potential; (ii) ψ_q and A^q_μ describing the quantum fields of virtual fermions and photons in the vacuum. To study this system, we start with a renormalized lagrangian density $L(x)$ with all necessary renormalization counterterms,

$$L(x) = -\frac{1}{4}(F^2 + F_q^2) + \bar{\Psi}\big[i\gamma^\mu\partial_\mu - m_p - e_p\gamma^\mu(A_\mu + A^q_\mu)\big]\Psi + \bar{\psi}_q\big[i\gamma^\mu\partial_\mu - m - e\gamma^\mu(A_\mu + A^q_\mu)\big]\psi_q + (\text{c.t.}), \quad (1)$$

where F and F_q are classical and quantum electromagnetic field tensors, e and m (e_p and m_p) and are electron(proton) charge and mass. This is a complex interacting system, the classical fields Ψ and A_μ, quantum fields

ψ_q and A^q_μ are coupled together. To the first order, we obtain an effective interacting lagragian (details will be presented elsewhere):

$$L_i^{\rm ext}(x)=-\bar{e}A_\nu^{\rm ext}\bar{\Psi}\gamma^\nu\Psi, \quad \bar{e}=e_p\frac{4\alpha^2}{3}\big(\ln\frac{m}{\mu}-\frac{7}{40}\big); \tag{2}$$

$$A_\nu^{\rm ext}(x)=\int\frac{d^4x'}{m^2}{\rm tr}\left[S_F(x-x')\gamma_\mu S_F(x'-x)\gamma_\nu\right]A^\mu(x'), \tag{3}$$

$$=\frac{1}{60\pi m^4}\left(g_{\mu\nu}-\frac{\partial_\mu\partial_\nu}{\Delta}\right)(\Delta)^2A^\mu(x). \tag{4}$$

In Feynman's prescription of particles and antiparticles, Eq.(3) shows that a pair of virtual fermion and antifermion (*virtual pair*) is created at one spacetime point x and annihilates at another x', behaving as an electric dipole $\vec{P}$ in its life-time. This *virtual pair* couples to the classical field $A^\mu(x')$ of the proton at x. As a result, an induced quantum dipole field $A_\nu^{\rm ext}(x)$ is created, attributed to *virtual pairs*, and this quantum field back interacts with the proton as an external field $A_\mu^{\rm ext}(\vec{E}^{\rm ext})$.

Induced quantum force and instability. In the case of the proton at rest or traveling with a constant velocity, we might conclude $A_\mu^{\rm ext}(x)\equiv 0$ for its transversality and the Lorentz invariance: $A^\mu(x)=\frac{e_p}{4\pi|\vec{x}|}g^{\mu\circ}$, being longitudinal in an instantaneous rest frame of the proton. However, we have to consider the quantum nature of quantum-induced field $A_\mu^{\rm ext}(x)$. In the absence of an external field, the quantum-field fluctuations of *virtual pairs* and their dipole fields are entirely random-fluctuating of a time-scale $\delta\tau_q\sim 1/m$ in the spacetime, we do not expect any quantum-induced field of life-time $>\delta\tau_q$ in(at) any particular direction(point) of the spacetime. In the presence of longitudinal electric field of the proton, (i) the transverse quantum-field fluctuations of *virtual pairs* and their dipole fields $A_\mu^{\rm ext}(x)$ are entirely random-fluctuating of a time-scale $\delta\tau_q\sim 1/m$ in the spacetime; (ii) the longitudinal quantum-field fluctuations of *virtual pairs* and their dipole fields $A_\mu^{\rm ext}(x)$, although their life-time can be larger than $\delta\tau_q$, are entirely spherically symmetric and total dipole field $A_\mu^{\rm ext}(x)$ acting on the proton is zero. Thus, indeed we do not expect any induced quantum field $A_\mu^{\rm ext}(x)$ of life-time $>\delta\tau_q$, acting on the proton in a peculiar direction of the instantaneous rest frame.

Nevertheless, in the instantaneous rest frame of the proton, we consider the case that an external trigger force $\vec{F}_{tri}$ accelerates the proton for a time interval $\Delta t_{tri}\gg\delta\tau_q$. As a result, proton's electric field $\vec{E}(x')$ gets a transverse component $\vec{E}_\perp(x')$, whose distribution (both value and direction) is axial symmetric with respect to the direction of $\vec{F}_{tri}$, as given by the Lien-

ard Wiechert field. This transverse field induces the transverse component $\vec{P}_\perp(x')$ of quantum electric dipoles of *virtual pairs* at x', $\vec{P}_\perp(x') \sim \vec{E}_\perp(x')$. The spatial distribution of $\vec{P}_\perp(x')$ is the same as that of $\vec{E}_\perp(x')$. These quantum electric dipoles create electric dipole fields $\vec{E}^{\rm ext}_\perp(x)$ (4) back reacting on the proton at x. Summing over all contributions of quantum electric dipoles $\vec{P}_\perp(x')$ of *virtual pairs*, we find that the total $\vec{E}^{\rm ext}_\perp(x)$ acts on the proton in the same direction of $\vec{F}_{tri}$. This total $\vec{E}^{\rm ext}_\perp(x)$ acting on the proton then plays the same role of $\vec{F}_{tri}$. This implies that quantum-field fluctuations of *virtual pairs*, triggered by $\vec{F}_{tri}$, could cause a quantum runaway instability that the proton is accelerated further and further by a quantum force $\vec{F}_q = \bar{e}\vec{E}^{\rm ext}_\perp(x)$ even after the trigger force is off. Such a quantum instability can take place, provided quantum electric dipoles $\vec{P}_\perp(x')$ and their electric fields $\vec{E}^{\rm ext}_\perp(x)$ have a life-time $\gg \delta\tau_q$. For the Lorentz invariance and homogeneity of the vacuum state, the quantum-induced field $\vec{E}^{\rm ext}_\perp$ or $F^{\rm ext}_{\mu\nu}$ must be constant.

In the following, we adopt a semi-classical model to qualitatively estimate the value of such an induced quantum driving force in the instantaneous rest frame of the proton. *Virtual pairs* in an external field can be possibly considered as unstable excitations of bound states of virtual fermions and antifermions. We approximately estimate their binding energy, size and life-time. The energy scale of quantum-field fluctuations of *virtual pairs* must be much smaller than the electron mass m, otherwise real electrons and positrons would be created. We thus adopt a non-relativistic description for *virtual pairs*, whose size is about $\frac{2}{\alpha m}$, binding energy $\sim \frac{\alpha^2 m}{2}$. This indicates the size of electric dipoles $|d| \sim |x - x'| \sim \frac{2}{\alpha m}$, and $\vec{P} = |e|\vec{d}$ in Eq.(3). The cross-section(probability) of the annihilation and creation of such a *virtual pair* is about $\pi(\frac{\alpha}{m})^2$. The life-time of such a *virtual pair* is then $\delta\tau_p \sim \frac{2}{\alpha^5 m} = 6.2 \cdot 10^{-11}$sec. This indicates the life-time of quantum electric dipole $\vec{P}_\perp$ and field $\vec{E}^{\rm ext}_\perp(x)$ is $\delta\tau_p \sim \frac{2}{\alpha^5 m}$, which is much larger than $\delta\tau_q \sim \frac{1}{m}$. Using $\vec{P}_\perp \cdot \vec{E}_\perp \lesssim e^2/(4\pi|d|)$, we can estimate $|\vec{E}_\perp| \lesssim |e|/(4\pi|d|^2)$.

The large wavelength modes k of proton's gauge field A_μ are sensitive to the low-lying states of *virtual pairs* of size $\sim \frac{2}{\alpha m}$. This suggests $k \sim \frac{\alpha m}{2}$ in Eq.(4) and the infrared cutoff $\mu \sim \frac{\alpha m}{2}$ in Eq.(2). The amplitudes of the induced quantum dipole fields $A^{\rm ext}_\mu$ and $\vec{E}^{\rm ext}$ are approximately given by,

$$A^{\rm ext}_\mu \simeq \frac{\alpha^4}{960\pi} A_\mu; \quad \vec{E}^{\rm ext}_\perp \simeq \frac{\alpha^4}{960\pi}\vec{E}_\perp. \tag{5}$$

Summing over the angular distribution of *virtual pairs*, we obtain the spon-

taneously induced quantum force:

$$\vec{F}_q = \frac{\delta E}{\delta \vec{x}} = \bar{e}\vec{E}_{\perp}^{\rm ext} \simeq 2.82 \cdot 10^{-5} ({\rm eV/cm})\vec{u}, \tag{6}$$

and its direction $\vec{u}(|\vec{u}| = 1)$ is kept in the same direction of proton's acceleration. The life-time of this induced quantum force is $\delta\tau_p \sim \frac{2}{\alpha^5 m} \gg \tau_q$, and it seems that the quantum instability ought to occurs. Eq.(6) holds for any charged particles and can be experimentally tested in a laboratory. The estimations and considerations are still very qualitative and speculative, need to be further improved and verified. It is highly deserved to have a quantitative computation of this quantum-induced force and instability.

Vacuum energy gain and lost. We turn to discuss Eq.(6) from the energetical point of view. In the absence of any external field, the quantum-field fluctuations of *virtual pairs* are entirely random in the spacetime. This determines the maximum value of the zero-point energy. However, in the presence of a proton and its external field that couples to *virtual pairs*, the quantum-field fluctuations of *virtual pairs* are re-oriented towards the direction of the external field, so that the zero-point energy is reduced. The variation of the zero-point energies due to the longitudinal component of the external field dissipates back to the vacuum and the external field. While, the variation of the zero-point energies due to the transverse component of the external field drains to the proton as a recoiling effect. This recoiling effect is realized by an induced quantum field $A_\mu^{\rm ext}$ (3) back reacting on the proton. The re-orientation of quantum-field fluctuations of *virtual pairs* towards external field's direction takes place during their life-time $\delta\tau_p \sim 6.2 \cdot 10^{-11}$sec. (corresponding to 1.86cm). The zero-point energy variation $\delta\epsilon \sim \alpha^5 m = 5.2 \cdot 10^{-6}$eV, given by the Heisenberg uncertainty relationship, consistently with the rate (6) of the zero-point energy variation.

We discuss a proton passing through the vacuum. After triggered, the proton driven by the quantum-induced force moves from one spacetime point to another, *virtual pairs* are involved in interacting with the transverse component of proton's electric field, more and more the zero-point energy drains into the proton. As a consequence, the constant quantum-induced force, which is rather analogous to the Casimir force, is built to accelerates the proton, as if the proton gets a continuous recoil from the vacuum and rolls down along a potential with a very small slop $\sim -10^{-5}$eV/cm. In this spontaneous process, the proton gains the zero-point energy and the vacuum reduces its zero-point energy in such a way that the whole interacting

system of the vacuum and proton minimizes its interacting energy. This causes the energetically favourable instability and accelerating the proton runaway.

However, any other trigger forces $\vec{F}'_{tri}$ acting on the proton can alter the direction of the quantum-induced force $\vec{F}_q$, since the later always keeps in the same direction of acceleration of the proton. Let us consider the following case: a proton driven by $\vec{F}_q$ (6) moves in velocity $\vec{v}$ that is in the same direction of $\vec{F}_q$; a trigger force $\vec{F}'_{tri}$ acts on such a proton in the opposite direction of $\vec{F}_q$ and $|\vec{F}'_{tri}| > |\vec{F}_q|$. The direction of $\vec{F}_q$ is altered to the direction of $\vec{F}'_{tri}$. After the trigger force $\vec{F}'_{tri}$ is off, the direction of $\vec{F}_q$ turns out to be opposite to the direction of proton's velocity $\vec{v}$. This causes the de-acceleration of the proton, Eq.(6) is negative for energy-lost, indicating that the kinetic energy of the proton drains back to the zero-point energy of the vacuum. In general, this happens for $\vec{F}_q \cdot \vec{F}'_{tri} < 0$ and $|\vec{F}'_{tri}| > |\vec{F}_q|$. Trigger forces $\vec{F}_{tri}$ acting on protons are attributed to all real particles and fields, rather than virtual particles in the vacuum. With respect to a proton, these trigger forces are totally random in the spacetime. This indicates that in our Universe, some protons gain the zero-point energy from the vacuum, whereas others instead lose their kinetic energy to the vacuum, both directions are equally probable and none of them is preferential. Our Universe is not continuously heated up by gaining the zero-point energy of the vacuum.

To discuss the energy conservation in such an spontaneously induced process of the matter and vacuum interaction, we would like to first take the Casimir effect (force) as an analogue. The Casimir force(vacuum) drives two separating plates moving closer and closer at the cost of the zero-point energy of the vacuum. On the other hand, any external force(matter) drives against the Casimir force to separate two plates moving further and further, and makes an energy-drain back to the vacuum. The induced quantum force $\vec{F}_q$ accelerates particles at the cost of the zero-point energy of the vacuum, and de-accelerates particles at the cost of the kinetic energy of particles. Energy-drain goes in bath directions, back and forth in between the matter and vacuum. The total energy of our Universe is conserved.

UHECRs. Based on the rate of energy-gain (6) and considering those primary protons that the energy-gain prevails in their traveling, we give a very preliminary discussion on UHECRs. With the present size of the Universe $\sim 10^{28}$cm, protons can possibly reach the energy more than 10^{21}eV, if they travel a distance D of $10^{27} - 10^{28}$cm before reaching us. In such a scenario,

primary protons, the candidates of UHECR events, could be originated from the astrophysical sources of large redshift z, like Quasars, or from the early Universe, and no particular arrival direction can be identified.

The GZK cutoff does not apply to such a process of protons gaining energy bit by bit on their way to us. The reason is that protons, beyond ~ 50Mpc from us, have an energy much smaller than the energy threshold 10^{20}eV. This explains the absence of the GZK cutoff in UHECR events. However, when protons near us reach the energy 10^{21}eV, the GZK effect acts and average energy loss is about $(10^{-5}-10^{-6})$eV/cm^2, which is roughly in the order of energy gain (6). This implies that ultra high energy protons would not have large possibilities to exceed the energy 10^{22}eV.

We set the origin of a spherical coordinate at the center of a primary proton's source, whose size is $R_\circ$, number-density $n_\circ$ and mean outgoing velocity $v_\circ$. The total flux out of the source is $4\pi R_\circ^2 n_\circ v_\circ$. The Earth is located at R distance away from the source. The total flux passing through the spherical surface $4\pi R^2$ is $4\pi R^2 nv$, where n is the number-density of UHECR protons and v the mean velocity. We have the conservation of total numbers of UHECR protons:

$$4\pi R^2 nv = 4\pi R_\circ^2 n_\circ v_\circ (1+z)^{-3}, \tag{7}$$

where the factor $(1+z)^{-3}$ is due to the effect of expanding Universe. Thus we obtain the flux of UHECRs measured on the Earth,

$$\Phi = 4\pi R_\circ^2 n_\circ v_\circ (1+z)^{-3} \frac{1}{4\pi R^2} \sim \frac{1}{R^2}. \tag{8}$$

Due to the distribution of intergalactic magnetic field and/or galactic wind etc, protons normally travel in a zigzag way with a mean-free path λ_p. The distance D that protons travel is certainly larger than R. In one extreme case, protons travel to us in a straightforward line, $D = R$. While in another extreme case, protons travel in a way of random walk, $D = \frac{R}{\lambda_p} R$. This gives rise to the spectrum of UHECR flux observed on the Earth:

$$\Phi(E) \sim \frac{1}{R^2} \sim \frac{1}{E^\gamma} \qquad 1 \le \gamma \le 2, \tag{9}$$

where $\gamma = 2$ is for proton traveling in a straightforward line ($\lambda_p = R$) and $\gamma = 1$ in random walk.

References

1. W. E. Lamb and R. C. Retherford, Phys. Rev. Vol. 72 (1947) 241.
2. J.W. Cronin, Nucl. Phys. (Proc. Suppl.) B28, 213 (1992).

ULTRA HIGH ENERGY COSMIC RAYS AND THE FLUORESCENCE IN AIR SHOWERS (FLASH) EXPERIMENT AT SLAC

JOHN N. MATTHEWS
FOR THE HIRES AND FLASH COLLABORATIONS
The University of Utah
Department of Physics and High Energy Astrophysics Institute
115 S 1400 E #201 JFB Salt Lake City, UT 84112 USA

The High Resolution Fly's Eye collaboration has measured the spectrum of cosmic rays above 10^{17} eV using the air fluorescence technique. It is now possible to observe structure within this spectrum including a steep fall which is consistent with a GZK cut-off. This steep fall is inconsistent with measurements made by the AGASA ground array detector which indicates a continuing spectrum above $10^{19.5}$ eV. A difference in energy scales between the experiments could be part of the problem. A new collaboration, FLASH, has been formed to re-measure the fluorescence yield and its contribution to the uncertainty in the energy scale. A test run successfully demonstrated the feasibility of making these measurements at the Stanford Linear Accelerator Center. A program of three short experiments (E-165) has been approved by the SLAC experimental program advisory committee and the experiment has now been scheduled for beam time.

1. Introduction

The cosmic ray spectrum is steeply falling and relatively featureless. Over many orders of magnitude it follows a simple power law dependence: $E^{-2.8}$. What structure there is presents itself near 10^{16} eV, "the knee", where the spectrum becomes slightly more steep and again at $10^{18.5}$ eV, "the ankle", where it becomes slightly less steep. The question remains; Does it end?

After the discovery of the Cosmic Microwave Background (CMB) it was quickly realized that collisions between Ultra High Energy (UHE) cosmic rays and these low energy (2.7 K) photons would result in photo-pion production (via a delta resonance). This should render the universe essentially opaque to UHE cosmic rays beyond the mean free path in the CMB: approximately 100 Mpc. Therefore, we expect to observe a cut-off in the cosmic ray spectrum near 1.6×10^{19} eV. Events observed above this energy

must come from "nearby" sources. This is known as the Greisen-Zatsepin-Kuzmin (GZK) cutoff. [1,2]

In 1991, the Fly's Eye experiment unexpectedly observed an event with an amazing 3.2×10^{20} eV, well above the GZK limit. The Volcano Ranch, Haverah Park, and Yakutsk experiments each also observed one "super-GZK" event. More recently, the AGASA (Akeno Giant Air Shower Array) experiment observed a significant flux of "super-GZK" events. With a significantly higher exposure, AGASA observed ten "super-GZK" events. The flux observed above the GZK limit in these experiments appears to be inconsistent. Is this a resolution problem, an energy scale problem, or something else?

2. Detector Description

The Fly's Eye and its successor the High Resolution Fly's Eye (HiRes) both use the earth's atmosphere as their calorimeter. When a cosmic ray enters the atmosphere, it collides with an air molecule. In this hard collision, many secondary particles are produced. These, in turn, go on to collisions of their own. Thus, a cascade of particles or Extensive Air Shower (EAS) potentially containing many billions of particles, results. As the charged particles of the shower pass through the atmosphere, they excite the gas. When the molecules return to their ground state, they emit fluorescence light, mostly in the ultra-violet. (See figure 1.) The fluorescence light is emitted isotropically, so that if one looks, a track glowing in the UV develops at the speed of light.

The HiRes experiment employs an array of telescopes to observe these tracks. (See figure 2.) Each telescope uses a 5 m^2 spherical mirror to gather light and focus it onto a 16×16 array of hexagonal PMTs in a hexagonal close-pack AKA honeycomb geometry. Each PMT subtends 1° of sky. The PMTs observe events though a 300-400 nm UV band-pass filter which transmits the strongest air fluorescence signals while filtering out background star and man-made light.

Like its predecessor, the High Resolution Fly's Eye is located at the US Army's Dugway Proving Ground in Utah's west desert. The observatory is composed of two detector sites separated by 12.6 km. The first site, HiRes-I, contains 22 telescopes arranged in a single ring geometry observing nearly 2π in azimuth and between 3° and 17° in elevation. Many of these telescopes were previously used in the HiRes prototype and they are instrumented with an older version sample and hold electronics. The 5.6 μs integration period

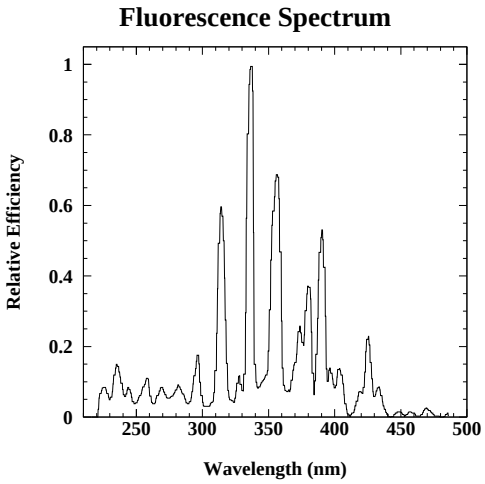

Figure 1. The fluorescence spectrum for air at sea level.
15

of these electronics is long enough to contain signals from all reconstructible events. The current HiRes-I site became operational in the spring of 1997. The second site, HiRes-II, is composed of 42 telescopes forming two rings. It observes nearly 2π in azimuth and between 3° and 31° in elevation. HiRes-II was completed late in 1999; considerably newer, these telescopes are instrumented with 100 ns FADC electronics.

With smaller pixels and larger mirrors than the Fly's Eye, the High Resolution Fly's Eye has an order of magnitude greater aperture than the original Fly's Eye or the present AGASA ground array (1000 km^2 str vs. 100 km^2 time averaged aperture). It also has significantly improved energy and shower profile resolution. It was designed for stereo observation of cosmic ray showers with energies above 3×10^{18} eV. The physics goals are to measure the cosmic ray spectrum and chemical composition of the incoming particles in addition to searching for point sources and/or anisotropy and Ultra High Energy neutrinos, gamma rays, and other exotic particles. For the present purposes, we concentrate on the Ultra High Energy Cosmic Ray (UHECR) spectrum and then only the monocular results (events observed by only one HiRes site), for which we have accumulated significant statistics. A typical event is shown in figure 3.

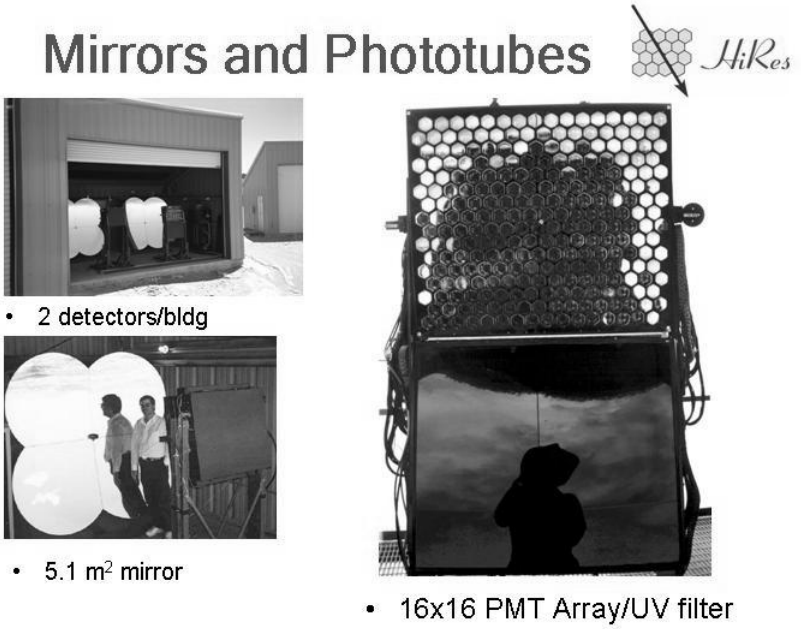

Figure 2. Some pictures of the HiRes detectors. Top left is a typical HiRes building housing two telescopes. Bottom left, one can see a mirror in the background and a PMT array in the foreground. The front side of the PMT cluster can be seen on the right where the UV filter has been opened to show the tubes.

3. Data Collection and Analysis

The HiRes detector collects data on clear, moonless nights and has a duty cycle approaching 10%. The current HiRes-I data set consists of events from the date of the detector's turn-on in June of 1997 through September of 2001. It contains 3100 hours of data, 2410 hours of which are "good weather" as identified by the operators. During that time, over 125 million triggers were written, however these mostly consist of noise and atmospheric monitoring data. Amongst these, 10,968 track candidates were found after cuts such as minimum track distance, minimum light level, and observation of the shower maximum.

Due to the limited angular coverage of HiRes-I, it is unable to completely reconstruct the event geometry using timing information alone. However, the HiRes Prototype, which had extensive zenith angle coverage, has previously shown that while the depth of shower maximum fluctuates, the shower shape has little variation. [3] That measurement also found that the

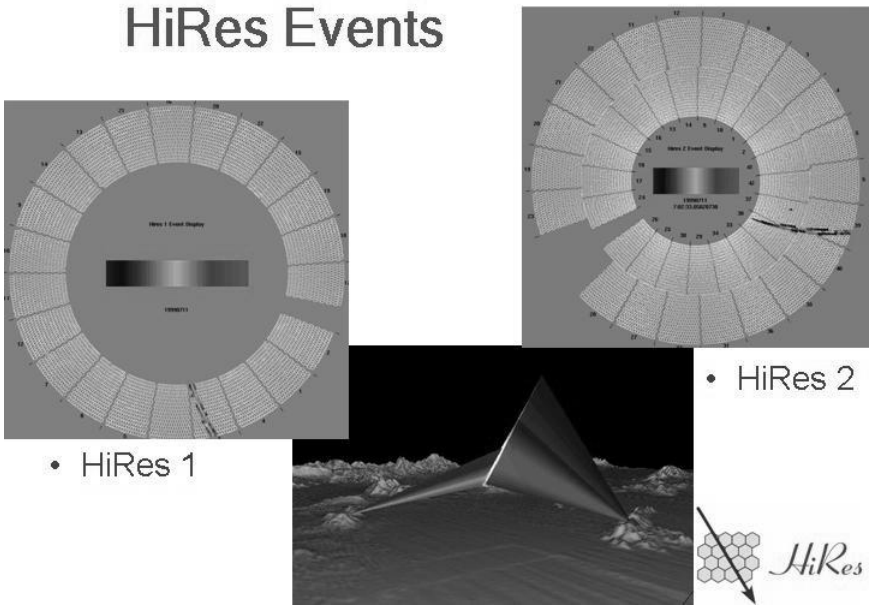

Figure 3. An event display for a typical stereo HiRes event. Top left, is the event display for HiRes-I. The center of the picture is up. The ring is what the portion of the sky which the detector sees. The outer edge is 3 degrees above horizon, the inner edge is 17 degrees above horizon. The top of the ring is north and the right side is east. The track can be seen, bottom right. The same event as seen by HiRes-II is top right. Below is a composite of what the two sites see overlayed with the local topology.

shower profile was a good fit to a parameterization previously presented by Gaisser and Hillas. [4] Using the additional constraint of the expected shower shape allows HiRes-I data to be reconstructed with significantly smaller uncertainties. We call this a profile constrained fit (PCF). After reconstruction and cutting on minimum track length, maximum Čerenkov light contamination, 5264 showers remained.

The HiRes-II data set covers December 1999 though May 2000, a period where the trigger conditions were stable. The analysis for these events is similar, except that the longer angular tracks and the improved timing resolution provided by the FADC system, the events can now be reconstructed based on timing information - the profile constraint is no longer necessary. For this period, 781 events remained after cuts. [5,6]

Monte Carlo (MC) studies were performed to assess the reliability of

the PCF method. The simulated events were subjected to the same selection criteria and cuts imposed on the data. Not including atmospheric fluctuations, an RMS energy resolution of better than 20% was seen above 3×10^{19} eV. However, the resolution degrades at lower energies to about 25% at 3×10^{18} eV. These MC results were cross-checked by examination of a small set of stereo events where the geometry is more precisely known. Comparing the reconstructed energies and geometric parameters using monocular and stereo geometries, we obtained resolutions in good agreement with those seen in the MC.

The MC simulation is also used to calculate the detector aperture. Here the simulated events were subjected to the same reconstruction algorithm and cuts applied to the data. To verify the reliability of this calculation, we compared, at different energies, the zenith angle (θ) and impact parameter (R_p) distributions, which define the detector aperture. The MC predictions for these are very sensitive to details of the simulation, including the detector triggering, optical ray-tracing, signal/noise, and the atmospheric modeling. We saw excellent agreement between data and MC. For example, we show the comparison of R_p distributions at three energies in Figure 4.

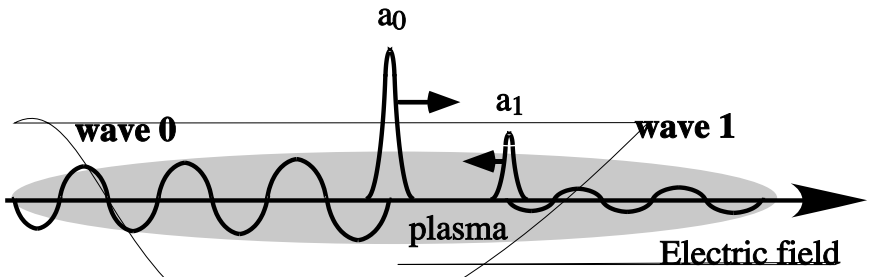

Figure 4. Comparison of HiRes-I simulated (histogram) and observed (points) R_p distributions at (a) $10^{18.5}$, (b) $10^{19.0}$, and (c) $10^{19.5}$ eV. The MC distributions are normalized to the number of data events.

The monocular reconstruction apertures are shown in figure 5; both HiRes-I and II approach 10^4 km^2 steradian above 10^{20} eV. We restrict our result for HiRes-I to energies $> 3\times10^{18}$ eV; below this the profile constraint technique is unstable. Due to longer tracks and additional timing information, the RMS energy resolution for HiRes-II remains better than 30% down to 10^{17} eV. However, due to the significantly shorter running time, the HiRes-II data sample becomes statistically depleted above 10^{19} eV. We deal with this problem by combining the two sets of monocular data to get

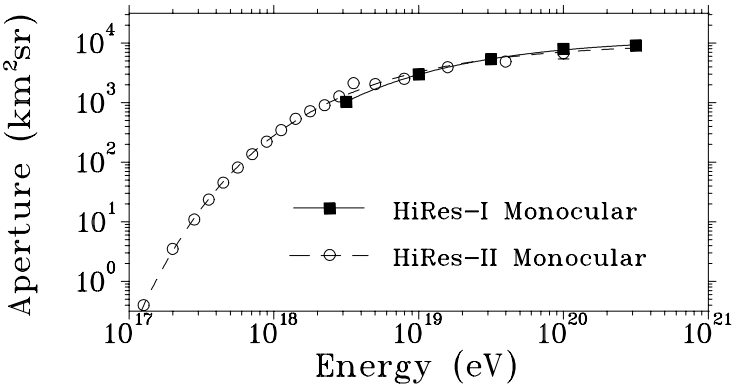

Figure 5. Calculated HiRes monocular Reconstruction aperture in the energy range $10^{17} - 3 \times 10^{20}$ eV. The HiRes-I and -II apertures are shown by the squares and circles, respectively.

one spectrum which stretches from near 10^{17} eV to beyond 10^{20} eV.

We calculated the cosmic ray flux for HiRes-I above 3×10^{18} eV, and for HiRes-II above 2×10^{17} eV. This combined spectrum is shown in Fig. 6, where the flux $J(E)$ has been multiplied by E^3. In the region of overlap, the HiRes-I and HiRes-II detectors are in excellent agreement. For comparison, current spectrum from the AGASA experiment[7] is also shown. The error bars represent the 68% confidence interval. The HiRes-I flux is the result of two nearly independent analyses [8,9], which yielded essentially identical flux values.

The largest systematic uncertainties are the absolute calibration of the detectors ($\pm 10\%$) [10], the yield of the fluorescence process ($\pm 10\%$) [11], the correction for unobserved energy in the shower ($\pm 5\%$) [12,13], and the modeling of the atmosphere. [14] To test the sensitivity of the flux measurement to atmospheric uncertainties, we generated new MC samples with atmosphere altered by ± 1 RMS value. The MC was then reconstructed using the expected average atmosphere. We found a $\pm 15\%$ change which represents a conservative over-estimate of the one sigma uncertainty from atmospheric effects. If we add in quadrature this uncertainty to the others mentioned above, we find a net systematic uncertainty in $J(E)$ of 21%. This uncertainty is common to the fluxes for HiRes-I and HiRes-II. There is an additional relative calibration uncertainty between the two sites which is less than 10%. [5]

Evident in the figure is a dip near an energy of 5×10^{18} eV and a subse-

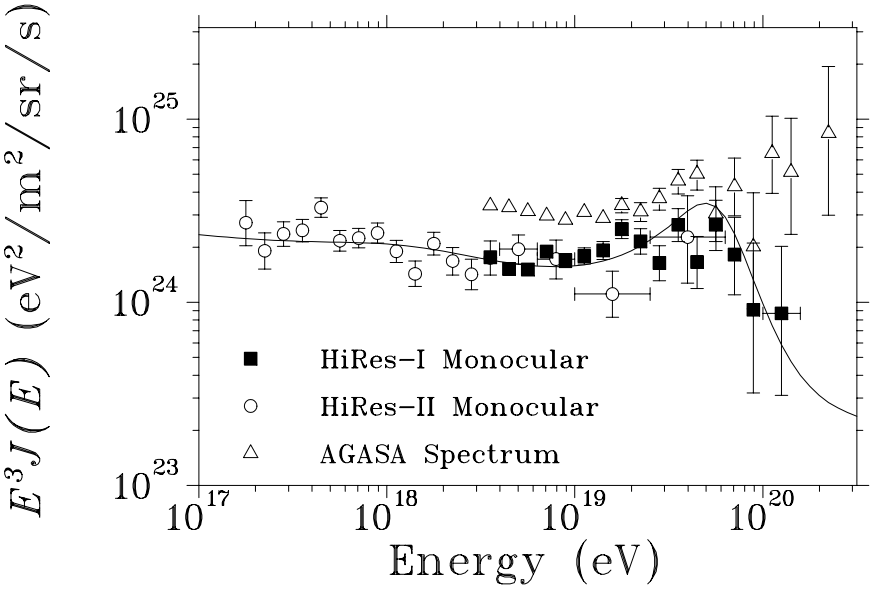

Figure 6. Combined HiRes monocular energy spectrum. The squares and circles represent the cosmic ray differential flux $J(E)$, multiplied by E^3, measured by HiRes-I and HiRes-II, respectively. The line is a fit to the data of a model, described in the text, of galactic and extra-galactic cosmic ray sources. The AGASA spectrum shown is taken from their Internet site[7].

quent flattening of the spectrum. The HiRes data is in disagreement with a constant power law. Fitting the slope at lower energies and extrapolating, one would expect to find 19 events above $10^{19.8}$ eV where we only observe four, a Poisson probability of 1.4×10^{-4}. This is in disagreement with the AGASA spectrum which seems to indicate a continuing power law. In addition, the dip structure is at a higher energy in the AGASA data and the overall normalization is higher in the AGASA data.

The discrepancies may be partially due to different energy scales. Scaling the AGASA data by 0.79 causes it to virtually overlay the HiRes data. Ground array experiments such as AGASA relate the surface particle density in an EAS measured about 1 km from the core to the primary particle's energy via a Monte Carlo calculation. The distance is chosen as the point at which the MC fluctuations are minimized. The energy scale for an air fluorescence measurement is much more direct. It depends upon knowledge of the air fluorescence efficiency and the atmospheric transmission of the light to the detector.

An uncertainty in the fluorescence yield folds directly into energy uncertainty in the HiRes measurement. In addition, as data continues to accumulate and statistical uncertainties are reduced, it becomes important to further reduce the systematic uncertainties. One effort to reduce the systematic uncertainties is a new measurement of the fluorescence yield.

HiRes currently traces its measurements back to the spectrum of Bunner. [15] Kakimoto *et al.* measured an overall fluorescence yield over the 300-400 nm range as well as the strength of a few lines. [11] Since Kakimoto only measured a few lines, HiRes monocular analysis uses the spectral shape provided by Bunner, with an overall yield (between 300 and 400 nm) normalized to Kakimoto.

At the 2001 International Cosmic Ray Conference in Hamburg, Germany, Nagano announced new fluorescence yield measurements which have recently been submitted for publication. [16] In this paper, the authors state that the photon yield which they believe HiRes is using is 13% smaller then their current measurement. Nagano *et al.* also disagree with previous measurements on specific spectral lines by factors of 2.8 - 3.5. Specifically, in this measurement, the 390 nm line is significantly less pronounced. The effect of this on the HiRes analysis is non-linear due to the λ^4 dependence of atmospheric attenuation. At 30 km, a 25% energy shift can result if there is a 40% reduction in light in the 390 nm line.

In addition to the potential problems pointed out by Nagano, there are two further weaknesses. The previous measurements of the fluorescence yield indicate that the yield is proportional to dE/dx, however, there were no measurements in the critical 100 keV - 1 MeV region. Finally, the pressure dependence is not well measured below 100 Torr. As a result of these uncertainties, some members of the HiRes group formed a collaboration with the Stanford Linear Accelerator Center, Laboratory Astrophysics group and the Taiwan Center for Cosmology and Particle Astrophysics. We proposed to make a new detailed measurement of the fluorescence yield and spectrum. A first pass of this, mostly a proof of principle, was performed in June 2002 as SLAC test T-461.

SLAC is an ideal place to perform this measurement since it can provide a very high intensity electron beam. Firstly, important nitrogen fluorescence transitions have been demonstrated to be inaccessible to proton or alpha excitations. Electrons are required to study all of the relevant transitions. An EAS produced by a cosmic ray of HiRes energies is a superposition of many electromagnetic sub-showers. By providing an electron bunch composed of 10^9 electrons each at 28.5 GeV, SLAC mimics an EAS

from a $\approx 10^{20}$ eV particle. (It reaches HiRes energy scales.) Finally, most of the energy in an EAS at shower maximum is carried by electrons near the critical energy in air ($\approx$100 MeV). This can be reproduced by dumping the SLAC beam into a thick target.

For T-461, we chose to simply measure the overall yield between 300 and 400 nm for a variety of gases and pressures. The measurements were performed in the Final Focus Test Beam at SLAC. The beam is of mm scale size and ps length. The energy of the electrons is 28.5 GeV and the pulse rate is 10 Hz. Into this beam, we put a vacuum vessel instrumented with two PMTs. Each PMT was fitted with a HiRes 300-400 nm UV band pass filter. On the opposite side of the tank from the PMTs were UV LEDs which could be pulsed to monitor PMT stability and gain. Two blind PMTs were also packed into the beam line next to the tank PMTs for the purpose of measuring the background. A sketch of the vessel is shown in figure 7.

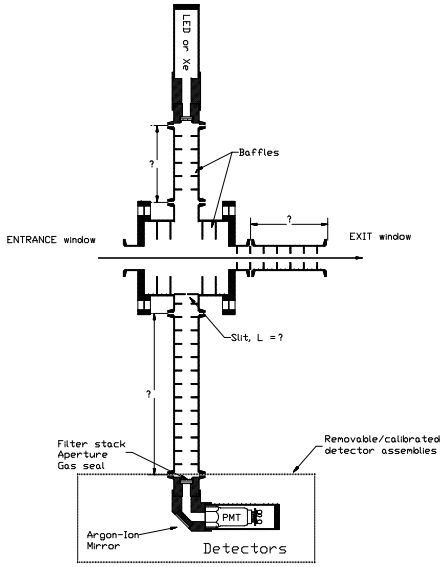

Figure 7. A sideview sketch of the SLAC T-461 fluorescence yield chamber. The beam enters via a vacuum window on the left and exits via another window on the right. The gas pressure and composition were controlled from outside the beam line. There were four side ports into the vessel. Two were instrumented with PMTs and two housed LED's which were flashed out of sync with the beam in order to monitor PMT gain and stability.

Data was collected during two, one week periods in June 2002. There were 707 individual data runs each with 2500 - 5000 events or beam pulses. Approximately two million events were recorded. The overall yield was measured between 300 and 400 nm. The pressure dependence for this same wavelength range was measured between 3 and 760 Torr. The average lifetime of the excitations was measured as a function of pressure. Measurements were made for nitrogen, air, nitrogen-air mixes, and ethylene (which does not fluoresce and hence is a background measurement).

In addition to the PMT stability, PMT high voltage, gas composition and pressure, vessel temperature, beam charge etc... were monitored. Lifetime measurements were made on the excitations to verify that indeed we were seeing fluorescence. (See figure 8) A preliminary measurement of the overall yield as a function of pressure is shown in figure 9. Despite their rough nature, the results are consistent with expectations based on Kakimoto and Nagano.

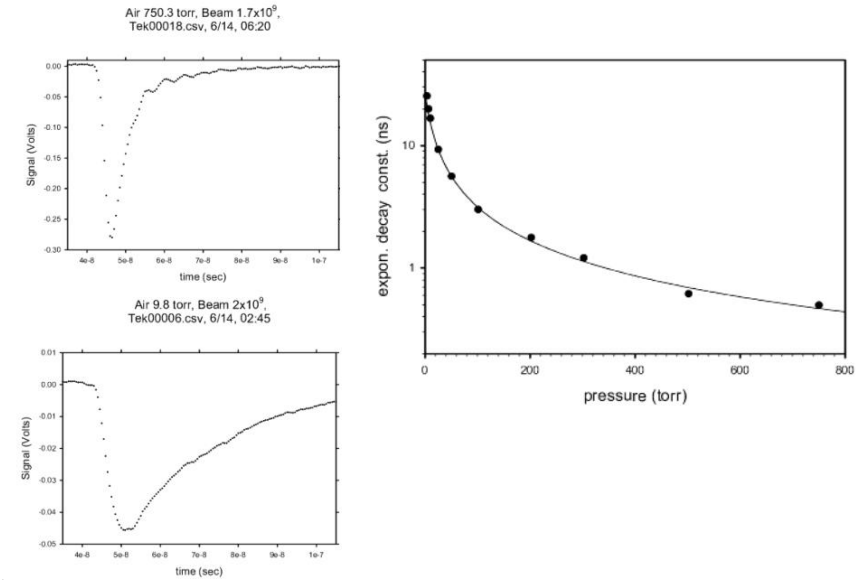

Figure 8. The two plots on the left show the lifetime of the decay in air at 750 torr (top) and 9.8 torr (bottom). On the right, the exponential decay constant is plotted as a function of pressure in torr. This is a good check that one is actually measuring fluorescence light.

Estimates of the larger uncertainties include the PMT calibration and

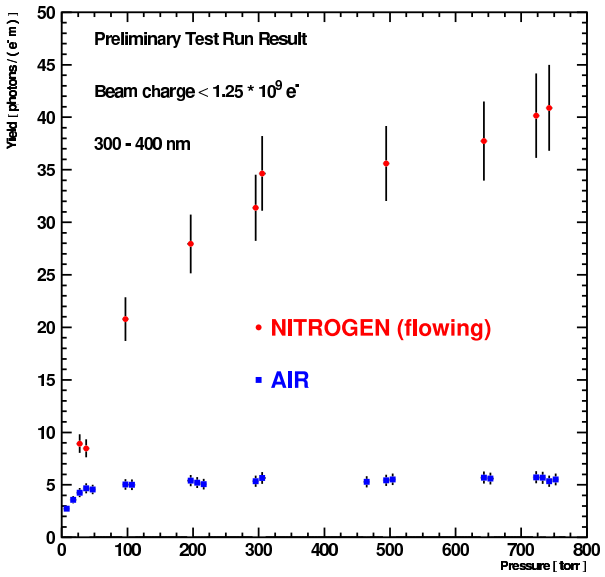

Figure 9. Preliminary results from the test run T-461. The fluorescence efficiency is plotted for nitrogen (circles) and air (squares) as a function of pressure from 10 - 760 torr. This is the integrated light through a 300 - 400 nm band bass filter with a beam charge of 1.25×10^9 e^-/pulse.

spectral assumption (∼10%), beam charge (∼5%), ADC to beam current conversion (∼3%), and geometrical acceptance (∼3%). The total uncertainty is of order 15-20%.

Having successfully demonstrated the detectability of nitrogen and air fluorescence in a thin gas chamber at SLAC, the collaboration submitted a proposal to the SLAC experimental program advisory committee (EPAC). The FLuorescence in Air Showers (FLASH) proposal was for a two part experiment - a thin target part and a thick target part. The objectives of FLASH are a) to produce a spectrally resolved yield to better than 10%, b) to measure the dependence on electron energy, c) to determine the effects of atmospheric impurities and d) to observe the showering of electron pulses in air equivalent material (Al_2O_3). FLASH/E-165 was presented to the EPAC in November of 2002 and approved. It was recently scheduled for beam time in September 2003 as well as February and June 2004.

In the thin target portion of the experiment, the yield will once again be studied using a variety of gases. These will again include air and nitrogen, however impurities of H_2O, CO_2, Ar, etc... will also be studied.

The wavelength dependence will be measured using filter wheels and a variety of narrow band filters to zoom in on the predicted emission lines. A spectrometer may also be used.

In the thick target stage, various thicknesses of alumina Al_2O_3, will be inserted into the beam to study the shower as it develops. The effects of low energy (<1MeV) electrons will be studied as will proportionality to dE/dx. Comparisons will be made to various shower models (EGS, GEANT, CORSIKA) to determine how closely they predict fluorescence light levels. In addition, we will measure how closely fluorescence yield tracks shower development.

Recently, several other groups interested in the fluorescence technique are pushing new initiatives to better understand air fluorescence. A variety of sources, energies, and techniques are under consideration. The efforts are largely complementary. A first international workshop to discuss these efforts was held in October, 2002 at the University of Utah. A follow-up meeting is already under consideration for Germany in October, 2003.

4. Conclusion

The High Resolution Fly's Eye has made monocular measurements of the UHE cosmic ray spectrum and observes significant structure in that spectrum. In particular, it sees a sharp decrease in the event rate at the highest energies. This is consistent with GZK cut-off expectation. It is inconsistent with the continuing spectrum which the AGASA experiment appears to observe. The collection of additional statistics are required to confirm this, especially in stereo mode where the geometry is precisely determined.

In an effort to resolve the discrepancy with AGASA and to decrease the systematic uncertainties associated with the fluorescence yield, a fluorescence yield experiment (FLASH) was proposed. FLASH aims to achieve an accuracy better than 10% in the total fluorescence yield and in the individual spectral lines. FLASH will be realized in two stages: thin and thick target modes. FLASH was approved by the SLAC EPAC and was recently scheduled for beam time.

We hope that FLASH will help to shed light on the apparent differences between HiRes and AGASA, and provide reliable information for future fluorescence-based UHECR experiments.

5. Acknowledgements

HiRes is supported by US NSF grants PHY-9322298, PHY-9321949, PHY-9974537, PHY-9904048, PHY-0071069, PHY-0140688, by the DOE grant FG03-92ER40732, and by the Australian Research Council. We gratefully acknowledge the contributions from the technical staffs of our home institutions and the Utah Center for High Performance Computing. The cooperation of Colonels E. Fischer and G. Harter, the US Army, and the Dugway Proving Ground staff is greatly appreciated.

References

1. K. Greisen, Phys. Rev. Lett. **16**, 748, (1966).
2. G.T. Zatsepin and V.A. K'uzmin, Pis'ma Zh. Eksp. Teor. Fiz. **4**, 114 (166) [JETP Lett. **4**, 78 (1966)].
3. T. Abu-Zayyad, *et al.*, Astroparticle Phys., **16**, 1, (2001).
4. T. Gaisser and A.M. Hillas, Proc. 15th Int. Cosmic Ray Conf. (Plovdiv), **8**, 353, (1977).
5. T. Abu-Zayyad, *et al.*, Submitted to Phys. Rev. Lett., (2002). Also astro-ph/0208301
6. T. Abu-Zayyad, *et al.*, Submitted to Astroparticle Phys., (2002). Also astro-ph/0208243
7. The AGASA Spectrum taken from http://www-akeno.icrr.u-tokyo.ac.jp/AGASA/
8. T. Abu-Zayyad, Ph.D Thesis, University of Utah (2000).
9. X. Zhang, Ph.D Thesis, Columbia University (2001).
10. T. Abu-Zayyad *et al.*, to be submitted to NIM.
11. F. Kakimoto, *et al.*, NIM **A372**, 527 (1996).
12. C. Song, Z. Cao *et al.*, Astropart. Phys. **14**, 7,(2000).
13. J. Linsley, Proc. 18th Int. Cosmic Ray Conf. (Bangalore), **12**, 135, (1983).
14. T. Abu-Zayyad *et al.*, in preparation, and http://www.cosmic-ray.org/atmos/.
15. A.N. Bunner, Ph.D. thesis (Cornell University) (1967).
16. M. Nagano, *et al.*, astro-ph/0303193 v1 (2003).

AN OVERVIEW OF ASTROPHYSICAL ACCELERATORS

FRANK C. JONES
NASA/Goddard Space Flight Center Greenbelt, MD USA

There have been many acceleration mechanisms proposed to explain the presence of energetic charged particles that appear to fill the observable universe. All of these processes share an underlying similarity and they also appear to share a common upper energy limit that the charged particles are able to attain. I will discuss some of these mechanisms, several of which are presented at this conference session, and point out there similarities and argue that all of them are subject to the same scaling law that limits their maximum attainable energy (the Hillas rule).

1. Introduction

In astrophysics there are two quite different scenarios that are invoked in the various theories of the origin of ultra high energy cosmic rays. One, called the Top Down picture describes the origin of such particles as the decay products of exotic particles or topological defects in space left over from the creation of the universe. Their energy is high because their parent particles were extremely massive and a great deal of energy was available in the decay. The Top Down scenario may be true but it is not what we usually mean by "acceleration". I will therefore devote my discussion to the Bottom Up scenario in which charged particles start at nominal energies and are subsequently accelerated to high energies by normal physical processes. I will, further, consider only charged particles because it is almost universally believed that energetic neutral particles are created in collisions of even more energetic charged particles.

2. What accelerates a particle?

Starting with the Lorentz force equation

$$\vec{F} = e(\vec{E} + \frac{\vec{v}}{c} \times \vec{B}) \tag{1}$$

we can compute the work done on a charged particle

$$\vec{F} \cdot \vec{v} = e\vec{E} \cdot \vec{v} \tag{2}$$

In a conducting plasma at rest $\vec{E} = 0$ but in a frame where the plasma moves with velocity $\vec{U}$ we have:

$$\vec{E} = -\frac{\vec{U}}{c} \times \vec{B} \tag{3}$$

and rearranging terms we obtain

$$\begin{aligned} \vec{F} \cdot \vec{v} &= -e \left(\frac{\vec{U}}{c} \times \vec{B} \right) \cdot \vec{v} \\ &= \vec{U} \cdot \left(e \frac{\vec{v}}{c} \times \vec{B} \right) \\ &= \frac{d\mathcal{E}}{dt} \text{ .. particle} \end{aligned} \tag{4}$$

and we see that the particle gains energy from the motion of the plasma working against the $v \times B$ force. The acceleration is, therefore, equivalent to a particle bouncing off of a blob or cloud of plasma with an embedded magnetic field. Such an interaction may be considered as a simple elastic (in the plasma frame) scattering.

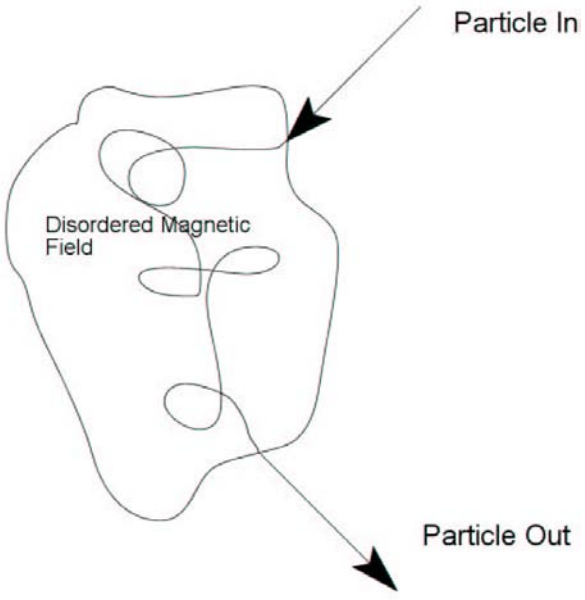

Figure 1. Particle scattering in disordered magnetic field in a plasma cloud.

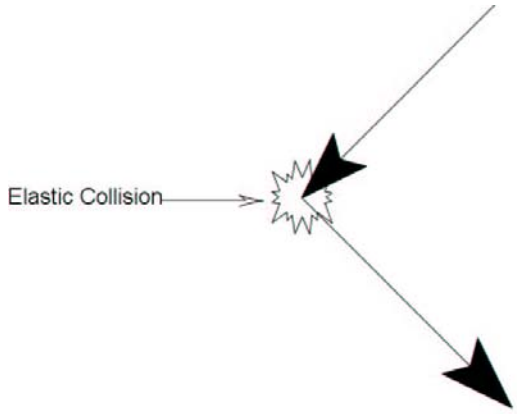

Figure 2. Scattering in Fig. (1)may be abstracted as a single scattering

3. Stochastic Acceleration

If U represents the speed of the moving clump of magnetic field and δw is the change of energy of a particle with energy w on colliding with a cloud, δt is the time between scatterings and λ is the mean free path between scatterings we have

$$\frac{\delta w}{w} = \left(\frac{U}{c}\right)^2 \; ; \delta t = \frac{\lambda}{v} \tag{5}$$

and α, the time rate of energy gain is given by

$$\alpha = \frac{1}{w}\frac{\delta w}{\delta t} = \frac{v}{\lambda}\left(\frac{U}{c}\right)^2 . \tag{6}$$

If we consider that a particle will continue to gain energy until it diffuses out of the region, of size L in which the moving magnetic scatterers are acting it will be accelerate, on the average, for a time T where

$$T = \frac{3L^2}{v\lambda}. \tag{7}$$

Then the theory of Fermi gives the resulting spectrum as

$$j = w^{-\nu} \tag{8}$$

where

$$\nu = 1 + \frac{1}{\alpha T} = 1 + \frac{1}{3}\left(\frac{UL}{c\lambda}\right)^{-2} . \tag{9}$$

Clearly we need $\frac{UL}{c\lambda} \geq 1$ or the exponent of the spectrum, ν will become large and the spectrum will be effectivly cut off. Since the mean free path must be at least as large as the gyroradius we have

$$\lambda = \eta r_g = \eta \frac{\gamma mcv}{ZeB} \approx \eta \frac{E}{ZeB} \tag{10}$$

where η is equal or greater than 1. This gives

$$Ze\frac{U}{c}\frac{BL}{\eta} \geq E \tag{11}$$

which is known as the Hillas limit.[1]

4. Diffusive Shock Acceleration

Shocks propagating through a diffusive (in the sense of Section 3) medium accelerate particles by scattering them in a more ordered fassion than in stochastic acceleration. In Fig. (3) we see how a particle scatters from one scattering to another and although the scattering centers are not moving at random with respect to each other whenever the particle crosses the shock it experiences converging flow and hence a compressiv heating or energization.

In a diffusive shock the e-folding time for acceleration is given by κ_n/U^2 where κ_n is the particle diffusion coefficient parallel to the shock normal. If the lateral extent of the shock is L the time required for a particle to diffuse to the shock's edge and escape is given by L^2/κ_p where κ_p is the particle diffusion coefficient pependicular to the shock normal. Clearly when the escape time becomes equal to or less than the acceleration time the prosess ceases to be effective and the spectrum is cut off.

This will occur when

$$\kappa_n/U = L^2/\kappa_p \tag{12}$$

rearranging gives

$$\kappa_n\kappa_p \approx \kappa_\perp\kappa_\parallel = L^2U^2 \tag{13}$$

Since it can be shown that

$$\kappa_\perp\kappa_\parallel = \frac{\kappa_\perp^2 r_g^2}{\lambda^2} \approx v^2 r_g^2 \tag{14}$$

Eqn.(13) becomes

$$r_g = L\left(\frac{U}{v}\right) \approx L\left(\frac{U}{c}\right) \tag{15}$$

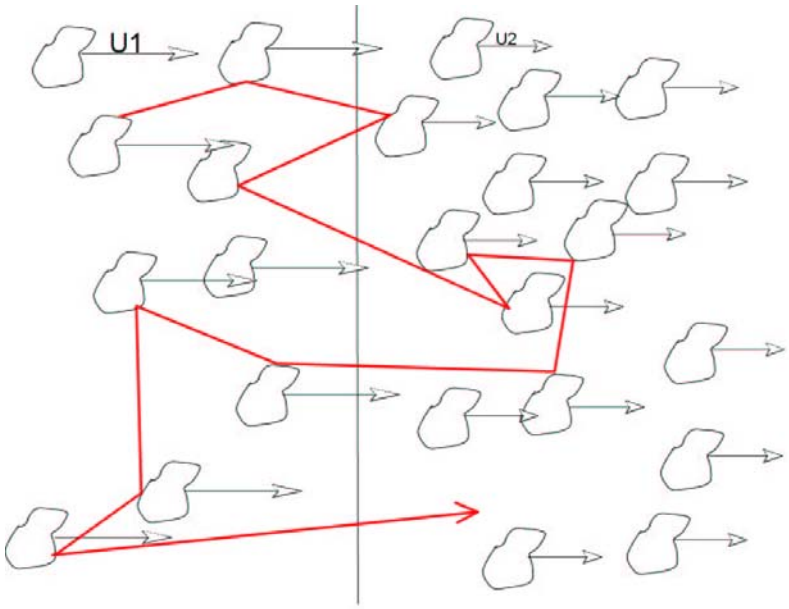

Figure 3. Particle scattering back and forth across a shock.

and since $r_g = \gamma mcv/ZeB$ where Z is the nuclear charge number we obtain the final expression

$$\gamma mc^2 = w_{max} = Ze\frac{U}{c}BL \tag{16}$$

which is just, once again the Hillas limit.

5. General Diffusive Acceleration

We saw that in stochastic acceleration

$$\frac{1}{w}\frac{\delta w}{\delta t} \propto \left(\frac{U}{v}\right)^2 \left(\frac{\lambda}{v}\right) \tag{17}$$

and in diffusive shock acceleration the energy gain per shock crossing (SC) is

$$\frac{1}{w}\frac{\delta w}{\delta(\mathrm{SC})} \propto \left(\frac{\Delta U}{v}\right) \approx \left(\frac{U}{v}\right) \tag{18}$$

but the rate of shock crossing is given by

$$\frac{\delta\ (\mathrm{SC})}{\delta t} \approx (U/v)\left(\frac{\lambda}{v}\right) \tag{19}$$

and thus

$$\frac{1}{w}\frac{\delta w}{\delta t} \propto \left(\frac{U}{v}\right)^2 \left(\frac{\lambda}{v}\right) \tag{20}$$

so even though the energy gain rate *per shock crossing* is first order in U/v the gain *per unit time* is second order in this quantity and hence the two processes proceed at similar rates. The main advantage that shock acceleration has over stochastic acceleration that the flow velocities are ususlly much faster (super Alfvénic) in shocks while the scattering centers in stochastic accleration usually are Alfvén waves and hence travel with the Alfvén speed.

6. Colliding Galaxies

Some believe that the highest energy particles are accelerated by the collision of galaxies where particles are trapped in the compressing magnetic fields of the galaxies. If the galaxy's velocity is greater than the Alfvén speed in the intracluster medium a bow shock will form. Further, if the medium is turbulent enough the diffusion scale will be smaller than the galaxy separation distance and single shock acceleration will be the picture.

In a typical case we will have

$$E_{max} = L_{100} U_{300} Z B_3 \times 10^{17} \text{ eV} \tag{21}$$

where

$$\begin{aligned} L &= L_{100} \times 100 \text{ kpc} \\ U &= U_{300} \times 300 \text{ km/sec} \\ B &= B_3 \times 3 \ \mu\text{g} \end{aligned} \tag{22}$$

Cesarsky and Ptuskin proposed [2] a "low entropy model" in the Calgary ICRC. Turbulence is assumed low and diffusion scales are much larger than the separation distance of the galaxies. In this picture particles go back and forth between the magnetic fields of the individual galaxies and are accelerated by the electric fields induced by the moving magnetic fields, $E = BU/c$.

We have, therefore, the rate of momentum gain given by $dp/dt = ZeE = ZeBU/c$. According to Cesarsky and Ptuskin the particle will stay in the system until it drifts across the size of the galactic field so the acceleration time is limited to $T = L/v_d$ where the drift velocity due to the curvature

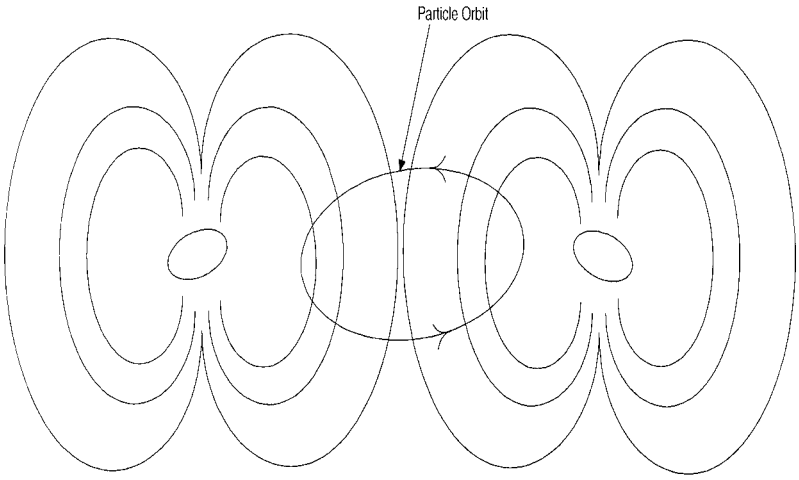

Figure 4. Particle orbit trapped between colliding galaxies.

and gradients of the magnetic field is approximately given by $v_d \approx cr_g/L$. Thus $p_{MAX} = ZeBL^2U/c^2r_g$ Inserting the expression given above for r_g this may be solved to obtain

$$E_{MAX} = ZeBL\left(\frac{U}{c}\right)^{1/2} \tag{23}$$

It would appear that, due to the fact that the term U/c appears under the square root, we have made a considerable gain in efficiency. It is true that the coherent type of acceleration described here is faster than the shock acceleration process which must rely on scattering of the particles to bring them back to the shock for further acceleration. This would seem to indicate that smooth, low turbulence, structures are better accelerators; they are if they are carefully designed. However, in nature, magnetic fields are rarely such good trappers of charged particles especially if they are dynamic. And, if the configuration *is* a trapping configuration, the question arises as to how the particles go there in the first place. In fact such configurations will

usually squirt out particles at about the particle speed v.

If the fields of the two approaching galaxies are aligned the geometry is a mirror and particles will reflect out of the system with $v_d \approx c$. If, on the other hand, the fields are opposed there is a neutral line or sheet and the scale of variation of the field is r_g rather than L and once again $v_d \approx cr_g/r_g = c$.

Employing this value yields:

$$p_{MAX} = \left(ZeB\frac{U}{c}\right)\left(\frac{L}{c}\right) \tag{24}$$

and

$$E_{MAX} = ZeBL\frac{U}{c} \tag{25}$$

Which is just the expression we obtained earlier for a diffusive shock.

7. Rotating Black Holes

It has been pointed out by several authors [3,4] that a maximally spun up Kerr black hole of $\approx 10^9$ solar masses threaded by an externally produced magnetic field of $\approx 10^4$ g would develop an electrical potential of $\approx 10^{20}$ volts. This is obtained by analyzing Maxwell's equations with simple dimensional arguments. In standard units where the black hole's mass and specific angular momentum, M and a respectively have the dimension of length and $\frac{ac}{M^2}$ has the dimension of frequency we have the approximation

$$\vec{\nabla} \times \vec{E} = \frac{\partial \vec{B}}{\partial t} \Longrightarrow \frac{E}{M} \approx \frac{ac}{M^2}B \tag{26}$$

assuming $a \approx M$ we have

$$\begin{aligned} V &= E \cdot M = acB \\ &= 4.4 \times 10^{20} B_4 M_9 \text{ eV} \end{aligned} \tag{27}$$

where $B = B_4 \times 10^4$g and $M = M_9 \times 10^9 M_\odot$ Some [4,5,6] argue that this potential is available to accelerate charged particles along the magnetic field lines thus producing the ultra high energy cosmic rays. Most authors ,however, assume that this electric field will have no component parallel to the magnetic field since it would be shorted out by the ambient plasma to produce the frozen field or degenerate field configuration.[7]

One can estimate the charge density required to short out the parallel electric field component. We recall that the magnetic field that threads the

black hole's (stretched) event horizon must be produced by currents exterior to the black hole. This requires a plasma with sufficient charge density to support the currents. This is given by the following considerations

$$\vec{\nabla} \times \vec{B} = \mu_0 \vec{j} \approx \frac{B}{M} \tag{28}$$

$$j \approx \rho_c v \Longrightarrow \rho_c \approx \frac{B}{\mu_0 v M} \tag{29}$$

The charge density required to short out the electric field is given by

$$\vec{\nabla} \cdot \vec{E} = \frac{1}{\epsilon_0}\rho_E \approx \frac{E}{M} \tag{30}$$

$$\Longrightarrow \rho_E \approx \epsilon_0 \frac{ac}{M^2} B \tag{31}$$

The ratio of these two charge densities is given by

$$\frac{\rho_E}{\rho_c} \approx (\epsilon_0 \mu_0 c^2 = 1)\frac{v}{c}\frac{a}{M} < 1 \tag{32}$$

There is plenty of plasma around to short out the field and make $\vec{E} \cdot \vec{B} = 0$. This indicates that models in which charged particles are accelerated directly to ultra high energies by a vacuum electric field are unlikely to be realized in nature.

8. Wakefield Acceleration

When a strong pulse from a laser passes through a plasma it excites a longitudinal electric wake field, shown symbolicly in Fig.(5). This pulse can trap charged particles around its potential minimum and because it is traveling very close to the speed of light these particles aquire very high energies. Furthermore, if this process is occuring in a jet of plasma which is itself moving with relativistic speeds, these accelerated particles recieve an additional boost in energy and can achieve ultra high energy.

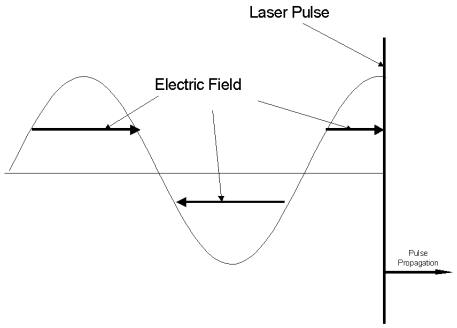

Figure 5. Symbolic view of wakefield of a laser pulse.

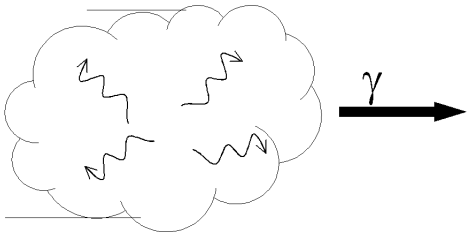

Figure 6. Particles accelerated inside a relativistic jet

$$F(E') = \frac{E'}{2\gamma} \int_{E/\gamma}^{\gamma E} \frac{f(E)}{E^2} dE \tag{33}$$

A*ssume*

$$f(E) = AE^{-q} \qquad E < E_{\rm M}$$
$$f(E) = 0 \qquad\quad E > E_{\rm M}$$
$$F(E') = \frac{A}{2(q+1)} \left(\frac{E'}{\gamma}\right)^{-q} \times \left(1 - \left(\frac{E'}{\gamma E_{\rm M}}\right)^{q+1}\right) \tag{34}$$

We see that the boosted spectrum is essentially the original spectrum shifted up in energy by a factor γ.

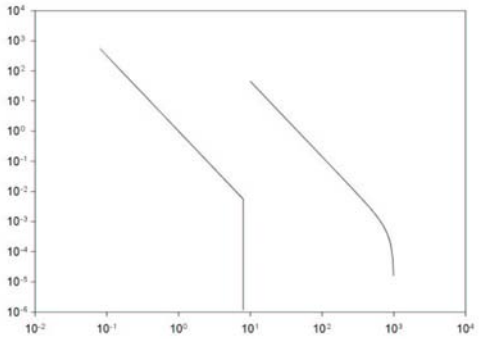

Figure 7. Curve to the right is the boosted spectrum

9. Hillas Violated?

From the above it might appear that relativistic boosts from jets violate the Hillas limit. However, if we designate quantities measured in the lab (or galaxy) frame with a prime we note that starting with the original Hillas formula $E_{\rm Max} = Ze(U/C)BL$ and transforming $E_{\rm Max} \Rightarrow E^{'}_{\rm Max} = \gamma E_{\rm Max}$ But! $B \Rightarrow B^{'} = \gamma B$ So $E^{'}_{\rm Max} = Ze(U/c)B^{'}L$ and we obtain the same expression in the boosted quantities.

References

1. Hillas, A. M. 1984, Ann. Rev. Astron. & Astop. 22, 425
2. Cesarsky, C. and Ptuskin, V., 1993, *23rd ICRC* (Calgary), **2**, 341
3. Thorne, K. S., Price, R. M. & MacDonald, D. A. 1986, *Black Holes: The Membrane Paradigm* (Yale University Press, New Haven CT)
4. Boldt, E. & Ghosh, P. 1999, MNRAS 307, 491
5. Boldt, E. & Loewenstein, M. 2000, MNRAS 316, l29
6. Levinson, A. 2000, Phys. Rev. Lett. 85, 912
7. Blandford, R. D. & Znajek, R. L. 1977, MNRAS 179, 433

COSMIC PLASMA WAKEFIELD ACCELERATION

PISIN CHEN
Stanford Linear Accelerator Center
Stanford University, Stanford, CA 94309, USA

TOSHIKI TAJIMA
Advanced Photon Research Center
Japan Atomic Energy Research Institute, Kyoto, 619-0215 Japan

YOSHIYUKI TAKAHASHI
Department of Physics, University of Alabama, Huntsville, AL 35899

Recently we proposed a new cosmic acceleration mechanism[1] which was based on the wakefields excited by the Alfven shocks in a relativistically flowing plasma. In this paper we include some omitted details, and show that there exists a threshold condition for transparency below which the accelerating particle is collision-free and suffers little energy loss in the plasma medium. The stochastic encounters of the random accelerating-decelerating phases results in a power-law energy spectrum: $f(\epsilon) \propto 1/\epsilon^2$. As an example, we discuss the possible production of super-GZK ultra high energy cosmic rays (UHECR) in the atmosphere of gamma ray bursts. The estimated event rate in our model agrees with that from UHECR observations.

1. Introduction

Ultra high energy cosmic ray (UHECR) events exceeding the Greisen-Zatsepin-Kuzmin (GZK) cutoff[2] (5×10^{19}eV for protons originated from a distance larger than $\sim$ 50 Mps) have been found in recent years[3,4,5,6]. Observations also indicate a change of the power-law index in the UHECR spectrum (events/energy/area/time $\propto \epsilon^{-\alpha}$) from $\alpha \sim 3$ to a smaller value, at energy around $10^{18} - 10^{19}$eV. These present an acute theoretical challenge regarding their composition as well as their origin[7].

So far the theories that attempt to explain the UHECR can be largely categorized into the "top-down" and the "bottom-up" scenarios. In addition to relying on exotic particle physics beyond the standard model, the main challenges of top-down scenarios are their difficulty in compliance with

the observed event rates and the energy spectrum[7], and the fine-tuning of particle lifetimes. The main challenges of the bottom-up scenarios, on the other hand, are the GZK cutoff, as well as the lack of an efficient acceleration mechanism[7]. To circumvent the GZK limit, several authors propose the "Z-burst" scenario[8] where neutrinos, instead of protons, are the actual messenger across the cosmos. For such a scenario to work, it requires that the original particle, say protons, be several orders of magnitude more energetic than the one eventually reaches the Earth.

Even if the GZK-limit can be circumvented through the Z-burst, the challenge for a viable acceleration mechanism remains, or becomes even more acute. This is mainly because the existing paradigm for cosmic acceleration, namely the Fermi mechanism[9], as well as its variants, such as the diffusive shock acceleration[10], are not effective in reaching ultra high energies[11]. These acceleration mechanisms rely on the random collisions of the high energy particle against magnetic field domains or the shock media, which necessarily induce increasingly more severe energy losses at higher particle energies.

From the experience of terrestrial particle accelerators, we learn that it takes several qualifications for an accelerator to operate effectively. First, the particle should gain energy through the interaction with the longitudinal electric field of a subluminous ($v \leq c$) electromagnetic (EM) wave. In such a setting the accelerated particle can gain energy from the field over a macroscopic distance, much like how a surfer gains momentum from an ocean wave. It is important to note that such a longitudinal field is Lorentz invariant, meaning that the acceleration gradient is independent of the instantaneous energy of the accelerating particle. Second, such a particle-field interaction should be a non-collisional process. This would help to avoid severe energy loss through inelastic scatterings. Third, to avoid excessive synchrotron radiation loss, which scales as particle energy squared, the accelerating particle should avoid any drastic bending beyond certain energy regime. We believe that these qualifications for terrestrial accelerators are also applicable to celestial ones.

Although they are still in the experimental stage, the "plasma wakefield accelerator" concepts[12,13], promise to provide all the conditions stated above. Plasmas are capable of supporting large amplitude electro-static waves with phase velocities near the speed of light. Such collective waves, or "wakefields", can be excited by highly concentrated, relativistic EM energies such as lasers[12] and particle beams[13]. A trailing particle can then gain energy by riding on this wakefield. Although hard scatterings be-

tween the accelerating particle and the plasma medium is inevitable, under appropriate conditions, as we will demonstrate below, the particle can be collision-free.

In our recent paper[1] we argued that magneto-shocks (Alfven shocks) in a relativistic plasma flow can also excite large amplitude plasma wakefields, which in turn can be highly efficient in accelerating ultra high energy particles. But with the limited space, many details and intermediate steps were omitted in that paper. Here we provide a more explicit discussion of our notions.

2. Alfven Waves and Plasma Wakefields

It is well-known that an ordinary Alfven wave propagating in a stationary magnetized plasma has a velocity $v_{_A} = eB_0/(4\pi m_i n_p)^{1/2}$, which is typically much less than the speed of light. Here B_0 is the longitudinal magnetic field and n_p is the density of the magnetized plasma. The relative strength between the transverse E and B fields of the Alfven wave is $E/B = v_{_A}/c$. Although the two components are not equal, being mutually perpendicular to the direction of propagation they jointly generate a non-vanishing ponderomotive force that can excite a wakefield in the plasma, which is slow: $v_{ph} = v_A \ll c$. For the purpose of ultra high energy acceleration, such a wakefield would not be too useful, for the accelerating particle can become quickly out of phase with the accelerating field.

Such a slow wave is ordinarily not suitable for accelerating relativistic particles. The situation changes when the plasma as a whole moves with a relativistic bulk velocity $V_p \leq c$. The standard method of obtaining the linear dispersion relation of waves in a magnetized plasma leads to

$$\frac{k_z^2 c^2}{\omega^2} = 1 - \frac{1}{\Gamma_p} \frac{(\omega_{pi}^2 + \omega_{pe}^2)(1 - V_p k/\omega)}{(\omega - V_p k \pm \omega_{Bi}/\Gamma_p)(\omega - V_p k \mp \omega_{Be}/\Gamma_p)} \ , \qquad (1)$$

where k and ω are the wave number and the frequency of the EM wave, respectively, $\omega_{pi,pe} = (4\pi e^2 n_p/m_{i,e})^{1/2}$ are the plasma frequencies for ions and electrons, and $\omega_{Bi,Be} = (eB_0/m_{i,e})^{1/2}$ are the ion and electron cyclotron frequencies. Here Γ_p is the Lorentz factor of the bulk plasma flow. Figure 1 shows the dispersion relations of various transverse EM waves that propagate along the direction of B_0 with and without the plasma bulk flow V_p. In Fig. 1(a) we see that outside the lightcone (superluminous, or $v_{ph} > c$) lie the regular EM waves, whose asymptotic dispersion is $\omega = kc$. Within the lightcone (subluminous), there are two additional branches, the

whistler wave (an electron branch mode) and the Alfven wave whose frequency remains quite low and its electric field is much smaller than the magnetic one, i.e., $E/B = v_A/c \ll 1$ in the absence of flow.

In the case where the bulk flow of the plasma approaches the speed of light, however, the Alfven waves acquire a phase velocity close to c and enhances the ratio of E/B to $\sim V_p/c \leq 1$, and it becomes indistinguishable from a bona fide EM wave. Preliminary results from simulations indicate that such relativistic Alfven waves can indeed excite plasma wakefields[14] Further simulation works are currently in progress, as reported in this workshop[15]. In this relativistic flow the excited wakefields are all in one direction, which contributes to the unidirectional acceleration. With our applications to astrophysical problems in mind, the Alfven-wave-plasma interaction relevant to us is in the nonlinear regime.

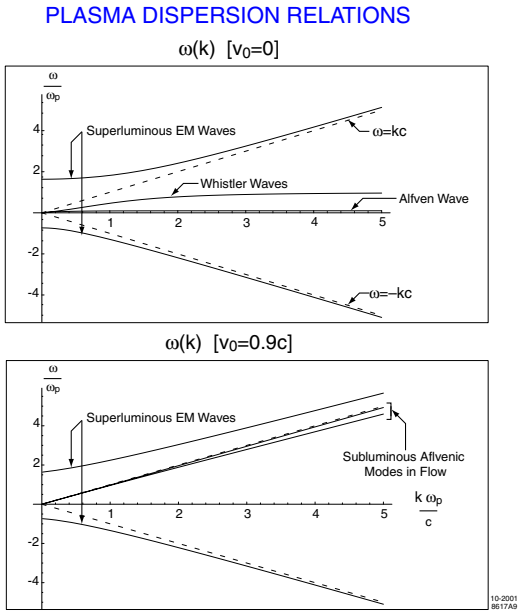

Figure 1. The dispersion relations for stationary and relativistic plasma flows.

The plasma wakefield in the nonlinear regime has been well-studied[16]. The nonlinearity is determined by the driving EM wave's *ponderomotive* potential, which is governed by its normalized vector potential $a_0 = eE/mc\omega$. When this parameter exceeds unity, nonlinearity is strong[12] so that addi-

tional important physics incurs. For a stationary plasma, the maximum field amplitude that the plasma wakefield can support is

$$E_{\rm max} \approx E_{\rm wb} a_0 = \frac{m_e c \omega_p}{e} a_0 \ , \tag{2}$$

which is enhanced by a factor a_0 from the cold wavebreaking limit (the naively assumed maximum field), $E_{\rm wb} = m_e c\omega_p/e$, of the linear regime. In a relativistic plasma flow with a Lorentz factor Γ_p, the cold wavebreaking field is reduced by a factor $\Gamma_p^{1/2}$ due to Lorentz contraction. The maximum "acceleration gradient" G experienced by a singly-charge particle riding on this plasma wakefield is then

$$G = eE'_{\rm max} \approx a_0 m_e c^2 \sqrt{\frac{4\pi r_e n_p}{\Gamma_p}} \ . \tag{3}$$

The plasma wavelength, in the mean time, is stretched also by a factor a_0 from that in the linear regime. So in a plasma flow the wavelength is

$$\lambda_{pN} = \frac{2}{\pi} a_0 \lambda'_p \approx a_0 \sqrt{\frac{\pi \Gamma_p}{r_e n_p}} \ , \tag{4}$$

where $r_e = e^2/m_e c^2 = 2.8 \times 10^{-13}$cm is the classical electron radius.

3. Maximum Energy Gain and Spectrum

To determine the maximum possible energy gain, we need to know how far can a test particle be accelerated. At ultra high energies once the test particle encounters a hard scattering or bending, the hard-earned kinetic energy would most likely be lost. The scattering of an ultra high energy proton with the background plasma is dominated by the proton-proton collision. Existing laboratory measurements of the total pp cross section scales roughly as $\sigma_{pp} = \sigma_0 \cdot \{1 + 6.30 \times 10^{-3} [\log(s)]^{2.1}\}$, where $\sigma_0 \approx 32$mb and the center-of-mass energy-squared, s, is given in $({\rm GeV})^2$. In our system, even though the UHE protons are in the ZeV regime, the center-of-mass energy of such a proton colliding with a comoving background plasma proton is in the TeV range, so it is safe to ignore the logarithmic dependence and assume a constant total cross section, $\sigma_{pp} \sim \sigma_0 \sim 30$ mb in the ZeV energy regime. Since in astrophysical settings an out-bursting relativistic plasma dilutes as it expands radially, its density scales as $n_p(r) = n_{p0}(R_0/r)^2$, where n_{p0} is the plasma density at a reference radius R_0 . The proton mean-free-path can be determined by integrating the collision probability up to unity,

$$1 = \int_{R_0}^{R_0 + L_{\rm mfp}} \frac{\sigma_{pp} n_p(r)}{\Gamma_p} dr = \int_{R_0}^{R_0 + L_{\rm mfp}} \frac{\sigma_{pp} n_{p0}}{\Gamma_p} \frac{R_0^2}{r^2} dr \ . \tag{5}$$

We find

$$1 = \frac{\sigma_{pp} n_{p0} R_0}{\Gamma_p} \Big[1 - \frac{R_0}{R_0 + L_{\rm mfp}} \Big] \ . \tag{6}$$

Since $L_{\rm mfp}$ is positive definite, $0 < [1 - R_0/(R_0 + L_{\rm mfp})] < 1$. Therefore the solution to $L_{\rm mfp}$ does not exist unless the coefficient, $\sigma_{pp} n_{p0} R_0/\Gamma_p > 1$. That is there exists a threshold condition below which the system is collision-free:

$$\frac{\sigma_{pp} n_{p0} R_0}{\Gamma_p} = 1 \ . \tag{7}$$

When a system is below this threshold, a test particle can in principle be accelerated unbound. In practice, of course, other secondary physical effects would eventually intervene.

In a terrestrial accelerator, the wakefields are coherently excited by the driving beam, and the accelerating particle would ride on the same wave crest over a macroscopic distance. There the aim is to produce near-monoenergetic final energies (and tight phase-space) for high energy physics and other applications. In astrophysical settings, however, the drivers, such as the Alfven shocks, will not be so organized. A test particle would then face random encounters of accelerating and decelerating phases of the plasma wakefields excited by Alfven shocks.

The stochastic process of the random acceleration-deceleration can be described by the distribution function $f(\epsilon, t)$ governed by the Chapman-Kolmogorov equation[17,18]

$$\frac{\partial f}{\partial t} = \int_{-\infty}^{+\infty} d(\Delta\epsilon) W(\epsilon - \Delta\epsilon, \Delta\epsilon) f(\epsilon - \Delta\epsilon, t) - \int_{-\infty}^{+\infty} d(\Delta\epsilon) W(\epsilon, \Delta\epsilon) f(\epsilon, t) \\ -\nu(\epsilon) f(\epsilon, t) \ . \tag{8}$$

The first term governs the probability per unit time of a particle "sinking" into energy ϵ from an initial energy $\epsilon - \Delta\epsilon$ while the second term that "leaking" out from ϵ. The last term governs the dissipation due to collision or radiation, or both. As we will demonstrate later, the astrophysical environment that we invoke for the production of UHECR is below the collision threshold condition, and so accelerating particles are essentially collision-free.

The radiation loss in our system is also negligible. As discussed earlier, in a relativistic flow the transverse E and B fields associated with the Alfven shock are near equal in magnitude. Analogous to that in an ordinary EM wave, an ultra relativistic particle (with a Lorentz factor γ) co-moving with

such a wave will experience a much suppressed bending field, by a factor $1/\gamma^2$. Furthermore, the plasma wakefield acceleration takes place in the region that trails behind the shock (and not in the bulk of the shock) where the accelerating particle in effect sees only the longitudinal *electrostatic* field colinear to the particle motion[16]. We are therefore safe to ignore the radiation loss entirely as well. We can thus ignore the dissipation term in the Chapman-Komogorov equation and focus only on the purely random plasma wakefield acceleration-deceleration.

Assuming that the energy gain per phase encounter is much less than the final energy, i.e., $\Delta\epsilon \ll \epsilon$, we Taylor-expand $W(\epsilon - \Delta\epsilon, \Delta\epsilon)f(\epsilon - \Delta\epsilon)$ around $W(\epsilon, \Delta\epsilon)f(\epsilon)$ in the sink term and reduce Eq.(9) to the Fokker-Planck equation

$$\frac{\partial f}{\partial t} = \frac{\partial}{\partial \epsilon}\int_{-\infty}^{+\infty} d(\Delta\epsilon)\Delta\epsilon W(\epsilon, \Delta\epsilon)f(\epsilon, t) + \frac{\partial^2}{\partial \epsilon^2}\int_{-\infty}^{+\infty} d(\Delta\epsilon)\frac{\Delta\epsilon^2}{2}W(\epsilon, \Delta\epsilon)f(\epsilon, t) \ . \tag{9}$$

We now assume the following properties of the transition rate $W(\epsilon, \Delta\epsilon)$ for a purely stochastic process:

a) W is an even function;

b) W is independent of ϵ;

c) W is independent of $\Delta\epsilon$.

Property a) follows from the fact that in a plasma wave there is an equal probability of gaining and losing energy. In addition, since the wakefield amplitude is Lorentz invariant, the chance of gaining a given amount of energy, $\Delta\epsilon$, is independent of the particle energy ϵ. Finally, under a purely stochastic white noise, the chance of gaining or losing any amount of energy is the same. Based on these arguments we deduce that

$$W(\epsilon, \Delta\epsilon) = \frac{1}{2c\tau^2 G} \ , \tag{10}$$

where τ is the typical time of interaction between the test particle and the random waves and G is the maximum acceleration gradient (cf. Eq.(4)). We note that there is a stark departure of the functional dependence of W in our theory from that in Fermi's mechanism, in which the energy gain $\Delta\epsilon$ per encounter scales linearly and quadratically in ϵ for the first-order and second-order Fermi mechanism, respectively.

To look for a stationary distribution, we put $\partial f/\partial t = 0$. Since W is an even function, the first term on the RHS in Eq.(10) vanishes. To ensure the positivity of particle energies before and after each encounter,

the integration limits are reduced from $(-\infty, +\infty)$ to $[-\epsilon, +\epsilon]$, and we have

$$\frac{\partial^2}{\partial \epsilon^2} \int_{-\epsilon}^{+\epsilon} d(\Delta\epsilon) \frac{\Delta\epsilon^2}{2} W(\epsilon, \Delta\epsilon) f(\epsilon) = 0 \ . \tag{11}$$

Inserting W from Eq.(11), we arrive at the energy distribution function that follows power-law scaling,

$$f(\epsilon) = \frac{\epsilon_0}{\epsilon^2} \ , \tag{12}$$

where the normalization factor ϵ_0 is taken to be the mean energy of the background plasma proton, $\epsilon_0 \sim \Gamma_p m_p c^2$. The actually observed UHECR spectrum is expected to be degraded somewhat from the above idealized, theoretical power-law index, $\alpha = 2$, not only due to possible departure of the reality from the idealized model, but also due to additional intermediate cascade processes that transcend the original UHE protons to the observed UHECRs.

We note that a power-law energy spectrum is generic to all purely stochastic, collisionless acceleration processes. This is why both the first and the second order Fermi mechanisms also predict power-law spectrum, if the energy losses, e.g., through inelastic scattering and radiation (which are severe at ultra high energies), are ignored. The difference is that in the Fermi mechanism the stochasticity is due to random collisions of the test particle against magnetic walls or the shock medium, which necessarily induce *reorientation* of the momentum vector of the test particle after every diffusive encounter, and therefore should trigger inevitable radiation loss at high energies. The stochasticity in our mechanism is due instead to the random encounters of the test particle with different accelerating-decelerating *phases*. As we mentioned earlier, the phase vector of the wakefields created by the Alfven shocks in the relativistic flow is nearly unidirectional. The particle's momentum vector, therefore, never changes its direction but only magnitude, and is therefore radiation free in the energy regime that we consider for proton acceleration.

4. Gamma Ray Bursts and Wakefield Acceleration

We now apply our acceleration mechanism to the problem of UHECR. GRBs are by far the most violent release of energy in the universe, second only to the big bang itself. Within seconds (for short bursts) about $\epsilon_{\rm GRB} \sim 10^{52}$erg of energy is released through gamma rays with a spectrum that peaks around several hundred keV. Existing models for GRB, such

as the relativistic fireball model[19], typically assume neutron-star-neutron-star (NS-NS) coalescence as the progenitor. Neutron stars are known to be compact ($R_{\rm NS} \sim O(10)$km) and carrying intense surface magnetic fields ($B_{\rm NS} \sim 10^{12}$G). Several generic properties are assumed when such compact objects collide. First, the collision creates sequence of strong magneto-shocks (Alfven shocks). Second, the tremendous release of energy creates a highly relativistic out-bursting fireball, most likely in the form of a plasma.

The fact that the GRB prompt (photon) signals arrive within a brief time-window implies that there must exists a threshold condition in the GRB atmosphere where the plasma becomes optically transparent beyond some radius R_0 from the NS-NS epicenter. Applying Eq.(8) to the case of out-bursting GRB photons, this condition means

$$\frac{\sigma_c n_{p0} R_0}{\Gamma_p} = 1 \ , \tag{13}$$

where $\sigma_c = (\pi r_e^2)(m_e/\omega_{\rm GRB})[\log(2\omega_{\rm GRB}/m_e) + 1/2] \approx 2 \times 10^{-25}{\rm cm}^2$ is the Compton scattering cross section. Since $\sigma_{pp} < \sigma_c$, the UHECRs are also collision-free in the same environment. There is clearly a large parameter space where this condition is satisfied. To narrow down our further discussion, it is not unreasonable to assume that $R_0 \sim O(10^4)$km. A set of self-consistent parameters can then be chosen: $n_{p0} \sim 10^{20}{\rm cm}^{-3}, \Gamma_p \sim 10^4$, and $\epsilon_0 \sim 10^{13}{\rm eV} \equiv \epsilon_{13}$.

To estimate the plasma wakefield acceleration gradient, we first derive the value for the a_0 parameter. We believe that the megneto-shocks constitute a substantial fraction, say $\eta_a \sim 10^{-2}$, of the total energy released from the GRB progenitor. The energy Alfven shocks carry is therefore $\epsilon_A \sim 10^{50}$erg. Due to the pressure gradient along the radial direction, the magnetic fields in Alfven shocks that propagate outward from the epicenter will develop sharp discontinuities and be compactified[20]. The estimated shock thickness is $\sim O(1)$m at $R_0 \sim O(10^4)$km. From this and ϵ_A one can deduce the magnetic field strength in the Alfven shocks at R_0, which gives $B_A \sim 10^{10}$G. This leads to $a_0 = eE_A/mc\omega_A \sim 10^9$. Under these assumptions, the acceleration gradient G (*cf.* Eq.(4)) is as large as

$$G \sim a_0 mc^2 \sqrt{\frac{4\pi r_e}{\sigma_c R_0}} \sim 10^{16} \Big(\frac{a_0}{10^9}\Big) \Big(\frac{10^9{\rm cm}}{R_0}\Big)^{1/2} {\rm eV/cm} \ . \tag{14}$$

Although the UHE protons can in principle be accelerated unbound in our system, the ultimate maximum reachable energy is determined by the conservation of energy and our assumption on the population of UHE protons. Since it is known that the coupling between the ponderomotive

potential of the EM wave and the plasma wakefield is efficient, we assume that the Alfven shock energy is entirely loaded to the plasma wakefields after propagating through the plasma. Furthermore, we assume that the energy in the plasma wakefield is entirely reloaded to the UHE protons through the stochastic process. Thus the highest possible UHE proton energy can be determined by energy conservation

$$\eta_a \epsilon_{\rm GRB} \sim \epsilon_{\rm A} \sim \epsilon_{\rm UHE} \sim N_{\rm UHE} \int_{\epsilon_{13}}^{\epsilon_m} \epsilon f(\epsilon) d\epsilon \ . \tag{15}$$

which gives

$$\epsilon_m = \epsilon_{13} \exp(\eta_a \epsilon_{\rm GRB} / N_{\rm UHE} \epsilon_{13}) \ . \tag{16}$$

This provides a relationship between the maximum possible energy, ϵ_m, and the UHE proton population, $N_{\rm UHE}$. We assume that $\eta_b \sim 10^{-2}$ of the GRB energy is consumed to create the bulk plasma flow, i.e., $\eta_b \epsilon_{\rm GRB} \sim N_p \Gamma_p m_p c^2 \sim N_p \epsilon_{13}$, where N_p is the total number of plasma protons. We further assume that $\eta_c \sim 10^{-2}$ of the plasma protons are trapped and accelerated to UHE, i.e., $N_{\rm UHE} \sim \eta_c N_p$. Then we find $\epsilon_m \sim \epsilon_{13} \exp(\eta_a / \eta_b \eta_c)$. We note that this estimate of ϵ_m is exponentially sensitive to the ratio of several efficiencies, and therefore should be handled with caution. If the values are indeed as we have assumed, $\eta_a / \eta_b \eta_c \sim O(10^2)$, then ϵ_m is effectively unbound until additional limiting physics enters. Whereas if the ratio is $\sim O(10)$ instead, the UHE cannot even reach the ZeV regime. The validity of our assumed GRB efficiencies then relies on the consistency check against observations.

5. UHECR Event Rate

In addition to the energy production issue, equally important to a viable UHECR model is the theoretical estimate of the UHECR event rates. The NS-NS coalescence rate is believed to be about 10 events per day in the entire Universe[21,22]. This frequency is consistent with the observed GRB events, which is on the order of $f_{\rm GRB} \sim 10^{3.5}$ per year.

In the Z-burst scenario an initial neutrino energy above 10^{21}eV[8] or 10^{23}eV[23] is required (depending on the assumption of the neutrino mass) to reach the Z-boson threshold. For the sake of discussion, we shall take the necessary neutrino energy as $\epsilon_\nu > 10^{22}$eV. Such ultra high energy neutrinos can in principle be produced through the collisions of UHE protons with the GRB background protons: $pp \to \pi + X \to \mu + \nu + X$. All UHE protons with energy $\epsilon_{>22} \geq 10^{22}$eV should be able to produce such neutrinos. The

mean energy (by integrating over the distribution function $f(\epsilon)$) of these protons is $\langle \epsilon_{>22} \rangle \sim O(100)\epsilon_{22}$. Therefore the multiplicity of neutrinos per UHE proton is around $\mu_{(p\to\nu)} \sim O(10) - O(100)$. At the opposite end of the cosmic process, we also expect multiple hadrons produced in a Z-burst. The average number of protons that Z-boson produces is ~ 2.7[24]. Finally, the population of UHE protons above 10^{22}eV is related to the total UHE population by $N_{>22} \sim (\epsilon_{13}/\epsilon_{22}) N_{\rm UHE} \sim \eta_b \eta_c \epsilon_{\rm GRB}/\epsilon_{22}$.

Putting the above arguments together, we arrive at our theoretical estimate of the expected UHECR event rate on earth,

$$N_{\rm UHECR}(> 10^{20}{\rm eV}) = f_{\rm GRB}\mu_{(p\to\nu)}\mu_{(Z\to p)} N_{>22} \frac{1}{4\pi R_{\rm GRB}^2}$$
$$\sim f_{\rm GRB}\mu_{(p\to\nu)}\mu_{(Z\to p)}\eta_b\eta_c \frac{\epsilon_{\rm GRB}}{\epsilon_{22}} \frac{1}{4\pi R_{\rm GRB}^2} \ . \quad (17)$$

The typical observed GRB events is at a redshift $z \sim O(1)$, or a distance $R_{\rm GRB} \sim 10^{23}$km. Our estimate of observable UHECR event rate is therefore

$$N_{\rm UHECR}(> 10^{20}{\rm eV}) = O(1)/100{\rm km}^2/{\rm yr}/{\rm sr} \ , \quad (18)$$

which is consistent with observations, or in turn this observed event rate can serve as a constraint on the various assumptions of our specific GRB model.

6. A Laboratory Astrophysics Experiment

History has shown that the symbiosis between direct observation and laboratory investigation was instrumental in the progress of astrophysics. Our cosmic plasma wakefield acceleration mechanism can in principle be tested in the laboratory setting[26]. A schematic diagram for such an experiment is shown in Figure 2.

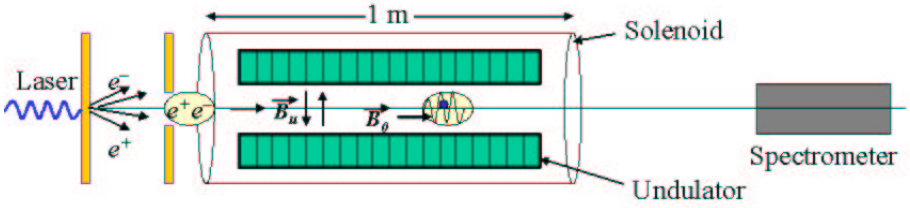

Figure 2. A schematic diagram of a possible laboratory experiment to verify the Alfven-induced plasma wakefield acceleration mechanism.

The main goals for such an experiment are

1. Generation of Alfven waves in a relativistic plasma flow;
2. Inducing high gradient nonlinear plasma wakefields;
3. Acceleration and deceleration of trapped e^+/e^-;
4. Power-law $(n\ -2)$ spectrum due to stochastic acceleration.

Although it is unlikely that the extremely high density, high intensity and high acceleration gradient involved in this acceleration mechanism can be reproduced in the laboratory setting, it is hoped that the key elements necessary for this mechanism can indeed be verified. In this regard, the value of the experiment lies in its validation of the underlying dynamics of the Alfven-induced plasma wakefield acceleration.

7. Accknowledgement

We appreciate helpful discussions with J. Arons, R. Blandford, P. Meszaros. This work was supported by Department of Energy contracts DE–AC03–76SF00515 and DE-AC03-78SF00098.

References

1. P. Chen, T. Tajima, Y. Takahashi, *Phys. Rev. Lett.* **89**, 161101 (2002).
2. K. Greisen, *Phys. Rev. Lett.* **16**, 748 (1966); G. T. Zatsepin and V. A. Kuzmin, *Pis'ma Zh. Eksp. Teor. Fiz.* **4**, 114 (1966) [*JETP Lett.* **4**, 78 (1966).
3. D. J. Bird et al., *Phys. Rev. Lett.* **71**, 3401 (1993); *Astrophys. J.* **424**, 491 (1994); **441**, 144 (1995).
4. M. Takeda et al., *Phys. Rev. Lett.* **81**, 1163 (1998); *Astrophys. J.* **522**, 225 (1999).
5. T. Abu-Zayyad et al., *Int. Cosmic Ray Conf.* **3**, 264 (1999).
6. M. A. Lawrence, R. J. O. Reid, and A. A. Watson, *J. Phys. G Nucl. Part. Phys.* **17**, 773 (1991).
7. A. V. Olinto, *Phys. Rep.* **333-334**, 329 (2000).
8. T. Weiler, *Astropart. Phys.* **11**, 303 (1999); D. Fargion, B. Mele, and A. Salis, *Astrophys. J.* **517**, 725 (1999).
9. E. Fermi, *Phys. Rev.* **75**, 1169 (1949); *Astrophys. J* **119**, 1 (1954).
10. W. I. Axford, E. Leer, and G. Skadron, in *Proc. 15th Int. Cosmic Ray Conf. (Plovdic)* **11**, 132 (1977); G. F. Krymsky, *Dokl. Acad. Nauk. SSR* **234**, 1306 (1977); A. R. Bell, *Mon. Not. R. Astro. Soc.* **182**, 147 (1978); R. D. Blandford and J. F. Ostriker, *Astrophys. J. Lett.* **221**, L29 (1978).
11. A. Achterberg, in *Highly Energetic Physical Processes and Mechanisms for Emission from Astrophysical Plasmas*, IAU Symposium, vol. 195, P. C. H. Martens and S. Tsuruta, eds. (1999).
12. T. Tajima and J. M. Dawson, *Phys. Rev. Lett.* **43**, 267 (1979).
13. P. Chen, J. M. Dawson, R. Huff, and T. Katsouleas, *Phys. Rev. Lett.* **54**, 693 (1985).

14. P. Romenesko, P. Chen, T. Tajima, in preparation (2002).
15. K. Reil, presented in this workshop and in these proceedings.
16. E. Esarey, P. Sprangle, J. Krall, and A. Ting, *IEEE Trans. Plasma Sci.* **24**, 252 (1996).
17. K. Mima, W. Horton, T. Tajima, and A. Hasegawa, in Proc. *Nonlinear Dynamics and Particle Acceleration*, eds. Y.H.Ichikawa and T.Tajima (AIP, New York, 1991) p.27.
18. Y. Takahashi, L. Hillman, T. Tajima, in *High Field Science*, eds. T. Tajima, K. Mima, H. Baldis, (Kluwer Academic/Plenum 2000) p.171.
19. M. J. Rees and P. Meszaros, *Mon. Not. R. Astro. Soc.* **158**, P41 (1992); P. Mezsaros and M. J. Rees, *Astrophys. J.* **405**, 278 (1993).
20. A. Jeffrey and T. Taniuti, *Nonlinear Wave Propagation*, (Academic Press, NY, 1964).
21. T. Piran, ApJ Letters 389, L45 (1992); A. Shemi and T. Piran, *Atrophys. J.* **365**, L55 (1990).
22. LISA collaboration, http://www.lisa.uni-hannover.de/
23. G. Gelmini and G. Varieschi, UCLA/02/TEP/4 (2002), unpublished.
24. Particle Data Group, Phys. Rev. D54, 187 (1996).
25. M. Punch et al., Nature 358, 477 (1992); J. Quinn et al., ApJ Letters 456, L63 (1996); C. M. Urry, *Advances in Space Research* **21**, 89 (1998).
26. P. Chen, Asso. Asian Pacific Phys. Soc. (AAPPS) Bull. **13**, 3 (2003).

ACCELERATOR EXPERIMENTS FOR ASTROPHYSICS *

JOHNNY S.T. NG

Stanford Linear Accelerator Center
Accelerator Research Department A, MS 26
P.O. Box 20450, Stanford, CA. 94309-2010, USA.
E-mail: jng@SLAC.Stanford.edu

Many recent discoveries in astrophysics involve phenomena that are highly complex. Carefully designed experiments, together with sophisticated computer simulations, are required to gain insights into the underlying physics. We show that particle accelerators are unique tools in this area of research, by providing precision calibration data and by creating extreme experimental conditions relevant for astrophysics. In this paper we discuss laboratory experiments that can be carried out at the Stanford Linear Accelerator Center and implications for astrophysics.

1. Introduction

Recent advances in high-energy astrophysics involve observations of extremely complex phenomena such as jets from active galactic nuclei (AGN), gamma-ray bursts (GRB), and ultrahigh-energy cosmic rays (UHECR). Observations of AGN jets, consisting of a highly collimated stream of material, show that the outflow expands at relativistic velocity and spans a distance scale of thousands of light-years. The collimation and production mechanism, most likely involving the dynamics of accretion disks around a black hole in the center of the AGN, are subjects of current research. Gamma-ray bursts, on the other hand, are some of the brightest observed light sources in the universe. The amount of electromagnetic energy output in a burst is equivalent to several times the solar mass released in a matter of seconds. The out-flowing materials of a GRB expand at relativistic velocity as well, and are possibly collimated, similar to an AGN jet. The nature of the progenitor and explanations for their observed characteristics are currently under debate. Much of our current understanding of these objects

*This work is supported by the U.S. Department of Energy under contract DE-AC03-76SF00515

are inferred from the properties of the observed radiation.

A strong magnetic field is believed to exist in both the GRB and the AGN jets. The interaction of the relativisticly expanding material with the environment can lead to nonlinear plasma phenomena that result in the acceleration of particles to high energies. Ultrahigh-energy cosmic rays, with energies observed up to around 10^{20} eV, are believed to come from extra-galactic sources. The nature and origin of these cosmic rays as well as their acceleration mechanism are still a mystery.

The study of these extreme phenomena requires tremendous effort. So far, progress in our understanding has required a combination of observation, numerical simulations, and theoretical modeling.[1] However, astrophysical observations must be carefully checked for instrumentation effects. And the complex numerical and theoretical calculations used to interpret these observations must be validated. Thus, it is important to calibrate the techniques used in the observations and to benchmark computer model calculations. Furthermore, since observational astrophysics deals with uncontrolled environments, laboratory experiments able to model the relevant extreme conditions would provide unique insight into the underlying physical mechanisms.

Laboratory studies, ranging from work on atomic spectroscopy, and the studies of hydrodynamics, radiation flow, and the equation-of-state using intense lasers[2], have been instrumental in astrophysics research. Recently, it has been suggested that accelerators can be used in the laboratory investigation of extreme astrophysical phenomena.[3] In this paper we discuss possible experiments using intense particle and photon beams to verify astrophysical observations and to study relativistic plasma dynamics and ultrahigh-energy cosmic acceleration mechanisms. An overview of the accelerator facility at the Stanford Linear Accelerator Center (SLAC) is given in Section 2. In Section 3, we discuss calibration experiments, focusing on the discrepancy in the UHECR spectrum measured by two large-aperture cosmic ray experiments, and describe an experiment that may help resolve it. In Section 4, we discuss laboratory experiments that may improve our understanding of the underlying dynamics of high-energy astrophysics phenomena. We conclude with an outlook in Section 5.

2. An Overview of the SLAC Facility

The 3-km long linear accelerator is the backbone for SLAC's high-energy physics research program. It is capable of delivering electrons and positrons

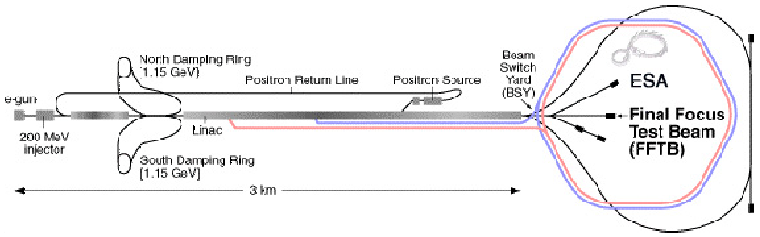

Figure 1. Layout of the SLAC facility.

with 50 GeV energy and 120 Hz repetition rate at 10^{10} particles per pulse. Currently it serves as the injector for the PEP-II storage ring to produce copious amount of B-meson particles for CP-violation measurements. It can also deliver beams to the fix-target experimental hall End-Station A (ESA) and the Final Focus Test Beam (FFTB). A schematic layout of the SLAC facility is shown in Figure 1. High intensity photon beams, tunable from X-ray to gamma-ray, can be derived using a variety of methods, such as undulators, laser-Compton back-scattering, and bremsstrahlung. Depending on the required wavelength, typical fluences of 10^9 photons per pulse can be provided.

3. Calibration Experiments

3.1. *Detector Calibration*

High energy beams from the linac can be used to generate a variety of secondary and tertiary beams for calibration purposes. A secondary pion and positron beam with well-defined momentum can be generated using a combination of target and selection magnet system, with a beam intensity that can be set to below 1 particle per pulse. With the addition of a tagger magnet, this secondary beam can be converted into a photon beam with known energy up to 20 GeV.

This test beam setup in the ESA has been used for the GLAST satellite mission, whose objective is to study energetic astrophysical gamma rays with energies in the 20 MeV to TeV range. The GLAST detector package consists of sophisticated silicon tracker and CsI calorimeter. It is important to calibrate its response and understand the various analysis algorithms in a controlled test beam environment before its space launch. Details on this experiment can be found elsewhere[4].

3.2. *X-ray Spectroscopy*

Recent X-ray observations of AGN galaxies have revealed features in the iron emission lines that are characteristic of Doppler shifts and gravitational redshifts expected from accretion disk models.[5] The emission lines can be thought of as "clocks" moving in various circular orbits around the black hole. To further probe the spacetime structure in the accretion disk, high resolution imaging and broad-band spectroscopy, such as those planned for the Constellation-X and MAXIM missions, are needed. A detailed laboratory measurement of heavy element atomic transitions and associated polarization effects will also be required for a proper interpretation of the observational data.[6]

For this purpose, an intense X-ray source, such as those available at a synchrotron light-source facility would be valuable. The next generation of linac-based light-source, with peak brilliance in the range of 10^{32}-10^{33} photons/sec/mrad^2/mm^2/0.1% bandwidth at 1-10 keV, could also play a role in this study.

3.3. *Air Fluorescence Efficiency Measurement*

The study of ultrahigh-energy cosmic rays has been based on observations of the secondary shower particles resulting from interactions in the atmosphere. For cosmic ray energies above $\sim 10^{14}$ eV, the shower particles can reach ground level and extend over a large area. One observation technique uses an array of sparsely spaced ground detectors to measure the density of these shower particles, which is related to the energy of the primary cosmic ray. The Akeno Giant Air Shower Array (AGASA) near Tokyo, Japan, for example, covers an area of approximately 100 km^2, with 100 detector units separated by about 1 km from each other.[7]

The cosmic ray shower also generates a trail of fluorescent light. The fluorescence is emitted nearly isotropically, mostly by the nitrogen molecules in air excited by shower secondaries. Instead of studying the transverse profile of the shower, as in the ground array approach, fluorescence-based detectors use a system of mirrors and photomultipliers to image the shower's longitudinal development. The fluorescence luminosity is related to the primary's energy; and the shape of the longitudinal profile provides information on the primary's composition. This technique is used by the Fly's Eye detector and its upgraded version, the High Resolution Fly's Eye (HiRes).[8]

Studies of UHECR events showed that they are not related to any known galactic sources. If they originated in extra-galactic sources, interactions

with the cosmic microwave background radiation would result in the attenuation of their energy. The flux above 10^{19} eV is expected to drop significantly due to the production of pions – the so-called GZK cutoff.[9] However, the Fly's Eye/HiRes and AGASA experiments have observed events greater than 10^{20} eV, well above the GZK cutoff. The two experiments have now accumulated similar exposure at the highest energies. With increased statistics, differences between the two measurements have become apparent. In particular, the flux measured by HiRes is systematically lower than that reported by AGASA above 4×10^{18} eV; there is also a difference in the energy at which the observed power-law spectrum changes slope, the so-called "ankle" structure.[10] This can be due to tails in the energy resolution function or other systematic errors, and is currently being investigated by both experiments.

One possible contribution to this discrepancy is the air fluorescence yield. Current understanding of air fluorescence, based on previous measurements, is incomplete. Many issues still remain: the detailed shape of the fluorescence spectrum, the pressure and atmospheric impurities dependences, and the dependence of fluorescence yield on shower particle energy. The associated systematic uncertainty is estimated to be 15%. A more precise measurement is desired as improvements are being made to other systematics in the observation.

Recently, it has been suggested that the high intensity electron beams at SLAC can be used for such study.[11] At the relevant energies, air showers produced by a cosmic ray hadron is a superposition of electromagnetic subshowers. At the shower's maximum, it consists of mostly electrons with energies dissipated to the 100 MeV level, near the critical energy of air. Further shower development is dominated by energy loss through ionization and excitation rather than shower particle creation. SLAC's electron beams interacting in an air-equivalent alumina target produce similar secondary electron energy distributions – see Figure 2. The SLAC E-165 experiment – Fluorescence in Air from Showers (FLASH) – has been proposed to study in detail the fluorescence yield in an air shower. It aims to make precision measurements of the total air fluorescence yield, as well as the spectral, pressure, composition, and energy dependencies. Details on this experiment have been presented elsewhere at this Workshop.[10]

Other examples of accelerator-based experiments that support astrophysical investigations are measurement of the Landau-Pomeranchuk-Migdal (LPM) effect, which has implication for photon/hadron identification at high energies, and observation of the Askarian effect, which can be

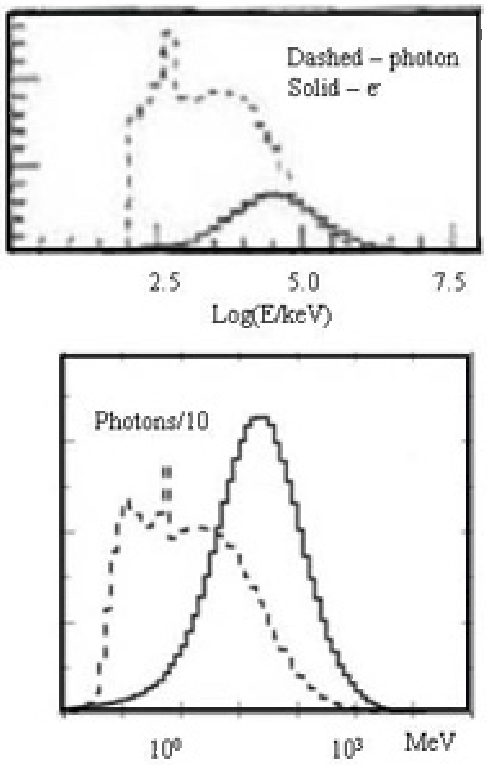

Figure 2. Simulations of shower secondary electron and photon energy distributions for a 10^{17} eV cosmic ray proton (top, CORSIKA) and a 28.5 GeV electron beam (bottom, GEANT) at the shower maximum.

used to detect UHE neutrinos. These experiments have been carried out using SLAC beams.[13]

4. Relativistic Plasma Experiments

While important issues remain to be resolved in the observational results of super-GZK events, the existence of extra-galactic UHECR above 10^{18} eV is well established. The nature of these cosmic rays and their acceleration mechanism are still a mystery, and various models have been proposed as solutions.[1] In the so-called "top-down" approach, the decay products of massive particles produced in the early universe could account for the observed UHECRs, especially those above the GZK cutoff. Certain "grand-

unification" theories predict the existence of particles with mass around 10^{16} GeV. Particles more massive than this, if they were to explain super-GZK events, would have to be produced continuously since their lifetimes would be extremely short. In some theories these particles can be emitted from topological defects created between causally disconnected regions during early epochs of cosmological phase transitions.

In the "bottom-up" approach, conventional particles accelerated in powerful astrophysical systems are thought to be responsible for the observed UHECR spectrum. The acceleration mechanisms are complex, involving strong magnetic fields and nonlinear plasma effects. Diffusive shock acceleration has been the generally accepted model.[14] More recent ideas include unipolar induction acceleration[15] and high gradient plasma acceleration in wakefields created by Alfvén shocks[16]. Possible acceleration sites are AGNs and gamma-ray bursts where typically relativistic plasma outflows are present. The key observational feature of UHECR is the power-law spectrum. The appropriate spectral index is predicted by existing models. Our goal is to experimentally test some of these models in the laboratory.

Typical beams delivered for experimentation in the FFTB are in short pulses pico-seconds long, 10 μm in radius, and consists of 10^{10} particles. Thus, the pulse power is approximately 40 Petawatts, and the intensity is $\sim 10^{20}$ W/cm^2. The energy density in the bunch is on the order of 10^{13} J/m^3. For comparison, the threshold for high-energy-density conditions, the energy density in a hydrogen molecule or the bulk moduli of solid-state materials, is 10^{11} J/m^3 The strong nonlinear and collective responses of a bunched relativistic particle beam to external stimuli are some of the important characteristics of a high-energy-density system relevant for astrophysical studies. Here we discuss possible relativistic plasma experiments. In particular, we explore the possibility of merging electron and positron beams to form a kinetically relativistic plasma, allowing the laboratory investigation of cosmic high-energy acceleration and radiation production phenomena.

4.1. e^+e^- *Beams as Relativistic Plasma*

Neutral co-moving e^+e^- beams have been investigated in an effort to improve the luminosity limit in high energy e^+e^- storage ring colliders. The disruptive effect of one beam's electromagnetic fields on the other can be compensated, in principle, by colliding neutral beams. This idea had been studied using two pairs of 0.8 GeV beams.[17] The experiment demonstrated

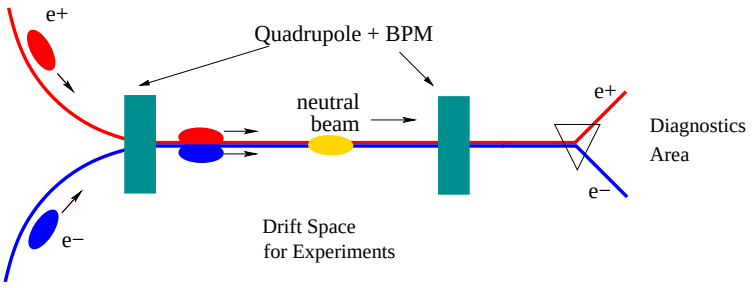

Figure 3. Combining electron and positron bunches to form a relativistic plasma.

beam-charge compensation with improved luminosity.

For our purpose, the 1-GeV electron and positron beams emerging from the damping rings at the beginning of the SLAC linac (see Figure 1) could be combined, forming an e^+e^- plasma streaming at relativistic velocity.[18] The transverse positions of the two beams would be aligned to micron precision using high resolution beam position monitors. The temporal locations would be synchronized using the damping rings' RF phase control, which is stable at the sub-picosecond level. This level of precision beam control has been demonstrated in measurements of wake-fields in accelerator structures.[19] The concept is illustrated in Figure 3.

For a relativistic bunched beam, temperature can be defined in terms of its emittance. Analogous to entropy, emittance is a measure of disorder. The discussions here follow those in Lawson[20]. The beam's transverse temperature is given by

$$kT_\perp = \frac{\beta^2\gamma mc^2\epsilon^2}{4\sigma_r^2} \tag{1}$$

where ϵ is the beam's emittance, γ the Lorentz factor, and σ_r the transverse beam size. The longitudinal temperature due to energy spread is negligible for relativistic beams.

The other plasma parameters can now be calculated. Results are shown in Table 1, using typical SLAC parameters at the exit of the damping rings. Plasma parameters are given in the frame co-moving with the beams. As can be seen, the number of particles inside a "Debye sphere" (N_D) is much greater than one, so that the effects of individual particles on each other are negligible compared to the collective effects, and the plasma description is indeed appropriate.

Table 1. Beam parameters in the laboratory frame and corresponding plasma parameters in the co-moving frame.

Beam Parameters (Lab frame)	Value	Plasma Parameters (Co-moving frame)	Value
Energy (E)	1.19 GeV	Density	4×10^{11} cm^{-3}
σ_E/E	10^{-3}	Debye Length (λ_D)	1.7 mm
Bunch Length	600 μm	Plasma Parameter (N_D)	6×10^6
Bunch Radius	50 μm	Frequency ($\omega_p/2\pi$)	6×10^9 (Hz)
Intensity	2×10^{10}	Wavelength (λ_p)	50 mm
Density	10^{15} cm^{-3}	Skin depth (c/ω_p)	8 mm
Emittance:		Temperature:	
ϵ_x	1.3×10^{-8} m-rad	Transverse ($kT_\perp$)	23 keV
ϵ_y	6.4×10^{-10} m-rad	Longitudinal	0.3 eV

For typical AGN jet parameters, the plasma length scales are much smaller than the jet dimensions. Thus, the AGN jet plasma is usually treated as having infinite extend. For typical relativistic bunched beams, however, the Debye radius (λ_D) is smaller than the bunch length but larger than the transverse beam size. As a consequence, the perpendicular plasma waves (involving particle motion in the transverse direction) have different properties compared to those excited in an infinite plasma. However, properties of the parallel propagating waves remain the same as those in an infinite plasma. The laboratory e^+e^- plasma discussed here can thus model the parallel propagating waves in an infinite plasma. As discussed below, this mode is most relevant for AGN jet dynamics.

So far our discussion have concentrated on neutral plasmas. The composition of astrophysical jets is, however, far from being understood. Magnetic confinement is generally accepted as the collimation mechanism, but it is also highly unstable. Models of current-carrying jets provide a possible alternative mechanism where the self-magnetic fields create a pinching force. This is very similar to the plasma-lens effect familiar to the beam-plasma physics community. Non-neutral plasma instabilities relevant for AGN jets could be studied using charged beams readily available at a facility such as SLAC. Possible experiments are under study.

4.2. *Scaling Laws and Relevance to Astrophysics*

The challenge for laboratory astrophysics is to create a terrestrial setting which can be scaled to the astrophysical environment. Magnetohydrodynamic (MHD) models have been used to describe many astrophysical processes such as bow-shock excitation in AGN jets or supernova explosions.

The MHD equations have the property that they are invariant under the appropriate scale transformations. This has been the basis, for example, for designing laser experiments to simulate supernova remnants.[2,21,22]

The MHD models are applicable when certain assumptions are satisfied. These, however, may not be applicable to the astrophysical conditions of interest here. In the following, we discuss a more general approach based on kinetic plasma theory. In particular, we concentrate on astrophysical plasma processes that might be investigated using high-energy-density particle beams.

The observed non-thermal radiation spectrum from AGNs is the subject of many recent studies. In some models, broad-band Blazar emission has been attributed to synchrotron radiation and/or various forms of Compton processes.[23] While in other models, it is described by the production of photon-pairs from the decay of mesons produced via the interaction of energetic protons with ambient photon and/or matter.[24] These models successfully describe various features in the observed spectrum, and thus are useful for understanding the radiation processes. But such phenomenological approach does not describe details of the underlying micro-physical dynamics of AGN jets. In particular, it does not address the issue of how the relativistic jet gives rise to energetic electrons and/or protons which subsequently produce the radiation. For example, these models typically assume that diffusive shock acceleration produces the required power-law spectrum.

In the plasma physics approach, details of the underlying dynamics for transferring kinetic energy in the relativistic jet into radiation are described. In the model proposed by Schlickeiser *et al.*[25], the jet is described by a one-dimensional outflow consisting of electron and positron pairs with bulk relativistic velocity, directed parallel to a uniform background magnetic field. The pairs have non-relativistic temperature in the co-moving frame. The e^+e^- jet propagates into an interstellar medium consisting of cold protons and electrons.

This two-stream multi-fluid system is studied in the jet rest frame. The analysis starts with a general phase space distribution, and the calculations then give the dispersion relations of the parallel propagating electrostatic (longitudinally polarized) and low-frequency transverse (Alfven-type) plasma waves. These waves are excited via a two-stream instability in the pair plasma. For typical AGN parameters, the calculations show that the jet kinetic energy is transferred via plasma turbulence to the initially cold interstellar protons and electrons, which then reach a plateau distri-

bution in momenta. The resulting radiation spectrum is consistent with observation.[26]

These kinetic plasma calculations also show that the instability build-up times and growth rates *scale* with the densities and the bulk relativistic factor, while the damping rates scales also with temperature. For example, the time it takes to build up the transverse instability in the protons is given by $t_{t,p} \sim (1/\omega_{p,e})(n_j/n_i)(m_p\Gamma/m_e)^{4/3}$, where $\omega_{p,e}$ is the electron plasma frequency, n_j and n_i are the jet and interstellar plasma densities, and Γ is the bulk Lorentz factor. The Landau damping rate is found to scale with $\Theta^{3/2}\omega_{p,e}\Gamma^2\exp[-(\Gamma-1)/\Theta]$, where $\Theta = kT/m_ec^2$ is the dimensionless temperature parameter.

4.3. *Parameters for Laboratory Experiments*

To determine whether the parameters of the relativistic plasma created by merging electron and positron bunches are relevant for an experimental investigation of AGN dynamics, the various dynamical time scales are calculated. The results are shown in Figure 4 for the parameters given in Table 1. In the setup being considered here, the pair plasma in the comoving frame appears to be ∼1-m long to the ambient plasma traveling through it. As can be seen from Figure 4, all dynamical time scales are shorter than the plasma traversal time: the time during which the relativistic plasma and the ambient plasma interact with each other. Typical plasma time scales are shown as the inverse plasma frequency. The build-up of the electrostatic waves is rather quick, for both the electrons and the protons, even with a fairly thin ambient plasma. The build-up of the transverse waves takes much more time, particularly for the protons, in which case an ambient plasma density of 10^{15} cm^{-3} in the laboratory is required.

Also, the maximum growth rate of the electrostatic turbulence is much greater than the Landau damping rate; similarly, the transverse turbulence growth rate is much larger than the cyclotron damping rate. Thus, this set of experimental parameters is in a regime where strong nonlinear plasma turbulence similar to those excited in AGN jets can be created and studied in detail experimentally in the laboratory. Further theoretical calculations are needed to guide the design of the experiment. A detailed numerical simulation using particle-in-cell techniques is needed as the next step.

The transverse magneto-hydrodynamic (Alfven-type) wave is especially interesting for testing various cosmic acceleration mechanisms. This type of turbulence is crucial in the formation of collisionless shocks and for efficient

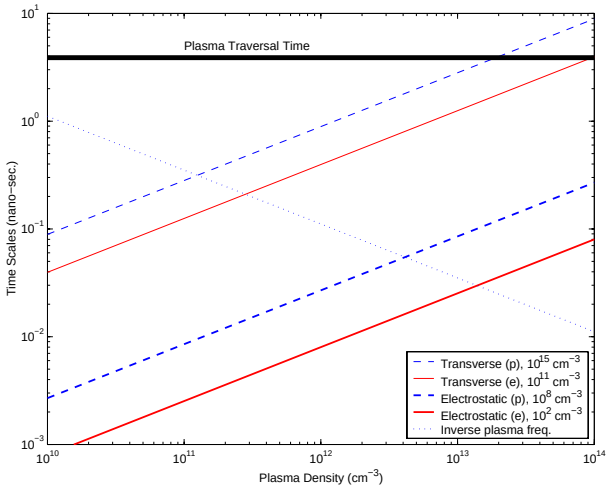

Figure 4. Various time scales for a laboratory experiment to test the dynamical model of AGN jets. The scaling of the plasma wave build-up times are shown as a function of the jet plasma density, for various interstellar medium densities – see text.

particle deflection in the diffusive shock acceleration process. The Alfven wave is also expected to excite plasma wakefields, which can provide high gradient particle acceleration. The spectrum and polarization properties of the radiation produced in the interaction of this e^+e^- "jet" with an ambient plasma can be measured and compared with astrophysical observations. Detailed simulation studies for these experiments are underway.

The laboratory experiments described here could have applications beyond the understanding of AGN jet dynamics. The dynamics in the polar caps of a spinning neutron star have been studied in the context of relativistic streaming electron-positron plasma.[27] Also, if GRB radiation is beamed, its dynamics would be similar to those found in AGN jets. Thus, our laboratory experiments would also shed light on these systems.

5. Summary and outlook

The field of laboratory astrophysics holds promise to the understanding of some of the most exciting astrophysical observations today. We have shown that particle accelerators are excellent tools for laboratory astrophysics, providing calibration data for observations and bench-marking computer models, as well as creating extreme conditions that make possible investigation of astrophysical dynamics in a terrestrial laboratory. SLAC, with the existing expertise and infrastructure, is well-positioned to contribute to this rapidly growing field.[28] The proposed ORION[29] facility for advanced accelerator research and beam physics will also be able to support dedicated laboratory astrophysics experiments with its unique combination of high quality electron beams and diagnostic lasers.

Acknowledgments

I would like to thank the Workshop organizers for their kind hospitality. I would also like to thank P. Chen, R. Noble, K. Reil, and P. Sokolsky for many fruitful discussions.

References

1. For a Review see collection of articles in *Science* **291**, 65-92 (2001).
2. B. Remington *et al.* it Science **284**, 1488 (1999); *Phys. Plasmas* **7**, No. 5, 1641 (2000); also see H. Takabe, proceedings of this Workshop.
3. P. Chen, Assoc. Asia-Pacific Phys. Soc. (AAPPS) Bull. **13**, 1(2003); *Proc. NASA Laboratory Astrophysics Workshop*, edited by F. Salama, Moffett Field, CA., 2002 (NASA/CP–2002-211863).
4. GLAST Collaboration (E. do Couto e Silva *et al.*), *Nucl. Instr. and Methods* **A 474**, 19-37 (2001).
5. Y. Tanaka *et al.*, *Nature* **375**, 659 (1995); A.C. Fabian *et al.*, *Mon. Not. R. Astron. Soc.* **335**, L1 (2002).
6. M. Begelman, *SLAC LabAstro Workshop*, SLAC, Stanford, Oct. 2001.
7. M. Takeda *et al.*, *Astrophys. J.* **522**, 225 (1999).

8. D.J. Bird *et al.*, *Phys. Rev. Lett.* **71**, 3401 (1993); *Astrophys. J.* **424**, 491 (1994); **441**, 144 (1995); S.C. Corbató *et al.*, *Nucl. Phys. B. (Proc Suppl.)* **28B**, 36 (1992).
9. K. Greisen, *Phys. Rev. Lett.* **16**, 748 (1966); G.T. Zatsepin and V.A. Kuzmin, *Zh. Eksp. Teor. Fiz.* **4**, 114 (1966) [*JETP Lett.* **4**, 78 (1966)].
10. J.N. Matthews, proceedings of this Workshop.
11. P. Sokolsky, *SLAC LabAstro Workshop*, SLAC, Stanford, Oct. 2001.
12. FLASH Collaboration (J. Belz *et al.*), *Proposal for an Experiment (E-165): Fluorescence in Air from Showers (FLASH)*, SLAC, Aug. 27, 2002 (unpublished).
13. P.L. Anthony *et al.*, *Phys. Rev.* **D56**, 1373 (1997); D. Saltzberg *et al.*, *Phys. Rev. Lett.* **86**, No. 13, 2802 (2001)
14. J.G. Kirk *et al.*, *J. Phys.* **G25**, R163 (1999); also see F. Jones, proceedings of this Workshop.
15. R. Blandford, astro-ph/9906026, June, 1999.
16. P. Chen *et al.*, *Phys. Rev. Lett.* **89**, No. 16, 161101 (2002); also proceedings of this Workshop.
17. J. Le Duff *et al.*, *Proc. 11^{th} Int. Conf. on High Energy Physics*, Geneva, W.S. Newman ed., 707(1980).
18. J.S.T. Ng, *SLAC LabAstro Workshop*, SLAC, Stanford, Oct. 2001.
19. C. Adolphsen *et al.*, *Phys. Rev. Lett.* **74**, No. 13, 2475 (1995).
20. J.D. Lawson, *The Physics of Charged-particle Beams*, Clarendon Press, Oxford, 1977.
21. D. Ryutov *et al.*, *Astro. Phys. J.* **518**, 821 (1999).
22. R.P. Drake *et al.*, *Phys. Plasmas* **7**, No. 5, 2142 (2000).
23. See, for example, M. Sikora *et al.*, *Astrophys. J.* **577**, 78 (2002).
24. See, for example, A. Atoyan *et al. Phys. Rev. Lett.* **87**, 221102 (2001).
25. R. Schlickeiser *et al.*, *Astron. Astrophys.* **393**, 69 (2002);
26. M. Pohl *et al.*, *Astron. Astrophys.* **354**, 395 (2000).
27. M. Lyutikov *et al.*, *Mon. Not. R. Astron. Soc.* **293**, 446 (1998).
28. Presentations at two recent SLAC workshops on LabAstro science and experiments can be found at the following web-sites:
http://www-conf.slac.stanford.edu/labastro/,
http://www-conf.slac.stanford.edu/orion/.
29. Details on the ORION project can be found at the web-site:
http://www-project.slac.stanford.edu/orion/.

CRITICAL ISSUES IN LINEAR COLLIDERS

VALERY TELNOV

Institute of Nuclear Physics, 630090 Novosibirsk, Russia
E:mail: telnov@inp.nsk.su; telnov@mail.desy.de

Linear colliders (LC) on the energy 0.5–1 TeV are considered as the next step in the particle physics. High acceleration gradients, small beam sizes, precision tolerances, beam collision effects are main problems for linear colliders. In this paper we discuss physics motivation, parameters and status of current LC projects, e^+e^-, $\gamma\gamma$ and γe modes of operation, physical limitations on the energy and luminosity. Present technologies allow to reach energies about 5 TeV with adequate luminosities. Advanced technique based on plasma and laser method of acceleration can provide much higher accelerating gradients, however, perspectives of these methods for high energy colliders are still under big question. Linear colliders with energies above 10 TeV are hard for any acceleration technology. Speculations on possibility of PeV linear colliders based on ponderomotive laser acceleration are just not serious and contain several mistakes on conceptual level. It is shown that due to radiation in the transverse laser field, methods of acceleration based on laser bunch "pressure" do not work at high energies.

1. Introduction: next steps in particle physics

Progress in particles physics in the last several decades was connected with the increase of accelerator energies. Historically, two types of colliders coexisted and gave main results, $pp(p\bar{p})$ and e^+e^-. Proton colliders give access to higher energies, but e^+e^- colliders have simple initial state, smaller background and allow much better precision. At proton colliders c, b, t quarks and W, Z bosons have been discovered, while at e^+e^- colliders c-quark, τ-lepton, gluon. In addition, at e^+e^- colliders c, b, W, Z, τ physics has been studied with a high accuracy providing a precision test of the Standard Model.

The next proton collider LHC with the energy $2E_0 = 14$ TeV will start operation in about 2007. It will certainly bring new discoveries. But, as before, for detail study of new physics and it's *understanding* a e^+e^- collider is very desirable. Such projects on the energy $2E_0$ =0.5–1.5 TeV already exist, but, unfortunately, approval is delayed due to a high cost and necessity of international cooperation. According to present understanding

the construction can start in about 2007.

As for long-term perspectives of particle physics, the future is even less clear. Three kind of facilities are under discussion: Very Large Hadronic Collider (VLHC) with pp beams on the energy up to 200 TeV, Compact e^+e^- Linear Collider CLIC on the energy $2E_0 = 3$–5 TeV and muon colliders which potentially can reach a c.m.s. energy even higher than in pp collisions.

Physics motivation for next generation of colliders (LHC, LC) is very strong, two examples are given below.

If the Standard Model is valid a new particle, the Higgs boson, should exist. Direct search at LEP and measurements of loop corrections indicate that the Higgs boson mass lays in the region 115–200 GeV. Such a particle should have very special properties, their coupling constants with other particles are proportional to particle masses. Linear colliders allow us to measure Higgs branchings with a high accuracy, So, experiments at LHC and LC can shed a light on the origin of particle masses.

The second physics goal is a search of a supersymmetry which assumes the existence of a new class of particles, superpartners of known particles but with different spins: particles with the spin 1/2 have partners with the spin 0 and vice versa. It is possible that the dark matter in the universe consists of the lightest neutral supersymetrical particles. At colliders, one could produce any kind of such particles, charged and neutral. A discovery of a "parallel" world (which according to astronomical data has a density even higher than that of the barionic matter) would mean a new revolution in physics.

Below we consider existing projects of linear colliders, their problems, energy and luminosity limitations, prospects of advanced accelerator methods.

2. Projects of linear colliders

It was realized already 30 years ago that the energy of circular e^+e^- linear colliders is limited by synchrotron radiation losses at a level of 100–200 GeV and further progress is only possible using linear e^+e^- colliders [1]. At the end of 1980-th the 2-mile electron linac at SLAC has been transformed into a (semi)linear collider SLC with the c.m.s. energy of 90 GeV. It gave nice physics results and a great experience of work at the first linear collider.

At the same time an international study on linear collider lead by SLAC, KEK, DESY, CERN and BINP has been launched with ambitious goal to

develop a linear collider with an energy about one TeV and a luminosity by a factor of 10^3–10^4 higher than it was at the SLC. Since that time a lot of developments have been done and now three projects TESLA (Europe),[2] NLC (US),[3] JLC (Japan)[4] are almost ready for construction. A fourth project CLIC(CERN)[5] is focused on multi-TeV energies and is considered as the next-to-next linear collider. Schemes of colliders are shown in Fig. 1, main parameters are presented in Table 1.

Table 1. Parameters of linear colliders

		TESLA		JLC/NLC		CLIC	
$2E_0$	GeV	500	800	500	1000	500	3000
Site L	km	–	33	–	32	–	40
Two linac L	km	30	30	12.6	25.8	5	27.5
Beam del. L	km	3.2	3.2	3.8	3.8	5	5
G(un.l/load)	MeV/m	23.4	35	70/55	70/55	172/150	172/150
Total AC	MW	95	160	120	240	100	300
AC-beam eff.	%	23	21	10	10	8.5	8.5
RF freq.	GHz	1.3	1.3	11.4	11.4	30	30
Rep. rate	Hz	5	4	120	120	200	100
bunch/train		2820	4886	192	192	154	154
Coll. rate	kHz	14.1	19.5	23	23	30.8	15.4
Bunch separ.	ns	337	176	1.4	1.4	0.67	0.67
Train length	μsec	950	860	0.267	0.267	0.1	0.1
Part./bunch	10^{10}	2	1.4	0.75	0.75	0.4	0.4
σ_z	μm	300	300	110	110	30	30
$\varepsilon_{nx}/\varepsilon_{ny}$	mm·mrad	10/0.03	8/0.015	3.6/0.04	3.6/0.04	2/0.02	0.68/0.02
β_x/β_y	mm	15/0.4	15/0.4	8/0.11	13/0.11	10/0.15	8/0.15
σ_x/σ_y	nm	553/5	391/2.8	243/3	219/2.3	200/2.5	43/1
D_x/D_y		0.2/25	0.2/27	0.16/12.9	0.08/10	0.12/7.9	0.03/2.7
Υ_0		0.06	0.09	0.14	0.29	0.3	8.1
δ	%	3.2	4.3	4.7	8.9	3.8	31
n_γ/e		2	1.5	1.3	1.3	0.7	2.3
$n_{e^+e^-}$/e							0.17
L(with pin.)	$10^{34}\,\mathrm{cm}^{-2}\mathrm{s}^{-1}$	3.4	5.8	2	3	1.4	10.3
L(w/o pin.)	$10^{34}\,\mathrm{cm}^{-2}\mathrm{s}^{-1}$	1.6	2.8	1.2	1.9	?	?
L(1%)/L	%	66		64		67	25.5
L(5%)/L	%	91		85		86	40.8

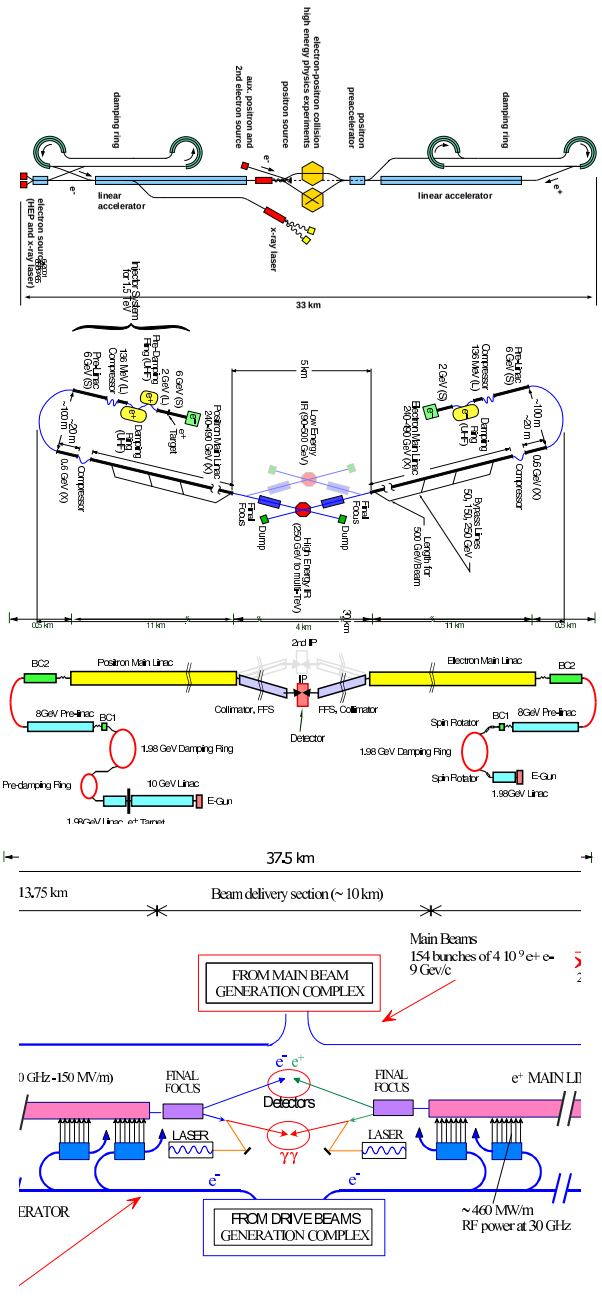

Figure 1. Schemes of linear colliders TESLA, NLC, JLC and CLIC (from up to down).

Each project has some distinctive features:

• TESLA: L band, 1.4 GHz, superconducting, $G_{max} \sim 35$ MeV/m, a good efficiency, a low wakefield, a relaxed alignment tolerances, a large distance between bunches;
• NLC/JLC: X-band, 11.4. GHz, warm cavities, a high gradient (55 MeV/m loaded);
• CLIC: 30 GHz, a two-beam accelerator (one of beams produces RF power), a very high gradient, 150 MeV/m, cost effective at multi-TeV energies.

So, there are three main technologies for LC developed by large teams, each project have certain advantages. It would be good to built two colliders almost simultaneously: TESLA for energies below 0.5 TeV, NLC/JLC for the energy region up to 1.5 TeV and a third collider, CLIC, on the energy 3–5 TeV one decade later. However, due to a high cost only one global linear collider is seen in the visible future.

3. General features of linear colliders

At storage rings, each bunch collides many times, the RF power is spent mainly for compensation of synchrotron radiation losses. At linear colliders, each bunch is used only once, radiation losses during the acceleration are negligible, but a lot of energy is needed for production and acceleration of bunches with a high rate. The total RF power consumption at LEP and at 0.5 TeV linear colliders are comparable, of the order of 100 MW from the wall plug.

The number of accelerated particles is limited by total AC power which is proportional to the beam power P. Due to the dependence of cross sections on the energy as $\sigma \propto 1/E^2$ the luminosity should increase as E^2, as a result the required transverse beam sizes at TeV energies should be very small.

Beams with small sizes have very strong fields that lead to large radiation losses during beam collisions (beamstrahlung). This effect does not allow us to use beams with simultaneously small horizontal and vertical beam sizes (σ_x, σ_y) (only very flat beams) and to get the required luminosity the beam power should be additionally increased. This leads to the "energy crisis" at the beam energy of about $2E_0 \sim 5\,\mathrm{TeV}$, see Sec. 4. In the $\gamma\gamma$ mode of operation (Sec. 5) only somewhat higher energies are possible due to conversion of high energy photons to e^+e^- pairs in the field of the opposing beam (coherent pair creation).

Beside traditional linear accelerators, there are ideas of using plasma and laser high gradient accelerator techniques for linear colliders. There are some speculations about colliders with 100 TeV and even PeV energies. Certainly, development of these techniques will lead to some practical applications, but obtaining colliding beams is very problematic due to required quality of beams and collision effects. Some considerations and critical remarks on plasma and laser acceleration are given Sec. 6.

4. Collision effects restricting luminosity and energy of linear colliders

In order to obtain a sufficient luminosity at linear colliders the beam sizes should be very small. This causes two sorts of problems: a) generation and acceleration of beams with very small emittances and focusing to a tiny spot, b) beam-beam collision effects which lead to degradation of the beam quality.

The first problem is very difficult but not fundamental, in principle, one can obtain emittance smaller than give damping rings using, for example, laser cooling. The second problem is even more severe: beam collision effects put restrictions on attainable luminosity and, correspondently, on the maximum energy of linear colliders.

In the absence of collision effects the luminosity of a collider

$$L \approx \frac{N^2 f}{4\pi\sigma_x\sigma_y} = \frac{P}{4\pi E_0} \times \frac{N}{\sigma_x\sigma_y}. \tag{1}$$

For $2P = 20$ MW(200 MW AC power), $N = 2\times10^{10}$, $\sigma_x = \sigma_y = 1$ nm $L = 10^{37}/E_0$[TeV], $\mathrm{cm}^{-2}\mathrm{s}^{-1}$, this luminosity is sufficient for production of 10^3 lepton pairs per 10^7 sec up to $2E_0 = 25$ TeV. Below we consider several limitations due to collisions effects.

4.1. *Pinch effect and instability of beam collisions*

During the collision beams attract (e^+e^-) or repulse (e^-e^-) each other. The characteristic disruption parameter[6,7]

$$D_y = \frac{2Nr_e\sigma_z}{\gamma\sigma_x\sigma_y}. \tag{2}$$

For flat beam and $D_y \sim 10$, the attraction leads to increase of the e^+e^- luminosity by a factor of $H_D \sim 2$. At $D_y \geq 25$ beams become unstable,

the corresponding luminosity

$$L \sim \frac{P}{mc^2 r_e \sigma_z}. \tag{3}$$

For $P = 10$ MW and $\sigma_z = 100$ μm $L \sim 5 \times 10^{34}$ cm^{-2}s^{-1}. So, this put limit on the luminosity for a given beam power and bunch length.

4.2. *Beamstrahlung*

A strength of a beam field is characterized by the parameter Υ [8,7]

$$\Upsilon = \frac{2}{3}\frac{\hbar\omega_c}{E} = \gamma\frac{B}{B_0}, \quad B_0 = \frac{\alpha e}{r_e^2} = 4.4 \cdot 10^{13}\text{G}. \tag{4}$$

For flat beams

$$\Upsilon_{av} \approx \frac{5 N r_e^2 \gamma}{6\alpha\sigma_x\sigma_z}. \tag{5}$$

The maximum value of σ_z is determined by disruption. Ideally, increasing σ_x to infinity and simultaneously decreasing σ_y to zero one can get arbitrary small Υ for any luminosity. However, if σ_y has some minimum value (there are many reasons), then $\Upsilon \propto L^2\gamma^2\sigma_y/P^2 D_y$. As P is always limited, $D_y < 25$ and the required L increases with the energy as γ^2, the value of Υ increases rapidly with the energy. In the current LC projects at 1 TeV $\Upsilon = \mathcal{O}(1)$, at higher energies inevitably $\Upsilon \gg 1$.

Synchrotron radiation of electrons in the field of the opposing beam (beamstrahlung) put severe limitations on performance of linear colliders. Energy losses are given by approximate formulae: [7]

$$\frac{dN_\gamma}{dt} = \frac{5}{2\sqrt{3}}\frac{\alpha^2 c\Upsilon}{r_e\gamma}U_0(\Upsilon), \qquad U_0 \approx \frac{1}{(1+\Upsilon^{2/3})^{1/2}}, \tag{6}$$

$$-\frac{dE}{Edt} = \frac{2}{3}\frac{\alpha^2 c\Upsilon^2}{r_e\gamma}U_1(\Upsilon) \quad U_1 \approx \frac{1}{(1+(1.5\Upsilon)^{2/3})^2}, \tag{7}$$

$$\frac{<\omega>}{E} = \frac{4\sqrt{3}}{15}\Upsilon\frac{U_1(\Upsilon)}{U_0(\Upsilon)} \quad = 0.462\Upsilon \ \ (\Upsilon \to 0), \quad 0.254 \ \ (\Upsilon \to \infty), \tag{8}$$

$$\delta_E = \frac{\Delta E}{E} = 1.24\left[\frac{\alpha^2\sigma_z\Upsilon}{r_e\gamma}\right]\Upsilon U_1(\Upsilon); \tag{9}$$

$\Upsilon \ll 1$ is the "classic" regime; $\Upsilon \sim 0.2$–200 the "transition" regime ($\Upsilon U_1(\Upsilon) \approx 0.1$–$0.2 \sim 0.15$); $\Upsilon \gg 200$ the "quantum" regime. Colliders in the TeV region belong to the transition regime, multi-TeV LC with dense short bunches can reach the quantum regime.

The luminosity (1) can be expressed via δ_E. In the transition regime it does not depend on σ_z:

$$L \sim \frac{6.45\delta_E}{4\pi\alpha r_e\gamma\sigma_y}\left(\frac{P}{mc^2}\right) = 1.5\times10^{34}\frac{P[\mathrm{MW}]\delta_E}{E_0[\mathrm{TeV}]\sigma_y[\mathrm{nm}]}\ \mathrm{cm}^{-2}\mathrm{s}^{-1}; \qquad (10)$$

In the quantum regime

$$L \sim \frac{1.95}{4\pi\alpha^2\sigma_y}\sqrt{\frac{\delta_E^3}{r_e\sigma_z\gamma}}\left(\frac{P}{mc^2}\right) = 5\times10^{34}\frac{P[\mathrm{MW}]}{\sigma_y[\mathrm{nm}]}\sqrt{\frac{\delta_E^3}{E_0[\mathrm{TeV}]\sigma_z[\mu\mathrm{m}]}}. \qquad (11)$$

For example, for $P = 10$ MW per beam (about 200 MW from wall plug) $\sigma_y = 1$ nm, $2E_0 = 5$ TeV, $\delta_E = 0.2$ we get (accuracy is about factor of 2–3) $L = 1.2\times10^{34}$ cm^{-2}s^{-1} in the transition regime (does not depend on σ_z) and $L = 3\times10^{34}$ cm^{-2}s^{-1} in the quantum regime (for $\sigma_z = 1$ μm), an additional factor of ~ 1.5 can give the pinch effect. We see that the quantum regime (short bunches) helps but not too much.

In order to produce 10^3 characteristic reactions $e^+e^-\to\mu^+\mu^-$ per 10^7 sec at the energy $2E_0 = 5$ TeV the required luminosity is 3×10^{34}, that is close to the above limit due to beamstrahlung. So, if $\sigma_{y,min}\sim 1$ nm (see Sec. 4.5), the maximum reasonable energy of linear colliders is about $2E_0\sim 5$ TeV.

In principle, there is a possibility to cancel beam fields by colliding four beams (e^+e^- from each side), then beamstrahlung is absent. The beams instability threshold remains at the same level of luminosity or may be only somewhat higher. This scheme can give some gain in luminosity, but technically it looks unrealistic.

4.3. *Coherent e^+e^- pair creation*

At $\kappa = (\omega/E_0)\Upsilon > 1$ a beamstrahlung photon can convert into e^+e^- pairs in the field of the opposing beam.[9] At $\kappa \gg 1$ the ratio of beamstrahlung/pair creation probabilities is about 3.8. The number of beamstrahlung photons at linear colliders $N_\gamma \sim N_e$ (in order to increse luminosity the horizontal size is decreased until each electron emit about one photon). Therefore the number of e^+e^- pairs at $\kappa \gg 1$ (or $\Upsilon \gg 1$), $N_{e^+e^-}/N_e = \mathcal{O}(0.1)$. For example, at CLIC(3000) $N_{e^+e^-}/N_e \sim 0.085$. The minimum energy of produce particles (important from a background point of view) $E_{min}\sim 0.05E_0/\Upsilon$.

4.4. *Deflection of soft particles*

The lowest energy charged particles produced in process of coherent pair creation with the same sign of the charge as that of the opposing beam are deflected by the opposing beam on the angle [9]

$$\theta \sim \left(\frac{4\pi N e^2}{\sigma_z E_{min}}\right)^{1/2} \sim 170 \frac{N}{\sigma_z}\left(\frac{r_e^3}{\sigma_x}\right)^{1/2}. \qquad (12)$$

For example, at CLIC $\theta \sim 15$ mrad. To avoid background from these large angle particles one should use the crab-crossing scheme.[10] Below we will see that crab-crossing angles below 20–30 mrad are acceptable, but larger angles lead to the increase of the vertical beam size.

So, deflection of soft particles put an additional constraint on the beam parameters. Beamstrahlung and instabilities may be OK (in case of very short bunches), but disruption angles are too large.

4.5. *Minimum value of σ_y*

The minimum vertical beam size at the interaction point (at $\beta_y \sim \sigma_z$) $\sigma_y = \sqrt{\varepsilon_{ny}\sigma_z/\gamma}$. Limitations:

a) Attainable value of the normalized vertical emittance from an injector;

b) Radiation in final quadrupoles (Oide effect). [11] Minimum achievable beam size $\sigma_{min}[\mathrm{m}] \approx 1.7\times 10^{-4}\varepsilon_{ny}[\mathrm{m}]^{5/7}$. For ε_{ny} considered in the current LC projects $\sigma_{min} \sim 0.5$ nm.

c) Radiation in the detector solenoid field due to the crab crossing[12,13,14]

$$\sigma_y^2 = \frac{55 r_e^2}{480\sqrt{3}\,\alpha}\left(\frac{eB_s\theta_c L}{2mc^2}\right)^5. \qquad (13)$$

For $B_s = 4$ T, $L = 4$ m $\sigma_y = 0.74$ nm for $\theta_c = 20$ mrad and 2 nm for $\theta_c = 30$ mrad. More accurate simulation of this effect (the number of emitted photon is about one) was done in Refs 13, 14. As a linear collider without a detector has no sense this effect put a limit on a minimum vertical beam size at the interaction point at the level of 0.5 nm at $\theta_c = 20$ mrad.

4.6. *Resume on maximum energies of linear colliders.*

For a reasonable wall plug AC power 100–300 MW the maximum energy of linear e^+e^- colliders with a luminosity sufficient for experiments, according to present understanding, is limited by collision effects at the level of $2E_0 =$ 5–10 TeV.

5. Photon colliders

In addition to e^+e^- physics, linear colliders provide a unique opportunity to study $\gamma\gamma$ and γe interactions at high energies and luminosities.[15,16] High energy photons can be obtained using Compton backscattering of laser light off high energy electrons. This option is foreseen in all other project of linear colliders.[2,3,4,5,18] The maximum energy of photons after Compton scattering

$$\omega_m = \frac{x}{x+1}E_0; \quad x \approx \frac{4E_0\omega_0}{m^2c^4} \simeq 15.3\left[\frac{E_0}{\mathrm{TeV}}\right]\left[\frac{\omega_0}{\mathrm{eV}}\right]. \tag{14}$$

For example: $E_0 = 250$ GeV, $\omega_0 = 1.17$ eV ($\lambda = 1.06$ μm) $\Rightarrow x = 4.5$ and $\omega_m = 0.82E_0 = 205$ GeV. The value $x = 4.8$ is the threshold for the process $\gamma\gamma_L \to e^+e^-$ in the conversion region. This determine the optimum laser wavelength: $\lambda_{opt} \sim 4E[\mathrm{TeV}]$ μm.[19] Nonlinear effects in Compton scattering increase the threshold value of x by a factor of $(1+\xi^2)$, where a parameter of nonlinearity $\xi^2 \sim 0.5$ is acceptable. [18] Most powerful solid state laser with $\lambda \sim 1.05$ μm can be used upto the energies $2E_0 \sim 800$ GeV. Detailed discussion of physics, and technical problem of photon colliders can be found elsewhere.[18,3,28] Below we consider only the most critical issues: luminosity, energy, laser system.

5.1. *Current projects of photon colliders*

Parameters of the photon colliders at TESLA[18] (as an example) are presented in Table 2, for comparison the luminosity in e^+e^- collisions is also given. Other parameters, constant for all energies, are: $\lambda = 1.06$ μm, $N = 2\times10^{10}$, $\sigma_z = 0.3$ mm, $f_{rep}\times n_b = 14.1$ kHz, $\varepsilon_{nx}/\varepsilon_{ny} = 2.5/0.03\times10^{-6}$ m·rad, $\beta_x/\beta_y = 1.5/0.3$ mm. For the same energy the $\gamma\gamma$ luminosity

Table 2. Parameters of the photon collider at TESLA, see also some fixed parameters above Table.

$2E_0$, GeV	200	500	800
$W_{\gamma\gamma,max}$	122	390	670
$W_{\gamma e,max}$	156	440	732
$\sigma_{x/y}$ [nm]	140/6.8	88/4.3	69/3.4
b [mm]	2.6	2.1	2.7
L_{ee}(geom) [10^{34}]	4.8	12	19
$L_{\gamma\gamma}(z > 0.8z_{m,\gamma\gamma})$[$10^{34}$]	0.43	1.1	1.7
$L_{\gamma e}(z > 0.8z_{m,\gamma e})$[$10^{34}$]	0.36	0.94	1.3
$L_{ee}(z > 0.65)$[10^{34}]	0.03	0.07	0.095
$L_{e^+e^-}$, [10^{34}]	1.3	3.4	5.8

in the high energy peak of the luminosity spectrum

$$L_{\gamma\gamma}(z > 0.8 z_{max}) \approx (1/3) L_{e^+e^-}, \tag{15}$$

where $z = W_{\gamma\gamma}/2E_0$. Note, that cross sections in $\gamma\gamma$ collisions are typically larger then in e^+e^- by one order of magnitude. A more universal relation $L_{\gamma\gamma}(z > 0.8 z_m) \approx 0.1 L_{ee}(geom)$ (for $k^2 = 0.4$). Expected $\gamma\gamma$, γe luminosity spectra at TESLA can be found elsewhere.[20,18,21]

The $\gamma\gamma$ luminosity at TESLA is limited by attainable electron beam sizes. Having beams with smaller emittances (especially the horizontal one) one would get a higher luminosity. In order to increase the geometric luminosity one should decrease the β-functions as much as possible, down to about a bunch length. In the current scheme of the final focus it was not possible to make β_x below 1.5 mm due to chromo-geometric abberations.[18] It is not clear whether this is a fundamental or just a temporary technical problem.

5.2. *Ultimate luminosity of photon colliders*

Though photons are neutral, $\gamma\gamma$ and γe collisions are not free of collision effects. Electrons and photons are influenced by the field of the opposite electron beam that leads to the following effects:[19]

- in $\gamma\gamma$: conversion of photons into e^+e^- pairs (coherent pair creation);
- in γe: coherent pair creation; beamstrahlung; beam displacement.

Beam collision effects in e^+e^- and $\gamma\gamma$, γe collisions are different. In particular, in $\gamma\gamma$ collisions there are no beamstrahlung and beam instabilities which limit the horizontal beam size in e^+e^- collisions on the level 550 (350) nm for TESLA (NLC/JLC). A simulation, which includes all collision effects has shown that in $\gamma\gamma$ mode at TESLA one can use beams with the horizontal size down to $\sigma_x = 10$ nm (at smaller σ_x may be problems with the crab–crossing scheme) and influence of collision effects will be rather small.[22,20,18] The $\gamma\gamma$ luminosity (in the high energy part) can reach 10^{35} $cm^{-2}s^{-1}$. Note that now in TESLA project $\sigma_x \approx 500$ nm in e^+e^- collisions and about 100 nm in the $\gamma\gamma$ collisions. Having electron beams with much smaller emittances one could build a photon collider factory with production rate of new particles by a factor of 10–50 higher than at e^+e^- colliders. A laser cooling of electron beams is one of the possible methods of reducting beam emittances at photon colliders,[23,24] but this method is not easy.

Note that small rate of coherent e^+e^- pair production at TESLA energies is partially explained by the beam repulsion which reduces the field act-

ing on the photons. For multi-TeV energies and short bunches such suppression is absent and photon colliders reach their energy limit (with adequate luminosity) approximately at the same energies as e^+e^- colliders.[25,26,27]

5.3. *Technical aspects of photon colliders*

A key element of photon colliders is a powerful laser system which is used for the $e \to \gamma$ conversion. Required parameters are: a few Joules flash energy, a few picosecond duration and 10–20 kHz repetition rate.

To overcome the "repetition rate" problem it is quite natural to consider a laser system where one laser bunch is used for the $e \to \gamma$ conversion many times. At the TESLA, the electron bunch train contains 3000 bunches with 337 ns spacing, here two schemes are feasible: an optical storage ring and an external optical cavity.[20,18,21] With the optical cavity a required laser power can be lower than in the case of a one-pass laser by factor of 50–100. There is no detailed scheme of such laser system yet.

At NLC, the electron bunch train consists of 96 bunches with 2.8 sec spacing therefore exploiting of the optical cavity is not effective. A current solution is a one-pass laser scheme based on the Mercury laser developed for the fusion program. The laser produces 100–200 J pulses which after splitting to 96 pulses can be used for $e \to \gamma$ conversion of one train.[3,21]

A laser system for a photon collider can certainly be built though it is not easy and not cheap.

6. Advanced accelerator schemes

Conventional RF linear colliders have accelerating gradients up to 150 MeV/m, corresponding lengths about 30–40 km and attainable energies up to 5 TeV (Sec.2). On the other hands, people working on plasma and laser methods of acceleration have obtained gradients of 100 GeV/m! Some people are thinking already about 100 TeV and even 1 PeV linear colliders or about 1–5 TeV LC with less than one km length.

Certainly, new methods of acceleration will make further progress and find certain applications, but it is less clear about possibility of super high energy colliders based on these technologies.

First of all, collision effects restrict the energy of linear colliders at about 10 TeV (Sec.4); secondly, the quality of electron beams should be very high; and thirdly, it is very likely that in considerations of very high acceleration gradients some important effects are just missed. Driven by my curiosity and for self-education I have spent some time for random check of these

conceptions and some remarks are presented below. Situation in this field is not bad, but some of existing proposals are certainly wrong.

6.1. *Plasma acceleration*

Laser or particle beams can excite waves in plasma with a longitudinal electrical field [29]. The accelerating gradient

$$G \sim mc\omega_p \sim 10^{-4}\sqrt{n_p[\mathrm{cm}^{-3}]}\left(\frac{\mathrm{MeV}}{\mathrm{m}}\right). \tag{16}$$

Typical parameters considered: $n_p \sim 10^{15}$ cm^{-3}, $G \sim 2$ GeV/m.

6.1.1. *Multiple scattering*

Let us consider the case $n_b \gg n_p$ when all plasma electrons are pushed out from the accelerated beam. The beams travel through ions with density n_p and experience a plasma focusing with the β-function[30] $\beta \sim \sqrt{2\pi\gamma/r_e n_p} = \sqrt{2\gamma}\lambda_p$. The r.m.s. angle due to multiple scattering

$$\Delta\theta^2 \approx \frac{8\pi Z^2 r_e^2 n dz}{\gamma^2}\frac{d\rho}{\rho}, \quad \rho_{min} \sim R_N, \;\; \rho_{max} \sim R_D, \tag{17}$$

where $R_D = (kT/4\pi ne^2)^{1/2}$ is the Debai radius. The increase of the normalize emittance $\Delta{\varepsilon_n}^2 = \gamma^2 r^2 \Delta\theta^2 = \varepsilon_n\ \gamma\beta\Delta\theta^2$. After integration on the energy we get the final normalized emittance

$$\varepsilon_n \sim 8\pi\sqrt{2\pi}Z^2(n_p r_e^3\gamma_f)^{1/2}(mc^2/G)\ L, \tag{18}$$

where $L = \ln\rho_{max}/\rho_{\min} \sim 20$. Substituting $n = 10^{15}$ cm^{-3}, $G = 2$ GeV/m, $Z = 1$, $\gamma_f = 5\times10^6$ ($2E_0 = 5$ TeV) we get $\varepsilon_n \sim 3\times10^{-7}$ cm. Note that the result does not depend on the plasma density because $G \propto \sqrt{n_p}$ (Eq.16). In present LC designs the minimum vertical emittance $\varepsilon_{ny} = 2\times10^{-6}$ cm, so multiple scattering in an *ideal* plasma accelerators look acceptable. It is assumed that sections with plasma have small holes for beams since any windows will give too large scattering angles.

6.1.2. *Synchrotron radiation*

Due to a strong focusing by ions (plasma electrons are pushed out from the beam), beam electrons lose their energy to radiation, the radiation power $P = (2/3)cr_e^2\gamma^2E_\perp^2$, where $E_\perp = 2\pi en_pZr$ (as before we assume $n_b \gg n_p$), $r \sim \sqrt{\varepsilon_n\beta/\gamma}$, $\beta = \sqrt{2\pi\gamma/r_e n_p}$. After integration on the energy we find

the difference of energies for the particle on the axis (no radiation) and one at the r.m.s distance form the axis

$$\Delta E/E \sim 25 r_e^{5/2} n_p^{3/2} Z^2 \gamma_f^{3/2} (mc^2/G) \varepsilon_n \ . \tag{19}$$

For $G = 2$ GeV/m, $n_p = 10^{15}$ cm^{-3}, $\varepsilon_{nx} \sim 10^{-4}$ cm (emittance from damping rings or from photo-guns), $\gamma_f = 5 \times 10^6$ ($2E_0 = 5$ TeV) we get $\Delta E/E \sim 10^{-3}$, that is acceptable. For several times larger energy spreads there are chromaticity problems in final focus systems. Note, that $G \propto \sqrt{n_p}$, therefore the energy spread is proportional to the plasma density. In Ref. 31 the case of the overdense plasma ($n_b < n_p$) was also investigated with the conclusion that it is not suited for TeV colliders.

So, synchrotron radiation puts a limit on a maximum plasma density (and acceleration gradient). A 10 TeV collider with a gradient 10 times larger that at CLIC is still possible.

6.1.3. *Some other remarks on plasma acceleration*

Though plasma accelerators pass the simple criteria discussed above, there are many other question.

At $E_0 = 1$ TeV, $n_p = 10^{15}$ cm^{-3}, ε_{ny}=10^{-6} cm the transverse electron beam size in plasma is about 0.1 μm ! This means that the accelerating sections should have relative accuracy better than $0.1\sigma_y \sim 10^{-6}$ cm !

The beam axis is determined in large extent by the drive beam. The transverse size of the drive beam (of it's head which is focused by external quadrupoles) is of the order of 10^{-2} cm. Small fluctuations in the beam profile will lead to dilution of the accelerated beam emittance.

To avoid radiation of the high energy accelerated beam in the field of kickers during the injection of the drive beam, the kickers should be very fast, in 100 GHz frequency range.[32] Then the required stability of the horizontal angle is about $\sim 0.1\sigma_x/L \sim 0.1 \times 10^{-4}/100 \sim 10^{-7}$ rad. If the kick angle is 10^{-2} rad, the required time stability is about $\sim \Delta x/c \times 10^{-5} \sim 10^{-16}$ sec.

In summary: a plasma acceleration is a perspective technique, it can find certain applications, but technical feasibility of plasma based linear colliders is not clear now.

6.2. *Laser acceleration in vacuum*

There are many ideas on this subject. [a] In general, in a space with some boundaries the accelerating gradient is proportional to the electric field, $G \propto E$, and $G \propto E^2$ in an open space. This is because the charged particle extracts the energy from the field due to interference of the external and radiated field:

$$\Delta\mathcal{E} \ \propto \int (E + E_{rad})^2 \, dV - E^2 \, dV \propto E E_{rad} \, dV, \tag{20}$$

where $E_{rad} \sim const$ when a particle radiates in a given structure without any field and in a free space the radiated field is proportional to a particle acceleration: $E_{rad} \propto E$.

6.2.1. $G \propto E$

In this case, a particle is accelerated by the axial electrical field E_z of a focused laser. For a radially polarized Gaussian beam $E_z \sim E(\lambda/\pi w_0)$, where E is the transverse laser field, w_0 is the radius of the focal spot.

The electron is in the accelerating phase of the wave on the length $\sim Z_R$ (Rayleigh length). In order to get a net acceleration one has to put some screen with a small hole to restrict the interaction length. The damage threshold of the optical components is a limiting factor of the method. For the damage threshold 5 TW/cm^2 the maximum energy gain ΔE(MeV) $\sim 20[P(\text{TW})]^{1/2}$, that is about 50 MeV for P = 10 TW.[33] There is a proposal to study this method at SLAC.[34]

One of the other approaches uses small cavities pumped by a laser. [35] This method needs very small beam sizes (emittances) and severe tolerances.

There are many laser accelerating schemes of such kind under development.

6.3. $G \propto E^2$

There are many fantasies on this subject.

1. Light pressure. If an electron is in the rest, a plane electromagnetic wave pushes it with a force $F = \sigma_T \times (E^2/4\pi)$, where σ_T is the Thomson cross section. This is because laser photons scatter isotropically and momenta of laser photons incident onto σ_T are transfered to the electron. At $I = 10^{28}$ W/cm^2 (in Ref.36), the accelerating gradient $d\mathcal{E}/dx = 1$ TeV/cm.

[a] In Secs 6.2, 6.3 $\mathcal{E}$ denotes an electron energy and E is the strength of a laser field.

Unfortunately, in a real wave, laser photons have the divergence $\theta \sim \sqrt{\lambda/4\pi Z_R}$. Therefore, if the electron has $\mathcal{E}/mc^2 > 1/\theta$, then in the electron rest frame laser photons come from the forward hemisphere and therefore the electron is deaccelerated! For $\lambda = 1$ μm and $Z_R = 100$ μm, $E_{max} \sim 15$ MeV only!

2. Ponderomotive acceleration. In a strong laser field an electron experiences a collective force from the whole laser bunch, so called a ponderomotive force,[37,38,39]

$$F_i \sim \frac{mc^2}{\gamma}\frac{d\xi^2}{dx_i}, \quad \xi^2 = \frac{e^2\overline{E^2}}{m^2c^2\omega_0^2} = \frac{2n_\gamma r_e^2\lambda}{\alpha}. \tag{21}$$

This opens a way to transfer the energy from large body (laser beam) to one microscopic particle (electron). There is an idea [40] to collide the laser pulse propagating in a rare gas (to have $v^* < c$, large effective γ^*) with the oncoming electron bunch with a relativistic factor γ_0, so that after elastic reflection the electron will have $\gamma = (\gamma^*)2/\gamma^0$. According to above Refs, for the laser power 4.3 EW (EW=10^{18} W) $\gamma^* = 1.6 \times 10^6$ and $\gamma_0 = 1400$, the energy of reflected electrons in the laboratory system is 1 PeV $\equiv$ 1000 TeV! The length of the collider is the laser bunch length or almost ZERO!

Unfortunately, the idea is wrong due to many reasons:

- The interaction length is not the bunch length but $L_{int} \sim l_{laser}/(1 - v^*/c) \sim l_{laser} \times (\gamma^*)^2 \sim 10^{-2} \times 10^{12} \sim 10^5$ km !
- Radiation of electrons (see below), and many other "NO".

6.3.1. *Radiation during a ponderomotive acceleration*

During the ponderomotive acceleration electrons radiate in the transverse laser field. This can be treated as Compton scattering. Radiated energy per unit length: $\frac{d\mathcal{E}}{dx} \sim \bar{\epsilon}\ n(1 - \cos\theta)\sigma_T$. Substituting $\theta^2 \sim \lambda/(2\pi Z_R)$, $\bar{\epsilon} \sim \omega_0\gamma^2\theta^2$, $n = \alpha\xi^2/(2r_e^2\lambda)$ we get

$$\frac{d\mathcal{E}}{dx} \sim \frac{\xi^2\gamma^2 r_e}{Z_R^2}mc^2. \tag{22}$$

For example: $\mathcal{E}_0 = 1$ TeV, $Z_R = 100$ μm, and $\xi^2 = 100$ (flash energy ~ 100 J), $d\mathcal{E}/dx = -200$ GeV/cm. For the mentioned 1 PeV project with $\xi^2 = 2 \times 10^6$, $d\mathcal{E}/dx = -10^9$ PeV/cm!

So, ponderomotive acceleration can be useful for low energy application, but not for linear colliders due to the decrease of the force with the increase of the energy and a huge radiation.

7. Conclusion

Linear e^+e^-, e^-e^-, $\gamma\gamma$, γe colliders are ideal instrument for study of matter in the energy region $2E_0 \sim 100$–1000 GeV. Three projects are almost ready for construction, a wise choice and political decision are needed.

A linear collider is not a simple machine, very high accuracies, stabilities and cleaver beam diagnostics are needed. Many critical elements have been tested experimentally.

According to present understanding a maximum attainable energy of linear colliders with adequate luminosity is about $2E_0 \sim 5$ TeV. There is technology for such "last" LC, that is CLIC.

Advance technologies (plasma, laser) can give higher accelerating gradients but their application for high energy linear colliders is under big question. Further complex studies of new accelerating methods in this context are needed.

Acknowledgement

I am grateful to Pisin Chen for a great work on organization of series of workshops on Quantum Aspects of Beam Physics, which motivated people to look deeply in topics related to beam physics at Earth and Cosmos and to Atsushi Ogata for organization of the present workshop in Hiroshima.

This work was supported in part by INTAS (00-00679).

References

1. A.N. Skrinsky, Usp. Fiz. Nauk, bf 138 (1982) 3.
2. *TESLA: Technical design report*, DESY 2001-011, ECFA 2001-209, March 2001.
3. Linear collider physics resource book for Snowmass 2001, T. Abe et al., SLAC-R-570, May 2001.
4. K. Abe et al., KEK-REPORT-2001-11, hep-ph/0109166.
5. R.W. Assmann *et al.*, CERN-2000-008.
6. V. Balakin, N. Solyak, Preprint INP 82-123, Novosibirsk, 1982; *Proc. of VIII Intern. Conf. on High Energy Accel.,* Novosibirsk, 1987, p.151.
7. K. Yokoya, P. Chen, *US-CERN Part. Accel. School*, Hilton Head, S.C., Nov 7-14, 1990. Proceedings. Edited by M. Dienes et al., Springer- Verlag, 1992. (Lecture Notes in Physics, 400).
8. R. Noble, *Nucl. Inst. Meth.*, **A256** (1987) 427.
9. P. Chen and V. I. Telnov, *Phys. Rev. Lett.*, **63** (1989) 1796.
10. R. B. Palmer, SLAC-PUB 4707.
11. K. Oide, *Phys. Rev. Lett.,* **61** (1988) 1713; K. Hirata, K. Oide and B. Zotter, *Phys. Lett.* **B224** (1989) 437; J. Irwin, AIP Conf. Proc. 335 (1995) 3.

12. The NLC Design Group. *Zeroth-Order Design Report for the NLC*, LBNL-5424, SLAC-474, UCBL-ID-124161, UC-414.
13. V. Telnov, Proc. of the APS/DPF/DPB Summer Study on the Future of Particle Physics (Snowmass 2001), ed. N. Graf, eConf **C010630** (2001) T104.
14. D. Schulte and F. Zimmermann, CERN-SL-2001-043-AP, PAC 2001, Chicago, Illinois, 18-22 Jun 2001.
15. I.F. Ginzburg, G.L. Kotkin, V.G. Serbo, and V.I. Telnov, *Pizma ZhETF*, **34** (1981) 514 (*JETP Lett.* **34** (1982) 491); *Nucl. Instr. &Meth.*, **205** (1983) 47.
16. I. F. Ginzburg, G. L. Kotkin, S. L. Panfil, V. G. Serbo, and V. I. Telnov. *Nucl. Inst. Meth.*, **A219** (1984) 5.
17. R. Brinkmann et al., *Nucl. Instr. &Meth.*, **A406** (1998) 13; hep-ex/9707017.
18. B. Badelek et al., *TESLA Technical Design Report, Part VI, Ch.1. Photon collider at TESLA*, DESY 2001-011, hep-ex/0108012.
19. V. Telnov, *Nucl. Instr. &Meth.*, **A294** (1990) 72; **A355** (1995) 3.
20. V. Telnov, *Nucl. Instr. &Meth.* **A472** (2001) 43; hep-ex/0010033.
21. V. Telnov, Nucl. Instr. Meth. **A 494** (2002) 35, hep-ex/0207093.
22. V. Telnov, Nucl. Phys. Proc. Suppl. **82** (2000) 359, hep-ex/9908005.
23. V. Telnov, Phys. Rev. Lett. **78** (1997) 4757 [Erratum-ibid. **80** (1998) 2747, hep-ex/9610008.
24. V. Telnov, Nucl. Instr. Meth., **A 455** (2000) 80, hep-ex/0001028.
25. V. Telnov, AIP Conf. Proc. **397** (1996) 259, physics/9706003.
26. V. Telnov, Nucl. Instr. Meth. **A 472** (2001) 280, hep-ex/0012047.
    V. Telnov, Proc. of the APS/DPF/DPB Summer Study on the Future of Particle Physics (Snowmass 2001), ed. N. Graf, eConf **C010630** (2001) E3026.
27. H. Burkhardt and V. Telnov, CERN-SL-2002-013-AP.
28. Proc. of Intern. Workshop on High-Energy Photon Colliders (GG 2000), Hamburg, Germany, 14-17 Jun 2000, ed. R.D. Heuer, V.I. Telnov, N.J. Walker, Nucl. Instr. Methods A **472** (2001) 1-321.
29. T. Tajima and J.M. Dawson, *Phys. Rev. Lett.* **43** (1979) 267.
30. D. Whittum, A. Sessler, *Phys. Rev. Lett.* **64** (1990) 2511-2514.
31. W.A. Barleta, E.P.Lee, R.Bonifacio, L.De Salvo, Nucl. Instr. and Meth. **A 423** (1999) 256.
32. J.Rozenzweig, N.Barov, A.Murokh, E.Colby, P.Colestock, Nucl. Instr. and Meth. **A 410** (1998) 532.
33. E. Esarey, P. Sprangle and J. Krall, Phys. Rev **E 52** (1995) 5443.
34. C.D. Barnes et al., SLAC-PROPOSAL E-163, 2001.
35. A.A. Mikhailichenko, SNOWMASS-2001-T401, Jun 2001, eConf C010630: T401, 2001.
36. T. Tajima, G. Mourou, Phys. Rev. ST Accel. and Beams, **5** (2002) 031301.
37. T. Kibble, Phys. Rev. Lett. **16** (1966) 1054; Phys. Rev, **150** (1966) 1060.
38. P. Mora, T. Antonsen, Jr. Phys. Plasma, **4** (1997) 217.
39. V. I. Telnov, BUDKER-INP-2003-15, hep-ex/0302038.
40. I.V. Smetanin, P.N. Lebedev, C. Barnes, K. Nakajima, Proceedings of HEACC2001, March 26–30, 2001, Tsukuba, Japan; K. Nakajima, in *Proc. of Snowmass 2001* ed. N. Graf, eConf **C010630** (2001) T803.

RECENT PROGRESS ON PHOTON COLLIDERS

TOHRU TAKAHASHI
Graduate School of Advances Sciences of Matter,
Hiroshima University,
Higashi-Hiroshima, 739-8530, Japan
E-mail: tohrut@hiroshima-u.ac.jp

Photon colliders have been studied for years as an option of future linear colliders. The studies revealed that physics in the high energy photon-photon interaction is attractive and the facility has to be ready not too much later than the e^+e^-collider. In this talk, we report recent status of technical aspect of development of the photon collier as an option of the future linear collider.

1. Introduction

The idea of converting the electron beam to the photon beam to was first proposed in 1981[1]. Since then, the idea has been discussed by many authors. Particularly, in the last decade, the understanding of photon collider has been grown very much both in physics opportunities and technical feasibility. So that the photon collider option is included all of linear collider projects as an important option which has to be started not too much later than the e^+e^-options. Activities and status of the photon colliders were reported from all linear collider groups, i.e., Asia , North America and Europe[2,3,4,5]. In Fig. 1, the JLC accelerator complex is illustrated as an example of the linear collider with the second interaction point. Thanks to these effort, general understanding for the photon collider is clear in both physics and technical aspect. Thus the R&D for the photon collider is in the stage that how we can really construct photon collider facility in the linear collider project.

In this talk, we briefly review principle and future of the photon collider and issues issue to be solved, then, report status and future prospect of the R&D effort toward the realization of the photon collider.

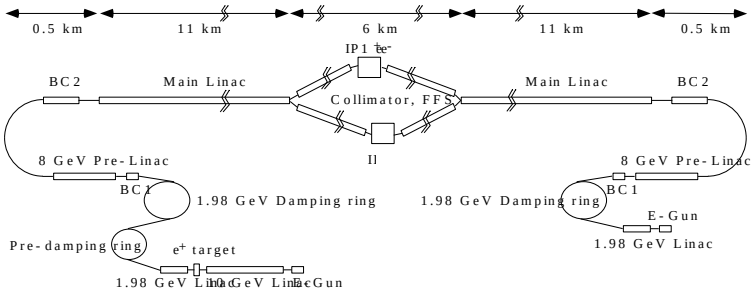

Figure 1. JLC schematic with the second interaction point.

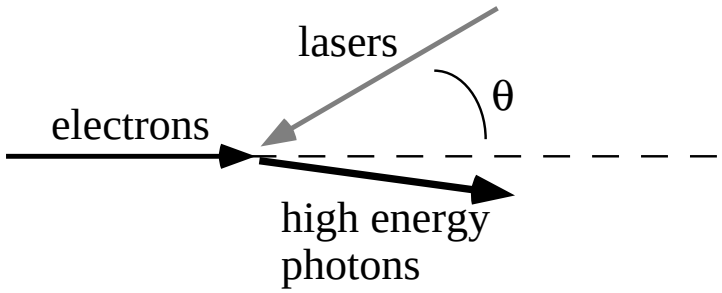

Figure 2. Kinematics of backward Compton scattering.

2. Principle of the Photon Collider

In the Photon collider, high energy photons are generated by the backward Compton scattering of the intense laser off the electron beam provided by the linear accelerator. The scheme of the backward Compton scattering is illustrated in Fig. 2. The maximum energy of the generated photon is expressed as;

$$E_\gamma\Big|^{max} = \frac{x}{x+1}E_e. \tag{1}$$

Here, x is a kinematics parameter of the Compton scattering, defined as

$$x = \frac{4E_e\omega_L}{m_e^2}\cos^2(\theta/2), \tag{2}$$

where E_e, ω_L and θ are the electron energy, laser photon energy and angle between the electron beam and the laser beam as shown in Fig. 2.

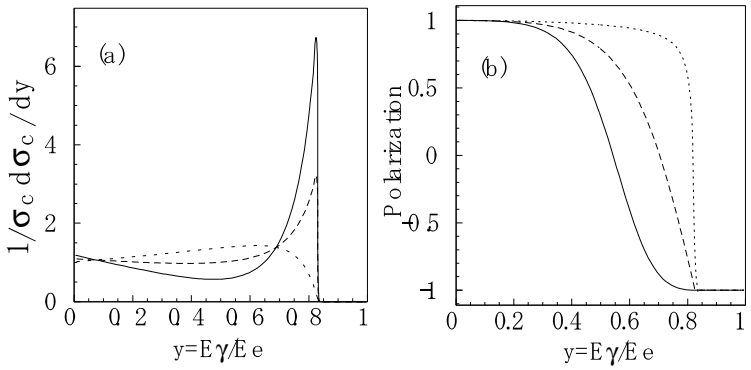

Figure 3. Calculated energy(a) and polarization(b) of back-scattered photons by laser-Compton scattering. Three lines are for different combination of the election and the laser polarization, i.e., $P_eP_L = -1$(solid), $P_eP_L = 0$(dash) and $P_eP_L = +1$(dots), respectively.

A calculated photon energy spectra and polarization generated by the backward Compton scattering is shown in Fig. 3. The energy distribution of the photons depends on the polarization of the electrons(P_e) and the laser(P_L)beam, i.e., one can obtain a broad ($P_eP_L = +1$) or peaked energy distribution($P_eP_L = -1$) by controlling the polarization. It is also found that the generated photon beam is highly polarized and is 100% polarized at the highest energy edge.

According to equation (1), the maximum photon energy increases as x becomes higher. However, when x exceeds $2(1+\sqrt{2}) \approx 4.83$, the energy of a Compton-scattered photon and a laser photon system exceeds the threshold of e^+e^- pair creation. This pair-creation process could waste generated high-energy photons and could be an additional source of detector background so that, at least as the first assumption, x parameter is restricted to be smaller than 4.83, corresponding to the maximum photon energy of about 80% of the electron energy. In the case that the electron beam energy of 250 GeV, laser wave length of 1μm, which matches wave length of typical solid state lasers, makes $x \approx 4.7$.

Ideally, we want to convert all electrons in an electron beam to photons, however, it requires infinite energy for the laser pulse. Therefore, in a typical parameters of the photon collider, the Compton-conversion probability for an electron, i.e., mean number of Compton interactions of an electron in a laser pulse, is assumed to be 1. Even for this assumption, the required energy for the laser system exceeds 1J/pulse and is still a key issue for the

Table 1. Proposed electron beam parameters of the $\gamma\gamma$ collider options for the JLC, NLC and TESLA

Parameter set			JLC	NLC	TESLA
e^-					
Beam energy	E_e	GeV	250	267.5	250
Particles/bunch	N		0.95@10	1.5@10	2.0@10
Repetition rate	f_{rep}	Hz	150	120	5
bunches/pulse	n_b		95	95	2.5k
bunch spacing	t	ns	2.8	2.8	≈ 300
Bunch length	σ_z	μm	120	156	300
Bunch sizes at IP	σ_x^*/σ_y^*	nm	67.8/12.8	166/3.0	88/4.3
Beta func. at IP	β_x^*/β_y^*	mm	0.5/0.8	4.0/0.065	1.5/0.3
Norm. emittance	$\varepsilon_{xn}/\varepsilon_{yn}$	nm·r	4500/100	3600/71	2500/30
CP-IP distance	d	mm	7.0	1.0	2.1
Geom. luminosity	L_{ee}	$cm^{-2}s^{-1}$	11.8@33	41.0@33	118@33

photon collider project. By this assumption, the conversion efficiency k, is calculated as;

$$k = \sum_{n=1}^{\infty} P_n^1 = 1 - e^{-1} \approx 0.63 \tag{3}$$

where P_n^1 is a probability that an electron encounters n laser photons when its average is one. Thus the number of scattered photons (N_γ) is $0.63N$, where N is the number of electrons in a bunch. As we are usually interested in the high energy part of the spectrum, we define effective conversion efficiency $k' \approx 0.3$ for the photons of its energy $E_\gamma > 0.65E_e$. Therefore, the luminosity of the $\gamma\gamma$ collider is expressed approximately as;

$$L_{\gamma\gamma} = k'^2 L_{ee} \approx 0.3^2 L_{ee} \approx 0.1 L_{ee}, \tag{4}$$

where L_{ee} is the geometric luminosity of e^-e^- collisions defined as;

$$L_{ee} = \frac{N^2 f}{4\pi\sigma_x^e\sigma_y^e} \tag{5}$$

with N, f, σ_x^e and σ_y^e being number of electrons in a bunch, its repetition rate, horizontal and vertical bunch size at the interaction point, respectively.

More precise estimation for the spectrum of the high energy photon and for luminosity spectrum can be performed using numerical simulation with specific parameters of the electron and the laser beam. Parameters of proposed photon colliders are summarized in table 1.

The energy spectrum for generated photon is shown in Fig.4. To simulate the distribution, CAIN, a program for the numerical simulation of the Compton scattering and the beam-beam simulation, is used[7].

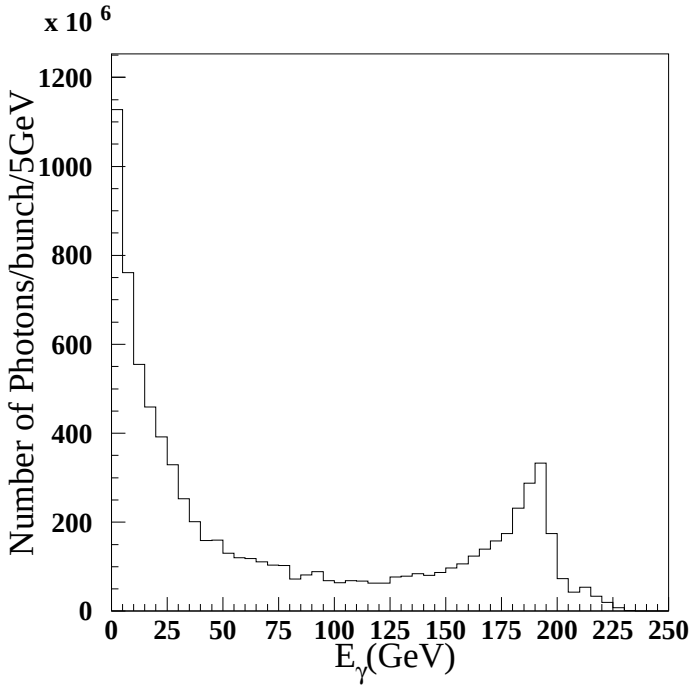

Figure 4. Simulated photon energy spectrum.

The simulated luminosity distributions simulated using CAIN is shown in Fig. 5. Since we are not going to sweep out used electrons from the interaction point, we have $\gamma\gamma$, $e\gamma$ and e^-e^- interaction simultaneously as well as low energy interaction caused by beamstrahlung photons.

3. Technical Issues

3.1. *Lasers*

To convert the electron beam to the photon beam effectively, the laser photon density n_{laser} has to satisfy

$$\sigma_{Compton} n_{laser} \approx 1.$$

It could be achieved using ultra-short pulse laser with relatively small flush energy. However, if the photon density of the laser, i.e., field strength of the laser pulse is too high, the non-linear effect in Compton scattering is

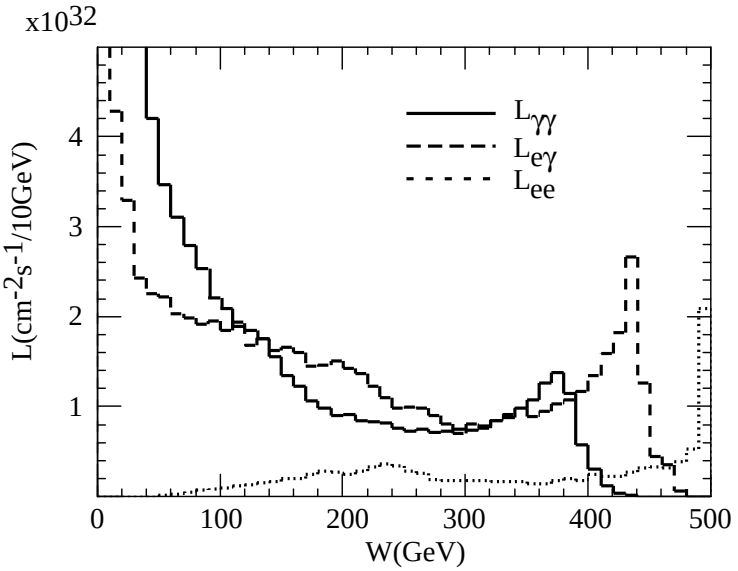

Figure 5. Luminosity distributions simulated by CAIN[7] for collisions, the solid, dashed and dotted lines are luminosities of $\gamma\gamma$, $e\gamma$ and e^-e^- collisions, respectively, and $\sqrt{s}$ is their center-of-mass energies.

not negligible. To suppress non-linear effect with in tolerable level, the laser field strength parameter ξ^2 has to be less than ≈ 0.3 which eventually results in longer O(ps) laser pulse with the energy of O(J/pulse) . Since the laser pulse must be synchronized with the electron bunch structure, the repetition of the laser pulse will be $\approx$ 15kHz and therefore the average laser power will be $\approx$ 15kW.

Although, number of pulse per second is more or less same for JLC/NLC and TESLA design, the difference in the bunch structure reflects design of the laser system. The bunch spacing of JLC/NLC design is 2.8 ns and the number of bunches in a bunch train is about 100 makes a bunch train of about 300ns. An important fact from this number is that 300ns is shorter than the life time of upper level state of lasing material of solid state laser. Therefore the laser system can be an extension of current LD pumped solid state laser technology.

A possible design of the laser system based on Mercury laser is discussed in [9]. The Mercury laser is 100J/pulse, 10Hz with 2-10ns pulse length which is now under development at Lawrence Livermore National Laboratory. In their scheme, a pulse train consists of 95 pulses with 2.8

ns spacing is formed before the amplification. Each pulse is chirped and overlapped temporarily so that the envelop is a $\approx$ 300ns pulse. However each pulse can still be identified because they are not overlapped in frequency. This pulse are put into the main amplifier and then high power laser pluses are compressed to 95 of 1ps pulses. Since the Mercury laser is design to operate 10Hz, it only needs 12 systems to provide the laser pulses to 95×120Hz electron bunches.

The other alternative is to develop the laser system which is capable to operate 150Hz with 1J/pulse energy[2]. Each laser is responsible for one of the bunch in a bunch train so that entire electron bunches can be covered if one can prepare the same number of laser system with the bunches in a train (200 in total for two beams). One of the issue to be solved for this scheme is a way to combine 100 laser pulses to a single pulse train of 2.8ns spacing. As each laser pulse is 1J/1ps, it requires high power/high speed Pockels Cells. Development of the Pockels Cells is still not trivial by current laser technology and more R&D is necessary for this point.

While the laser system for JLC/NLC scheme may be possible by extension of conventional laser technology, TESLA may need more sophisticated laser handing. The pulse structure of the TESLA system is 3000 bunch with 337ns spacing, resulting in length of a train of $\approx$ 1ms. The length of the pulse is longer than the life time of the upper level of the lasing material. Therefore, pumping power of the laser system will be too large to make 3000 of 1J pulse. To reduce pulse energy from the laser system, they designed a ring resonator at the interaction region of the detector[4]. The system aims to build up laser power of 100 in the resonator so that laser power can be reduced to 1/100 ($\approx$ 0.05J/pulse).

3.2. *Interaction Region*

The basic requirement for the interaction region is the same as those of e^+e^- collider, i.e.,

- Protect detectors from the beam-beam backgrounds.
- Extract spent electron beam.

However, for the photon collider, we have to satisfy these requirement with the optical system for the TW laser pulse. The beam related background is more or less similar to the e^+e^- collider except for the energy spectrum of the spent electron. Since the electron beam already interacted with the laser pulse at the conversion point, energy of the electron beam is widely

spread and hence its disruption angle is larger than the e^+e^-collider as shown in Fig. 6. Due to the large disruption angle, the beam crossing

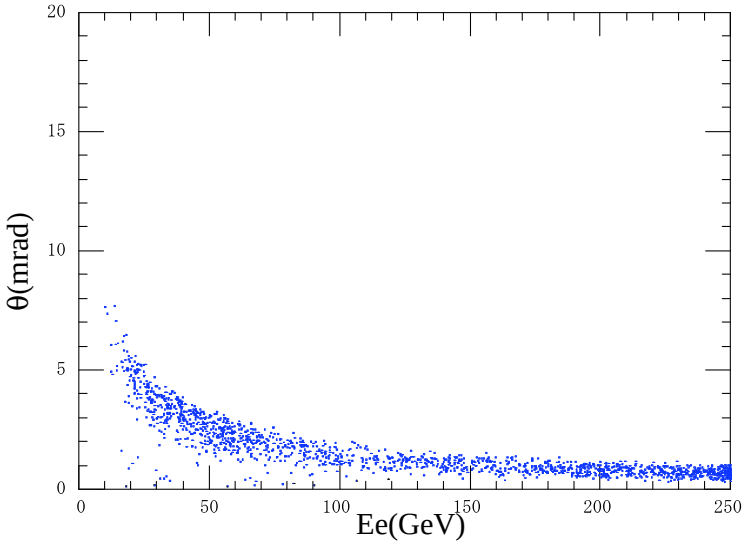

Figure 6. Disrupition angle of spent electrons.

angle have to be larger than the e^+e^-collider and the beam extraction line must have larger aperture to accommodate the spent electrons.

The engineering level design of the interaction region including the laser optics and masking system are still under consideration. A design close to the engineering level at this moment is shown in Fig. 7[10].

In this design, the aperture of the electron beam exaction line is about 10mr to accommodate the spent electrons and the beam crossing angle is enlarged to 30mr to avoid interference between the extraction line and the final focus magnet. The laser path is also shown in Fig. 7. The final focus mirror is mounted on the tungsten mask(M1) which is 3 m from the interaction point. The mirror is 38cm in diameter with a hole of 15 cm diameter for the electron lines. The detail description of this design is found in [10].

4. Prospect and Plan

According to the studies in the last decade, physics opportunities and technical feasibility of the $\gamma\gamma$ collider have been understood. Community

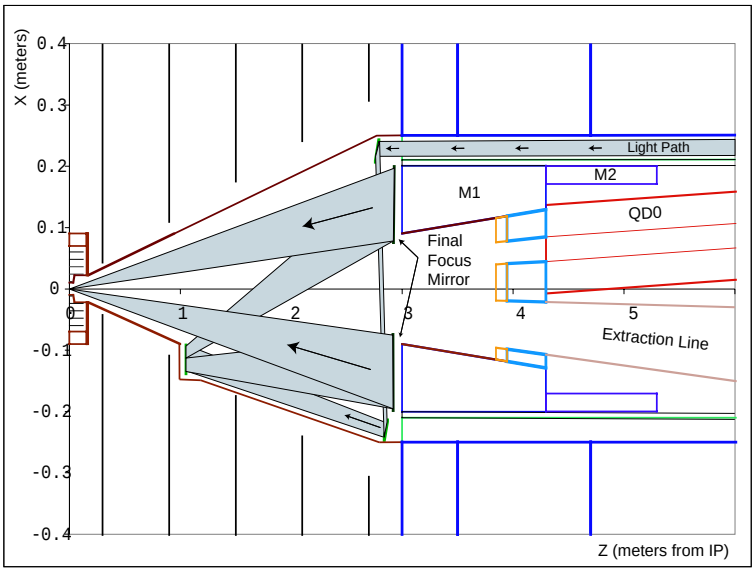

Figure 7. A schematic of the interaction region of the $\gamma\gamma$ collider.

reached consensus that this option has to be build. In technical aspect, we now have a realistic design of the laser system and the interaction region. The R&D effort is now in the phase to consider systematic and collaborative way to construct the photon collider in the e^+e^-collider project including possibility of a demonstration of photon-photon collision with a prototype.

Acknowledgements

The author would like to thank workshop organizer giving an opportunity to present this work. This work is based on the collaboration with members of photon collider group in Asia, North-America and European linear collider working groups.

References

1. I. Ginzburg, G. Kotokin, V. Serbo and V. Telnov, *ZhETF* **34**, 514 (1980), *JETP Lett.* **34**, 491 (1982).
2. I. Watanabe, S. Hiramatsu, K. Nakajima, T. Tauchi, K. Yokoya, I. Endo, K. Matsukado, T. Ohgaki, T. Takahashi, I. Ito, T. Kon, N. Matsuda and T. Takeshita, $\gamma\gamma$ *Collider as an Option of JLC*, *KEK Report 97-17* (1998), K. Abe et.al, *Particle Physics Experiment at JLC*, *KEK Report 2001-11* (2001)

3. *Zeroth Order Design Report for the Next Linear Collier SLAC-474* (1996); *Physics and Technology of the Next Linear Collider*, *SLAC Report 485* (1996).
4. TESLA Technical Design Report, Part 6, Chapter 1, hep-ex/0108012.
5. Proc. International Workshop on High-Energy Photon Colliders (GG 2000), Hamburg, Germany, 14-17 Jun 2000, Nucl.Instrum.Meth.A472:100-120,2001.
6. H. Müller and B. D. Serot, *Phys. Rev.* **C52**, 2072 (1995).
7. K. Yokoya, `http://www-acc-theory.kek.jp/members/cain/default.html`.
8. V. Baran, M. Colonna, M. Di Toro and A. B. Larionov,
9. J.Early, in *Proc. LCWS2000* ed. P. Para and H. E. Fisk, AIP conf. proc. 578, 713 (2000).
10. Linear Collider Physics, Resource Book for Snowmass 2001, SLAC-R-570.

BEAM-SIZE EFFECT IN BREMSSTRAHLUNG*

V. N. BAIER AND V. M.KATKOV
Budker Institute of Nuclear Physics,
Novosibirsk, 630090, Russia
E-mail: baier@inp.nsk.su; katkov@inp.nsk.su

The smallness of the transverse dimensions of the colliding beams leads to suppression of bremsstrahlung cross section. This beam-size effect was discovered and investigated at INP, Novosibirsk. Different mechanisms of radiation are discussed. Separation of coherent and incoherent radiation is analyzed in detail. For linear collider this suppression affets the whole spectrum. It is shown that objections to the subtraction procedure in [9] are groundless.

1. Introduction

The bremsstrahlung process at high-energy involves a very small momentum transfer. In the space-time picture this means that the process occurs over a rather large (macroscopic) distance. The corresponding longitudinal length (with respect to the direction of the initial momentum) is known as the *coherence* (formation) length l_f. For the emission of a photon with the energy ω the coherence length is $l_f(\omega) \sim \varepsilon(\varepsilon-\omega)/m^2\omega$, where ε and m is the energy and the mass of the emitting particle (here the system $\hbar = c = 1$ is used).

A different situation arises in the bremsstrahlung process at the electron-electron(positron) collision. For the recoil particle the effect turns out to be enhanced by the factor ε^2/m^2. This is due to the fact that the main contribution to the bremsstrahlung cross section gives the emission of virtual photon with a very low energy $q_0 \sim m^2\omega/(\varepsilon(\varepsilon-\omega))$ by the recoil particle, so that the formation length of virtual photon is $L_v(\omega) = l_f(q_0) = 4\varepsilon^3(\varepsilon-\omega)/m^4\omega$. This means that the effect for the recoil particles appears much earlier than for the radiating particles and can be important for contemporary colliding beam facilities at a GeV range [1].

*This work is partially supported by grant 03-02-16154 of the Russian Fund of Fundamental Research.

The special experimental study of bremsstrahlung was performed at the electron-positron colliding beam facility VEPP-4 of Institute of Nuclear Physics, Novosibirsk [2]. The deviation of the bremsstrahlung spectrum from the standard QED spectrum was observed at the electron energy $\varepsilon = 1.84$ GeV. The effect was attributed to the smallness of the transverse size of the colliding beams. In theory the problem was investigated in [3], where the bremsstrahlung spectrum at the collision of electron-electron(positron) beams with the small transverse size was calculated to within the power accuracy (the neglected terms are of the order $1/\gamma = m/\varepsilon$). After the problem was analyzed in [4], and later on in [5] where some of results for the bremsstrahlung found in [3] were reproduced.

It should be noted that in [3] (as well as in all other papers mentioned above) an incomplete expression for the bremsstrahlung spectrum was calculated. One has to perform the subtraction associated with the extraction of pure fluctuation process. This item will be discussed in Sec.2. In Sec.3 an analysis is given of incoherent radiation in electron-positron linear collider.

2. Mechanisms of Radiation

2.1. *Dispersion of momentum transfer*

We consider the radiation at head-on collision of high energy electron and positron beams. The properties of photon emission process from a particle are immediately connected with details of its motion. It is convenient to consider the motion and radiation from particles of one beam in the rest frame of other beam (the target beam). In this case the target beam is an ensemble of the Coulomb centers. The radiation takes place at scattering of a particle from these centers. If the target consists of neutral particles forming an amorphous medium, a velocity of particle changes (in a random way) only at small impact distances because of screening. In the radiation theory just the random collisions are the mechanism which leads to the incoherent radiation. For colliding beams significant contributions into radiation give the large impact parameters (very small momentum transfers) due to the long-range character of the Coulomb forces. As a result, in the interaction volume, which is determined also by the radiation formation length (in the longitudinal direction), it may be large number of target particles. Let us note that in the case when the contribution into the radiation give impact parameters comparable with the transverse size of target, the number of particles in the interaction volume is determined by the ratio of the radiation formation length to the mean longitudinal distance between

particles.

However, not all cases of momentum transfer should be interpreted as a result of random collisions. One have to exclude the collisions, which are macroscopic certain events. For elaboration of such exclusion we present the exact microscopic momentum transfer to the target particle in the form: $\mathbf{q} =< \mathbf{q} > +\mathbf{q}_s$. Here $< \mathbf{q} >$ is the mean value of momentum transfer calculated according to standard macroscopic electrodynamics rules with averaging over domains containing many particles. The longitudinal size of these domains should be large with respect to longitudinal distances between target particles and simultaneously small with respect to the radiation formation length. The motion of particle in the averaged potential of target beam, which corresponds to the momentum transfer $< \mathbf{q} >$, determines the coherent radiation. While the term $\mathbf{q}_s$ describes the random collisions which define the process of incoherent radiation (bremsstrahlung). Such random collisions we will call "scattering" since $< \mathbf{q}_s >= 0$.

We consider for simplicity the case when the target beam is narrow, i.e.when the parameter $1/q_{min}$ characterizing the screening of Coulomb potential in bremsstrahlung is much larger than the transverse dimensions determining the geometry of problem. When a particle crosses the mentioned domain the transverse momentum transfer to particle is

$$\mathbf{q} = \sum_{a=1}^{N} \mathbf{q}_a, \quad \mathbf{q}_a = 2\alpha \frac{\boldsymbol{\varrho} - \boldsymbol{\varrho}_a}{(\boldsymbol{\varrho} - \boldsymbol{\varrho}_a)^2}, \tag{1}$$

where α=1/137, N is the number of particles in the domain under consideration of the counter-beam, $\boldsymbol{\varrho}$ is the impact parameter of particle, $\boldsymbol{\varrho}_a$ is the transverse coordinate of Coulomb center. The mean value of momentum transfer is

$$\langle \mathbf{q} \rangle = N \langle a|\mathbf{q}_a|a\rangle , \quad \langle a|\mathbf{q}_a|a\rangle = \int \mathbf{q}_a w_c(\boldsymbol{\varrho}_a) d^2\varrho_a, \tag{2}$$

here $w_c(\boldsymbol{\varrho}_a)$ is the probability density of target particle distribution over the transverse coordinates normalized to unity. Then

$$\left\langle \mathbf{q}_s^2 \right\rangle = N \left\langle a|\mathbf{q}_a^2|a\right\rangle + N(N-1) \langle a|\mathbf{q}_a|a\rangle^2 - \langle \mathbf{q} \rangle^2 = N(\left\langle a|\mathbf{q}_a^2|a\right\rangle - \langle a|\mathbf{q}_a|a\rangle^2). \tag{3}$$

The same expression for the dispersion of transverse momentum gives the quantum analysis of *inelastic* scattering of emitting particle on *a sepa-*

rate particle of target beam in the domain under consideration

$$\overline{\mathbf{q}_{in}^2} = \sum_{n\neq a} |\left\langle n|\mathbf{q}_a|a\right\rangle|^2 = \sum_n \left\langle a|\mathbf{q}_a|n\right\rangle \left\langle n|\mathbf{q}_a|a\right\rangle - \left\langle a|\mathbf{q}_a|a\right\rangle^2$$
$$= \left\langle a|\mathbf{q}_a^2|a\right\rangle - \left\langle a|\mathbf{q}_a|a\right\rangle^2 . \quad (4)$$

Granting that $N = n_z \Delta z$ we find for the mean value of transverse electric field of target beam

$$\mathbf{E}_\perp(\boldsymbol{\varrho}, z) = 2en_z(z) \int \frac{\boldsymbol{\varrho} - \mathbf{x}}{(\boldsymbol{\varrho} - \mathbf{x})^2} w_c(\mathbf{x}) d^2x \quad (5)$$

For the rate of variation of function $\left\langle \mathbf{q}_s^2 \right\rangle$ we get

$$\frac{d\left\langle \mathbf{q}_s^2 \right\rangle}{dz} = 4\alpha^2 n_z(z) \left[\int \frac{w_c(\mathbf{x}) d^2x}{(\boldsymbol{\varrho} - \mathbf{x})^2} - \left(\int \frac{\boldsymbol{\varrho} - \mathbf{x}}{(\boldsymbol{\varrho} - \mathbf{x})^2} w_c(\mathbf{x}) d^2x \right)^2 \right]. \quad (6)$$

We don't discuss here applicability of Eq.(6) at $|\boldsymbol{\varrho} - \mathbf{x}| \leq \lambda_c$ (see e.g. Sec.III in [9])

It should be noted that in the kinetic equation which describes the motion of emitting particle

$$\frac{\partial f}{\partial t} + \mathbf{v}\frac{\partial f}{\partial \mathbf{r}} + \dot{\mathbf{p}}\frac{\partial f}{\partial \mathbf{p}} = \mathbf{St} f \quad (7)$$

the value of electric field $\mathbf{E}_\perp$ (5) determines the coefficient $\dot{\mathbf{p}}$ in l.h.s of equation (7) while r.h.s of equation arises due to random collisions and is determined by Eq.(6). The kinetic equation for description of radiation was first employed in [6] and later in [7] and [8]. We consider the case when the mean square angle of multiple scattering during the whole time of beams collision is smaller than the square of characteristic radiation angle. It appears, that this property is sufficient for applicability of perturbation theory to the calculation of the bremsstrahlung probability.

2.2. *Main characteristics of particle motion and radiation*

One of principal characteristics of particle motion defining the properties of coherent radiation (*the beamstrahlung*) is the ratio of variation of its transverse momentum to the mass during the whole time of passage across the opposite beam T

$$\frac{\Delta \mathbf{p}_\perp}{m} \sim \frac{eE_\perp \sigma_z}{m} \sim \frac{2\alpha N_c \lambda_c}{\sigma_x + \sigma_y} \equiv \delta, \quad (8)$$

where N_c is the number of particles in the opposite beam, σ_x and σ_y is its transverse dimensions ($\sigma_y \leq \sigma_x$), σ_z is the longitudinal size of opposite beam. The dispersion of particle momentum during time T is small comparing with m. It attains the maximum for the coaxial beams:

$$\frac{\left\langle \mathbf{q}_s^2 \right\rangle}{m^2} = \gamma^2 \left\langle \vartheta_s^2 \right\rangle \sim \frac{8\alpha^2 N_c \lambda_c^2}{\sigma_x \sigma_y} L \ll 1, \tag{9}$$

here ϑ_s^2 is the square of mean angle of multiple scattering, L is the characteristic logarithm of scattering problem ($L \sim 10$). This inequality permits one to use the perturbation theory for consideration of bremsstrahlung, and to analyze the beamstrahlung independently from the bremsstrahlung[a].

Another important characteristics of motion is the relative variation of particle impact parameter during time T

$$\frac{\Delta \varrho_i}{\varrho_i} \sim \frac{eE_\perp \sigma_z^2}{\varepsilon \sigma_i} \sim \frac{2\alpha N_c \lambda_c \sigma_z}{\gamma(\sigma_x + \sigma_y)\sigma_i} \equiv D_i, \tag{10}$$

here i is x or y. When the disruption parameter $D_i \ll 1$, the collision doesn't change the beam configuration and the particle crosses the opposite beam on the fixed impact parameter. If in addition the parameter $\delta \ll 1$ (this situation is realized in colliders with relatively low energies) then the beamstrahlung process can be calculated using the dipole approximation. The main contribution into the beamstrahlung give soft photons with an energy

$$\frac{\omega}{\varepsilon} \leq \frac{\gamma \lambda_c}{\sigma_z} \ll 1. \tag{11}$$

In the opposite case $\delta \gg 1$ the main part of beamstrahlung is formed when the angle of deflection of particle velocity is of the order of characteristic radiation angle $1/\gamma$ and the radiation formation length l_m is defined by

$$\frac{eE_\perp l_m}{m} \sim \frac{2\alpha N_c \lambda_c l_m}{(\sigma_x + \sigma_y)\sigma_z} = 1, \quad l_m = \frac{\sigma_z}{\delta}; \tag{12}$$

and the characteristic photon energy is

$$\omega \sim \omega_m = \frac{\gamma^2}{l_m} = \varepsilon \chi_m, \quad \chi_m \equiv 2\alpha N_c \gamma \frac{\lambda_c^2}{(\sigma_x + \sigma_y)\sigma_z} (\chi_m \ll 1). \tag{13}$$

[a]Actually more soft condition should be fulfilled:

$$\left\langle \mathbf{q}_s^2(l_f) \right\rangle / m^2 = \left\langle \mathbf{q}_s^2 \right\rangle / m^2 \; l_f/\sigma_z \ll 1$$

Here $\chi = |\boldsymbol{\chi}|$ is the invariant parameter

$$\boldsymbol{\chi} = \frac{\gamma}{E_0}\left[\mathbf{E}_\perp + \mathbf{v}\times\mathbf{H}\right], \quad \mathbf{E}_\perp = \mathbf{E} - \mathbf{v}(\mathbf{vE}), \tag{14}$$

where $E_0 = m^2/e = 1.32\cdot 10^{16}$V/cm, which defines properties of magnetic bremsstrahlung in the constant field approximation (CFA). For applicability of CFA it is necessary that relative variation of $\mathbf{E}_\perp$ in Eq.(5) was small on the radiation formation length l_m. As far l_m is shorter than σ_z in $\delta \gg 1$ times the characteristic parameter becomes

$$D_{mi} = D_i\frac{l_m}{\sigma_z} = \frac{D_i}{\delta} = \frac{\sigma_z}{\gamma\sigma_i},\ (i = x, y) \tag{15}$$

to that extent. The condition $D_{mi} \ll 1$ is fulfilled in all known cases. The mean number of photons emitted by a particle during the whole time of passage across the opposite beam T is $\langle N_\gamma\rangle \sim \alpha\delta$, it include the electromagnetic interaction constant. Using the estimate (13) we get an estimate of relative energy loss

$$\frac{\Delta\varepsilon}{\varepsilon} \sim \alpha\delta\chi_m\ (\chi_m \ll 1) \tag{16}$$

In the case $\chi_m \ll 1$ (this condition is satisfied in all existing facilities and proposed collider projects) the soft photons with energy $\omega \sim \omega_m = \varepsilon\chi_m \ll \varepsilon$ are mainly emitted. For $\omega \gg \omega_m$ the emission probability is exponentially suppressed. So, such photons are emitted in the bremsstrahlung process only. The boundary photon energy ω_b, starting from which the bremsstrahlung process dominates, depends on particular parameters of facility. If $\chi_m \sim 1/10$ the energy is $\omega_b \sim \varepsilon$. The formation length for $\omega \gg \omega_m$ is much shorter than l_m. On this length the particle deflection angle is small comparing with $1/\gamma$ and one can neglect the variation of transverse beam dimensions (see Eq.(15)). This means that all calculations of bremsstrahlung characteristics can be carried out in adiabatic approximation using local beam characteristics $\sigma_{x,y}(t), \mathbf{v}(t)$ etc, with subsequent averaging of radiation characteristics over time. Note that actually we performed a covariant analysis and the characteristic parameters are defined in a laboratory frame.

2.3. *Separation of coherent and incoherent radiation*

As an example we consider the situation when the configuration of beams doesn't change during the beam collision (the disruption parameter $D \ll 1$), and the total particle deflection angle during intersection of whole beam is

small comparing with the characteristic radiation angle $1/\gamma$ (the dipole case). The target beam in its rest frame is the ensemble of classical potentials centers with coordinates $\mathbf{r}_a$ $(\mathbf{x}_a,\ z_a)$ and the transverse coordinate of emitting particle is $\mathbf{r}_\perp$. In the perturbation theory the total matrix element of the radiation process can be written as

$$\mathbf{M}(\mathbf{r}_\perp) = \sum_{a=1}^{N_c} \mathbf{m}(\mathbf{r}_\perp - \mathbf{x}_a) \exp(iq_\parallel z_a) \tag{17}$$

We represent the combination $M_i M_j^*$ in the form

$$\begin{aligned} M_i M_j^* &= \sum_{a=b} m_i(\mathbf{r}_\perp - \mathbf{x}_a) m_j(\mathbf{r}_\perp - \mathbf{x}_b) \\ &+ \sum_{a\neq b} m_i(\mathbf{r}_\perp - \mathbf{x}_a) m_j(\mathbf{r}_\perp - \mathbf{x}_b) \exp(-iq_\parallel\,(z_a - z_b))\,. \end{aligned} \tag{18}$$

In the expression Eq.(18) we have to carry out averaging over position of scattering centers. We will proceed under assumption that there are many scattering centers within the radiation formation length $l_f = 1/q_\parallel$

$$N_f = n_z l_f \gg 1, \tag{19}$$

where for the Gaussian distribution

$$n_z = \frac{N_c}{\sqrt{2\pi}\sigma_z} \exp\left(-\frac{z^2}{2\sigma_z^2}\right), \tag{20}$$

here N_c and σ_z are introduced in Eq.(8). Note that in the situation under consideration $\varrho_{max} = |\mathbf{r}_\perp - \mathbf{x}_a|_{max} \geq \sigma_t$, where σ_t is the characteristic transverse size of target beam. Let us select terms with approximately fixed phase $q_\parallel(z_a - z_b) = \phi_{ab}$ in the sum with $a \neq b$ in Eq.(18). If the condition (19) is fulfilled, there are many terms for which the phase variation is small ($\Delta\phi_{ab} \ll 1$). For this reason one can average over the transverse coordinates $(\mathbf{x}_a, \mathbf{x}_b)$ of target particles in Eq.(18) without touching upon the longitudinal coordinates (z_a, z_b)

$$\begin{aligned} M_i M_j^* &= N_c \left\langle m_i m_j \right\rangle_\perp + \left\langle m_i \right\rangle_\perp \left\langle m_j \right\rangle_\perp \sum_{a\neq b} \exp(-iq_\parallel\,(z_a - z_b)) \\ &= N_c \Big(\left\langle m_i m_j \right\rangle_\perp - \left\langle m_i \right\rangle_\perp \left\langle m_j \right\rangle_\perp \Big) + \left\langle m_i \right\rangle_\perp \left\langle m_j \right\rangle_\perp \left| \sum_a \exp(iq_\parallel z_a) \right|^2, \end{aligned} \tag{21}$$

where

$$\langle m_i \rangle_\perp = \int m_i(\mathbf{r}_\perp - \mathbf{x}) w_c(\mathbf{x}) d^2x,$$
$$\langle m_i m_j \rangle_\perp = \int m_i(\mathbf{r}_\perp - \mathbf{x}) m_j(\mathbf{r}_\perp - \mathbf{x}) w_c(\mathbf{x}) d^2x, \tag{22}$$

here $w_c(\mathbf{x})$ is the probability density of target particle distribution over the transverse coordinates normalized to unity. In Eq.(21) in the sum with $a \neq b$ we add and subtract the terms with $a = b$. The first term (proportional to N_c) on the right-hand side of Eq.(21) is the incoherent contribution to radiation (*the bremsstrahlung*). The second term gives the coherent part of radiation. For Gaussian distribution Eq.(20) performing averaging over the longitudinal coordinate z_a one has

$$\left| \sum_a \exp(iq_\parallel z_a) \right|^2 \to \left| \int_{-\infty}^{\infty} n_z \exp(iq_\parallel z) dz \right|^2 = N_c^2 \exp(-q_\parallel^2 \sigma_z^2). \tag{23}$$

3. Incoherent Radiation

The correction to photon emission probability due to the small transverse dimensions of colliding beam for unpolarized electrons and photon was calculated in [9] basing on subtraction procedure as in Eq.(21). It is obtained after integration over the azimuthal angle of the emitted photon

$$dw_1 = \frac{\alpha^3}{\pi m^2} \frac{\varepsilon'}{\varepsilon} \frac{d\omega}{\omega} U(\zeta) F(\omega, \zeta) d\zeta, \quad \zeta = 1 + \gamma^2 \vartheta^2, \tag{24}$$

where ϑ is the photon emission angle, $\varepsilon' = \varepsilon - \omega$,

$$U(\zeta) = v - \frac{4(\zeta - 1)}{\zeta^2}, \; v = \frac{\varepsilon}{\varepsilon'} + \frac{\varepsilon'}{\varepsilon}, \quad F(\omega, \zeta) = F^{(1)}(\omega, \zeta) - F^{(2)}(\omega, \zeta),$$
$$F^{(1)}(\omega, \zeta) = \frac{\eta^2}{\zeta^2} \int \left[K_0(\eta\varrho) K_2(\eta\varrho) - K_1^2(\eta\varrho) \right] \varrho \frac{d\Phi(\boldsymbol{\varrho})}{d\varrho} d^2\varrho$$
$$F^{(2)}(\omega, \zeta) = \frac{2\eta^2}{\zeta^2} \int \left(\int K_1(\eta\varrho) \frac{\boldsymbol{\varrho}}{\varrho} w_c(\mathbf{x} - \boldsymbol{\varrho}) d^2\varrho \right)^2 w_r(\mathbf{x}) d^2x, \tag{25}$$

here

$$\eta = q_{min}\zeta, \; q_{min} = m^3\omega / 4\varepsilon^2\varepsilon', \; \Phi(\boldsymbol{\varrho}) = \int w_r(\mathbf{x} + \boldsymbol{\varrho}) w_c(\mathbf{x}) d^2x, \tag{26}$$

where $w_c(\mathbf{x})$ is defined in (22), $w_r(\mathbf{x})$ is the same but for the radiating beam, value q_{min} is defined in c.m.frame of colliding particles. The term $F^{(2)}(\omega, \zeta)$ is the subtraction term. The total probability is $dw_\gamma = dw_0 + dw_1$, where

dw_0 is standard QED probability. The analysis in [9] was based on Eqs.(24)-(25).

We considered in [9] the actual case of the Gaussian beams. The Fourier transform was used

$$w(\mathbf{x}) = \frac{1}{(2\pi)^2}\int d^2q \exp(-i\mathbf{qx})w(\mathbf{q});$$

$$w_r(\mathbf{q}) = \exp\left[-\frac{1}{2}(q_x^2\Delta_x^2 + q_y^2\Delta_y^2)\right],\ w_c(\mathbf{q}) = \exp\left[-\frac{1}{2}(q_x^2\sigma_x^2 + q_y^2\sigma_y^2)\right], \quad (27)$$

where as above the index r relates to the radiating beam and the index c relates to the target beam, Δ_y and Δ_x (σ_y and σ_x) are the vertical and horizontal transverse dimensions of radiating (target) beam. Substituting (27) into Eq.(26) we find

$$\Phi(\boldsymbol{\varrho}) = \frac{\Sigma_x\Sigma_y}{\pi}\exp[-\varrho_x^2\Sigma_x^2 - \varrho_y^2\Sigma_y^2];\ \Sigma_x^2 = \frac{1}{2(\sigma_x^2+\Delta_x^2)},\ \Sigma_y^2 = \frac{1}{2(\sigma_y^2+\Delta_y^2)}. \quad (28)$$

Using the relation $d\sigma_1 = \Phi^{-1}(0)dw_1$ the following expression for the correction to spectrum was found in [9] starting from (24)

$$d\sigma_1^{(1)} = \frac{2\alpha^3}{m^2}\frac{\varepsilon'}{\varepsilon}\frac{d\omega}{\omega}f^{(1)}(\omega),\ f(s) = \frac{\sqrt{\pi}}{2s}(v-8s^2)\mathrm{erfc}(s) + 4e^{-s^2} + 2\mathrm{Ei}(-s^2),$$

$$f^{(1)}(\omega) = -\frac{1}{\pi\Sigma_x\Sigma_y}\int_0^{2\pi}\frac{d\varphi}{\Sigma_x^{-2}\cos^2\varphi + \Sigma_y^{-2}\sin^2\varphi}\int_0^{\infty}F_2(z)f(s)sds, \quad (29)$$

$$z^2 = \frac{s^2q_{min}^{-2}}{\Sigma_x^{-2}\cos^2\varphi + \Sigma_y^{-2}\sin^2\varphi},\ F_2(x) = \frac{2x^2+1}{x\sqrt{1+x^2}}\ln(x+\sqrt{1+x^2}) - 1,$$

where $\mathrm{Ei}(x)$ is the exponential integral function and $\mathrm{erfc}(x)$ is the error function. This formula is quite convenient for the numerical calculations.

The subtraction term ($F^{(2)}(\omega,\zeta)$ in (25)) gives for coaxial beams

$$d\sigma_1^{(2)} = -\frac{2\alpha^3}{m^2}\frac{\varepsilon'}{\varepsilon}\frac{d\omega}{\omega}J^{(2)}(\omega), \quad (30)$$

where

$$J^{(2)}(\omega) = \frac{\sqrt{ab}}{\Sigma_x\Sigma_y}\int_0^{\infty}ds_1\int_0^{\infty}ds_2 g\left(\frac{q_{min}\sqrt{s}}{2}\right)G(s_1,s_2),$$

$$G(s_1,s_2) = \frac{1}{2}\left(\frac{a_1a_2b_1b_2}{AB}\right)^{1/2}\left[\frac{a_1a_2}{A} + \frac{b_1b_2}{B}\right] \quad (31)$$

Here the function $g(q)$ is:

$$g(q) = \left(v-\frac{2}{3}\right)e^{-q^2} - 2q^2\left[\frac{\sqrt{\pi}}{2q}\left(v-\frac{8}{3}q^2\right)\mathrm{erfc}(q) + \frac{4}{3}e^{-q^2} + \mathrm{Ei}(-q^2)\right]. \quad (32)$$

In (31) we introduced the following notations

$$a = \frac{1}{2\Delta_x^2}, \quad b = \frac{1}{2\Delta_y^2}, \quad a_{1,2} = \frac{1}{s_{1,2} + 2\sigma_x^2}, \quad b_{1,2} = \frac{1}{s_{1,2} + 2\sigma_y^2},$$
$$A = a_1 + a_2 + a, \quad B = b_1 + b_2 + b, \quad s = s_1 + s_2. \tag{33}$$

In the case of narrow beams one has $q_{min}/(\Sigma_x + \Sigma_y) \ll 1$. In this case of coaxial beams $d\sigma_\gamma = d\sigma_0 + d\sigma_1$ is

$$d\sigma_\gamma = \frac{2\alpha^3}{m^2}\frac{\varepsilon'}{\varepsilon}\frac{d\omega}{\omega}\left\{\left(v - \frac{2}{3}\right)\left[2\ln\frac{m}{\Sigma_x + \Sigma_y} + C + 2 - J_-\right] + \frac{2}{9}\right\}, \tag{34}$$

where

$$J_- = \frac{\sqrt{ab}}{\Sigma_x \Sigma_y}\int_0^\infty ds_1 \int_0^\infty ds_2 G(s_1, s_2) \tag{35}$$

The dimensions of beams in the experiment [2] were $\sigma_y = \Delta_y = 24\ \mu m, \sigma_x = \Delta_x = 450\ \mu m$, so this is the case of flat beams. The estimate for this case gives $J_- \simeq (4/3\sqrt{3})\pi\sigma_y/\sigma_x \ll 1$. This term is much smaller than other terms in (34). This means that for this case the correction to the spectrum calculated in [3] is very small. The parameters of beam in the experiment [11] were (in our notation): $\sigma_y = \Delta_y = (50 \div 58)\mu m$, $\sigma_x = \Delta_x = (250 \div 290)\mu m$. Since the ratio of the vertical and the horizontal dimensions is not very small, the contribution of subtraction term (Eq.(30)) is essential (more than 10%). For details of comparison of experimental data [2], [11] with theory see [9], where we discussed also possible use of beam-size effect for linear collider tuning. It should be noted that for linear collider the condition of strong beam-size effect $\sigma_y q_{min} \ll 1$ ($\sigma_y \ll \sigma_x$) is fulfilled for the whole spectrum. This can be seen in Fig.1, where the lower curve is calculated using Eq.(29) and the subtraction term is very small since $\sigma_y/\sigma_x < 0.01$. As far as the narrow beams are considered in Fig.1, the lower curve is consistent also with Eq.(34). This curve depends on the energy and the transverse sizes of beams. It will be instructive to remind that the analysis in [9] (see Eq.(2.8)) and here is valid if $\chi_m/u \ll 1$ (see Eq.(13), $u = \omega/\varepsilon'$). The parameter χ_m depends also on number of particles N_c and the longitudinal beam size. So, for low N_c Fig.1 is valid for any x, but for TESLA project (χ_m=0.13) it holds in hard part of spectrum only. In fact, the probability of incoherent radiation becomes larger than the probability of coherent radiation only at $x > 0.7$ where the lower curve in Fig.1 is certainly applicable.

Beam-size effect was considered using different approaches which are more or less equivalent formulations of QED perturbation theory where the

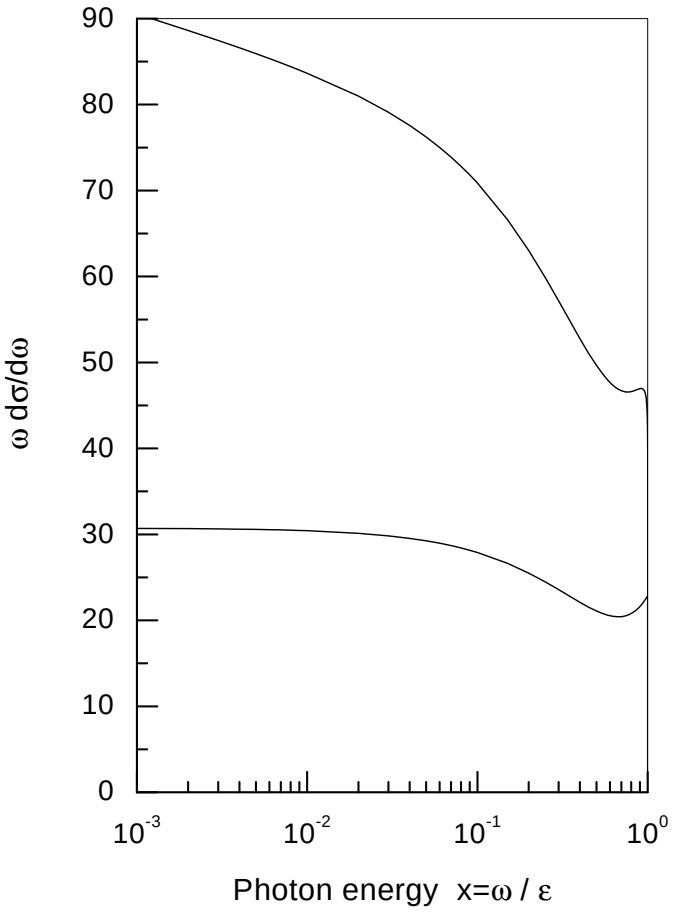

Figure 1. The bremsstrahlung intensity spectrum $\omega d\sigma/d\omega$ in units $2\alpha r_0^2$ versus the photon energy in units of initial electron energy ($x = \omega/\varepsilon$) for linear collider with beam energy $\varepsilon = 250$ GeV. The upper curve is the standard QED spectrum. The curve below is calculated with the beam-size effect taken into account for $\sigma_x = 553nm, \sigma_y = 5nm$.

incident particles consists of wave packets. In [3] the universal method was used which permits to obtain any QED cross section within the relativistic

accuracy (up to terms $\sim 1/\gamma$). A "general scheme" in [5] doesn't fall out the scope of [3] and particular derivation follows method used in [4]. As it was shown above, the subtraction procedure is necessary to extract pure fluctuation process, this was done in [9].

Recently in [10] this subtraction procedure was questioned. An objection is based on correlator Eq.(28) in [10]. If one takes integrals over $\mathbf{r}$ and $\mathbf{r}'$ from both sides of this correlator, one obtains using Eq.(21) in [10]:$N_p^2 = N_p(N_p + 1)$. It is evident that the last relation as well as correlator Eq.(28) in [10] are not adequate for the discussed problem since the subtraction term is of the same ($\propto N_p$)as the relation error. According to [10] (see text before Eq.(19)) the correlator Eq.(28) is obtained as result of "the averaging over fluctuation of particle in the field connected, for example, with the fluctuations of particle positions *for many collisions of bunches in a given experiment*" (our italics BK). This statement has no respect to the problem under consideration. As it is shown in Secs.2.1 and 2.3 the main aspect is *the presence of many scattering centers within the radiation formation length*. An analysis in Appendix A confirms this conclusion for radiation in crystals. The reference (Ref.21 in [10]) to the textbooks is senseless because different problems are discussed in these books.

The only correct remark in [10] is that in [9] there was no derivation of the starting formulas. This derivation is given here above. In Sec.2.1 a generic picture of particle motion in the field of counter-beam (in its rest frame) is given. A smooth variation of transverse momentum in an averaged field of counter-beam is considered. It determines the coherent radiation (the beamstrahlung). Along with smooth variation there are the fluctuations of particle velocity due to multiple scattering on the formation length. Just these fluctuations ensure the incoherent radiation (the bremsstrahlung). The mean square of transverse momentum dispersion at multiple scattering on the formation length (see Eqs.(3), (4), (6)) determines the bremsstrahlung probability. The mentioned equations contain both the singular and the subtraction terms accordingly to [9]. In Sec.2.3 we separated the coherent and incoherent parts of radiation explicitly just under the same conditions as in [10]. The result (Eq.(21)) agrees with Eq.(3.6) in [9] which is input formula for analysis in [9].

Appendix A. Radiation in crystals

Separation of coherent and incoherent radiation in oriented single crystals was considered using different approaches in [12],[13] and in [14], [15]. We give here

a sketch of the analysis in one-chain approximation neglecting correlations due to collision of projectile with different chains. In this case

$$\left\langle \sum_{a\neq b} m_i(\mathbf{r}_\perp - \mathbf{x}_a) m_j(\mathbf{r}_\perp - \mathbf{x}_b) e^{-iq_\parallel (z_a - z_b)} \right\rangle$$
$$= \langle m_i \rangle_\perp \langle m_j \rangle_\perp e^{-q_\parallel^2 u^2} \sum_{a\neq b} e^{-iq_\parallel \left(z_a^{(0)} - z_b^{(0)} \right)}, \tag{A.1}$$

where u is the amplitude of the thermal vibrations, in averaging over the thermal vibrations we used the distribution

$$w(z_a) = \frac{1}{\sqrt{2\pi}u} \exp\left(-\frac{(z_a - z_a^{(0)})^2}{2u^2} \right). \tag{A.2}$$

The sum in the r.h.s. of (A.1) one can present as

$$\sum_{a\neq b} \exp(-iq_\parallel \left(z_a^{(0)} - z_b^{(0)} \right)) = -N_c + \left| \sum_a \exp(iq_\parallel z_a^{(0)}) \right|^2, \tag{A.3}$$

where

$$\sum_a \exp(iq_\parallel z_a^{(0)}) = \sum_{n=-\infty}^{\infty} \exp(inq_\parallel d) = 2\pi \sum_{k=-\infty}^{\infty} \delta(q_\parallel d - 2\pi k),$$
$$\left| \sum_a \exp(iq_\parallel z_a^{(0)}) \right|^2 = \frac{N_c}{d} 2\pi \sum_{k=-\infty}^{\infty} \delta(q_\parallel - 2\pi \frac{k}{d}), \tag{A.4}$$

where d is the distance between atoms forming the chain. Substituting Eqs.(A.1)-(A.4) in Eq.(18) we get

$$\left\langle M_i M_j^* \right\rangle = N_c \left(\langle m_i m_j \rangle_\perp - \exp(-q_\parallel^2 u^2) \langle m_i \rangle_\perp \langle m_j \rangle_\perp \right)$$
$$+ N_c \frac{2\pi}{d} \exp(-q_\parallel^2 u^2) \langle m_i \rangle_\perp \langle m_j \rangle_\perp \sum_{k=-\infty}^{\infty} \delta(q_\parallel - 2\pi \frac{k}{d}). \tag{A.5}$$

This expression agrees with Eq.(11) in [12]. The incoherent term in Eq.(A.5) ($\propto N_c$) coincide with the incoherent term in Eq.(23) if $q_\parallel u \ll 1$. This is true if the condition Eq.(19) ($l_f/d \gg 1$) is satisfied.

References

1. V.N.Baier and V.M.Katkov, *Sov.Phys.Doklady*, **17**, 1068 (1973).
2. A.E.Blinov, A.E.Bondar, Yu.I.Eidelman et al., *Preprint INP 82-15, Novosibirsk 1982; Phys.Lett.* **B113**, 423 (1982).

3. V.N.Baier, V.M.Katkov, V.M.Strakhovenko, *Preprint INP 81-59, Novosibirsk 1981; Sov.J.Nucl.Phys*, **36**, 95 (1982).
4. A.I.Burov and Ya.S.Derbenev, *Preprint INP 82-07, Novosibirsk 1982*.
5. G.L.Kotkin, S.I.Polityko, and V.G.Serbo, *Yad.Fiz.*, **42** 692, 925 (1985). G.L.Kotkin et al., *Z.Phys.*, **C39**, 61 (1988).
6. A.B.Migdal, *Phys. Rev.*, **103**, 1811 (1956).
7. V.N.Baier, V.M.Katkov, V.M.Strakhovenko, *Sov.Phys.JETP*, **67**, 70 (1988).
8. V.N.Baier and V.M.Katkov, *Phys. Rev.* **D57**, 3146 (1998).
9. V.N.Baier and V.M.Katkov, *Phys. Rev.* **D66**, 053009 (2002).
10. G.L.Kotkin, and V.G.Serbo, hep-ph/0212102, 2002.
11. K.Piotrzkowski, *Z.Phys.* **C67** 577 (1995).
12. Bazylev V.A, Golovoznin V.V., and Demura A.V. *Zhurn.Teor.i Eksp. Fiziki*, **92**, 1921 (1987).
13. Bazylev V.A, and Zhevago N.K.,*Radiation from Fast Particles in Solids and External Fields* "'Nauka', Moscow, 1987, (in Russian).
14. V.N.Baier, V.M.Katkov, V.M.Strakhovenko, *phys.stat.sol.(b)* **149**, 403 (1988).
15. V.N.Baier, V.M.Katkov, V.M.Strakhovenko, *Electromagnetic Processes at High Energies in Oriented Single Crystals*, World Scientific Publishing Co, Singapore, 1998.

CRITICAL ISSUES FOR VACUUM LASER ACCELERATION*

E. R. COLBY

Stanford Linear Accelerator Center
2575 Sand Hill Road MS 07
Menlo Park, CA 94025 USA
E-mail: ecolby@slac.stanford.edu

Recent technological progress in lasers has renewed interest in applying high power lasers to accelerate charged particles. Outstanding gains in efficiency and power, and the first demonstration of optical phase-locking have moved the laser closer to competitive standing with microwave vacuum tubes as power sources for accelerators. We explore some of the questions that will determine the suitability of both low-field ($a_o \ll 1$) and high-field ($a_o > 1$) acceleration methods, and identify some of the challenges ahead. Possible applications include a laser-driven linear collider and novel, compact particle and radiation sources, each with its own performance requirements.

1. Introduction

The acceleration of charged particles by laser radiation has long been a dream for accelerator designers [1]. Achieving the correct conditions to permit efficient acceleration over long distances has been and remains the primary challenge in using lasers to accelerate particles. The extraordinary electric fields laser can produce make this a challenge worth pursuing.

Several applications drive the exploration of laser-driven particle acceleration. Future generations of linear colliders will be required to attain successively higher energies and higher luminosities and will place a premium on accelerating gradient, power efficiency, and the ability to preserve excellent emittances. Compact particle and radiation sources for university and industry generally operate at much lower energies and beam powers, but find a broad spectrum of applications with wide ranging requirements, hence laser accelerators built for this purpose will instead have low cost and versatility as key attributes.

A natural consequence of using optical wavelengths for acceleration is that conditions can be arranged such that the accelerated beams will be bunched at the optical wavelength. The resultant sub-femtosecond particle bunches will produce ultrafast radiation pulses that are tunable in energy, and sufficiently

* This work is supported by DOE contract DE-AC03-76SF00515 (SLAC).

short in duration to permit the study of attosecond phenomena, such as the rearrangement of atomic electron distributions that occurs as chemical bonds are formed.

2. Coupling Mechanisms

The primary challenge in using lasers for particle acceleration is in devising means to couple energy efficiently over macroscopic distances. Efficient use of laser power requires strong focusing of the laser, making diffraction effects important. Some means to guide the laser, either with a series of focusing optics, or with a continuous waveguide is therefore required.

. The available methods for coupling radiation to charged particles are quite different depending on the strength of radiation fields. The methods divide into two groups, "low-field", for which the normalized vector potential of the radiation $a_o=eE/2\omega mc\ll 1$ is sufficiently small that the oscillatory motion of electrons responding to the alternating optical fields remains subrelativistic, and "high-field", for which $a_o>1$ and electrons acquire relativistic velocities during each half cycle of the optical fields. At optical wavelengths $a_o\sim 1$ corresponds to very high laser intensities, $\sim 10^{18}$ W/cm^2 which, roughly speaking, is possible for lasers in the $\geq$30 TW class over an interaction distance of $z_R=\pi w_o^2/\lambda\sim 30$ μm.

Generally speaking, low-field accelerators must rely on material (metals, dielectrics, gases) placed within a few wavelengths of the particle beam to sufficiently diffract the optical waves to produce an axial electric field component that has a phase velocity somewhat below the speed of light [2]. The exception to this rule is the inverse free electron laser (IFEL), which achieves synchronous interaction by bending the particle trajectories in a periodic manner such that the transverse motion permits energy transfer directly from transversely polarized fields. As such, most low-field accelerators will be limited in gradient by the voltage breakdown characteristics of the materials used, which is unlikely to exceed the atomic binding fields, $\sim 10^{10}$ V/m. The interaction between fields and particles is exclusively linear in the field strength, and particles must remain in phase synchronism with the optical wave to receive continuous acceleration. Further, there is no requirement (except for the IFEL) that the particles deflect from straight-line trajectories to achieve coupling to the fields, so there is no high-energy limit to the maximum energy that can be attained.

Material damage is a key issue determining what accelerating gradients are possible. At present, energy fluences above ~2 J/cm^2 cause damage to surfaces made of fused silica [3,4], an excellent candidate material for its ease of handling

by lithography and resistance to radiation damage. Crystalline materials perform marginally better, potentially due to their improved strength and thermal conductivity. The damage threshold exhibits a $\tau_p^{1/2}$ dependence on pulse length above 10 picoseconds, but is insensitive to pulse length below about 1 psec, motivating the use of very short laser pulses. For ~100 fsec laser pulses, 2 J/cm^2 corresponds to field levels approaching the atomic binding limit, 10^{10} V/m. Much can be gained by designing efficient structures that tightly couple the particles to the radiation fields, permitting lower fields on the structure surfaces for a given accelerating gradient.

The structures used to couple the particles and radiation fields will generally have geometric features at or somewhat smaller than the radiation wavelength. For laser-driven structures, this means features on the order of microns or less. Making such tiny structures with the required accuracy from materials with good optical properties is a challenge, but a similar task is accomplished by the semiconductor industry using lithographic techniques. Present UV lithography techniques can mass produce feature sizes as small as ~107 nm [5] with critical dimensions held to ±5.3 nm (3σ) in silicon and silica. Next-generation XUV lithography promises to reduce both feature size and absolute dimensional tolerances significantly. Learning the capabilities of the lithography process and the implications for structure design will be key steps to making laser accelerator structures.

For high energy physics machines, the overall power efficiency is very important. Present collider designs call for 9.6 MW of beam power (total) at the collision point, which with ~8% overall power efficiency wall-plug-to-beam requires 121 MW total AC power, which is already a significant fraction of the power output of even the largest power plants[6]. Lasers have made significant progress in total efficiency both from high efficiency pumping with diode lasers, and through the engineering of materials with very small energy differences between the pumping and lasing transitions. High power diode bars with 50% electrical-to-light efficiency are commercially available [7], with further improvement possible. Lasing media with 86.9% slope efficiencies ($Yb:KY(WO_4)_2$ [8], λ=1.025 μm) have already been used to make high average power lasers achieving better than 10% wall-plug-to-light efficiencies [9], with limiting efficiencies approaching 40% possible.

Strongly coupling the radiation to the particles is essential to getting good power efficiency, but strong coupling means structures must place material within a wavelength or so of the beam. The particles beams must pass through these very small holes, which presents a number of challenges. Long-range wakefields must be carefully managed with a combination of very small bunch

charges and aggressive suppression of the most dangerous higher-order modes. Additionally, the beam must be kept in alignment with these tiny structures to very tight tolerances (less than an optical wavelength) over the entire accelerator length. With noise and ground motion constantly shifting the accelerator components, this will be very challenging.

High-field accelerators generally produce acceleration through the combined action of the electric and magnetic fields, with the requirement that the particles must deflect appreciably within each optical cycle to obtain strong coupling to the fields. This requirement makes accelerating very high-energy particles problematic, with the deflection resulting in rapidly growing synchrotron radiation losses with increasing particle energy. However, there is no rigid requirement that the particles remain in phase synchronism with the wave to receive acceleration. Instead, particles experience force arising from several mechanisms, including the usual first-order force, second-order $\boldsymbol{E}\times\boldsymbol{B}$ forces, and possibly higher-order terms, depending on the field intensity.

Optics must still be used to direct and focus the laser light, but may be placed many Rayleigh ranges from the interaction point, permitting a significant reduction in field strengths. As laser power grows, the optics must also grow in size and be moved still further from the focus, making the problem of obtaining sufficient surface accuracy to achieve diffraction-limited focused spot sizes rapidly more challenging.

A number of lasers exist worldwide that produce focused energy densities high enough for high-field acceleration. Many of these lasers are primarily intended for inertial confinement fusion research, but with suitable broadband seed lasers and appropriate optics, are also used for high field physics. These lasers operate in the near infrared, and are mostly optical parametric chirped-pulse amplifier (OPCPA) based systems employing large energy-storage volumes of flashlamp-pumped Nd:glass. The GEKKO XII laser at ILE Osaka [10] is a petawatt-class laser and the Vulcan laser at Rutherford Appleton Laboratory [11] will soon complete upgrades to operate at the petawatt level, with each laser storing several kilojoules of energy. The High Peak Power T^3 Laser at Jaeri-Kansai [12] is a Ti:sapphire system, and will also shortly complete upgrades to operate at the petawatt level. These kilojoule-class petawatt systems are capable, in principle, of producing fields in the $a_o \sim 10$ range (assuming twice the diffraction-limited spot size for *f*/2 optics), making them suitable for a range of high-field experiments. Two megajoule-class facilities are under construction, the National Ignition Facility (NIF) at Livermore Laboratory [13], and the Laser

MegaJoule (LMJ) facility at CEA-Limeil [14]. These are also Nd:glass systems, which in principle could reach fields strengths beyond a_o~*100*.

These megajoule class flashlamp-pumped glass lasers are very large, complicated systems, occupying several hundred square meters of floor space. They are also not power-efficient, with most of the pump power dissipated as heat in the lasing media. For the NIF and LMJ facilities, the total weight of lasing media (a glass, and hence a poor heat conductor) is over 150 tons, and consequently requires long cooling periods (8 hours for the megajoule lasers listed here) between successive shots. Ti:sapphire offers some improvement over Nd:glass both through its broader bandwidth (and hence shorter ultimate pulse lengths) and through its higher heat conductivity, but has a significantly lower saturation fluence (1 J/cm^2 vs 7 J/cm^2 for Nd:glass) requiring physically large transverse dimensions to produce high powers, is crystalline, requiring large crystals to be grown, and has a large difference between the pumping wavelength (532 nm) and lasing wavelength (800 nm), resulting in poor optical efficiency. Even so, Ti:sapphire systems offer shorter laser pulses and much higher repetition rates (e.g. 10 Hz for the Jaeri-Kansai system) making them attractive for this application. The development of better lasing media (e.g. Yb:$LiYF_4$) with high saturation fluence, good thermal properties, better efficiency, and the capability of being produced in very large, optical quality volumes will greatly improve the utility of these laser systems.

Focusing and steering such large energy laser pulses requires that very large optics (with apertures in the 1 m^2 range) be used to avoid damage. The surfaces of the optics must be accurate to produce an aberration-free focus, and hence the highest fields. Significant advances in the production of large, highly accurate, actively stabilized optics for telescopes and advances in adaptive optics have made the production of such optics possible.

3. Future Research

Rapid progress in laser technology, driven by a $5 billion/year market, has led to a number of exciting developments [15]. High power diode pumping at high efficiency is continually evolving, and offers to replace flash lamp pumping for many applications. Advances in solid-state lasing media have produced highly efficient media with good thermal conductivity that together allow very high average powers to be produced. Carrier phase locking has been demonstrated [16], a key step towards synchronizing two or more lasers at the optical level to drive multiple acceleration stages.

Experimental demonstrations of low-field laser acceleration [17] and high-field laser acceleration [18] have been made. Experiments to explore different coupling mechanisms are needed to establish the most efficient methods that are within reach of fabrication technologies. Expanded experimental efforts will be needed to understand the impact of technical issues on ultimate gradient and on the quality of accelerated beams that may be produced. Material science advances, and improvements in the accuracy with which optical components may be produced will impact both low- and high-field efforts. A handful of laboratories are pursuing experiments to explore these issues, including CEA-Limeil-Valenton, and Brookhaven National Laboratory, and two more are under construction: the Relativistic Photon-Electron Dynamics Lab at National Tsinghua University, Taiwan, and the ORION facility at SLAC.

Remarkable progress over the last decade in laser technology has brought the possibility of laser driven acceleration closer to reality. Dedicated efforts to identify and test the most promising acceleration methods, and to characterize their impact on beam quality are the next steps towards realizing the promise of laser acceleration.

Acknowledgments

The author wishes to thank Bob Siemann, Levi Schächter, Tomas Plettner, and Bob Byer for many stimulating conversations on laser acceleration. Preparation of this manuscript was supported under DOE contract number DE-AC03-76SF00515 (SLAC).

References

1. K. Shimoda, “Proposal for an Electron Accelerator Using an Optical maser,” Appl. Opt., **1**, p.33 (1962) and A. Lohmann, “Electron Acceleration by Light Waves,” IBM Technical Note TN5, San Jose, CA, October 3 (1962).
2. J. D. Lawson, “Laser Accelerators?,” RL-75-043, (1975), but see also P. M. Woodward, J. D. Lawson, “The Theoretical Precision with which an Arbitrary Radiation-Pattern may be Obtained from a Source of Finite Size,” *J. I. E. E.* **95** (III), 363, (1948), and R. B. Palmer, “A Laser-Driven Grating Linac”, *Part. Accel.*, **11**, 81, (1980).
3. M. D. Perry, *et al*, “Ultrashort-Pulse Laser Machining of Dielectric Materials”, J. Appl. Phys., **65**(9), p. 6803 (1999).
4. T. Plettner, “Proof-of-Principle Experiment for Crossed Laser Beam Electron Acceleration in a Dielectric Loaded Vacuum Structure”, Ph.D. dissertation, Stanford University, (2002).

5. "International Technology Roadmap for Semiconductors, 2002 ITRS Update", URL: http://public.itrs.net/Files/2002Update/Home.pdf, p. 64 (2002).
6. "Zeroth-Order Design Report for the Next Linear Collider", v. I, SLAC-474, (1996).
7. *n*LIGHT Photonics, Vancouver, WA, URL: www.nlight.net .
8. Opt. Lett., **22** (17), p.1317, September (1997).
9. F. Brunner, *et al*, "240-fs Pulses with 22-W Average Power from a Mode-Locked Thin-Disk Yb:$KY(WO_4)_2$ Laser", Opt. Lett., **27**(13), p. 1162 (2002).
10. M. Nakatsuka, *et al*, "Class Laser System, GEKKO XII Upgrade for ICF Ignition", in Proc. 11th Top. Mtg. On the Tech. Fusion Energy, New Orleans, LA, June (1994).
11. C. B. Edwards, "Vulcan Petawatt Upgrade Overview", CLF/RAL Annual Report, URL: http://www.clf.rl.ac.uk/Reports/2001-2002/pdf/75.pdf (2002).
12. See URL: http://www.jaeri.go.jp/english/research/re07.html .
13. J. A. Paisner, *et al*, "National Ignition Facility Design, Schedule and Cost", in Proc. 11th Top. Mtg. On the Tech. Fusion Energy, New Orleans, LA, June (1994).
14. J. Coutant, *et al*, "The French Megajoule-Laser Project", in Proc. 11th Top. Mtg. On the Tech. Fusion Energy, New Orleans, LA, June (1994).
15. K. Kincade, "Review and Forecast of the Laser Markets", Laser Focus World, p. 73, January, (2003).
16. D. J. Jones, *et al*, "Carrier-Envelope Phase Control of Femtosecond Mode-Locked Lasers and Direct Optical Frequency Synthesis", Science, **288**, p.635 (2000).
17. W. D. Kimura, *et al*, "Detailed Experimental Results for Laser Acceleration Staging", PRST-AB, **4**, 101301 (2001).
18. P. H. Bucksbaum, *et al*, "Scattering of Electrons by Intense Coherent Light", Phys. Rev. Lett., **58**(4), p.349 (1987), P. Monot, "Energy Measurements of Electrons Submitted to an Ultrastrong Laser Field", Phys. Rev. Lett., **70**(9), p.1232 (1993), C. I. Moore, *et al*, "Observation of the Transition from Thomson to Compton Scattering in Multiphoton Interactions with Low-Energy Electrons", Phys. Rev. Lett., **74**(13),p.2439 (1995), G. Malka, *et al*, "Experimental Observation of Electrons Accelerated in Vacuum to Relativistic Energies by a High-Intensity Laser", Phys. Rev. Lett., **78**(17), p.3314 (1997).

CRITICAL ISSUES IN PLASMA ACCELERATOR

M. UESAKA and T. HOSOKAI
Nuclear Engineering Research Laboratory School of Engineering, University of Tokyo
22-2 Shirane-shirakata, Tokai, Naka, Ibaraki,319-1188. Japan

Updated achievements and critical issues in plasma accelerators are summarized As to laser plasma accelerators, we cover the results of plasma cathodes by U.Michigan, LBNL, LOA and U.Tokyo. Although many new results of accelerated electrons have been reported, the electrons do not yet form a bunch with narrow energy spread. Several injection schemes and measurements to verify ultrashort bunch (tens fs) with narrow energy spread, low emittance and many charges are planned. E-162 experiments by UCLA / USC / SLAC and a newly proposed experiment on density transition trapping are introduced for electron beam driven plasma accelerators. Their main purpose is realization of GeV plasma accelerator, but application to pump-and-probe analysis for investigation of ultrafast quantum phenomena is also promising.

1. Introducton

Acceleration of electrons by plasma wave is of current interest because the acceleration gradient of ~100GV/m is much larger then conventional RF linac. Several methods have been proposed for driving a large amplitude plasma waves, such as plasma wakefield accelerator (PWA), the beat wave accelerator (PBWA), the self-modulated accelerator (SMLWFA), and the laser wakefield accelerator (LWFA). The LWFA and SMLWFA have rapid progress due to recent development of intense ultra-short pulse lasers. On the other hand, the electron driven plasma accelerators are also at an exciting stage of development. E-162 experiments by UCLA/USC/SLAC and a newly proposed experiment on density transition trapping are introduced for electron beam driven plasma accelerators.

2. Laser plasma accelerator

2.1. *Injection Schemes*

Injection of energetic electrons into wakefields for their further acceleration is a crucial part of LWFA. Usually the injection of a high quality electron beam from a RF accelerator is assumed [1]. Another way for electron injection exploits an injection produced by the laser pulse itself, so-called 'self-injection'. There are three major injection schemes of LWFA. In these schemes not only single but also two or several laser pulses are employed for the injection, which called the transverse optical injection[2], colliding pulse injection [3], and injection by wavebreaking of plasma waves [4,5] respectively. Figure 1(*a*)-(*c*) shows the major schemes of the injection of LWFA. First, in the transverse optical injection shown in (*a*), a transverse pulse injects energetic electrons into a longitudinal wakefields excited the pump pulse. Second, in the

colliding optical injection shown in (*b*), the collision of two counterpropagating laser pulses produce the beat wave which traps background elecrons and put into wakefields excited by the pump laser pulse. Third, in the injection by wavebreaking of plasma waves shown in (*c*), the plasma wave produced by a single intense laser pulse breaks at a steep change of plasma density with ejection of plasma electrons, which is injected into further wakefield. These injection schemes are described in the next sections in details.

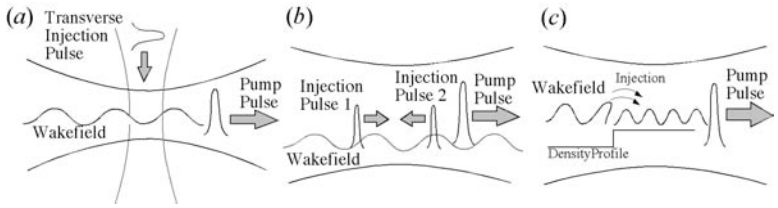

Fig.1 Injection scheme of LWFA
(*a*) Transverse optical injection
(*b*) Colliding optical injection
(*c*) Injection by wavebreaking of plasma waves

2.2.University of Michigan

As shown in Fig.1(*a*), the transverse optical injection method uses two laser pulses; one pump pulse and one injection pulse. The two pulses cross at a focal point. This method was proposed by D.Umustadter of University of Michigan as the laser injected laser accelerator concept (LILAC).[2] The basic idea is that once a laser wake field is excited by the longitudinal ponderomotive force of one laser pulse (the pump pulse), the momentum kick due to a second, orthogonally directed, laser pulse (the injection pulse) can then be used to locally alter the trajectories of some of the plasma wave electrons such that they become in phase with the wave's electric field and thus accelerated to the trapping velocity [2]. In the original concept, it was the transverse ponderomotive force of the injection pulse that delivered the required kick.

The experiment has been done with a Ti:sapphire/Nd:glass laser system. It delivered short pulses (400 fs, 1.053 μm) in a single shot with high-peak-power (~10 TW). The laser beam was split to two beams by a beam splitter. The 20% beam was used as the pump pulse in the experiment and the 80% beam as the injection pulse. In the experiment these two beams were focused with two *f* /3 parabolic mirrors. The laser intensities were about $3x10^{17}$-$5x10^{17}$ W/cm^2 for pump beam and $1.2x10^{17}$-$2x10^{18}$ W/cm^2 for injection (corresponding to the laser powers were about 1.0-1.5 TW for pump beam and 4.0-6.0 TW for injection. These two laser beams were perpendicularly overlapped onto the edge of a supersonic helium gas jet. The pressure of the helium gas was 800 psi and the

gas was fully ionized by the laser beams all above 10^{17} W/cm^2) and the corresponding plasma density was about $4x10^{19}$/cm^3. The background air pressure in the experiment was less than 100 mTorr. The electron beams were observed by LANEX scintillating screen with CCD camera. Figures 2 and 3 show the spatial profile and electron spectrum of the electron beam with and without injection pulses, at a pump laser power of 1.0 TW respectively. As shown in Figure 2 the divergence angle decreased with injection, indicating an improvement in transverse geometrical emittance. From Fig.3 it can be seen that with injection there was an increase in the number of the electrons whose energies are greater than 400 keV. Multi-temperature components were observe in the electron spectra. For the low temperature part, the temperature of the electrons increased from 240 keV (without injection) to 390 keV (with injection), >60% increase. The increase of electron temperatures was 30% to 70%.

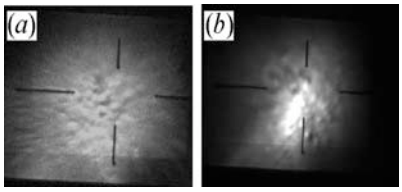

Fig.2 Profiles of pump and injection electron-beams on the LANEX screens. *(a)* with injection pulses (*b*)without injection pulses (by D.Umstadter)

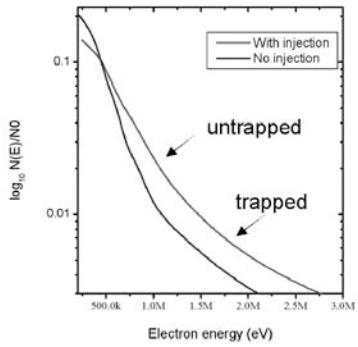

Fig.3 The longitudinal electron energy spectrum in the direction of the low power beam with and without the injection beam. (by D.Umstadter)

2.3. Lawrence Berkeley National Laboratory

As shown in Fig.1(*b*), the colliding pulse injection method uses three laser pulses ; a pump pulse for wakefield excitation and two injection pulses for trapping electrons in plasma. This method has been proposed by E.Esary of Lawrence Berkeley National Laboratory (LBNL)[3], which based on the beat wave produced by the collision of two counterpropagating laser pulses. In beat wave injection, injection is the result of the ponderomotive force associated with the slow beat wave of two intersecting pulses. Colliding pulse injection uses three short laser pulses: an intense ($a_0^2 \sim 1$) pump pulse (denoted by subscript 0) for plasma wake generation, a forward going injection pulse (subscript 1), and a backward going injection pulse (subscript 2). The frequency, wavenumber, and normalized intensity are denoted by ω_i, k_i, and a_i (i=0,1,2). Furthermore, it is

assumed that $k_1 \sim k_0$, $k_2 \sim k_0$, and $\omega_1 - \omega_2 = \Delta\omega >> \omega_p$. The pump pulse generates a plasma wake with phase velocity near the speed of light ($v_{p0} \sim$ c). The forward injection pulse travels at a fixed distance behind the pump pulse, which determines the position (i.e., phase) of the injected electrons. The injection pulses are orthogonally polarized to the pump laser pulse, such that the pump pulse and backward going injection pulse do not beat. When the injection pulses collide some distance behind the pump, they generate a slow ponderomotive beat wave of the form $a_1 a_2 \cos(\Delta k\, z - \Delta\omega\, t)$ (here $\Delta k = k_1 - k_2 \sim 2k_0$) with a phase velocity $v_{pb} \sim |\Delta\omega|/2k_0 << c$. During the time in which the two injection pulses overlap, a two-stage acceleration process can occur, i.e., the slow beat traps and heats background plasma electrons which, as a result of shifts in their momentum and phase, can be injected into the fast wakefield for acceleration to high energies. This three pulses scheme require highly precise At LBNL, the colliding pulse experiments have been underway with only two pulses: a pump pulse for wakefield generation and a single backward propagating injection pulse [6]. Fig.4 shows the electric field profiles and corresponding wakefields plotted during collision of the drive pulse and colliding pulse versus *x* and *z-ct* (were *z* is the drive pulse propagation direction), for the two-pulse configuration with 30 degree interaction geometry. Here the pump and injection pulses have the same polarization such that injection results from the slow ponderomotive beat wave that is produced when the injection pulse collides with the tail of the pump pulse. Two intense short laser pulses were produced by a 10,Hz, Ti:Sapphire CPA laser system(λ=800nm,45fs). The pulse split into two, and

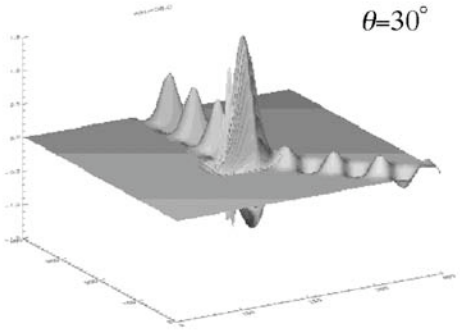

Fig.4 Electric field Profiles and corresponding wakefields.
(by W.Leemans and E.Esarey)

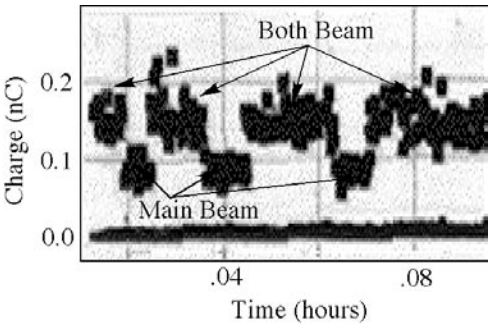

Fig.5 Result of electron beam charge measurement at LBNL.
(by W.Leemans and E.Esarey)

then amplified to 1J/pulse and 0.3J/pulse, respectively. The main drive laser pulse was focused to a 6μm spot size with a 30cm focal length F/4off-axis parabola (OAP) onto the pulsed gas jet. The colliding pulse was focused to a 8μm spot size with an identical OAP onto the pulsed gas jet with a 30 degree angle with respect to the drive beam. The total charge per bunch and spatial profile of the electron beam were measured using an integrating current transformer (ICT) and phosphor screen imaged onto a 16 bit CCD camera, respectively. Figure 5 shows preliminary experimental results, which indicate electron yields have been affected by the second laser beam which intersected the forward going drive laser beam at 30 degrees. Note that the peak power in the drive beam was lowered to reduce the charge production to about 0.1,nC. The charge enhancement resulting from the second pulse could be due to several mechanisms, such as generation of a beat wave (*i.e.*, colliding pulse injection), heating of the background electrons, or other stochasticprocesses.

2.4. Laboratoire d'Optique Appliquée (LOA)

Very recently LOA group demonstrated the first experimental evidence for the relativistic electrons due to wavebreaking in a laser wakefield acceleration (LWFA). [7]. The detection of electrons accelerated up to a maximum beyond 200MeV in a well-collimated beam. The measured emittance of the high-energy electron is small, comparable to those found in conventional rf accelerators. The experiment was performed with Ti:Sapphire laser based on CPA technique generates 30TW, 30fs pulses at 820nm with a 10 Hz repetition rate. The laser beam was focused with a long-focal-length optics of an f/18 off axis parabolic mirror onto the edge of a supersonic helium gas jet. The focusing intensity of the pulse is order of $3x10^{18}$ W/cm^2 and the gas density is between $2x10^{19}$ and $3x10^{19}$ cm^{-3}. Energy and angular distributions of the generated electrons from gas jet are characterized by electron energy spectroscopy and nuclear activation technique. Figure 6 shows electron spectra obtained in the experiment. An effective longitudinal electron temperature of 18 MeV is

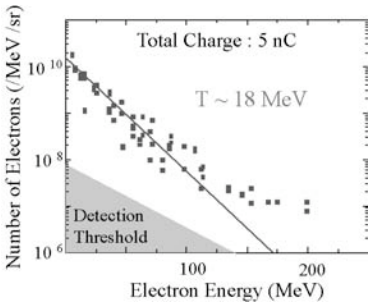

Fig.6 Electron spectra obtained in the experiment. (by V.Malka)

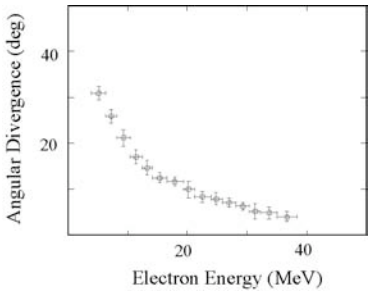

Fig.7 FWHM of the angular distribution of the generated electrons. (by V.Malka)

obtained from an exponential fit for 130MeV (solid line). Figure 7 shows the collimation of the electrons as a function of the energy. The high-energy part of the beam is shown to be well-collimated, whereas the low-energy electrons are accelerated broader cone in the forward direction.

2.5. University of Tokyo

At University of Tokyo, similar experiment of the wavebreaking scheme has been performed with a short Rayleigh length optics. However, the prepulse can be used to form a proper condition for the wave-breaking injection of electrons to the wake-field while the main pulse can produce injection by itself due to relativistic effects. At real condition, a laser prepulse, with approximately a few ns duration, precedes the main laser pulse [7,8]. If the Raleigh length, L_R, is short enough, the prepulse can form a cavity with a shock wave in the front of laser propagation. In contrast to the plasma channel produced by long Raleigh length laser beam [7], the length of the cavity is determined by this small L_R, because the energy is deposited in the plasma mostly near the focus point x=0 as $W(x)\sim 1/(1+(x/L_R)^2)$.

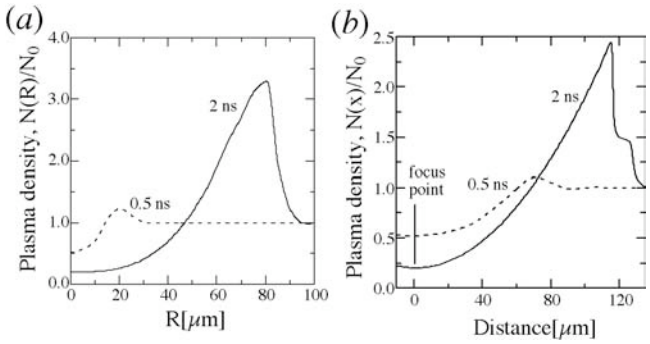

Fig..8 Density distributions of He-jet after the laser pre-pulse calculated by 2D (*r*,*x*) hydrodynamic simulation [8]. The power density of the pre-pulse is 10^{13} Wcm^{-2}, and Rayleigh length is 50 μm. (a) Radial direction (*x*= 0), (b) Longitudinal direction (*r* = 0).

If the shock wave relaxation depth $Dx \sim (M/m)^{1/2}\, l_i$ (M is the ion mass, l_i the ion free path) less than the plasma wave wavelength l_{pl}, the strong wave-breaking of wake-field produced by the main pulse there can be a good source of injection. A typical calculated distribution of the plasma density after the laser prepulse is shown in Fig.8. A strong shock wave is clearly seen. The density gradient at the shock wave is steep and effective wave-breaking is expected. The above conditions has been achieved in the experiments [8]. In the experiment, spatial and energy distribution of energetic electrons produced by an ultra-short, intense laser pulse with short focal length optical system (Ti:Sapphire, 12 TW, 50 fs, l= 790 nm, *f* /3.5) in a He gas jet are measured. They are shown to depend strongly on contrast ratio and shape of the laser pre-pulse. Figure 9(a)-(c) show

spatial distribution of electrons deposited on a bottom plate of the cup-shaped I.P. obtaind for different pre-pulse conditions. The wave-breaking of the plasma waves at the front of shock wave formed by a proper laser pre-pulse is found to make a narrow-coned (0.1p mm mrad) electron injection (Fig.9(a)).

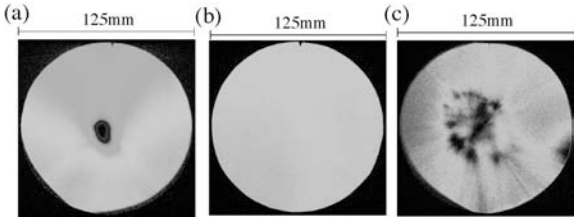

Fig.9 IP image of ejected electrons for the prepulse

These electrons are further accelerated by plasma wake-field generated by the laser pulse up to tens MeV forming a Maxwell-like energy distribution. In the case of non-monotonic pre-pulse (Fig.9(c)), hydrodynamic instability at the shock front leads to a broader, spotted spatial distribution. The numerical analysis based on a 2D hydrodynamic (for the laser pre-pulse) and 2D particle-in-cell (PIC) simulation justify the mechanism of electron acceleration. The PIC calculation predict that electrons with energy from 10 to 40 MeV form a bunch with pulse duration about 40 fs. In Fig.10 energy distribution of electrons accelerated by the laser wake field after wave-breaking injection in a cavity formed by the laser prepulse is shown. The self-injection of plasma electrons which have been accelerated to relativistic energies by a laser pulse moving with a group velocity less than the speed of light appears when $a_0 \geq \sqrt{2}(\omega/\omega_{pl})^{2/3}$ where a_0 is normalized laser field.

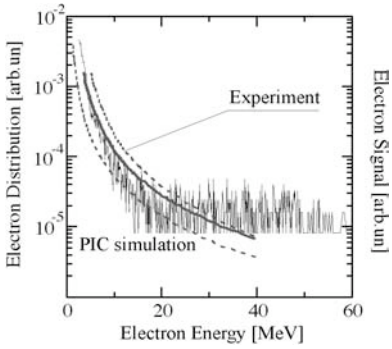

Fig. 10 The measured and calculated time-integrated energy distribution of electrons in the bunch for the laser power of 4TW.

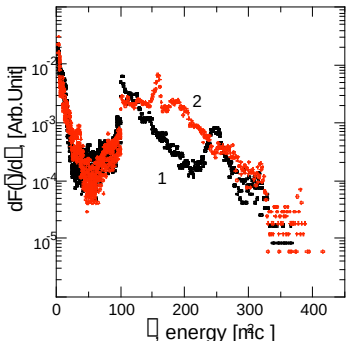

Fig.11 Electron energy distribution in 2D PIC simulation; I=10^{20} W/cm^2, τ=20 fs, Δt=6000 (b) Δt=12000 (b) at the plasma density N_e=10^{19} cm^{-3}

In contrast to the injection due to wave-breaking processes, self-injection allows extraction of a beam-quality bunch of energetic electrons. This injection is also expected to be useful in generation of very short pulse, ~10 fs, electron beams with the charge ~100 *p*C. A typical energy distribution of electron self-injected in the wake field by the main pulse obtained by 2D PIC simulation is given in Fig.11. A peaky distribution is clearly seen. The energy spread is less than 5%.. Formal calculation of the emittance in the bunch gives that of 0.1 *p* mm mrad at total charge *Q*~100 pC. [9]

3. Highlights of electron driven plasma wakefield accelerator

3.1. E-164 experiment by USC / UCLA / SLAC

A new imaging spectrometer eliminating the effect of beam divergence was developed and used at SLAC wakefield experimental line (E-162) under collaboration of USC/UCLA/SLAC/etc. Here, the Cherenkov radiation by the electro beam in air after the achromatic optics was imaged by the CCD camera. As results the energy loss/gain of 15 GeV beam with several charges were successfully obtained as 159+/-40, 156+/-40 MeV with the resolution of ~10MeV, respectively.

3.2. Density transition trapping by UCLA

M.Thompson *et al*. of UCLA is working for the plasma density transition trapping as a possible high brightness electron beam sources. The plasma density transition trapping is a recently purposed self-injection scheme for plasma wake-field accelerators. It has a new self-trapping scenario that uses the rapid change in the wakefield wavelength at a steep drop in the plasma density to diphase plasma electrons into an accelerating phase of wake. This technique uses a sharp downward plasma density transition to trap and to accelerate background plasma electron in a plasma wake-field. They examined

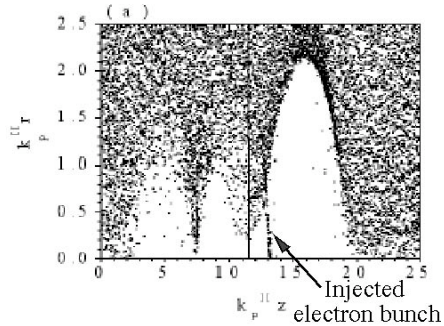

Fig.12 Illustration of transition trapping obtained by PIC simulation. (by H.Suk et al)

the quality of electron beams captured using this scheme in terms of emittance, energy spread, and brightness. Two-dimensional Particle-In-Cell (PIC) simulations show that these parameters can be optimized by manipulation of the plasma density profile [10]. Figure 12 illustrates the transition trapping obtained by the PIC simulation. It clearly shows automatic injection of substantial charge of ~100pC into an accelerating phase. They also develop, and support with simulations, a set of scaling laws that predict how the brightness of transition trapping beams scales with the plasma density of the system. These scaling laws indicate that transition trapping can produce beams with brightness > $5x10^{14}$ Amp/(m-rad$)^2$. A proof-of-principle transition trapping experiment is planned for the UCLA Neptune Laboratory in the near future.

4. Critical Issues

As described above experiments on laser injection methods using multiple laser pulses are being pursued at several laboratories world-wide. As a summary of previous section typical electron beam parameters achieved in the laser plasma wake field acceleration experiments are shown in table 1.

Lab.	Injection	Laser	E_{max}	Energy spread	Emittance [mm mrad]	Charge /shot
LOA	Wave -breaking (Long Rayleigh length)	30TW 30fs	200MeV	100%	$< 3\pi$	5nC (total)
Univ. Michigan	Colliding two pulses	1.5TW 400fs (pump) 6TW 400fs (injection)	2MeV	100%	$< 2\pi$	1.6 nC
LBNL	Colliding three/two pulses	10TW 45fs 3TW 45fs	40MeV	100%	$< \pi$	0.2nC (Two) 0.1nC(One)
Univ. Tokyo	Wave -breaking (Short Rayleigh length)	4-5TW 50fs	40MeV	100%	$< 0.1\pi$	0.1nC (beam)

Table 1 Typical electron beam parameters obtained by LPWA.

The laser plasma wakefield acceleration (LPWA) have rapid progress because of recent development of intense ultra-short pulse lasers. However it is still in the stage of proof-of-principle. Though several injection schemes using multiple laser pulses are being demonstrated at many laboratories, there are several critical issues. First, the injections give a broad Maxwell-like energy distribution of accelerated electrons. This is because some fraction of the background electrons are continually being swept up and trapped in the wakefield as the laser pulse propagates into fresh plasma, and typically the self-guided propagation distance of the laser pulse is much greater than the detuning length for trapped electrons. This implies that deeply trapped electrons will

circulate many revolutions within the separatrix, again resulting in a large energy spread. Second, experimental result shows that spatial and energy distribution of the trapped electrons depend strongly on the laser prepulse. It means proper prepulse control is essential for the high quality electron beam. Third, adding plasma channel for further acceleration is necessary for acceleration into higher energy. It means extending the acceleration distance larger than the vacuum diffraction length by plasma channels. Several methods for production of plasma channel have been proposed: relativistic self-guiding in a plasma and guiding in preformed plasma channels generated by a focused laser pulse or by slow discharge through a capillary in vacuum. or fast Z-pinch discharge through a gas-filled capillary.

The electron driven plasma wakefield accelerator is also still in the stage of proof-of-principle. More new ideas (plasma density transition trapping, THz acceleration, etc), numerical simulations, experiments (at USC / UCLA / SLAC, Fermi) and new diagnostics (imaging spectrometer, etc) are needed. The linear scaling law should be checked and up-graded.

Acknowledgements

The authors are grateful to Dr. V.Malka, Prof. D.Umstdater, Dr. W.Leemans, Dr. E.Esarey, Prof. K.Nakajima, Dr.H.Kotaki, Dr. M.Kando, Prof. J.Rosenzweig, Mr.Thompson, Dr. P.Muggli, Dr.H.Suk, Dr. A.Ting, and Dr. Sprangle for their contribution for this paper, and also acknowledges the support of the research stuffs, Drs. T.Watanabe, A.Zhidkov, K.Kinoshita, Mr.T.Ohkubo, and Mr. Kanegae of University of Tokyo.

References

1. K. Nakajima et al., Phys. Rev. Lett. 74, 4428(1995); F. Amiranoff et al., Phys. Rev. Lett. 81, 995 (1998); F. Dorchies et al., Phys. Plasmas 6, 2903 (1999).
2. D. Umstadter et al., Science 273, 472 (1996); D. Umstadter, J.M. Kim, and E. Dodd, Phys. Rev. Lett. 76, 2073 (1996)
3. E. Esarey, R.F. Hubbard, W.P. Leemans, A. Ting, and P. Sprangle, Phys. Rev. Lett. 79, 2682 (1997); E. Esarey, P. Sprangle, J. Krall, and A.Ting, IEEE Trans. Plasma Sci.,24,252 (1996)
4. S. Bulanov, N. Naumova, F. Pegoraro, J. Sakai, Phys. Rev. E58, R5257 (1998)
5. J. D. Kmetec, C. L. Gordon III, J. et al., Phys. Rev. Lett. 68, 1527 (1992)
6. W.P. Leemans, P.Catravas, E.Esarey *et al*., Phys. Rev. Lett. 89, 174802-4 (2002)
7. V. Malka, J. Faure, J.R. Marques *et al.*, Phys. Plasmas 8, 2605 (2001); Science, 298, 1600 (2002); F. Dorchies, F. Amiranov, V. Malka et al., Phys. Plasmas 6, 2903 (1999); J. Faure, V. Malka, J.-R. Marques, F. Amiranoff, et al., Phys. Plasmas 7, 3009 (2000)
8. T. Hosokai, K. Kinoshita, A. Zhidkov *et al*., Phys. Rev. E67, 036407 (2003)
9. A. Zhidkov, J. Koga, K. Kinoshita, M. Uesaka, Phys. Rev. Lett. (in press)
10. H.Suk,et al., Phys. Rev. Lett. 86, 1011(2001)

PROPOSED LASER DRIVEN PHOTONIC BAND GAP ACCELERATOR

J. H. HAN AND I. S. KO

Department of Physics, Pohang University of Science and Technology, Pohang, 790-784, Korea
E-mail:jhhan@phys.postech.ac.kr

Accelerating gradient field can be guided in a waveguide made out of a photonic band gap structure. The electron beam which has the same velocity as the phase velocity of the guided accelerating field can be accelerated during passing the photonic band gap accelerator structure. A ratio of the surface electric field to the central accelerating gradient field can be made low because the field does not penetrate into the photonic band gap structure composed of the dielectric material and the vacuum. Calculated maximum accelerating gradient is 150 MeV/m for the 1 cm accelerating structure.

1. Introduction

Photonic crystals (PCs) with an artificially constructed periodic structure inhibit the electromagnetic radiation with a frequency inside the photonic band gap (PBG).[1] A central defect which is carefully made inside the PBG structure makes it possible to induce the radiation corresponding to the defect modes.[1] The vacuum-guiding becomes possible when the central vacuum defect is surrounded by the 2D PBG structure and the defect modes satisfy the vacuum-guiding condition.[2,3]

In the photonic band gap accelerator (PBGA), the 2D PBG structure blocks a leakage of the electromagnetic radiation and the central vacuum defect guides both the radiation and the charged particle beams. A fundamental TE_{11}-like mode generally used in communication is useless for the charged particle acceleration, but the TM_{01}-like mode with the longitudinal electric field gains an attention in the PBGA. Tuning of the guided mode is carried out by changing the size and the shape of the central defect and the PBG structure geometry.

The acceleration mode guided in the PBGA structure propagates with the longitudinal phase velocity greater than the speed of light, c. Synchro-

nization between the phase velocities of light and the propagation velocity of the electron beam is achieved by inserting the iris which is made by partly building a wall in the defect region as shown in Fig. 1. In this paper, we introduce an effective geometry of the PBG structure with large out-of-plane PBG composed of GaAs and a vacuum. Then the PBGA which is composed of the 2D PBG structure, a central vacuum defect and dielectric irises is presented. The proposed PBGA will be able to accelerate the electron beam in a straight way because of the rigid well-aligned structure.

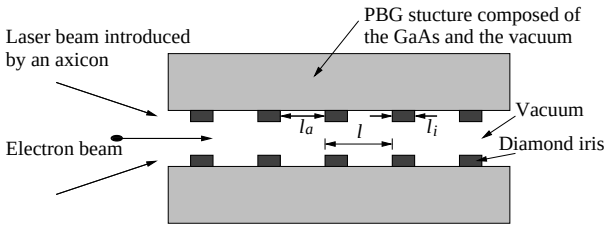

Figure 1. Schematic of proposed laser driven PBGA

2. Design

2.1. *Accelerating Frequency and Materials*

The power of acceleration is increased with the square of the laser wavelength.[4] On the other hands, the electromagnetic radiation with the wavelength longer than 10 μm is hardly transmitted through most dielectric materials. The CO_2 laser with the wavelength of 10.6 μm may be a solution as an acceleration field source because the CO_2 laser is the longest wavelength source among conventional laser sources and can be easily made to the high power source with the pulse length of hundreds picoseconds.

Dielectric materials constructing the frame of the PBGA must have a good transmission property and the high laser induced damage threshold (LIDT) at given wavelength. In addition, the frame material should satisfy high thermal conductivity, appropriations for precise fabrication, and the mechanical strength enough for maintaining PBG architecture when the high intensity laser field is loaded.

In this study, the GaAs with the refractive index of 3.12 at 10.6 μm was selected as the frame dielectric material of the PBGA because its properties fairly well satisfy previously discussed demands for 10.6 μm wave.[5] Due to

high LIDT, heat capacity, and hardness, the diamond is selected as the iris material.[5,6]

2.2. *Calculation Method*

To calculate the properties of the accelerating gradient field guided in the PBGA, the absolute PBG map for a unit lattice of the PBG structure is configured as a function of the variation of the normalized propagation constant, βa, where a is a lattice constant, assuming the perfect periodicity. Then the normalized frequency, ka, and the field profile of defect modes at the given βa are calculated for the entire two-dimensional PBGA structure including the PBG structure and the central defect.

We use the MIT Photonic-Bands (MPB) package[7] to obtain the dispersion relation in the first Brillouin zone of the PBG structure and to calculate the physical properties of the accelerating mode of the entire PBGA structure by using supercell approximation. One unit lattice of our PBG structure has the values of 12.45 μm horizontally (a) and 24.9 μm vertically ($2a$) and the dielectric-filling fraction of 21.7 %. The width of horizontal and vertical slabs are $0.1a$ and $0.13a$, respectively.

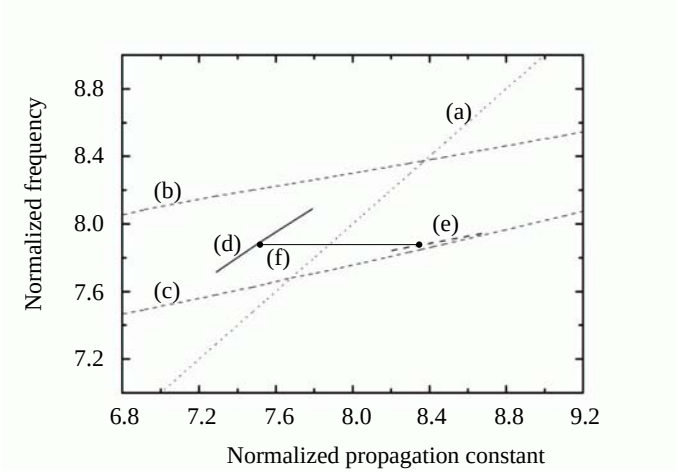

Figure 2. Variations of the radiation modes. (a) is the line corresponding to the speed of light, (b) and (c) are upper and lower photonic band gap boundaries, (d) is the TM_{01}-like mode formed in the region without iris, (e) is the TM-like mode formed in the region with iris, and (f) indicates the operating frequency.

3. Acceleration Process in PBGA

3.1. *Accelerating Structure*

The band gap is positioned to cross the line corresponding to the speed of light because the longitudinal phase velocity of the guided accelerating gradient mode settled in the gap must equal to the propagation velocity of the electron beam. Strong confinement of the guided-mode is the key to raise the acceleration gradient field against the maximum electric field of the dielectric limited by the LIDT. Confinement is roughly dependent on the photonic band gap size and the position of the defect mode. The position of the acceleration mode has to be settled in the middle of the gap boundaries for strong confinement. Figure 2 shows the absolute PBG map of the out-of-plane 2D PBG structure, where the variation of the gap is represented as the function of the normalized propagation constant. As can be seen in Fig. 2, only one gap exists, and higher-order modes are suppressed.

As mentioned above, the defect breaking the perfect symmetry of the PBG structure can induce the defect modes. The size and the shape of the defect determine the properties of the defect modes. The size of the defect is large enough to guide almost all electromagnetic field inside the defect. As can be seen in Fig. 3, the central vacuum defect consists of the vacuum area corresponding to 9.5 unit lattices.

3.2. *Description on Accelerating Field*

The accelerating mode, the second-order TM_{01}-like mode, has a Bessel function-like distribution in the vacuum defect region and the central accelerating gradient field is 0.762 times the peak electric field inside the GaAs frame. The phase velocity of the accelerating mode is 1.047 c. Therefore, the phase slippage becomes $\pi/11$ per one accelerating mode wavelength, 10.6 μm. In the waveguide region with the iris, most electric field is concentrated to the iris. Because the refractive index of diamond is 2.39, the phase velocity of the accelerating wave becomes slow down. According to our simulation, the phase velocity of the waveguide region with the iris is 0.930 c. The longitudinal length of the iris, l_i, is chosen to 0.373 l for the synchronization, where a unit length, l, is chosen to be four wavelength (42.4 μm). The fundamental TE_{11}-like mode, which is composed of two orthogonal, quasi-linear polarization states, does not contain the longitudinal component of the electric field.

3.3. *Calculation of the Maximum Accelerating Gradient*

The velocity of the relativistic electron beam is equivalent to the speed of light, c, otherwise the energy of the accelerating gradient field propagates with the velocity slower than c. Therefore, the electron beam can expe-

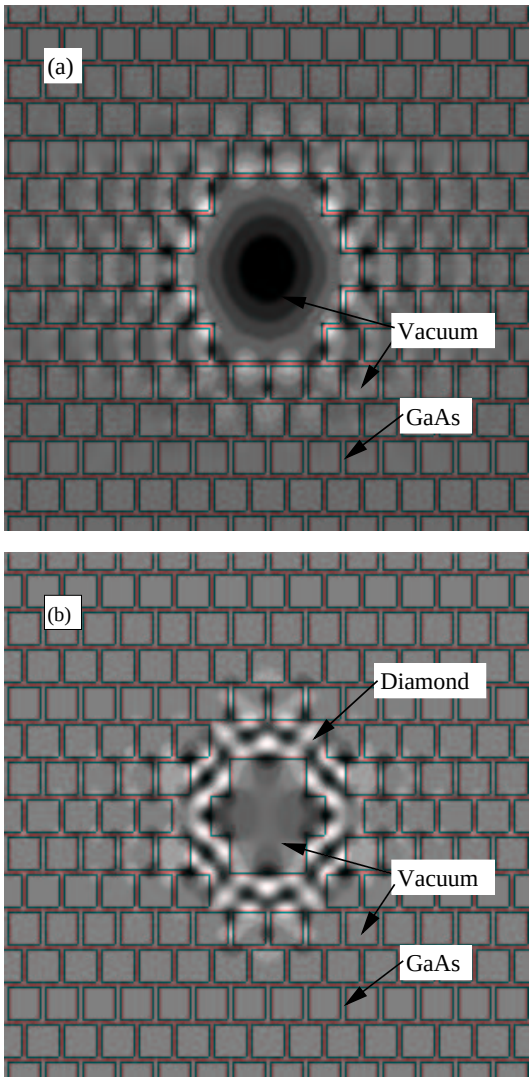

Figure 3. Acceleration field profiles. (a) and (b) show the longitudinal electric field profile in the region without iris and with iris, respectively.

rience the acceleration throughout the entire waveguide length only when the pulse length is larger than $n[(c - v_{ag})l_a + (c - v_{ig})l_i]/c^2$, where n is the number of the sections composed of no iris and iris region, v_{ag} and v_{ig} are the group velocities, and l_a and l_i are the length in each regions as shown in Fig 1. Our calculation shows $v_{ag} = 0.738\ c$ and $v_{ig} = 0.217\ c$. When a four-inch GaAs wafer is used, we can get the 10 cm long acceleration structure and the minimum pulse length is 144 ps. For the laser pulses of hundreds pico seconds or less, the laser-induced material damage can be caused by a mixture of the joule heating, the avalanche ionization, and the multiphoton and the tunneling ionization. Therefore, the damage threshold is determined by both the laser-pulse width and the peak laser field[6] and in our case, about 4.83 J/cm^2.[5] The peak electric field at the GaAs which composes PC structure, is 271 MV/m and the corresponding peak acceleration field at the center of the vacuum defect is 207 MV/m for the 10 cm accelerating structure. Because the maximum acceleration gradient is a half of the peak accelerating field[8] and the l_a/l is 0.627, the proposed PBGA with the 10 cm structure have a gradient of 64.8 MeV/m. The pulse length can be shortened by dividing the accelerating structure into several serial arrays. The LIDT of the frame material can be raised by shortening the pulse length. When one accelerating structure is set to 1 cm, the minimum pulse length is 14.4 ps and LIDT is 1.53 J/cm^2 and the expected gain is 150 MeV/m.

4. Proposed Fabrication Procedure

In order to fabricate the discussed structure, we propose to use a conventional semiconductor microfabrication technique.[9] When a wafer-fusion and alignment technique is used, one long PBGA structure with the length equivalent to the diameter of a GaAs wafer or a serial array of several short PCA structures may be constructed on the wafer substrate. A pattern of the diamond iris to carry out the synchronization can be etched by synchrotron[10] or focused-ion-beam.[11] The diamond layer on the GaAs structure may be grown by the chemical vapor deposition (CVD) technique.[12] In the process of the PBGA fabrication, the surface roughness of the dielectric materials is not crucial.[13]

5. Conclusion

We have designed the PBGA with a rigid and accurately machinable structure which has a large absolute band gap. To synchronize the phase veloc-

ity of the accelerating mode to the velocity of the electron beam, we have adopted the diamond iris with higher refractive index than the vacuum. Introducing the iris in the defect region have made it possible to enlarge the transverse area of the waveguide also. In our simulation, the diameter of the defect is set to 26.5 μm, and it can be expanded to the diameter of 50 μm or more. Calculated maximum accelerating gradient is 150 MeV/m for the 1 cm accelerating structure.

Acknowledgments

This work has been supported by the Korea Science and Engineering Foundation through the Center for High Energy Physics at Kyungpook National University.

References

1. J. D. Joannopoulos, R. D. Meade, and J. N. Winn, *Photonic Crystals* (Princeton University Press, Preston, NJ, 1995).
2. R. F. Cregan, B. J. Margan, J. C. Knight, T.A. Birks, P.St. J. Russel, P. J. Roberts, and D. C. Allan, Science **285**, 1537 (1999).
3. J. Broeng, S. E. Barkou, T. Søndergaard, and A. Bjarklev, Opt. Lett. **25**, 96 (2000).
4. X. E. Lin, Phys. Rev. ST Accel. Beams **4**, 051301 (2001).
5. R. M. Wood, *Laser Damage in Optical Materials* (Adam Hilger, Bristol, 1986)
6. A. C. Chiang, Y. Y. Lin, and Y. C. Huang, Opt. Lett. **27**, 164 (2002)
7. S. G. Johnson and J. D. Joannopoulos, Opt. Express **8**, 173 (2001)
8. P. B. Wilson, SLAC-PUB-2884 (1991)
9. S. Noda, N. Yamamoto, M. Imada, H. Kobayashi, and M. Okano, J. Lightwave Technol. **17**, 1948 (1999)
10. H. Ohashi, E. Ishiguro, T. Sasano, and K. Shobatake, Appl. Phys. Lett. **68**, 3713 (1996)
11. J. Taniguchi, N. Ohno, S. Takeda, I. Miyamoyo, and M. Komuro, J. Vac. Sci. Technol. B **16**, 2506 (1998)
12. M. C. Salvadori, J. W. Ager III, I. G. Brown, and K. M. Krishnan, Appl. Phys. Lett. **59**, 2386 (1991)
13. S. Fan, P. R. Villeneuve, and J. D. Joannopoulos, J. Appl. Phys. **78**, 1415 (1995)

USE OF MACROSCOPIC SOLID STRUCTURE IN ACCELERATORS

A. OGATA, N. SAITO*AND T. ISHIMARU
AdSM, Hiroshima University,
Kagamiyama, Higashi-Hiroshima 739-8530, Japan
E-mail:ogata@sci.hiroshima-u.ac.jp

Use of structures of a solid in accelerators is discussed, which have sizes around the wavelength of lasers. An example is a photonic band-gap crystal, an artificial periodic structure made from two materials with different dielectric constants. Another simpler example is a fine hole in a solid, in which electromagnetic waves transmit as low-dimensional waves. One of the applications of the photonic band-gap crystal is guiding of laser pulses over a Rayleigh length. The hole in a metal holds plasmons on the inner wall, whose electric fields can accelerate charged particles. A plasmon linac, a linac based on this principle, can realize an emittance on the order of nm.

1. INTRODUCTION

Size of structure of a solid is characterized by a lattice constant. Use of such structures has once been proposed to hold the electric field to accelerate charged particles,[1,2] but no experiments have been performed so far. This is mainly because the power source has not been readily available in the form of a wave with wavelength around the lattice constant. The present paper proposes use of an artificial macroscopic structure whose lattice constant is around the laser wavelength, 1μm or less, but much larger than the real lattice constant. An example of such structures available is a photonic band-gap crystal.[3] Another simpler example is a hole in a solid whose diameter is around the laser wavelength[4]. Their applications to accelerators have already been discussed in several papers.[5,6,7,8]

The next section of this paper reviews the photonic band-gap crystal and its application to accelerators. The electromagnetic waves with the

*Present address : Mazda Motor Corporation, 3-1 Shinchi, Fuchu-cho, Aki-gun, Hiroshima 730-8670, Japan.

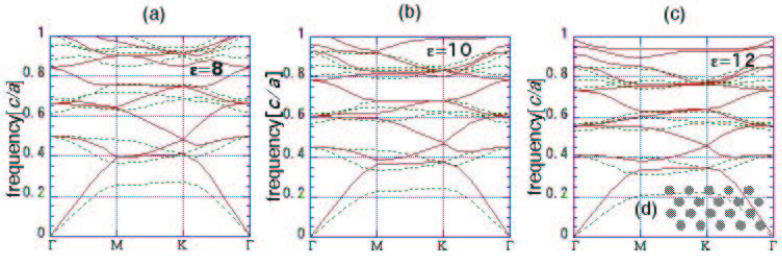

Figure 1. Dispersion curves of (a)bulk solid, (b)one-dimensional periodic structure from homogeneous material, and (c)one-dimensional periodic structure of two materials with different dielectric constants.

band-gap frequencies are channeled, which property is useful to lengthen the acceleration distance of a laser-plasma accelerator. Group velocity of a light decreases in the crystal, which could be used in the laser acceleration of "slow" particles such as ions. The third section first reviews a low dimensional light, which is realized in a hole in a metal with diameter around the laser wavelength. A specific application of the low dimensional light, a plasmon linac, is then described. The last section contains conclusion.

2. PHOTONIC BAND GAP CRYSTAL

Photonic band-gap crystals (often called simply photonic crystals) are regular array of materials with different refractive indices. Their spatial periods (lattice constants), can be on the order of any electromagnetic wave. It is about 1μm or less for visible lasers. The two features of the photonic crystal are channel guiding of a light and slowing down of the group velocity of a light.

Another topic is generation of radiation in the interaction between charged particle beams and a photonic crystal. If charged particle beams run close to a surface of the periodic structure such as the photonic crystal, Smith-Purcell radiation is generated.[7] We experimentally measured the intensities of the visible radiation and depicted them on the $k-\omega$ plane, which will be published elsewhere.[9]

2.1. *use of band-gap for channel guiding*

Figure 1(a) shows the dispersion diagram or the Brillouin diagram of a bulk solid with the dielectric constant ϵ. It is of two straight lines $\omega = \pm v_p k$,

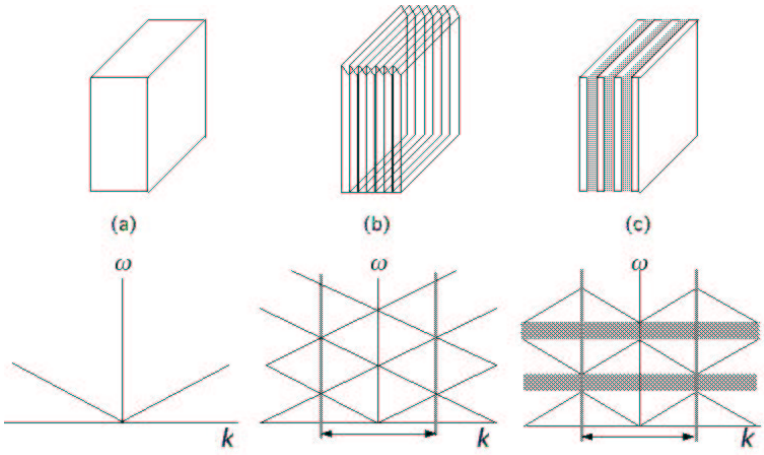

Figure 2. Brillouin diagrams of two-dimensional triangular photonic crystals schematically given in (d), made of columns with radius $r = 0.3a$, where a is the lattice constant, from materials with $\epsilon = 8$(a), $\epsilon = 10$(b) and $\epsilon = 12$(c). Lines show those in the TE mode and broken lines show those in the TM mode.

where $v_p = c(\epsilon_0/\epsilon)^{1/2}$. If a single material has a periodic structure like a grating, the dispersion is folded at the periods of the wave-numbers as shown in (b). Usually only the part indicated by the arrow is depicted. If two or more materials make a period, the dispersion becomes such that shown in (c), which has band-gaps.

Figure 2 shows Brillouin diagrams of real two-dimensional photonic crystals, made of columns with radius $r = 0.3a$ where a is the lattice constant, from materials with $\epsilon = 8$(a), $\epsilon = 10$(b) and $\epsilon = 12$(c). The figures were depicted by the MIT program.[10] The eigenmodes are classified into two categories according to the polarization of the optical waves; that is, the TE mode for which the electric field is perpendicular to the 2D plane and the TM mode for which the magnetic field is perpendicular to the 2D plane. These definitions are common in solid-state physicists but different from those of accelerator scientists. Three diagrams in Fig. 2 looks same except their aspect ratios. It is found that existence of the bandgaps is different between the TE and the TM modes. Careful inspection finds that the TE mode has a band-gap only in (c) and has not in (a) and (b).

Existence of band-gaps enables the channel guiding of light waves. Waves with frequencies in the band-gaps cannot exist in the photonic crystal. If defects are introduced into the crystal, such waves are localized in the

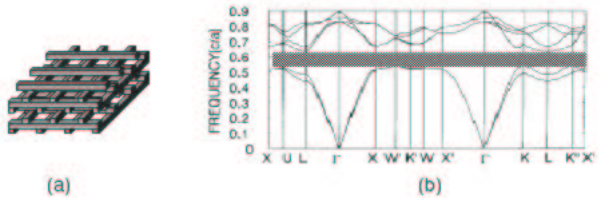

Figure 3. Three dimensional photonic crystal(a), and its Brillouin diagram(b).
12

defects. A line defect thus guides waves with the band-gap frequencies.[11] This phenomenon can be used to guide lasers in the laser wake-field acceleration to lengthen the acceleration distance far over a Rayleigh wavelength.

A three dimensional photonic crystal shown in Fig. 3(a) has the Brillouin diagram of (b), in which both the TE and TM modes have a band-gap in all directions of the crystal.[12] Let us assume use of a Ti:Sapphire pump laser and a crystal made from Si; i.e., laser wavelength is 800nm and refractive index of the crystal is 3.2. We specify the thickness of the stripe as $0.2a$. The a value should be designed so that the laser wavelength exists in the band-gap, 416nm$< a <$496nm in these conditions. The thickness of the defect should be a bit larger than the waist size of the laser, say 4μm, so we have to pull out about 10 stripes to make the waveguide.

In order that the line defect is used as a waveguide of a plasma accelerator, the Debye length, $\lambda_D = (\lambda_p/2\pi c)(k_B T_e/m_e)^{1/2}$, should be small enough compared with the size of the defect, where λ_p is the plasma wavelength, T_e is the plasma electron temperature and k_B is the Boltzman constant. In the mechanism of linear laser wake-field acceleration using laser pulses with longitudinal width σ_z, the plasma wavelength should be around $\pi\sigma_z$ to maximize the acceleration gradient.[13] If we assume use of 40fs laser pulses in a plasma with $T_e = 1$eV, these relations specify $\lambda_p = 47.1\mu$m and $\lambda_D = 10.5$nm. The Debye length is thus small enough than the defect size. Though the plasma wavelength is larger than the defect size, excitation of the plasma wave in such situation has already been verified.[14]

2.2. *use of slow group velocity*

Group velocity is indicated by a gradient of the dispersion curve in a Brillouin diagram. Curves in Fig. 2 and Fig. 3(b) have a lot of points with slow group velocities. The slow group velocity in a photonic crystal is because of two reasons. First is a so-called whispering gallery mode, in which photons

repeat random reflection inside the bulk solid and do not come out immediately. Second is the macroscopic Bragg reflection. Photons turn to and fro in the structural layers and cannot go straight. Experiments have measured the velocity of a laser pulse propagation in the crystal and verified that it was lowered down to $c/20$.[15]

The state density of photons becomes large as the group velocity decreases, so the slow group velocity enhances the electric field. Such properties could be useful in energy manipulation of heavy particles, not only ions but also neutrals. The idea is to confine particles by the ponderomotive force of a laser pulse, or load the laser pulse with particles. The particles consequently have to move in the speed of the laser pulse. Further calculations show, however, this method can hardly accelerate the heavy particles in MeV range. This is because the ponderomotive force is given by

$$f = \frac{1}{4}\frac{e^2}{M\omega^2}\nabla E^2, \tag{1}$$

with ω, the laser frequency and M, the ion mass, which is at least $\sim$2,000 times larger than the electron mass. A rough estimation shows that a laser power density of 10^{15} W cm^{-2} gives a ponderomotive force of 3.27 10^{-12} N or a ponderomotive potential of $\sim$20eV, assuming the electric field enhancement due to the small group velocity as 20. This method is rather useful to manipulate the particle energies in keV range.

In the acceleration of heavy particle beams, velocity of the laser pulses has to increase along the beam path. Figure 2 gives a hint, showing that the higher dielectric constant gives smaller group velocity. If the dielectric constant of the material was controlled so that its value at the particle entrance is larger than that at the exit, the group velocity could be increased with the particle acceleration. Both change of a value and change of the r/a ratio could fulfill the same requirement.

3. LOW-DIMENSIONAL LIGHT

3.1. *low-dimensional light*

A plane wave in a material with dielectric constant ϵ is expressed by

$$k_x^2 + k_y^2 + k_z^2 = \epsilon\omega^2/c^2. \tag{2}$$

If one is real among k_x, k_y and k_z, we call the wave one-dimensional, and if two are real, we call it two-dimensional. These two are low-dimensional waves. Because the dielectric constant of a metal is negative in visible-IR range, the light in the metal has to be low-dimensional. Imagine a boundary

between a metal and vacuum. If a condition $k_\parallel > (\epsilon_0\omega/c)^{1/2}$, $k_\parallel$ being the wave number along the boundary, is satisfied, $k_\perp$ is imaginary and the wave becomes two dimensional in both sides. Dispersion of the light becomes $k_\parallel = \omega/c[\epsilon\epsilon_0/(\epsilon+\epsilon_0)]^{1/2}$, which mode is called surface plasmon-polariton or simply surface plasmon. If we replace ϵ_0 by 1 and ϵ by $1-(\omega_p/\omega)^2$, ω approaches $\omega_p/(2^{1/2})$, as $k_\parallel$ gets ∞.

The low-dimensional light can transmit in a waveguide with a diameter much smaller than its wavelength in a free space. It will enable construction of optical integrated circuits with sizes smaller than the wavelength used in them. Its another feature is a slow phase velocity,[16] which could be useful in acceleration of heavy particles.

3.2. *plasmon linac*

A plasmon linac is a miniature linac that uses a hole in a metal as an acceleration tube. A laser pulse excites plasmons, the low-dimensional waves, along the inner wall of the tube, whose radius is around the laser wavelength. Test beams are then accelerated by the potential of the plasmons. One can regard this method as a laser wake field acceleration in a hollow channel,[17] though it uses an overdense metal plasma instead of an underdense gaseous plasma. The structure resembles that of a dielectric linac,[18] which has once been studied as a rival of a linac with periodic structure. It features beam size in the nanometer range and good conversion efficiency from laser power to acceleration gradient; it attains a GeV/m gradient by a MW laser instead of a TW one, though the current is very small.

Suppose a hole with radius a in a medium with dielectric function $\epsilon_1(\omega)$. Axial symmetric components of electric and magnetic fields inside the hole ($r \le a$) are

$$\begin{aligned} E_r &= -(ik/K_0)A_0J_1(K_0r), \\ E_z &= A_0J_0(K_0r), \\ B_\theta &= -[i(K_0^2+k^2)/\omega K_0]A_0J_1(K_0r), \end{aligned} \tag{3}$$

and those in the medium ($r > a$) are

$$\begin{aligned} E_r &= -(ik/K_1)A_1H_1^{(1)}(K_1r), \\ E_z &= A_1H_1^{(0)}(K_1r), \\ B_\theta &= -[i(K_1^2+k^2)/\omega K_1]A_1H_1^{(1)}(K_1r), \end{aligned} \tag{4}$$

where

$$K_i^2 = \omega^2\epsilon_i(\omega)/c^2 - k^2, \quad i = 0 \text{ or } 1, \tag{5}$$

and $J_n(x)$ and $H_n^{(1)}(x)$ are Bessel function and Hankel function of the first kind, respectively.[19]

Using the boundary conditions at $r = a$, we obtain a so-called transcendental equation. Inserting the dielectric functions of vacuum $\epsilon_0 = 0$ and that of the medium

$$\epsilon_1 = 1 - [\omega_p^2/\omega(\omega + i\gamma)], \tag{6}$$

with ω_p and γ being plasma frequency and relaxation constant, respectively, into the transcendental equation, we obtain the dispersion relation,

$$K_1 H_0^{(1)}(K_1 a) J_1(K_0 a) - [1 - \omega_p^2/\omega(\omega + i\gamma)] K_0 H_0^{(1)}(K_1 a) J_1(K_0 a) = 0. \tag{7}$$

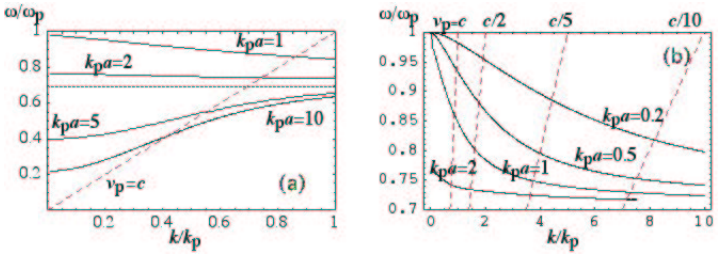

Figure 4. Real part of the dispersions of the plasmons inside the hole. Straight lines give those of particle beams with various velocities.

Figure 4 shows the real part of the dispersion relations for various $k_p a$ values. Frequencies in time and space are normalized by ω_p and $k_p = \omega_p/c$, respectively. All ω values approach $\omega_p/\sqrt{2}$, the surface plasmon-polariton frequency, with increasing k. Straight lines show particle beams with various velocities. Lasers with frequencies at the crossing points between straight lines and curves are able to excite the plasmons mating with the relativistic beams in Fig. 4(a). Figure 4(b) suggests acceleration of slow heavy particles. If we use a laser with a single frequency throughout the acceleration, we have to increase the hole radius along the particle orbit in accordance with the increase of the particle velocity.

One of the features of the dispersions in Fig. 4(b) is in their negative group velocity, $\partial\omega/\partial k < 0$. Laser pulses and test beams should have counter directions each other in the accelerator configuration. A backward-wave tube produces similar waves, in which a forward-flowing electron beam converts its energy into a backward wave.[20]

Integration of Poynting vector gives the laser power transmitting along the hole. Using the boundary conditions of the field components, and by inserting E_z in Eq. (4), we find that the accelerating field E_z inside the hole is proportional to the square root of the laser power P;

$$E_z(0) = \alpha k_p P^{1/2}. \tag{8}$$

The $k_p a$ dependency of the coefficient α of the above equation is numerically calculated and given in Fig.5 for various particle velocities, $v_p = c$ in (a) and slower velocities in (b).

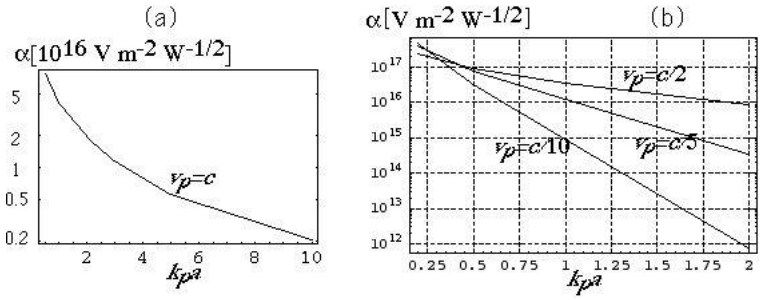

Figure 5. Conversion coefficient α between $k_p P^{1/2}$ and the acceleration field $E_z(0)$, as a function of $k_p a$ for various phase velocities, $v_p = c$ (a) and $v_p < c$ (b).

Use of silver ($\omega_p = 13.2 \times 10^{15}$ s^{-1} and $\gamma = 68.9 \times 10^{12}$ s^{-1}) under the design conditions $k_p a = 10$ and $v_p = c$ give $a = 227$ nm and the laser wavelength as 344 nm. According to Fig.5(a), a laser with a power of 1 MW attains an acceleration gradient of 45.0 GeV·m^{-1}. The acceleration length $\sim c/\gamma$ is, however, only 4.32 μm, giving an energy gain of 194 keV.

This short length is due to the ohmic loss, which raises the temperature and destroys the accelerator structure. The solution is to keep the structure at a low temperature. The resistivity ρ is in proportion to γ. That of silver at 300 K, 16.29×10^{-9} Ω·m, is reduced to 0.0115×10^{-9} Ω·m at 10 K.[21] The acceleration length and the energy gain at 10K instead increase to 6.11 mm and 273 MeV, respectively, with the same 1 MW laser. The laser intensity at the inner wall is 1 MW/($2\times\pi\times$ 227 nm $\times$ 6.11 mm) = 11.48×10^9 Wcm^{-2}. This value can be below the damage threshold of silver, if the laser repetition rate is moderate.

This linac with a fine acceleration tube is capable of producing so-called nano electron beams. Reiser expressed normalized emittance of an electron

beam as a function of T and κ,[22]

$$\epsilon = \frac{k_B T}{\kappa m_e c^2}, \tag{9}$$

where T is the beam temperature, k_B is the Boltzman's constant, m_e is the electron mass. A transverse linear restoring force F on an electron at r is expressed by using κ,

$$F = -\gamma m_e c^2 \kappa^2 r. \tag{10}$$

In the case $v_p = c$, Eq. (4) gives $J_0(0) = 1$ and $E_z = A_1$. The acceleration field is therefore independent of the radial position in the hole. The transverse field contains $J_1(K_1 r)$. Since $K_1 r << 1$, we can make approximation $J_1(K_1 r) \sim (K_1 r/2)(1/\Gamma(2)) = K_1/2$, to obtain $E_r = -ikA_1 r/2$. The transverse force F thus becomes $F = eE_r = -iekE_z r/2$. We can express κ as

$$\kappa = \left(\frac{eke_z}{c^2 ek_p m_e}\right)^{1/2} \frac{k_B T}{E_z^{1/2}}. \tag{11}$$

Substituting the result in eq.(9), we find that the emittance is inverse-proportional to the square root of E_z,

$$\epsilon = \left(\frac{2}{c^2 ek_p m_e}\right)^{1/2} \frac{k_B T}{E_z^{1/2}}. \tag{12}$$

In the case of a silver tube with $k_p a = 10$, this becomes

$$\epsilon = \frac{4.61 \times 10^{-7} \times k_B T[\mathrm{eV}]}{(\mathrm{E_z[eV]})^{1/2}}.$$

If E_z=45GeV/m and $k_B T$ =1keV, we have ϵ =2.1nm.A carbon-nanotube electron source will provide source beams for this linac.[23] Such beams with nanometer emittances will contribute to further investigation, manufacture and measurement in the nanometer range.

Acceleration of ions in the plasmon linac is more difficult than acceleration of electrons. Certainly, Fig. 4(b) tells that plasmons can interact with beams with a slow phase velocity, and we can even calculate the acceleration gradient based on Fig. 5(b). We, however, have no practical way to excite the plasmons by lasers with $v_p = c$. The present trend of low-dimensional wave generation is not to transfer them from outside but to excite them directly in a fluorescent material. It is reported that a high k wave is experimentally excited in two-dimensional geometry.[16] However, this method may not excite waves with power high enough for the particle acceleration.

4. CONCLUSION

Use of photonic band-gap crystals and holes in a metal in accelerators is discussed, which have sizes around the wavelength of lasers. The photonic band-gap crystal can guide laser pulses over a Rayleigh length to lengthen acceleration length of a laser-plasma accelerator. The fine hole in a metal holds plasmons on the inner wall, whose electric fields can accelerate charged particles. A plasmon linac, a linac based on this principle, can realize an emittance on the order of nm. A light wave in the photonic crystals have slow group velocity, while a plasmon has slow phase velocity. Such properties could be useful in acceleration of heavy particles, though further studies are necessary.

References

1. T. Tajima and M. Cavenago, Phys. Rev. Lett. 59 (1987) 1440.
2. P. Chen and R. J. Noble, in R. A. Calligan, Jr and J. A. Ellison (eds.), Relativistic Channeling, Plenum, New York, 1987, p517.
3. E. Yablonovitch and T. M. Gmitter, Phys. Rev. Lett. 58 (1987) 2059.
4. J. Takahara and T. Kobayashi, Opt. Lett. 22 (1997) 475.
5. M. A. Shapiro et al., Phy. Rev. St Accel. Beams 4 (2001) 042001.
6. X. E. Lin, Phy. Rev. St Accel. Beams 4 (2001) 051301.
7. S. Yamaguchi, J. -I. Inoue and K. Ohtaka, Phys. Rev.B66 (2002) 085209.
8. N. Saito and A. Ogata, J. Plasma Fusion Res. 78 (2002) 613.
9. T. Ishimaru, private communication.
10. S. G. Johnson and J. D. Joannopoulos, Optics Express 8 (2001) 173.
11. A. Meksis et al., Phys. Rev. Lett. 77 (1996) 3787.
12. S. Noda et al., J. Lightwave Technol. 17 (1999) 1948.
13. A. Ogata and K. Nakajima, Laser Part. Beams 16 (1998) 381.
14. N. E. Andreev et al., Phys. Plasmas, 4 (1997) 1145.
15. K. Inoue et al., Phys. Rev. B65 (2002) 121308.
16. J. Takahara and T. Kobayashi, in S. Kawata, M. Ohtsu and M. Irie, eds., "Near Field Nano Optics" (Springer, in press).
17. T. C. Cuiou, T. Katsouleas and W. B. Mori, Phys. Plasmas 3 (1996) 1700.
18. S. Frankel, J. Appl. Phys. 18 (1947) 650.
19. J. A. Stratton, "Electromagnetic Theory" (McGraw-Hill, 1941).
20. Y. Carmel et al., Phys. Rev. Lett. 69 (1992) 1652.
21. D. R. Lide and F. P. R. Frederikse, eds., "CRC Handbook of Chemistry and Physics" 75th ed. (1994-1995), CRC Press, p12-40.
22. M. Reiser, "Theory and Design of Charger Particle Beams", (1994), Weiley.
23. Y. Saito and S. Uemura, Carbon 38 (2000) 169.

OBSERVATIONS ON BUNCHED CRYSTALLINE BEAMS

U. SCHRAMM, M. BUSSMANN, T. SCHÄTZ [*], D. HABS
Sektion Physik, Ludwig-Maximilians-Universität München, Germany
E-mail: ulrich.schramm@physik.uni-muenchen.de
http://www.ha.physik.uni-muenchen.de/uschramm/

Recently, crystalline ion beams have been realized and systematically studied in the table-top rf quadrupole storage ring PALLAS by means of laser cooling. Here, the phase transition of a longitudinally modulated, bunched ion beam in the regime of a linear string of ions is followed monitoring the full spatial distribution of the ion bunch. Structural transitions are investigated as a function of the ratio of the transverse to the longitudinal confinement strength. Surprisingly, the length of crystalline ion bunches was found to be shorter by a factor of up to three with respect to dedicated models, considerably increasing the luminosity of such beams.

1. Introduction - Crystalline Ion Beams

The phase transition of an ion beam to the Coulomb-ordered "crystalline" state, the state of ultimate brilliance and stability, can occur when the mutual Coulomb-energy of stored ions overcomes their mean kinetic energy by about two orders of magnitude [1,2,3]. As typical inter-ion distances of stored singly charged ions amount to of the order of $10\,\mu$m, beam temperatures in the range of mK are required to fulfill this condition.

The first experimental evidence of this phase transition was recently observed at the table-top storage ring PALLAS with a laser cooled beam of low-energy $^{24}Mg^{+}$ ions [4]. Meanwhile, PALLAS has been used as a model system for synchrotron storage rings mapping the focusing parameters required to attain and maintain crystalline ion beams [4,5,6] and for the detailed investigation of heating mechanisms specific to crystalline beams. These result from envelope modulations due to the strong focusing [5], from bending shear when the beam is cooled to constant linear velocity, but also from longitudinal laser cooling itself due to the inevitable random scattering of photons [7].

[*] New address: NIST Boulder, CO, USA

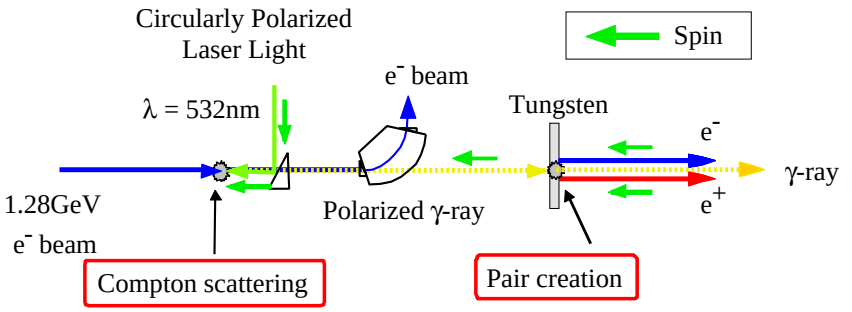

Figure 1. Sketch of the rf quadrupole storage ring PALLAS. Four ring electrodes enclose the ion orbit in quadrupole geometry. For the storage of $^{24}Mg^{+}$ ion beams voltages between $U_{rf} = 150$ and 450 V are applied at a fixed radio frequency of $\Omega = 2\pi \times 6.3$ MHz. Additionally, sixteen segmented drift tubes are distributed around the ring. The accented tubes are used to localize ions in the laser cooling section during loading, for taking images of stationary ion crystals, or to bunch an ion beam. The scheme for the measurement of the longitudinal spatial ion distribution of bunched beams is indicated, details are explained later in the text.

Here, we focus on systematic measurements on bunched crystalline ion beams in PALLAS [8,9], where the ion current is additionally modulated by a harmonic pseudo-potential in the co-moving system, the so-called "bucket" potential, thereby splitting and compressing the beam into short "bunches". On the one hand, this technique offers further control over the longitudinal phase space. Except for the collective motion of the ions in the beam, the situation is equivalent to the situation commonly found in linear Paul traps. Yet, the length of the bunches can be considerably larger as compared to the typical situation of a stationary ion crystal in a linear Paul trap, challenging theoretical models as will be discussed. On the other hand, laser cooling of bunched beams facilitates the cooling of high energy ion beams [10,11], as discussed in the outlook.

2. Experimental Techniques - the PALLAS Storage Ring

In the table-top storage ring PALLAS [4,5,6,12] ion beams are guided on a closed orbit of circumference $C = 2\pi \times 57.5$ mm by the circular quadrupole electrode structure sketched in Fig. 1. Similar to the more common case of strong magnetic focusing in large-scale storage rings, an electric quadrupole field alternating at the radio-frequency Ω results in a bound transverse motion of the particles at the secular or betatron frequency ω_{sec}. In terms of the stability parameter $q = 2eU_{rf}/(m\Omega^2 r_0^2)$ of the underlying Mathieu

differential equation [13], this frequency amounts to $\omega_{sec} = q\Omega/\sqrt{8}$, where e and m stand for the charge and mass of the stored ion, U_{rf} for the voltage applied between the quadrupole electrodes, and $r_0 = 2.5\,\mathrm{mm}$ for the aperture radius.

After the loading of the ring with a cloud of $^{24}Mg^+$ ions, the resonant light pressure of the co-propagating laser beam, addressing the Doppler-shifted optical $3s^2S_{1/2} - 3p^2P_{3/2}$ transition of the $^{24}Mg^+$ ion, is used for the acceleration of the stored ions [4,5,7]. The frequency of this laser beam $\omega_1(t)$ is continuously increased, while the frequency of a second counter-propagating laser beam ω_2 is maintained at a constant detuning that determines the final beam velocity to $v \approx 2600\,\mathrm{m/s}$, typically. The longitudinal velocity spread of the ion beam is efficiently reduced by the friction force that results from the combination of both accelerating and decelerating laser forces, sketched in the right graph of Fig. 2. Providing sufficient confinement, the transverse ion motion can be coupled to the longitudinal and thus be indirectly cooled. This point turned out to be delicate [4,5,7] as dissipative hard Coulomb-collisions are strongly suppressed in the crystalline state [14,15], where ions reside on well-separated lattice positions. The resonance fluorescence is recorded either with a fast photo-multiplier or imaged with an intensified CCD video camera. From the latter images time averaged vertical beam profiles can be deduced with a spatial resolution of $\sigma^{res} \approx 5\,\mu\mathrm{m}$.

For the bunching of the ion beam [8,9], discussed in more detail, a small alternating voltage $U_0\,\cos(2\pi\nu_b t)$ that is tuned to a harmonic h of the revolution frequency

$$\nu_b = h\nu_{ref} = hv/C \tag{1}$$

is applied to one of the 16 drift tubes sketched in Fig. 1. In the co-moving frame, the ions experience a position dependent longitudinal force, depicted in the upper graph of Fig. 2. The corresponding longitudinal pseudo-potential, the bucket, can be characterized by the synchrotron frequency

$$\nu_{syn} = \sqrt{\frac{eU_b\,h}{2\pi C^2\,m}}\quad , \tag{2}$$

or directly by its velocity acceptance $\Delta v_{sep} = 2v\nu_{syn}/\nu_b$. Here, eU_b amounts to the maximum energy change per passage of an ion through a drift tube of length $L = 22\,\mathrm{mm}$

$$eU_b = 2eU_0\,\sin\left(\frac{\pi hL}{C}\right)\quad . \tag{3}$$

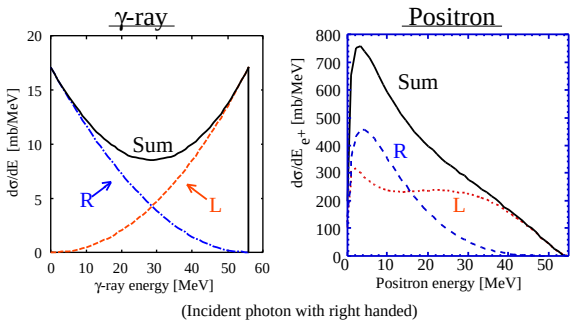

Figure 2. Illustration of the motion of a single ion in the bucket (co-moving frame). The ion experiences the velocity dependent accelerating force of the co-propagating laser beam and the position dependent restoring force of the bucket, as indicated in the right and the upper graph, respectively. The sample phase space trajectory starts 25 m/s below the synchronous velocity $v_s = C\nu_b/h$ and the force of the scanning co-propagating laser beam first damps, then inhibits (over-damps), and finally drives the synchrotron oscillation of the ion. Note, that for the overdamped case, which represents optimum cooling, the ions are shifted out of the bucket center as a consequence of the required equilibrium of forces. For technical reasons, the decelerating force of the second counter-propagating laser beam (dashed line), acting on ions with a velocity slightly above the synchronous velocity, is used for long-term cooling.

This energy change does not lead to a considerable displacement of an ion from its lattice position in a string, although the multiple passage in phase leads to the bunching of the beam.

As illustrated in Fig. 2, the synchrotron oscillation of a singe particle in the bucket can be efficiently damped by the velocity dependent force of only one laser beam [10,11,8], counteracted by the restoring force of the bucket. A stable over-damped situation at $v = v_s$ is achieved when the decelerating force of the counter-propagating laser beam (dashed line in Fig. 2) is tuned into resonance with a velocity class slightly above the synchronous velocity v_s. The decelerating laser force at v_s is then compensated by the restoring pseudo-force (accelerating phase) of the bucket which leads to a shift of the ion out of the bucket center. A modification of the longitudinal cooling strength can thus be achieved by a fine-tuning of the bunching frequency.

From the measurement of the ion fluorescence signal in coincidence with the bunching frequency, the longitudinal shape [16] of bunched laser-cooled ion beams can be deduced [9], as demonstrated in Fig. 1.

3. Crystallization of Bunched Beams

The common emittance dominated (gaseous) state of a cold bunched ion beam can be described by Gaussian distributions in the longitudinal and in the transverse directions. From the width of the spatial profiles, depicted in Fig. 3 ($\sigma_\parallel \approx 4\,\mathrm{mm}$, $\sigma_\perp = ((\sigma^c)^2 - (\sigma^{res})^2)^{1/2} = 8.8\,\mu\mathrm{m}$), the following beam temperatures can be deduced (k denoting the Boltzmann constant)

$$\begin{aligned} T_\parallel &= m\omega_{syn}^2\sigma_\parallel^2/k \approx 1.5\,\mathrm{K} \\ T_\perp &= m\omega_{sec}^2\sigma_\perp^2/(2k) = 2.2\,\mathrm{K} \quad . \end{aligned} \tag{4}$$

The transverse narrowness of this cold bunched beam indicates that, in contrast to the case of non-crystalline coasting beams, where the motion in the transverse and the longitudinal degrees of freedom was found to be strongly decoupled [4,5], presumably non-linear effects in the bunching increase the coupling and thus the overall cooling efficiency [9].

A gradual increase of the cooling rate leads to a significant change in the shape of the longitudinal profile from a broad Gaussian to an inverse parabola, characteristic of the space-charge dominated (cold fluid as well as crystalline) regime. In this regime, the repulsive space-charge force and the harmonic confining forces of the bucket and the storage ring are balanced at constant volume charge density n_0 [17]. The shape of the bunch is not determined by its temperature anymore. However, this distinct change in the longitudinal profile of this specific sample beam is only accompanied by a small change in the transverse ($T_\perp = 1.5\,\mathrm{K}$).

The latter temperatures correspond to a value of the plasma parameter, basically the ratio of the mutual Coulomb-energy of ions to their thermal energy kT, of

$$\Gamma_p = \frac{1}{4\pi\varepsilon_0}\,\frac{e^2}{a_{ws}}\,\frac{1}{kT} \approx 1 \tag{5}$$

where

$$a_{ws} = \left(\frac{3}{4\pi n_0}\right)^{1/3} = \left(\frac{1}{4\pi\varepsilon_0}\,\frac{3e^2}{2m\omega_{sec}^2}\right)^{1/3} \quad , \tag{6}$$

the Wigner-Seitz radius, is used as a measure of the inter-ion distance to account for the strength of the transverse confinement [18]. The value of $\Gamma_p \approx 1$ is consistent with the observed shape and should justify the description of the bunch as a cold fluid [17] as long as correlations between the ions remain negligible.

Similar to the case of coasting beams [5], the phase transition to the crystalline state (uppermost curve [19] in Fig. 3) is identified by a sudden

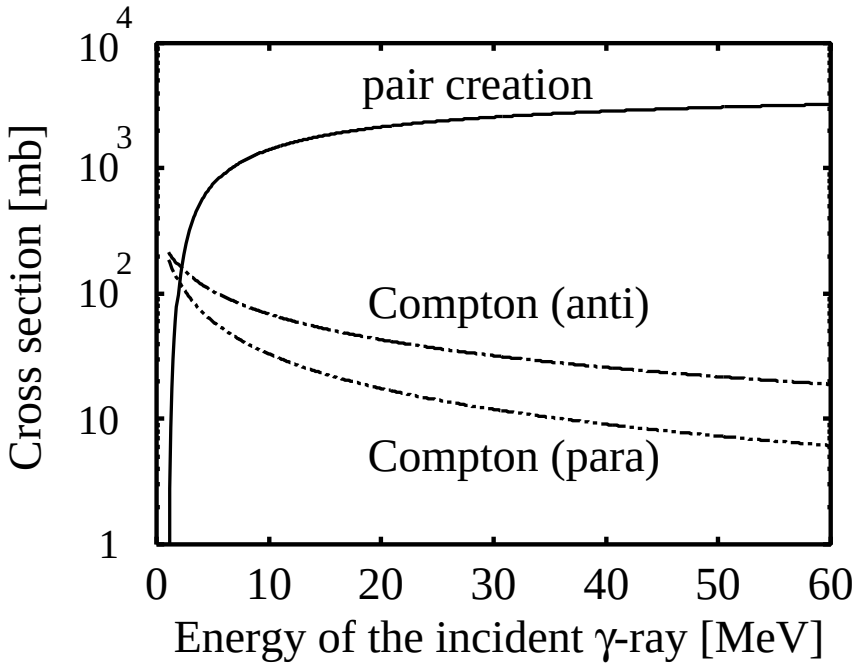

Figure 3. Left: Longitudinal spatial profiles of the sample ion beam, presented in Fig. 1. With increasing cooling strength, achieved by rising the bunching frequency ν_b or, in other words, reducing the velocity detuning Δv as explained in the text and in Fig. 2, the profile changes from a broad Gaussian ($l_b \approx 11.5\,\mathrm{mm}$ FWHM) to a sharp inverse parabola. During the crystallization (from the middle to the upper black curve) the length of the bunch again increases from $l_b = 3.7 \rightarrow 5.3\,\mathrm{mm}$. All curves are vertically displaced for a better visibility. Right: Vertical beam profiles corresponding to the three situations mentioned above (black curves). The width of the uppermost profile corresponds to the formation of a linear string of ions.

reduction of the width of the transverse beam profile to the (resolution limited) width of a string of ions [4,8]. The structural formation of the string is confirmed when the value of the dimensionless linear density $\lambda(z) = N(z)/\Delta z \times a_{ws}$ remains below the threshold value [18] of 0.71.

The bunching compresses the linear ion density of this crystalline beam by a factor of about 11. This compression is directly visible in Fig. 1, and, though favorable, surprisingly high, as discussed in the next section. Yet, for the given particle number of $N_b = N/h = 500$, it only leads to an average [20] linear density of $\bar{\lambda} = N_b/(\sqrt{2} l_b) \times a_{ws} = 0.5 < 0.71$.

The fact that the non-crystalline but space-charge dominated beam (at

$\Delta v = -3\,\mathrm{m/s}$ in Fig. 3) was observed to be another factor of 2/3 shorter may be qualitatively explained by the onset of Coulomb-ordering into a disc-like distribution of the ions. Subjected to strong direct longitudinal laser cooling the ions experience the diffusive transverse heating due to the random scattering of the laser photons [19,7] that cannot be fully compensated by the indirect transverse cooling. The effective longitudinal inter-ion distance increases when the transverse localization of the ions on axis is reduced compared to the fully ordered string. The bunch can be further compressed.

4. Shape and Structure of Bunched Crystalline Beams

The anisotropy of the confining harmonic well is characterized by the ratio $\beta = \omega_\perp^2/\omega_\parallel^2 = \omega_{sec}^2/\omega_{syn}^2$. Though in the range of $\beta \approx 1...25$ the shape of three-dimensional ion crystals, characterized by the aspect ratio $\alpha^* = l_b/(2\sigma)$ of the resulting prolate spheroid, can be calculated with high accuracy [17,21], the situation turns out to be more complicated for large values of β. For the extreme case of a one-dimensional (1D) Coulomb-string, where the length should intuitively not depend on the strength of the transverse confinement, both mean-field (repulsive) and correlation energy ('attractive' in the sense that the sum is less repulsive) are of the same order and thus the pure mean-field (cold fluid) description, implying constant volume density, becomes inadequate [22]. The inter-ion spacing varies with the position of the ions in the string [22,24,25] especially for short strings or close to their ends, as illustrated by the image of a stationary ion crystal that will be presented in Fig. 5.

Two different models are compared with the experimental results. In both models, the linear ion density is well described by the observed inverse parabola and thus the analysis of its length is sufficient. For the full length of a crystalline string of ions $L_b = \sqrt{2}\,l_b$, Dubin [22] derived

$$L_{Dubin} \approx \left[\left(\ln(6N_b) + \gamma - \frac{7}{2}\right) 12 N_b \frac{e}{\epsilon_0}\frac{R^2}{U_b h}\right]^{\frac{1}{3}}, \qquad (7)$$

where $\gamma = 0.577$ denotes Euler's constant and parameters are adopted to the conditions at the storage ring PALLAS. This approach takes into account the ordering of the ions, but the determination of the correlation energy is still related to the cold fluid model. Equation 7 then results from minimizing the total energy with respect to L_b. It comes out to be almost identical to the 1D limit of the cold fluid approach [22]. It agrees with related MD simulations [23] and direct calculations of few-ion strings [24]

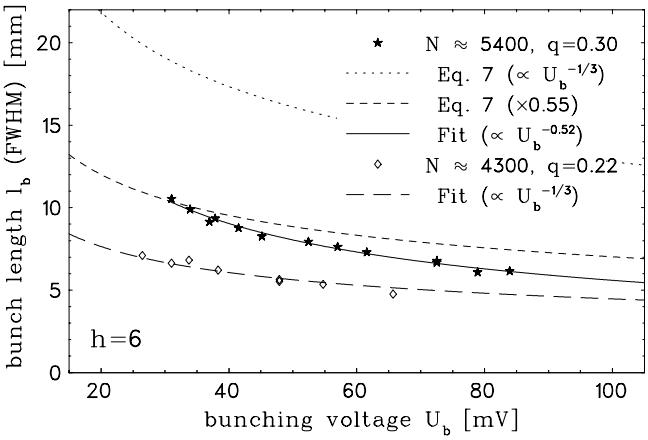

Figure 4. Dependence of the bunch length l_b of crystalline (filled stars) and hot, non space-charge dominated (open rhombs) ion beams on the bunching voltage U_b. For the crystalline bunch, the measured length not only deviates from the theoretical expectation (dotted line) by a factor of 0.55, but also shows a stronger dependence on U_b. However, the length of the non-crystalline bunch scales $\propto U_b^{1/3}$ as expected.

and describes the length of short few-ion strings in PALLAS [25] and other experiments. Yet, it fails to describe the length of the elongated crystalline bunches observed in PALLAS by about a factor of up to three, which is illustrated by the ratio of the dotted (Eq. 7) and the dashed line (Eq. 7 scaled by a factor of 0.55 to fit the first data point) in Fig. 4.

This fact becomes more evident when Eq. 7 is compared with the result of a straight-forward calculation of the length of a space-charge dominated bunch, treated as a charged cylinder of edge radius 2σ inside a conducting beam pipe of radius r_0, which has originally been used by Ellison et al. to describe the length of electron cooled ion bunches [26,10,9]

$$L_{Ellison} = \left[\ln\left(\frac{r_0}{2\sigma}\right) 12 N_b \frac{e}{\epsilon_0} \frac{R^2}{U_b h} \right]^{\frac{1}{3}} . \qquad (8)$$

Though based on completely different approaches, both equations give about equal results for N_b of the order of 1000.

The decreasing of the bunch lengths with increasing bunching voltages is analyzed in Fig. 4. Besides the obvious discrepancy between the models presented and the measurements concerning the absolute value of the bunch length, also the dependence on the confinement strength (solid line in Fig. 4) considerably deviates from the expected (dashed line). For any Coulomb-

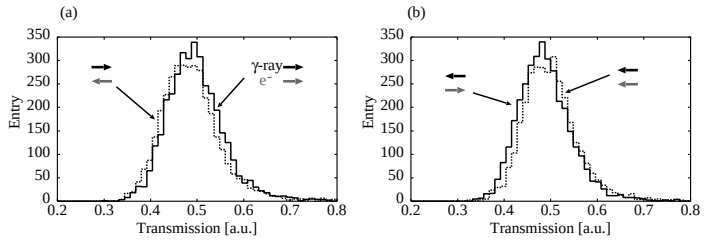

Figure 5. Fluorescence image of a stationary ion crystal of length $L_b \approx 1.5\,\mathrm{mm}$ taken in the storage ring PALLAS. Illustrating the presently unresolvable structure of an ion bunch, the spatial dependence of the ion density in the outer wings and the rather constant linear density and radius in the center, where the zig-zag structure is fully developed, are discernible. The "digital" appearance of $1/d$ in the lower graph is due to the finite pixel size (approximate inter-ion distance ≈ 7 pixel) of the CCD chip.

system confined in 3D in an anisotropic harmonic well the length of the crystalline bunch should scale as $l_b \propto U_b^{-1/3}$. The much faster shortening (close to $l_b \propto U_b^{-1/2}$) could be explainable with an augmenting structural transition of the string into a 2D zig-zag, specially as the peak linear density [20] of the first data point at $U_b = 31\,\mathrm{mV}$ already amounts to $\lambda_p = 0.72$. The structure of the elongated bunched beam might gradually extend into the transverse plane and thus shorten faster than expected for the pure string before finally a dominant zig-zag structure is formed in the central region. This final situation is illustrated in Fig. 5 with the image of a stationary ion crystal stored in PALLAS ($N_b = 110 \ll 900$), that contains a large fraction of the ions at a rather constant linear density of $\lambda_{zz} = 0.93$.

This structural transition of the bunched crystalline beam can be followed in more detail in Fig. 6. The data points in this figure correspond to different combinations of the transverse (U_{rf}) and the longitudinal (U_b) confinement strength which had to be carefully chosen to attain and maintain the crystalline state. Previous systematic studies of the transverse beam size of different crystal structures for coasting beams [5,7] allow for for the distinguishing of three structural regimes, string, zigzag and helix, although the transverse beam size has to be reconstructed from a time averaged picture. Again, the assumption of a gradual evolution of a zig-zag structure in the center of a dominant ion string is consistent with the measurement, starting from the upper right data point. Moreover, a distinct structural transition to a dominant zig-zag structure, identified by a sudden broadening of the width of the beam, was observed [25] at $\bar{\lambda} = 0.83$, similar to the situation in the stationary crystal.

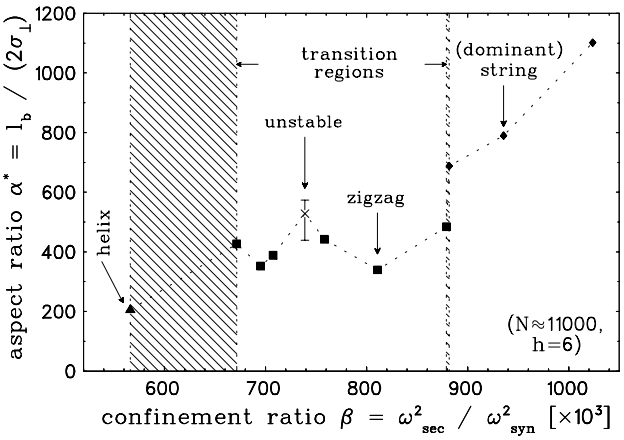

Figure 6. Mapping of the structural transition of a sample bunched crystalline ion beam as a function of the anisotropy parameter of the confining potential and the resulting aspect ratio of the ion crystal. The structure is identified by means of the transverse profiles as explained in the text. The dashed line is meant to guide the eye.

5. Conclusion and Future Prospects of Crystalline Beams

The question now arises how these elongated crystalline ion bunches can be properly described. Their central part behaves similar to an infinite system, where the constant inter-ion distance on axis [18] is given by $d_\parallel(z) = a_{ws}/\lambda(z)$. Moreover, the peak linear density seems to be always close to the threshold value above which a structural transition should occur. In other words, the length l_b of a bunched ion string can be approximated surprisingly well by $N_b \times a_{ws}/0.71$. This observation cannot be fully explained at the moment and will be further investigated at PALLAS.

More generally, bunched beam laser cooling will be the method of choice for the anticipated attainment of dense crystalline ion strings at relativistic energies. The huge Doppler-shift associated with these energies only allows for counter-propagating laser and ion beams and thus the restoring force of the bucket is required to counteract the laser force. Furthermore, the longitudinal confinement prevents complete ion losses from the narrow-band cooling process due to hard Coulomb-collisions. After such a collision, ions circulate in the bucket and are recycled into the laser cooling process. A test experiment is currently prepared for the ESR of GSI, where a beam of Li-like C^{3+} ions at a velocity of $v/c = 0.47$ will be subjected to a combination of transverse electron and longitudinal laser cooling [6]. With the operation of larger heavy ion synchrotrons (SIS 300 at GSI), laser cooling of Li-like

ions of the order of uranium becomes possible with fascinating possibilities for the forward scattering of laser light into the keV range. On the other hand, the application of refined cooling techniques could strongly enhance the luminosity of radioactive beam colliders, presently under discussion.

Acknowledgments

This work has been supported by the DFG (HA1101/8) and the MLL. We acknowledge fruitful discussions with P. Kienle and J.P. Schiffer and generous technical support by R. Neugart.

References

1. J.P. Schiffer, P., Kienle, Z. Phys. A **321**, 181 (1985), and A. Rahman, J.P. Schiffer, Phys. Rev. Lett. **57**, 1133 (1986).
2. D. Habs, R. Grimm, Ann. Rev. Nucl. Part. Sci., **45**, 391 (1995).
3. D.M. Maletic, A.G. Ruggiero, (Editors.), "Crystalline Beams and related issues" (World Scientific, Singapore 1996).
4. T. Schätz, et al., Nature **412**, 717 (2001).
5. U. Schramm, et al., Phys. Rev. **E 66**, 036501 (2002).
6. U. Schramm, et al., Plasma Physics and Controlled Fusion **44**, B375 (2002).
7. U. Schramm, et al., J. Phys. **B 36**, 561 (2003).
8. U. Schramm, et al., Phys. Rev. Lett. **87**, 184801 (2001).
9. U. Schramm, et al., Physics Scripta (at press 2003).
10. J.S. Hangst, et al., Phys. Rev. Lett. **74**, 4432 (1995).
11. H.-J. Miesner, et al., Nucl. Instr. Meth. **A 383**, Letter to the Editor, 634 (1996), and U. Eisenbarth, et al., Nucl. Instr. and Meth. **A 441**, 209 (2000).
12. T. Schätz, et al., Applied Physics **B 76**, 183 (2003).
13. P.G. Gosh, "Ion Traps", (Clarendon Press, Oxford 1995).
14. M. Seurer, et al., Hyperfine Interactions **99**, 253 (1996), Q. Spreiter, et al., Nucl. Instr. Meth. **A 364**, 239 (1995).
15. J. Wei, et al., Phys. Rev. Lett. **80**, 2606 (1998).
16. Note, that (although favorable) a stroboscopic observation of the ion crystal cannot be realized at present [25].
17. L. Turner, Phys. Fluids **30**, 3196 (1987), and D. H. E. Dubin, Phys. Rev. **E**, 5268 (1996), and refs. therein.
18. Hasse, R.W., Schiffer, J.P., Annals of Phys. **203**, 419 (1990).
19. Here, the phase-transition of the longitudinally cold ensemble was observed after a slight reduction of the cooling rate which reduced the amount of diffusive transverse heating associated with the scattering of photons [7].
20. The peak linear density amounts to $1.5 \times \bar{\lambda}$ (parabolic profile).
21. M. Drewsen, et al., Phys. Rev. Lett. **81**, 2878 (1998).
22. D.H.E. Dubin, Phys. Rev. Lett. **71**, 2753 (1993), Phys. Rev. **E 55**. 4017 (1997).
23. J.P. Schiffer, Phys. Rev. Lett. **70**, 818 (1993).

24. D.F.V. James, Appl. Phys. **B 66**, 181 (1998).
25. M. Bussmann, et al., J. Phys. **A**, (in press 5/2003).
26. T.J.P. Ellison, et al., Phys. Rev. Lett. **70**, 790 (1993).

APPROACH TO ULTRA COLD BEAM AT LSR, KYOTO UNIVERSITY *

A. NODA, H. FADIL, M. IKEGAMI, Y. IWASHITA, T. SHIRAI, H. TONGU

Institute for Chemical Research, Kyoto University.
Gokano-sho, Uji-city
611-0011,Kyoto, Japan
E-mail: noda@kyticr.kuicr.kyoto-u.ac.jp

K. NODA, S.SHIBIYA, T. TAKEUCHI

National Institute of Radiological Sciences.
4-9-1Anagawa, Inage-ku, Chiba-city,263-8555, Chiba, Japan
E-mail: koji_noda@nirs.go.jp

Laser equipped Storage Ring (LSR) with the circumference and radius of curvature of 22.197 m and 1.05 m, respectively is now under construction. The ring has six-fold symmetry and satisfies the so-called maintenance condition. Experimental approach to 3-D laser cooling for $^{24}Mg^{+}$ is planned together with the studies of 1-D string by the electron beam cooling of highly charged ion beam.

1. Introduction

Ordering of high-energy ion beam circulating in a ring has been claimed for proton beam with kinetic energy of 65 MeV for the first time by the electron beam cooling at NAP-M in Budker Institute for Nuclear Physics at Novosibirsk [1]. The momentum spread of the cooled beam is reported to suddenly jump into a certain small level when the number of the circulating beam is reduced to a certain level. Recently similar phenomena are reported for highly charged ion beam by experiments utilizing ESR and SIS at GSI, Darmstadt, Germany [2] and CRYRING at Man Siegbahn Laboratory, Stockholm University, Sweden [3]

At Institute for Chemical Research, Kyoto University, an ion storage/cooler ring, LSR (Laser equipped Storage Ring) is now under construction for the purpose of compact accelerator development for charged-particle cancer-therapy, which aims at quantitative experimental studies of beam cooling for hot beam (beam with rather wide energy spread) peculiar to laser-produced ion beam [4].

* The work presented here is supported by the funds of Advanced Compact Accelerator Research Project of Ministry of Education, Sports, Culture, Science and Technology of Japan.

LSR is also to be utilized for the purpose of fundamental physics studies, one of which is the pursuit of 1-dimensional string of highly charged ion beam above mentioned with use of the electron beam cooling. The other is 3-dimensional laser cooling proposed by H. Okamoto and others [5]. For such purpose, LSR lattice is designed to have a rather higher super periodicity as 6 [6]. In the present paper, the LSR project is reviewed briefly at first and then proposed electron beam cooling and laser cooling systems are described together with present status and future time-schedule of the project.

2. LSR Project

LSR is a storage/cooler ring to show feasibility of matching the characteristics of laser produced ion beam with the rather limited momentum acceptance of a pulse synchrotron [7]. Laser produced carbon ions with rather wide energy spread is rotated in a longitudinal phase space by an RF electric field phase locked with the pulse laser and then injected into LSR and cooled down another one order of magnitude in energy spread by an electron beam cooling [4]. As it aims at the realization of compact accelerator for cancer therapy, compact size is the item to be pursued and its circumference and radius of curvature are taken to be 22.197 m and 1.05 m, respectively. Main parameters of LSR are given in table 1.

In order to suppress the envelope instability, it is desirable to use the phase

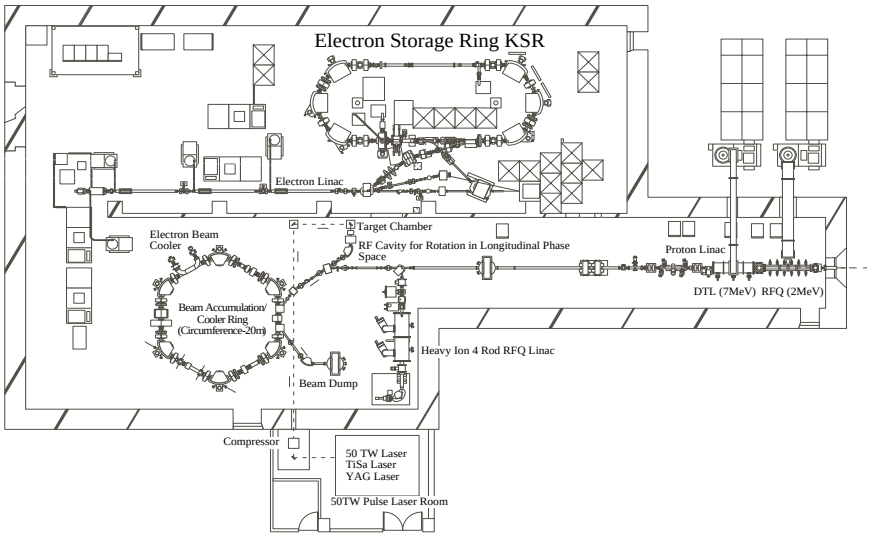

Fig. 1 Layout of LSR

Table 1. Parameter List of LSR

Ion Species	H^+, $^{12}C^{6+}$, $^{24}Mg^+$
Energy	7 MeV (2MeV), 2MeV/u, 35 keV
Radius of Curvature	1.05 m
Circumference	22.7 m
Super periodicity	6

advance of betatron oscillation per cell smaller than 90° and operation point for beam crystallization mode is chosen at (1.43, 1.42). For the purpose of reducing the stop-band width of lower order resonances, the dipole and quadrupole magnets of LSR are carefully designed and fabricated making emphasis on suppression of nonlinear components. In Fig. 2, the overall design of the dipole magnet (a), fabricated coil combining usual winding and saddle shape winding to avoid the saturation in the field clamp with a limited coil space (b), the shape of iron core used for 3-D calculation by TOSCA (c) and obtained magnetic field distribution by calculation for higher and lower magnetic fields (d) are given.

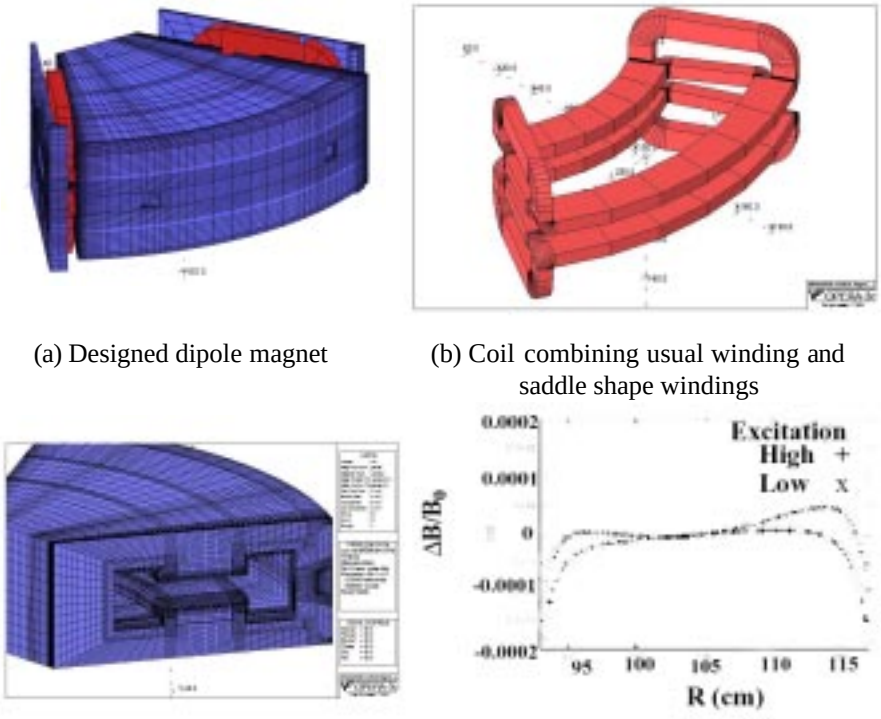

(a) Designed dipole magnet

(b) Coil combining usual winding and saddle shape windings

(c) Shape of the iron core

(d) Calculated magnetic field distribution

Fig.2 Dipole magnet of LSR

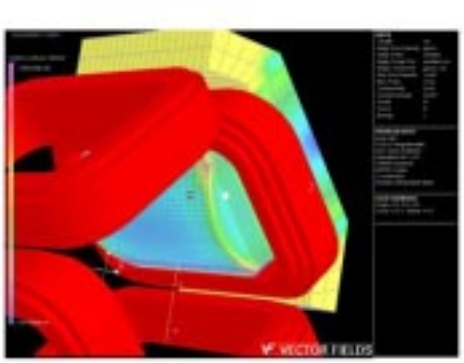

(a) Coils attached to the iron pole

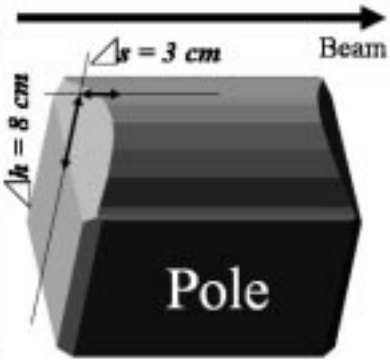

(b) End cut shape of the iron pole

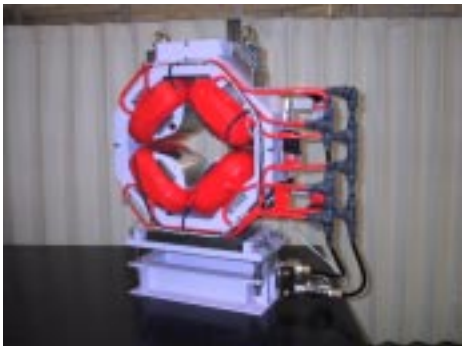

(c) Overall view of the fabricated magnet

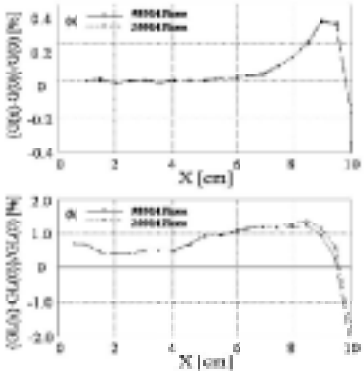

(d) Calculated distribution of field gradient

Fig.3 Quadrupole magnet of LSR

The coils attached to the iron poles of the lattice quadrupole magnet are illustrated in Fig.3 (a). The end cut shape of the iron pole is given in Fig.3 (b). An overall view of the fabricated quadrupole magnet and calculated deviation of field gradient (central and integrated along the beam direction) are shown in Fig.3 (c) and (d), respectively. As is known from these figures, the nonlinear components are expected to be well suppressed by the computer-aided design. It is expected by such characteristics of the ring lattice magnets free from nonlinear components, LSR will provide us an ideal playground for beam physics mainly related beam cooling and crystallization. Real achieved characteristics are to be evaluated by field measurements from now on.

The main obstacle against the 3-D beam crystallization for the case of storage ring, where ion beam is circulating rapidly, is the shearing force caused by dipole magnets in the lattice. Recently, we noticed the fact that the

dispersion caused by the dipole magnet could be compensated if the electric field with certain strength to deflect ions to opposite direction is superposed [8]. It is expected that appropriate condition for 3-dimensional beam crystallization will be possible with such compensation, which is to be studied in detail by computer simulation including space charge forces from now on.

3. Electron Beam Cooling

An electron beam cooling is to be applied for laser-produced $^{12}C^{6+}$ beam with the kinetic energy of 2MeV/u. The energy spread of ±1% after phase rotation is to be reduced to $\pm 0.1\%$ with this method. By the requirements of compactness and high super periodicity as 6, the length of long straight section is limited as 1.8m and installation of the electron cooler into this limited size is the hard technical challenge, which is inevitable item for compact accelerator development. In table 2, main parameters of the electron cooler of LSR are listed up.

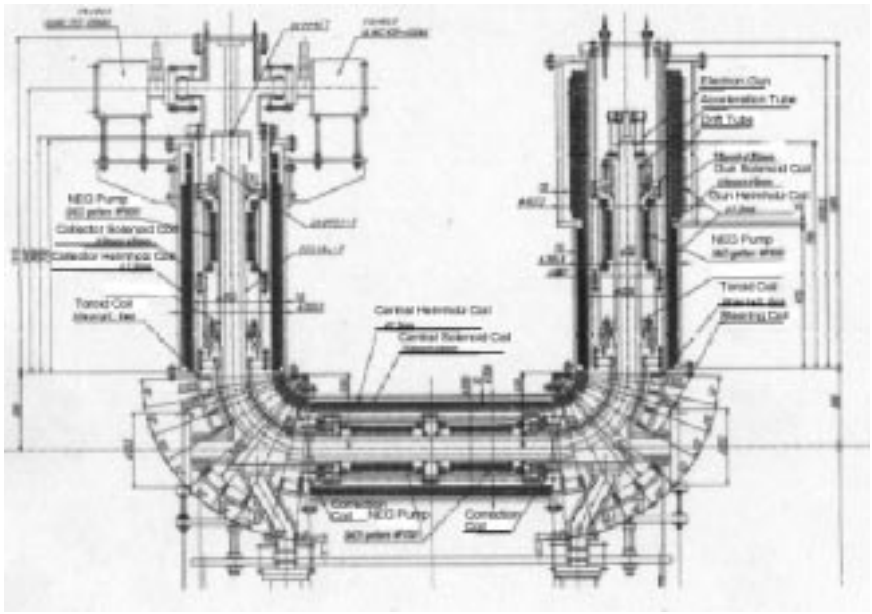

Fig. 4 Electron Cooler of LSR now under design study

As the cooling force of the electron cooling is efficient only in the limited region $\sim \pm 0.1\%$ of energy spread as shown in Fig. 5, cooling time for such a hot ion beam as has energy spread of ±1% becomes long usually [9]. In order to improve this situation, we have proposed the possibility of energy sweep with use of an induction accelerator illustrated in Fig. 6. This scheme is tested with use of TSR at Max-Planck-Institut für Kernphysik, Heldelberg and cooling time of 2.8 sec without induction voltage is f reduced to 0.6 sec by application of induction voltage of 0.4 V (maximum value applicable at TSR). The scheme of electron energy sweep is also studied at TSR. The cooling time is found to be reduced to 0.35 sec for small horizontal size beam (8mm), while it increases to ~0.8 sec for larger horizontal size beam

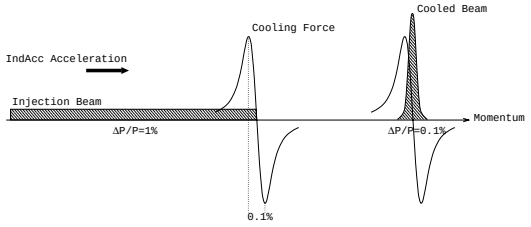

(a) Scheme with induction accelerator

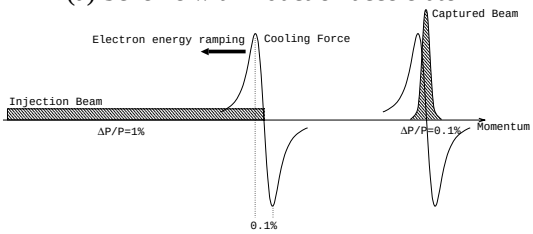

(b) Scheme with electron energy sweep

Fig. 5 Cooling force of the electron cooling

Table 2 Main Parameters of LSR Electron Cooler

Ion Species	$^{12}C^{6+}$
Ion Energy	2MeV/u
Electron Energy	1.2 keV (Max.3 keV)
Solenoid Field	500 G
Electron Current	200 mA (Max)
Length of Central Solenoid	0.8 m
Troid Radius	250 mm

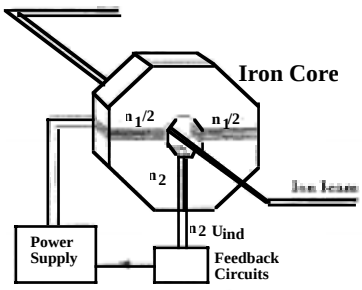

Fig. 6 Induction accelerator

(16mm) [10]. In these measurements, vertical size of the beam is left to be small (a few mm). Real evaluation of the cooling time with large transverse temperature both in horizontal and vertical directions together with wide momentum spread is left to be performed at LSR.

Possibility of making experiments on one-dimensional string by application of the electron cooling to the highly charged heavy ion beam is also being studied. As we are now considering direct injection of extracted ion beam from the ion source, the ion beam energy is considered to be very low except for the case of laser produced ion beam, which will results in rather limited electron current for electron cooling. Careful study is needed on this approach.

4. Laser Cooling

Laser cooling of circulating ion beam in the storage ring has been limited for $^{7}Li^{+}$ (meta-stable state), $^{9}Be^{+}$ and $^{24}Mg^{+}$ due to available wavelength of the CW laser with enough power up to now. Because metal Be is highly poisonous, it is difficult to handle. So $^{24}Mg^{+}$ is chosen as the ion to be laser cooled. Second harmonic of ring dye laser utilizing the dye Rhodamine pumped by a solid state green laser is to be utilized to provide the needed

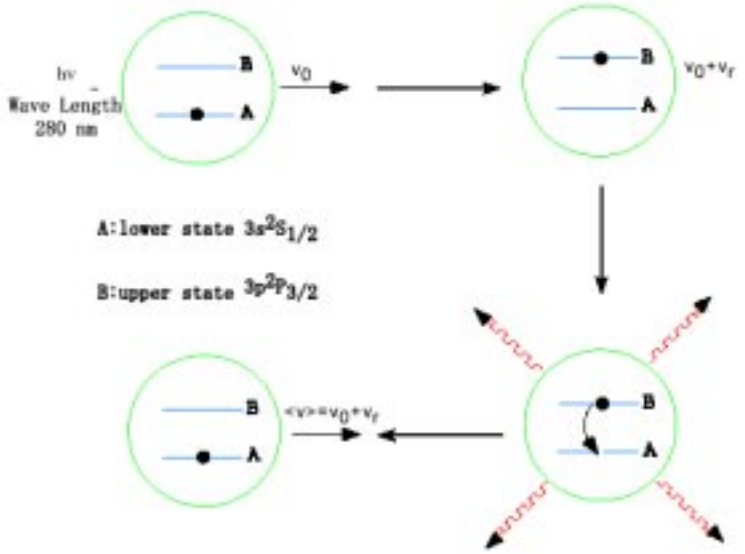

Fig. 7 Scheme of laser cooling of $^{24}Mg^{+}$ ion

wavelength of 280 nm. In Fig. 7, the scheme of laser cooling for $^{24}Mg^{+}$ ion is illustrated with the energy levels. So as to sweep the energy region of the initial energy spread of the stored ion beam, induction accelerator described in the previous section is to be used following the results at TSR for cooling of $^{9}Be^{+}$[11]..

For the purpose of cooling down transverse temperature, synchro-betatron coupling resonance is to be utilized [5,12]. Computer simulation with use of molecular dynamics is highly required and is now under preparation.

5. Present Status and Future Time Schedule

Main magnets of LSR lattice have been already fabricated and are now to be evaluated in its field characteristics by field measurement in coming several months. The vacuum chambers are now just to be ordered, modification on which is now seriously discussed to incorporate the dispersion compensation by superposing the electric field [8]. The fabrication of beam injection line and alignment of the LSR ring will be completed until the end of 2004 and early in 2005, beam commissioning is expected to be started.

Acknowledgments

The authors would like to present their sincere thanks to Prof. Y. Hirao and Dr. S. Yamada for their continuous supports to the present work. Their thanks are also due to Dr. H. Okamoto for his fruitful discussions on beam cooling and crystallization.

References

1. Parkhomchuk, Proc. of ECOOL84, Karlsruhe, Germany, 71 (1984).
2. M. Steck et al., Hyperf. Int. **99**, 245 (1996).
   M. Steck et al., Nucl. Phys. **A626**, 473c (1997).
3. H. Danared et al.,Proc. of the Workshop on Ion Beam Cooling-Toward the Crystalline Beam, Kyoto, Japan, 43 (2001).
4. A. Noda et al., Beam Science and Technology, **6**, 21 (2001).
5. H. Okamoto, A.M. Sessler, and D. Möhl, Phys. Rev. Lett. **72**, 3977 (1994)..
6. T. Shirai et al., Proc. of EPAC2002, Paris, France, 623 (2002).
7. K. Endo et al., Proc. of EPAC2002, Paris, France, 2733 (2002).
8. M. Ikegami and A. Noda, Submitted to Phys. Rev. Lett.
9. D. Möhl, Proc. of ECOOL84, Karlsruhe, Germany, 293 (1984).

10. H. Fadil et al., Submitted to Nucl. Instr. and Meth. In Phys. Res.
11. W. Petrich et al., Phys. Rev. **A48**, 2127 (1993).
12. T. Kihara et al., Phys. Rev. **E59**, 3594 (1999).

Appendices

COMMITTEES

INTERNATIONAL ADVISORY COMMITTEE

Chien-Te Chen (SRRC), He-Sheng Chen (IHEP, Beijing), Jia-Er Chen (Peking U.), J. Dorfan (SLAC), W-Y. P. Hwang (CosPA), T. Muta (Hiroshima U), W. Namkung (PosTech), Y. Kato (JAERI Kansai), A. Sessler (LBL), A. Skrinsky (BINP), H. Sugawara (KEK), D. Sutter (USDOE), S. Tazzari (Rome), A. Wagner (DESY), T. Wilson (CERN), M. Witherell (Fermilab), J. Wood (RAL) ICFA Beam Dynamics Panel and Advanced Accelerator Research Panel members

PROGRAM COMMITTEE

D. Barber (DESY), S. Chattopadhyay (LBL), P. Chen (SLAC, Chairperson), A. Dragt (U. Maryland), K. J. Kim (Argonne), K. McDonald (Princeton), C. Pellegrini (UCLA), M. Pusterla (Padova), F. Ruggiero (CERN), R. Ruth (SLAC), T. Tajima (JAERI), Y. Takahashi (UA Huntsville), V. Telnov (BINP), E. Uggerhoj (Aarhus), K. Yokoya (KEK)

ORGANIZING COMMITTEE

P. Chen (SLAC), I. Endo (Hiroshima Univ.), K. Hirata (Graduate University for Advanced Studies, Japan), T. Hirose (Waseda Univ.), K. Nakajima (KEK/GUAS/JAERI), A. Ogata (Hiroshima Univ., Chairperson), H. Okamoto (Hiroshima Univ.), T. Takahashi (Hiroshima Univ.), M. Uesaka (Univ. of Tokyo)

LIST OF PARTICIPANTS

Akimoto, Kazuhiro	Teikyo University, Japan
Baier, Vladimir N.	Budker Institute of Nuclear Physics (BINP), Russia
Bingham, Robert	Rutherford Appleton Laboratory, England
Bulanov, Sergei V.	Advanced Photon Research Center, JAERI, Japan
Chen, Pisin	Stanford Linear Accelerator Center, USA
Colby, Eric R	Stanford Linear Accelerator Center, USA
Date, Schin	Spring 8, Accelerator Division, Japan
De Martino, Salvatore	Dipartimento Di Fisica, Universita Di Salerno, Italy
De Siena, Silvino	Dipartimento Di Fisica, Universita Di Salerno, Italy
Dong, Dong	Chinese Academy of Science, P. R. China
Ebisuzaki, Toshikazu	Advanced Computing Center, RIKEN, Japan
Ellison, James A	Math and Stat, U. of New Mexico, USA
Endo, Ichita	ADSM, Hiroshima University, Japan
Esirkepov, Timur	Advanced Photon Research Center, JAERI, Japan
Fukuda, Masafumi	Tokyo Metropolitan University, Japan
Hamatsu, Ryosuke	Tokyo Metropolitan University, Japan
Hartemann, Frederic V.	Lawrence Livermore National Laboratory, USA
Hirata, Koji	Graduate School for Advanced Studies, Japan
Hirose, Tachishige	Waseda University, Japan
Hwang, W-Y. Pauchy	Dept. of Physics, National Taiwan University, Taiwan
Jaganathan, Ramaswamy	The Institute of Mathematical Sciences, India
Kamiya, Yoshio	Tokyo Metropolitan University, Japan
Karataev, Pavel V	Tokyo Metropolitan University, Japan
Ko, In Soo	Pohang University of Science and Technology, Korea
Kotaki, Hideyuki	JAERI, Japan
Kumita, Tetsuro	Tokyo Metropolitan University, Japan
Kuroda, Ryunosuke	Waseda University, Japan
Li,Dongguo	Dept. of Phys. Tokyo Metropolitan University, Japan
Li,Hui	Los Alamos National Laboratory, USA
Mais,Helmut	DESY, Germany
Maltsev,Anatoly A	Joint Institute for Nuclear Research, Russia
Masuda,Shinichi	JAERI, KANSAI, Japan

Matthews,John N	University of Utah, USA
Morozumi,Takuya	Hiroshima University, Japan
Nakajima,Kazuhisa	KEK/JAERI, Japan
Ng,Johnny S.T.	Stanford Linear Accelerator Center, USA
Noda,Akira	Inst. for Chemical Research, Kyoto University, Japan
Ogata,Atsushi	AdSM, Hiroshima University, Japan
Ohgaki,Tomomi	KEK, Japan
Okamoto,Hiromi	Hiroshima University, Japan
Potylitsyn,Alexander P	Tomsk Polytechnic University, Russia
Pusterla, Modesto	Dipartimento Fisica, Italy
Reil,Kevin A	Stanford Linear Accelerator Center, USA
Ringwald,Andreas	Deutshes Elektronen-Synchrotron, DESY, Germany
Rosu,Haret C	IPICyT, Mexico
Sato,Humitaka	Dept. Phys., Konan Univ., Japan
Schramm,Ulrich	Sektion Physik, lmu Muenchen (Munich), Germany
Sergi,Antonino	Univrsity of Rome@ La Sapienza, Italy
Shchagin,Alexander V	VBL, Hiroshima University, Ukraine
Smetanin,Igor V.	Advanced Photon Research Center, JAERI, Japan
Suwada,Tsuyoshi	KEK, Japan
Suzuki,Toshio	KEK, Japan
Tajima,Toshiki	JAERI, Kansai, Japan
Takabe,Hideaki	Institute of Laser Energetics, Osaka University, Japan
Takahashi,Tohru	ADSM Hiroshima University, Japan
Takahashi,Yoshiyuki	The University of Alabama in Huntsville, USA
Telnov,Valery I	Institute of Nuclear Physics, Russia
Uesaka,Mitsuru	University of Tokyo, Japan
Uggerhoj,Ulrik I	Dept. of Physics and Astronomy, Denmark
Vitagliano,Luca	University of Rome, La Sapienza, Italy
Xue,She-Sheng	University of Rome, La Sapienza, Italy
Yuri,Yosuke	ADSM, Hiroshima University, Japan
Zeitlin,Michael G	Math.Methods in Mechanics Group, IPME RAS, Russia

CONFERENCE PROGRAM

1/7		**Tue Morning, Topics A and E**
0830	0930	Registration
0930	0945	Opening
0945	1015	H. Mais (DESY): Quantum Fluctuations in Beam Dynamics
1015	1045	V.N. Baier (BINP): Coherent radiation in Electron-Positron Colliders
1045	1115	Coffee break
1115	1145	R. Jaganathan (IMS, India): Quantum mechanics of electron beam transport through optical elements with curved axes
1145	1215	M. Zeitlin (IPME, Russia): Quasiclassical Calculations for Wigner Functions
1215	1245	S. De Siena (Salerno): A Stochastic-Hydrodynamic Model of Halo Formation in Charged Particles
1245	1315	Discussion
1315	1445	Lunch
1/7		**Tue Afternoon, Topic B**
1445	1515	T. Tajima (JAERI-APRC): A Low Emittance Laser-Plasma Electron Gun
1515	1545	F. Hartemann (LLNL): Compton Scattering and its Applications
1545	1615	T. Morozumi (Hiroshima U.): CP violation in the early universe and the mass scale of heavy Majorana neutrinos
1615	1645	Coffee break
1645	1705	A. Maltsev (JINR): Infrared Radiation in Accelerator Experiments
1705	1725	R. Kuroda(Waseda U.): Soft X-ray generation using laser Compton scattering at Waseda University
1725	1745	T. Ohgaki (KEK): Design Studies for Laser-Compton Backscattering at PLS Storage Ring
1745	1805	T. Kumita (Tokyo Metropolitan U.): Study of laser-Compton scattering in a plasma channel
1805	1845	Discussion
1900		Concert/Dinner

1/8		**Wed Morning, Topic C**
0900	0930	A. Ringwald (DESY): Boiling the Vacuum with an X-Ray Free Electron Laser
0930	1000	H. Rosu (IPICyT, Mexico): Possible Experimental Searches for Unruh Effect
1000	1030	A. Yashin (SLAC): Wave-Packet Approach to Unruh E.ect (presented by P. Chen)
1030	1100	Coffee break
1100	1130	U. Uggerhoj (Aarhus U.): On the radiative cooling of positrons in a crystal.
1130	1150	T. Esirkepov (JAERI): To achieve the Schwinger limit on Earth
1150	1210	R. Hamatsu: (Tokyo Metropolitan U.) Experimental investigations on a new kind of positron source using oriented crystals
1210	1230	Discussion
1300	1430	Lunch
1/8		**Wed Afternoon, Topic D1**
1430	1500	H. Takabe (ILE, Osaka U.): Astrophysics with Intense Lasers
1500	1530	R. Chiao (UC Berkeley) Quantum Fields in Curved Spacetime
1530	1600	D. Dong (IHEP, Beijing): Gravitational-Wave Induced E.ects in Storage Rings Beam Dynamics
1600	1630	J. Irwin (SLAC): Gravitational Lensing as Cosmic Final Focus (presented by J. Ng)
1630	1700	Coffee break
1700		**Poster Session**
	1	M. Fukuda (Tokyo Metropolitan University): Production of a short-bunch polarized positron and design of a positron polarimeter
	2	Y. Kamiya (Tokyo Metropolitan University): X-ray spectrometer for observation of nonlinear Compton scattering
	3	P. Karataev (Tokyo Metropolitan University): Application of Optical Diffraction Radiation to a Non-Invasive Low-Emittance High-Brightness Beam Diagnostics
	4	H. Kotaki (JAERI): Generation of high quality electron beam by laser-plasma interaction
	5	D. Li (Tokyo Metropolitan University): Polarization of .nial photons in nonlinear Compton scattering for linearly polarized laser

	6	A. Potylitsyn (Tomsk Polytechnic University): Is it possible to obtain polarized positrons during multiple compton backscattering process?
	7	I. Smetanin (JAERI): Quantum theory of laser and beam Compton interaction in a strong field
	8	J. Koga and S. Bulanov (JAERI):Radiation Reaction effects on the Evolution of an Intense Laser Pulse Propagating in a Plasma
	9	S. Masuda (JAERI): 1D PIC Simulation of Plasma Cathode
	10	H. Okamoto (Hiroshima University): Lattice dependence of beam crystallization
	11	S.-S. Xue(ICRA, and Physics Department, University of Rome): The Lamb Shift and Ultra High Energy Cosmic Rays
	12	M.V. Goussakova(JINR): Detector for Measurement of Angular Divergence of the Sinchrotron Radiation
	13	M. G. Zeitlin(IPME RAS): Energy con.nement/fusion/localization in general kinetics (BBGKY approach to beam dynamics/kinetics)
	14	M. G. Zeitlin(IPME RAS): Beam-beam dynamics: e.cient calculations
	15	H. Takahashi (BNL): Quantum aspect of strong laser field
	16	S.S. Xue (ICRA, and U. Rome):The Casimir e.ect and energetic sources for gamma ray bursts
1900		Dinner
1/9		**Thu Morning, Topic Z**
0830	0900	J. Matthews (Utah): Ultra High Energy Cosmic Rays and the Fluorescence in Air Showers (FLASH) Experiment at SLAC
0900	0930	Y. Takahashi (U. Alabama): Extremely high energy cosmic rays and status and suggested origins
0930	1010	Very short coffee break
1010	1040	H. Li (LANL): Magnetic Energy Dissipation in Force-Free Plasmas
1040	1110	P. Chen (SLAC): Plasma Wake.eld Acceleration for Ultra High Energy Cosmic Rays
1110	1140	K. Reil (SLAC): Simulations on Alfven-Wave Induced Plasma Wake.eld
1140	1200	Discussion
1200		Excursion
1/10		**Fri Morning, Topic D2**
0900	0930	R. Bingham (RAL): Neutrino-Induced Electroweak Plasma Instability
0930	1000	J. S. T. Ng (SLAC): Astrophysics with High Energy Particle Beams
1000	1030	H. Sato (Konan U.): Ultrahigh Energy Cosmic Rays and Violation of Lorentz Invariance
1030	1100	Coffee break

1100	1130	P. W-Y. Hwang (CosPA): Bridging Particle Astrophysics and Cosmology via Ultra High Energy Cosmic Rays
1130	1200	S. -S. Xue (ICRA/U. Rome): Plasma oscillations in a Strong Electric Field
1200	1240	L. Vitagliano (ICRA/U. Rome): Evolution of an Electron-Positron-Photon Plasma around a Collapsing Star
1240	1300	L. Tsintsadze (VBL, Hiroshima U.): New Aspects of Physics of a Photon Gas
1300	1320	Discussion
1330	1430	Lunch
1/10		**Fri Afternoon, Topic X1**
1430	1500	E. Colby (SLAC): Critical Issues for Vacuum Laser Acceleration
1500	1530	M. Uesaka (U. Tokyo): Critical Issues in Plasma Accelerators
1530	1600	S. Bulanov (JAERI): Radiation Dominant Laser-Plasma Interaction
1600	1630	Coffee break
1630	1650	A. Ogata (Hiroshima U.): Use of macroscopic solid structure in accelerators
1650	1720	K. Nakajima (KEK/JAERI): Electron-Positron Pair-beam Production and Acceleration in Ultrastrong Laser-plasma interactions
1720	1800	Discussion
1900		Banquet
1/11		**Sat Morning, Topic X2 and Y**
0900	0930	V. Telnov (BINP): Critical Issues in Linear Colliders
0930	1000	T. Takahashi (Hiroshima U.): Recent Progress on Photon-Photon Colliders
1000	1030	V.N. Baier (BINP): Beam-Size E.ect in Bremsstrahlung
1030	1100	Coffee break
1100	1130	U. Schramm(LMU, Munchen): Observations on Crystalline Beams
1130	1200	H. Okamoto (Hiroshima U.): Dynamics of ultra-cold beams
1200	1220	A. Noda (ICR, Kyoto U.): Approach to ultra-cold beam at LSR, Kyoto University
1220	1240	Discussion
1240	1300	Closing Remark


1/7 Tue
Morning
QUASICLASSI
FOR WIGNER
ENERGY CON
LOCALIZATIO
KINETICS (BB
TO BEAM DY
M-BEAM I
CIENT CA

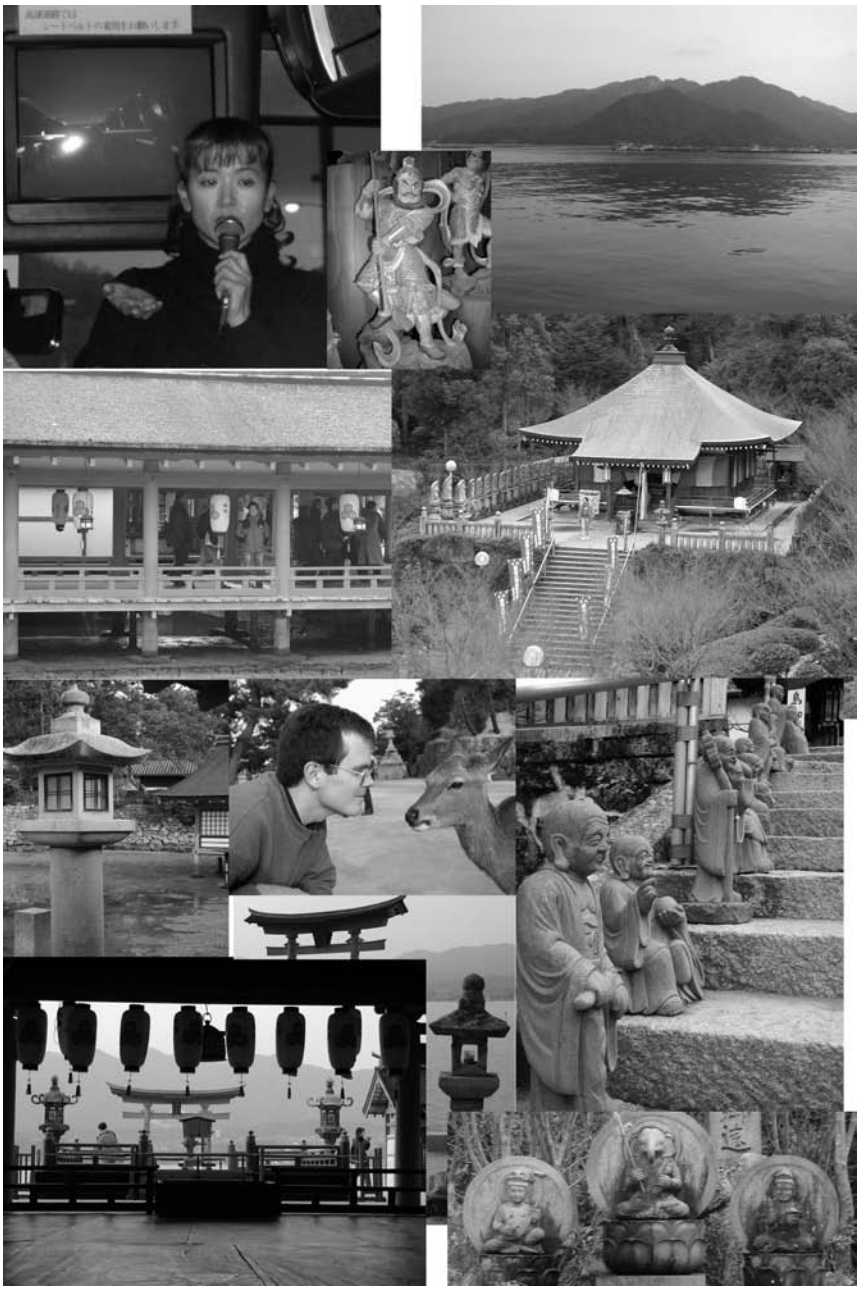

AUTHOR INDEX